



HAL
open science

Intracontinental tectonics in the South China block: example of the Xuefengshan belt

Yang Chu

► **To cite this version:**

Yang Chu. Intracontinental tectonics in the South China block: example of the Xuefengshan belt. Earth Sciences. Université d'Orléans; Institute of geology and geophysics, Chinese academy of sciences, 2011. Chinese. NNT : 2011ORLE2019 . tel-00626808v2

HAL Id: tel-00626808

<https://theses.hal.science/tel-00626808v2>

Submitted on 7 Dec 2011

HAL is a multi-disciplinary open access archive for the deposit and dissemination of scientific research documents, whether they are published or not. The documents may come from teaching and research institutions in France or abroad, or from public or private research centers.

L'archive ouverte pluridisciplinaire **HAL**, est destinée au dépôt et à la diffusion de documents scientifiques de niveau recherche, publiés ou non, émanant des établissements d'enseignement et de recherche français ou étrangers, des laboratoires publics ou privés.



ÉCOLE DOCTORALE [SCIENCES ET TECHNOLOGIE]

INSTITUT DES SCIENCES DE LA TERRE D'ORLEANS

INSTITUT DE GEOLOGIE AND GEOPHYSIQUE (CAS)

THÈSE EN COTUTELLE INTERNATIONALE présentée par :

Yang CHU

soutenue le : 15 septembre 2011

pour obtenir le grade de :

**Docteur de l'Université d'Orléans
et de l'Institute de Géologie et Géophysique**

Discipline : Sciences de la Terre et de l'Univers

**TECTONIQUE INTRACONTINENTALE DANS LE BLOC DE CHINE DU SUD.
EXEMPLE DE LA CHAÎNE DU XUEFENGSHAN**

THÈSE dirigée par :

M. Michel Faure

M. Wei Lin

Professeur, ISTO, Université d'Orléans

Professeur, IGG, CAS, Chine

RAPPORTEURS :

M. Junlai Liu

M. Bei Xu

Professeur, Université de Geoscience, Pekin

Professeur, Université de Pekin

JURY :

M. Yan Chen

M. Dominique Cluzel

M. Michel Faure

M. Wei Lin

M. Junlai Liu

M. Bei Xu

Professeur, ISTO, Université d'Orléans **Président de jury**

Professeur, Université de la Nouvelle-Calédonie

Professeur, ISTO, Université d'Orléans

Professeur, IGG, CAS, Chine

Professeur, Université de Geoscience, Pekin

Professeur, Université de Pekin

INVITÉ :

M. Xianhua Li

M. Qingchen Wang

Professeur, IGG, CAS, Chine

Professeur, IGG, CAS, Chine

Intracontinental tectonics in the South China block: Example of the Xuefengshan Belt

Chu Yang (Majored in Structural geology)

Directed by:

Prof. Lin Wei (Institute of Geology and Geophysics, CAS)

Prof. Faure Michel (University of Orléans, France)

Abstract

Intracontinental orogens remain less understood than accretionary or collisional orogens that are related to plate margin interactions. The mechanisms of intracontinental orogeny have long been discussed, since intraplate mountain belts cannot be ascribed to the plate margin interaction paradigm that assumes that the interiors of a continent are rigid and hard to deform. It is now well accepted that the deformation of continental crust can be a far-field consequence of collision, as exemplified by the Miocene tectonics of Asia, but still controversial.

The Xuefengshan Belt is located in the center of the South China block, in Hunan Province. To the west, the eastern Sichuan fold belt is characterized by Jura-type anticlines formed during Late Jurassic to Early Cretaceous; to the north, the foreland fold-thrust belt of the Triassic Qinling-Dabie orogen is represented by folds and faults of S-SW vergence; to the south, the Nanpanjiang basin is filled with Early Triassic flysh; to the east, the dominant structures are resulted from the Early Paleozoic orogen in Jiangxi-Zhejiang-Fujian provinces. The Xuefengshan Belt provides a well-exposed and unique example of an intracontinental orogen, but its structural style and evolution are still on debate. Recent studies proposed that this intracontinental belt was formed by large scale over-thrust in the Late Mesozoic or by Triassic transpressional tectonics. An Early Mesozoic flat slab subduction to the NW

is also suggested.

Detailed field observations indicate that the Xuefengshan Belt can be divided into a Western Outer Zone (Wuling Mountain), and an Eastern Zone, separated from the Western Outer Zone by the Main Xuefengshan Thrust, also corresponding to the cleavage front. The Western Outer Zone is characterized by km-scale box-fold structures with layer-slip and collapse folds in the hinges. In the Eastern Zone, NW verging folds coeval with a pervasive slaty cleavage and a NW-SE trending lineation are the dominant structure. From west to east, the dip of the cleavage surface exhibits a fan-like pattern. Basement rocks are sparsely located around some Triassic plutons.

The rocks of the Xuefengshan Belt are generally ductilely deformed but weakly metamorphosed, however, below these upper crustal level, a high strain decollement accommodates the difference of deformation between the sedimentary and the basement rocks. In Chengbu, Fengjia-Shuiche, Weishan and Shuangfeng areas, intensely deformed rocks like mylonite, granitic gneiss and sheared schist are mainly outcropped around Triassic plutons, indicating a domed high strain layer during the emplacement. According to our mesoscopic to microscopic observations and quartz c-axis measurements, the ductile deformation occurred at low temperature (ca. 300 to 400 °C) coincident with regional greenschist facies syn-tectonic metamorphism. Monazite chemical dating by Electron microprobe on micaschist of the decollement layer gives a range from 243 to 226 Ma, constraining the timing of the deformation and metamorphism.

The bulk architecture of the Xuefengshan Belt results from polyphase deformation: the first one (D1), characterized by a top-to-the-NW shearing, controls the bulk architecture of the Xuefengshan, and is responsible for the crustal thickening of the Lower Unit of the Eastern Zone. The second one (D2) corresponds to the back-folding and back-thrusting stage with preferential cleavages or foliations that dip to the NW. The S1 cleavages were refolded by F2 fold with relics preserved in some muddy layers. The last phase (D3) is a NW-SE or W-E shortening event associated with upright folds with vertical axial plane cleavages. Both D1 and D2 structures were affected in the D3 event. The high strain zone, corresponding to the ductile

decollement, accommodated at depth the folding and shearing of the Neoproterozoic to Early Triassic sedimentary series. These three events are interpreted as a continuum of a single NW-SE compression in the interior of the South China block, and finally shaped the landscape by the formation of the Xuefengshan Belt.

Two generations of magmatism are recorded in the Xuefengshan Belt. Our precise SIMS zircon U-Pb dating shows that the Early Paleozoic granites, which were deformed into orthogneiss, occurred during 440-410 Ma while the undeformed Early Mesozoic ones were emplaced between 225 Ma and 215 Ma. Together with structural observations, it is implied that the Xuefengshan Belt is partly involved in the Early Paleozoic deformation, but affected by the extension-induced magmatism. During Early Mesozoic, late-orogenic magmatism intruded the folded strata, following the Triassic contractional deformation. Zircon Lu-Hf isotopic data show that the granites of both periods are of similar features, with $\varepsilon_{\text{Hf}}(t)$ values ranging from -10 to -1, with a peak at -5, indicative of Paleo- to Middle Proterozoic crustal source. Thus, we can infer that these granites are both intracontinental late- or post-orogenic products with addition of depleted mantle source, for example, from the plate boundary suture zones.

Combined with geochronological data, the Xuefengshan Belt is interpreted as an Early Mesozoic intracontinental orogen, which possibly originated from the continental underthrusting or continental subduction to the SE of a piece of the South China Block in response to northwest directed subduction of the Pacific plate. The Chenzhou-Linwu fault played a key role in the orogeny as a preexisted weak zone which was activated by the far-field effect of the subduction, as well exemplified by the Cenozoic Tianshan and the Indo-Asia collision.

Key Words: the Xuefengshan Belt, South China block, intracontinental, basal decollement, polyphase deformation, late-orogenic magmatism, thin-skinned tectonics, far-field effect.

Contents

Chapter 1 Introduction	1
Section 1. Research background	1
1. Intracontinental belts.....	1
2. Early Mesozoic structures in the South China block.....	5
Section 2 Research topics and contents	7
1. Subject.....	7
2. Contents of research.....	8
2.1 Contents	8
2.2 Methods.....	9
3.1 Work.....	10
3.2 Results.....	11
Chapter 2 Geological setting.....	12
Section 1 Geological setting of the South China block	12
1. Location	12
2. Polyphase events.....	13
2.1 Neoproterozoic.....	13
2.2 Early Paleozoic	15
2.3 Early Mesozoic	16
2.4 Late Mesozoic.....	18
Section 2 Geological setting of the Xuefengshan belt	19
1. Geology.....	19
2. Geodynamic models.....	21
Section 3 Early Mesozoic tectonic evolution of the South China block.....	23
1. Collision.....	23
2. Transpression	24
3. Flat-slab subduction.....	25
Section 4 Summary	26
Chapter 3 Structural analysis of the sedimentary cover in the Xuefengshan belt.....	27

Section 1 Early Paleozoic structures.....	28
Section 2 Tecotnic division.....	29
Section 3 Main Xuefengshan Thrust.....	31
Section 4 Western Zone.....	35
Section 5 Eastern Zone.....	37
1. Anhua area.....	38
2. Xupu area.....	43
3. Dongkou area.....	45
4. Lianyuan area.....	48
Section 6 Summary.....	51
Chapter 4 Structural analysis of the high strain layer in the Xuefengshan belt.....	53
Section 1 Chengbu area.....	54
1. Mesoscopic fabrics.....	54
2. Microscopic fabrics.....	57
3. Quartz fabrics.....	59
Section 2 Fengjia-Shuiche area.....	61
1. Mesoscopic fabrics.....	61
2. Microscopic fabrics.....	64
Section 3 Weishan area.....	68
Section 4 Shuangfeng area.....	70
Section 5 Summary.....	72
Chapter 5 Time constraints of the Xuefengshan belt.....	74
Section 1 Analytical methods.....	74
1. Zircon SIMS U-Pb dating.....	74
2. Monazite U-Th-Pb dating.....	75
Section 2 Sample description.....	76
1. Granites.....	76
2. Metamorphic rocks.....	77
Section 3 Zircon SIMS U-Pb dating results.....	78
1. Early Paleozoic granites.....	79

2. Early Mesozoic granites.....	83
Section 4 Monazite dating results	86
Section 5 Implications and summary	90
Chapter 6 Phanerozoic crustal evolution of the Xuefengshan belt	95
Section 1 Analytical method	95
Section 2 Results.....	96
1 Early Paleozoic granites.....	96
2 Early Mesozoic granites.....	98
Section 3 Discussion and summary	102
Chapter 7 Early Mesozoic tectonic evolution of the Xuefengshan belt.....	105
Section 1 Polyphase deformation.....	105
Section 2 Timing constraints of polyphase deformation.....	107
Section 3 Early Mesozoic tectonic evolution of the Xuefengshan belt	109
Section 4 Early Mesozoic tectonic evolution of the South China block: Insights from the Xuefengshan belt.....	113
Section 5 Insights for intracontinental orogenic belts.....	117
Chapter 8 Conclusion.....	119
References.....	121
Published papers	140
Acknowledgement	142
Appendix table 1 Zircon U-Pb data	144
Appendix table 2 Monazite U-Th-Pb data	153
Appendix table 3 Lu-Hf data	172
Appendix table 4 Index of figures	184
Article 1: Tectonic evolution of the Early Mesozoic (Indosinian) intracontinental Xuefengshan Belt, South China.....	185
Article 2: Structural analysis and chronological constraints on the decollement layer in an intracontinental orogen: Example of the Early Mesozoic Xuefengshan Belt, South China.....	229

Article 3: Phanerozoic tectonothermal events of the Xuefengshan Belt, central South China: implications from U-Pb age and Lu-Hf determinations of granites.....	271
Discussion (in English).....	300
Conclusion (in English).....	317

第一章 引言

第一节 研究现状

1. 陆内造山带

造山作用一词“orogeny”起源于19世纪中期，Gilbert (1890) 将其定义为一个特定时期段内山脉形成作用。之后，造山作用主要被用来解释地槽的形成与演化过程 (Schuchert, 1925)。而当板块构造理论最终确立后，造山带演化中最为著名的理论为威尔逊旋回 (Wilson cycle)，描述了从新洋盆的形成、拉张，到大洋俯冲、消减，洋盆消失形成陆陆碰撞造山带的一整套连续过程 (Wilson, 1966)。现在，造山作用经常与板块边界的俯冲和碰撞过程联系起来 (Dewey and Bird, 1970; Sengör, 1991)。造山过程中构造变形的生成、变质作用的叠加以及岩浆的生成和侵位，均发生在岩石圈尺度，因此岩石圈是研究造山的主要对象。相对于大洋岩石圈，大陆岩石圈记录了地质历史演化中不断进行或重复的构造过程，而大陆地壳密度较低，难于俯冲，因此构造作用可以在地壳中反复的发生，后期的构造叠加，或者说大陆的再造过程，可以强烈地影响地壳乃至岩石圈的性质 (Sutton and Watson, 1986)。

通常，造山带分为两种：碰撞型和增生型 (图 1-1a 和 b)。碰撞型造山带表现为两个“漂浮的”刚性大陆板块相互碰撞，由于俯冲、会聚等作用产生的阻力所引起的岩石圈增厚和二者的变形，如喜马拉雅造山带；而增生型造山带的构造变形、变质作用以及地壳生长均发生在长期的洋壳—陆壳俯冲的环境下，缺少陆壳间的碰撞和漂浮的岩石圈间的挤压，如阿尔泰山脉 (Murphy and Nance, 1991; Windley, 1992; Sengör et al., 1993; Windley, 1993; Nance and Murphy, 1994; Sengör and Natal'in, 1996a,b; Cawood, 2007)。以上两种经典造山带的形成均建立在相对刚性的大陆板块基础上，即大多数大陆都有太古代陆核。而这些太古代陆核又被元古代和显生宙构造体系所包围。太古代之后大陆的演化不仅包括新生地壳的加入，也包括部分已有的大陆岩石圈在构造重新活动中被重新改造 (Holdsworth et al., 2001)。在这种演化所带来的结果是大陆板块中不可避免的保留了先前构造的遗迹，产生了相对薄弱的区域。于是，刚性板块理论就被板块内部广泛的地壳变形所打破 (Molnar and Tapponnier, 1975)，并由此开辟了陆内造山研究领域。

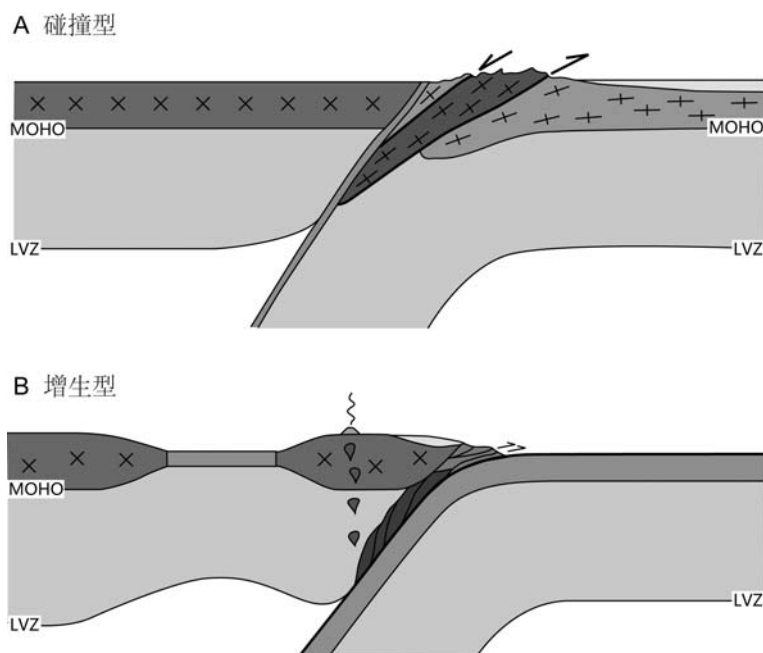


图 1-1 造山带分类示意图 (a) 碰撞型造山带 (b) 增生型造山带

与碰撞型和增生型造山带类似，陆内造山带也存在的大规模的构造变形、低级至高级变质作用和陆壳重熔形成的花岗岩。因此，地质学家们可以通过应用在板缘造山带中的各种方法和范式来剖析陆内造山带。但是动力学机制却无法借鉴，故一直成为争论的焦点。世界上典型的陆内造山带如澳大利亚的 Petermann 造山带和 Alice Spring 造山带、欧洲的比利牛斯山、北美洲的 Laramide 造山带、西亚的 Zagros 山以及中国的天山都成为陆内造山研究的热点区域(Dickinson and Snyder, 1978; Choukroune, 1992; Allen et al., 1999; Hand and Sandiford, 1999; Sandiford et al., 2001; McQuarrie, 2004; English and Johnston, 2004; Raimondo et al., 2010)。这些造山带最显著的特点就是位于远离板块边界几百甚至上千公里的内陆地区，无法通过传统的板块间俯冲、碰撞理论来解释。人们尝试用过许多模型来解释陆内造山带，平板俯冲和远程效应成为较为常用的两种解释机制(Molnar and Tapponnier., 1975; Tapponnier and Molnar, 1979; Dickinson and Snyder, 1978; Hendrix et al., 1992; Avouac et al., 1993; English and Johnston, 2004)，同时先前存在的薄弱构造带也是产生陆内变形的重要原因之一(Choukroune, 1992; Hand and Sandiford, 1999)。

位于法国与西班牙交界的比利牛斯山与阿尔卑斯山均为造山带研究的经典地区，不同的是后者是碰撞造山带，而前者是陆内造山带。前人研究表明，比利

牛斯山在海西期造山之后，经历了地壳伸展作用，一直持续到早白垩世，并形成了陆内裂谷，位于欧洲板块的内部。在晚白垩世开始挤压，在裂谷位置形成造山，Iberia 块体向欧洲板块之下俯冲，与欧洲板块相聚合。而欧洲板块西南部沿原先的裂谷带位置俯冲，形成了比利牛斯山（Choukroune, 1992）。比利牛斯山主要分为三个构造单元：北比利牛斯区（NPZ），轴心区（Axial zone）和南比利牛斯区（SPZ）。北区与北部的 Aquitaine 盆地以北比利牛斯前缘逆冲断层（NPFZ）相隔，南区与南部 Ebro 盆地以南比利牛斯前缘逆冲断层（SPFT）相隔（图 1a）。比利牛斯山的核心地带为海西期的变质基底，在造山过程中形成了背形构造。通过精细的地球物理剖面，我们看到比利牛斯山下存在着陆内俯冲的证据，形成了类似于扇状构造的样式。这个俯冲带是在中生代的裂谷基础上形成的，欧洲板块的南部连同 Iberia 板块向北俯冲于欧洲板块北部之下。整个比利牛斯山形成过程中共造成了 100 至 150 公里的地壳缩短（Dérmond et al., 1993; Muñoz, 1992）。

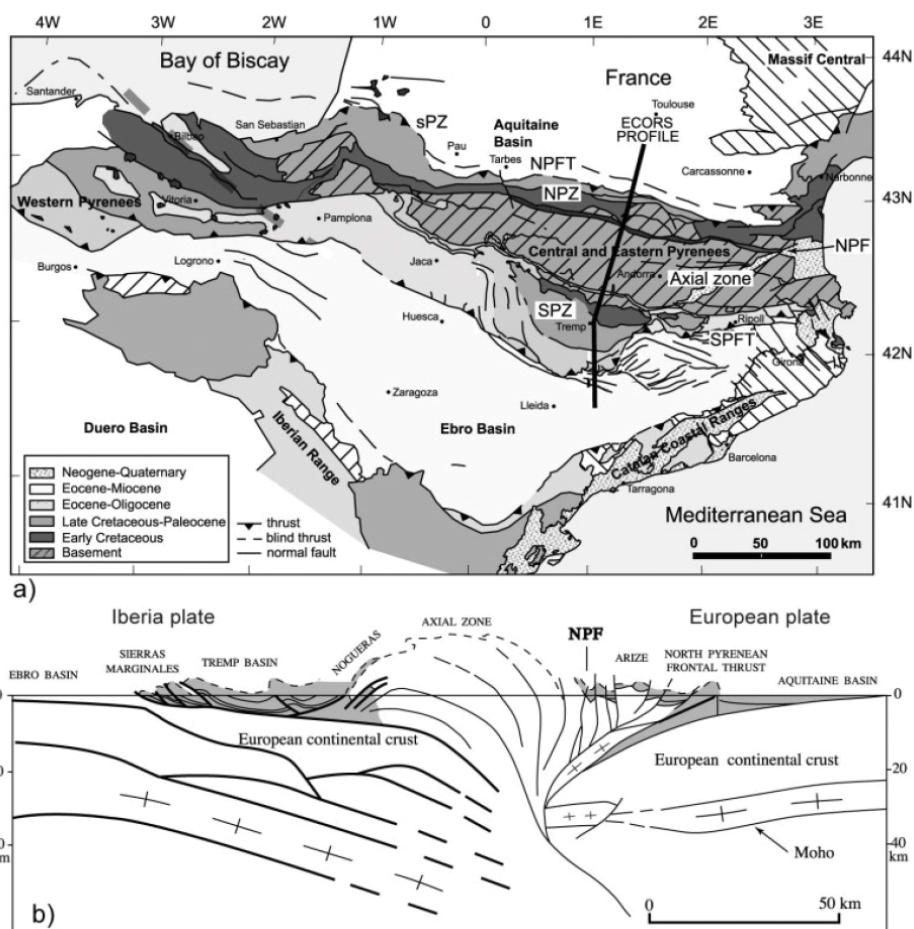


图 1-2 (a) 比利牛斯山构造剖面图 (Choukroune, 1992)。 (b) ECORS 剖面图 (Roure et al., 1989; Sibuet et al., 2004)。

位于澳大利亚中部的 Alice Springs 造山带是另一条经典的陆内造山带，其所在区域在晚元古代形成了 Petermann 造山带，并形成了一系列的断裂构造。在泥盆纪至石炭纪，这种薄弱区域由于晚古生代巨厚的沉积使得下部岩石圈的地温上升，使其软化而易于变形或重新活化了先存断裂，形成了切割岩石圈的逆冲断裂带（Goleby et al., 1989; Hand and Sandiford, 1999; Sandiford et al., 2001）。Alice Springs 造山构造主要发育于 Amadeus 盆地的北边（图 2a），而先前的 Petermann 造山中的断裂构造局部也发生了活化（图 2b）。

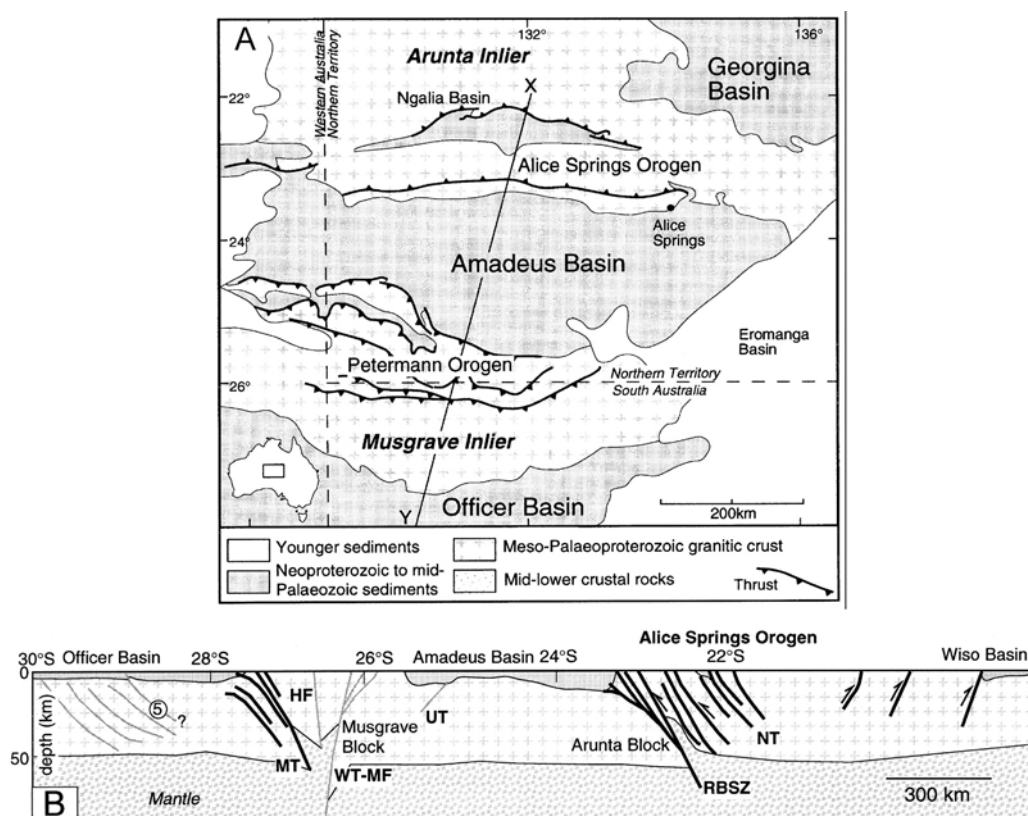


图 1-3 (a) Alice Springs 造山带构造剖面图 (Hand and Sandiford, 1999)。 (b) 造山带剖面图 (Hand and Sandiford, 1999; Sandiford et al., 2001)。

由于陆内造山带的特殊性，其研究一直没有板块边缘造山受到的关注多。但是陆内造山也是板块构造的重要组成部分，也是研究板块边缘构造对于板块内部影响的重要载体之一，因此它的形成、格架以及动力学机制越来越受到地质学家们的重视，各种研究手段诸如构造地质学、地球化学、地球物理等方法都被应用于分析陆内造山带的形成和演化过程。与板缘造山带不同，陆内造山带并不是板块间俯冲、增生或碰撞的直接结果，但是了解陆内造山过程，对于研究板块内部

构造变形、区域应力的展布、以及板内构造如何对板缘变形的响应，都具有重要的科学意义。

2. 华南板块早中生代构造

早中生代是华南构造变形最为强烈的时期，板块边缘几乎被造山带所包围，而板块内部强烈的构造变形、区域性的变质作用以及大规模的花岗岩的生成和侵位，均显示着华南板块经历了强烈的大陆再造过程。

①在其北缘，华南板块向华北板块之下俯冲，形成了出露大量超高压变质岩的秦岭—桐柏—大别—苏鲁造山带 (Mattauer et al., 1985; Hacker and Wang, 1995; Faure et al., 1999, 2008; Webb et al., 1999; 张国伟等, 2001; 徐树桐等, 2002; Ratschbacher et al., 2003; Hacker et al., 2006; Lin et al., 2009a; Li SZ et al., 2010b, 2011), 同时形成了前缘大规模向南西方向的逆冲褶皱推覆带以及同构造伸展作用 (Faure et al., 1998; Lin et al., 2001)。早中生代经历了陆壳深俯冲作用产生的超高压榴辉岩于晚中生代折返至地表，并在白垩纪接受了广泛的重熔作用，形成了花岗岩穹窿构造 (Lin et al., 2000; Hacker et al., 2000; Ratschbacher et al., 2000)。

②西缘，龙门山构造带记录了早中生代逆冲作用。龙门山西侧为松潘—甘孜复理石带，研究表明其主要物源来自于秦岭造山带、华北板块，少部分来自华南板块 (Weislogel et al., 2006, 2010; Enkelmann et al., 2007)。在中晚三叠世，松潘—甘孜带被逆冲到四川盆地之上，同时记录了三叠纪的构造变形和大规模的岩浆活动 (Wallis et al., 2003; Harrowfield and Wilson, 2005; Roger et al., 2008, 2010)。

③在西南和南缘，一条从云南一直延伸到广西、越南的造山带分隔了华南板块和印支板块 (Carter et al., 2001; Lèpvrier et al., 2004, 2008, 2011; Carter and Clift, 2008)，其中西缘为右江造山带，而南部则是真正意义上的印支造山带 (王清晨和蔡立国, 2008)。印支造山带在越北地区、广西和广东云开地区均有明显的表现，中三叠世的浊积岩卷入变形并发生了强烈的具有向北极性的褶皱，而我国广西地区由于上三叠统不整合覆盖在这套褶皱-逆冲推覆构造之上 (广西壮族自治区地质矿产局, 1985; Lèpvrier et al., 2004; 林伟等, 2011)。

④在东南缘和东缘，Li XH et al. (2006) 提出古太平洋向 W 的俯冲从晚二叠世就已经开始，形成了海南岛五指山岛弧型花岗岩 (267-262 Ma)；而在华夏

板块之上也分布着大量的 A 型花岗岩 (254-220 Ma), 均可能与太平洋俯冲形成的转换伸展作用相关 (Wang Q et al., 2005; Li and Li, 2007; Sun et al., in press)。

与华南板块周缘经历了的多个方向强烈变形相比较, 板块内部现今保存的构造行迹主要是以 NE-SW 向占主导, 表明早中生代事件对于华南板块构造格架的定型起到了决定性的作用。最早 Hsü et al. (1988, 1990) 认为早中生代华南经历了类似阿帕拉契亚型的远程推覆, 板溪群为华南造山带所产生的碰撞杂岩, 但经过大量地质学家的工作证明, 板溪群与上下地层关系为连续的沉积接触, 而非构造接触 (Rodgers, 1989; Rowley et al., 1989); 在武夷山地区, Chen (1999) 通过结合地球物理剖面与构造认为, 武夷山地区早中生代至晚中生代经历了持续的 SE 向的挤压作用; 而在浙北地区, Xiao and He (2005) 则得出了相反的构造挤压方向, 即由 SE 向 NW 挤压。雪峰山地区, 早三叠纪之前的岩层全部卷入了构造变形, 晚三叠世-早侏罗世的陆相沉积不整合的覆盖在老地层之上, 而且发育了大量的造山后岩浆岩 (丁兴等, 2005; 陈卫锋等, 2006, 2007; Chen et al., 2007; Wang et al., 2007b; Li and Li, 2007; 李华芹等, 2008; 罗志高等, 2010)。丘元禧等 (1998, 1999) 通过开拓性的工作, 认为雪峰山的陆内造山过程主要形成于早古生代末期, 但是也叠加了早中生代的构造作用; Yan et al. (2003) 的研究表明, 雪峰山和武陵山是飞来峰, 形成于晚中生代; 而 Wang et al. (2005) 通过在雪峰山的构造学和年代学研究认为, 雪峰山在早中生代处于以走滑为主的扭压环境之下。然而, 由于缺少精细的构造学与年代学约束, 这一造山带还存在着诸多争议。

针对雪峰山造山带的动力学来源, 现在还存在的广泛的争论, Yan et al. (2003) 认为是华南板块和华北板块穿时闭合过程中, 在白垩纪形成了大规模的多层次逆冲推覆带; Wang et al. (2005, 2007a, 2007c) 通过在雪峰山和云开大山的构造学和年代学研究认为, 华南板块为力学性质较弱的板块, 而华北板块和印支板块则相对而言较为刚性的块体, 处于二者的共同挤压之下, 形成了以走滑为主的大规模山系; 而 Li and Li (2007) 通过对华南中生代花岗岩年代学进行全面的总结, 于是将整个华南 1300km 宽的褶皱带归结为古太平洋板块的平板俯冲, 类似于北美 Laramide 造山带的形成 (Dickinson and Snyder, 1978)。虽然太平洋板块俯冲是否在早中生代就开始了现在还有不同的观点 (Engebretson et al., 1985; Li XH et al., 2006), 而且也缺少详细的构造学证据作为支持, 但毋庸置疑, 这给

华南早中生代（印支期）构造演化提供了新的思路，即陆内造山的动力来源是在板块东南缘的挤压。

第二节 选题依据和研究内容

1. 选题依据

长久以来，由于板块碰撞所产生的大型造山带为地质学家所研究的重点，这其中包括著名的欧洲的阿尔卑斯造山带、美洲的阿帕拉契亚山脉、亚洲的喜马拉雅山脉等等。这些造山带的形成时代不同，但其强烈的构造活动引起的明显的地壳缩短、岩石的强烈变形、大规模的变质作用以及广泛发育的同/后造山的岩浆活动。近 20 年来，陆内造山带逐作为板块构造理论在大陆内部的重要补充，渐走入人们的视野，引起的地质学家的广泛关注。典型的陆内造山带包括欧洲比利牛斯（Pyrenees）山、非洲的 Atlas 山、北美的 Laramide 造山带和澳大利亚的 Petermann 造山带和 Alice Springs 造山带等等（Dickinson and Snyder, 1978; Goleby et al., 1989; Choukroune, 1992; Teixell, 1998; Allen et al., 1999; Hand and Sandiford, 1999; Sandiford et al., 2001; Teixell et al., 2003; McQuarrie, 2004; English and Johnston, 2004; Raimondo et al., 2010）。我国的新生代天山造山带、中生代的阴山—燕山造山带也是陆内造山带的典型代表（Molnar and Tapponnier., 1975; Tapponnier and Molnar, 1979; Avouc et al., 1993; Davies, et al., 1998, 2001）。这些造山带随远离传统的板块边界多达上千公里，却形成了巨大的山链，产生了大量的地壳缩短，出露了高级变质岩，也改变了多数人板块内部刚性而稳定的传统观点。同时由于身处板块内部，对陆内造山带的研究为探索板块内部变形机制、应力场分布以及板内构造对板缘构造的响应关系提供了独一无二的平台，因此这已成为造山带研究的一个重要方向。

中国拥有广阔的土地，其中 60%为山地或丘陵地区，之中也分布着为数众多的碰撞造山带。地质学家对秦岭-大别造山带、中亚造山带、喜马拉雅造山带等均进行了深入的构造学、岩石学和地球化学等多学科研究，涌现出了一大批高质量的研究成果（Ye et al., 2000a, 2000b; Yin and Harrison, 2000; Chung et al., 2005; Zheng et al., 2006; Xiao et al., 2008; Lin et al., 2009b; Yin et al., 2010 等等）。然而对于华南板块，其造山期次多，构造叠加关系复杂，构造学研究却相对分散，未形

成系统的、详细的多期构造的区域格架，远远落后于岩石学和地球化学的研究。华南板块从新元古代由扬子板块和华夏地块拼贴以来，就在不断遭受着构造改造。从早古生代的“加里东运动”到中生代的“印支运动”和“燕山运动”，都对华南板块产生的巨大的影响（Zhou et al., 2006; Wang et al., 2007b, 2007c; Lin et al., 2008）。正是由于多期构造叠加和广泛发育的岩浆作用，使得华南板块的作用及其复杂，为不同期次的构造识别设置了障碍。雪峰山构造带位于华南板块核部，远离板块边界，其构造几何形态、变形年代仍存在争议，但是它的构造演化却是研究华南板块早中生代演化的基础，非常具有代表性。因此要想解决华南中生代的构造问题，雪峰山造山带的演化历史就成为一个很好的切入点。虽然前人进行了构造学、年代学和地球化学等方面的研究，但对构造现象的解释上存在明显分歧，同时缺少完整的构造剖析与造山带剖面，也无法形成一个全局性的构造格架。所以本论文将关键科学问题定位于“雪峰山早中生代构造演化”，目的是为了能够通过详细的研究，将雪峰山这一华南陆内造山带从几何学、运动学和动力学上进行完整的分析，为研究华南地质演化提供构造学和年代学的证据，并使其成为典型的陆内造山带之一。

2. 研究内容与技术路线

2.1 研究内容

本论文的研究主要围绕“雪峰山早中生代构造演化”这一关键科学问题进行多尺度的构造学研究，从野外地质观察分析入手，分析雪峰山地区的构造对于早中生代造山过程的响应，进而剖析其演化过程，并探讨华南板块的地质演化。研究内容包括以下三个方面：

（1）雪峰山造山带的构造几何学和运动学

在现有的研究基础上，通过对雪峰山地区的进行大范围、详细的野外勘察，勾画出详细的几何形态，理清不同构造期次变形关系，研究构造变形样式之间的匹配关系，同时结合地球物理学数据揭示深部与表层构造之间的响应关系及差异，最终厘定雪峰山造山带及其前陆地区完整的构造演化历史，逐步完善对这一地区构造演化的认识。

(2) 雪峰山造山带的年代学约束

在构造学研究的基础上,通过对典型的强应变带内岩石进行观察分析,选取典型样品进行锆石原位二次离子探针或激光多接收等离子质谱仪进行 U-Pb 定年、独居石 U-Th-Pb 电子探针定年以及同变形矿物的 Ar-Ar 年代学定年,并结合年代学和地层变形叠加关系,限定出相应的变形时限。

(3) 华南板块早中生代构造演化

在对雪峰山详细构造学、年代学研究的基础上,讨论其地球动力学背景;并以此为切入点,分析早中生代期间华南板块整体的变形特征与构造样式,从而为理解华南早中生代构造变形的动力学来源提供帮助。

2.2 技术路线

(1) 资料调研:全面收集评估与课题相关的地质、地球化学、地球物理资料,掌握国内外研究动态,为野外和室内研究提供依据;在及时了解、消化研究领域的国际前沿动态和该区研究资料的基础上,“去粗取精”、“去伪存真”,恢复该区早古生代构造事件的基本构造格架。

(2) 野外地质研究:以 1:20 万区域地质图为基础同时结合 1:5 万区域地质资料,选择雪峰山地区主要剖面,对主要变形构造、重要韧性-脆韧性剪切带、典型造山后花岗岩(汾山岩体和紫云山岩体等)及卷入变形的花岗岩体(白马山岩体、越城岭岩体和苗儿山岩体)开展系统和细致的野外构造-岩浆-沉积观察和系统的样品采集。

(3) 构造地质学研究:以关键地段关键剖面和辅助性构造剖面为重点、结合面上观察点,点面结合并重点突出地开展区内构造层构造要素的对比分析研究、解析不同构造层构造不连续面(带)及构造岩的宏微观变形构造的几何学、运动学标志;协调构造样式的排列组合与配套;详细观察和分析各类构造的先后顺序和变形期次、突出不同期次构造变形与构造要素的相互协调等;详细观察和变形期次划分与构造要素的相互协调,全面收集和利用该区已有的地球物理资料对构造进行解释;恢复不同期次构造规模、强度及相应的几何学、运动学特征等,分析多层多重多种推滑构造与先存构造叠加、置换、继承与反转的影响及与时空规律,运动学标志及构造样式的排列组合与配套的野外观察、素描与剖析。

(4) 年代学研究：在野外地质和岩相学研究的基础上，拟选择区内构造岩或同构造新生矿物独居石开展电子探针分析，或同构造期和侵入变形体中花岗岩或岩脉和碎屑岩的 LA-ICPMS 或 SIMS 的锆石 U-Pb 定年，构建研究区多重复杂变形和沉积物源时序格架。系统研究变质岩和构造岩的岩相(石)学和矿物学研究，获得其变质 P-T 轨迹等基础性资料。对目标地区进行详细构造几何学和运动学的分析，同时结合进行区域构造进行加深对研究区的理解。同时有计划采集有代表性的样品进行室内岩石变形分析。通过详细的薄片观察进行组构分析，以验证并进一步确定剪切方向、变形过程的变质条件以及每一期变形过程与变质过程之间的先后关系。野外过程中特别关注岩石单元与变形之间的时序关系，以确定特定的岩石单元的形成于构造前、同构造，还是构造后。构造变形的时代可以通过同构造的侵入体和变质矿物（如榍石、磷灰石和独居石）的同位素年龄直接确定，或者通过构造前和构造后的侵入体时代加以限定。本研究将选取适合测年的岩石和矿物将采用 U-Pb (TIMS 或 SIMS)和/或电子探针法进行。

3. 工作量和研究成果

3.1 论文工作量

序号	工作内容	数量	单位	主要完成人
1	野外地质考察	6	月	褚杨、林伟、Faure M
2	野外观测点	898	个	褚杨、林伟、Faure M
3	实测剖面	25	条	褚杨、林伟、Faure M
4	样品采集	212	块	褚杨、林伟、Faure M
5	野外照片	925	张	褚杨
6	岩石学薄片鉴定	308	片	褚杨
7	构造定向薄片观察	354	片	褚杨
8	绘制地质图	10	张	褚杨、林伟、Faure M
9	绘制剖面	14	条	褚杨、林伟、Faure M
10	锆石阴极发光实验	13	件	褚杨
11	锆石 SIMS U-Pb 定年	13	件	褚杨、冀文斌
12	锆石 Hf 同位素测定	13	件	褚杨、冀文斌
13	独居石扫描电镜实验	6	件	褚杨
14	独居石电子探针定年	6	件	褚杨

3.2 主要研究成果

1. 将雪峰山造山带划分为两个构造单元，西部区与东部区，二者以雪峰山主逆冲断层为边界，这条断层同时也是劈理前缘。西部区以箱型褶皱为特征，劈理不发育；东部区广泛发育褶皱和逆冲断层，并伴随着渗透性劈理的出现。
2. 雪峰山出露岩石以沉积岩或浅变质岩为主，地表无绿片岩相以上变质岩出现，故在强烈挤压变形的沉积盖层之下存在着一条基底滑脱带，将盖层与变质基底隔开，以薄皮构造模式解释了雪峰山盖层与基底岩石的变形差异。
3. 划分了雪峰山多期构造变形。雪峰山造山带早中生代共经历了3期构造变形： D_1 期为主变形期，以上部指向NW的剪切变形为特征，产生了大量不对称褶皱、逆冲断层及劈理（面理）； D_2 期为反冲构造期，以上部指向SE的剪切为特征，褶皱和断层的极性均为SE； D_3 期为直立褶皱期，在局部地区形成了直立的褶皱和劈理。
4. 雪峰山存在两期岩浆活动，早古生代和早中生代，通过SIMS锆石U-Pb定年，确定了两期花岗岩的时间分别是440-410 Ma和225-215 Ma。其中早古生代花岗岩经历了早中生代构造作用而发生糜棱岩化，而早中生代花岗岩为造山后期铝质-过铝质花岗岩，未经历变形。
5. 通过电子探针独居石的原位化学法定年，确定了雪峰山主滑脱带中含石榴石云母片岩的同构造变质作用时间在243 Ma，含矽线石云母片岩的高温变质作用发生在226 Ma，稍早于岩体的大规模侵位时间，说明高温变形之后引起了地壳熔融，形成了花岗岩。
6. 雪峰山为典型的陆内造山带，其形成机制与新生代的天山类似，晚二叠世太平洋板块在华南板块边缘的俯冲作用产生的挤压应力，至早三叠世传递至华南板块内部，先存的薄弱带发生活化，产生了NW向的逆冲推覆，从而形成了雪峰山造山带。

第二章 雪峰山及其邻区区域地质背景

第一节 华南板块区域构造背景

1. 地理位置及构造简介

自然地理上以中国淮河、秦岭以南地区称为华南，而华南板块区域更为广泛，包含了沿海各省之外，区划一直延伸到四川省、贵州省和云南省中部。从地形上看，整体处于丘陵地带，地表侵蚀切割强烈，植被生长茂盛，覆盖较好，未有海拔 4000 米以上山峰，主要山脉有南岭、武夷山、雪峰山等，平原地区包含四川盆地和江汉盆地两个大盆地以及长江中下游和珠江三角洲平原区；从地质上看，主要由位于东南部的华夏板块和位于西北部的扬子板块组成，周边主要为中生代造山带所围限（图 2-1），分别为北部的秦岭—大别造山带、西北的龙门山褶皱冲断带以及西缘和西南缘的金沙江缝合带和 Songchay 缝合带，而南缘和东缘则为欧亚大陆的大陆架一边缘海区域。

但是华南板块现今的构造格架主要经历了多期构造叠加之后的最终产物，以下将逐一介绍。

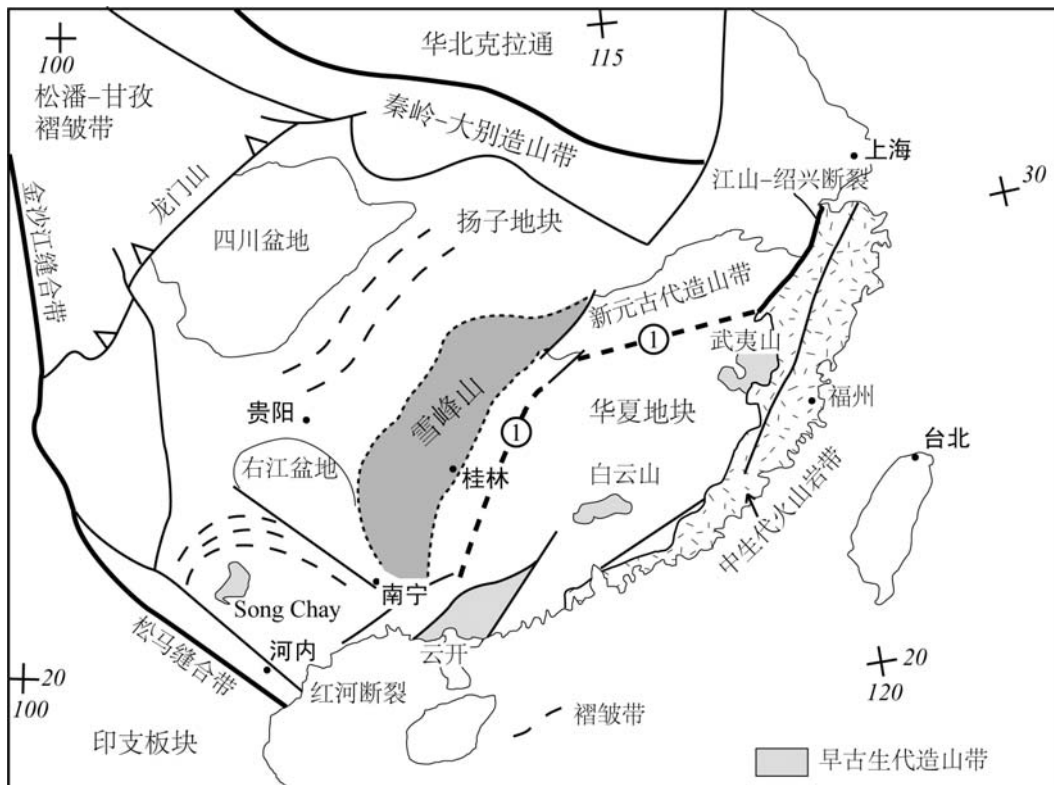


图 2-1 华南构造简图。①为推测的华夏和扬子的缝合线。

2. 多期构造事件

2.1 晚元古代

晚元古代, 扬子地块和华夏地块沿江绍断裂带拼合之后 (Charvet et al., 1996; Li XH et al., 2009a), 经历了一次区域性早古生代的构造事件 (Huang, 1960; Ren, 1991; Huang et al., 1980), 主要表现在高级变质作用 (局部可达麻粒岩相) (于津海等, 2007; Li ZX et al., 2010; Wan et al., 2010; Li LM et al., 2011), 强烈的构造变形 (舒良树等, 1997, 1999; 舒良树, 2006; Faure et al., 2009; Charvet et al., 2010) 以及大范围的岩浆作用 (江西省地质矿产局, 1984; 福建省地质矿产局, 1985; 邓希光等, 2004; 周新民, 2007; Li ZX et al., 2010; Yang et al., 2010; Chen et al., 2011; Xu et al., 2011)。而在早中生代华南板块在其演化历史上可谓多灾多难。除了四川盆地内部, 基本没有一个地方可以逃离不同期次构造作用对其的影响, 主要表现在华南板块边缘在早中生代经历了强烈的构造作用。晚中生代, 华南板块上最明显的特征当属沿海大面积的火成岩省, 代表了晚中生代太平洋板块平板俯冲所产生的研究活动 (Charvet et al., 1994; Li XH, 2000; Zhou and Li, 2000; Zhou et al., 2006; 周新民, 2007)。

华南板块之上覆盖着从新元古代开始至早中生代厚度大于 10 km 的沉积盖层, 因此, 其前寒武纪变质基底并不如华北克拉通出露广泛, 仅分布在零星地区, 如扬子地块之上的湖北崆岭群, 华夏地块上的浙江麻源群和八都群, 以及广东的云开群等。崆岭群主要由闪长质—英云闪长—奥长花岗—花岗闪长质片麻岩和花岗片麻岩 (TTG) 组成, 同时伴生有变泥质岩和斜长角闪岩。研究表明, 崆岭杂岩的奥长片麻岩形成于 2.95-2.90 Ga (Qiu et al., 2000), TTG 质岩浆活动主要在 3.0-2.9 Ga, 而莲沱组中高达 3.8 Ga 继承锆石以及锆石的 Hf 模式年龄表明扬子地块的基底地壳在至少在上古太古代就已形成, 可能存在冥古代的残片 (高山等, 1990; Gao et al., 1999; Zhang et al., 2006a, 2006b; Gao et al., 2011)。相比扬子地块, 华夏地块的基底分布就更为广泛。胡建雄等 (1991, 1994) 认为浙西南的八都群形成年龄 >1.8 Ga, 于津海等通过对粤北的龙川和潭溪地区锆石年代学研究认为, 华夏地块的地壳主要生长期在 ~3.6 Ga、3.3-3.0 Ga、~2.5 Ga 和 ~1.8 Ga, 同时也存在 >4.0 Ga 的古老地壳残余, 这同时也被再广西发现的火山岩中碎屑锆石年龄所支持 (广东地质调查局, 1988; 胡雄健, 1994; 于津海等, 2006a, 2006b, 2007; Yu et

al., 2008, 2010; Zheng et al., 2010)。由此可见, 无论是扬子地块还是华夏地块, 均存在着广泛分布的前寒武纪基底, 且很可能太古代就已经存在了陆核, 并经历了后期多期的地壳增生作用。

新元古代末, 是华南板块形成的关键时期, 扬子板块和华夏板块在这一时期沿江南造山带拼合为一整体(图 2-2, Charvet et al., 1996; Li ZX et al., 2002, 2007; Li XH, 1999; Li XH et al., 2009a)。江南造山带, 又称江南古陆, 是一条从广西北部、贵州东南经湖南西北、江西北部至安徽南部和浙江的带状晚前寒武纪浅变质岩系(黄汲清, 1945)。然而由于后期沉积的覆盖, 针对这一造山带的构造记录并不多, 其东段江山—绍兴断裂被确认为是新元古代的板块缝合带(郭令智等, 1980, 1984; 水涛, 1987, 1988), 赣东北东乡—德兴—歙县一带形成了含有高压蓝片岩的蛇绿混杂岩, 年代集中在 1034 至 866 Ma 之间(徐备和乔广生, 1989; 周新民等, 1989; Chen et al., 1991; 徐备等, 1992; 李献华等, 1994; Shu et al., 1996; Charvet et al., 1996)。而缝合带的其余部分都还不甚明了, 研究也多集中在岩石学和同位素地球化学的证据之上(Li ZX et al., 2002, 2007; Wang XL et al., 2004, 2006, 2007; Greentree, 2006; Li XH et al., 2009a)。

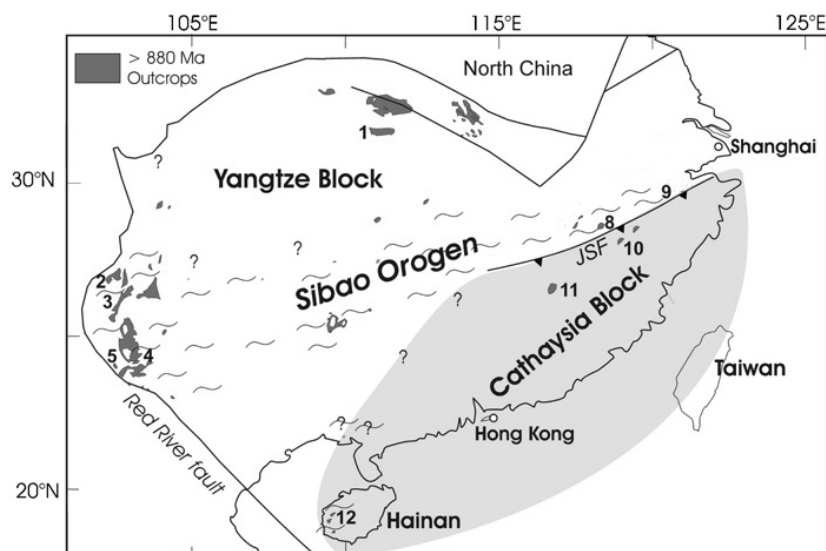


图 2-2 新元古代四堡(晋宁)造山带及扬子和华夏地块位置(引自 Li XH et al., 2009)

曾经在上世纪八十至九十年代, 一些学者认为这个导致形成华南统一整体的造山作用发生于早中生代(Hsu et al., 1988, 1990)或者早古生代(李继亮等, 1993; 马力, 2004)。但随后越来越多的新证据挑战着这些观点(Rogers, 1989; Rowley et

al., 1989; Charvet et al., 1996; Li and McCulloch, 1996)。现在大多数学者认为扬子与华夏板块在新元古代拼合,称之为晋宁造山带或者四堡造山带,但是造山带的时间还有所争议。一种观点认为晋宁造山带属于全球格林威尔造山带(Grenvillian orogen)的一部分,即 Rodinia 大陆聚合时期,又称四堡造山带(Li ZX et al., 2002, 2007; Greentree, 2006; Li XH et al., 2009a),而另一种观点则表明晋宁造山带一直持续到 0.82 Ga 或者更晚(Zhou et al., 2002, 2006; Wang XL et al., 2004, 2006, 2007, 2008)。岩浆与火山活动也广泛分布在江南造山带之中,其中岩浆活动通常认为造山后的产物,年龄在 820 Ma 左右(Li XH et al., 1999; Zheng et al., 2007);双溪坞岛弧火山岩在 950-890 Ma 之间(Li XH et al., 2009a)。

在扬子地块和华夏地块完成拼合之后,伴随着 Rodinia 大陆的裂解,华南板块内部也产生了大量的双峰式火山岩,830-820 Ma 的火山岩被认为是裂解前产物,而 790-740 Ma 之间的则为裂解过程中形成的火山岩(Li ZX et al., 1999; Li XH et al., 2002, 2003; Zheng et al., 2007)。随后,华南板块进入了平静期,沉积了从巨厚的砂岩—泥岩系列(Wang and Li, 2003)。

2.2 早古生代

早古生代末期,华南板块经历了一次区域性的构造事件。黄汲清先生于 1945 年就依据中泥盆世的不整合和底砾岩认为江南古陆为加里东褶皱带。郭令智等(1980)将云开—武夷一带划分为加里东期岛弧褶皱系。李继亮等(1993)认为赣南存在一个极性 W 或 NW 混杂岩推覆带,是早古生代赣南海俯冲消减,湘中南地块和华夏地块拼合的结果。刘宝珺(1994)认为华南早古生代造山作用源于古洋盆的关闭。由此可见,华南早古生代造山带的存在毋庸置疑,而突出的证据表现为:(1)震旦系—下古生界的强烈褶皱与韧性剪切变形;(2)强烈的花岗岩浆活动;(3)泥盆纪与前泥盆纪地层间的区域性角度不整合。

早古生代的构造事件影响区域主要在武夷山、白云山和云开大山一带及周边地区,但由于这一区域既保留了晚元古代的构造遗迹,同时也经历了强烈的中生代构造改造,因此早古生代造山带的研究一直无法明细化,有些原本认为是新元古代的构造,在年代学数据不断更新的情况下被证明是早古生代造山事件的产物,而且造山环境也趋于统一,即陆内造山带(水涛等, 1988; Zhao and Cawood,

1999; Wan et al., 2007, 2010; Wang et al., 2007a; Faure et al., 2009; Li ZX et al., 2010)。在同位素年代学的推动下, 早古生代构造事件的格架逐渐清晰化。舒良树等(1997, 1999)认为武夷山北缘发生了由 N 向 S 的逆冲推覆, 其 Ar-Ar 年龄为 420 Ma 和 390 Ma。Faure et al. (2009) 和 Charvet et al. (2010) 分别通过在江西和福建的工作得出早古生代陆内造山从 460 Ma 开始, 持续了近 20 My, 440 Ma 之后为造山后伸展引起的混合岩化和岩浆作用。Lin et al. (2008) 在云开大山进行了详细的构造学分析, 认为早古生代变形为上部指向 NW 的韧性剪切, 这与 Li ZX et al. (2010) 的观点一致, 认为武夷山至云开大山一线早古生代均存在着极性 NW 的陆内造山作用, 并将其命名为武夷—云开造山带。综合上述年代学数据, 早古生代的陆内造山的挤压期主要发生在 460 Ma 至 440 Ma 之间, 产生了大规模的韧性变形和高级变质作用(局部可达麻粒岩相), 使得原有的前寒武纪的基底都遭受了强烈改造。变质峰期温压条件分别是 600-700°C 和 1.0-1.2 GPa (Wang et al., 2007a; Wan et al., 2007, 2010; Faure et al., 2009; Charvet et al., 2010; Li ZX et al., 2010)。大范围的岩浆作用代表了造山后的垮塌, (江西省地质矿产局, 1984; 福建省地质矿产局, 1985; Li XH, 1991, 1994; 邓希光等, 2004; Wang et al., 2007a; Wan et al., 2007; Li ZX et al., 2010; Yang et al., 2010; Chen et al., 2011; Xu et al., 2011), 这一作用还影响到了越南与我国交界的 Songchay 地区 (Roger et al., 2004)。420-390 Ma 间的 Ar-Ar 年龄则为造山后的伸展冷却年龄(舒良树等, 1997, 1999; Faure et al., 2009)。

早古生代造山作用之后, 华南板块进入了平静的沉积期。中-晚泥盆世开始为造山结束后的陆相砂岩, 并逐渐向灰岩到过渡。随后的石炭纪至二叠纪海侵使华南板块全部被海水淹没, 成为广阔的碳酸盐岩台地, 直到早三叠世(王清晨和蔡立国, 2007)。

2.3 早中生代

早中三叠世开始, 华南板块进入又一个构造活跃期, 尤其以周缘的碰撞造山为主(图 2-1)。华南板块在早中生代处于四面围限的状态, 处于各向挤压的应力场之下。以北, 为华北克拉通, 二者之间形成秦岭—大别—苏鲁造山带, 以出露了大量高压—超高压变质岩而闻名, 为三叠纪陆陆碰撞时大陆深俯冲产物, 记录

了多期构造变形 (Mattaueer et al., 1985; Hacker and Wang, 1995; Faure et al., 1999, 2008; Webb et al., 1999; 张国伟等, 2001; 徐树桐等, 2002; Ratschbacher et al., 2003; Hacker et al., 2006; Lin et al., 2009a)。同时在造山带的南缘在形成了前陆褶皱冲断带, 呈现出单一的 SW 或者 SE 向的逆冲推覆, 尽管冲断带的宽度在不同区域差异明显, 但整体不超过 100 公里 (Liu and Hao, 1989; Faure et al., 1998; Schmid et al., 1999; Li SZ et al., 2010b)。西北部, 龙门山褶皱冲断带记录了三叠纪松潘—甘孜地块向四川盆地南西方向的逆冲, 同时产生了大量三叠纪岩浆活动 (Harrowfield and Wilson, 2005; Roger et al., 2008, 2010); 而在西缘和西南部分, 存在着一条从云南一直延伸到越南境内的晚古生代—早中生代的缝合带, 代表了印支板块与华南板块的板块界限, 形成了一系列的逆冲带 (钟大赟, 1998; Carter et al., 2001; Lepvrier et al., 2004, 2008, 2011; Yan et al., 2006; Carter and Clift, 2008; Roger et al., 2008, 2010)。与印支造山带相对应的, 华南板块西南缘也记录了其造山前陆的 NE 向逆冲 (林伟等, 2011)。在云开地块, Lin et al. (2008) 通过详细的构造野外观察认为早中生代构造主要为上部指向 NE 的韧性剪切, 包括一些列极性 NE 的褶皱和 NE-SW 走向的矿物拉伸线理, 对应着印支板块向华南板块的挤压; 而 Wang et al. (2007c) 认为云开大山的三叠纪变形分为两期, 早期为走滑挤压, 晚期为走滑伸展, 是华北板块和印支板块的联合挤压使得华南板块内部产生了走滑山系。此外, 在武夷山地区也记录了早中生代韧性剪切的年代学证据 (Xu et al., 2011)。

在华南板块东南缘, 研究表明古太平洋板块俯冲可能从晚二叠世-早三叠世就已经开始 (Li XH et al., 2006; Li ZX and Li XH, 2007), 并由此提出了平板俯冲模式来解释华南板块内部 NE-SW 走向的陆内造山带。在福建—浙江—江西一带, 早中生代花岗岩以 A 型为主, 年龄在 254-220 Ma 之间, 表明当时的环境可能并不是处在挤压造山之中, Wang Q et al. (2005) 认为这些三叠纪花岗岩是在太平洋板块的斜向俯冲从而产生了走滑伸展的区域构造背景之下形成的 (Wang et al., 2005; Sun et al., in press)。

中三叠世至早侏罗世沉积相由于华南板块的整体抬升而发生了剧烈的改变, 从之前的浅海或边缘海沉积转变成陆相地层, 沉积的砂岩和砾岩地层较为局限地分布于山间盆地之中, 不整合于下伏地层之上。这次区域上的不整合为早中生代

造山事件的响应（江西省地质矿产局，1984；广西壮族自治区地质矿产局，1985；湖南省地质矿产局，1988；福建省地质矿产局，1989；Shu et al., 2009）。

2.4 晚中生代

侏罗纪至白垩纪，华南板块上构造主要以伸展走滑作用为主，表现为 NE-SW 向的走滑或者正断作用，伸展穹窿，同构造岩浆作用以及断层相关盆地的形成（Xu et al., 1987; Gilder et al., 1991; Faure et al., 1996; Lin et al., 2000; Zhou and Li, 2000; Li XH et al., 2001; Zhou et al., 2006; Shu et al., 2009）。形成的晚侏罗世与白垩纪沉积岩包括红色陆相碎屑岩夹有火山碎屑岩（湖南省地质矿产局，1988）。在华南板块东南缘，由于太平洋板块的俯冲作用，形成了大面积的花岗岩以及同时期的火山活动，极大地改造了燕山期之前的构造形迹（Zhou et al., 2000, 2006）。

在这一时期，整个华南处于伸展应力状态之下，白垩纪盆地边界多为正断层或者走滑断层（Shu et al., 2009）。在断裂带方面，Zhu et al. (2005) 发现郟庐断裂的左行走滑剪切在早白垩世早期最为剧烈，可能对应着太平洋板块的快速俯冲；长乐—南澳断裂在 120-105 Ma 期间也发生了走滑剪切构造（Wang et al., 2000）。在华南板块内部，左行走滑构造也较为强烈，在雪峰山地区，大规模左旋走滑断层切割了早中生代的花岗岩，使得岩体发生了明显的错段（湖南省地质矿产局，1988; Li JW et al., 2001）。伸展穹窿在晚中生代也较为发育。庐山穹窿与洪镇变质核杂岩均记录了 130-125 Ma 的 NE-SW 向的伸展构造，略微不同的是，庐山在 NE-SW 伸展同时有花岗岩的侵位，洪镇则没有。而最后一期构造都伴随着花岗岩就位，形成了 NW-SE 向的伸展构造（Lin et al., 2000; Zhu et al., 2010）。东南沿海区域，广泛分布着 145-105 Ma 的流纹质火山岩和强过铝质花岗岩（Jahn et al., 1990; Wang et al., 1990; Lapierre et al., 1997; Zhou and Li, 2000）。Zhou et al. (2000, 2006) 运用“太平洋板块俯冲+玄武质岩浆底垫作用”来解释这些火山—侵入岩系列的地球动力学成因。于此同时，但是在四川盆地东部，著名的川东褶皱带主要在晚侏罗纪至早白垩世早期形成，说明在华南板块内部局部存在着挤压应力场（Yan et al., 2003, 2009; 梅廉夫等, 2010）。

第二节 雪峰山区域地质背景

1. 地质简介

雪峰山位于华南板块中部，走向 NNE-SSW，南北长 300 公里，东西宽 100 公里，主要分布在湖南省和广西壮族自治区境内。海拔最高峰为苗儿山，2068 米高，位于桂林市资源县境内。雪峰山地区出露的最老地层为冷家溪群，主要由砂岩、砾岩、粉砂岩、千枚岩和板岩组成，出露于雪峰山的北区和西北区，主要位于常德、安化、桃源一带，其沉积环境应属活动海槽或浅海、半深海环境（湖南省地质矿产局, 1988; 丘元禧等, 1999）。冷家溪群之上为板溪群，为近 3 千米厚的复理石沉积，为新元古代晋宁（四堡）期造山作用后剥蚀的产物，主要分布于靖州、溆浦、安化一线（湖南省地质矿产局, 1988）。板溪群与下部冷家溪群在北部呈不整合接触，但向南逐渐转变成假整合乃至整合接触。震旦系为冰碛岩、砂岩、硅质岩和灰岩所组成，其中著名的南沱冰碛岩代表了全球性的冰川事件。从震旦系一直到志留系，雪峰山地区未有明显的沉积间断（图 2-3）。但是在雪峰山地区，寒武纪和奥陶纪沉积体现出明显的南北差异。北部为灰岩和页岩，而南部则以泥岩或者浅变质板岩为主（广西自治区地质矿产局, 1985; 湖南省地质矿产局, 1988）。寒武纪至早志留世，雪峰山的沉积物源即有来自扬子地块，又有来自华夏地块，表明雪峰山地区在这一时期位于地势较低的浅海环境，而 NW 和 SE 两侧的地势较高，为本区提供了物源（丘元禧等, 1999; Wang et al., 2010）。

志留纪末至早中泥盆世，华南经历了大规模的造山作用，这一过程在雪峰山主要体现在区域性地层缺失，即中晚泥盆统直接覆盖在早古生代地层之上。但在研究区，从南东到北西，体现出一种渐变态势，即从角度约为 25 度不整合逐渐转变为假整合接触关系，而且在不整合两边并没有出现明显的构造变形的差异。早古生代末期，华南板块恢复平静，晚泥盆世-石炭纪-二叠纪-早三叠世的浅海至滨海相沉积作用在雪峰山地区沉积了几公里厚的灰岩、白云岩和碎屑岩。以上地层均卷入了早中生代的构造变形之中，发育了强烈的褶皱和逆冲推覆构造（湖南省地质矿产局, 1988; Wang et al., 2005; Shu et al., 2009）。

晚三叠世至早侏罗世的沉积相发生了明显的变化，从浅海-滨海相转变成陆相沉积，红色砾岩和砂岩局部地分布在山间盆地之中，不整合于老地层之上。中

晚侏罗世至白垩纪陆相砂岩发育在半地堑或走滑拉分盆地之中, 均与整个华南燕山期的构造岩浆活动相对应(江西省地质矿产局, 1984; 湖南省地质矿产局, 1988; Zhou et al., 2006; Shu et al., 2009; 张进等, 2010)。

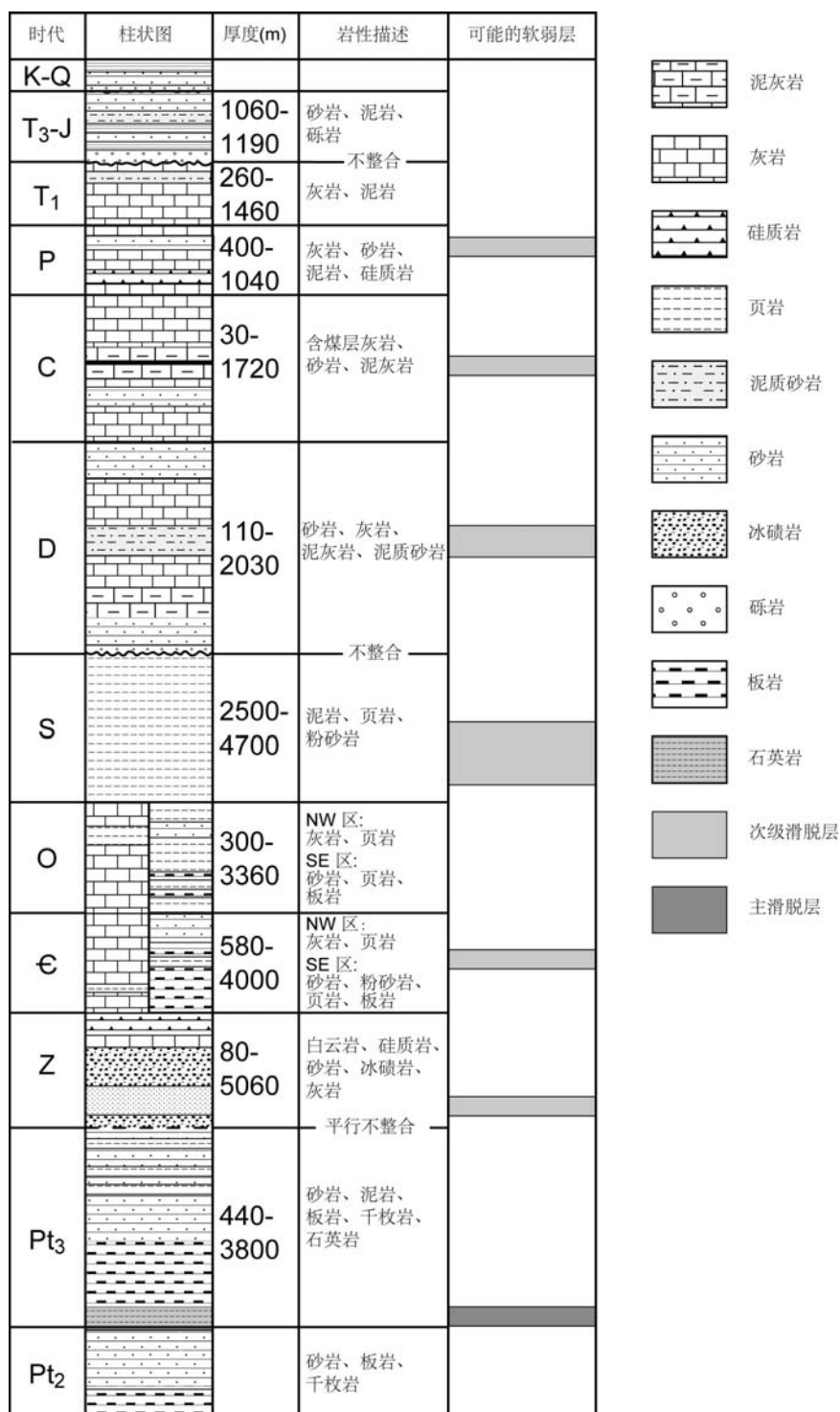


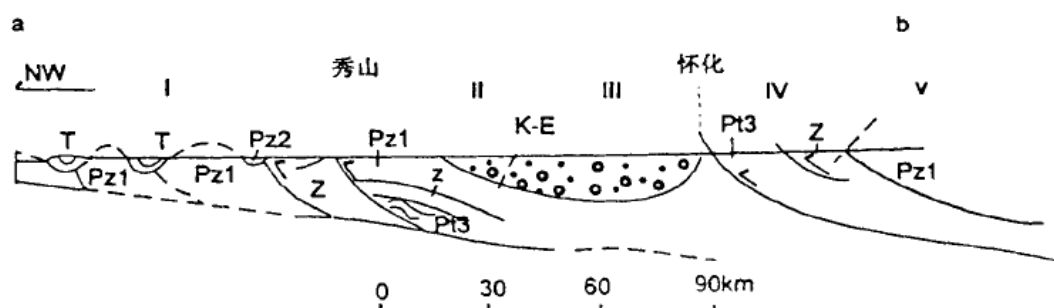
图 2-3 雪峰山的综合地层柱状图 (据湖南省地质矿产局, 1988)。

在晚三叠世之前的沉积序列之中包含了若干层泥质岩，而有些包括了煤层，如震旦系、寒武系和二叠系等。在早中生代造山作用之中，这些软弱层在构造变形中起了重要作用，即吸收了大部分的缩短作用（丘元禧等，1999；Yan et al., 2003），变形在这些次级滑脱带中会表现的尤为强烈。

2. 动力学模式

前人通过对雪峰山及其西缘地区的构造学和年代学工作，对雪峰造山带形成不同的观点，其中具有代表性的有如下几个：

1) 丘元禧等（1998, 1999）对雪峰山地区进行了详细的地质工作，认为其地质构造以具有多期次、多层次的层滑构造为主要特点。他们将雪峰山至川东划分了5个构造分区（图2-4），特点包括在垂向剖面上存在多个区域滑脱层，且上下构造不协调。厚皮构造是从早期薄皮构造演化而来的从基底滑移进一步推动前缘的盖层滑脱，形成侏罗山式褶皱。同时表现出长期渐进递变发育和阶段发展而形成的演化序列，即层滑—切层滑移—逆冲推覆—伸展滑覆。



K-E 白垩系及下第三系; T 三叠系; Pz₂ 上古生界; Pz₁ 下古生界; Z 震旦系; P₃ 板溪群
 I 川东南—湘西北燕山期弧形梳状褶冲带 II 湘西北—黔东南慈利—大庸—保靖—铜仁燕山期弧形断褶带
 III 沅麻中生代前渊盆地 IV 雪峰山基底褶皱—冲断带 V 湘中印支期弧形褶皱带

图 2-4 雪峰山中段的综合地质剖面（引自丘元禧等, 1999）

雪峰山主要以逆冲叠瓦推覆构造为主，并兼具飞来峰和构造窗等构造样式。其推覆模式为近原地推覆，不存在大规模的远程推覆。伴随着雪峰山主体加里东期构造，还发育了变质核杂岩以及伸展拆离断层，但在拆离断层下盘并未发现糜棱岩和糜棱岩化岩石，而拆离断层上部发育了滑脱层，发育强烈变形，倒转和平

卧褶皱。雪峰山的多期构造运动主要发生在雪峰期、加里东期和印支期，每次陆内造山过程均形成了地壳加厚，在逆掩推覆后伴随伸展构造以及地壳熔融，形成了花岗岩的侵位。雪峰山陆内造山带发生于陆内裂陷旋回的基础上，发生了陆内原地地块之间的拼贴碰撞和仰冲。

2) Yan et al. (2003) 的观点与 Hsu et al. (1988, 1990) 的类似，推断雪峰山与武陵山的新元古代板溪群为飞来峰，与下伏的震旦系和寒武系为构造接触。他们通过结合地震剖面进行了平衡剖面的恢复，认为深处华南腹地的大规模推覆作用表现为多层次推覆构造，兼具薄皮构造和厚皮构造。整个湘西北—川东南褶皱带可以分为两个大区，以大庸断裂为界，以东为厚皮构造，以西为薄皮构造，薄皮构造区中又以齐岳断裂为界分为尖楞向斜区和尖楞背斜区（图 2-4）。构造变形以极性向 NW 的逆冲为主，同时伴生次级的 SE 向逆冲断层。从西向东，由雪峰山的厚皮构造向川东华蓑山的薄皮构造过渡，经过平衡剖面的恢复计算得出薄皮构造带的缩短量在 18-21%，借此推断厚皮构造带的缩短量应在 20% 以上。这一推覆系统形成于晚侏罗世至白垩纪，属于晚燕山期构造，对应着华南与华北板块之间剪刀式闭合后华南内陆的构造调整。

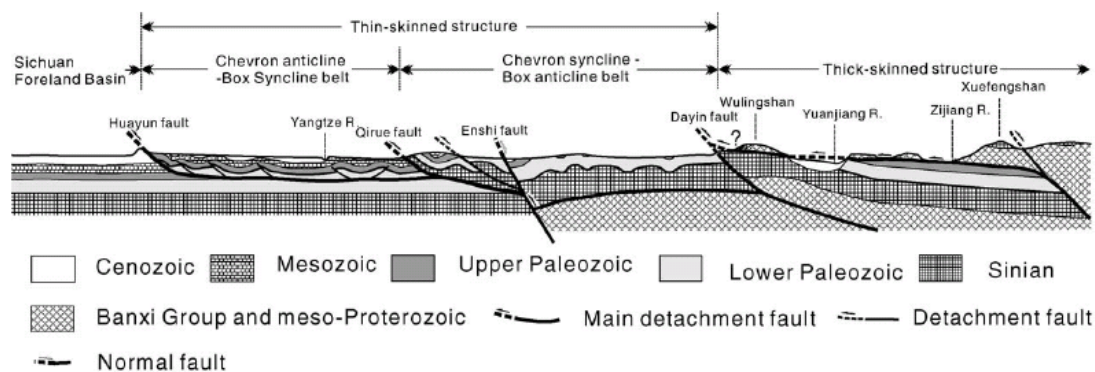


图 2-5 华蓑山至雪峰山的综合地质剖面（引自 Yan et al., 2003）

3) 与前两种模式不同的是，Wang et al. (2005) 结合了断层构造与年代学研究认为雪峰山构造带形成于早中生代，即印支期，其主要变形样式以走滑为主，同时在基底滑脱带之上形成一系列逆冲-反冲推覆断层，类似走滑断层的逆花状构造（图 2-5）。

Wang et al. (2005) 以雪峰山的区域性断裂为突破口，通过细致的野外观察，测得的线理均为近 N-S 走向，而构造变形主要表现为上部指向 NW 的韧性剪切

为主，认为这些断层具有压性兼左行走滑性质。沿基底滑脱带的挤压形成了浅表极性 NW 的逆冲断层和极性 SE 的反冲断层，沿断层带发育有糜棱岩。糜棱岩中云母矿物的 Ar-Ar 年代学结果显示，雪峰山的造山期在 217 至 195 Ma 之间，属于印支晚期至燕山早期。

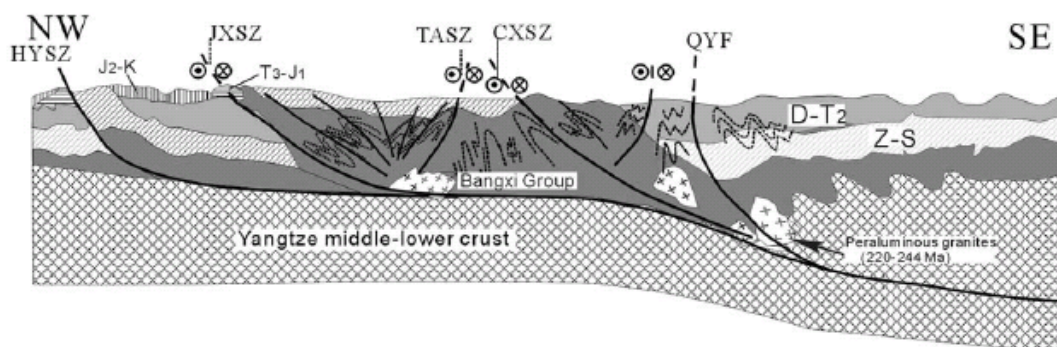


图 2-6 雪峰山地质剖面图（引自 Wang et al., 2005）

第三节 华南中生代构造演化模式

最初在黄汲清命名江南古陆时，就将雪峰隆起置于华南加里东褶皱带之中，（黄汲清, 1945; Huang, 1960, 1978）。郭令智等（1980）通过板块构造理论阐述了江南古陆实际为雪峰新元古代岛弧，同时将华南分为 5 条不同时代的沟-弧-盆体系；朱夏（1980）认为华南的变形样式和盆地演化是在“硅铝层之上的大陆岩石圈内部拆离的结果”；崔盛芹和李锦蓉（1983）将东南滨海分为 3 个带，在大地质构造角度上分析了中国东部“印支运动”的影响。从上世纪 80 年代末开始，中国地质学家对华南的构造演化模式提出了多种不同的动力学模式，其中以下为最具代表性的三个演化模式。

1. 俯冲碰撞模式

Hsu et al. (1988, 1990) 认为，扬子地块和华夏地块在中生代之前仍是独立的块体，二者之前存在一个华南洋。在三叠纪，华南洋的洋壳发生向 SE 的俯冲消减，闭合后扬子地块继续向华夏地块下俯冲，形成了大面积的构造混杂岩，即板溪群，同时形成了以雪峰山飞来峰和蓝田构造窗为特征的大规模的远程推覆构

造（图 2-6A）。但这一观点的提出立即在学术界引起了巨大的争议，大多数地质学家认为板溪群是新元古代连续沉积，与上下地层没有构造接触关系（Gupta, 1989; Rodgers, 1989; Rowley, 1989）。之后，Xiao et al. (2005) 在其基础上提出了一个改进的构造模式，在三叠纪并没有扬子地块和华夏地块间的洋壳消减，但由于东缘古太平洋板块俯冲的挤压作用，促使了多岛洋中小地块的最终聚合，最终拼合成统一的华南板块（图 2-6B）。整体上两个模式都是建立在三叠纪陆块聚拢拼合基础上的。

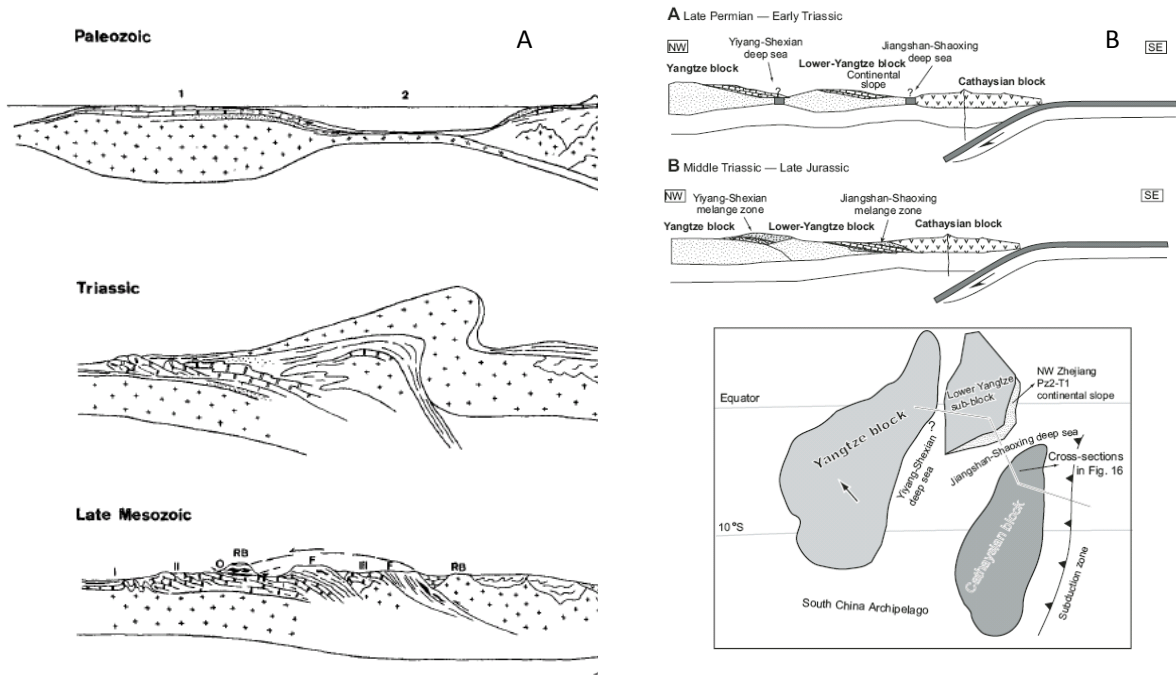


图 2-7 华南板块构造演化模式 (A) 引自 Hsu et al., 1988。(B) 引自 Xiao et al., 2005。

2. 韧性走滑挤压模式

Wang et al. (2007a) 结合了雪峰山和云开大山的构造和年代学研究，提出在早中生代华南板块内部经历了一个陆内转换挤压过程，雪峰山和云开大山都位于这套转换挤压系统之间（图 2-7）。在三叠纪，华南板块体现出两期构造特征。早期（250-230 Ma），构造样式主要以左行走滑兼挤压为主，而到了晚三叠世

（230-200 Ma），则以走滑拉张为主，花岗岩侵位也与这两期构造相对应，分别为同造山花岗岩和造山后花岗岩（Wang et al., 2007b）。

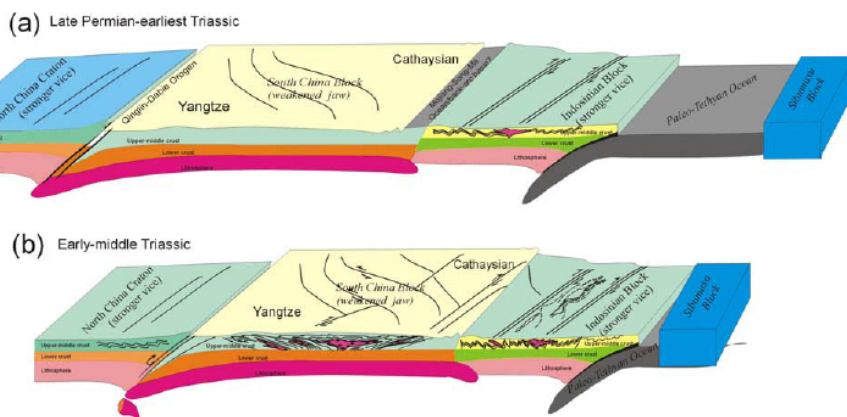


图 2-8 华南板块构造挤压模式 (引自 Wang et al., 2007c)。

3. 平板俯冲模式

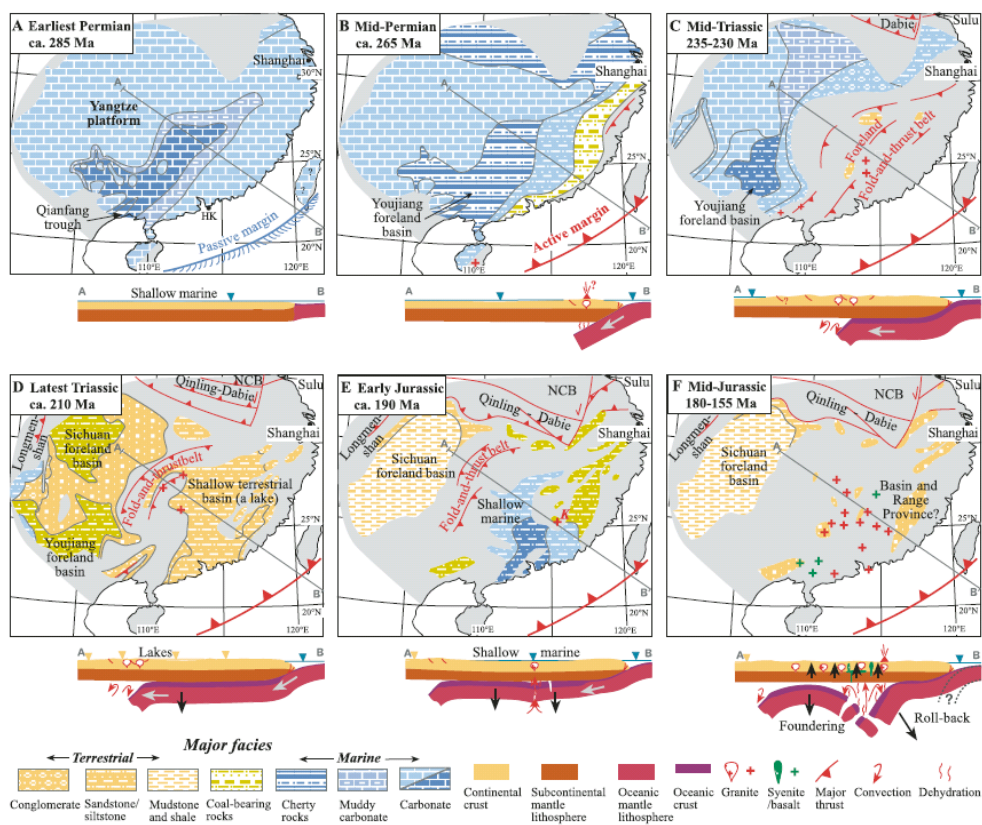


图 2-9 华南板块构造挤压模式 (引自 Li ZX and Li XH, 2007)。

Li and Li 在 2007 提出了一个平板俯冲模式来解释华南的古地理和岩浆活动的演化。他们通过总结从东南沿海到内陆的中生代花岗岩年代学,认为从 250-190

Ma 之间在华南板块之上形成一个宽达 1300 公里的向内陆迁移的造山带（图 2-8），并伴随着世界上最大规模的盆岭岩浆活动（Zhou and Li, 2000; Liu et al., 2003; Zhou et al., 2006; Shu et al., 2009; Yan et al., 2011）。

第四节 小结

雪峰山位于华南板块的核心部位，其构造属性和地球动力学的演化对于理解华南板块中生代地质历史的关键因素之一。

华南板块由扬子地块和华夏地块组成，二者均具有前寒武纪基底，并经历了多次地壳增生作用。新元古代，两个地块沿江山—绍兴断裂碰撞拼合。虽然扬子地块和华夏地块的拼合时间已趋于统一，但是南部缝合带的位置还不明确。从新元古代开始到早三叠世，华南板块接受了巨厚的沉积。华南板块经历了多期构造变形，分别是新元古代、早古生代末、早中生代和晚中生代。各个构造期次存在叠加关系，给构造解析提出了挑战。早古生代和早中生代造山带都具有陆内属性，产生了广泛的地壳变形和变质作用，分别对应着区域地层不整合现象。晚中生代以大量的岩浆活动和伸展构造为主，形成了大面积的伸展盆地。

早中生代变形作为华南板块的主控构造，对格架的定型起了决定性作用。现有的模式表明，华南的早中生代构造还是以陆内变形为主。无论哪种动力学模型，雪峰山造山带都是研究陆内变形的关键点。

针对构造模式，可以明确的是古太平洋的俯冲对于华南陆内的变形起到了关键性的作用，但是如何实现以及表现形式，现在还存在着争议，急需进行详尽的构造学工作。前人对雪峰山地区以及华南板块进行了详细的研究，或者缺少详尽的构造学解析，或者对构造期次划分缺少明晰的思路。相对于花岗岩岩石学、年代学及地球化学的研究，构造工作已较为落后，需要通过基础的野外工作来弥补这一差距。

第三章 雪峰山盖层早中生代构造变形分析

雪峰山地区广泛分布着从晚元古代至早三叠世的沉积盖层,经历了强烈的早中生代的挤压褶皱作用,并在中三叠世产生了区域性的不整合面(湖南省地质矿产局,1988)。与此相类似的,在早古生代末期,雪峰山地区也存在早古生代的一期构造事件,但是此次事件在雪峰山构造影响较弱。尽管如此,在此还有必要将早古生代做必要的阐述,以明确雪峰山造山带的时代归属性。本章选取了5个典型地区(图3-1),着重对雪峰山早中生代构造进行详细解析。

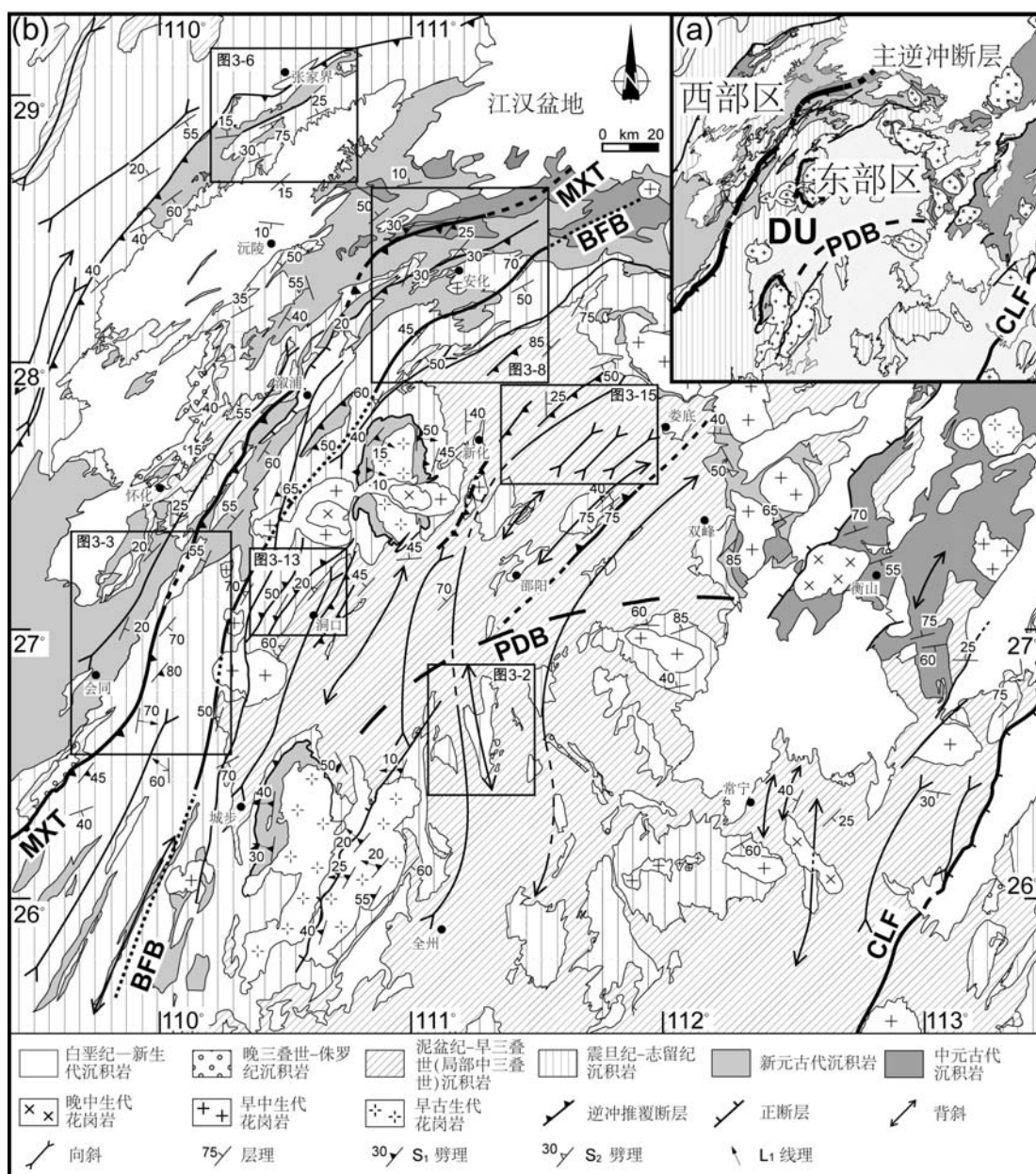


图3-1 雪峰山构造地质图(修改自湖南省地质矿产局,1988)。MXT:雪峰山主逆冲断层。BFB:反向褶皱边界。PDB:古生代构造边界。CLF:郴州-临武断层。DU:深部单元。

第一节 早古生代构造

由于雪峰山地区存在着泥盆纪不整合面，所以一些地质学家将雪峰山的主构造期次归于早古生代（黄汲清, 1945; 李继亮, 1993; 丘元禧等, 1998, 1999; 马力, 2004）。但是通过我们的野外考察证明早古生代造山带在雪峰山地区的影响被过高估计了。

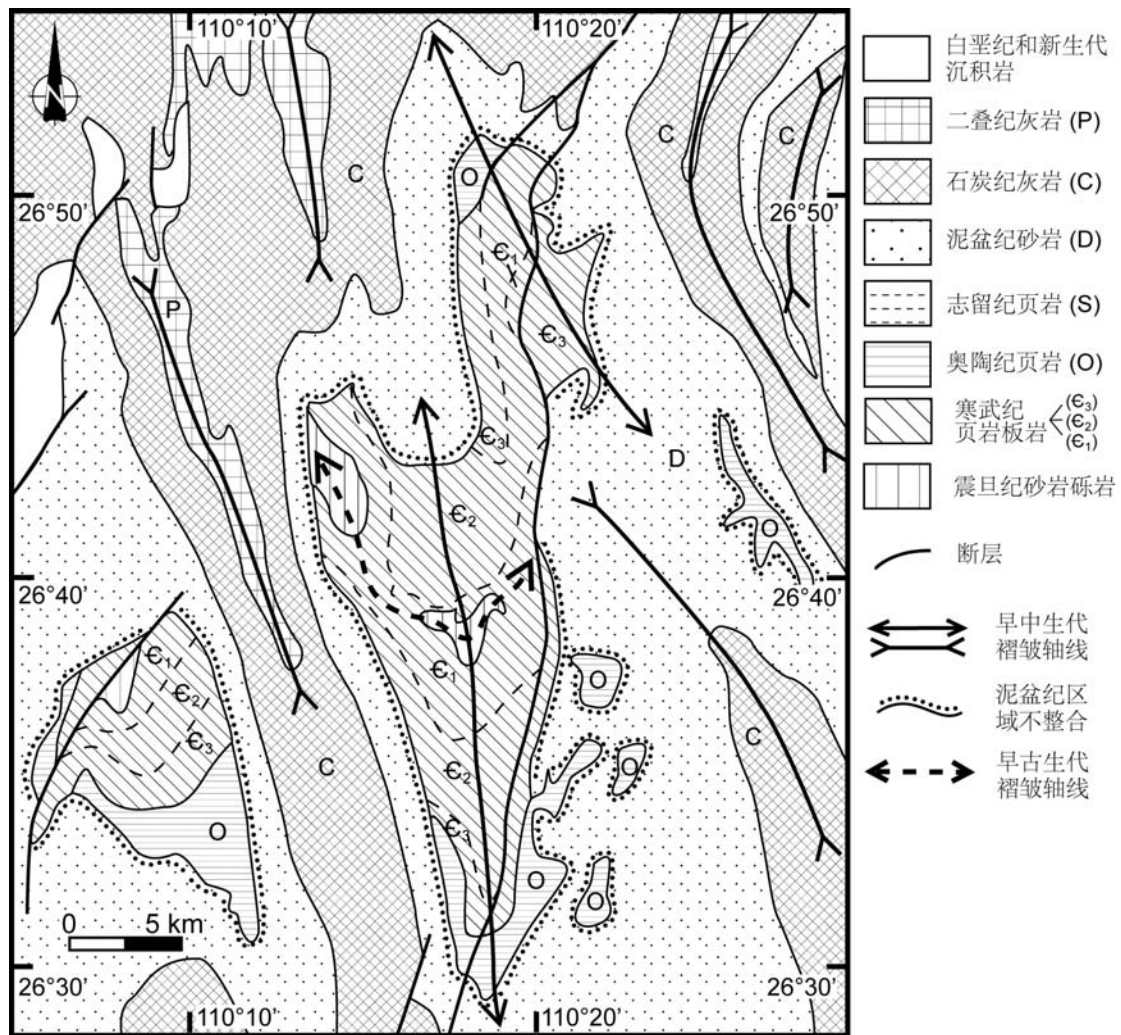


图 3-2 雪峰山南部永州东北地质简图。褶皱轴迹可以看出早中生代 N-S 或 NNW-SSE 向褶皱叠加在早古生代 E-W 向褶皱之上（修改自湖南省地质矿产局, 1988）。

在雪峰山南部地区，可以看到新元古代、寒武纪和奥陶纪的地层卷入了轴向 E-W 的褶皱（图 3-2）。这些早期的褶皱轴迹与研究区东侧江西的古生代造山带构造行迹平行，因此可以推断是华南板块早古生代陆内造山的产物（Faure et al.,

2009)。之后褶皱的地层被泥盆纪的砾岩和砂岩地层不整合的覆盖。从晚泥盆世开始,这一区域接受了稳定的台地相沉积,直到早三叠世,在早中生代构造作用下,整个沉积盖层,包括经历过早古生代构造的地层,均卷入了 N-S 走向的褶皱与冲断作用之中。

丘元禧等(1996, 1999)和侯光久等(1998)认为雪峰山早古生代构造线走向为 NEE-SWW,与印支期的构造方向一致,形成了 NW 向推覆和 SE 向反冲。Faure et al.(2009)认为江西早古生代造山作用形成的褶皱轴迹为 WNW-ESE 方向,这与湖南东南部早古生代地层构造线方向相同。而张岳桥等(2009)和李三忠等(2011)则认为近 E-W 向的褶皱形迹为印支早期构造,印支晚期构造为 NE-SW 走向尽管存在着早古生代的构造遗迹。通过野外工作我们发现,早古生代构造线应为 E-W 走向,表现为这期褶皱仅仅发育在早古生代地层之中,晚古生代地层不整合覆盖在上面,而且在研究区内分布较为局限,仅在南部地区较为清楚,北部由于早中生代 NW-SE 向挤压已被后期构造全部替代。同时作为早古生代造山带的主要证据的泥盆纪不整合,在雪峰山地区也呈现一个渐变的趋势。结合文献及野外观察,雪峰山大部分区域的泥盆纪地层与下伏地层的产状夹角大致在 15° 至 30° 之间,高角度相交的现象较少。在雪峰山东北部,不整合角度逐渐减小,进而演变成区域的平行不整合(湖南省地质矿产局, 1988; 李三忠等, 2011)。此外,早古生代的褶皱样式多为宽缓型,未见任何大规模的劈理发育区域,甚至褶皱轴面劈理都较为少见。而且在早中生代劈理发育的地区,不整合面上下地层均可见渗透性劈理的存在,而且劈理方向一致。因此可以推断,雪峰山的早古生代构造影响较弱,大规模的挤压、逆冲和劈理构造均为早中生代,我们将主要精力集中于早中生代构造研究之上。

第二节 雪峰山的构造单元划分

前人通过对雪峰山的构造学研究也对其进行过构造区划。陈海泓等(1993)将雪峰山分为 5 个构造单元:扬子板块前陆盆地,前陆褶冲带,华南板块刚性基底推覆体,盖层推覆体和碰撞混杂带。这个划分主要建立在 Hsu et al.(1990)中生代华南为碰撞造山带的构造格架之下,同时认为沅麻盆地为前陆盆地,白垩纪红层为磨拉石沉积(陈海泓等, 1992)。丘元禧等(1998, 1999)对雪峰山做了非

常详尽的构造学工作,认为雪峰古陆及其邻区地质构造形迹总体表现为向北西突出的弧形构造带,自北西向南东可以依次划出:川东南—湘西北燕山期弧形梳状褶冲带,湘西北—黔东南慈利—大庸—保靖—铜仁弧形断褶带,中生代沅麻弧形沉积盆地,安化—怀化—黔东南—桂北雪峰山多期复合逆冲推覆断褶带,以及湘中印支期弧形梳状褶皱带。但是这个分区的依据是雪峰山多期构造后的框架,对主变形期早中生代的构造并没有详细区分。Yan et al. (2003) 依据构造变现阶段的不同,将湘西雪峰山至川东区域分为尖楞背斜薄皮构造区、齐岳山断裂、尖楞向斜薄皮构造区、大庸断裂、厚皮构造区这三区夹两断裂的分区模式,同样的,他们并没有将雪峰山的早中生代构造变形和川东晚中生代变形区分开。

在详细的野外地质考察基础上,我们将雪峰山早中生代造山带分为两个主要构造单元(图 3-1a):西部区和东部区。两个构造单元之间以雪峰山主逆冲断层为界限(图 3-1a 和 3-1b),同时这个断层也是区域上的劈理前缘,导致下部韧性变形岩石被逆冲至地表。断层以西,则没有劈理发育或者仅仅存在于少数褶皱的轴面转折位置;而在断层以东,发育了大量的渗透性劈理构造,同时伴随着 NE-SW 走向的褶皱、逆冲断层以及 NW-SE 向拉伸线理等构造现象。

西部区从湖南西北的张家界地区向 SW 方向延伸至湖南西部和贵州东部,为大范围箱型褶皱发育区,这与丘元禧等(1999)的湘西北—黔东南弧形断褶带位置大致相当。武陵山处于西部区之中,主体构造也以公里尺度的大型箱型褶皱为代表。区域内主要以新元古代冷家溪群和板溪群和早古生代沉积岩为主,沅陵—麻阳盆地分布在武陵山以南,主要以白垩纪红色沉积为主,其东侧也沉积了晚三叠世至侏罗纪的地层。

东部区主要由雪峰山山脉主体和其东部低地构成,其中山脉主体由密集发育劈理的绿片岩相变质的板岩、变砂岩所组成,这里的变质作用和变形最为强烈,是雪峰山的核心区域。前人将这一块区域划归为江南(雪峰山)基底褶皱—冲断带的主体区域(陈海泓等, 1993; 马文璞等, 1993; 丘元禧等, 1998, 1999)。板溪群、震旦系以及下古生界在该区大片出露,背斜的核心为冷家溪群,以经历了低绿片岩相变质作用的变砂岩为主。在东部低地,主要为泥盆纪到早三叠世的沉积岩所覆盖,发育了褶皱和轴面劈理,灰岩中发育断裂构造。早三叠世薄层灰岩分布在向斜的核部,局部可见紧闭褶皱和尖楞褶皱。东部区的变质程度最深,但除了少

数地区（如城步），高级变质岩如角闪岩、混合岩等在研究区内并未出露。

此外，另一个重要的构造边界便是反向褶皱边界（BFB，图 3-1a），主要通过发育极性 SE 的褶皱和逆冲断层来区分，即在反向褶皱边界以西，没有或少见极性向 E 或 SE 的反向构造，而在以东，则出现了大量的极性 SE 的逆冲断层和褶皱（同斜褶皱），包括洞口地区大范围的地层倒转。总体上看，在雪峰山地区的构造边界在野外表现并不是非常鲜明，劈理的发育程度呈现一种渐变性，这一特点也表现在强应变带的周围——从弱变形砂砾岩到强变形或糜棱岩化石英岩。

整个雪峰山造山带在早中生代经历了复杂的多期构造变形。在构造解析劈理几何学、褶皱极性的基础上，我们在主变形分析研究区——东部识别出 3 组不同形式的构造特征，分别是以上部指向 NW 的韧性变形为特征，伴随着褶皱、劈理及线理的变形；以上部指向 SE 的韧性剪切，并伴随着极性 SE 褶皱和逆冲构造为特征的变形；以及在局部地区发育直立褶皱以及直立的轴面劈理的变形，在劈理面上可见直立拉伸线理。对于各个单元，将在下面各节对典型构造样式进行详细的介绍。

第三节 雪峰山主逆冲断层（会同县）

雪峰山主逆冲断层为一条近南部 N-S 走向、北部 NE-SW 走向、运动学指向 W 或 NW 的逆断层，同时也是主期次 S_1 劈理的前锋面（图 3-1b 和 3-3a）。其南北长约 200 公里，以北延伸至江汉盆地白垩纪和新生代沉积之下，向南至中生代右江盆地（图 2-1）。这条断层在地质图上大致与湖南省区域地质志上所述的靖州-溆浦断裂相对应，从北至南经过安化县、溆浦县、怀化市、会同县、靖州县等地区。

作为雪峰山造山带中最明显的线性构造，主逆冲断层带中发育了渗透性、密集的劈理构造，断层面倾角从近直立至近水平，但都倾向 SE 方向。断层上盘和下盘岩石的变形性质差异明显。上盘岩石为新元古代或早古生代浅变质砂岩或板岩，劈理发育；而下盘为新元古代至早中生代岩石，劈理微弱，仅发育在断层引起的褶皱核部。主逆冲断层还有一个明显特征为在造山之后晚中生代重新活动。由于白垩纪的伸展作用，在溆浦和怀化一带附近，这条断层又重新活动成为正断层，控制溆浦盆地和安江盆地的白垩纪沉积（图 3-1）。

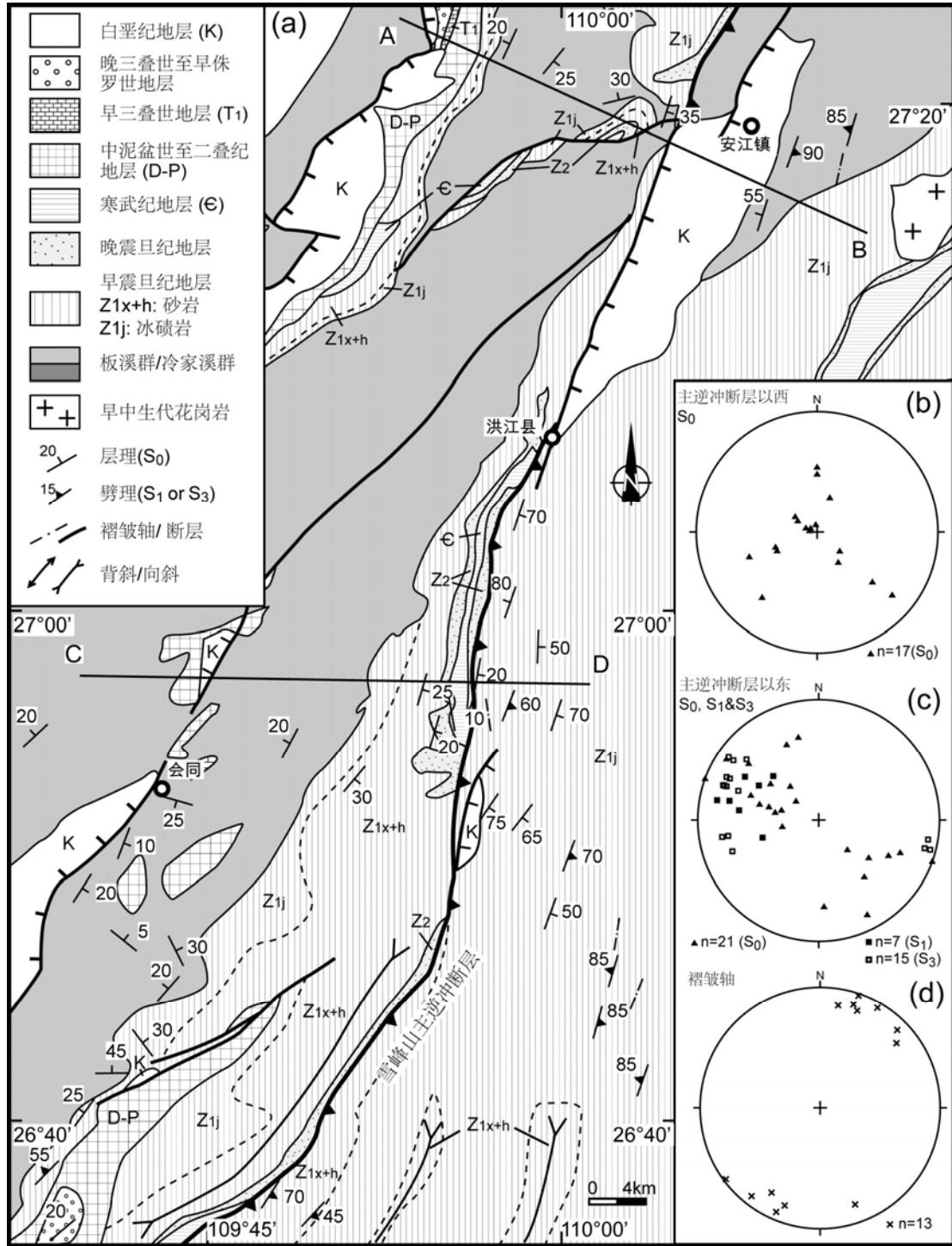


图 3-3 (a): 主逆冲带南端区域地质简图。构造要素施密特网下半球赤平投影 (b) 主逆冲断层以西层理; (c) 主逆冲断层以东层理、第一期劈理 S₁ 和第三期劈理 S₃; (d) 褶皱轴。

在主逆冲断层的北端 (图 3-1b), 安化县以北的板溪群砂岩中, 并没有观察到明显的断层面, 而是发育了大量的极性 NW 的褶皱。但是根据野外劈理的发育程度, 可以判断出断层的存在。断层东侧, 板劈理和同斜褶皱大量出现, 褶皱

两翼非常紧闭，轴面劈理几乎取代原生层理；断层西侧的褶皱随着与断层带距离的增加，褶皱由紧闭逐渐宽缓，进而转变为箱状褶皱。

本节，我们选取研究区南部会同县作为重点分析区域。会同县东侧的震旦系和寒武系之中主逆冲断层构造较为明显（图 3-3a）。一条厚约 10 米、向东部缓倾的高应变断层带，发育在寒武纪黑色页岩、板岩和片岩之中。这条应变带使得东侧断层上盘的弱变质、劈理化的震旦纪砂岩、砾岩逆冲至断层下盘产状水平、未经历变质作用的新元古代-寒武纪沉积岩之上（图 3-4a 和 3-4b）。在断层带上，岩石被强烈剪切，形成 σ 型剪切透镜体，指示上部向 W 的运动学方向（图 3-5a）。寒武系局部层位含碳质成分较多，因此变形也较为集中于这些能干性较弱的层位，发育了顺层滑脱构造（图 3-5c）。而在洪江县附近，断层带则以脆性为主，发育了碎裂岩和断层角砾岩。

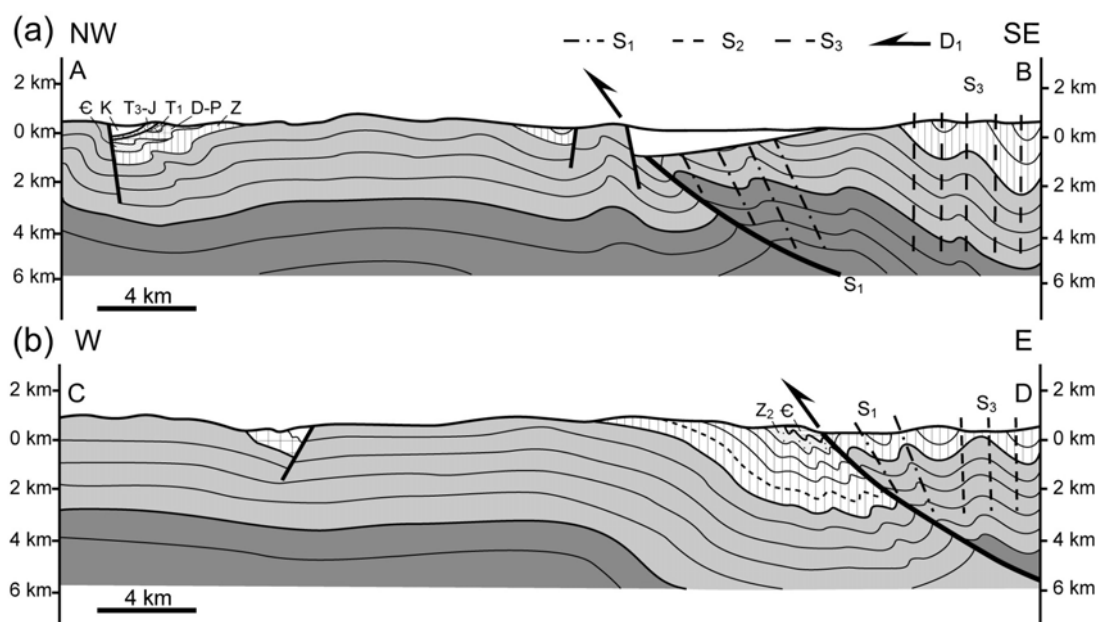


图 3-4 主逆冲带南端构造剖面图 (a) 安江, (b) 会同 (位置见图 3-3a)。

断层作用使得下盘形成了紧闭的同斜褶皱，指示了上部向 W 的韧性剪切（图 3-4b）；离断层带约两百米的地方，也有十米左右的较大型不对称褶皱，极性向 W（图 3-5b）。此外，在震旦系冰碛岩中，还发育了一组由定向砾石组成的劈理面（图 3-5d）。这组倾向朝西的劈理代表了一期极性向 SE 的构造，但是由于在反向褶皱边界以东，这是唯一一处见到的韧性反向构造，这并不能代表大范围的

SE 向的构造变形，因此我们倾向于将这个特殊的构造解释为由 NW 向逆冲断层构造产生的局部对冲（pop-up）构造。

随着远离与断层带之间距离的增加，剪切应变程度迅速降低。在断层带往西，地层产状逐渐变得平缓，层理主要为近水平或低角度的缓倾，同时在断层附近的强变形构造也消失了，除了宽缓的褶皱之外，不发育渗透性的劈理构造(图 3-3b)。断层带上盘往东，地层产状变化较大，表明褶皱构造较多，轴迹 NE-SW 向(图 3-3d)，劈理多以高角度(60°-80°)向 SE 陡倾(图 3-3c)，并逐渐转为直立(图 3-4a 和 3-4b)。

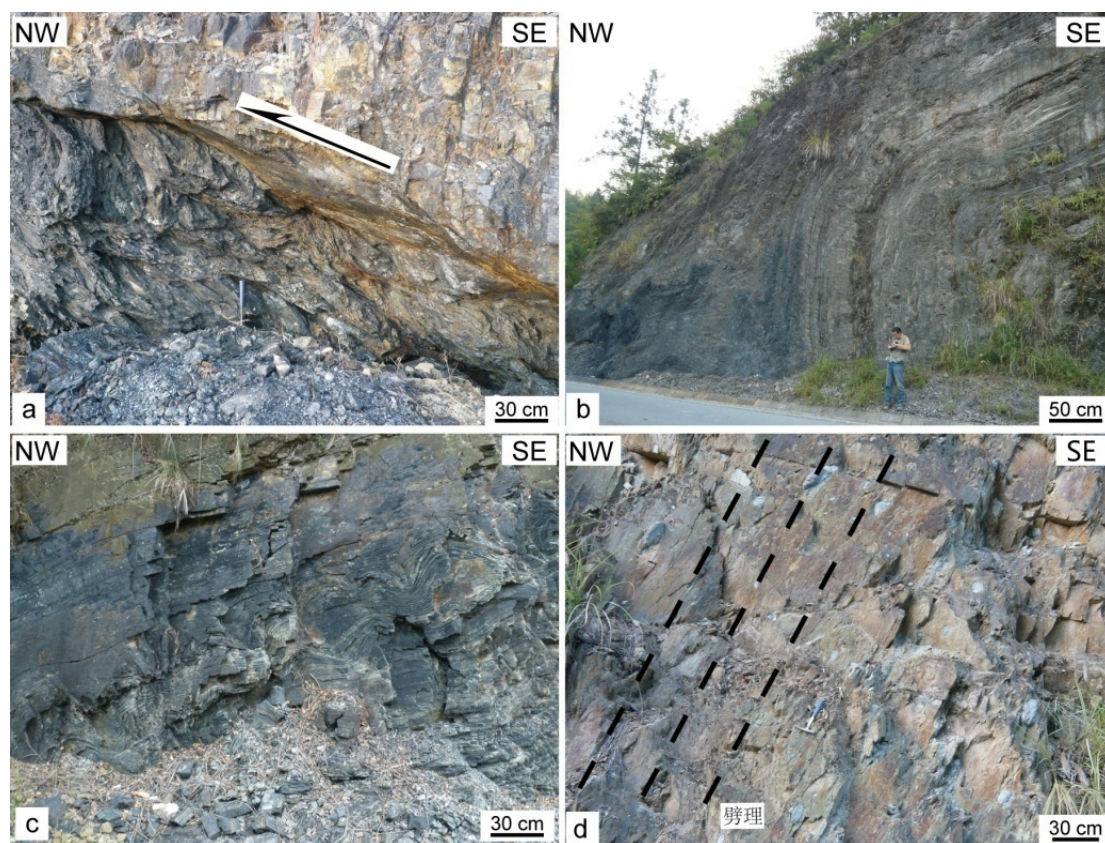


图 3-5 主逆冲带南端野外构造照片。(a) 寒武纪板岩之中发育的主逆冲断层，岩石受到强烈剪切之后呈 S 形，指示上部向 NW 的运动学方向。(b) 震旦纪岩石中发育的中等尺度、极性 NW 的褶皱。(c) 寒武纪页岩中的顺层滑脱现象。(d) 震旦纪冰碛岩中砾石定向构成的劈理面，倾向朝 NW，指示向 SE 的构造方向。

从区域上看，在雪峰山主逆冲断层以西出露的整个新元古代地层变形相当微弱，甚至没有变形迹象。地层总体上近水平，发育了少量的脆性节理构造，褶皱

多为呈现为公里等级的起伏。相反的，断层以东沉积地层卷入了强烈褶皱作用之中，褶皱相关的渗透性轴面劈理也广泛发育（图 3-3）。丘元禧等（1999）对这一地区也进行了构造分析，发现了早期向 W 的逆掩推覆构造和晚期反向滑覆现象。

第四节 西部区（武陵山）

西部区与东部区相比，变形强度较东部区弱，无变质作用和韧性变形。我们对武陵山地区，即张家界市以南进行了详细的地质考察（图 3-6a）。这一区域的构造线方向以 NNE-SSW 为主，形成了大规模的箱型褶皱，新元古代至志留纪地层均卷入了褶皱，变形以脆—韧性为主，劈理未见。

武陵山地区主要出露了从新元古代板溪群至早古生代志留纪的一套地层，岩石包括灰岩、砂岩、泥岩，均未经历变质作用。研究区南部，沅麻盆地的白垩纪红层不整合的覆盖着下伏的寒武纪至奥陶纪地层之上。北部，大庸（张家界）断裂切过研究区，通过野外观察，主要变现为逆冲断层性质，寒武纪或奥陶纪岩石被逆冲推覆至志留纪泥页岩之上（图 3-6b）。整个区域的地层产状走向均为 NE-SW 向，与褶皱的轴迹相同（图 3-6c 和 3-6d）。

大规模的箱状褶皱表明构造变形较强，但变现多集中背斜和向斜的翼部，核部区域地层水平，宏观上的变形几乎未见。如张家界南的背斜—向斜构造中，翼部的地层直立，不对称褶皱随处可见；一旦离开翼部，进入向斜或背斜核部，岩层产状迅速变缓，呈近水平状态，倾角多为 10-15 度（图 3-6a 和 3-6b）。在翼部，也并不是所有岩石均卷入变形。由于泥岩层固有的较弱的能干性，寒武纪黑色页岩和震旦纪泥岩、含煤层系中变形就强于灰岩和砂岩。因此当地层倾角在 70° 到 90° 之间时，沿着上述软弱岩层产生了大量的米到厘米尺度的滑脱褶皱和层滑作用（图 3-6b）。滑脱褶皱的极性总是背向背斜的核部，即位于背斜南东翼的指向 SE，反之亦然（图 3-7a 和 3-7b）。在能干性强的灰岩之中，层滑表现在断层的擦痕以及方解石脉之上，褶皱现象不明显。在岩层与岩层之间，可以观察到由于滑动形成的阶步（图 3-7c）；在武陵山南坡，方解石脉因为受到重力滑动而产生的剪切作用而发生了旋转，呈 S 型，表明剪切力为左行（图 3-7d）。本区域即使是出露最深的中晚元古代冷家溪群也没有经历过变质作用，由此可见西部区

处于整个雪峰山造山带构造层次的上部，缺少韧性变形和变质作用。

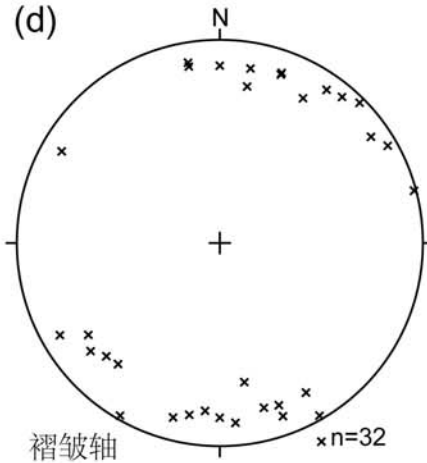
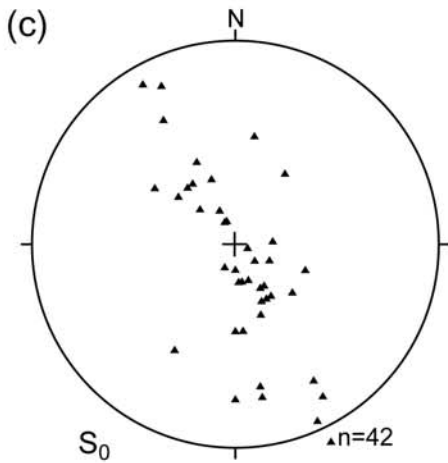
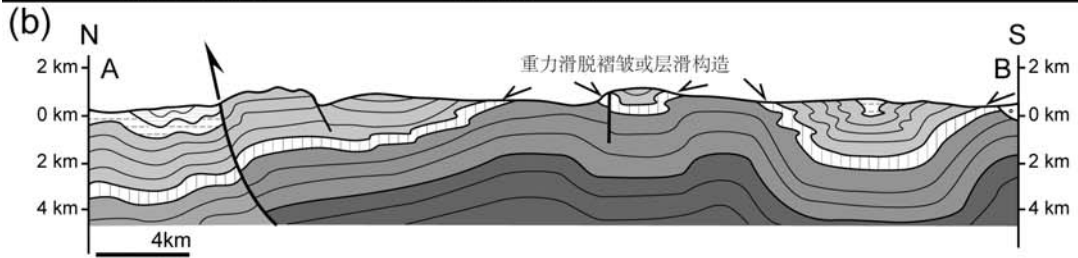
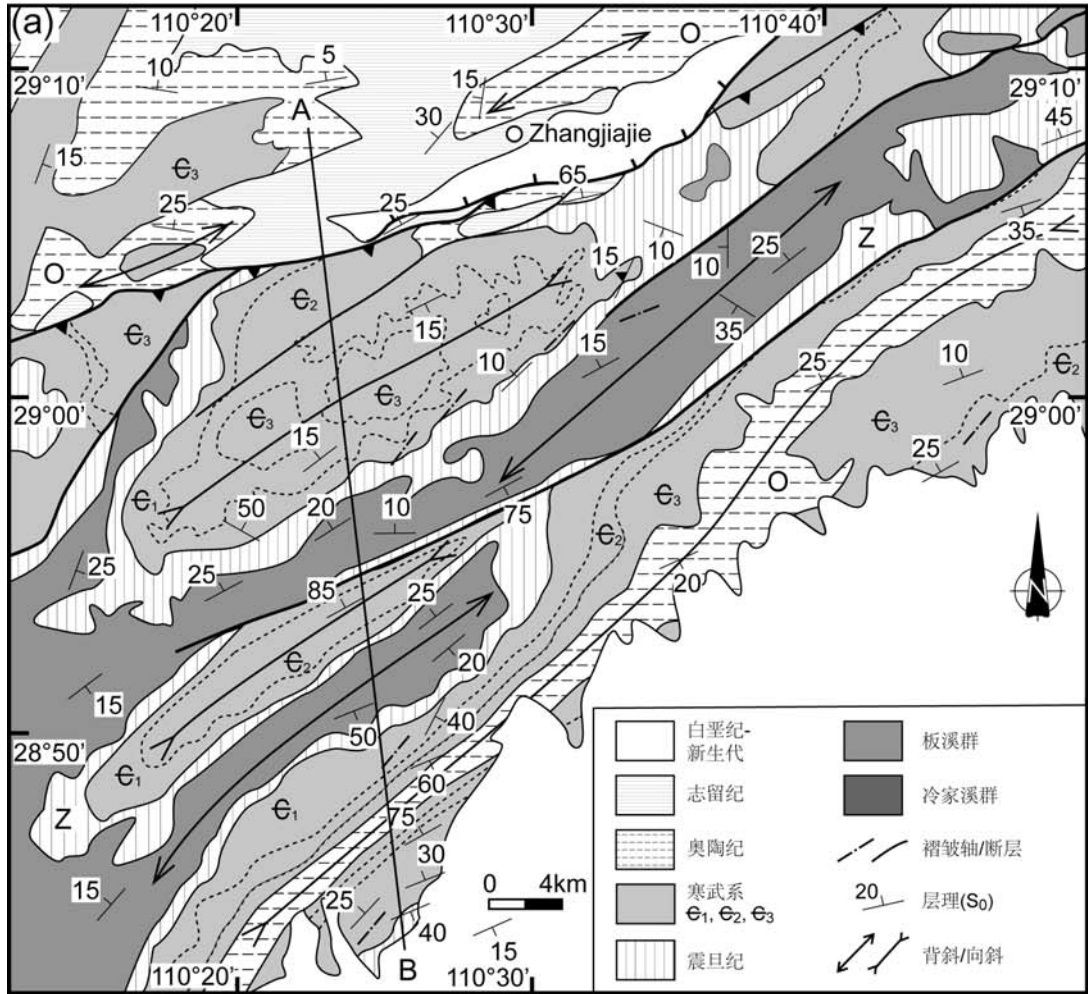


图 3-6 (a) 西部区武陵山地质简图。(b) 构造剖面图。构造要素施密特网下半球赤平投影
(c) 层理; (d) 褶皱轴。

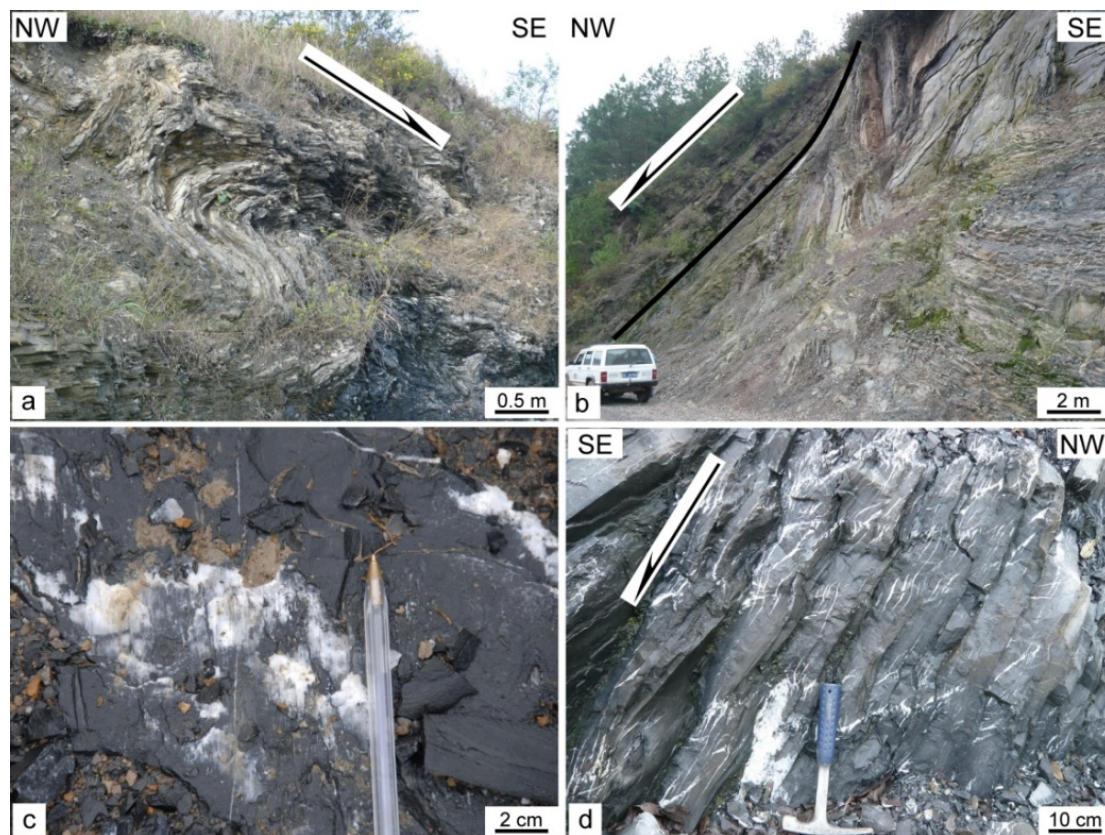


图 3-7 西部区（武陵山）野外构造照片。(a) 寒武纪灰岩之中发育重力滑脱褶皱。(b) 新元古代砂泥质岩石之中发育的正断层。(c) 寒武纪灰岩岩中的顺层滑脱产生擦痕。(d) 寒武纪灰岩中的方解石脉指示向 SE 的构造运动方向。

朱宝贵等（1988）曾对同一构造单元下的古丈背斜进行了详细的研究，认为主要存在三种变形机制，韧性剪切基底、盖层褶皱和盖层滑脱褶皱。而我们通过对武陵山的构造分析表明，主要变形机制为大型箱型褶皱，所谓的韧性剪切基底的构造并未出现，冷家溪群与板溪群和下古生界同属沉积构造单元，一起卷入了这一褶皱作用之中，并形成了逆冲推覆构造。在挤压抬升的同时，发生盖层滑脱褶皱。

第五节 东部区

东部区作为雪峰山造山带的主体区域，经历了强烈的构造变形和区域性低绿片岩相变质作用。东部区西部为地理上的雪峰山主体，出露了大量的中新元古代

沉积岩，这些岩石的变质与变形最大，而且在花岗岩体周边，由于隆升作用将深部的强应变主滑脱带抬升出地表。随着向东构造层次逐渐升高，出露岩石也转变为以泥盆纪至早三叠世沉积岩为主，变形逐渐减弱，变质作用消失。从东部区我们识别出 3 期构造变形，分别为上部向 NW 和上部向 SE 的剪切以及直立褶皱变形。本节将分区域详细讨论东部区沉积层的构造变形。

1 安化地区

安化地区位于雪峰造山带的北部，主要出露强烈劈理化的中晚元古代的砂岩和泥质岩（图 3-8a 和 3-8b）。安化以北的冷家溪群和板溪群砂岩、泥岩之中发育了走向 N70-90E、向 SE 陡倾的渗透性劈理，这一期劈理向南越来越强，逐渐替代了 S_0 原生层理（图 3-9a）。但是在褶皱的不同部分，劈理面的倾角会稍微有所变化，有的地方近水平，有的地方则近直立（图 3-8d）。例如在同斜或横卧褶皱中，正常翼的劈理倾角较陡，大于地层倾角。但在褶皱的轴部劈理面则逐渐变缓；在褶皱倒转翼则地层倾角大于劈理倾角。

安化以北，一条数米厚、运动学指向 NNW 的强烈变形带将新元古代砂岩逆冲至古生代地层之上（图 3-8a）。而在有些区域，新元古代地层在逆冲至泥盆纪灰岩之上。断层带上砂岩被强烈剪切破碎，形成大量的断层角砾岩，同时砂岩碎块在剪切作用下与碎基构成 σ 形构造，指示上盘向北西的运动学方向（图 3-9b）。在冲断层的下盘，灰岩被强烈褶皱和剪切（图 3-9c）；而在断层上盘，砂岩不仅被褶皱，同时形成了渗透性轴面劈理，倾向南西。在新元古代砾岩中，由于强烈的剪切变形，砾石发生定向拉长现象，沿 100-120 方向定向，并可见基质围绕在砾石变上形成的剪切压力影。

安化以南，劈理面从倾向 SE 逐渐演变成直立，随后倾向 NW（图 3-8a, 3-8b 和 3-8d）。在震旦纪到奥陶纪的岩层之中，原生层理也由于直立褶皱的作用倾角逐渐变大，同时发育直立的轴面劈理（图 3-9d）。这一块区域可以称为直立劈理区，但是整体上与 SE 倾向的劈理区呈过渡关系，并没有明显的界限。

直立劈理区以南，劈理面再次变化，开始倾向 NW，广泛的存在于震旦纪到泥盆纪地层之中，也可以和雪峰山中部洞口地区、南部的绥宁地区相对应（图 3-1b）。因此我们在本文中将这从北至南的雪峰山山地东侧的条带区域成为反向

褶皱区，作为东部区的一个重要次级分区，其所涵盖的区域大致为山脉隆起东缘的泥盆纪砂岩、灰岩至震旦系的连续地层区域。

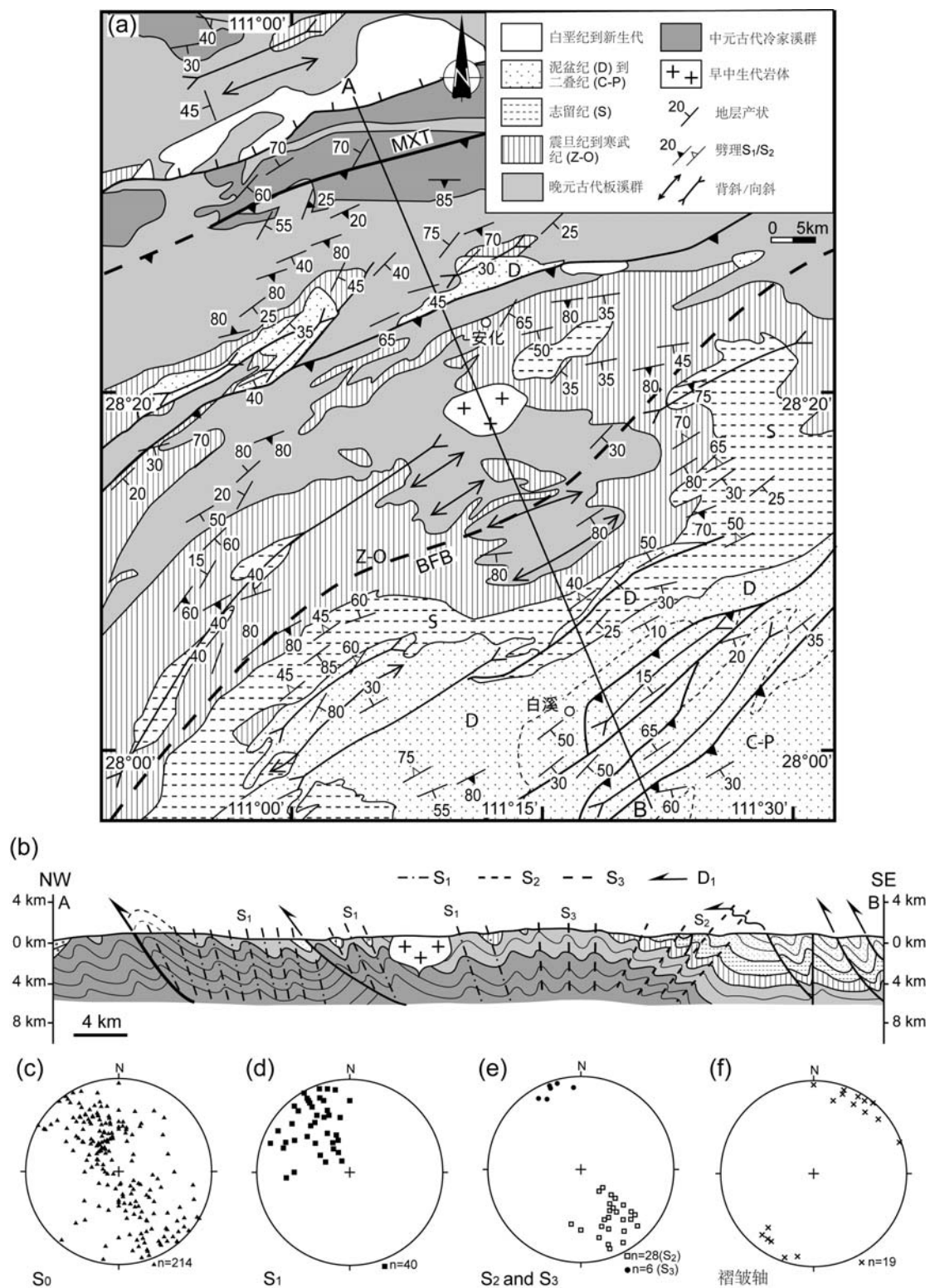


图 3-8 (a) 安化区域地质简图。(b) 构造剖面图。构造要素施密特网下半球赤平投影 (c) 层理；(d) S₁；(e) S₂ 和 S₃；(f) 褶皱轴。

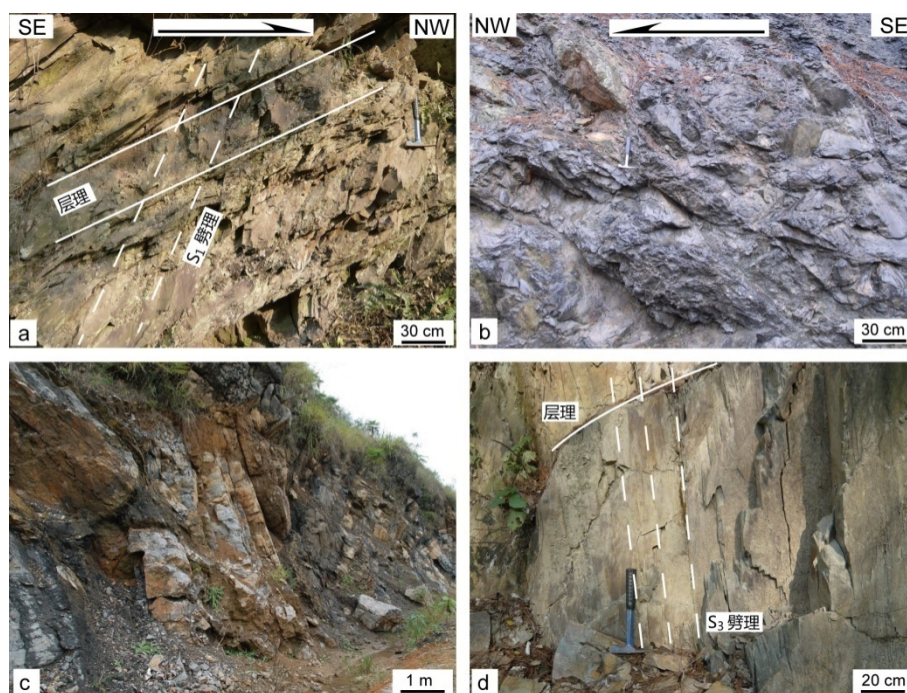


图 3-9 安化地区西北区构造典型照片。(a) 新元古代砂岩发育强烈劈理，指示上部指向 NW 的变形。(b) 构造破碎带，岩石被强烈剪切，局部与基质构成 σ 构造，运动学为上部指向 NW。(c) 安化县城附近逆冲断层下盘强烈褶皱破碎的泥盆纪灰岩。(d) 直立褶皱区近直立发育的劈理构造，层理因为褶皱作用而弯曲。

在这个与 NW 极性变形反向的褶皱区域里，构造现象发育最为强烈的是在洞口地区，形成了大面积的地层倒转，我们将在本节第三部分进行详细阐述。而在安化地区，极性向 SE 的褶皱虽不及洞口地区强烈，但是也形成了大规模的 NW 倾向的褶皱、逆冲断层和褶皱。安化以南，志留纪泥岩中发育了密集的劈理构造，地层也被褶皱，劈理和褶皱均指示了上部向 SE 的剪切变形（图 3-10a）。类似的，泥盆纪的砂岩层在褶皱作用下直立，存在大量的极性 SE 的褶皱形成的劈理，虽然由于岩性的差异并没有志留纪泥岩中强烈（图 3-10a），但这些劈理连续的发育在不整合面之上的泥盆纪和之下的志留纪岩石之中，清楚地表明这期构造在不整合作用之后，不可能是早古生代造山事件的产物。

在野外考察过程中我们发现，在极性 NW 的构造作用明显的地方，没有上部向 SE 的剪切构造出现；而在后者发育的地方，虽然 NW 方向的构造不发育，但是总会残留一些构造作用的痕迹。如图 3-11 所示，新元古代泥砂岩被极性 SE

的褶皱所变形，整体上倾向 NW 的劈理占主导地位，同时，我们也观察到一些倾向 SE 的劈理不和谐的出现泥岩层中，而且在背斜的两翼均有发育，因此不能用顺层滑脱来解释。因为若是在褶皱过程中发生了顺层滑脱，两翼的泥岩层中形成的劈理倾向应是向对的，而不是统一的倾向。

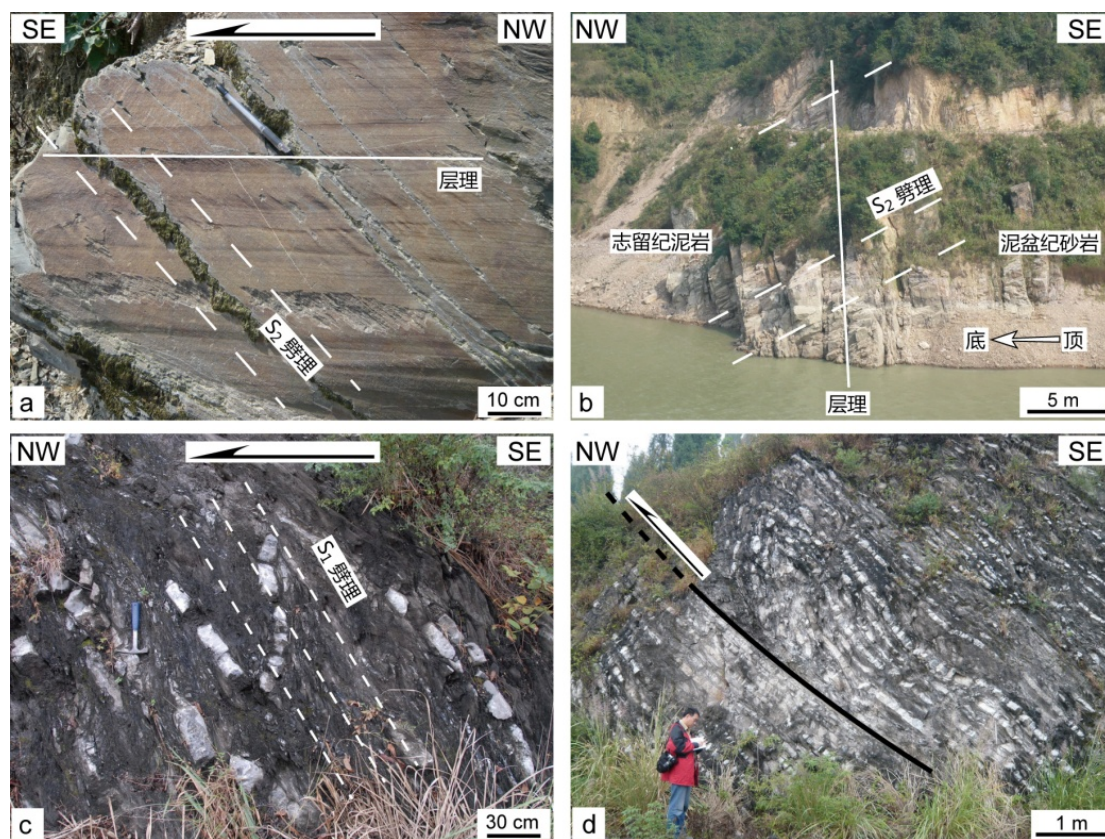


图 3-10 安化地区东南区构造典型照片。(a) 志留纪泥岩中密集发育劈理，指示上部指向 SE 的变形。(b) 泥盆纪砂岩和志留纪页岩中不整合，页岩因为风化层理不清楚，而砂岩层理直立，同时可见劈理向 NW 缓倾。(c) 白溪镇附近互层泥岩灰岩中，泥岩发育劈理，而能干性较强的灰岩则布丁化，褶皱明显。(d) 白溪镇附近运动学指向 NW 的断层极其伴生褶皱。

白溪镇以北，志留纪到泥盆纪地层整体上向 NW 方向缓倾，走向 N20-50E。整个地区都经历了上部指向 SE 的剪切作用。而到了白溪镇，构造样式发生了转变（图 3-8a 和 3-8b）。在石炭纪和二叠纪互层的灰岩和泥岩中，形成了大量的向 NW 推覆的逆冲断层及断层相关褶皱，构造形迹又以上部指向 NW 的剪切变形为主。在石炭纪岩石中，当互层的灰岩泥岩以泥岩为主时，由于灰岩的能干性强，成为褶皱的标志性岩层，并且在外力作用下以布丁的形式夹杂于基质的黑色泥岩

之中。相反的，泥岩能干性弱，则发育了密集排列的 SE 倾向的劈理（图 3-10c）。在剪切变形的作用之下，泥岩中劈理与原生层理的相互作用下形成了类似铅笔构造的现象。在以中薄层灰岩为主的地方，沿层理发育了多组逆冲断层，及由于逆冲作用而产生的不对称同斜褶皱（图 3-10d）。

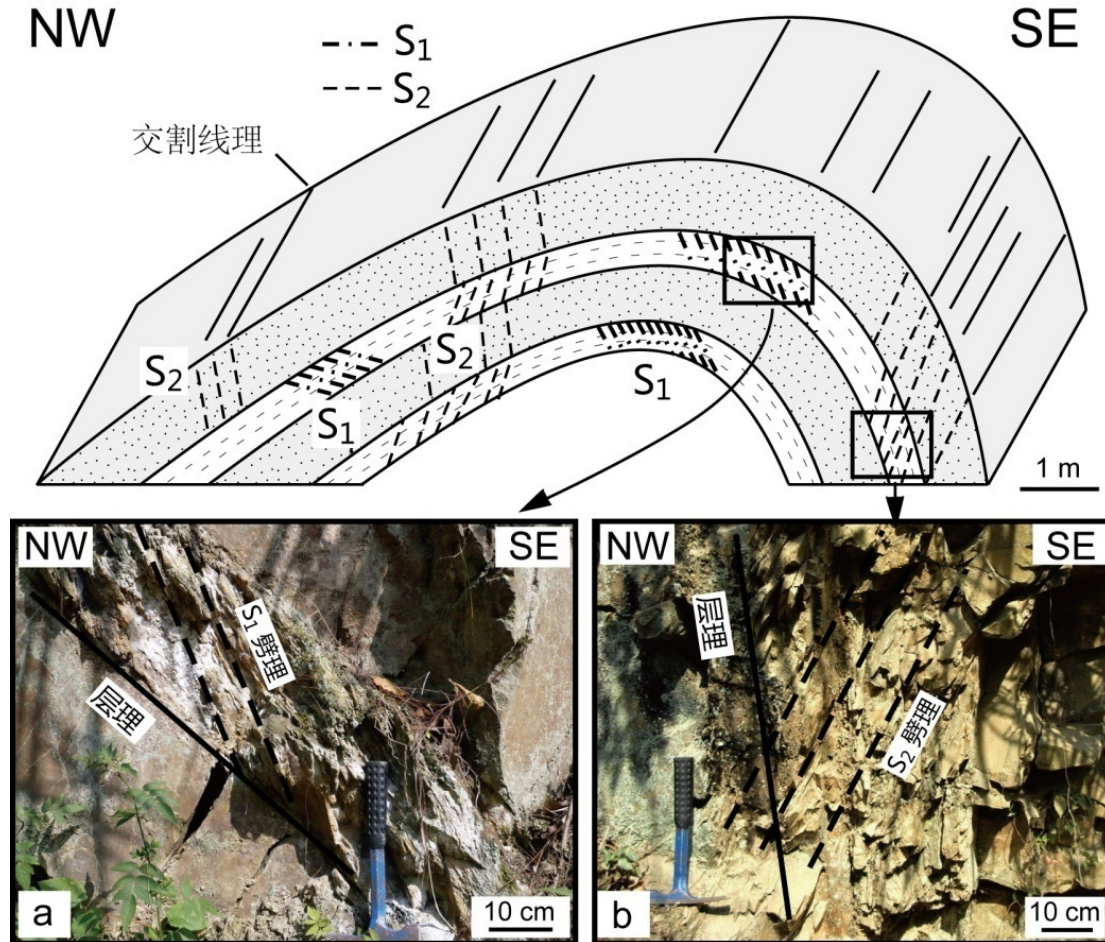


图 3-11 安化地区构造叠加示意图及野外照片。(a) 泥质岩层中残留的 S_1 劈理。(b) 在泥质岩层和砂岩层均发育的倾向 NW 的 S_2 劈理。

安化地区是雪峰山造山带变形最为强烈的区域之一，集中发育了雪峰山的 3 期构造变形。其中上部指向 NW 的变形最为强烈，在安化西北部表现最为明显。Wang et al. (2005) 通过对主要断层的构造工作，认为在怀化—沅陵断裂和靖县—溆浦断裂间构造以 NW 向逆冲为主，并对新元古代地层中的强应变岩石进行 Ar-Ar 定年，获得了 194.7 ± 0.3 Ma 的全岩年龄。对于上部指向 SE 的剪切，Wang et al. (2005) 认为是次级的反冲构造，以通道—安化断裂为代表。而我们依据野

外获得的构造叠加关系认为, 极性 SE 的韧性剪切改造了极性 NW 的构造, 如劈理等, 因此二者并不是同期形成的。而且, 安化南部大神山岩体侵位于褶皱地层之中 (图 3-8a), 续海金等 (2004) 对其进行锆石 SHRIMP 测年后结果为 211 Ma, 因此这与韧性变形时间有近 20 Ma 的差距, 我们认为 Wang et al. 所获得的 Ar-Ar 年龄应该代表了冷却年龄, 而不是变形的时间。

2 溆浦地区

溆浦县位于白垩纪盆地之内, 而雪峰山的主逆冲断层经过溆浦县城东北, 这个断层同时也是溆浦盆地的边界断裂, 这说明主逆冲断层在白垩纪时再次活动, 但是以正断层的形式, 控制了溆浦盆地内的白垩红层的沉积 (图 3-1)。由于靠近主逆冲断层, 因此溆浦县附近的构造作用也相当强烈, 岩石遭受明显的褶皱作用, 形成了密集发育的劈理。

在溆浦县东, 寒武纪和奥陶纪的灰岩被强烈的剪切变形, 这在雪峰山地区都非常少见。灰岩和泥岩互层的地方可以观察到明显的灰岩层的错断, 而同时错断方向相互平行, 表明劈理很发育, 倾向 SE, 表明与安化县北部一起经历了强烈的上部指向 NW 的韧性变形。在泥质成分更多的地方, 剪切作用产生大量密集发育的劈理, 与原生层理形成 30-40 度的夹角, 结合灰岩中的劈理, 二者均指示了上部指向 NW 的运动学方向 (图 3-12a 和 3-12b)。

强烈的构造作用同时也发生在震旦纪和新元古代的地层之中。如图 3-12c 所示, 震旦系砂岩中形成了非常紧闭的同斜褶皱, 褶皱轴面劈理广泛发育, 并几乎取代了原生的沉积层理, 成为岩石的主要特征。因此我们认为在这一区域的面状构造均为劈理, 而不是层理。低角度的逆冲断层也时常可见, 虽然逆冲幅度不大, 但均代表了上部指向 NW 剪切变形构造的产物 (图 3-12d)。直立褶皱在溆浦地区东南也较为常见, 主要表现为密集发育的直立劈理以及大规模的直立褶皱。在新元古代砂岩中, 岩层在被褶皱的同时, 由于强水平应力的影响, 局部形成的直立劈理已经将岩石沉积层理彻底抹去 (图 3-12e), 有些区域则可以观察到原生的层理在整体褶皱的基础上, 还产生类似缝合线的次级褶皱构造。此外, 我们还观察到了波长达上百米的直立褶皱 (图 3-12f)。

前人通过对雪峰隆起区的研究认为, 怀化—溆浦地区存在着大规模的推覆

带，形成了辰溪—怀化飞来峰构造带，存在着大大小小数十个飞来峰，同时对方解石包裹体测温推测推覆前岩石所处深度在 7-8 公里（据成都地质学院，四川黑水至福建泉州地学大断面构造地质研究报告）。结合我们的研究表明，这一地区的挤压推覆构造相当明显，发育了大规模的上部指向 NW 的剪切变形。岩石中劈理构造强烈，表明形成在韧性剪切变形域，深于 5 公里，与前人研究吻合。

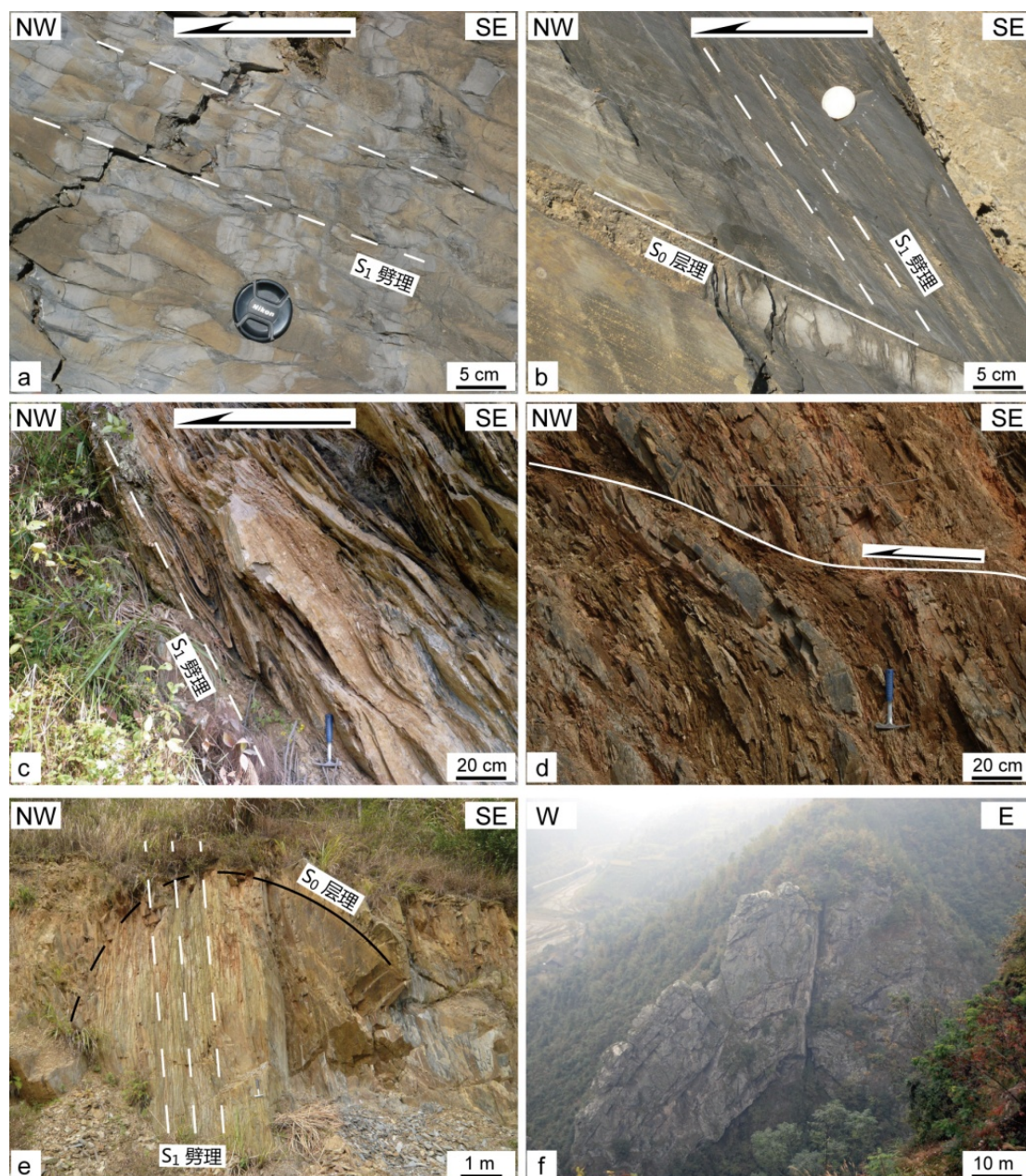


图 3-12 溆浦地区构造野外照片。(a) 被强烈剪切的寒武纪灰岩。(b) 泥岩中形成的 S_1 劈理。(c) 震旦纪粉砂岩夹泥岩中形成的同斜紧闭褶皱， S_1 劈理已基本取代 S_0 层理。(d) 砂泥岩中的逆冲断层。(e) 新元古代砂岩中的直立褶皱以及轴面劈理。(f) 大型直立褶皱。

3 洞口地区

洞口县附近最明显的构造表征是存在着大规模的地层反转现象, 这些与区域上广泛分布的 NW 极性构造方向相反, 因此我们认为是反向褶皱的产物, 其中反转构造所卷入的地层主要包括了新元古代上部、震旦系至泥盆系底部的岩层 (图 3-13a 和 3-13b)。

在月溪镇西北, 寒武纪至志留纪泥岩和粉砂岩受到浅变质作用而转变成板岩, 卷入了 NE-SW 走向、极性 SE 的褶皱之中, 并伴生倾向 NW 的轴面劈理广泛的发育于这一区域的岩石之中, 倾角随着处在褶皱的位置不同而变化 (图 3-13c)。先前存在的极性 NW 的褶皱在上部指向 SE 的剪切作用中被再褶皱, 形成了叠加褶皱, 而新生的褶皱极性均是极性朝向 SE。

在寒武纪和奥陶纪浅变质泥岩之中, 原生的沉积构造仍被较好的保存下来, 如重荷模和波痕构造。在褶皱作用之下, 原来应该在底面的重荷模出现在地层顶面之上, 相应地, 波痕则出现在底面之上, 这些证据充分证明了地层倒转现象的存在 (图 3-14a 和 3-14b)。洞口县城以西和以北, 在志留纪粉砂岩和泥岩中可见极性 SE 的褶皱以及 S₂ 劈理构造 (图 3-14c 和 3-14d), 其中劈理主要发育在泥岩或含泥质岩石, 能干性相对较强的砂岩中则较为少见, 或者时而可见劈理折射现象, 即由于性质不同, 不同岩石产生的劈理角度有所不同, 形成类似光线折射的构造现象。紧闭的横卧褶皱也是反向构造的直接产物 (图 3-14e)。

洞口县城西约 5 公里处, 泥盆纪砂岩以角度不整合的形式覆盖在志留纪的砂岩和页岩之上, 不整合面与地表呈~70 度角 (图 3-14f)。丘元禧等 (1999) 在文中特别提到了这个不整合面, 认为在不整合面下志留纪地层中发育了一组轴面劈理, 但是没有穿过不整合面, 所以认为劈理构造是发生于加里东期变形的产物 (丘元禧等, 1999)。我们通过详细观察发现, 在野外露头中, 不整合面的上下均为砂岩, 二者交角在 30-40 度, 说明早古生代的构造事件影响到了这一区域。但是在不整合面的上下由于砂岩的能干性较强, 劈理均为发育。而在离不整合面向东 50 米的地方, 泥盆系的砂岩中可以观察到向 SE 倾斜的渗透性劈理 (图 3-14g), 而且在洞口以西的泥盆纪灰岩中, 我们还发育有极性 SE 的褶皱和倾向 NW 的轴面劈理。与之相对应的, 不整合面以西大片的连续露头里, 志留系中发育了同样

的极性 SE 的剪切构造和倾向 NW 的劈理，充分表明这次构造事件发生在早古生代构造活动之后切穿了不整合面。区域上的褶皱作用不仅造成不整合面的掀斜现象，还使得泥盆纪地层直立（图 3-14g）。同样的地层直立现象在在安化地区也有出现，说明整个雪峰山构造带均遭受了极性 SE 的反向褶皱作用，但向南东反向出了泥盆纪地层之后，反向褶皱就明显减弱，直至重新以 NW 极性的褶皱和逆冲构造为主导（图 3-13a 和 3-13b）。

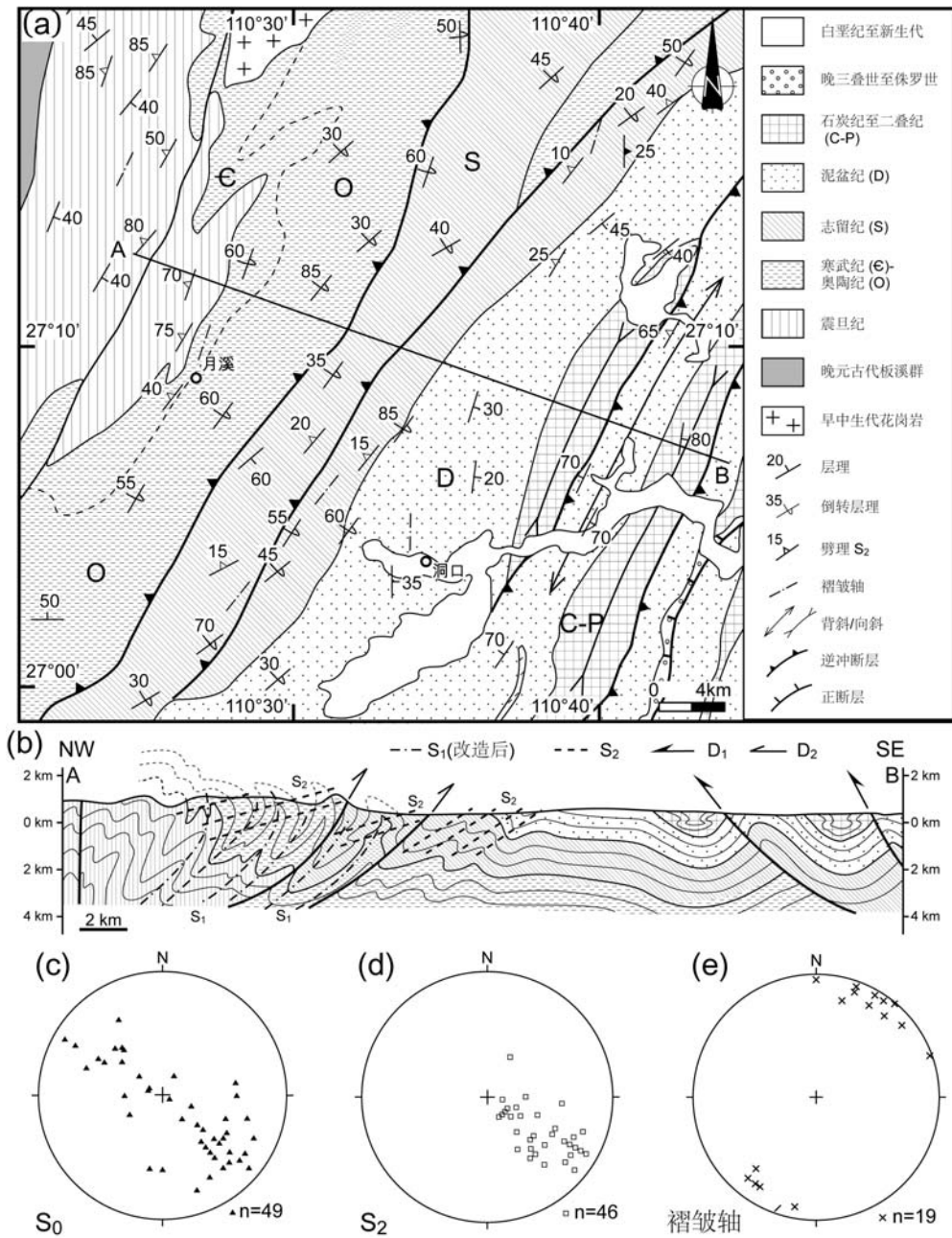


图 3-13 (a) 洞口区域地质简图。(b) 构造剖面图。构造要素施密特网下半球赤平投影 (c) 层理 S₀; (d) S₂; (e) 褶皱轴。

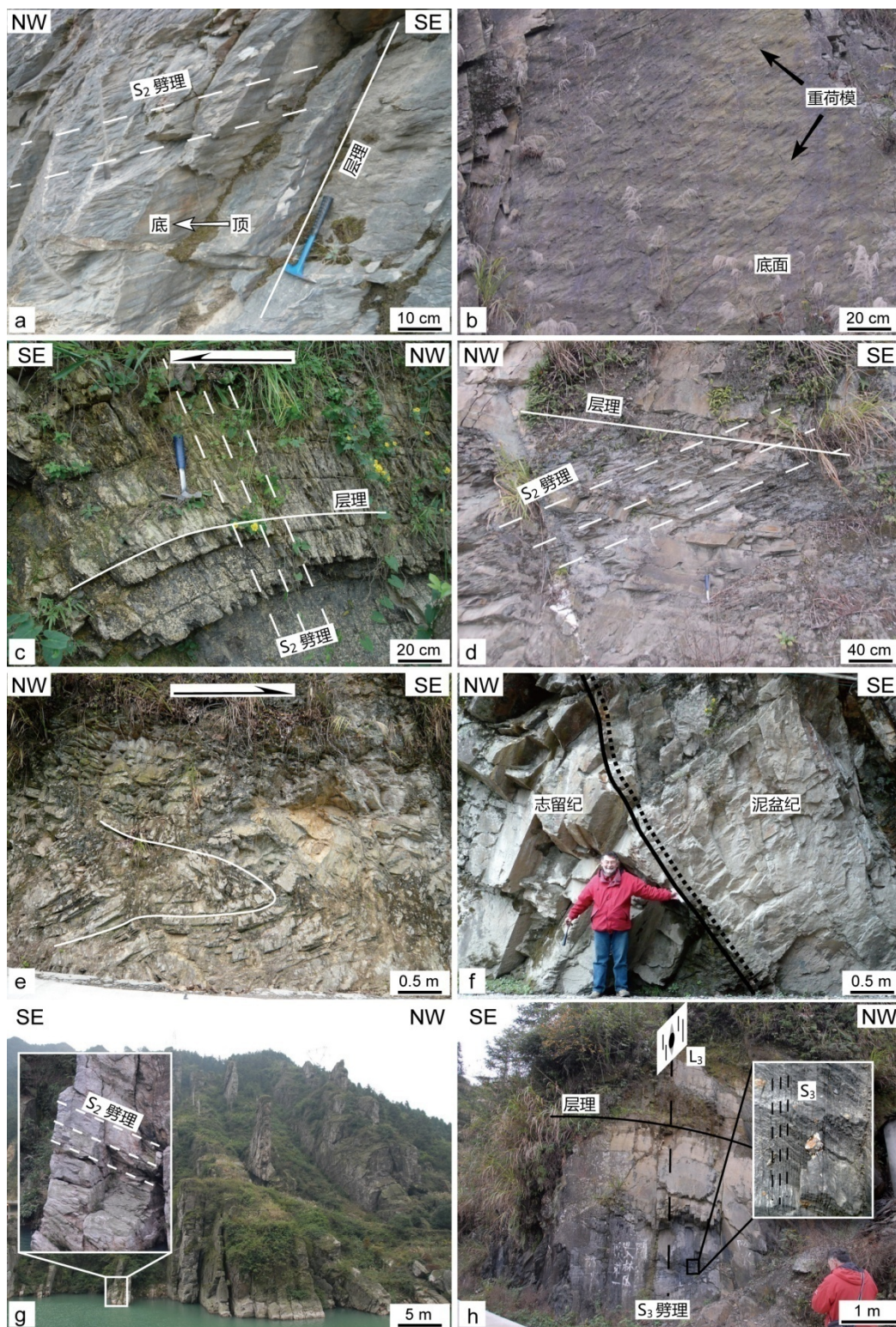


图 3-14 洞口地区构造野外照片。(a) 倒转的奥陶系泥岩层，具有波痕的顶面朝下，同时发育了劈理。(b) 砂岩底面重荷模朝上指示着地层倒转现象。(c) 志留纪粉砂岩夹泥岩中形成的极性 SE 的褶皱，劈理强烈发育。(d) 砂泥岩中的倾向 NW 的劈理。(e) 志留纪砂岩和泥岩中的横卧褶皱，运动学指向 SE。(f) 志留系和泥盆系之间的不整合界面，劈理构造同时发育于不整合面上下。(g) 泥盆纪砂岩的直立地层。(h) 奥陶系板岩中发育的直立褶皱以及直立劈理，劈理面上发育了黄铁矿压力影构造的直立线理。

最后,直立褶皱作为雪峰山早中生代造山带多期构造变形中的一期也在寒武纪和奥陶纪的板岩之中发育。轴面劈理形成的 S_3 面上还形成了流体成因的黄铁矿,同时在黄铁矿周边产生了压力影构造,压力影的长轴方向直立,代表了 L_3 线理方向(图 3-14h),这一期的构造影响较弱,仅在局部发育。

4 涟源地区

本区位于雪峰山东部区的东缘,沉积盖层主要以泥盆纪至早三叠世地层,晚三叠世陆相砂岩和砾岩不整合的沉积在下伏地层之上,局限地分布在山间盆地之中。震旦纪至志留纪地层在本地区出露非常局限(图 3-15a)。尽管如此,本区的构造线方向为 NEE-SWW,主要以广泛发育的褶皱和逆冲断层为主,但是劈理的发育程度明显弱于东部区的西缘,如安化和洞口地区(图 3-15b, 3-15c, 3-15d 和 3-15e)。这些特征表明涟源地区处于构造层次相对较高的地区。

冷水江以北,泥盆纪砂岩向 NW 逆冲至石炭纪灰岩之上,而相应的,石炭纪灰岩在局部则逆冲至二叠纪的灰岩之上(图 3-15b)。在夹有灰岩的泥岩中,倾向 SE 的劈理密集的发育在泥质层中,指示了朝向 NW 的构造变形(图 3-16a)。在这个逆冲推覆系统中,泥盆纪、石炭纪和二叠纪的含煤岩层由于强度较弱,起到了滑脱带的作用。而在砂岩和灰岩岩层之中,劈理很少发育。有时,在强烈的挤压作用影响下,断层下盘的岩层发生的明显的褶曲,局部形成了大型平卧褶皱(图 3-16b)。

此外,上部指向 SE 的剪切构造变形在本区也局部发育,但没有形成密集发育的劈理,主要表现为极性 SE 的褶皱和断层(图 3-16c)。例如,在冷水江东北的石炭纪岩层中,宏观上构造现象以上部指向 SE 的韧性剪切形成的反向褶皱和反向逆冲断层为主,但是在泥质岩夹层里可以观察到残留的早期倾向 NW 劈理构造形迹(图 3-15c)。此外,在泥盆纪的互层砂岩泥岩之中,早期形成的倾向 SE 劈理被极性 SE 的褶皱弯曲,劈理的倾角随着褶皱而改变(图 3-16d),而且同样的褶皱也发育于志留系复理石层系之中。

东部区的另一个构造特征与西部区类似,就是形成了大量的背斜边缘的重力滑脱褶皱、层滑构造以及正断层。在区域尺度上的背斜边缘,存在滑脱带的地层例如三叠纪的含泥质岩层,就容易形成滑脱褶皱(图 3-16e)。局部地区这些构造

更加明显,如在一个数十米的露头上,在第一级的褶皱两翼分别形成次级正断层,同时形成了极性相反的重力滑脱褶皱(图 3-16g)。在向斜的核部,由于挤压作用以及后期两侧重力滑脱使得早三叠世的薄层灰岩的空间受到横向的强烈压缩,因此形成非常紧闭的尖楞褶皱(图 3-16f)。

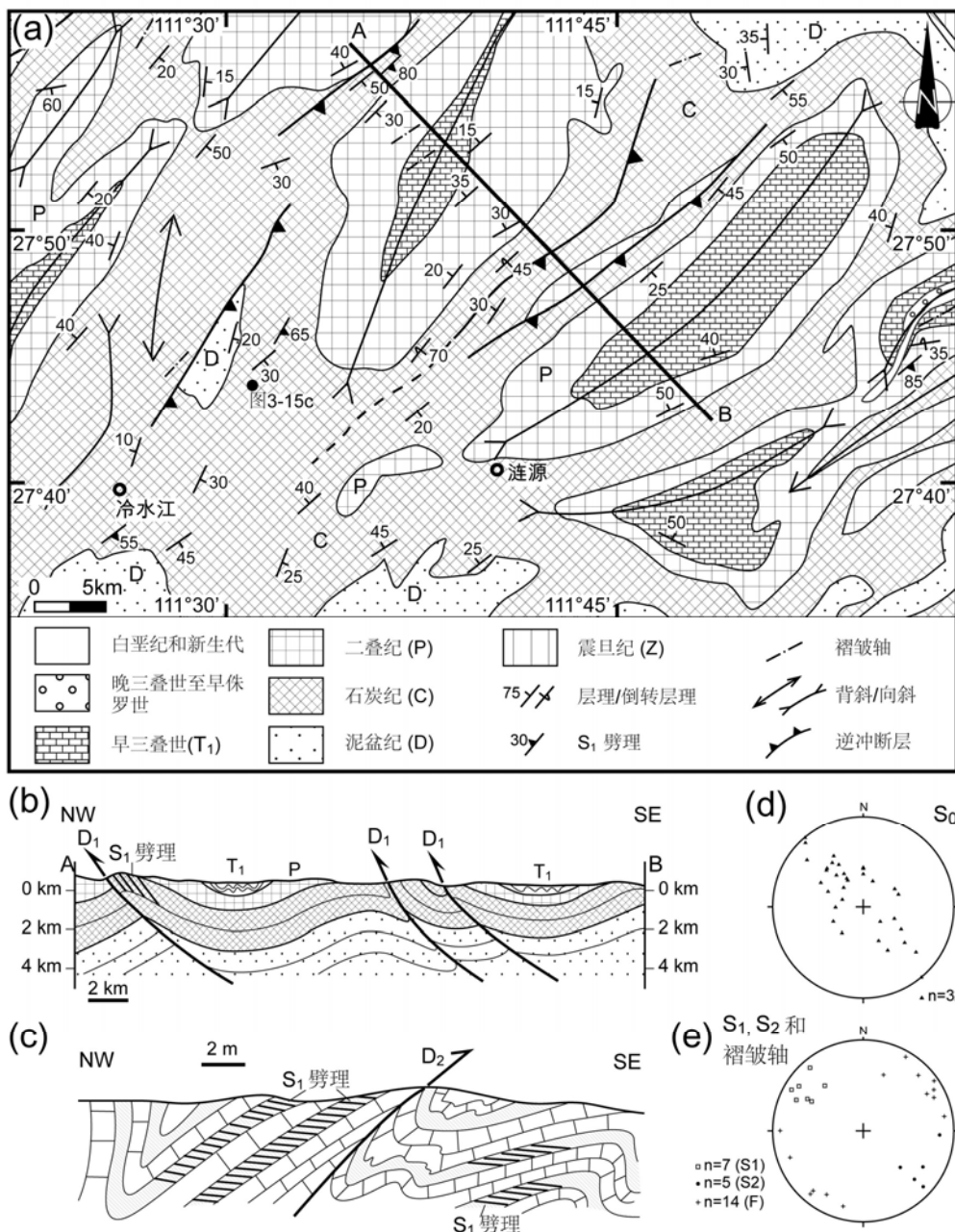


图 3-15 (a) 涟源区域地质简图。(b) 和 (c) 构造剖面图。主要构造要素施密特网下半球赤平投影 (d) 层理 S₀; (e) S₁、S₂ 和褶皱轴。



图 3-14 东部区东缘涟源地区的典型构造的野外照片。(a) 石炭纪泥岩夹灰岩中的泥岩层发育的 S_1 劈理，而灰岩层则未见劈理。(b) 石炭纪灰岩中逆冲断层，下盘在冲断过程中形成了大型横卧褶皱，断层运动学指向 NW。(c) 石炭灰岩中的极性 SE 的逆断层及断层伴生褶皱。(d) 泥盆纪粉砂岩夹泥岩中早期 S_1 劈理被 F_2 褶皱所改造，同时可见劈理折射现象，表明构造作用发生于早古生代不整合作用之后。(e) 重力滑脱褶皱，褶皱极性指向向斜核部。(f) 向斜核部的早三叠世灰岩遭受强烈挤压。(g) 直立褶皱及其两翼形成的次级重力滑脱褶皱和正断作用。

在衡阳市的北东，柏道远等（2009）根据钻孔数据发现新元古代浅变质砂岩

向北西逆冲到泥盆纪的砂岩之上，表明东部区广泛存在着 NW 向的构造变形，而且构造变形时间在早古生代之后。

此外，在邵阳市北边（图 3-1），震旦纪至泥盆纪岩层中发育了大量的倾向 NW 的劈理、极性 SE 的褶皱和断层，这些构造都是上部指向 SE 剪切变形的产物，与前面洞口和安化地区的反向构造一致。因此整个东部区的格架是以运动学指向 NW 的构造为主，包括不对称褶皱和逆冲断层，之后这些构造又被极性 SE 的褶皱和断层所叠加，从北至南的构造完整性非常好，各构造带呈连续分布。

第六节 小结

整个雪峰山造山带主要以沉积岩盖层为主，仅仅在局部花岗岩侵位过程中将深部变质岩揭露出地表。从中-新元古代至早三叠世，雪峰山地区接受了厚度在 10 公里以上的沉积，晚三叠世至早侏罗世的砾岩和砂岩不整合的覆盖在下伏地层之上。其间还存在着一个中晚泥盆世砂岩与早古生代岩石间的不整合。

我们通过详细构造分析将雪峰山分为两个主要构造带，西部区和东部区，二者由雪峰山主逆冲断层相分隔。作为雪峰山的主要分界线，同时也是劈理前缘，主逆冲断层在地表主要以逆冲断层和两侧劈理构造的差异性发育为野外特征。作为劈理前缘，主逆冲断层在构造层次分析上具有重要的意义。Mattauer（1980）根据不同的变形机制，并结合构造几何学、深度、变形强度及动力学条件等因素综合考虑，把山脉的整体划分为上中下三个构造层（或构造域），劈理发育的区域属于下构造层，劈理前缘为此构造层的顶界，深度约为 5 公里，此界面以下岩石以强塑性压扁和韧性剪切为主，并过渡至流动变形域（许志琴, 1984）。因此，沿雪峰山主逆冲断层，深层次韧性变形物质被逆冲至地表。主逆冲断层的断层面在南部会同地区出露最为完整。发育在寒武纪黑色片岩之中逆冲断层，将上盘密集发育劈理的新元古代-震旦纪砂岩、粉砂岩逆冲至下盘的无明显构造变形的新元古代-寒武纪岩层之上。而北部安化地区未见明显的断裂带构造，而以劈理的发育差异为标志，断层带以南发育渗透性劈理构造，以北密集劈理不再出现。

西部区以大型箱状褶皱为特征，同时在箱状褶皱两翼地层近直立处出现了极性背向背斜的重力滑脱褶皱，二者向斜和背斜的核部，地层产状近水平，仅可见宽缓的褶皱。东部区可再细分为雪峰山主体部分——经历了低绿片岩相变质作用

及韧性变形, 以及东缘延伸部分——以未变质但强烈变形的泥盆纪至早三叠世岩石为主。这两个部分均发育有上部指向 NW 的和上部指向 SE 的剪切, 以及水平缩短产生的挤压构造。其中, 在安化、洞口、涟源等地区均能见到早期倾向 SE 的劈理被后期褶皱所改造。在区域性的中晚泥盆世不整合面上下, 泥盆纪和志留纪的岩石均强烈变形, 发育了同样的劈理和褶皱构造, 证明二者遭受变形的时间一致, 是同一期构造变形的产物。丘元禧等 (1999) 在绥宁—城步地区也发现了大量的叠加褶皱, 早期轴面倾向 SE 的褶皱被晚期轴面倾向 NW 的褶皱所改造, 这与我们的观察非常一致, 只是他们认为这些现象是加里东期构造变形, 即早期的 NW 向逆冲推覆和晚期 SE 向的滑覆。

通过构造叠加关系, 我们将三期构造变形的划定出时间序列: 运动学指向 NW 的韧性剪切构造为 D_1 期构造变形, 形成了大范围的逆冲断层和不对称褶皱以及倾向 SE 的轴面劈理, 在劈理面上可见 NW-SE 向矿物拉伸线理; D_2 为反向褶皱和冲断构造期, 表现为极性 SE 的逆冲断层和褶皱, 并改造了 S_1 劈理; 直立褶皱期为 D_3 构造变形的产物, 局部形成了轴面直立的褶皱以及近直立的劈理, 同时形成直立的 L_3 线理。三期构造的区域动力学背景均为三叠纪的 NW-SE 向挤压作用。

第四章 雪峰山强应变带构造变形分析

雪峰山地区地表广泛分布着从晚元古代至早三叠世的沉积盖层,经历了多期构造变形,但是与大多数经典的造山带不同的是,雪峰山地区并没有大面积的基底高级变质岩如片麻岩或混合岩的出露,缺少中下地壳部分熔融的证据。但是,早中生代花岗岩却广泛分布在造山带之中。就在这些中生代花岗岩体周边,出露了一些强应变的岩石。经过我们详细的野外考察,我们在不同区域均观察到了在新元古代沉积岩之下存在着的强应变带。以下我们在雪峰山造山带中选取了 4 个强应变岩石出露地区进行了几何学、运动学构造分析,并讨论了其构造意义。

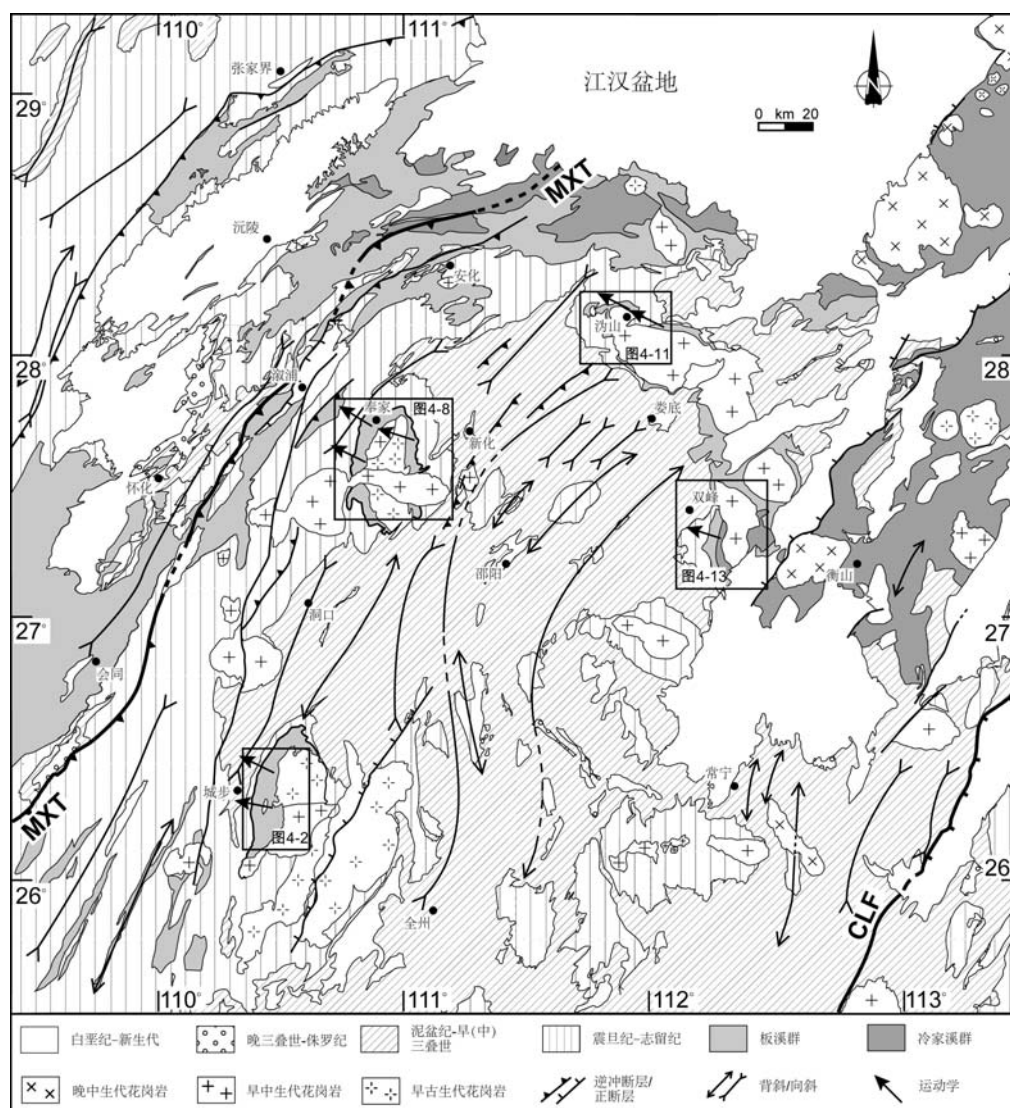


图 4-1 雪峰山构造地质图及强应变带出露区域 (修改自湖南省地质矿产局, 1988)。MXT: 雪峰山主逆冲断层。CLF: 郴州—临武断层。

第一节 城步地区

城步地区位于雪峰山造山带的南部, 出露苗儿山早古生代岩体和其中部早中生代岩体(孙涛等, 2007)。研究区东部为震旦系至寒武系, 包括砂岩、灰岩和泥岩, 倾向以 NW 为主(图 4-2a 和 4-2c)。地质志上将岩体周边位于震旦系之下的岩石标定为新元古代板溪群岩石, 但并未做详细描述。实际上, 与湖南省其他地区的板溪群不同, 此处的新元古代岩石由板岩、片理化砂岩和含石榴石二云母片岩组成(图 4-2a)。这些浅变质岩经历了绿片岩相变质作用, 并且发育了渗透性的面理构造, 并由于早中生代花岗岩的侵位而形成背斜构造(图 4-2b)。NW-SE 方向拉伸线理以及 NE-SW 方向的细褶纹(图 4-2d、4-2e 和 4-2f)。强变形的糜棱岩化岩石主要出露于兰蓉附近以及浆坪的东南区域。因此, 城步地区为雪峰山地表出露出的造山带最深的单元, 代表了一条基底之上的强应变带。

1 宏观构造

在强应变带之上的震旦纪和寒武纪岩石受到了上部指向 NW 的剪切构造作用而强烈变形, 褶皱极性均指向 NW, 但是基本没有遭受过变质作用。相反, 在强应变带之中, 岩石受到了强烈的剪切, 局部可见糜棱岩。糜棱岩化的砂岩和泥岩形成了厚度在 1 到 5 毫米的矿物分异条带, 其中深色以云母居多, 而浅色的则以石英和长石占多数(图 4-3a)。这些糜棱岩面理倾角多为 15-45 度, 倾向 NW 或 SE(图 4-2d)。在一些露头上, 矿物集合体被强烈拉伸, 沿 N110° 方向排列, 构成了拉伸线理(图 4-2e)。在云母片岩之中, 有许多石英脉产出于其中, 代表了地质过程中重要的流体作用。在垂直面理、平行线理的岩石面上, 石英脉受到强烈剪切, 形成了不对称的 σ 形, 指示了上部指向 NW 的运动学方向(图 4-3b 和 4-3c)。而有时剪切作用造成的石英脉的垂向缩短, 剪切面与面理面相平行(图 4-3d)。同时糜棱岩面理也被后期的厘米-毫米尺度的 NNE-SSW 方向细褶纹所叠加, 这些直立的细褶纹可能与后期盖层中记录的水平挤压构造的改造相关。

褶皱构造在糜棱岩带中也随处可见, 尤其在强应变作用下, 形成了褶皱轴与线理方向平行的 a 型褶皱(图 4-3e)。在花岗岩的围岩之中, 与岩体一起侵位时形成的岩脉也被剪切成不对称的 σ 构造, 运动学方向为上部指向 NW(图 4-3f)。在早古生代兰蓉岩体的周边云母片岩之中, 存在着大量的岩体侵位时形成的接触

变质产物——红柱石。这些红柱石在面理面上定向明显，延伸方向沿~N100度，与区域变形的线理方向一致，表明早古生代侵位时生成的红柱石片岩在后期受到构造作用重新定向，所以这期构造发生在早古生代之后（图 4-3g）。

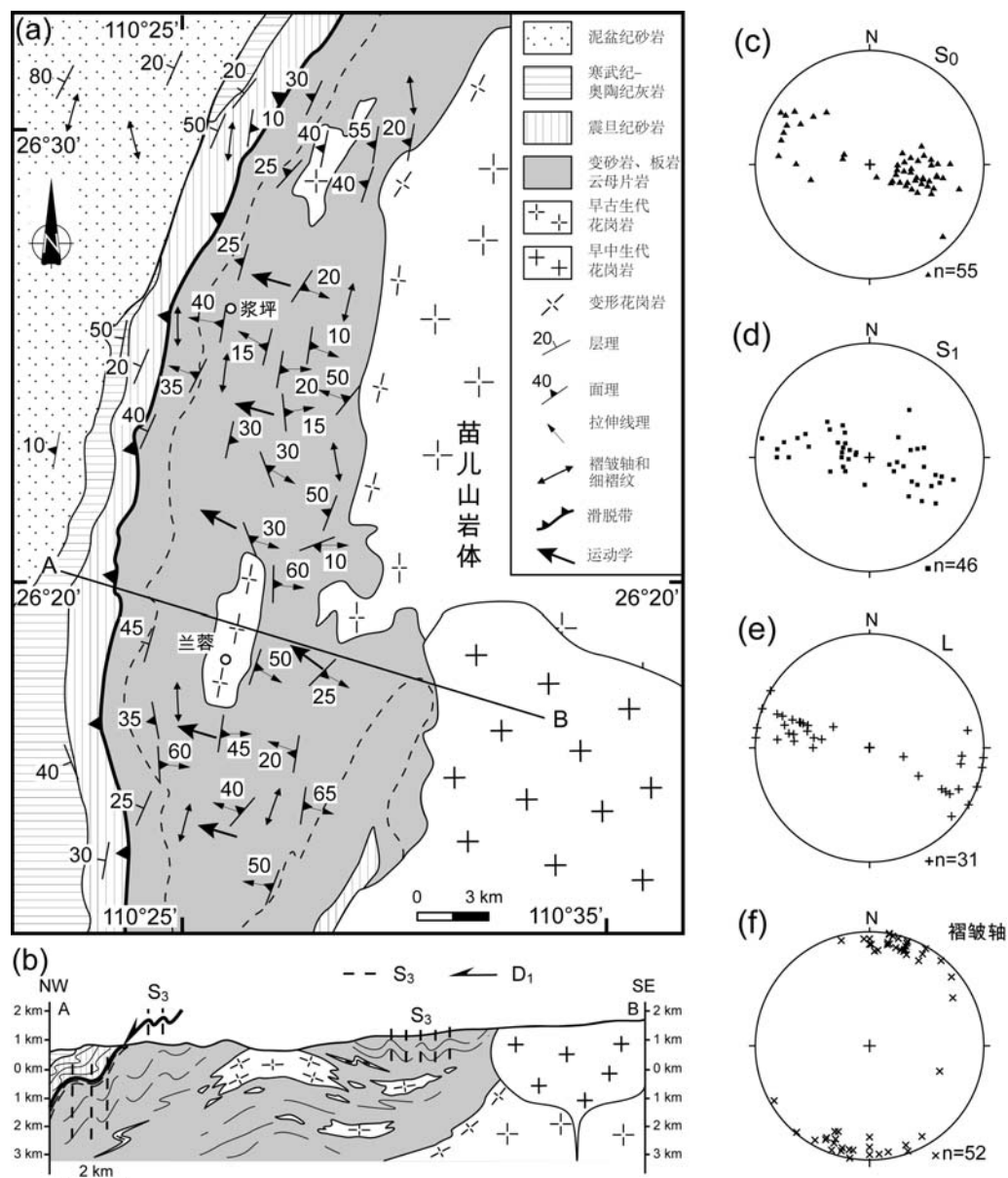


图 4-2 (a) 城步地区构造地质图。(b) 构造地质剖面。主要构造要素的持平投影图（施密特网下半球投影）：(c) 层理 S_0 。(d) S_1 面理。(e) 线理。(f) 褶皱轴。

与围岩变形相对应，花岗岩体也卷入了早中生代变形之中。在兰蓉镇附近，兰蓉岩体的周缘均受到了构造剪切变形的影响。在岩体的东缘和西缘，黑云母花岗岩被强烈的糜棱岩化，转变成了花岗片麻岩（图 4-3h），而暗色和淡色条带分别对应着云母矿物和长英质矿物的集合体。这些特征表明花岗岩的变形发生在固

相之后，即在早古生代侵位之后。

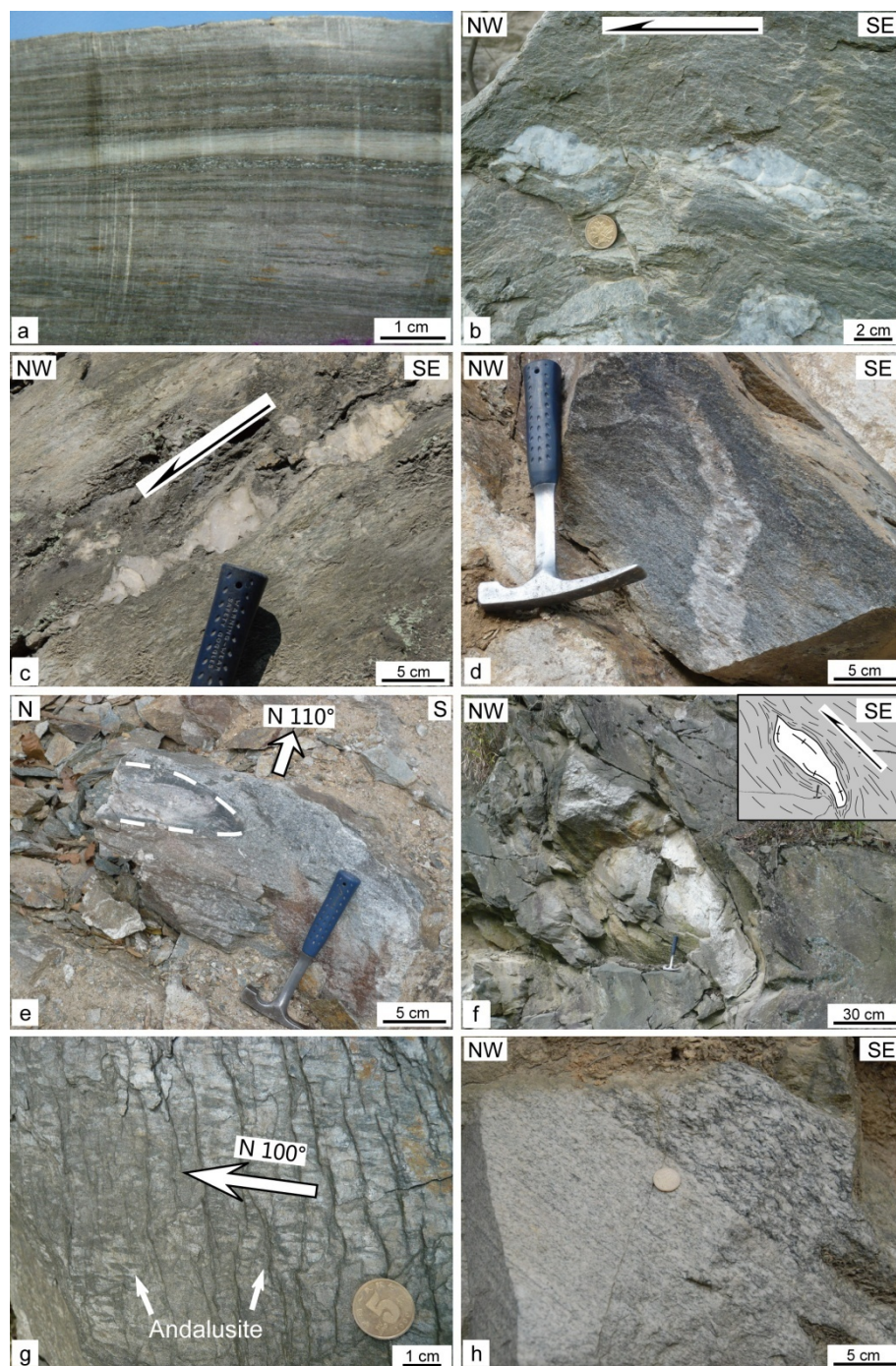


图 4-3 城步地区典型构造的野外照片。(a) 糜棱岩化的石英岩，形成了浅色的石英条带和深色的黑云母等暗色矿物条带。(b) 石英砂岩中的石英脉被强烈剪切成 σ 形，指示极性 NW 的剪切方向。(c) 云母片岩中的剪切石英脉布丁构造，上部指向 NW 的运动学方向。(d) 砂岩中石英脉被强烈剪切缩短，缩短方向平行于面理方向。(e) 石英岩中 a 型褶皱，褶皱轴方向垂直于区域矿物拉伸线理方向。(f) 围岩中被剪切的花岗岩团块。(g) 花岗岩接触带上片岩中红柱石组成的矿物线理。(h) 片麻岩化的兰蓉花岗岩体。

整个城步的深部变质单元均被上部指向 NW 的剪切所影响，但是与盖层变形类似，这些石英岩和云母片岩也被后期构造所叠加，受到直立褶皱的改造。例如糜棱岩和云母片岩的面理乃至矿物拉伸线理均被褶曲，广泛发育了近直立的轴面劈理。在兰蓉东约 10km，一处石榴子石云母片岩的露头之上，多次弯曲的石英脉很好的阐释出褶皱的叠加现象（图 4-4）。早期石英脉由于流体作用而顺岩石的层理面生成，由于上部指向 NW 的剪切作用形成了极性 NW 的不对称褶皱，并形成面理；在晚期时，这些早期褶皱和面理被直立褶皱褶曲，形成了新的直立的劈理面。

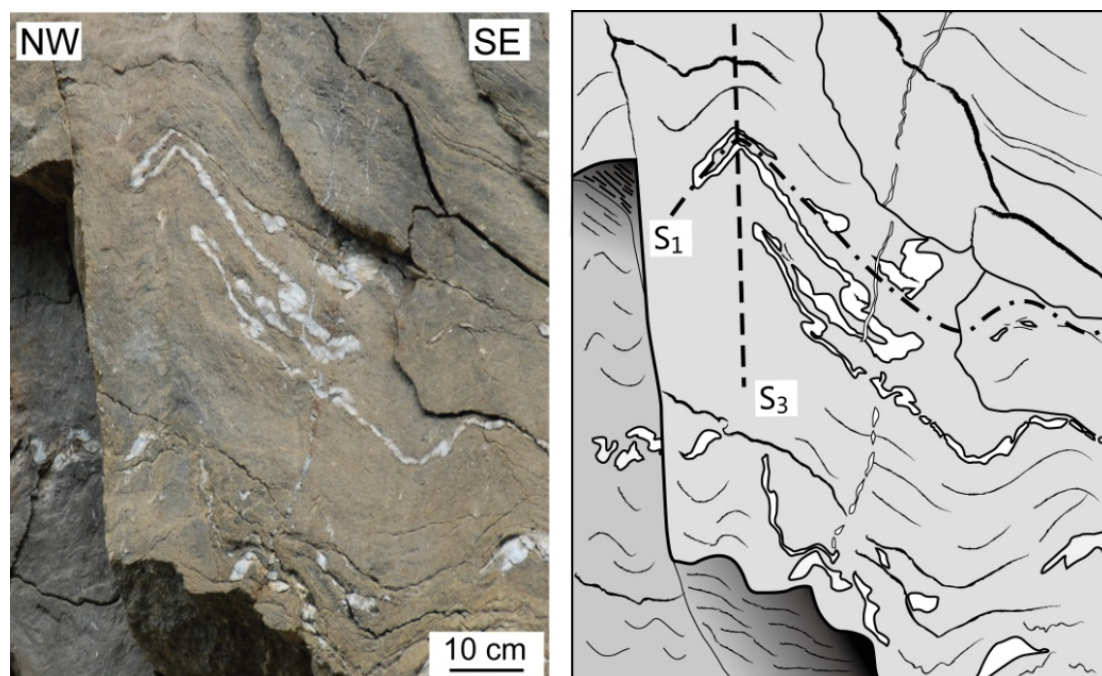


图 4-4 云母片岩中石英脉的叠加褶皱。早期极性 NW 的褶皱被后期直立褶皱所改造。

2 显微组构

在显微尺度上，我们主要通过 σ 形旋转残斑、云母鱼和剪切条带等构造特征判断构造变形的运动学。在变砂岩之中，石英碎屑颗粒被绿泥石和云母所围绕，并且在剪切应力作用之下形成了压力影构造，同时在基质之中还生成了剪切条带（图 4-5a）。石英岩中，长石的旋转残斑在剪切力作用下与基质矿物如黑云母、石英和绿泥石等组成 σ 构造，运动学方向指示上部指向 NW 的剪切（图 4-5b）。

在薄片上，层状硅酸盐在面理面上、碎斑的压力影中的分布状况表明主要的变形机制为压溶作用。压溶作用作为一种重要的变形机制，发生在存在着高差异应力的中低温绿片岩相变质作用之中。这种机制一般作用于石英颗粒的接触点周边，因为在这一区域被流体接触且应力较高。所以相应的溶解性就较强。当接触点的颗粒晶格受到强烈的挤压，物质就会被溶解并迁移至低应力区再次沉淀下来。所以压力影一般都形成于矿物拉伸的方向（Passchier and Trouw, 2005）。

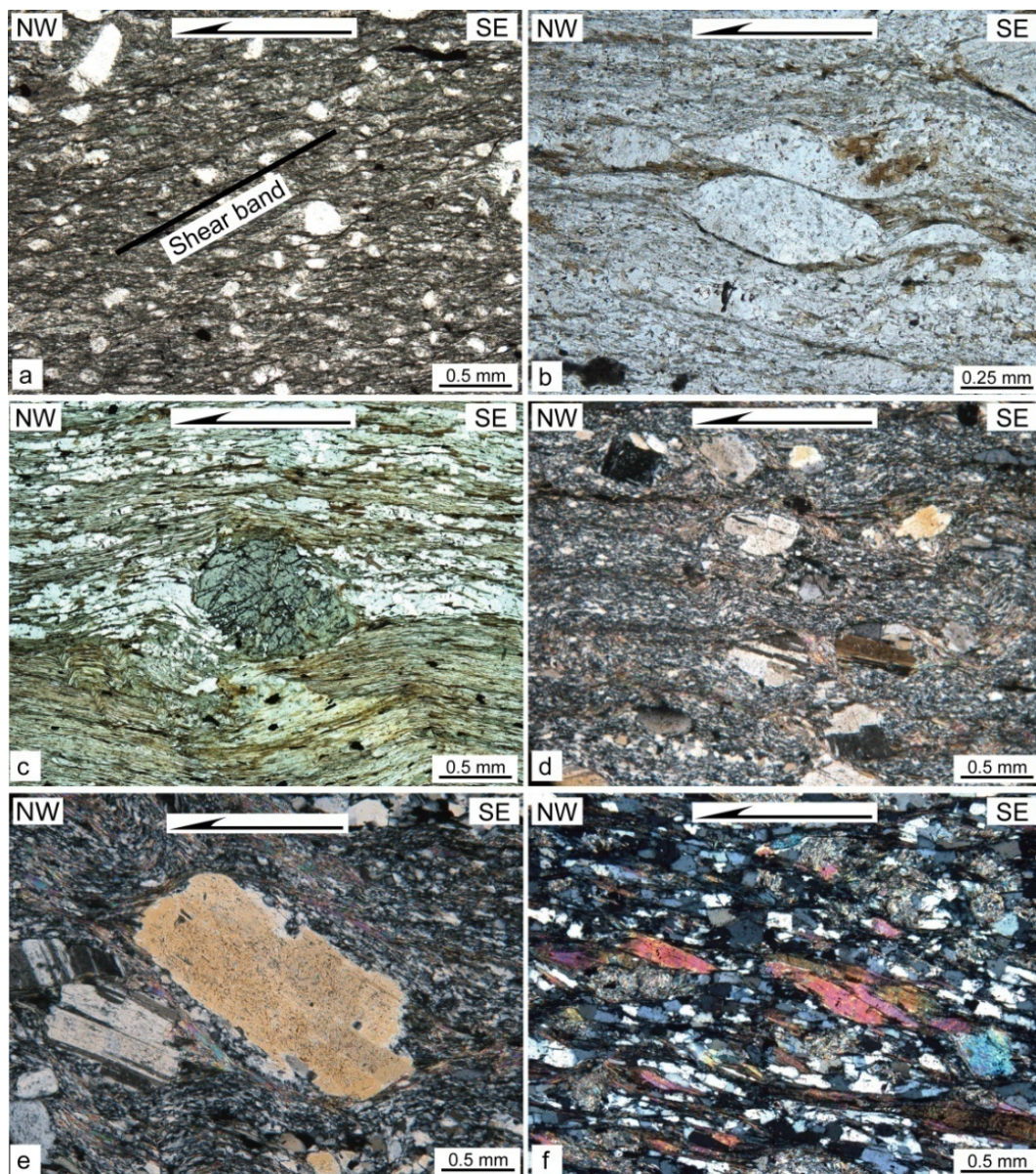


图 4-5 城步地区典型构造的显微照片。(a) 变砂岩中石英颗粒组成的 σ 构造，局部形成了剪切条带。(b) 长石颗粒的旋转残斑，剪切指向 NW。(c) 石榴子石云母片岩中石榴石的旋转残斑，石英构成了压力影，运动学方向 NW。(d) 糜棱岩的显微照片，石英因动态重结晶细化而长石作为斑晶存在。(e) 长石残斑及边缘的石英压力影组成 σ 构造。(f) 石英云母片岩中云母鱼构造，上部指向 NW 的剪切指向。

兰蓉以东（图 4-2a），在石榴子石云母片岩中，尽管石榴子石在后期地质过程中经历了其他作用而转变成绿泥石—石英集合体，但是构造形迹并没有被改造。围绕在残存的石榴子石边缘形成了不对称的石英和绿泥石压力影，指示着上部指向 NW 的剪切运动学（图 4-5c）。

浆坪以东约 3km 处（图 4-2a），是本地区乃至整个雪峰山造山带之中强应变糜棱岩出露最好的地区。在显微尺度上我们可以清楚地观察到中低温的糜棱岩组构。石英由于变形温度较低，因此在薄片里被强烈细粒化，组成基质矿物；长石的变形温度较高，为残斑的主要组成矿物。石英的粒度基本在 $50\ \mu\text{m}$ 以下，表明变形的温度低于 500°C ，而且围绕着长石形成典型的 σ 构造，运动学清晰的显示为 NW 方向的剪切（图 4-5d 和 4-5e）。垂直构造线往西，变形程度降低，在石英云母片岩中，石英的细粒化程度不高，但发育了典型的云母鱼构造（图 4-5f）。

3 石英组构

为了更好的分析强应变滑脱带的变形样式，我们结合显微构造，对糜棱岩带中的样品进行了石英组构分析，主要是针对石英 c 轴的优选方位的测量。

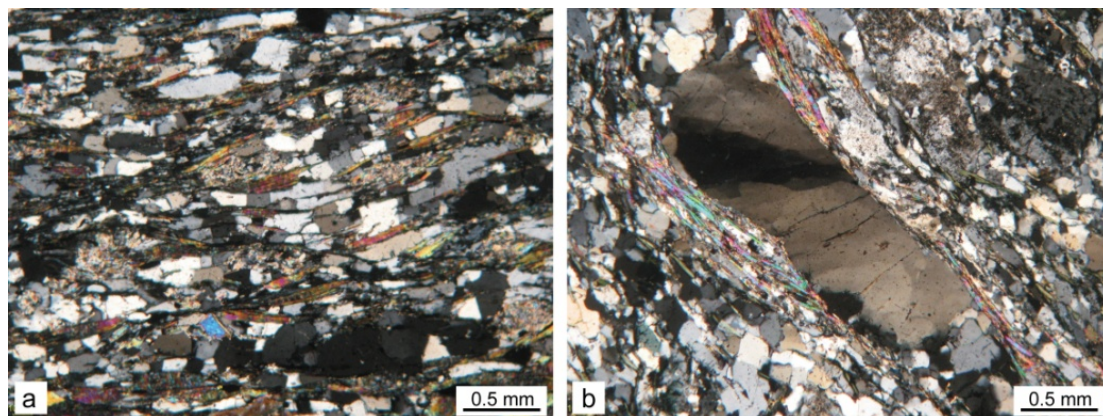


图 4-6 城步糜棱岩中两种石英组构的样式

在分析的糜棱岩样品之中，主要存在了两种石英显微组构。第一种发育于云母片岩之中，包含了他形和半自形的石英颗粒，这些石英颗粒边界较为平直，多数呈拉扁的多边形（图 4-6a）。此外，在有些薄片里，石英三联点的颗粒边界呈等角度，即以近 120° 的边界角接触，而且没有或少见动态重结晶的迹象。第二

种石英组构主要发育在石英岩或含云母石英岩之中。在这类岩石中，石英颗粒大小可以分为两组，一组在 1 mm 左右，而另一组为基质，约 70 μm (图 4-6b)。石英碎斑在应力作用下被拉长，长轴的方向平行于面理。同时碎斑在矿物边缘出被分解成若干亚颗粒，亚颗粒的边界与碎斑的边界呈斜交关系。碎斑颗粒通常有波状消光现象，而且沿着碎斑边缘，新生他形石英细粒主要通过亚颗粒旋转的重结晶方式生成。

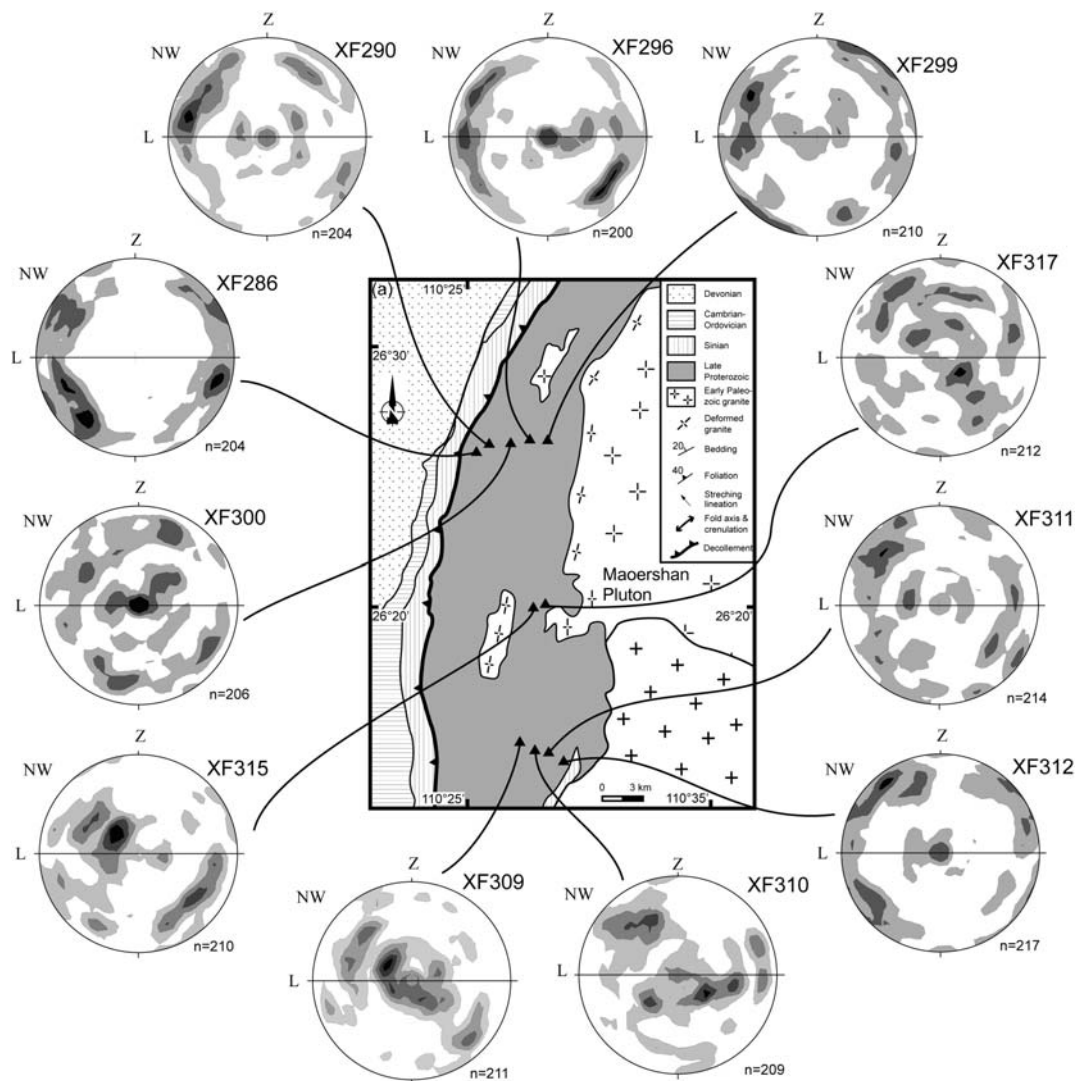


图 4-7 城步糜棱岩石英 c 轴持平投影图 (施密特网下半球投影)。

石英 c 轴的测量工作在 XZ 岩石切面的薄片上进行 (垂直于面理、平行于线理的平面)，我们选取了 11 个样品进行了测量，包含了上述两种石英组构种类。类似的，石英 c 轴组构也可以分为两类：第一类主要由边缘的四个极密点和中间一个极密点组成，边缘的四组极密点两两组成的交叉环带的交角在 75° 左右，极

密点更靠近 Y 轴。沿着环带分布的极密点表明主要以底面<a>滑移系为主，而靠近 Y 轴的石英 c 轴代表了柱面<a>滑移系。存在这一类石英 c 轴样式的样品包括 XF286、XF290、XF296、XF299、XF311、XF312（图 4-7）。另一组石英 c 轴组构中极密点更加接近 Y 轴，并且只存在一组斜交的环带，表明底面、菱面和柱面滑移系同时存在于滑移系统之中。这一类的组构样式主要发育在 XF300、XF309、XF310、XF315、XF317 之中（图 4-7）。尽管存在着部分差异，但是两种石英组构的样式均表明，城步地区的糜棱岩中的石英优选方位形成于低温变质条件之下，并且在变形过程之中还存在着流体作用（Passchier and Trouw, 2005）。

综上所述，城步地区出露了雪峰山地区揭露出的变质最深的岩石，这些石英岩和含石榴子石云母片岩经历了低绿片岩相的变质作用。同时，这些岩石由经历了强烈的剪切作用，局部形成了糜棱岩，代表了基底与沉积盖层之间发育的强应变滑脱带，其中变形的温度在 300-400°C 之间（Tullis et al., 1973; Stipp et al., 2002）。

第二节 奉家-水车地区

在白马山岩体为早古生代和早中生代两期花岗岩所组成的复式花岗岩体，但是其各时代岩体的展布还不甚明了，在前人文献中存在争议（湖南省地质矿产局, 1988; Wang et al., 2005）。岩体的周边地区出露了包括变砂岩、石英岩和云母片岩等低绿片岩相的变质岩（图 4-8a）。这些变质岩出露于一个大型的背斜核部，可能是由于晚三叠世花岗岩侵位时的抬升作用所致。在沉积岩层之下，存在着一条强应变带，带中发育了受到强烈剪切变形的岩石，局部还形成了糜棱岩（图 4-8a 和 4-8b）。

1 宏观构造

在白马山岩体周边的强应变带之中，渗透性的面理广泛的发育于变形岩石之中（图 4-8d）。在区域尺度上，面理在岩体的西边倾向 NW 或者 W，而在东侧则倾向 SE 或者 E，呈现出一个背斜的形态（图 4-8b, 4-8c 和 4-8d）。在露头尺度上，变质与变形程度在岩体的东西两侧呈现出差异。

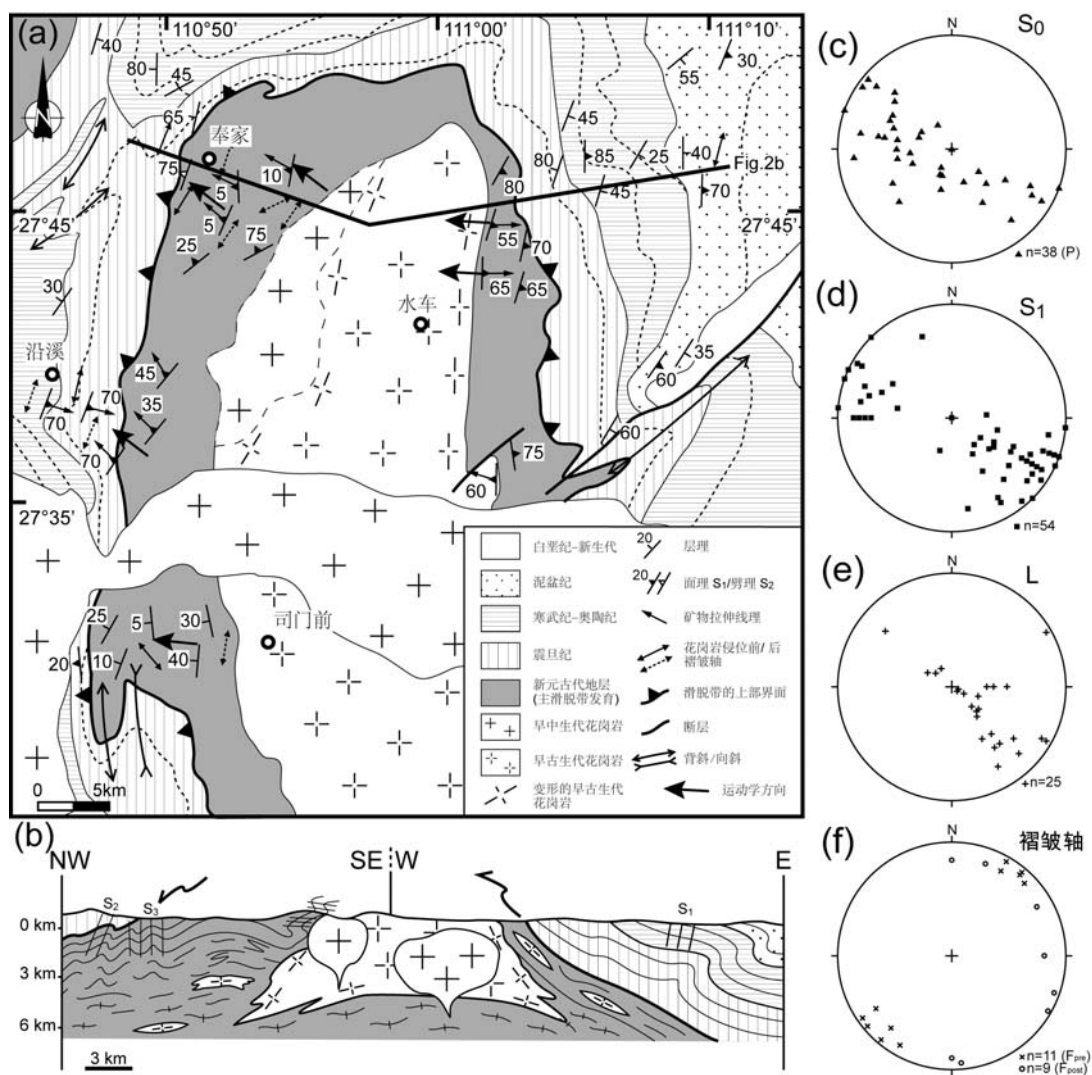


图 4-8 (a) 奉家-水车地区构造地质图。(b) 构造地质剖面。主要构造要素的持平投影图(施密特网下半球投影): (c) 层理 S₀。(d) S₁ 面理。(e) 线理。(f) 褶皱轴 F_{pre} 为中生代花岗岩侵位前褶皱轴线; F_{post} 为侵位之后发育的褶皱轴线。

在白马山岩体两侧,新元古代至古生代沉积岩尽管经历了韧性变形,但沉积构造仍较好的保存了下来,层理倾向 WNW 或 ESE,褶皱轴线为 NE-SW 走向(图 4-8c 和 4-8f)。在西侧,奉家镇的西边,当我们向东逐渐靠近花岗岩时,随着变形和变质作用的强度不断增加,原生的沉积层理就慢慢地被新生面理所取代。在奉家镇周边岩石中,面理的倾角平缓的或近水平,但仍然存在倾向上的变化,表明可能是后期的直立褶皱对面理的改造。局部可以观察到轴面直立的尖棱褶皱以及褶皱的面理上形成厘米尺度的细褶皱纹构造(图 4-9a)。当逐渐靠近花岗岩体,面理角度开始倾斜,变成近直立形态,同时形成了 NE-SW 走向褶皱轴面近水平的细褶皱纹或微褶皱。有时面理上发育了优选定向的云母片。这些微型褶皱的成因可能有两种:一种是在花岗岩侵位前就形成的近直立的褶皱或细褶皱纹,即在后期水平缩短作用下,之后在花岗岩侵位隆升时产生的掀斜作用造成了面理面的直立以及褶皱面的水平;另一种则是这些褶皱或细褶皱纹是在花岗岩侵位隆升造成面理面掀斜成近直立之后形成的,即在垂向缩短作用下(图 4-8b 和 4-9b)。通过我们的野外调查表明,本区域出露最深、变形最强烈、变质作用最高的岩石出现在有新生黑云母的地方,而没有像城步地区的石榴子石二云母片岩。

奉家镇以南,沿溪附近,一组渗透性密集发育的劈理构造产出于新元古代的砾岩之中。在劈理面之上,砾石因剪切而沿 $N120^{\circ}$ 方向定向,其组成的线理方向与雪峰山造山带中变砂岩和云母片岩的韧性变形产生的矿物拉伸线理方向一致(图 4-9c)。在砾石周边形成的剪切压力影也指示了强应变造成的上部指向 NW 的构造作用。而在沉积盖层之中,岩石变形与主滑脱带中变形具有较好的一致性。例如,密集发育的 NE-SW 走向劈理构造和 NW-SE 矿物集合体组成的拉伸线理等等。

在研究区域南部,司门前镇以西(图 4-8a),大面积遭受过强变形的变砂岩、变砾岩或石英岩代表了揭露至地表的强应变带。在这一地区,面理水平,后期的褶皱也较为少见。在 XZ 切面上(平行线理垂直面理),剪切作用使得石英脉拉伸并布丁化,有的石英脉布丁被剪切成 σ 型,并指示了上部指向 NW 的运动学方向(图 4-9d)。此外,在这些我们还发现了层间紧闭的横卧褶皱发育在弱变质的石英砂岩之中,这印证区域上我们所观察到的水平面理不是原始层理,而是面理,原生层理已经在强烈构造变形之中被面理所取代(图 4-9e)。在这一区域,

岩石主要经历了低绿片岩相的变质作用，并没有更深层次的变质岩出露。

在白马山岩体以东，水车镇北东部约 8km 处，与岩体西边岩石单元类似，此处岩石组合主要有变质砾岩、变泥岩和绢云母片岩，也代表了出露至地表的主滑脱带，但是变质程度较西部高。在新元古代的变质砾岩中，面理面主要是渗透性的泥劈理，而其中的砾石也沿着劈理面方向定向，有的被剪切拉伸，有的与泥质的基质成分构成了 σ 组构。从新元古代到震旦纪和早古生代岩石，劈理的强度逐渐降低，在后者仅发育褶皱相关的轴面劈理。运动学方向在强变形的砾岩中被识别出，如围绕砾石的不对称剪切压力影构造和长石质的砾石中书斜构造等等（图 4-9f）。与城步地区相类似，在早古生代花岗岩周边的围岩之中，接触变质作用产生的红柱石随处可见。这些在白马山早古生代岩体侵位时形成的红柱石之后由于变形作用而定向排列，其定向方向与区域线理方向一致，即 $N110^{\circ}E$ （图 4-9g）。与围岩中的变形相对应的，在水车镇以南，花岗岩体在韧性变形以及变质作用下转变成了正片麻岩（图 4-9h）。在变形的花岗岩中，糜棱岩面理表现为深色与浅色条带的交替，其中深色条带对应着长英质矿物聚集区，而浅色条带则对应着黑云母富集的部分。此外，在局部也可以观察到基性包体或析离体的定向，整体上也呈 NW-SE 排列。白马山的运动学标志均指示了上部指向 NW 的韧性剪切变形。

2 显微构造

在 XZ 切面的薄片上，可以观察到明显的岩石显微特征。在变泥质岩或石英岩之中，由于强烈的剪切作用，在刚性的磁铁矿周边形成了石英的压力影构造，压力影的纤维从 0.1 mm 至 0.5 mm 长，剪切方向均代表了上部指向 NW 的运动（图 4-10a）。在砾岩或粗碎屑岩中，主要变形机制为压溶作用，压溶劈理与石英颗粒的定向平行。相对刚性的石英颗粒平行劈理的两侧应力较弱，因此也形成了对称的压力影构造（图 4-10b）。随着变形的增强，不对称构造也越来越发育。在奉家镇东主滑脱带中的变石英砂岩中，长石的旋转残斑及其不对称剪切压力影构造指示了主变形期 D_1 极性 NW 的构造方向（图 4-10c）。

在奉家镇出露的主滑脱带最深和最强的变形仅限于此，但是在沿溪以东，我们在强变形的石英岩中观察到了石英的动态重结晶现象，主要以颗粒的隆凹构造

(bulging) 和亚颗粒旋转的变形机制为主 (图 4-10d)。因此, 从主滑脱带上部至下部, 变形机制的改变主要控制因素在于温度。在上部的变砂岩和变砾岩中, 石英颗粒拉伸平行于面理方向, 同时在流体作用之下, 形成了以压溶为主的平行面理面的层状硅酸盐矿物以及与碎斑延展方向一致的压力影构造。这种变形样式说明岩石处于低温变质作用下, 而且流体的参与阻碍了颗粒内部变形的进行 (Passchier and Trouw, 2005)。往滑脱带的下部走, 颗粒大小在 $\sim 50 \mu\text{m}$ 至 $\sim 400 \mu\text{m}$ 之间的石英或长石的多晶集合体在动态重结晶的作用下主要呈现出核幔构造 (图 4-10e)。先形成的石英大颗粒被细小的石英集合体所取代, 这些在边缘新生的石英颗粒主要通过隆凹构造 (bulging) 和亚颗粒旋转与母颗粒分开, 有些早期的石英颗粒甚至完全被新生的重结晶颗粒所取代, 表明变形温度在 300 到 400 度之间。

因此, 由于差异应力和温度的增加, 晶粒间滑移成为了主导的变形机制。在奉家-水车地区, 强应变岩石也是通过三叠纪岩体而隆升揭露至地表, 这些由低绿片岩相变质岩组成的岩石为基底滑脱带的组成部分, 分隔了浅表的韧性变形的沉积盖层和下部未出露的高级变质的基底岩石。在这条强应变滑脱带之中, 新元古代沉积岩和早古生代花岗岩分别被转变成低温糜棱岩或正片麻岩。沿着 NW-SE 的线理方向, 不同的运动学标志均指示了上部指向 NW 的剪切。在矿物尺度上, 流体参与的变形 (压溶作用) 为主要的变形机制, 但是在局部滑脱带出露较深的区域, 动态重结晶的颗粒聚集体表明塑性变形成为了主导的变形机制。



图 4-9 奉家-水车地区典型构造的野外照片。(a) 奉家镇东部滑脱带中的直立尖棱褶皱。(b) 奉家镇滑脱带后期直立褶皱影响使得面理面直立,同时在面理面上由于重力作用而产生了垂向缩短的细褶皱或微褶皱。(c) 滑脱带中新元古代砾岩中砾石强烈拉长并定向,拉伸方向为 $N120^{\circ}E$ 。(d) 石英岩中的石英脉体在剪切应力的作用下布丁化。(e) 石英岩中非常紧闭的横卧褶皱,表明原生的 S_0 已被 S_1 面理所取代。(f) 新元古代-震旦纪砾岩中中长石质砾石被剪切错断,形成书斜构造,指示上部指向 NW 的剪切构造。(g) 早古生代白马山花岗岩体周边接触变质的红柱石定向排列,方向 $N110^{\circ}E$ 。(h) 白马山岩体中早古生代部分受到剪切变形而糜棱岩化,并形成淡色与暗色条带的分异。

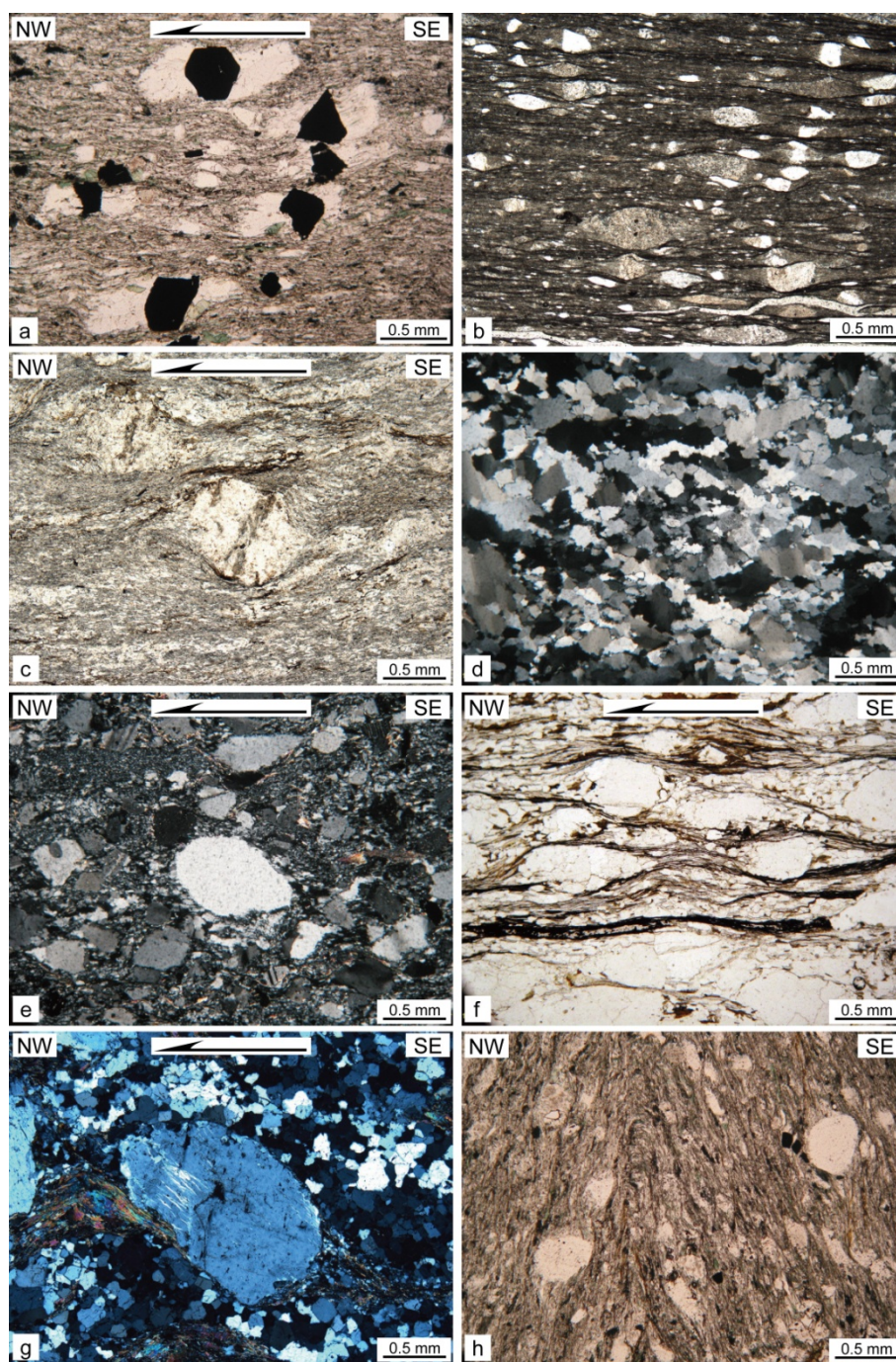


图 4-10 奉家-水车地区显微构造照片。(a)变泥质岩之中围绕磁铁矿发育的剪切压力影构造。(b)碎屑岩中石英或长石碎斑沿面理面定向,同时可见压力影构造。变形主要以压溶作用为主。(c)石英岩中发育的长石旋转残斑的 σ 构造,指示了上部NW的运动学方向。(d)石英岩中石英可以发生动态重结晶作用,变形机制以bulging和亚颗粒旋转为主。(e)石英岩中的核幔构造。(f)片岩中的剪切条带。(g)早古生代花岗岩中发育的剪切构造,同样指示了上部指向NW的运动学方向。(h)在砂岩中发育的两期构造叠加现象。 S_{0-1} 面理被直立褶皱改造,但仍保存了上部指向NW的 σ 剪切构造。

第三节 沅山地区

沅山岩体为雪峰山地区地表出露面积最大的早中生代花岗岩体，但是基底滑脱带的出露区域仅限于岩体的西北部（图 4-1 和 4-11a）。在主滑脱带之上，震旦纪至泥盆纪均遭受了早期极性 NW 的褶皱变形和晚期极性 SE 的反向褶皱变形。沅山岩体以西，区域发育的 NE-SW 走向的褶皱轴在岩体的周边转变成 NNE-SSW 或 N-S 走向。原岩为新元古代的变质砂岩和云母片岩出露在黄材镇的西部和南部（图 4-11a）。由于后期沅山岩体的侵位和掀斜作用，初始形成的面理被改造成围绕岩体周边发育，即在北东缘倾向 NE，而在西缘倾向 W（图 4-11a）。除此之外，沅山岩体周缘还广泛发育了接触变质环带。因此，为了避免接触变质作用的影响，我们主要在接触变质环带之外的变质岩区域进行了详细的构造学分析。

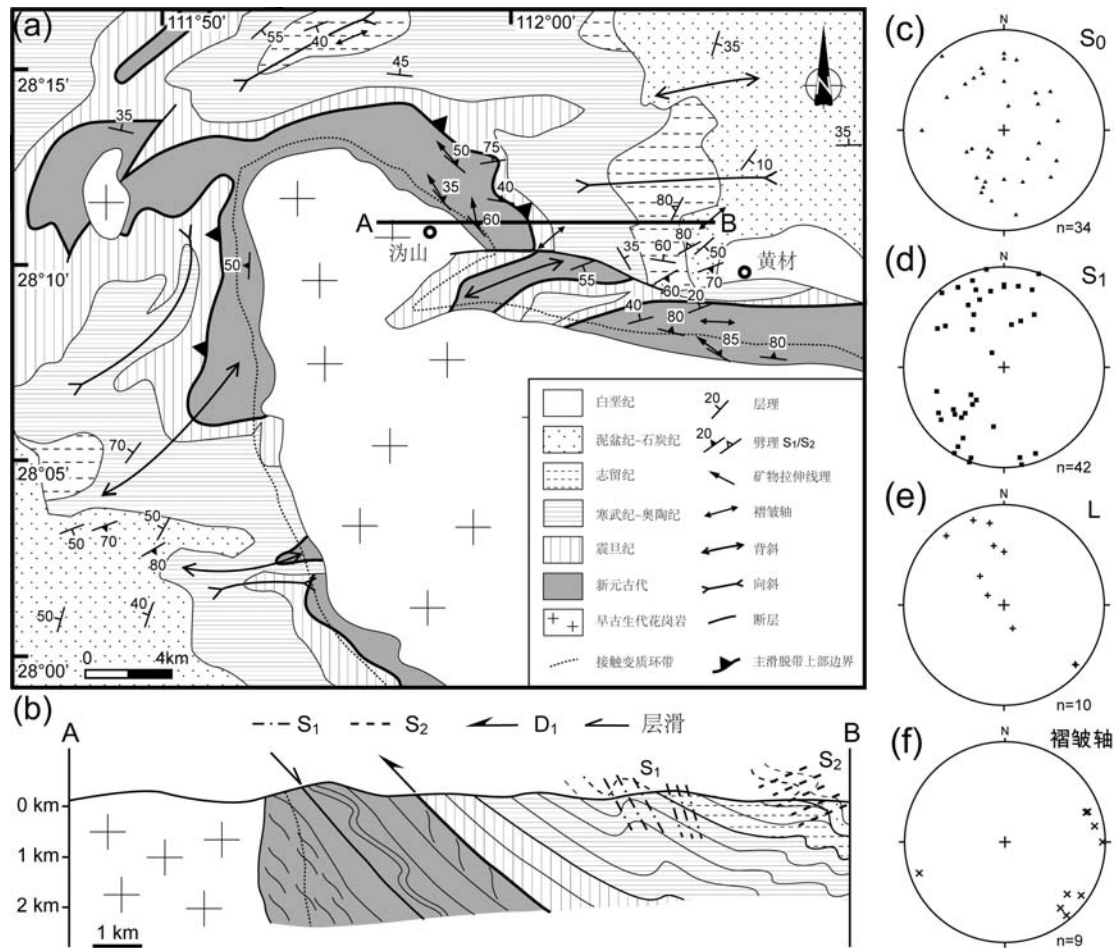


图 4-11 (a) 沅山地区区域构造地质图。(b) 构造剖面图。主要构造要素的持平投影图（施密特网下半球投影）：(c) 层理 S₀。(d) S₁ 面理。(e) 线理。(f) 褶皱轴。

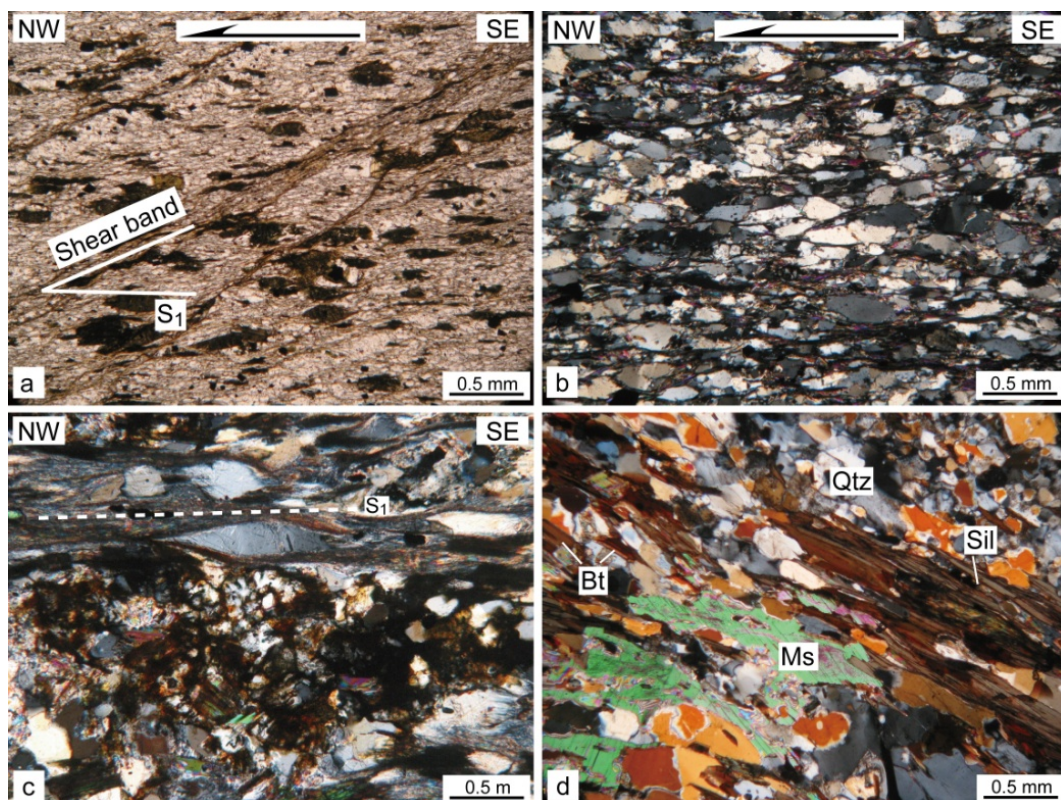


图 4-12 沔山地区显微构造照片。(a) 变砂岩中定向的碎屑颗粒和剪切条带的发育。(b) 定向排列的石英颗粒并有局部的动态重结晶作用。(c) 石英在剪切条带中发育 σ 构造指示上部朝向 NW 的剪切。(d) 含矽线石的二云母片岩。

沔山镇以东的石英岩和云母片岩之中，面理主要由定向的白云母、黑云母和石英颗粒组成，倾向 NE（图 4-11a），同时 NNW-SSE 的矿物线理和拉伸线理与产出于沉积盖层中的区域的矿物拉伸线理相一致，只是表现形式不同，此处的线理通过定向的黑云母和石英集合体表现出来。在显微尺度下，变砂岩中碎屑石英颗粒在剪切变形作用下被拉长并发育有波状消光。石英岩中，碎屑矿物在剪切作用下平行 S_1 面理定向，同时伴随剪切条带的发育，指示了上部指向 NW 的运动学方向（图 4-12a）。随着应变的增强，石英集合体中的单个石英颗粒边界从平直向锯齿状转变，局部可见边界与母颗粒斜交的新生颗粒，并指示了极性 NW 的运动学（图 4-12b）。石英云母片岩中也可见强应变条带，条带之中的石英拉伸明显，具有 σ 构造（图 4-12c）。此外，有些石英颗粒具有自形、平直的颗粒边界以及等角度的三联节点等特征，均指示了石英集合体经历了后期热事件主导的静态重结晶作用，很可能发生于沔山岩体的侵位过程之中。但是，我们的野外和室内

观察均表明上部指向 NW 的 D_1 与变质同期产生的构造变形发生于沱山岩体侵位之前。此外,在变泥质岩中,纤维状矽线石的存在指示了高温变质作用(图 4-12d)。其中,矽线石、黑云母和石英均平行于面理发育,而白云母则分为两类,一类为较为细小的白云母,其节理面平行于面理面发育,且长轴方向平行于面理,代表了与矽线石+黑云母同期变质作用的产物;另一类白云母颗粒较大,有时包裹了矽线石和早期白云母,其长轴和节理面方向无定向,与面理斜交,表明是在岩体侵位后热接触变质作用时产生。

因此,综合沱山地区的变质与变形的观察与分析,说明早中生代岩体的侵位时间晚于雪峰山造山带的上部指向 NW 的主变形期。而在本区域上部指向 SE 的剪切变形和直立褶皱的发育较为局部。

第四节 双峰地区

双峰地区位于雪峰山造山带的东部,主滑脱带的地表出露也主要产出于紫云山早中生代岩体的周边(图 4-13a),与前面三个区域类似,由于花岗岩的就位,造成了变质岩和强变形的岩石的抬升。

通过详细的野外观察,韧性变形的岩石主要出露在岩体的西缘,位于双峰县的南东。研究区内,所有的面状组构如层理、劈理和变质岩的面理均为 NE-SW 走向(图 4-13c 和 4-13d)。在远离紫云山岩体的地方,如双峰南东 3-4 km 处,新元古代至泥盆纪的岩石均卷入了极性 SE 的褶皱作用之中。在靠近岩体的地方,砂岩和冰碛岩地层在掀斜作用下逐渐直立,相应地,由于重力作用而引起的垂向缩短以及重力滑脱褶皱在泥质岩中较为发育。这些褶皱虽然极性指向 NW,但均是岩体侵位之后的产物,因此是在侵位同期或者更晚的时期形成的(图 4-14a 和 4-14b)。这一地区云母片岩和石英岩也有分布,但非常局限,仅仅在 1-2 个露头上观察到,而且变形作用较弱,表明强应变带着这一地区并没有因为岩体的隆升而完全抬升至地表,我们所观察到的还属于强应变带的上部。垂直的密集发育劈理在变砂岩中可以观察到,同时伴生的有被强烈挤压的石英脉体(图 4-13c)。在显微尺度下,原生的面理被密集发育的近直立劈理改造(图 4-13d)。

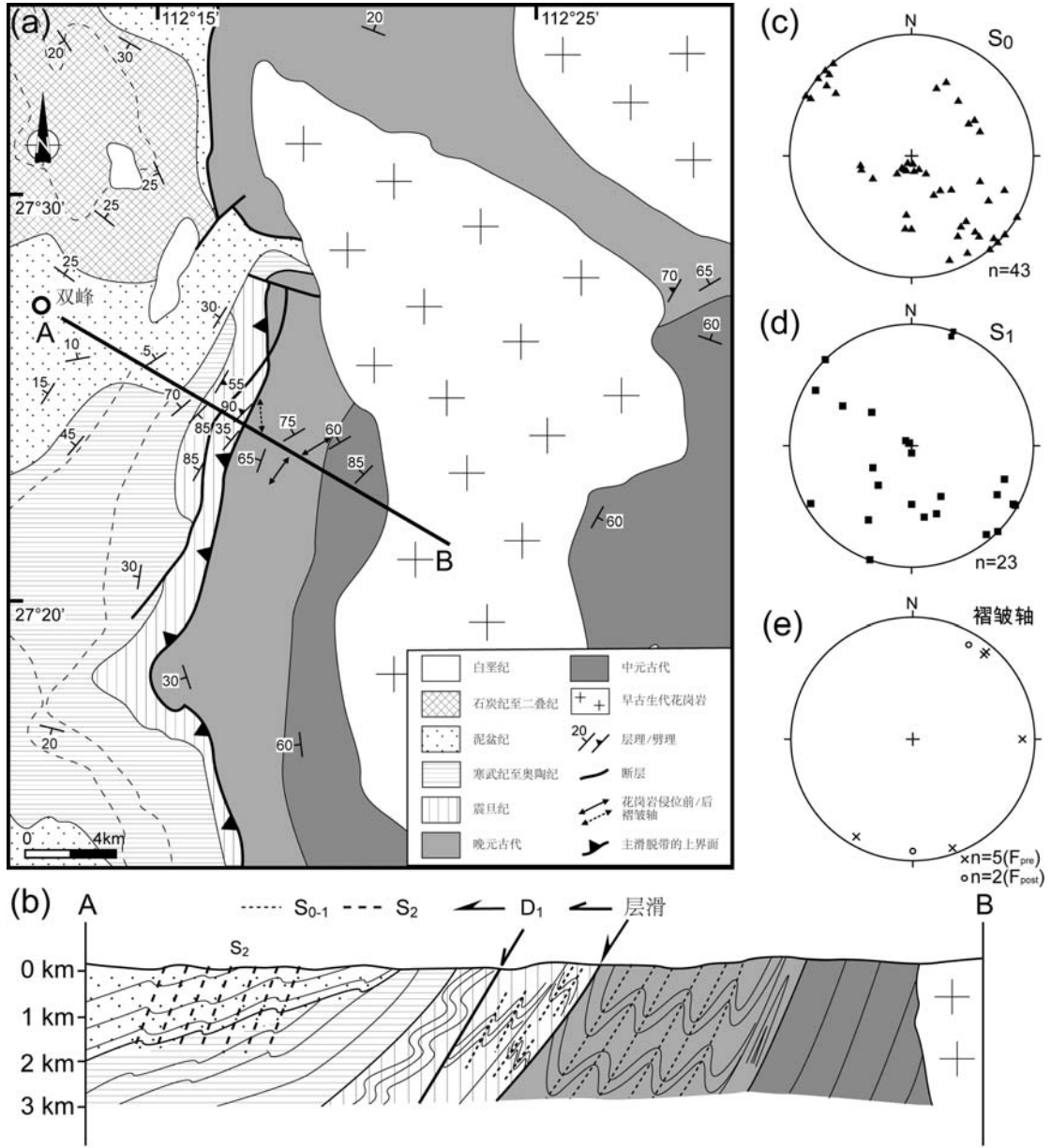


图 4-13 (a) 双峰地区区域构造地质图。(b) 构造剖面图。主要构造要素的持平投影图(施密特网下半球投影): (c) 层理 S₀。(d) S₁ 面理。(f) 褶皱轴。

尽管研究区仅仅出露了弱变质的岩石，但在岩体周边则存在了一圈接触变质环带，产出有角岩和含红柱石与黑云母的变砂岩。与前三个区域不同，在双峰地区，矿物拉伸线理相当不发育，因此剪切指向较为少见。结合地表构造，我们认为双峰地区的变砂岩和变泥岩处于雪峰山主滑脱带的上部，或者在后期岩体侵位过程中，线性构造如线理等被后期的重结晶作用所抹去。

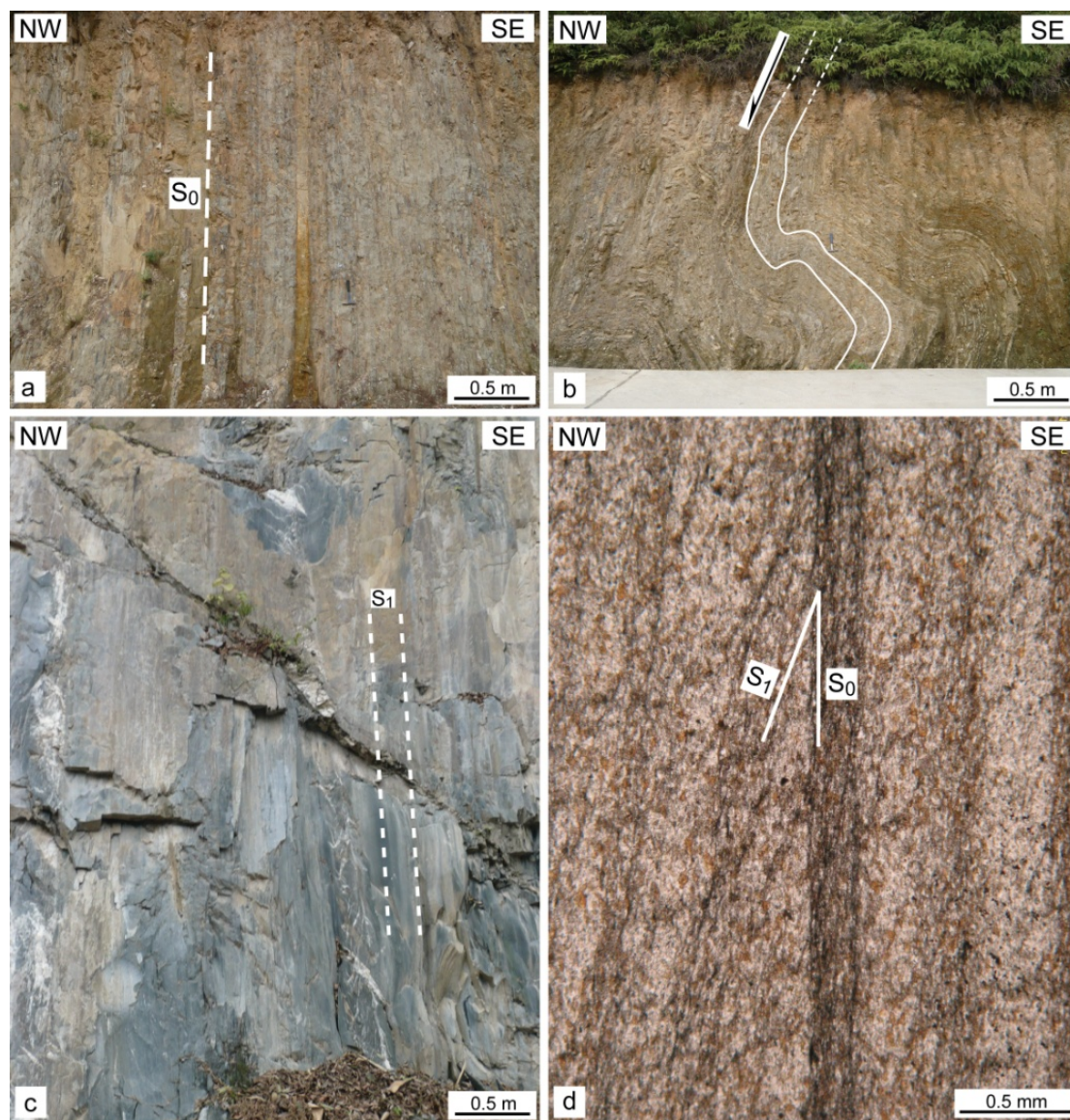


图 4-14 双峰地区野外与显微构造照片。(a) 互层的泥岩和砂岩原生层理由于岩体的掀斜作用而直立。(b) 泥质岩中发育重力滑脱褶皱。(c) 浅变质砂岩中密集发育的直立劈理构造。(d) 变泥质岩显微照片中可见 S_0 层理直立，而 S_1 劈理与其斜交。

第五节 小结

雪峰山陆内造山带在早中生代经历了多期构造变形，其中以 D_1 期上部指向 NW 的剪切作用为主导变形期，之后是 D_2 期以极性 SE 的褶皱和冲断为主的反向褶皱期以及最后的 D_3 直立褶皱期 (Wang et al., 2005)。与上部沉积盖层缺少变质作用不同，主滑脱带中岩石均经历了低绿片岩相的变质作用，以变砂岩、石英岩和云母片岩为主，局部可见含石榴子石二云母片岩。这些揭露在早中生代岩体周边的强应变岩石经历了 D_1 期的韧性变形，发育了平缓的面理、NW-SE 的拉伸线

理以及上部指向 NW 的剪切指向, 这些构造均与盖层中发育的变形构造相类似。

前人对雪峰山的研究报道了多条强应变带, 如安化—溆浦断裂等(丘元禧等, 1999; 杨奎峰等, 2004; Wang et al., 2005), 并对其进行了构造学分析。经过我们的野外观察, 这些断裂带之上的强应变岩石多为片理化强烈的千枚岩或板岩, 并未见真正的糜棱岩。雪峰山中的强应变带主要出露在早中生代岩体周边, 我们选取了城步、奉家、沅山和双峰四个地区从宏观尺度和显微尺度上进行了详细的几何学和运动学分析。在强应变带中, 发育了大量的上部指向 NW 的剪切构造, 如剪切的 σ 型石英脉、石榴子石旋转残斑以及长石的剪切斑晶, 后期上部指向 SE 的剪切对其几乎没有影响, 而直立褶皱叠加在强应变带的岩石之上。结合矿物变形和石英组构分析, 我们认为强应变带的变形温度在 300-400 度之间, 变形深度在 10 公里左右。

在早中生代构造事件中, 这些原岩为新元古代的砂岩和泥岩经历了强烈变形作用, 而上覆的震旦纪至古生代地层则没有变质作用的痕迹, 因此在二者之间存在着构造间断面, 代表着基底岩石和盖层之间的解耦, 说明在雪峰山造山带形成的时候, 地壳中可能存在一个滑脱层。朱夏先生在上世纪 80 年代初就提出华南内部的变形是在大陆岩石圈内部拆离的结果(朱夏, 1980), 而丁道桂等人结合地震剖面资料也提出华南内部早中生代构造变形存在着基底拆离带(丁道桂等, 2007); Wang et al. (2005) 也提出雪峰山底部存在一个基底拆离带, 但是没有出露至地表, 靖县—溆浦断裂、安化—通道断裂等均是基底拆离带的分支。我们结合典型地区的构造分析认为, 所有的强变形岩石组成的强应变带均位于新元古代的沉积岩之下, 而所有强变形带综合起来则代表了一个滑脱带, 即雪峰山主滑脱带。通过现有的地球物理资料分析, 雪峰山造山带地壳中存在着连续的低导层, 这很可能就对应着主滑脱带, 并控制了整个早中生代的构造变形(秦葆瑚, 1991; 范小林等, 1993, 1994; 袁学诚, 1997)。

第五章 雪峰山造山带的年代学约束

通过前文对雪峰山造山带的描述,我们对雪峰山的不同构造单元进行了详细的、多尺度的构造学解析,针对雪峰山的主变形期次的NW向构造,也是前人研究主要立足点。然而针对同样的构造,在形成年代上却存在分歧。丘元禧等(1998, 1999)认为造山作用为多期次,但主变形期在早古生代末期,即加里东期;Yan et al. (2003)则认为雪峰山主构造活动期于川东的褶皱带相类似,即中生代晚期;Wang et al. (2005)依据其糜棱岩中全岩和矿物Ar-Ar定年认为雪峰山构造带的时间在晚三叠世至早侏罗世。作者在对雪峰山构造带详细剖析的基础上,根据构造切割关系,对切穿三期构造的早中生代花岗岩和卷入变形的早古生代花岗岩进行锆石SIMS U-Pb和独居石U-Th-Pb电子探针的精确定年,以限定构造变形的上限,同时对同构造的变质岩中独居石测年,确定构造变形时间。

第一节 实验方法

1 锆石SIMS U-Pb定年

用于U-Pb年龄测定的样品用常规的重选和磁选技术分选出锆石。将锆石样品颗粒和锆石标样Plésovice (Sláma et al., 2008)和Qinghu (Li XH et al., 2009)粘贴在环氧树脂靶上,然后抛光使其曝露一半晶面。对锆石进行透射光和反射光显微照相以及阴极发光图象分析,以检查锆石的内部结构、帮助选择适宜的测试点位。样品靶在真空下镀金以备分析。

U、Th、Pb的测定在中国科学院地质与地球物理研究所CAMECA IMS-1280二次离子质谱仪(SIMS)上进行,详细分析方法见Li XH et al. (2009b)。锆石标样与锆石样品以1:3比例交替测定。U-Th-Pb同位素比值用标准锆石Plésovice (337Ma, Sláma et al., 2008)校正获得,U含量采用标准锆石91500 (81 ppm, Wiedenbeck et al., 1995)校正获得,以长期监测标准样品获得的标准偏差(1SD = 1.5%, Li XH et al., 2010)和单点测试内部精度共同传递得到样品单点误差,以标准样品Qinghu (159.5 Ma, Li XH et al., 2009b)作为未知样监测数据的精确度。普通Pb校正采用实测 ^{204}Pb 值。由于测得的普通Pb含量非常低,假定普通Pb主要来源于制样过程中带入的表面Pb污染,以现代地壳的平均Pb同位素组成(Stacey and Kramers, 1975)作为普通Pb组成进行校正。同位素比值及年龄误差均为 1σ 。数据

结果处理采用ISOPLOT软件 (Ludwig, 2001)。

2 独居石 U-Th-Pb 电子探针定年

独居石 U-Th-Pb_{tot} 定年主要有以下几个假设: (1) 与通过铀与钍衰变产生的放射性成因铅相比, 独居石中的普通铅含量可以忽略 (Parrish, 1990); (2) 在系统封闭之后, 没有放射性成因铅丢失的发生 (Cocherie et al., 1998; Crowley and Ghent, 1999; Zhu et al., 1997; Zhu and O'Nions, 1999); (3) 每个测试点都可以获得一个单独的年龄。由于电子探针的测试点径一般为 1 微米, 与传统的 U-Pb 同位素定年, 可以进行精确的原位定年, 避免了矿物中所存在的晶格缺陷以及包裹体的影响, 因此能更准确的给出年代学约束。

通常对独居石定年采取两种方法, 一种是将独居石从岩石中挑选出来, 用树脂固定在靶之上; 另一种则是直接在岩石光薄片上进行真正意义上的原位定年。本文中选用的是在岩石薄片上进行直接定年。实验所用仪器为 Cameca SX50 电子探针 (法国地质调查局和奥尔良大学)。在实验之前, 通过背散射成像在岩石薄片中寻找独居石, 并对其显微结构进行照相和详细分析, 选取合适的点进行同位素测试。

详细的分析流程见 Cocherie et al. (1998) 和 Cocherie et al. (2005b)。实验所使用的加速电压为 20 kv, 电流为 100 nA, 因为 Th 和 U 的含量一般均高于 7500 ppm, 为了避免 U 含量高的颗粒造成的异常低误差, 对于 U、Th 和 Pb 的检测下限 (2σ) 均设定为 150 ppm (Cocherie and Legendre, 2007)。独居石测年的标准矿物选取如下: Pb—方铅矿 (PbS), U—晶质铀矿 (UO₂), Th—方钍石 (ThO₂), 稀土元素和 Y—合成磷酸盐 (XPO₄), P—磷灰石, Si 和 Ca—钙铁榴石。

当在独居石之中存在两个或者两个以上均一的、形成时代不同的区域, 而且年龄间隔要小于分析检测误差, 我们可以通过选取合适的等时线投图将其分开 (Suzuki and Adachi, 1991; Suzuki et al., 1994; Cocherie et al., 1998; Cocherie and Albarède, 2001; Suzuki and Kato, 2008)。Cocherie et al. (2005b) 证明, 根据实验矿物颗粒的地球化学性质的不同, 通过选取合适的投图, 可以获得误差范围在 5 到 10 Ma (2σ) 之间的精确年龄。

通过电子探针显微分析仪 (EPMA: Electron Probe MicroAnalyzer) 得到的数

据经过一个 Excel 的宏程序处理后即可获得单点的 U-Th-Pb_{tot} 年龄。这些数据再通过 ISOPLOT 程序进行 U/Pb-Th/Pb 投图处理(Ludwig, 2001)。最终获得 U-Th-Pb 的年龄、Th-Pb 年龄(与 Th/Pb 坐标轴的交点)和 U-Pb 年龄(与 U/Pb 坐标轴的交点)。所有的计算均在 2σ 误差下进行。最后, MSWD 的大小对于年龄的可靠性有着重要的作用, 即所获得的年龄的 MSWD 必须低于 $1+2/(2/f)^{0.5}$, 其中 f 为自由度, 等于测试点数减去热事件数(Wendt and Carl, 1991)。

第二节 样品描述

1 花岗岩

雪峰山地区出露的花岗岩主要为两个时代——早古生代和早中生代, 其中早古生代的花岗岩卷入了早中生代的变形之中, 而早中生代花岗岩则切割了之前的变形, 限制了变形的上限。

早古生代花岗岩主要分布在雪峰山的南部和东部地区, 出露面积超过 3000 平方公里。实验样品(XF76、XF93、XF99、XF219、XF270、XF274 和 XF314) 主要为中粗粒黑云母二长花岗岩、黑云母花岗岩和含角闪石花岗岩。矿物成分为: 钾长石(~25%)、斜长石(~35%)、黑云母(~10%)和石英(~30%), 同时含少量的角闪石、白云母和其他副矿物。

早中生代花岗岩在雪峰山花岗岩中出露面积最大、分布最广, 超过了 5000 平方公里(湖南省地质矿产局, 1988)。与早古生代花岗岩类似, 早中生代花岗岩(XF17、XF73、XF205、XF208、XF213、XF216 和 XF221) 主要是黑云母二长花岗岩和黑云母花岗岩, 根据是否含有角闪石或白云母又可分为两类(图 5-1a 和 5-1b)。矿物组合主要为黑云母(~8%)、斜长石(~40%)、钾长石(~20%)和石英(30%), 同时含有少量角闪石(~2%)或白云母(~2%)。两类花岗岩与 A/CNK 指数有较好的一致性(Wang et al., 2007b), 即含角闪石(XF17、XF216 和 XF221)的 A/CNK 指数在 1.0 至 1.1 之间, 为铝质花岗岩; 而含白云母(XF73、XF205、XF208 和 XF213)的 A/CNK 指数大于 1.1, 表明为过铝质花岗岩。

除此之外, 早古生代和早中生代花岗岩的构造变形也有不同的表现。在早古生代岩体的边部, 如白马山岩体, 由于卷入了早中生代的构造作用, 形成了数十米到数百米的变形带。在这个带之中, 石英受到了强烈的剪切作用而强烈重结晶

化，围绕在长石的周边。长石在外力之下也发育了波状消光或火焰状的消光（图 5-1c）。相比于早古生代花岗岩，早中生代花岗岩则缺少韧性变形，仅仅可见岩浆在固相之前的变形现象，如蠕英构造，在岩浆未固结前在长石与石英之间发生交代作用而产生的石英进入长石的蠕虫型包裹体（图 5-1d）。

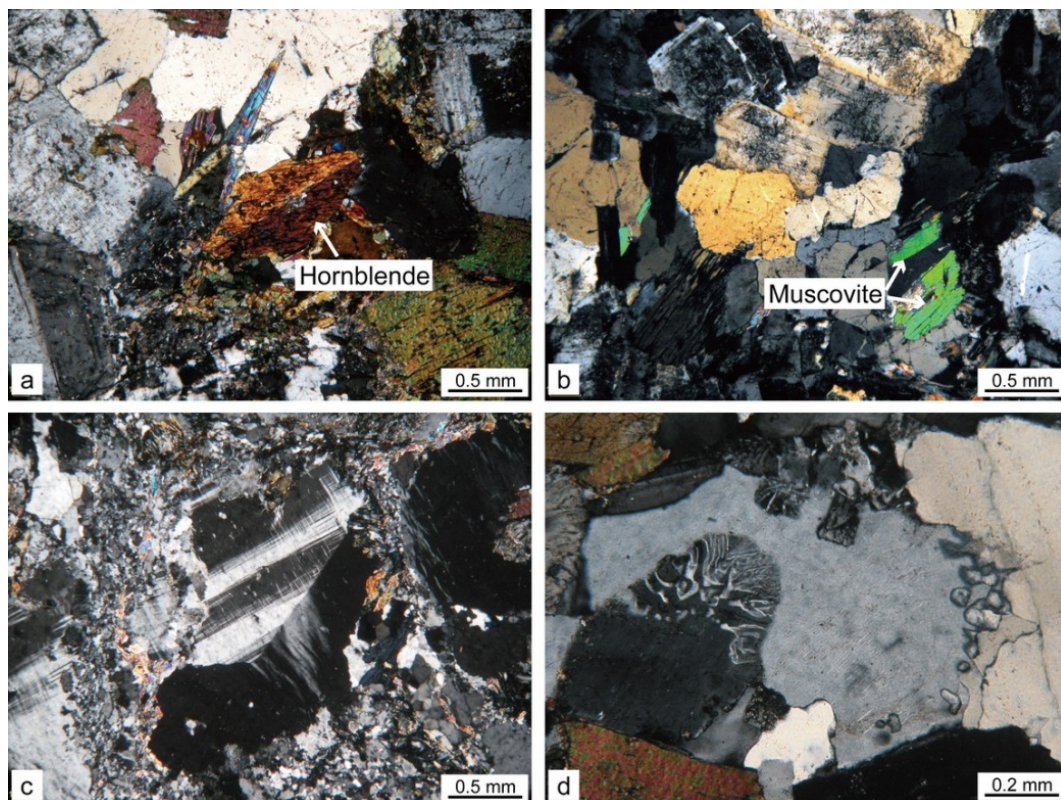


图 5-1 雪峰山花岗岩的显微照片。(a) 含角闪石 (hornblende) 早中生代花岗岩。(b) 含白云母 (muscovite) 早中生代花岗岩。(c) 早古生代花岗岩中石英的动态重结晶和斜长石中的机械双晶构造。(d) 不发育韧性变形的早中生代花岗岩，但有固相前变形的指示标志——蠕英构造。

2 变质岩

雪峰山的变质岩最高经历了低绿片岩相的变质作用，以含矽线石二云母片岩或含石榴子石云母片岩为主，代表了早中生代变质峰期的产物(图 5-2a 和 5-2b)。我们在云母片岩中选取了两个样品进行了独居石的电子探针原位测年，分别为含石榴子石 (XF365) 和含矽线石 (XF376)，以期获得同构造变质作用的年龄，从而从年代学上更好地限定雪峰山造山带主变形期。

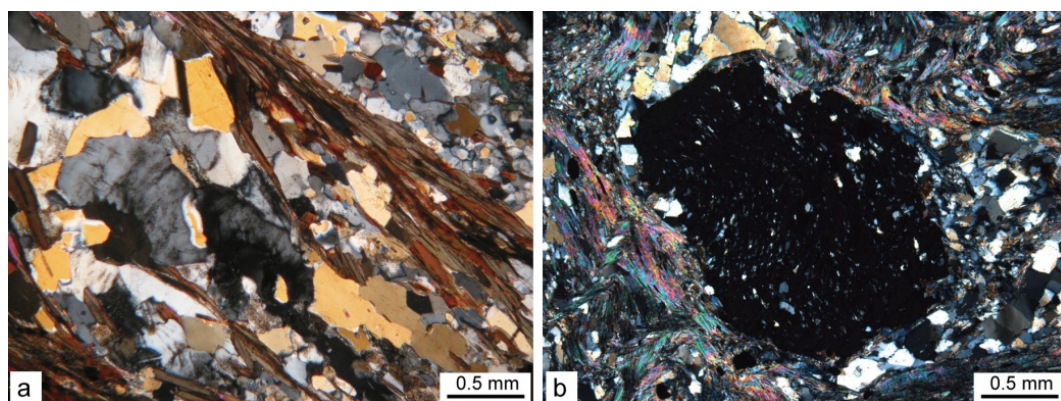


图 5-2 雪峰山变质岩的显微照片。(a) 含矽线石石英云母片岩。(b) 含石榴子石云母片岩。

第三节 锆石 SIMS U-Pb 年代学结果

我们一共在研究区选取了 14 个代表性的花岗岩体（早古生代 7 个、早中生代 7 个）进行锆石 SIMS U-Pb 的年代学测定，详细的 GPS 位置和岩性如表 5-1 所示，并在图 5-3 中标出。

表 5-1 雪峰山早古生代和早中生代花岗岩采样点及年龄表。

岩体	样品	岩性	GPS	年龄 (Ma)
早中生代				
桃江	XF17	黑云母花岗岩	N28°28.624', E112°04.268'	220 ± 2
油榨坪 (资源)	XF73	黑云母花岗岩	N25°56.121', E110°38.082'	219 ± 2
塔山	XF213	二云母花岗岩	N26°11.709', E112°16.528'	224 ± 2
关帝庙	XF216	二长花岗岩	N26°57.392', E112°08.094'	225 ± 2
白马山 (高坪)	XF221	角闪石花岗岩	N27°35.756', E110°58.355'	217 ± 2
汾山	XF205	二长花岗岩	N28°00.255', E112°00.455'	222 ± 3
紫云山	XF208	二长花岗岩	N27°27.802', E112°22.327'	225 ± 2
早古生代				
都庞岭	XF76	二长花岗岩	N25°20.102', E111°05.427'	428 ± 4
桂东	XF93	角闪石花岗岩	N26°05.496', E113°58.364'	438 ± 3
万洋山	XF99	二云母花岗岩	N26°27.393', E113°49.097'	437 ± 4
白马山 (主体)	XF219	角闪石花岗岩	N27°27.948', E110°57.279'	411 ± 4
苗儿山	XF270	黑云母花岗岩	N26°27.690', E110°30.608'	412 ± 4
越城岭 (主体)	XF274	黑云母花岗岩	N26°10.109', E110°43.674'	424 ± 3
兰蓉	XF314	黑云母花岗岩	N26°19.743', E110°26.519'	418 ± 3

1 早古生代花岗岩

七个早古生代花岗岩样品经过粉碎选矿后挑选出的锆石大多数为自形至半自形, 呈现出黄色-粉色的透明形态, 锆石大小一般从 50 μm 至 250 μm , 长宽比从 1:1 到 4:1。同时在阴极发光下显现出较为发育的成分环带 (图 5-4)。结合绝大多数测试点的 Th/U 比值 (0.1 至 1.6 之间), 表明早古生代花岗岩中的锆石为岩浆成因, 仅有几个年龄较老的锆石具有较低的 Th/U 比值, 为继承锆石。所有测试数据详见附录表 1。以下将对早古生代花岗岩一一阐述。

XF76 采自广西壮族自治区北部都庞岭岩体的二长花岗岩。对本样品的 16 个锆石进行两个分析测试, 这些分析点具有相对较低的 U 含量 (210-564 ppm) 和 Th 含量 (45-283 ppm), Th/U 比值在 0.128 至 0.652 之间, 只有一个点年龄在 832.5 Ma 的比值低于 0.1。除了 3 个继承锆石分别给出 926 Ma、833 Ma 和 822 Ma, 剩余的 13 个点在谐和图上较为集中, 给出了一个和谐年龄为 428 ± 4 Ma (图 5-5a), 代表了岩浆的冷却结晶年龄。

XF93 采自湖南省与江西省交界地区的桂东岩体。通过 16 个点的分析, 岩体中典型锆石的 U 含量在 272 至 673 ppm 范围之内, Th 含量在 88 到 235 ppm 之间, 而 Th/U 比值分布在 0.286 到 0.503 范围之间, 显示岩浆锆石的成因性质。所有的测试点分布集中, 谐和年龄为 438 ± 3 Ma (图 5-5b), 代表了岩体形成时代。前人在上世纪九十年代初也对此岩体进行了单颗粒锆石 TIMS 定年, 得出了 426 ± 2 Ma 和 427 ± 2 Ma 的锆石年龄, 这比我们的结果稍年轻 (李献华, 1991, 1994), 但均表明岩体形成于早古生代。

样品 XF99 为二云母花岗岩采自于湖南省和江西省交界的万洋山岩体。通过对 13 个锆石的原位 U-Pb 分析, U 含量从 122 到 812 ppm, Th 含量在 49 到 297 ppm 之间, Th/U 比值在 0.146 到 0.907。所有的测试点均落在谐和线之上, 给出 437 ± 4 Ma 的谐和年龄 (图 5-5c), 代表了岩浆结晶年龄。这与前人通过 TIMS 实验所得的锆石 U-Pb 年龄 434 ± 1 Ma 在误差范围内一致 (Li XH, 1991)。

样品 XF213 采自白马山岩体南缘, 14 个锆石点测试的 U 含量范围较大, 从 318 至 2086 ppm, Th 含量从 191 至 1271 ppm, Th/U 比值也分布在岩浆锆石成因区间之内, 0.327 至 0.910。所有的测试点位于谐和线之上, 给出了 411 ± 4 Ma 的谐和年龄 (图 5-5d), 说明白马山岩体主要在 411 Ma 左右冷却结晶。

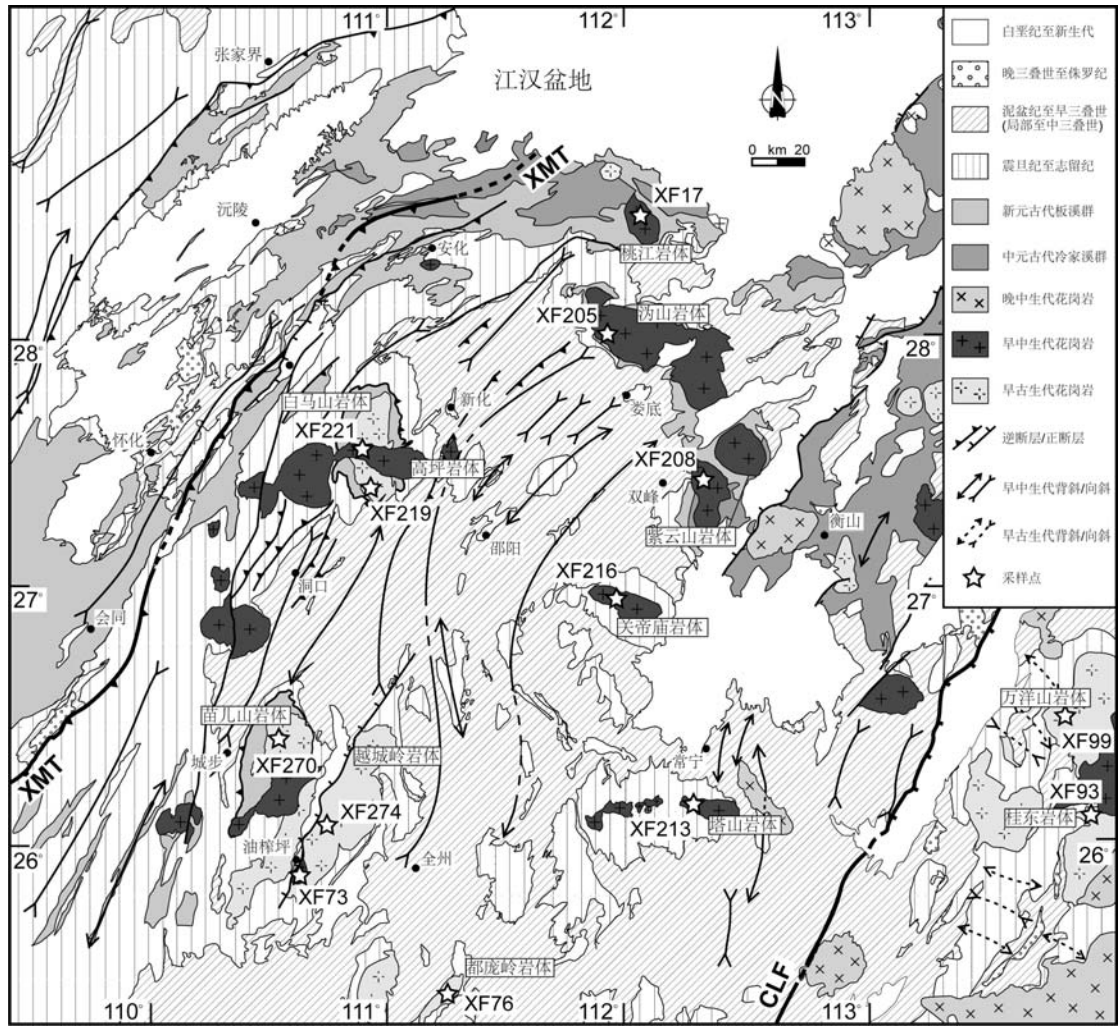


图 5-3 研究区所采的花岗岩样品在区域上的分布。XMT：雪峰山主逆冲断层。

样品 XF270 采自苗儿山岩体，进行了 14 个锆石点的分析，测得 U 含量的变化范围在 480 到 1827 ppm 之间，Th 含量在 160 至 1223 ppm 范围之间，Th/U 比值在 0.288 至 0.692。在 U-Pb 谐和图中，所有的点位于谐和线之上，表明锆石形成之后的 U-Pb 体系封闭未有 U、Pb 同位素的丢失或加入（图 5-5e）。在岩浆韵律环带之上的测试点给出 412 ± 4 Ma 的谐和年龄，表明花岗岩于此年龄侵位于地表浅部。

样品 XF274 采自越城岭岩体，为糜棱岩化的花岗片麻岩，但这次的糜棱岩化为晚中生代构造作用产物（湖南省地质矿产局，1988）。23 个锆石测试点得出 U 含量在 116 至 2453 ppm、Th 含量在 139 至 951 ppm 之间，而 Th/U 比在 0.230

至 1.263 之间，均为为岩浆成因锆石。在锆石 U-Pb 谐和图之中，所有的测试点均落在谐和线之上，说明锆石形成之后的 U-Pb 体系一直保持着封闭的状态（图 5-5f）。23 个点给出 424 ± 3 Ma 的谐和年龄，这代表了岩体的结晶年龄。

XF314 采自苗儿山岩体以西的一个较小的兰蓉岩体。这个岩体整体均经历早中生代韧性剪切作用，岩石受到了糜棱岩化，边部强烈变形，形成了成分层，而岩体中心的岩石也因剪切而使得长石发生明显的定向排列。15 个测试点测得锆石 U 含量为 163-1581 ppm，Th 含量在 195-500 ppm，Th/U 比值在 0.280-1.322 范围之内。锆石 U-Pb 谐和图之中，15 个测点同样都落在谐和曲线之上，得到 418 ± 3 Ma 的谐和年龄，说明岩体在此年龄上升至地表并冷却结晶，固结成岩。

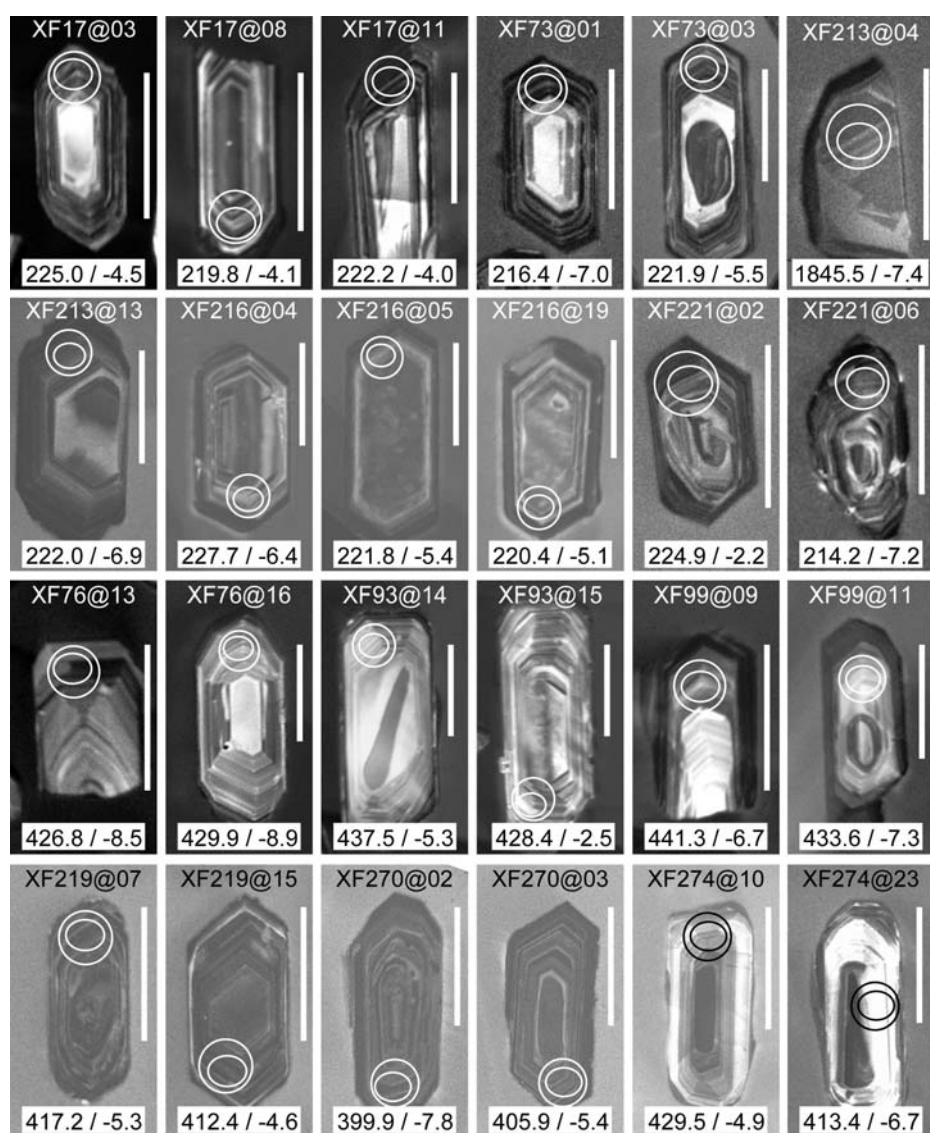


图 5-4 雪峰山早古生代和早中生代花岗岩中锆石阴极发光图像。大圈为 U-Pb 年龄，小圈为 Hf 同位素值。

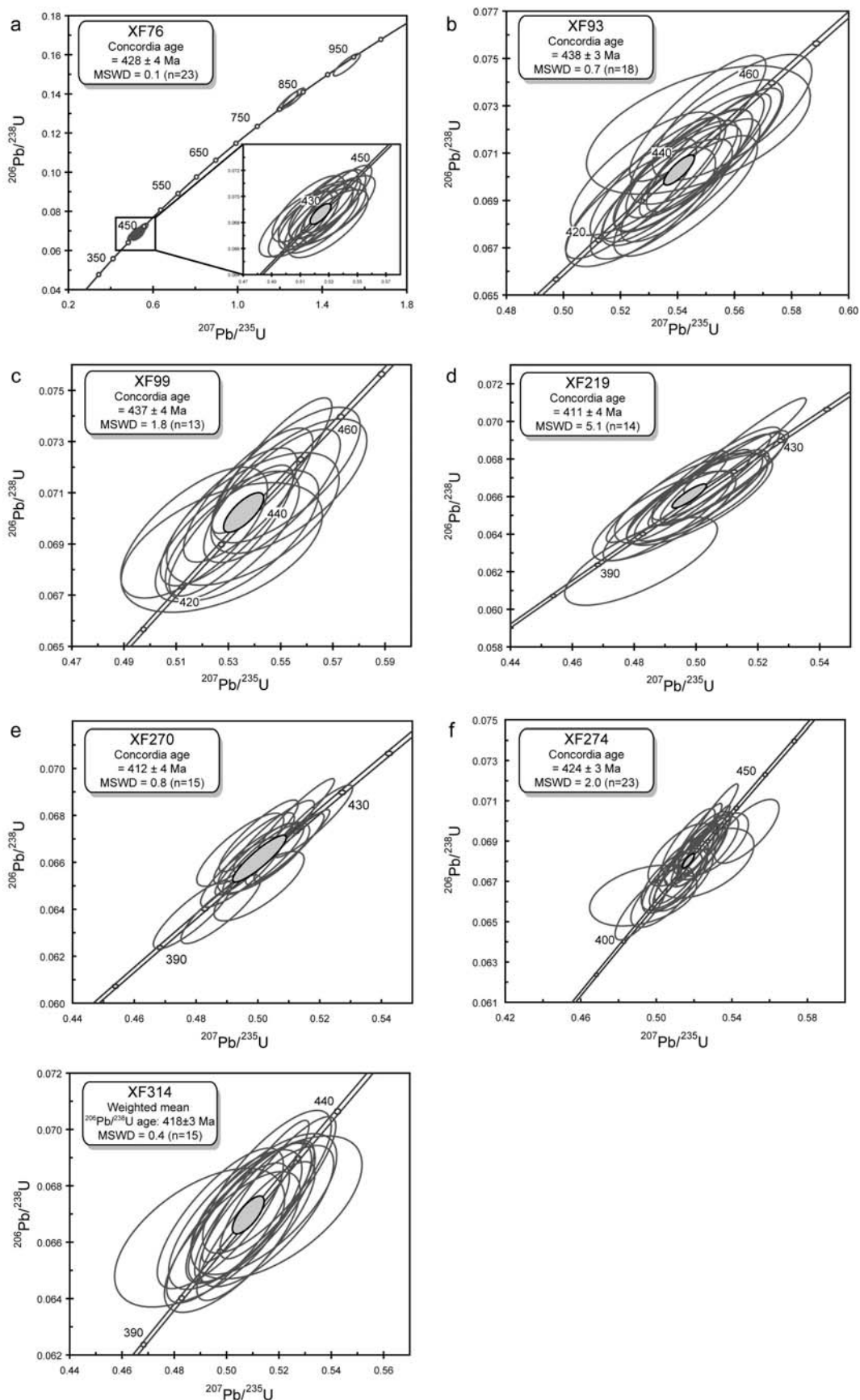


图 5-5 研究区早古生代花岗岩锆石 U-Pb 谐和图。

2 早中生代花岗岩

由于印支期构造活动的重要性,前人对雪峰山地区的印支期花岗岩也进行了同位素年代学的研究,并获得了 245-235 Ma 和 230-215 Ma 两个岩浆活动阶段(王岳军等, 2005; Wang et al., 2007b; Li and Li, 2007; 李华芹等, 2008; 罗志高等, 2010)。对于研究区内的早中生代花岗岩,我们也同样选取了 7 个代表性岩体进行了年代学的测定。通过我们对这一期次的重新定年,我们精确限定了岩浆活动的时间,同时也为限定早中生代构造活动的年代学上限提供了重要依据。

早中生代花岗岩体中的锆石大多数为淡黄色或无色透明,呈自形至半自形的形态,以短柱状或长柱状为主,锆石大小一般从 50 μm 至 300 μm ,长宽比主要集中在 2:1 到 4:1 之间,少数可达 6:1。在阴极发光下,多数锆石具有清晰的成分环带,只有在 XF213 的锆石中具有云雾状或港湾状的形态,韵律环带不发育(图 5-4)。绝大多数锆石分析点的 Th/U 比值大于 0.1,表明早中生代花岗岩中的锆石为岩浆成因,仅在 XF213 中广泛存在着年龄较老的锆石,具有较低的 Th/U 比值,说明为继承锆石或者可能经历了后期的重结晶作用(Vavra et al., 1996; Pidgeon, 1992; 吴元保等, 2001)。所有测试数据详见附录表 1。

XF17 采自雪峰山北部桃江岩体,进行了 13 个锆石点的分析,测得 U 含量的变化范围在 238 到 1520 ppm 之间,Th 含量在 131 至 871 ppm 范围之内,Th/U 比值在 0.277 至 0.710。成分相对稳定,使得锆石单点年龄的分布也较为集中。在 U-Pb 谐和图中,所有的点位于谐和线之上,表明锆石形成之后的 U-Pb 体系封闭未有 U、Pb 同位素的丢失或加入(图 5-6a)。在岩浆韵律环带之上的测试点给出 220 ± 2 Ma 的谐和年龄,代表了花岗岩的侵位年龄。

样品 XF73 采自雪峰山资源县越城岭岩体的油榨坪附近,通过对 16 个锆石进行单点的 U-Pb 同位素分析,U 含量范围在 162 到 2486 ppm 之间,Th 含量在 154 至 1416 ppm 范围之内,Th/U 比值从 0.221 至 1.575,指示了岩浆成因。成分相对稳定,使得锆石单点年龄的分布也较为集中。在 U-Pb 谐和图中,所有的点位于谐和线之上,表明锆石形成之后的 U-Pb 体系封闭未有 U、Pb 同位素的丢失或加入(图 5-6b),后期的流体作用也没有影响这一封闭体系。在岩浆韵律环带之上的测试点给出 220 ± 2 Ma 的谐和年龄,代表了花岗岩的侵位年龄。

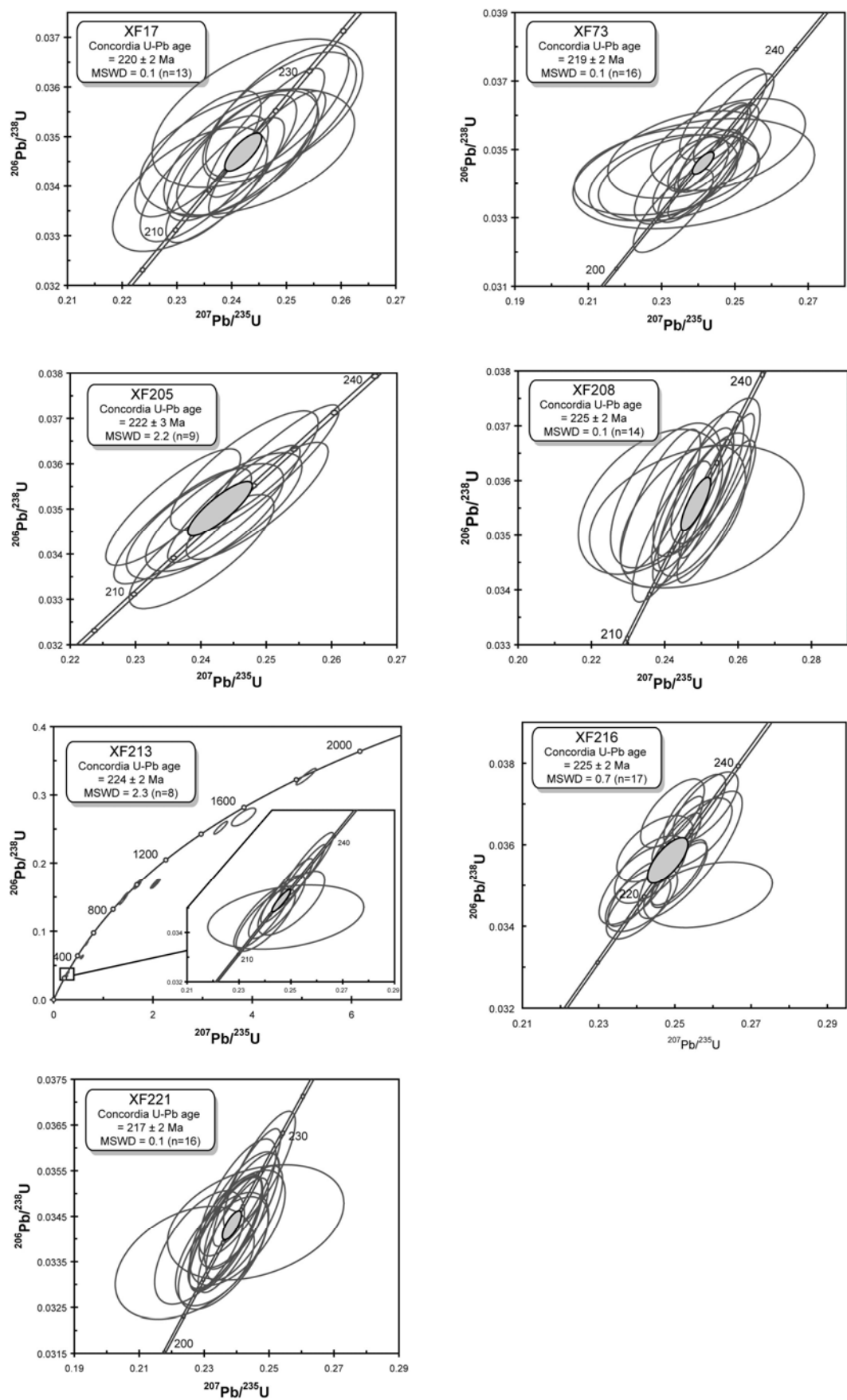


图 5-6 研究区早中生代花岗岩锆石 U-Pb 谐和图。

XF205 采自湖南省娄底以北沅山岩体，为一黑云母二长花岗岩，通过对 14 个锆石进行单点的 U-Pb 同位素分析，结果显示此岩体锆石 U 含量较高，范围在 1202 到 7648 ppm 之间，Th 含量也相对丰富，在 192 至 2176 ppm 范围之间，Th/U 比值从 0.067 至 0.347。在 U-Pb 谐和图中，所有的点位于谐和线之上，表明锆石形成之后的 U-Pb 体系封闭未有 U、Pb 同位素的丢失或加入（图 5-6c）。但是在所有的测试点中有 5 个点的 U 含量高于 4000 ppm，而这 5 个点的也选在岩浆韵律环带之上，但是得到的年龄也相对较老。同样的现象前人也在 SIMS 锆石 U-Pb 分析中报道过（如 Li QL et al., 2010）。因此，去除这 5 个点，剩下的 9 个测试点给出 222 ± 3 Ma 的谐和年龄，代表了花岗岩的侵位年龄（图 5-6c）。前人通过 SHRIMP 或 LA-ICP-MS 方法也对这一岩体进行了 U-Pb 同位素测年，但是结果却有着较大的差异。丁兴等（2005）在沅山岩体中选取了两个样品，测得年龄分别为 215 Ma 和 211 Ma；而 Wang et al.（2007）同样选取了两个样品，却分别为 243 Ma 和 210 Ma。此次我们通过更为精确的 SIMS 将沅山岩体的年代学确定为 222 Ma。

XF208 采自湖南省双峰县以东紫云山岩体，为一块新鲜的黑云母二长花岗岩。湖南省地质矿产局（1988）曾经对此岩体进行过锆石 U-Pb 定年，认为是侏罗纪岩体。但是我们通过对 14 个锆石进行单点的 U-Pb 同位素分析认为此岩体为三叠纪花岗岩。结果显示此岩体锆石 U 含量范围在 851 到 1603 ppm 之间，Th 含量在 172 至 817 ppm 范围之间，Th/U 比值从 0.203 至 0.538。在 U-Pb 谐和图中，所有的点位于谐和线之上，表明锆石形成之后的 U-Pb 体系封闭未有 U、Pb 同位素的丢失或加入。图中 14 个测试点分布集中，给出 226 ± 2 Ma 的谐和年龄，代表了花岗岩的侵位年龄（图 5-6d）。

样品 XF213 采自雪峰山南部常宁市以南塔山岩体。这个样品中锆石显示出非岩浆锆石的属性，如锆石阴极发光中有的锆石为港湾状。而且通过对 17 个锆石进行单点的 U-Pb 同位素分析，U 含量范围相当大，在 47 到 3964 ppm 之间，Th 含量在 23 至 373 ppm 范围之间，Th/U 比值从 0.009 至 1.191，部分锆石指示了岩浆成因，而部分 Th/U 比值较低的锆石，通过结合阴极发光表明为变质锆石。在 U-Pb 谐和图中，两种锆石也较好的体现出来。如 XF213@5、XF213@6、XF213@9 和 XF213@9-1 这四点位于谐和线之右，表明锆石形成之后的 U-Pb 体

系封闭有 U、Pb 同位素的丢失, 或者是后期的流体作用影响了这一封闭体系(图 5-6e)。而在谐和线接近 220 Ma 的附近, 有 8 个点集中分布于谐和线之上, 为样品中锆石的最小年龄, 表明花岗岩的形成年龄。这些位于岩浆韵律环带之上的测试点给出 224 ± 4 Ma 的谐和年龄, 代表了花岗岩在此时侵位于浅表。其余的测试锆石的表面年龄在 251 至 1823 Ma 之间, 为岩浆源区中继承的锆石。

XF216 采自湖南省邵阳市以东关帝庙岩体, 为一含角闪石花岗岩样品。我们通过对 19 个锆石进行单点的 U-Pb 同位素分析认为此岩体为三叠纪花岗岩。结果显示此岩体锆石 U 含量范围在 280 到 4484 ppm 之间, Th 含量在 189 至 4577 ppm 范围之间, Th/U 比值从 0.386 至 1.021。在 U-Pb 谐和图中, 所有的点位于谐和线之上, 表明锆石形成之后的 U-Pb 体系封闭未有 U、Pb 同位素的丢失或加入。图中 19 个测试点分布集中, 给出 225 ± 2 Ma 的谐和年龄, 代表了花岗岩的侵位年龄(图 5-6f)。同样的, 关帝庙岩体前人也做了年代学研究, 但是年龄数据仍然差距较大, Wang et al. (2007) 得到了 236 Ma 的 U-Pb 年龄, 而陈卫锋等(2007) 的 LA-ICP-MS 锆石 U-Pb 年龄为 203 和 208 Ma, 二者有着较为明显的差距。由于激光锆石 U-Pb 的准确性没有 SIMS 准确, 同时由于束斑大而受到的干扰会较大; Wang et al. 的年龄则可能受到了 U 含量较高的影响, 所以我们的精确测定给出了 225 Ma 应该最为接近岩体侵位的真实年龄。

XF221 采自湖南省新化县白马山复式岩体中的高坪附近岩体, 样品为一块新鲜的黑云母二长花岗岩。通过对 16 个锆石进行单点的 U-Pb 同位素分析显示, 此岩体锆石 U 含量范围在 191 到 1559 ppm 之间, Th 含量在 87 至 713 ppm 范围之间, Th/U 比值从 0.263 至 0.746。在 U-Pb 谐和图中, 16 个点均位于投在谐和线之上, 表明锆石形成之后的 U-Pb 体系封闭, 没有遭受后期变质作用、流体作用的改造而改变系统的封闭性。16 个测试点分布集中, 给出 217 ± 2 Ma 的谐和年龄, 代表了花岗岩的侵位年龄(图 5-6g)。这与 Wang et al. (2007) 的 241 Ma 有着较大出入, 但是与 Li and Li (2007) 的年龄完全一致, 说明 217 Ma 正是岩体冷却结晶的年龄。

第四节 独居石电子探针定年

对于现在应用越来越广泛的独居石电子探针化学定年法, 我们也选取了 4

个花岗岩样品（XF205、XF208、XF326 和 XF366）和 2 个变质的云母片岩样品（XF365 和 XF376）进行测年。这些独居石主要以包裹体的形式存在于黑云母之中，大小主要在 50 至 200 μm 之间（图，但也有直径在 500 μm 以上的巨大的独居石（图）。详细的独居石测试数据见附表 2。

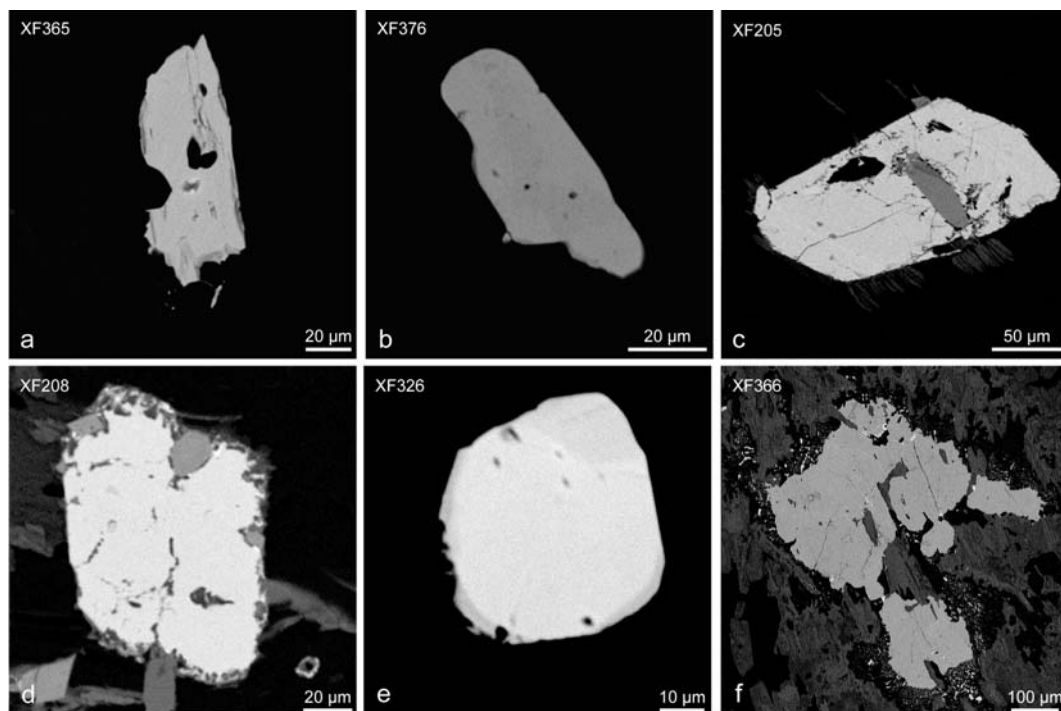


图 5-7 研究区云母片岩（a-b）和早中生代花岗岩（c-f）中独居石照片。

样品 XF365 采自城步以东兰蓉镇附近 ($N26^{\circ}16.467'$, $E110^{\circ}24.269'$)，为一块含石榴子石、白云母、黑云母、石英和绿泥石的二云母片岩，位于雪峰山的主滑脱带之上。在薄片之中， S_1 面理为最主要的构造表征，在石榴子石旋转残斑边部形成的不对称压力影构造，指示了上部指向 NW 的剪切方向，与在 D_1 的构造作用下形成的宏观与微观构造特征相似。在 XF365 之中，独居石的矿物颗粒主要位于边部有绿泥石化黑云母之中，大小从 10 至 80 μm 不等，环带构造不发育，表明都是在同一期构造事件中形成的独居石（图 5-7a）。样品中独居石颗粒均为长柱状，其长轴的优选方位平行于 S_1 面理。由此我们可以确定这些独居石都是在 D_1 构造作用下结晶形成的同变质矿物。正是由于电子探针的精确性，使得我们可以在原位选择最大的而且没有环带构造的颗粒进行定年，以期获得同变质-

变形年龄。通过 74 个有效测试点的分析和计算，我们获得了一个加权平均年龄 243 ± 9 Ma，MSWD 为 1.2，表明年龄属于有效范围之内（图 5-8a）。我们将其解释为韧性变形的时间。

样品 XF376 采自沩山镇以东附近 ($N28^{\circ}11.317'$, $E111^{\circ}58.108'$)，为一块含矽线石、白云母、黑云母、石英的二云母片岩，同样采自位于雪峰山的主滑脱带之上。在薄片之中， S_1 面理清晰可见，矽线石和云母等矿物定向排列明显，薄片剪切指向为上部指向 NW，为 D_1 的构造作用下构造特征。在 XF376 之中，背散射电子图像显示独居石的矿物颗粒主要产出于黑云母或基质之中，大小从 20 至 50 μm ，环带构造不发育，表明都是在同一期构造事件中形成的独居石（图 5-7b）。样品中独居石颗粒均为长柱状，其长轴的优选方位也近似平行于 S_1 面理。由此我们可以确定这些独居石也都是在 D_1 构造作用下结晶形成的。由于放射性成因铅含量较低，因此单点测试所得的年龄较大，但通过对 13 个颗粒上 28 个有效测试点的分析和加权平均计算，我们获得了一个加权平均年龄 226 ± 18 Ma，MSWD 为 0.95，表明年龄属于有效范围之内（图 5-8b）。故我们可以将其解释为与矽线石相变质作用同时发生的韧性变形时间。

样品 XF205，采自沩山岩体，由于其分布范围较大的 Th/U 比值较为适用 Th/Pb-U/Pb 投图 (Cocherie and Albarede, 2001)。通过 91 个单点测试，我们得到了较好的上下交点年龄 (U/Pb 年龄: $222 + 24/ - 25$ Ma 和 Th/Pb 年龄: 239 ± 7 Ma)。最后计算得出的年龄为 236 ± 4 Ma (图 5-8c)。

样品 XF326 采自瓦屋塘岩体，位于白马山岩体和苗儿山岩体之间的早中生代岩体。在 10 个独居石颗粒上进行 68 个点分析之后，我们发现该样品的独居石之中 Th/U 比值较 XF205 更为集中，因此分析点在 Th/Pb 对 U/Pb 的投图中较为集中，并产生了误差较大的上下交点年龄 (U/Pb 年龄: $219 + 75/ - 87$ Ma 和 Th/Pb 年龄: $236 + 18/ - 16$ Ma)。尽管如此，其回归线与理论的等时线较为接近 (图 5-8d)，所以我们认为计算得出的 233 ± 6 Ma 可以代表独居石年龄。

样品 XF366 采自城步以东苗儿山岩体以西的兰蓉岩体，与 XF314 位置相近。整个兰蓉岩体均受到了韧性剪切变形，边部呈糜棱岩化，中心部分变形稍弱，但长石定向明显 (详细介绍见第四章第一节)。独居石原位电子探针测试结果显示，相对恒定的 Th/U 的比值并不适用于 Th/Pb 对 U/Pb 的投图，而最适合的则是

Suzuki and Adachi 的 Pb-U* 投图 (1991)。在 Pb-U* 图解中, 所有分析点所形成的回归线与 X 和 Y 轴的交点非常接近原点, 符合使用此投图的要求。112 个测试点给出 414 ± 18 Ma 的年龄, 在误差范围之内与 XF314 的 SIMS 锆石 U-Pb 定年结果几乎一致。

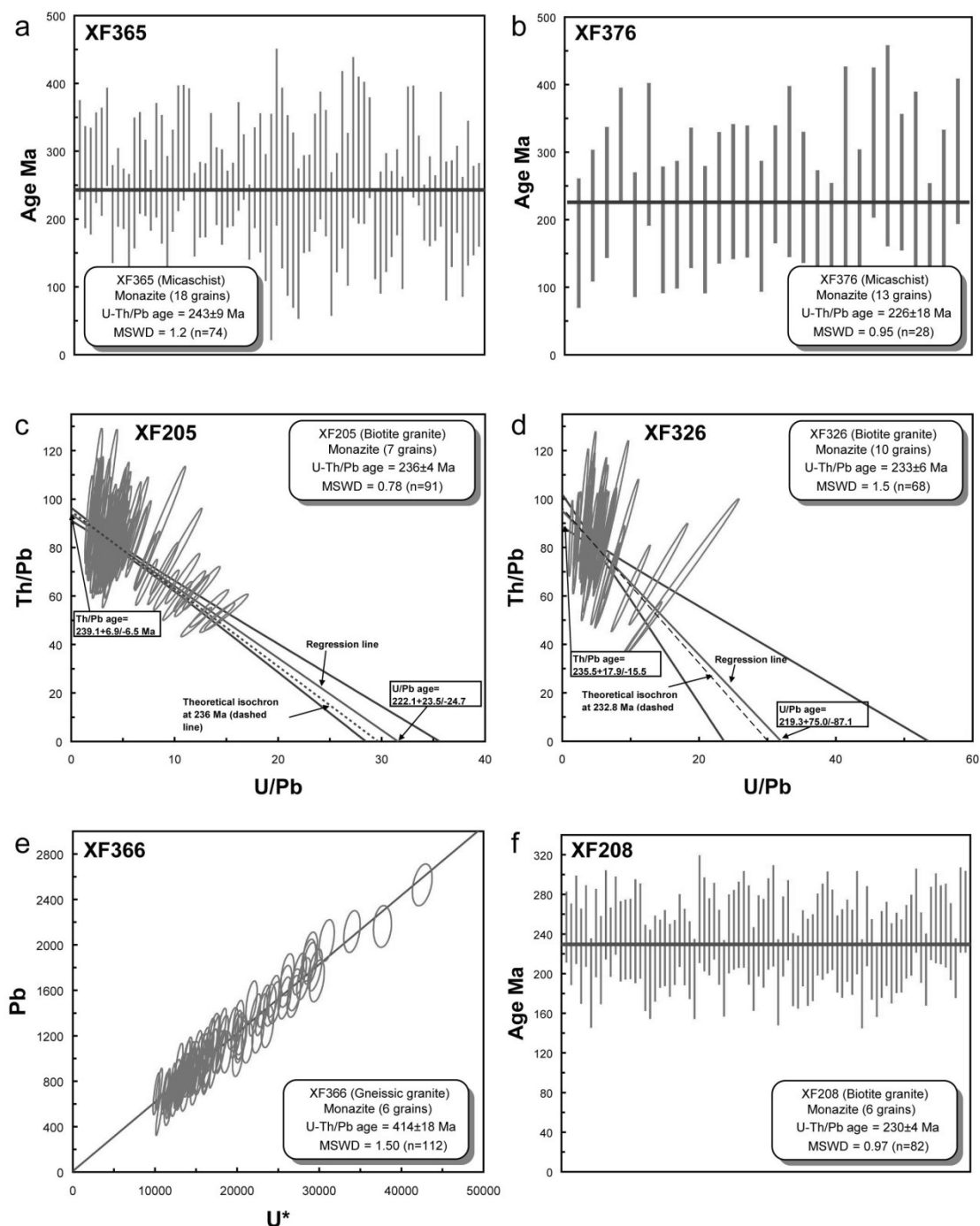


图 5-8 研究区云母片岩 (a-b) 和早中生代花岗岩 (c-f) 的独居石年代学投图。

样品 XF208 通过 U-Pb 定年得到的结果为 225 ± 2 Ma。通过独居石电子探针测试, 我们发现由于 Th/U 比值过于集中, 因此无论是 Th/Pb 对 U/Pb 的投图还是 Pb-U*投图, 都无法得到准确的年龄, 因此只能使用加权平均年龄 230 ± 4 Ma 来代表所得的独居石年龄, MSWD 为 0.97, 表明得到的年龄真实可信。同时在误差范围内与锆石 U-Pb 年龄较为一致。

第五节 年代学意义及小结

雪峰山地区的花岗岩主要形成于两个时代: 早古生代和早中生代。早古生代片麻花岗岩年龄为 440-410 Ma, 而早中生代则在 225-215 Ma 之间。

如前文所述, 早古生代构造作用在雪峰山地区并没有形成明显的挤压作用和地壳缩短。相反, 早古生代造山作用在雪峰山以东地区, 及华南板块东南部形成了强烈的构造变形 (舒良树等, 1997, 1999; Lin et al., 2008; Faure et al., 2009; Charvet et al., 2010), 大范围的高级变质作用 (Wang et al., 2007a; Wan et al., 2007, 2010; Faure et al., 2009; Li ZX et al., 2010)。早古生代构造最为明显的结果就是大规模的地壳重熔性花岗岩的侵位 (江西省地质矿产局, 1984; 福建省地质矿产局, 1985; Li XH, 1991, 1994; Wang et al., 2007a; Wan et al., 2007; 张爱梅等, 2010; 张菲菲等, 2010; Li ZX et al., 2010; Yang et al., 2010; Chen et al., 2011; Xu et al., 2011)。前人的年代学结果表明, 早古生代的构造变形发生在 460-440 Ma 之间, 从 440 Ma 开始, 地壳均衡作用引起了陆内造山形成的加厚地壳的松弛与垮塌, 从而形成了面积广阔的 440-400 Ma 的花岗岩体。尽管没有经历强烈的早古生代末期的陆内造山过程, 雪峰山却经历造山后期的伸展作用, 说明整个华南板块中部和东部在造山之后处于伸展的区域应力场之下。造山后岩浆侵入了新元古代至早古生代的地层, 形成了白马山、苗儿山、越城岭、都庞岭、万洋山等等诸多的岩体。本文的锆石 SIMS U-Pb 年龄表明这些岩体的形成于 440-410 Ma 之间, 与东部早古生代岩体形成于同一时代, 可能具有相同的构造背景。

雪峰山地区经历了早中生代强烈的挤压构造变形, 与世界上大多数造山带类似, 形成了众多的造山后期的铝质-过铝质的花岗岩 (Montel et al., 1992; Harris and Massey, 1994; Faure et al., 2003; Brown, 2005; Chung et al., 2005)。这些花岗岩分布在整个东部区, 表明这个区域经历了早中生代强烈的地壳加厚作用, 而西部

区则没有花岗岩体的出露。

雪峰山造山带的三叠纪的花岗岩最明显的特征有两个,分别为(1)切穿了整个变形地层,以及(2)没有任何韧性变形痕迹(图 5-1)。尽管前人对于这些花岗岩进行了详尽的、多方法的(SHRIMP 和 LA-ICP-MS)年代学测试,但是岩体的年龄仍存在着大量争议(图 5-9)。王岳军等认为这一地区的花岗岩分为 243-228 Ma 和 220-206 Ma 两期岩浆活动,第一期岩浆是由于印支期造山过程中增厚地壳均衡调整,从而引起含水矿物脱水产生的熔体,第二区是造山结束后幔源物质在造山带下部底垫作用导致的,地幔熔体的将热量向上传导引起下部地壳部分熔融(王岳军等, 2005; Wang et al., 2007a; 罗志高等, 2010)。而另一种观点认为雪峰山的岩浆活动主要在 225-205 Ma 之间,其动力学背景源于华南板块和印支板块间的碰撞(丁兴等, 2005; 陈卫锋等, 2006, 2007a, 2007b)。在 258-243 Ma 之间,碰撞造山引起华南板块上的地壳增厚,在 20 My 之后,造山后的应力松弛引起了大面积的造山后的岩浆活动。Li ZX and Li XH (2007) 结合华南板块的花岗岩认为,雪峰山的岩浆活动是由于太平洋平板俯冲引起的,陆内造山带不断向内陆迁移从而引起的同造山花岗岩。

本文中独居石电子探针 U-Th-Pb 化学法测得的年龄与 SIMS 锆石 U-Pb 年龄相比较,除了 XF366 这块早古生代样品与 U-Pb 法测试年龄误差范围内几乎相等外,其余 2 个样品(XF205 和 XF208)均比 U-Pb 法年龄要老,使用加权平均计算得到的年龄要比投图得出的年龄要年轻,而且更接近 U-Pb 年龄。锆石 U-Pb 系统的封闭温度在 700-900 度,独居石 U-Th-Pb 的封闭温度在 600-700 度,一般情况下应该是锆石年龄老于独居石年龄,而本文的情况却恰恰相反。虽然具体原因仍不明了,但获得的年龄整体在误差范围内可以认为是一致的。由于锆石 U-Pb 法已经非常成熟,在花岗岩冷却结晶年龄的确定上,其准确度与精确度均是其他年代学方法所无法比拟的,所以我们认为锆石 U-Pb 年龄应该更接近花岗岩的侵位冷却年龄。故本文倾向于使用 SIMS 锆石 U-Pb 年龄代表雪峰山地区三叠纪岩浆活动的时代。

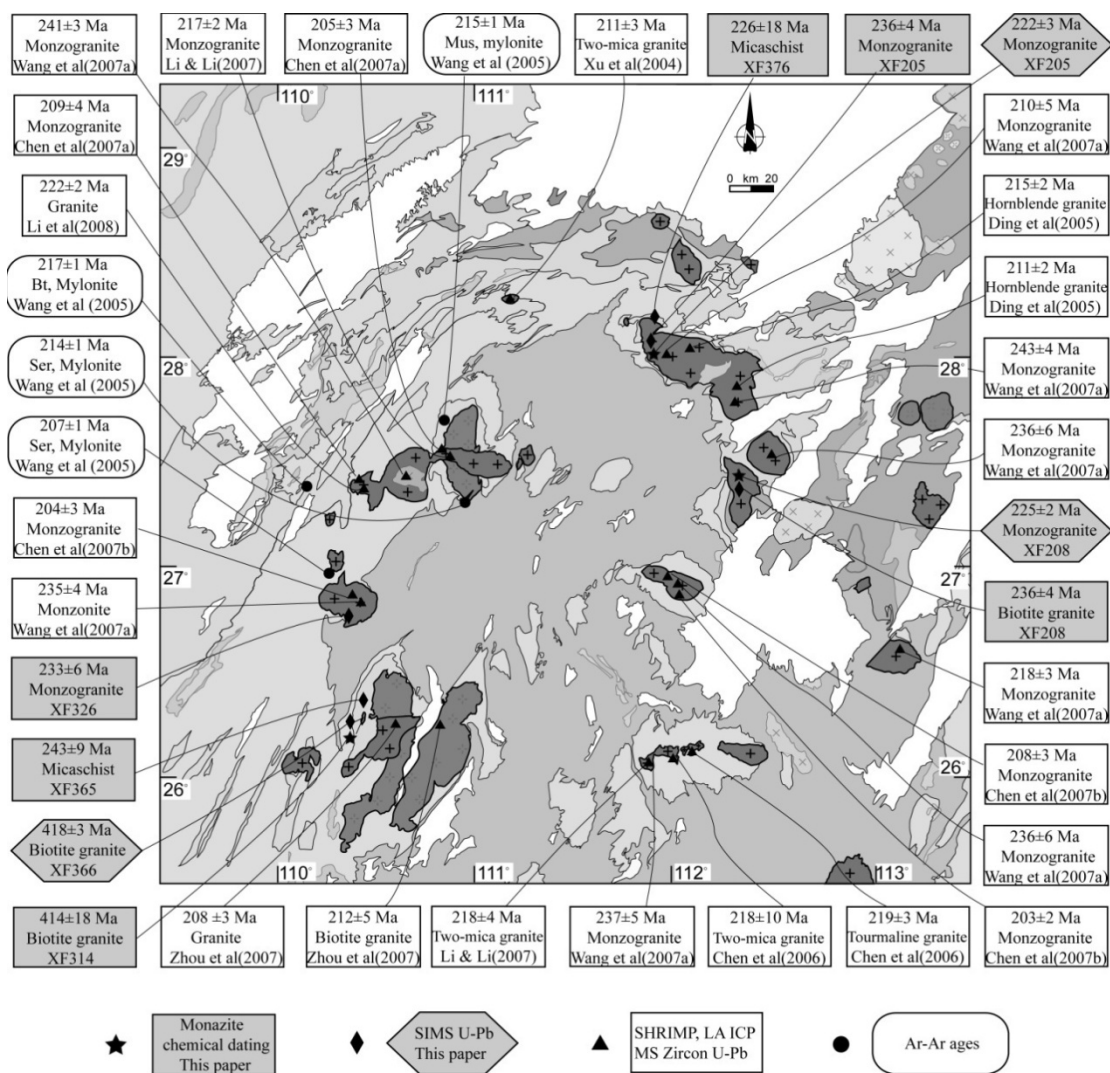


图 5-9 研究区年代学数据总结

通过 SIMS 锆石 U-Pb 法的精确定年，我们认为雪峰山早中生代造山作用后期的岩浆活动在 225-215 Ma，峰值在 222 Ma (图 5-10)，并且只有一期，而不是前人所认为的两期岩浆活动。结合地质构造背景，这期岩浆是雪峰山陆内造山带的产物，而不是由印支和扬子板块拼合后导致的加厚陆壳伸展引起的。

雪峰山的高级变质岩和达到糜棱岩化的强变形岩石出露较少，因此雪峰山地区的变形年代学研究较少，仅仅有 Wang et al. (2005) 获得的 5 个 Ar-Ar 年代学数据，而且变形年代在 217-195 Ma，明显晚于造山后期的花岗岩年龄，因此这些数据的具体构造学意义仍值得商榷。杨奎峰等(2004)应用电子自旋方法(ESR)断层中的石英脉测年获得了 160-130 Ma 和 110-90 Ma 的两个阶段年龄，认为安化—溆浦断裂活动期在晚中生代。然而在其文中也说明这一断裂最深的岩石也仅

为绢云母化千枚岩，同时石英脉很容易受到后期流体作用影响，所以这一年龄可能记录的为燕山期断层的重新活动时留下的证据。最近，胡召齐等（2010）对板溪群板岩中的伊利石进行了 K-Ar 测年，获得了 419-389 Ma 的年龄，表明在早古生代雪峰山地区也经历了区域性的隆起，这与中晚泥盆世的不整合相对应。

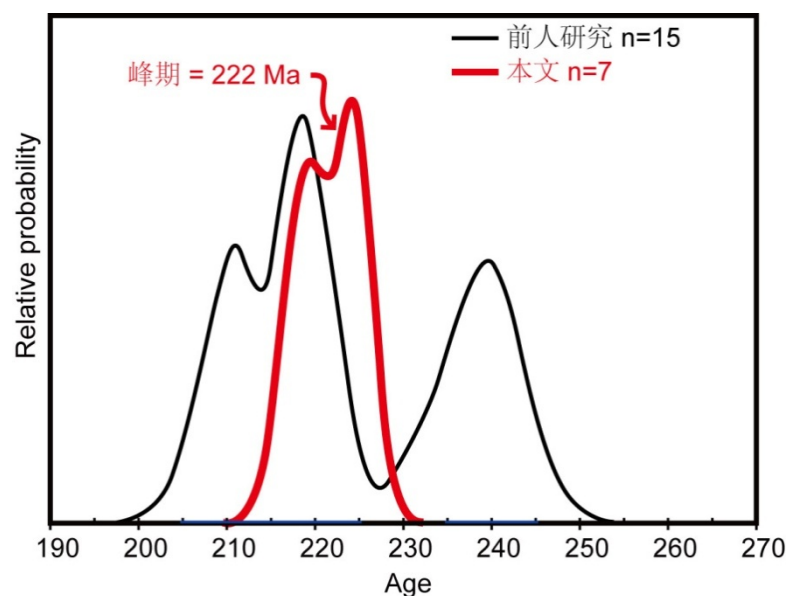


图 5-10 研究区花岗岩前人的年代学数据与本文对比

本文中独居石 U-Th-Pb 年代学提供了针对雪峰山构造演化的新数据。通过在主滑脱带出露的城步和沩山地的强变形云母片岩中进行了原位的独居石 U-Th-Pb 测年，获得 243-226 Ma 的年龄。结合构造学证据，这些独居石平行面理生长，表明为同构造新生产物，因此我们获得的年龄代表了主滑脱带的活动的年龄。主滑脱带中以 D_1 的上部指向 NW 剪切变形为主，所以 D_1 构造发生于早中三叠世。

此外，值得注意的是我们在沩山岩体东边采得的 XF376 样品给出了 226 Ma 的独居石年龄，这与岩体的年龄 222 Ma 较为接近。XF376 是一块含矽线石云母片岩，矽线石的出现表示变质的温度较高，可能代表着构造事件引起的高温变质作用，同时也促使之后的地壳熔融而产生了三叠纪的花岗岩。这也精确限定了构造变质作用和岩浆侵位的时间序列关系。

针对雪峰山的主构造变形时间，主要存在两种认识，早古生代（贾宝华，1994；

丘元禧等, 1998, 1999) 和早中生代 (Hsu et al., 1988, 1990; 马文璞等, 1993; 陈海泓等, 1993; Wang et al., 2005), 此外侏罗纪的挤压也不可忽视 (Yan et al., 2003)。结合构造学和年代学数据, 我们认为雪峰山是一条早中生代陆内造山带, 为定型构造, 同时也经历了早古生代抬升和晚中生代的伸展作用, 分别对应着区域性的泥盆纪不整合和白垩纪伸展穹窿及断陷盆地。

第六章 雪峰山地区显生宙的地壳演化

Lu 与 Hf 均为难熔(highly refractory)的中等-强不相容性亲石元素, 这一点与 Sm-Nd 体系有很大的类似性。因此, Hf 同位素示踪的基本原理与 Nd 同位素相同。随着质谱技术的不断发展, 同时由于锆石封闭温度高、稳定等特性, 应用锆石 Hf 同位素来探讨岩石的演化、地壳的形成以及大陆增生等问题具有其明显的优越性, 因此本文试图通过激光锆石原位 Hf 同位素分析手段对研究区早古生代和早中生代花岗岩进行测试, 从而来探讨雪峰山的显生宙地壳演化。

第一节 实验方法

锆石 Hf 同位素测试在中国科学院地质与地球物理研究所 Neptune 多接收器电感耦合等离子体质谱仪 (MC-ICP-MS) 和 193 nm 激光取样系统上进行, 分析时激光束直径为 44 或 63 μm , 激光剥蚀时间约 26s。测定时用锆石国际标样 GJ-1 和 MUD 作外标, 分析中所用的激光脉冲速率为 10 Hz, 激光束脉冲能量为 100 mJ。仪器的运行条件及详细的分析过程可参见 Wu et al. (2006)。本次实验测定过程中, GJ-1 和 MUD 的测定结果分别是 $0.281999 \pm 6 (2\sigma, n=34)$ 和 $0.282503 \pm 7 (2\sigma, n=34)$, 该值与目前用溶液法获得的值在误差范围内一致 (Woodhead and Hergt, 2005; Morel et al., 2008)。以下是 Hf 同位素研究中的有关公式:

$$\varepsilon\text{Hf}(0)=10000[(^{176}\text{Hf}/^{177}\text{Hf})_{\text{S}}/(^{176}\text{Hf}/^{177}\text{Hf})_{\text{CHUR},0}-1].$$

$$\varepsilon\text{Hf}(t)=10000\{[(^{176}\text{Hf}/^{177}\text{Hf})_{\text{S}}-^{176}\text{Lu}/^{177}\text{Hf})_{\text{S}}\times(e^{\lambda t}-1)]/[(^{176}\text{Hf}/^{177}\text{Hf})_{\text{CHUR},0}-(^{176}\text{Lu}/^{177}\text{Hf})_{\text{CHUR}}(e^{\lambda t}-1)]-1\}.$$

$$T_{\text{DM}}=1/\lambda\times\ln\{1+[(^{176}\text{Hf}/^{177}\text{Hf})_{\text{S}}-(^{176}\text{Hf}/^{177}\text{Hf})_{\text{DM}}]/[(^{176}\text{Lu}/^{177}\text{Hf})_{\text{S}}-(^{176}\text{Lu}/^{177}\text{Hf})_{\text{DM}}]\}$$

$$T_{\text{DM}}^{\text{C}}=1/\lambda\times\ln\{1+[(^{176}\text{Hf}/^{177}\text{Hf})_{\text{S},t}-(^{176}\text{Hf}/^{177}\text{Hf})_{\text{DM},t}]/[(^{176}\text{Lu}/^{177}\text{Hf})_{\text{C}}-(^{176}\text{Lu}/^{177}\text{Hf})_{\text{DM}}]\}+t$$

$(^{176}\text{Lu}/^{177}\text{Hf})_{\text{S}}$ 和 $(^{176}\text{Hf}/^{177}\text{Hf})_{\text{S}}$ 分别是样品的测试值, 而 $(^{176}\text{Lu}/^{177}\text{Hf})_{\text{CHUR}}$ 为 0.0332, $(^{176}\text{Lu}/^{177}\text{Hf})_{\text{CHUR},0}$ 为 0.282772 (Bichert-Toft and Albarède, 1997); $(^{176}\text{Lu}/^{177}\text{Hf})_{\text{DM}}=0.0384$, $(^{176}\text{Hf}/^{177}\text{Hf})_{\text{DM}}=0.28325$ (Griffin et al., 2000), $(^{176}\text{Lu}/^{177}\text{Hf})_{\text{C}}=0.015$, t 则是锆石的结晶年龄, ^{176}Lu 的衰变常数 $\lambda=1.867 \times 10^{-5}$ m.y. (Soderlund et al., 2004)。

第二节 实验结果

1 早古生代花岗岩

此次共选取了 6 个早古生代花岗岩样品 (XF76、XF93、XF99、XF219、XF270 和 XF274) 进行锆石 Hf 同位素的测定, 分析点基本上与前文 SIMS 锆石 U-Pb 测点一致。锆石 U-Pb 测试所获得的谐和年龄用于计算样品初始 Hf 以及模式年龄。详细数据见附表 3。

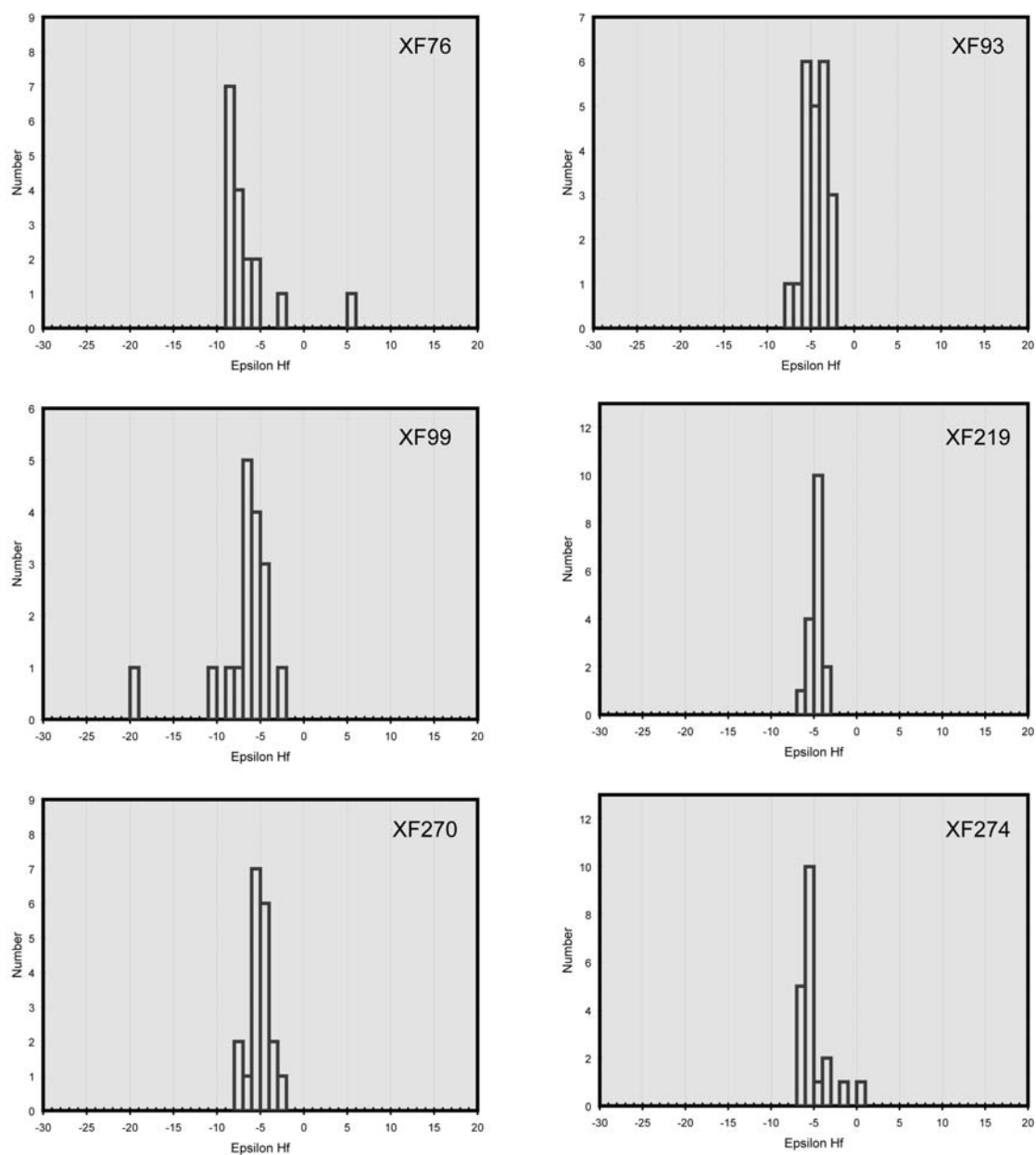


图 6-1 雪峰山早古生代花岗岩的 $\epsilon\text{Hf}(t)$ 的柱状分布图。

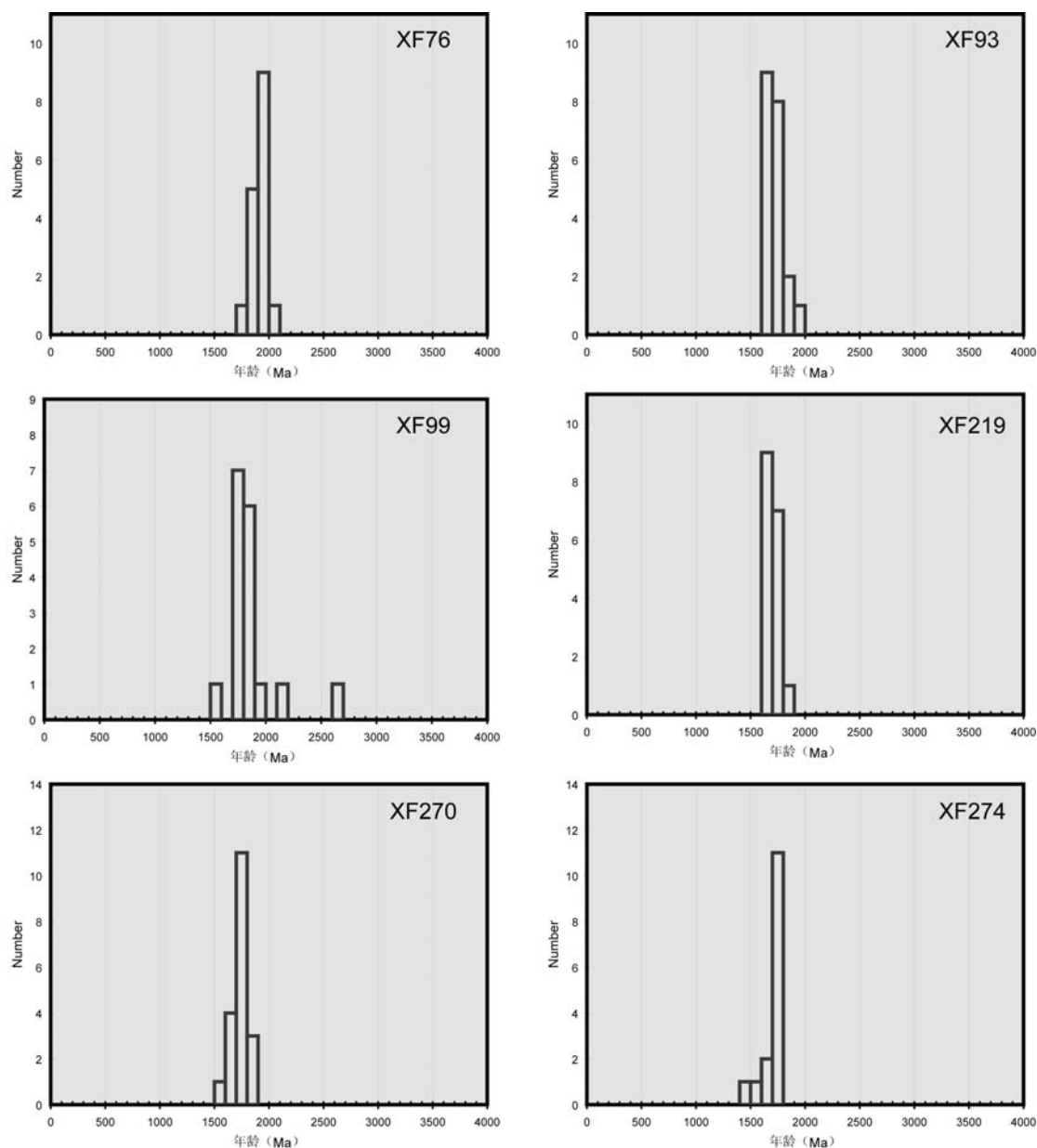


图 6-2 雪峰山早古生代花岗岩样品的 T_{DM}^C 的柱状分布图。

XF76 采自都庞岭岩体，年龄为 428 Ma。共进行了 17 个点测试，其中 16 个颗粒的 $^{176}\text{Lu}/^{177}\text{Hf}$ 比值在 0.002 以下，表明锆石形成之后有较低的放射性成因 Hf 同位素的累积。测试结果显示， $\varepsilon_{\text{Hf}}(t)$ 数值较为集中，在 -8.9 至 -6.1 之间（图 6-1），同样地，模式年龄 T_{DM}^C 分布范围较小，从 1807 至 1979 Ma（图 6-2）。在 XF76 的分析点中，存在着 3 个继承锆石。其中一个 956 Ma 的锆石具有正的 $\varepsilon_{\text{Hf}}(t)$ 值，其 T_{DM}^C 模式年龄为 1475 Ma，表明可能有亏损地幔的加入。而另外两个 ~800 Ma 的锆石的 $\varepsilon_{\text{Hf}}(t)$ 值分别是 -3.0 和 -5.4，模式年龄分别为 1914 Ma 和 2050 Ma。

样品 XF93 采自桂东岩体, 年龄为 438 Ma, 我们共分析了 22 个锆石点。样品中没有继承锆石, 年龄均在 438 Ma 左右, 所有的点 $^{176}\text{Lu}/^{177}\text{Hf}$ 比值均在 0.002 以下, 也说明了锆石形成之后有较低的放射性成因 Hf 同位素的累积。 $\varepsilon_{\text{Hf}}(t)$ 数值在 -7.5 至 -2.5 之间 (图 6-1), 峰值在 -6.0 左右, 而模式年龄 T_{DM}^{C} 分布范围在 1583 至 1903 Ma 之间, 峰值在 1700 Ma (图 6-2)。

XF99 采自万洋山岩体, 锆石年龄为 437 Ma。共进行了 17 个点分析测试, 所有颗粒的 $^{176}\text{Lu}/^{177}\text{Hf}$ 比值在 0.002 以下, 表明较低的放射性成因 Hf 同位素的累积。 $\varepsilon_{\text{Hf}}(t)$ 数值较为分散, 在 -11.0 至 -2.2 之间, 峰值在 -4.0 左右 (图 6-1), 同样地, 模式年龄 T_{DM}^{C} 分布范围较大, 从 1720 至 2118 Ma, 峰值在 1800 Ma 左右 (图 6-2)。在 XF76 的分析点中, 有 1 个继承锆石年龄为 939 Ma 的锆石具有正的 $\varepsilon_{\text{Hf}}(t)$ 值, 其 T_{DM}^{C} 模式年龄为 2372 Ma, 表明可能是古老地壳物质的残余。

XF219 为白马山岩体, 锆石年龄为 411 Ma。共进行了 18 个点测试, 其中有 17 个颗粒的 $^{176}\text{Lu}/^{177}\text{Hf}$ 比值在 0.002 以下。测试结果显示, $\varepsilon_{\text{Hf}}(t)$ 数值在 -7.0 至 -2.9 之间 (图 6-1), 模式年龄 T_{DM}^{C} 分布范围从 1590 到 1846 Ma (图 6-2)。

XF270 为苗儿山岩体, 锆石年龄 412 Ma, 共对 19 个锆石进行了 19 个点测试。所有点的 $^{176}\text{Lu}/^{177}\text{Hf}$ 比值在 0.002 以下, $^{176}\text{Hf}/^{177}\text{Hf}$ 比值也在 0.282323 至 0.282463 之间, 表明锆石成分较为均一, 同时形成之后放射性成因 Hf 同位素的累积量也较低。 $\varepsilon_{\text{Hf}}(t)$ 数值分布范围在 -7.8 至 -4.1 之间 (图 6-1), 除了两个点在 -3.2 和 -2.2。模式年龄 T_{DM}^{C} 分布在 1546 至 1900 Ma 之间, 峰值为 1750 Ma (图 6-2)。

XF274 为越城岭岩体, 锆石年龄 424 Ma, 共对 20 个锆石进行了 20 个点的测试。所有点的 $^{176}\text{Lu}/^{177}\text{Hf}$ 比值在 0.002 以下, $^{176}\text{Hf}/^{177}\text{Hf}$ 比值也在 0.282325 至 0.282522 之间。 $\varepsilon_{\text{Hf}}(t)$ 数值分布范围在 -6.7 至 -1.8 之间 (图 6-1), 除了一个点在 0.2。模式年龄 T_{DM}^{C} 分布在 1531 至 1843 Ma 之间, 峰值为 1750 Ma (图 6-2)。

2 早中生代花岗岩

XF17 采自桃江岩体, 锆石年龄 220 Ma, 共对 18 个锆石进行了 18 个点测试。所有点的 $^{176}\text{Lu}/^{177}\text{Hf}$ 比值在 0.002 以下, 多数在 0.001 以下, $^{176}\text{Hf}/^{177}\text{Hf}$ 比值分布在 0.282500 至 0.282583 之间, 表明锆石成分较为均一, 同时形成之后放射性成因 Hf 同位素的累积量也较低。 $\varepsilon_{\text{Hf}}(t)$ 数值分布范围在 -5.0 至 -2.1 之间 (图 6-3),

峰值在-4.5左右。模式年龄 T_{DM}^C 相对年轻，在 1386 至 1572 Ma 之间，峰值为 1400 Ma（图 6-4）。

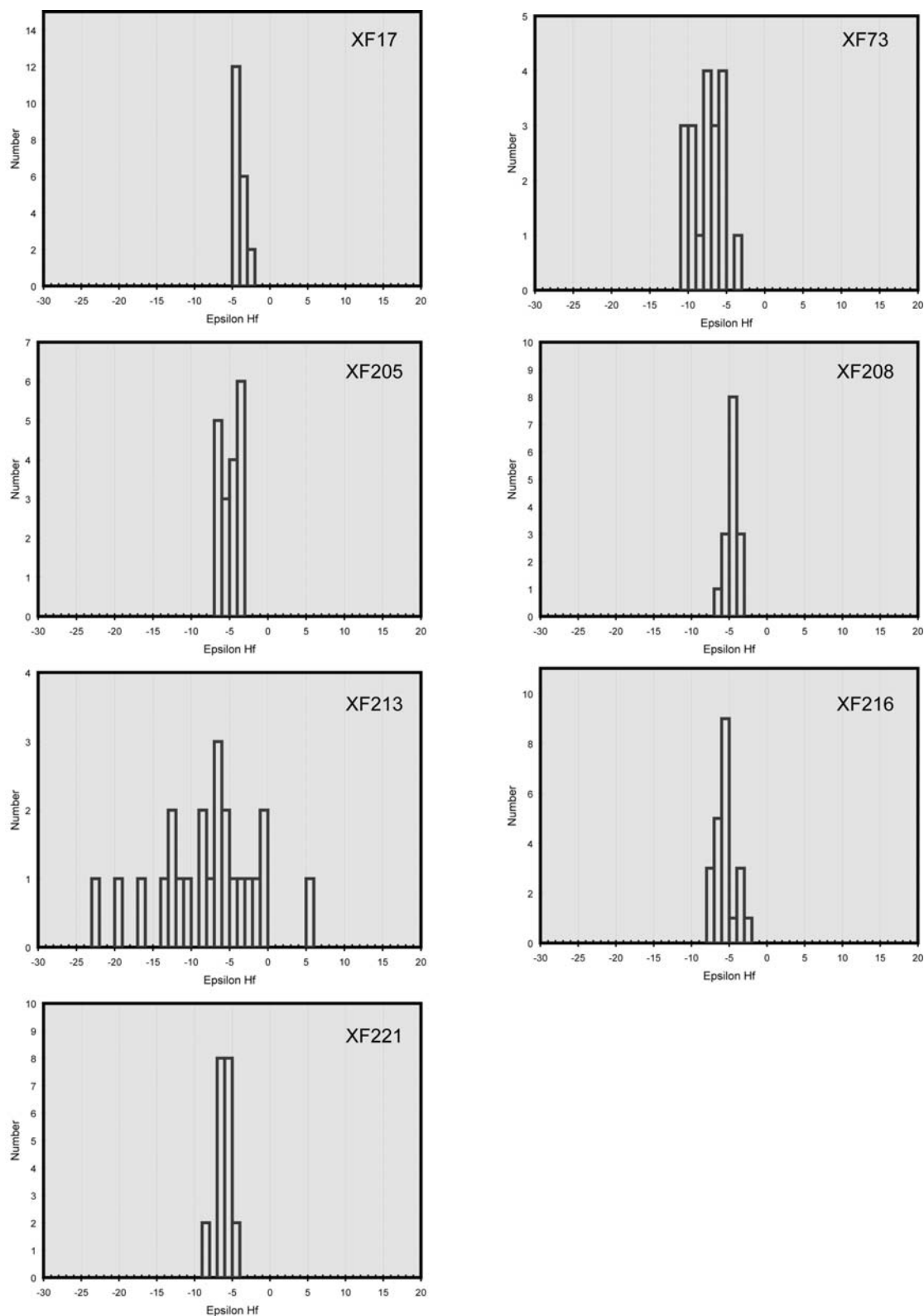


图 6-3 雪峰山早中生代花岗岩的 $\epsilon Hf(t)$ 的柱状分布图。

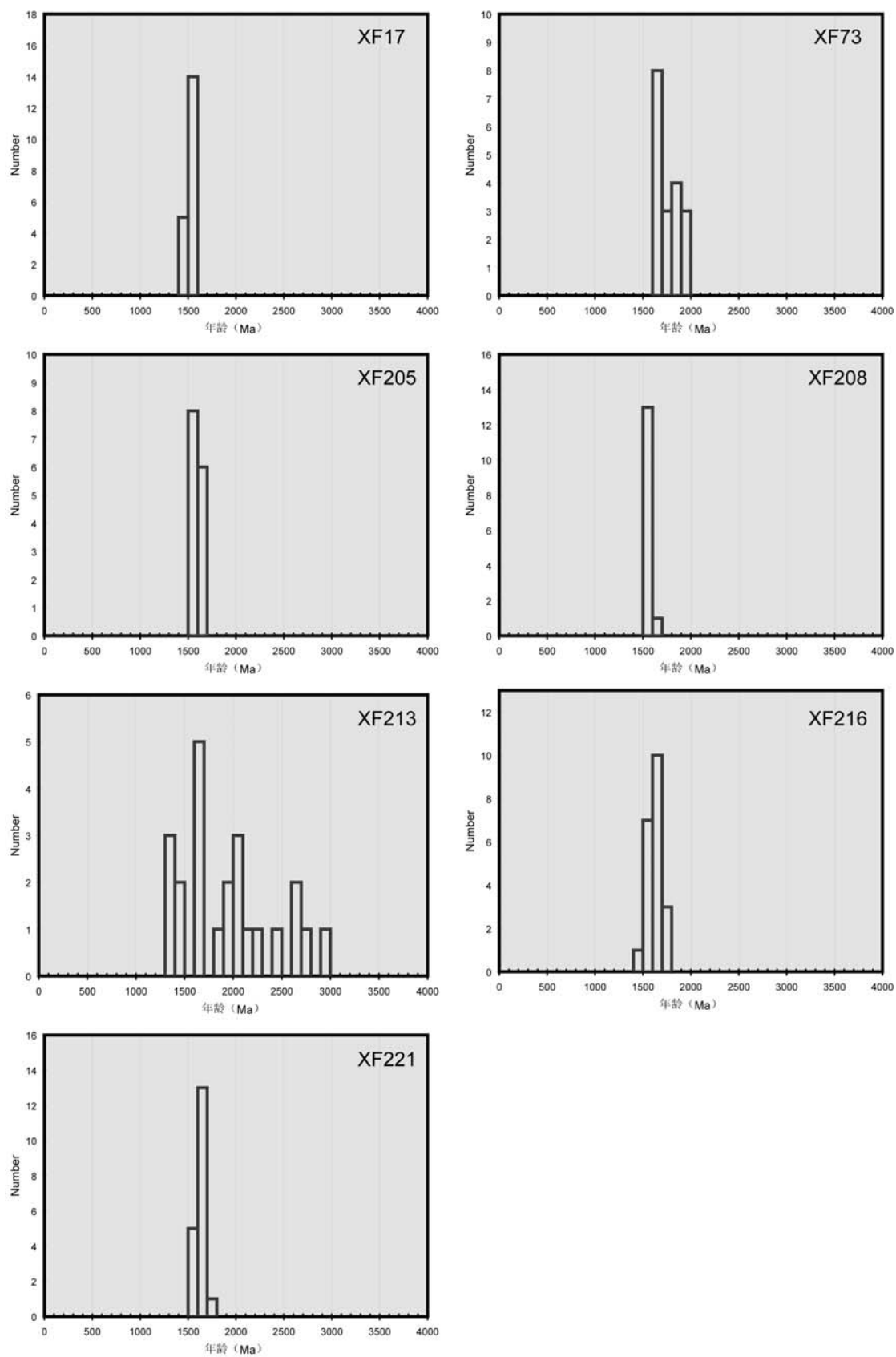


图 6-4 雪峰山早中生代花岗岩样品的 T_{DM}^c 的柱状分布图。

XF73 采自越城岭岩体的油榨坪, 锆石年龄 219 Ma, 共对 19 个锆石进行了 19 个点测试。测试点的 $^{176}\text{Lu}/^{177}\text{Hf}$ 比值在 0.002 以下, $^{176}\text{Hf}/^{177}\text{Hf}$ 比值也在 0.282348 至 0.282558 之间, 放射性成因 Hf 同位素的累积量也较低。 $\varepsilon_{\text{Hf}}(t)$ 分布范围在 -10.4 至 -3.1 之间 (图 6-3)。模式年龄 T_{DM}^{C} 分布在 1451 至 1912 Ma 之间, 峰值在 1600 Ma 左右 (图 6-4)。

XF205 采自浏山岩体, 锆石年龄 222 Ma, 通过对 18 个锆石进行了 18 个点测试表明, $^{176}\text{Lu}/^{177}\text{Hf}$ 比值在 0.002 以下, $^{176}\text{Hf}/^{177}\text{Hf}$ 比值相当均一, 在 0.282457 至 0.282556 之间。 $\varepsilon_{\text{Hf}}(t)$ 分布范围在 -6.6 至 -3.1 之间 (图 6-3)。模式年龄 T_{DM}^{C} 分布在 1452 至 1674 Ma 之间 (图 6-4)。

XF208 采自紫云山岩体, 锆石年龄 225 Ma。对 17 个锆石进行了 17 个点测试结果显示, $^{176}\text{Lu}/^{177}\text{Hf}$ 比值在 0.000893 到 0.002425 之间, $^{176}\text{Hf}/^{177}\text{Hf}$ 比值也在 0.282461 至 0.282558 之间, 表明锆石中的 Hf 同位素成分非常的均一。 $\varepsilon_{\text{Hf}}(t)$ 分布在 -6.3 至 -2.6 之间 (图 6-3)。模式年龄 T_{DM}^{C} 分布在 1427 至 1662 Ma 之间, 峰值非常突出, 在 1600 Ma 左右 (图 6-4)。

XF213 采自塔山岩体, 锆石年龄 224 Ma。在这个样品中, 如 U-Pb 结果显示, 含有大量的继承锆石组分。对继承锆石的测试结果显示 $\varepsilon_{\text{Hf}}(t)$ 分布在 -10.8 至 -2.2 之间, 除了一个 U-Pb 年龄在 909 Ma 的锆石具有 +5.5 的 $\varepsilon_{\text{Hf}}(t)$ 值, 这可能表明在 900 Ma 左右有亏损地幔的物质加入, 这也与样品 XF76 中 956 Ma 的锆石具有同一成因。这些锆石的 $^{176}\text{Lu}/^{177}\text{Hf}$ 比值在 0.002 以下。相反的, 三叠纪岩浆成因的锆石中的 $^{176}\text{Lu}/^{177}\text{Hf}$ 比值分布散乱, 从在 0.000106 至 0.003325, 变化范围很大, $^{176}\text{Hf}/^{177}\text{Hf}$ 比值也在 0.282176 至 0.282630 之间。 $\varepsilon_{\text{Hf}}(t)$ 分布范围在 -16.4 至 -0.7 之间 (图 6-3)。所有的锆石 Hf 模式年龄 T_{DM}^{C} 分布在 1444 至 2117 Ma 之间, 三个年龄为 1366、1692 和 1846 Ma 的继承锆石分别给出了 2676、2701 和 2991 的 Hf 模式年龄, 表明雪峰山地区也存在古老地壳的残存物质 (图 6-4)。

XF216 采自关帝庙岩体, 锆石年龄 223 Ma。对 22 个锆石进行了 22 个点测试结果显示, $^{176}\text{Lu}/^{177}\text{Hf}$ 比值在 0.000820 到 0.002640 之间, $^{176}\text{Hf}/^{177}\text{Hf}$ 比值也在 0.282437 至 0.282584 之间, 说明锆石中的 Hf 同位素成分相对均一, 后期放射性成因 Hf 的累积不多。 $\varepsilon_{\text{Hf}}(t)$ 分布在 -7.3 至 -2.2 之间 (图 6-3)。模式年龄 T_{DM}^{C} 分布在 1395 至 1718 Ma 之间, 峰值较突出, 在 1600 Ma 至 1700 Ma 之间 (图 6-4)。

XF221 采自白马山岩体的高坪镇附近, 锆石年龄 217 Ma。对 20 个锆石进行了测试后, 锆石的 Lu、Hf 同位素较为均一, $^{176}\text{Lu}/^{177}\text{Hf}$ 在 0.000581 到 0.001163 之间, 比值较低, 说明后期累积的放射性 Hf 同位素少。 $^{176}\text{Hf}/^{177}\text{Hf}$ 比值集中分布在 0.282398 至 0.282525 之间。 $\varepsilon_{\text{Hf}}(t)$ 分布在 -8.7 至 -4.1 之间 (图 6-3)。模式年龄 T_{DM}^{C} 分布在 1516 至 1801 Ma 之间, 峰值非常突出, 在 1650 Ma 左右 (图 6-4)。

第三节 讨论

根据花岗岩的地球化学性质, 雪峰山构造带的早古生代和早中生代的岩体均为铝质或过铝质的造山后期产物 (Li XH, 1991, 1994; Zhou and Li, 2000; Zhou et al., 2006; 丁兴等, 2005; 王岳军等, 2005; 陈卫锋, 2007a, 2007b; Wang et al., 2007b; 罗志高等, 2010)。此外, 在花岗岩中出现的继承锆石为岩浆源区可能是沉积成因的中下地壳岩石提供了些许线索。

从图 6-5 中可见, 早古生代花岗岩的 $\varepsilon_{\text{Hf}}(t)$ 较为集中, 从 -10 至 -1, 峰值在 -5 左右, 除了 XF76@03 号锆石 (956 Ma) 具有 +5.6 的 $\varepsilon_{\text{Hf}}(t)$ 值。所有样品的 Hf 模式年龄 (T_{DM}^{C}) 都落在 2.4 至 1.5 Ga 之间, 峰值在 ~1.75 Ga (图 6-5b), 这与前人针对桂东岩体实验所得的 Nd 同位素模式年龄也较为一致 (Li XH, 1994), 由此推断, 这些岩浆可能具有类似的源区。结合 $\varepsilon_{\text{Hf}}(t)$ 和 Hf 模式年龄, 古元古代至早中元古代形成的地壳物质可能是早古生代的岩浆源区。

早中生代花岗岩样品的 $\varepsilon_{\text{Hf}}(t)$ 值与早古生代岩体类似, 主要分布在 -10 至 -1 之间, 峰值在 -5 (图 6-5c)。但是早中生代花岗岩的 Hf 模式年龄基本上分布在 2.3 至 1.4 Ga, 峰值在 ~1.55 Ga, 比早古生代岩体的模式年龄要年轻 150 Ma (图 6-5d)。因此, 我们认为早中生代岩体也主要是晚古元古代-早中元古代形成的地壳物质在早中生代部分熔融形成的, 但是熔融的部分要年轻于早古生代部分熔融部分。Wang et al. (2007a) 对雪峰山早中生代花岗岩进行了 Nd 同位素研究, 其 $\varepsilon_{\text{Nd}}(t)$ 分在 -11 至 -6 之间, Nd 模式年龄集中在 1.5 Ga 之中, 与我们的实验结果类似, 即早中生代花岗岩的源区集中于早中元古代的岩石。而且, 在样品的锆石中, 1.8 Ga、1.6 Ga 和 1.0 到 0.9 Ga 的继承锆石也表明一些古老的地壳物质并没有在岩浆形成过程中被熔融掉。值得注意的是, 在 XF213 和 XF76 分别有一个新元古代锆石具有正的 $\varepsilon_{\text{Hf}}(t)$ 值, 年龄分别为 909 Ma 和 956 Ma (图 6-6), 表明在新元古

代时发生了亏损地幔的抽取作用,这与前人这一时代发生的华夏地块和扬子地块间板块碰撞拼合作用可能有一定的联系 (Shu et al., 1994; Charvet et al., 1996; Li XH, 1999; Li ZX et al., 2002, 2007; Li XH et al., 2009b)。但是这些具有正的 $\epsilon_{\text{Hf}}(t)$ 值的锆石并没有出现在早古生代和早中生代岩浆锆石之中,因此早古生代和早中生代岩浆的生成没有幔源物质的加入,仅仅是陆壳物质的部分熔融。

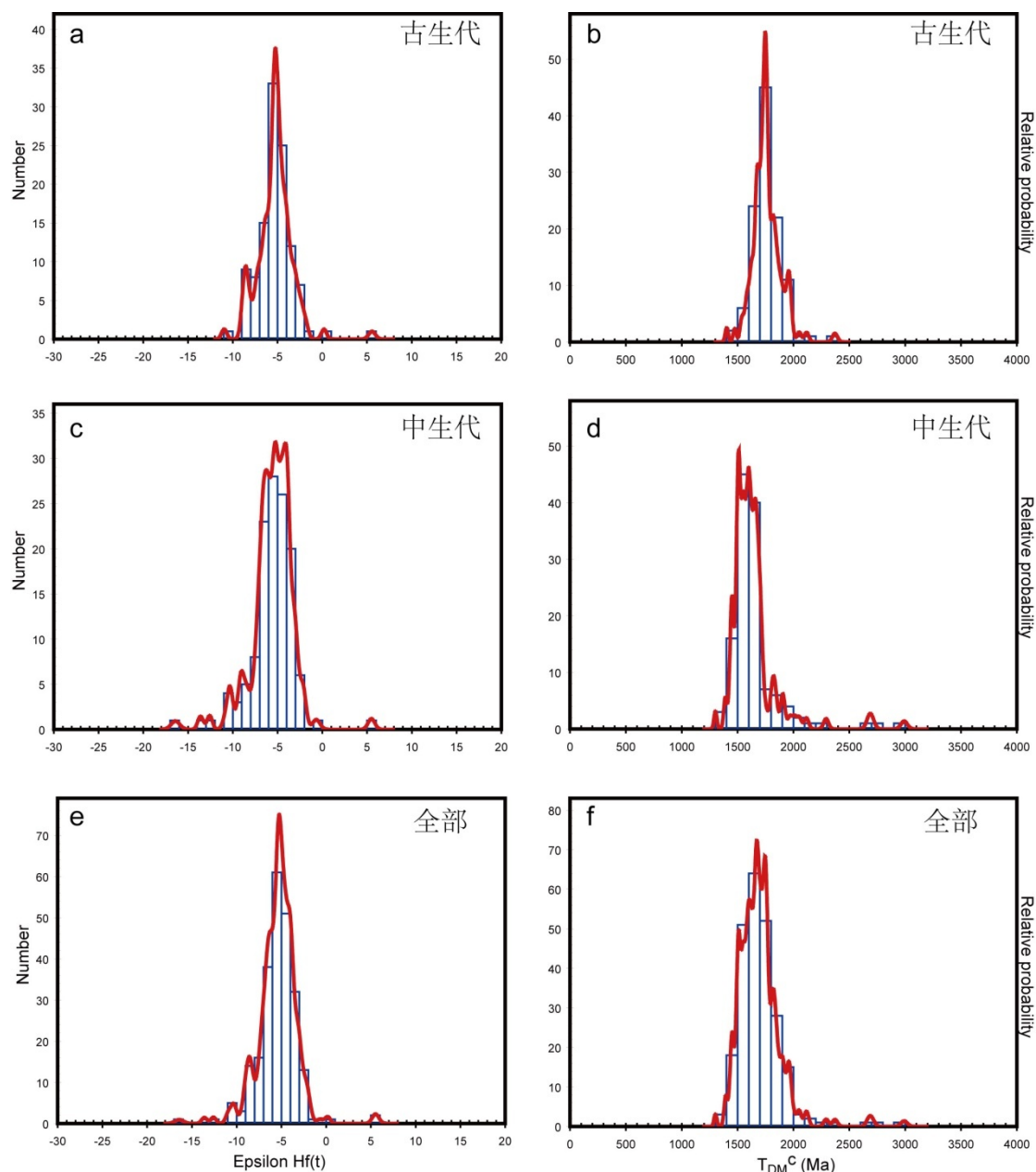


图 6-5 雪峰山早古生代和早中生代花岗岩的 $\epsilon_{\text{Hf}}(t)$ 以及 T_{DM}^{c} 的综合柱状分布图。

综上所述,雪峰山地区经历了两期岩浆作用,分别对应着早古生代和早中生

代的造山时间，不同的是，早古生代造山事件并没有造成雪峰山地区地层的强烈变形和褶皱，但是早中生代造山作用大范围的影响了雪峰山地区，形成了陆内造山带。产出的两个世代的岩体具有接近的 Hf 同位素组成，而且 $\epsilon_{\text{Hf}}(t)$ 值也颇为相似，表明具有近似的岩浆源区（图 6-6）。但是与典型的地壳熔融含有大量的继承锆石不同，这两期岩浆的继承锆石并不发育，说明岩浆部分熔融较为完全，溶解了早期的锆石；少量的继承锆石也多数具有负的 $\epsilon_{\text{Hf}}(t)$ 值，表明古老地壳的残余。两期岩浆活动均没有亏损的幔源物质加入，而两颗~900 Ma 的继承岩浆锆石给出了正的 $\epsilon_{\text{Hf}}(t)$ 值表明这一时期的岩浆活动有新生地壳的加入，这些 900 Ma 的岩体也为早古生代和早中生代的岩浆提供了物源。结合构造学和岩石学证据，表明这些岩浆均为陆内造山后地壳部分熔融的产物。

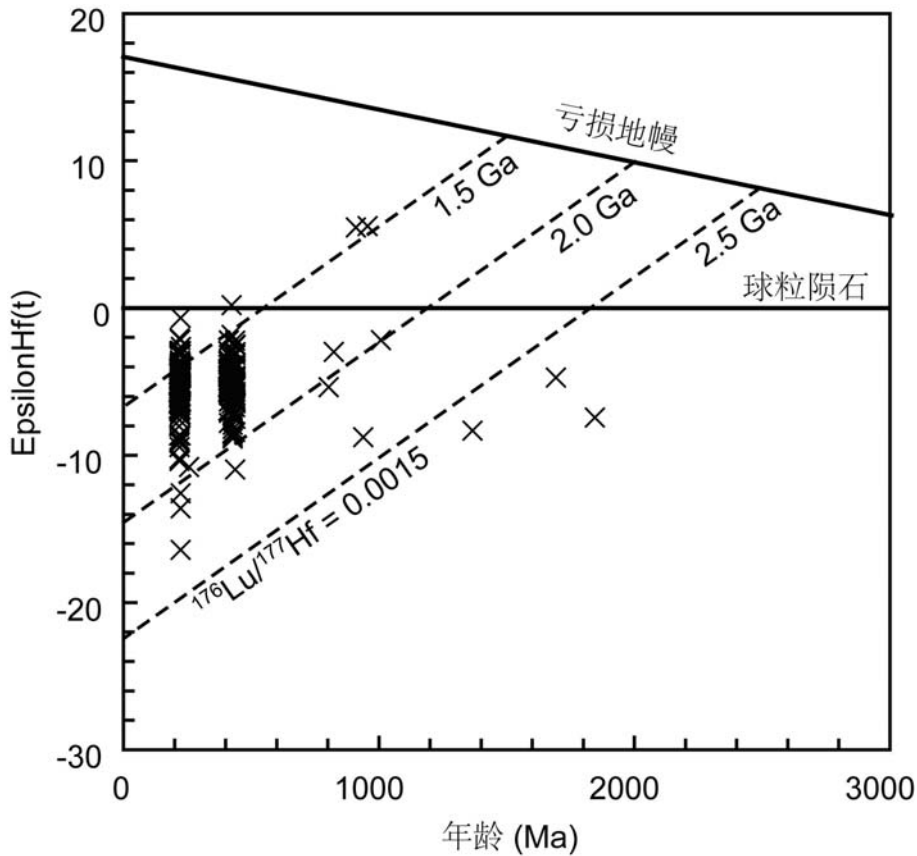


图 6-6 雪峰山早古生代和早中生代花岗岩的年龄- $\epsilon_{\text{Hf}}(t)$ 图解。

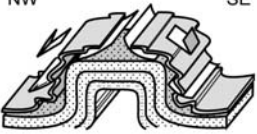
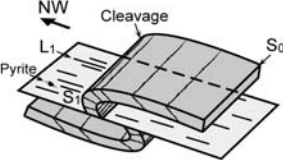
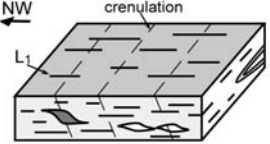
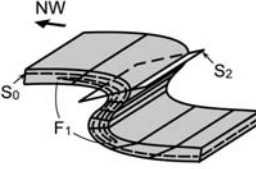
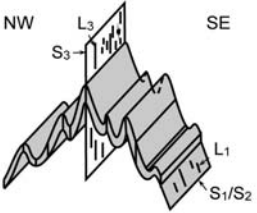
第七章 雪峰山造山带早中生代的构造演化

第一节 多期构造变形

雪峰山造山带位于华南板块的中心位置,是研究华南板块构造变形的关键位置。在雪峰山早中生代造山带中,存在着一条区域性断裂,分隔西部区和东部区,我们称之为雪峰山主逆冲断层。这条断裂既是构造边界,也劈理前缘带,即劈理开始出现的边界。断层向 SE 缓倾,断层带内岩石强烈剪切变形,运动学方向指向 NW。研究区内,新元古代至早三叠世岩石地层经历了三期构造事件。 D_1 期对应着上部指向 NW 逆冲推覆和褶皱作用,这一期事件在整个雪峰山地区都有发育,为早中生代构造作用的主变形期次(图 7-1)。在西部区,箱型褶皱为最明显的特征,形成了近直立的向斜和背斜的翼部,而在核部,地层近水平变形集中在褶皱翼部。除了区域性公里尺度的褶皱缩短外,顺层滑脱、不对称褶皱等脆-韧性构造是变形的载体。而在东部区, D_1 期次的变形程度更深,基本上集中在韧性域。密集发育的极性 NW 的同斜褶皱中发育了渗透性的 S_1 轴面劈理,在 S_1 劈理或面理面上,可以观察到 NW-SE 走向的矿物拉伸线理或压力影中矿物的定向拉伸现象。在 XZ 面上,即平行线理垂直面理的平面上,剪切标志如不对称的石英或方解石压力影, σ 型的石英脉,震旦纪冰碛岩中剪切的砾石,无一不具有上部指向 NW 的剪切运动方向。伴随着这一期构造,东部区的岩石还经历了绿片岩相的变质作用。

而在东部区东缘的大片区域,为构造层次相对浅表的部分,岩石地层为泥盆纪至早三叠世。同样在这片区域,构造特征与西缘类似,发育了大面积、渗透性 D_1 的变形构造,但是岩石没有经历同构造变质作用。变形主要表现为不对称的褶皱作用和逆冲断层。在涟源地区,泥盆纪至早三叠世的灰岩和泥岩中发育了众多的逆冲断层和断层相关褶皱,均指示了剪切方向指向 NW。

相比 D_1 的广泛分布, D_2 期构造事件仅广泛发育在东部区。野外观察表明极性 SE 的褶皱伴随着倾向 NW 的 S_2 轴面劈理叠加在了 D_1 构造之上。这一期构造并没有 D_1 期次强,仅仅可见区域性的褶皱作用,没有同构造变质作用和强应变带的产出。由于上部指向 SE 的强烈剪切作用,在安化—新化—洞口—绥宁这一线区域内,震旦纪至泥盆纪岩层之中,发育了由于极性 SE 的褶皱作用而产生大规模的地层倒转构造。

变形期次	西部区	东部区	深部变质单元和滑脱带
D ₁	 <p>NW SE</p> <p>箱型褶皱发育，在褶皱两翼倾角较大处发育重力滑脱褶皱。劈理未见。</p>	 <p>NW Cleavage L₁ S₀ Pyrite</p> <p>S₁、L₁和F₁都具有上部指向NW的运动学方向。低绿片岩变质作用（绢云母+绿泥石）。</p>	 <p>NW crenulation L₁</p> <p>发育有面理S₁水平的糜棱岩。NW-SE线理具有上部指向NW的剪切方向。绿片岩相变质作用（黑云母+石榴子石+白云母）。</p>
D ₂	无	 <p>NW S₀ F₁ S₂</p> <p>S₁和F₁均被极性SE的F₁褶皱所改造，同时发育S₂劈理，局部见S₁残留。</p>	无
D ₃	无	 <p>NW L₃ S₃ SE L₁ S₁/S₂</p> <p>S₁、L₁和S₂均被F₃所改造。同时发育S₃面理和L₃矿物拉伸线理。</p>	

雪峰山主逆冲断层

主滑脱带

图 7-1 雪峰山造山带早中生代多期构造变形图解。

最后一期, D_3 期构造变形以直立褶皱为主, 发育了大量直立的 S_3 轴面劈理和直立 L_3 拉伸线理, 这些构造主要也集中发育在东部区。在野外露头之上, 有时直立的 S_3 劈理和倾角较大的 S_1 劈理之间比较难于区分, 但是, 在某些情况下, 我们可以观察到 S_1 面理也被褶皱, 与卷入原生层理的褶皱相比, S_1 面理之上存在韧性变形的痕迹, 如矿物拉伸线理, 同样的, 这些线理也随着面理面而弯曲。这些证据表明 S_1 面理在 D_3 期被 F_3 所改造。同样的, S_2 劈理被 F_3 所改造的现象也存在, 如在城步以北, F_2 褶皱的轴面劈理在直立褶皱作用下弯曲, 并形成了直立劈理构造。

Wang et al. (2005) 认为雪峰山地区上部指向 WNW 的逆冲构造伴随着明显的 N-S 或 NE-SW 走向的左旋走滑分量, 而且他们所测到的线理方向均为近 N-S 向水平延伸。上部指向 SE 的逆冲构造作为与上部指向 NW 构造的反冲构造, 与 D_1 同期形成, 而不是时间前后的关系。但是基于我们的工作, D_1 的构造变形主要以极性 NW 的逆冲推覆和褶皱作用为主, 线理方向也为 NW-SE 走向, 相反地, 近水平的矿物拉伸线理和近直立的面理在雪峰山地区并不多见。丘元禧等(1999) 将 NW 向的构造归为雪峰山造山带的准原地推覆构造, 仅仅影响了泥盆纪之前的地层, SE 向的构造则为造山后期的滑覆构造, 形成了劈理和褶皱等现象。泥盆纪至早三叠世的地层中的构造变形, 他们将其解释为印支构造的叠加。

综上所述, 东部区中 S_1 - S_2 、 S_1 - S_3 和 S_2 - S_3 的相互叠加构造表明雪峰山造山带经历了多期的构造变形, 并且这些变形发育在从新元古代至早三叠世的地层之中。整体上, 三期变形均对应着 NW-SE 的构造缩短, 是一期事件的不同时间序列段上的产物。

第二节 多期构造变形的年代学约束

在雪峰山地区, 早古生代事件影响主要体现在南部轴向 E-W 的褶皱(震旦纪至志留纪)以及较为分散的早古生代岩体。但是研究区并未出露有早古生代的构造变质作用以及地壳熔融现象(混合岩化作用)。在雪峰山以东区域, 志留纪晚期至泥盆纪早期的岩体侵位于早古生代之前的褶皱层系, 并且没有变形(Faure et al., 2009; Charvet et al., 2010)。这些花岗岩体直接被中晚泥盆世砾岩-砂岩所不整合覆盖。因此, 我们可以推断, 在雪峰山造山带之中, 早古生代花岗岩所发育

的固相后的韧性变形在早古生代构造事件之后,类似的证据在武夷山和云开地区也都有发育(Wang et al., 2007b, 2007c; Yang et al., 2010; Xu et al., 2011)。不同的是,雪峰山并没有早古生代造山作用的明显痕迹。

从新元古代到早三叠世,卷入雪峰山造山带中的沉积岩大部分沉积于浅海环境之下,除了在晚志留统至早泥盆统之间由于华南整体的地壳抬升而产生的沉积间断以及随后的陆相沉积(江西省地质矿产局, 1984; 福建省地质矿产局, 1985; 湖南省地质矿产局, 1988; 浙江省地质矿产局, 1989)。但中三叠世开始,整个雪峰山的地层发生了明显的变化,从海相沉积完全转变为陆相沉积,而华南大陆也几乎全部抬升成陆地,一直延续至今。晚三叠世至早侏罗世的沉积序列主要由碎屑岩如砾岩、粗砂岩和泥岩等组成,这些岩石的物源主要来自隆升成山的雪峰山剥蚀的碎屑物,分布在小型山间盆地中(张进等, 2010)。相对的,中三叠世之前的地层则全部卷入了褶皱与逆冲构造之中。

贾宝华(1994)和丘元禧等(1999)均认为雪峰山的主构造期在早古生代,其依据是区域性发育的中泥盆世不整合,以及志留纪中的劈理没有穿不整合面。然而我们观察的结果显示,作为造山后期伸展的产物,早古生代岩体卷入了构造变形,而且在不整合面的上下地层中,无论是劈理还褶皱都有较好的一致性,泥盆纪和志留纪地层的变形特征几乎完全一致,所以雪峰山的主变形期应在早中生代,而不是早古生代。Yan et al. (2003, 2009)认为雪峰山为晚中生代厚皮推覆构造,为飞来峰,新元古代地层与古生界是构造接触。这一推覆至川东转变成薄皮构造。川东的侏罗山褶皱的确发育在晚中生代,大约在晚侏罗世至早白垩世,而雪峰山的构造与之不同,主体构造在晚三叠世就已停止,这一时期雪峰地区已抬升成陆,不再接受大范围的海相沉积,而开始形成山间的磨拉石盆地,接受雪峰山造山后的剥蚀产物。

在雪峰山地表构造之下,存在着一个主滑脱带,而且早古生代的花岗岩及其也卷入了主滑脱带的韧性变形之中,并产生了糜棱岩化现象,花岗岩形成正片麻岩,围岩则为糜棱岩化的云母片岩和变砂岩。主滑脱带的构造变形以上部指向NW的剪切为主,因此属于D₁期的构造产物,形成在早中生代。我们在主滑脱带中选取了两个新鲜的强变形的云母片岩,获得了243和226 Ma独居石U-Th-Pb年龄,表明雪峰山主滑脱带的变形时间在243 Ma至226 Ma之间,限定了挤压

构造的发生时间,也就是 D_1 期和 D_2 期的变形年代。除此之外,晚三叠世铝质-过铝质花岗岩体切穿了褶皱变形的地层,侵入至古生代地层之中,广泛的分布于整个雪峰山造山带。这些花岗岩类没有经历过任何变形,为造山后产物,因此这些可以作为雪峰山造山带的时间下限。结合前人和本文的数据,主要侵位于 225-215 Ma 之间(丁兴等, 2005; 陈卫锋等, 2006, 2007a, 2007b; Wang et al., 2007b; Li and Li, 2007; 柏道远等, 2007; Li HQ et al., 2008), 暗示着挤压造山过程在 225 Ma 的时候就已停止, 转入了伸展状态。三叠纪的岩体广泛侵位于背斜的核部, 再次形成了局部的弱挤压构造, 尽管无法获得 D_3 褶皱的同位素年代学上的直接证据, 我们认为与花岗岩侵位同期的挤压变形可能对应着 D_3 直立褶皱变形期。

Wang et al. (2005) 对雪峰山的糜棱岩定年结果为 217-195 Ma 之间, 表明造山带在晚三叠世晚期至早侏罗世活动。这还要晚于晚三叠世的岩浆侵位。他们重点研究的左行走滑断层还明显错断了造山后期的花岗岩岩体, 如瓦屋塘和白马山岩体中的早中生代小沙江单元, 这表明走滑构造是发生在岩体侵位之后。因此, 我们认为 217-195 Ma 的 Ar-Ar 年龄代表了早中生代岩体侵位之后造山带的冷却年龄, 而并不是韧性剪切变形的年龄。

总而言之, 雪峰山造山带早中生代的三期构造变形可以理解成一个大构造背景下的三期连续变形, D_1 期和 D_2 期剪切变形发生在 243-226 Ma 之间, D_3 期挤压构造在 225-215 Ma 之间, 与花岗岩同期, 而 217-195 Ma 代表着岩体侵位后的冷却年龄。

第三节 雪峰山造山带的早中生代构造演化

前人对雪峰山造山带中的上部指向 NW 的韧性剪切和褶皱作用都有过研究, 但是他们的构造模式与本文所阐述的地质构造描述对比, 均不符合雪峰山的实际构造格局。丘元禧等认为, 虽然早中生代的构造也有影响, 但是雪峰山的主体构造是早古生代, 在其核心区——黔东南—桂北雪峰山逆冲推覆断褶带中发育了大规模准原地的逆冲推覆, 之后发生了滑覆构造(丘元禧等, 1998, 1999); Yan et al. (2003) 认为雪峰山和武陵山分别为飞来峰, 并且形成了多层次的逆冲推覆, 这与 Hsu et al. (1988, 1990) 的观点类似, 即华南板块经历的大规模、长距离的推覆, 不同点在于前者认为板溪群在晚中生代被推覆, 而后者认为板溪群是早中生

代的构造混杂岩。但是实际上,老地层盖在新地层之上也可能是由于地层陡倾出发生切层的重力滑脱现象导致 (Faure et al., 1998)。Wang et al. (2005) 指出雪峰山形成于早中生代的转换挤压环境下,走滑是构造起因,而挤压则是主要表现形式。但实际上走滑构造切过了晚三叠世花岗岩体,因此是发生在造山后花岗岩侵位之后。

在西部区,以大型箱状褶皱为主,在武陵山前的大庸断裂使得武陵山的寒武纪—奥陶纪地层逆冲至志留纪地层之上,同时也使得上盘背斜核部的板溪群抬升至地表。在东部区的西缘,从雪峰山主逆冲断层以东 50 km 宽的条带区域中,劈理广泛发育于新元古代至古生代的地层之中,并呈现出扇形样式 (图 7-2), 即在西侧,劈理倾向 SE, 褶皱极性指向 NW; 而在东侧,劈理倾向 NW, 褶皱极性指向 SE。我们将这些极性 SE 的剪切变形解释为反冲构造。反冲构造在造山带挤压过程中较为常见,如台湾山脉、喜马拉雅和阿尔卑斯山中均可见到 (Godin et al., 1999; Willett et al., 1993; Malavieille, 2010)。

在郴州—临武断层以东 (图 3-1 和图 7-2), 早古生代构造变形被较好的保存下来,而三叠纪变形的影响范围相对局限。早古生代末期的构造作用基本影响了整个华南板块东部,主要表现为中晚泥盆世地层区域不整合地覆盖在泥盆纪之前的地层之上,大范围的造山后岩浆作用以及闽—赣—粤地区广泛的混合岩化 (福建省地质矿产局, 1985; 广东省地质矿产局, 1988; 广西壮族自治区地质矿产局, 1985; 江西省地质矿产局, 1984; 舒良树等, 1997, 1999; Wang et al., 2007a; Wan et al., 2007, 2010; 陈科等, 2008; Faure et al., 2009; Charvet et al., 2010; Li ZX et al., 2010; 张爱梅等, 2010; 张菲菲等, 2010; Yang et al., 2010; Chen et al., 2011; Xu et al., 2011)。在江西,晚元古代至奥陶纪的沉积地层被走向 E-W 或 NW-SE 的褶皱所变形,形成了倾向 NE 的轴面劈理和极性 SW 的不对称褶皱及断层。早古生代的基底滑脱带将上部褶皱的沉积盖层和下部变质岩石分开,下部向 N 发生陆内俯冲,而上部盖层则受到强烈挤压向南推覆。同时由于造山后花岗岩的侵位才使得高级变质岩如角闪岩甚至混合岩等滑脱带以下的中下地壳部分抬升至地表 (Faure et al., 2009)。这些早古生代 N-S 向的构造在郴州-临武断裂以西则表现得很微弱,早古生代的挤压作用不明显,而造山后的伸展却影响了这个区域,造成了大面积的早古生代岩体侵位。泥盆系的角度不整合在湘东南局部较为明显,而

在湘中地区呈微—低角度不整合，在常德—沅陵一线以西则转变成平行不整合，表明早古生代的构造作用在雪峰山地区没有产生明显的强烈褶皱作用、韧性变形和变质作用（湖南省地质矿产局，1988）。因此我们认为，郴州-临武断裂代表了早中生代雪峰山造山带的东部边界，分隔了雪峰山早中生代（印支期）构造区和以东的早古生代（加里东期）构造区。

通常情况下，在碰撞造山带的外部区，（例如阿尔卑斯山西部的侏罗山和扎格斯山前陆褶皱冲断带），滑脱带主要发育在能干强度低的岩石如蒸发岩或黑色页岩中，从而吸收了整个区域的构造缩短（Beaumont et al., 1994; Escher and Beaumont, 1997; Mcquarrie, 2004）。在主滑脱带之下，基底岩石没有经历强烈的变形。而在雪峰山造山带，新元古代至早三叠世沉积盖层之下应当存在着一条区域范围的基底滑脱带，从而来吸收 NW-SE 向的构造缩短。新元古代早期形成的沉积岩如泥岩和粉砂岩很好的扮演了强应变带的角色，成为雪峰山的基底滑脱带。由于 D_3 期直立褶皱和岩体侵位的作用，基底滑脱带的局部被抬升至地表，如在城步地区或白马山地区（见第四章）。在部分花岗岩体的周边，分布着雪峰山地区出露的最深的岩石。主要有云母片岩、石英岩、变砂岩和少量正片麻岩所组成，这些岩石均经历了绿片岩相变质，也是滑脱带的组成部分，糜棱岩化作用明显，代表了基底与盖层之间的强应变带。然而，雪峰山早中生代造山带的基底岩石至今还未有报道，缺少绿片岩相以上的高级变质岩或混合岩化岩石。

研究区内，由于地壳尺度的地震资料较为缺乏。秦葆瑚（1991）曾根据四川黑水至福建泉州的地球物理大断面的地震资料分析给出了雪峰山下的地壳模型，也证明雪峰山地区主要发育了向 NW 的逆冲构造，但是缺少更为细致的地壳结构模型。而丁道桂等（2007）通过重新解释地震资料之后认为，在地震反射剖面中，一条倾向 SE 的低速层可能代表了位于东部区之下的深部基底滑脱带，并行成了雪峰山的现今构造格架。因此，我们认为雪峰山主逆冲断层和其他的次级逆冲断层在地下最终都汇入主滑脱带之中。雪峰山造山带中的上部地壳变形，如逆冲断层、褶皱和劈理构造均是主滑脱带之上的薄皮构造，并不是厚皮构造（Yan et al., 2003）。但是在没有详细的地震深部资料的情况下，基底卷入逆冲和褶皱的可能性并不能排除。因此需要更为详尽的地球物理资料来观察雪峰山的下部构造，从而与上部地表的逆冲推覆相耦合。

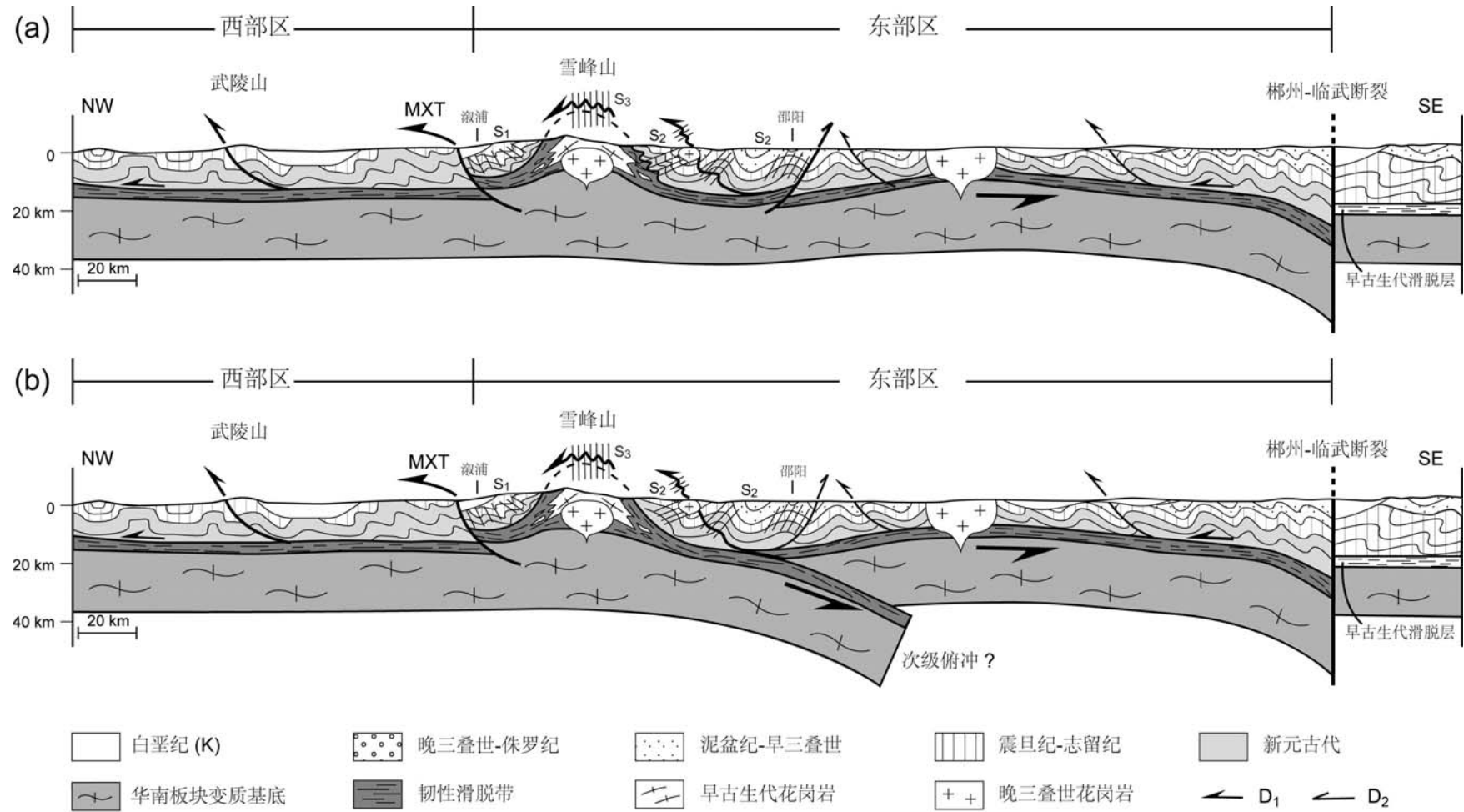


图 7-2 雪峰山造山带早中生代构造剖面图。

对于主滑脱带向东如何延伸,这里有两种可能的模型。第一种较为简单,即只存在一个滑脱层,在郴州-临武断层向 SE 俯冲。在这种模型下,这个主滑脱带延伸了超过 300 km,超过了世界上任何一个造山带中的基底滑脱带的长度。此外,这种情况下, D_2 的反向褶皱也是产生于切穿基底滑脱带的 SE 极性的逆冲(图 7-2a)。第二种模式中给出了一个次级俯冲引起的滑脱带(图 7-2b)。这个滑脱带在邵阳附近向 SE 倾伏,形成次级俯冲。这样的几何学格架表明 D_2 期反向褶皱和反向逆冲源自基底滑脱带的反向构造。无论是那种解释,雪峰山陆内造山带中必然存在一条区域范围的强应变基底滑脱带,分隔了上部地壳的沉积盖层和未出露的中下地壳变质岩。为了吸收早中生代发生在晚元古代至早三叠世沉积地层中的大规模地层缩短,下伏的基底岩石一定经历了陆内俯冲/底冲,从而形成了现今的雪峰山造山带的构造样式。

第四节 从雪峰山透视华南板块早中生代的地质演化

放眼于整个华南板块,其板块边缘在早中生代经历了强烈的构造作用。北缘,华南板块向华北板块之下俯冲,形成了出露大量超高压变质岩的秦岭—大别—苏鲁造山带(Hacker and Wang, 1995; Faure et al., 1999; 2008); 西缘,松潘—甘孜和龙门山构造带记录了三叠纪的构造变形和岩浆活动(Wallis et al., 2003; Harrowfield and Wilson, 2005; Roger et al., 2008, 2010); 在西南和南缘,一条从云南一直延伸到广西、越南的造山带分隔了华南板块和印支板块(Wang et al., 2000; Lepvrier et al., 1997, 2004, 2008, 2011; Carter et al., 2001; Carter and Clift, 2008; Zhang et al., 2011)。

其实自从黄汲清(1945)提出江南古陆之后,华南内部的构造就引起了广泛的关注。尤其在 80 年代之后的十多年中,一时间各种构造模式均喷薄而出,形成了百家争鸣的现象。首先是时代的争议,究竟是早古生代还是早中生代构造。提出者黄汲清先生认为主要是早古生代构造为主,支持他的观点的还有任纪舜(1991)、李继亮(1993)、贾宝华(1994)和丘元禧(1999)等人。提出早中生代造山的是许靖华先生(1988, 1990),此外陈海泓(1993)、马文璞(1993)也支持这一观点。郭令智先生(1980)则认为是新元古代的沟弧盆体系。其次争议的是造山模式,是陆内造山还是碰撞造山。许靖华、陈海泓和李继亮等先生都支

持早碰撞造山的模式，而陆内造山则被马文璞、丘元禧等先生所推荐。随着实验技术和研究工作的不断深入，陆内造山模式已逐渐被人所接受。

前人曾经将雪峰山的逆冲推覆体系的成因归为扬子板块和华北板块在晚侏罗世至早白垩世向西的递进变形，但是却忽略了早中三叠世的构造事件，如晚三叠世的造山后期岩体以及区域不整合，并没有与川东白垩纪的构造变形区分开（Yan et al., 2003, 2009）。Wang et al. (2005, 2007b, 2007c) 通过在雪峰山和云开大山的构造学和年代学研究认为，早中生代华南板块在华北板块和印支板块两个刚性块体的作用下，处于以走滑为主的扭压环境之下，形成了走滑挤压山系，雪峰山作为山系的西缘，运动学方向指向 NW；而福建省的褶皱冲断带代表了山系的东缘，挤压逆冲方向指向 SE，两者组成了双向逆冲构造。但是福建省的挤压构造主要发生在晚侏罗世，而雪峰山主要为早中生代构造，因此二者的形成时间有所不同。所以，由于动力学方向的不同以及构造影响的范围，这些造山事件都无法解释雪峰山的构造成因。

近些年来，对于华南中生代褶皱逆冲构造的一种新的解释跃然于纸面。Li and Li (2007) 提出，整个华南板块在早中生代均卷入了陆内造山过程，整个陆内造山带宽达 1300 km。局限地分布在山间盆地中的晚三叠世陆相或湖滩相沉积代表着造山后的沉积物，而湖南和江西从石炭-二叠纪的厚层白云质灰岩至早三叠世的海相薄层灰岩则表明沉积环境逐渐变浅的一个过程（江西省地质矿产局, 1984; 湖南省地质矿产局, 1988）。依据这个模式，对应于太平洋板块的平板俯冲，褶皱和逆冲断层的发育、同造山岩浆作用以及前陆盆地的沉积均向华南板块内部迁移。但是，太平洋板块俯冲的开始时间依旧存在争议，一些作者认为西向俯冲一直到~125 Ma 才开始（Engebreston, et al., 1985），但是其他人却认为板块俯冲从早三叠世甚至是晚二叠世就已经开始了（Li XH et al., 2006）。除此之外，华南板块上的三叠纪岩体年龄主要分布在 235 至 210 Ma，并且分布并没有明显的规律（丁兴等, 2005; 陈卫锋等, 2006, 2007a, 2007b; Wang et al., 2007b; Li and Li, 2007; Li HQ et al., 2008; 罗志高等, 2011）。尽管这些岩体的年代学数据并不支持从 SE 向 NW 逐渐迁移年轻的岩浆带，进而使得平板俯冲最重要的基础并不那么可靠，但是三叠纪 W 或者 NW 向的俯冲作用的证据似乎更为充足，不仅仅因为海南岛上存在晚二叠世的岛弧岩浆岩，而且在日本岛弧之上，也存在着晚二叠世至早中

三叠世的高压变质作用 (Faure and Charvet, 1987; Faure et al., 1988; Li XH et al., 2006)。因此, 如同新生代的天山在欧亚和印度大陆碰撞作用下重新活化一样, 早中生代的雪峰山造山带就在华南板块东缘的古太平洋板块俯冲作用下而形成。

作者通过详细的构造学、岩石学和年代学的分析, 综合和前人的工作, 提出了新的模式, 试图解释华南板块早中生代的构造演化 (图 7-3)。自从扬子和华夏地块在新元古代拼合之后, 其碰撞拼合带就位于板块内部, 而之后的南华期张裂期, 华南板块之上又形成了大范围的裂谷构造。这些都可能以薄弱带的形式存在于刚性板块之中。早古生代中晚期, 华南板块在挤压应力作用下, 经历了强烈的 S 或 SE 向推覆构造, 形成了早古生代陆内造山带, 地壳缩短变形时间为 460-440 Ma (图 7-3a)。虽然这一期造山作用的动力学背景还不清楚, 但华南板块东缘清楚地记录了早古生代的韧性变形和同构造的变质作用。在 440 Ma 之后, 造山过程结束, 加厚地壳开始受到重力均衡的调整, 出现了地壳伸展和造山带的垮塌。相伴随的是区域性走滑断层的调整和大面积造山后花岗岩的侵入 (图 7-3b)。早古生代造山作用造成了华南板块抬升成陆, 在中东部整体缺失了晚志留世—上泥盆世的沉积, 中晚泥盆世的砾岩不整合地覆盖着造山带褶皱地层之上。这一影响随着向华南内陆逐渐减小, 不整合在湖南西部和四川东部转变成假整合或整合接触。在泥盆纪至早三叠世, 华南板块进入了平静期, 没有大范围构造活动迹象 (图 7-3c)。至晚二叠世, 华南板块在经历了长距离的漂移之后, 逐渐停滞下来。在其东南侧古太平洋板块俯冲, 形成了二叠纪末的岛弧岩浆岩, 并在板块边缘的区域形成了 NW 的逆冲构造, 或者走滑伸展构造 (图 7-3d)。在三叠纪, 约 250 Ma 开始, 板块边缘的挤压应力传递至华南板块内部, 一直以薄弱带存在的郴州-临武断裂在此时活化, 在其西部区域发育大面积的逆冲断层和褶皱, 形成了雪峰山陆内造山带 (7-3e)。

综上所述, 华南板块内部的构造变形是以陆内造山的形式实现的, 其动力学来源于板块边缘的挤压作用而产生的远程效应。整个华南板块上早中生代发育了长达几百公里的、从广西北部经湖南至江西的陆内褶皱带, 从而奠定了华南板块现今我们所见的构造格架。

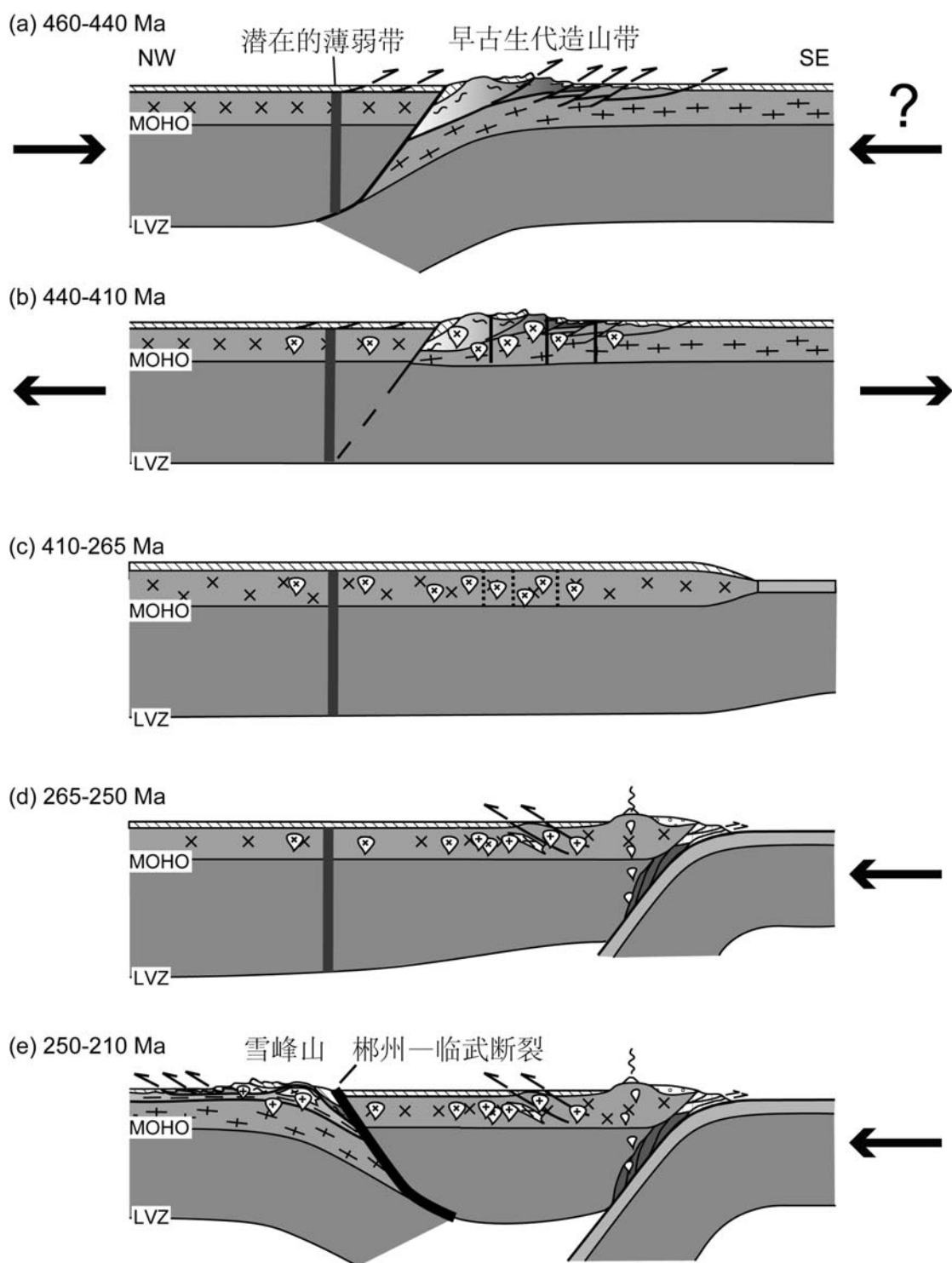


图 7-3 华南板块早古生代至早中生代的构造演化模式图 (a 和 b 修改自 Faure et al., 2009; Charvet et al., 2010)。

第五节 对陆内造山带的启示

针对陆内造山带的动力学来源,现在还存在的广泛的争论,但平板俯冲和远程效应成为较为常用的两种解释机制(Dickinson and Snyder, 1978; Avouac et al., 1993; English and Johnston, 2004)。现今的天山就是在新生代印度和欧亚大陆碰撞的基础上,古生代的构造带受到板块碰撞的远程效应而重新活动,发育了新生代的逆冲和隆升等构造事件(Molnar and Tapponnier, 1975; Hendrix et al., 1992; Avouac et al., 1993)。

Li and Li (2007) 通过对华南中生代花岗岩年代学进行全面的总结,于是将整个华南 1300 km 宽的褶皱带归结为古太平洋板块的平板俯冲,类似于北美 Laramide 造山带的形成(Dickinson and Snyder, 1978)。雪峰山位于平板俯冲形成陆内造山系统中的西缘。在早中生代,之前长期漂移的华南板块受到周边板块的围限而导致东南缘的应力累积,进而在板块内部的薄弱区域形成断裂并造成板块内部岩石圈的俯冲。这个薄弱区域可能是郴州-临武断裂,同时前人也认为是扬子和华夏地块的拼合线(Wang et al., 2003)。由于晚古生代巨厚的沉积使得下部岩石圈的地温上升,使其软化而易于变形或重新活化了先存断裂,就如同 Alice Spring 造山带一样,形成了切割岩石圈的逆冲断裂带(Goleby et al., 1989; Hand and Sandiford, 1999; Sandiford et al., 2001)。澳大利亚大陆上的新元古代 Petermann 造山带和古生代的 Alice Springs 造山带都是陆内构造活化的典型代表。Sandiford and Hand (1998) 研究表明, Petermann 造山带和 Alice Springs 造山带都是形成在原有的构造薄弱带之上。在 Petermann 造山带活动之前,造山区域沉积了超过 15 公里厚的沉积物,从而引起地温的升高, Woodroffe 断层活化后产生了大于 120 公里的地壳缩短,并揭露了榴辉岩向变质的岩石。Alice Springs 造山带也类似,首先造山前沉积了超过 8 公里的物质,之后沿 Redbank 断层形成了向 S 的推覆和地壳缩短。根据地球物理资料, Redbank 断层切穿了地壳,将 Moho 面错断了 10 公里,使得岩石圈地幔逆冲至下地壳之上(Goleby et al., 1989)。比利牛斯山也同样存在着薄弱带。在海西期造山之后,经历了地壳伸展作用,形成了陆内裂谷,一直持续到早白垩世。裂谷作用将欧洲板块拉分成两块。在晚白垩世开始,南部的 Iberia 块体向欧洲板块之下俯冲。在欧洲板块内部,早先形成的裂谷位置发生陆内俯冲造山,在 Iberia 板块与欧洲板块相聚合之后,造山作用一

直延续，最终形成了比利牛斯山（Choukroune, 1992）。

因此对于典型的陆内造山带而言，刚性板块内部的薄弱带是发生造山的绝佳位置。在板块边缘的持续挤压之下，首先变形的是板块边界。但是当板块边界的地壳不断加厚至临界值之后，挤压作用在重力均衡的作用下就很难使板缘增生型或碰撞型的造山带的地壳继续加厚。此时，板块内部的挤压应力无法得到释放，而聚集了巨大的应力累积。此时板块内部的薄弱带就成了应力释放最佳的位置，当应力累积到一定程度，先存薄弱带就会发生构造活化，从而可以在远离板块边界上千公里的地方形成大规模的造山作用。

雪峰山造山带正是在这种机制下形成的，但由于缺少较为可信的地球物理数据，我们暂时无法将雪峰山的地表变形与深部构造有机的结合起来，也无法预计郴州—临武断裂是否切穿了岩石圈，更难估计地壳的缩短量。但随着研究的不断深入，地表地质和深部地球物理资料的不断丰富，雪峰山造山带的深部地壳结构势必会被揭示出来，从而对雪峰山造山带乃至华南板块的早中生代构造格局起到巨大的推动作用，也能加深对陆内造山过程的理解。

第八章 结论

本文选取华南板块内陆的雪峰山造山带作为研究对象,研究了该造山带的构造格架和地质演化。本文主要分为两部分,前一部分建立在详细的构造几何学和运动学研究的基础上,通过不同尺度的分析,得出了雪峰山造山带的几何学模型。第二部分包括同位素年代学和锆石 Hf 同位素的研究,为研究造山带的演化建立年代学格架,并探讨了雪峰山地区的岩浆活动和地壳演化。本文主要取得了如下结论:

1. 早中生代雪峰山造山带卷入了从新元古代至早三叠世的地层。早古生代构造作用在华南板块东部产生剧烈的作用,如挤压推覆、高角闪岩相的变质以及广泛的地壳重熔,但在雪峰山地区却影响微弱,仅表现为早古生代零星的岩浆活动和南部地区震旦纪至奥陶纪地层中残留的 E-W 走向的褶皱作用。

2. 雪峰山造山带可以分为 2 个构造单元:以主逆冲断层(MXT)为界,以西为西部区,以大型箱状褶皱为特征,在背斜的两翼地层陡立处,发育了大量的滑脱褶皱和层滑;以东为东部区,劈理发育呈扇状,是雪峰山构造带的核心区域,变形向东逐渐减弱,构造层次逐渐提高。在东部区局部出露了基底滑脱带和经历了绿片岩相变质作用的石榴石云母片岩,这些属于基底变质岩的表层部分。整个雪峰山没有出露角闪岩、麻粒岩等高级变质岩。

3. 雪峰山造山带经历了多期构造事件。 D_1 为上部指向北西的韧性剪切,广泛发育于整个区域,产生了大量的极性 NW 的不对称褶皱和逆冲断层, S_1 劈理倾向 SE,在劈理面上发育了 NW-SE 向的矿物拉伸线理; D_2 代表了一期反向褶皱—逆冲构造事件,以极性 SE 的褶皱和倾向 NW 的劈理为主要构造, D_1 期形成的褶皱和劈理均被 F_2 所改造; D_3 则以水平挤压为主,形成了直立的 F_3 褶皱、 S_3 劈理和 L_3 线理,褶皱改造了 D_1 和 D_2 期的构造。

4. 雪峰山地区存在两期构造热事件——早古生代和早中生代两期岩浆活动。早古生代挤压构造影响虽然较为小,但是后期的造山后伸展可能影响到了雪峰山地区,从而产生了 440-410 Ma 的岩浆活动;三叠纪的花岗岩侵位于背斜的核部,并造成了基底滑脱带的抬升,年龄主要分布于 225-215 Ma 之间。

5. 早古生代与早中生代花岗岩的 $\epsilon_{\text{Hf}}(t)$ 值均在 -10 至 -1 之间, Hf 模式年龄在 2.4-1.3 Ga 之间,表明两期岩浆活动的源区均为早中元古代的中下地壳物质。

6. 在雪峰山地区卷入早中生代构造事件中最年轻的地层为早三叠世薄层灰岩，因此构造作用开始于~245 Ma；而造山后期的岩浆活动止于 215 Ma，因此雪峰山造山带的活动时间为 245-215 Ma。

7. 郴州-临武断裂被认为是新元古代扬子地块和华夏地块的拼合带。作为雪峰山造山带的重要边界，分隔了雪峰山早中生代构造域和以东的早古生代构造域，作为潜在的薄弱带，在其中生代构造演化中起到了重要作用。

8. 雪峰山造山带作为典型的陆内造山带，是华南板块东缘古太平洋板块早三叠世向 NW 俯冲的远程效应的产物。与新生代的天山类似，雪峰山在郴州-临武断裂这条薄弱带活化的基础上，形成大面积的逆冲推覆构造。

参考文献

1. Allen, M. B., Vincent, S. J., and Wheeler, P. J., 1999. Late Cenozoic tectonics of the Kepingtage thrust zone: Interactions of the Tien Shan and Tarim Basin, northwest China. *Tectonics*, 18(4), 639-654.
2. Avouac, J. P., Tapponnier, P., Bai, M., You, H., and Wang, G., 1993. Active Thrusting and Folding Along the Northern Tien Shan and Late Cenozoic Rotation of the Tarim Relative to Dzungaria and Kazakhstan. *J. Geophys. Res.*, 98(B4), 6755-6804.
3. Beaumont C., Fullsack, P., and Hamilton, J., 1994. Styles of crustal deformation in compressional orogens caused by subduction of the underlying lithosphere. *Tectonophysics*, 232, 119-132.
4. Brown, M., 2005. Synergistic effects of melting and deformation: an example from the Variscan belt, western France. In: Gapais, D., Brun, J.P., Cobbold, P. (Eds.), *Deformation mechanisms, rheology and tectonics: from minerals to the lithosphere*: Geological Society, London, Special Publication, 243, pp. 205-226.
5. Carter, A., and Clift, P. D., 2008. Was the Indosinian orogeny a Triassic mountain building or a thermotectonic reactivation event?. *CR Géosci.*, 340(2-3), 83-93.
6. Carter, A., Roques, D., Bristow, C., and Kinny, P., 2001. Understanding Mesozoic accretion in Southeast Asia: Significance of Triassic thermotectonism (Indosinian orogeny) in Vietnam. *Geology*, 29(3), 211-214.
7. Cawood, P. A., Buchan, C., 2007. Linking accretionary orogenesis with supercontinent assembly. *Earth-Science Reviews* 82, 217-256.
8. Charvet, J., Lapiere, H., Yu, Y., 1994. Geodynamic significance of the Mesozoic volcanism of southeastern China. *Journal of Southeast Asian Earth Sciences* 9, 387-396.
9. Charvet, J., Shu, L. S., Shi, Y. S., Guo, L. Z., and Faure, M., 1996. The building of south China: Collision of Yangzi and Cathaysia blocks, problems and tentative answers. *J. Southeast Asian Earth Sci.*, 13(3-5).
10. Charvet, J., Shu, L., Faure, M., Choulet, F., Wang, B., Lu, H., and Le Breton, N., 2010. Structural development of the Lower Paleozoic belt of South China: Genesis of an intracontinental orogen. *J. Asian Earth Sci.*, 39(4), 309-330.
11. Chen, A., 1999. Mirror-image thrusting in the South China Orogenic Belt: tectonic evidence from western Fujian, southeastern China. *Tectonophysics*, 305(4), 497-519.
12. Chen, C.-H., Hsieh, P.-S., Lee, C.-Y., Zhou, H.-W., 2011. Two episodes of the Indosinian thermal event on the South China Block: Constraints from LA-ICPMS U-Pb zircon and electron microprobe monazite ages of the Darongshan S-type granitic suite. *Gondwana*

- Research 19, 1008-1023.
13. Chen, J. F., Foland, K. A., Xing, F. M., Xu, X. A., Zhou, T. X., 1991. Magmatism along the southeast margin of the Yangtze block - Precambrian collision of the Yangtze and Cathaysia blocks of China. *Geology* 19, 815-818.
 14. Chen, W. F., Chen, P. R., Zhou, X. M., Huang, H. Y., Ding, X., and Sun, T., 2007. Single Zircon LA-ICP-MS U-Pb Dating of the Guandimiao and Wawutang Granitic Plutons in Hunan, South China and its Petrogenetic Significance. *Acta Geol. Sin.*, 81, 81-89.
 15. Choukroune, P., 1992. Tectonic evolution of the Pyrenees. *Annu. Rev. Earth Planet. Sci.*, 20, 143-158.
 16. Chung, S. L., Chu, M. F., Zhang, Y., Xie, Y., Lo, C. H., Lee, T.-Y., Lan, C. Y., Li, X., Zhang, Q., Wang, Y., 2005. Tibetan tectonic evolution inferred from spatial and temporal variations in post-collisional magmatism. *Earth-Science Reviews* 68, 173-196.
 17. Cocherie, A., Legendre, O., Peucat, J. J., Kouamelan, A. N., 1998. Geochronology of polygenetic monazites constrained by in situ electron microprobe Th-U-total lead determination: implications for lead behaviour in monazite. *Geochimica et Cosmochimica Acta* 62, 2475-2497.
 18. Cocherie, A., Albarede, F., 2001. An improved U-Th-Pb age calculation for electron microprobe dating of monazite. *Geochimica et Cosmochimica Acta* 65, 4509-4522.
 19. Cocherie, A., Mezeme, E. B., Legendre, O., Fanning, C. M., Faure, M., and Rossi, P., 2005. Electron-microprobe dating as a tool for determining the closure of Th-U-Pb systems in migmatitic monazites. *American Mineralogist* 90, 607-618.
 20. Crowley, J.L., Ghent, E.D., 1999. An electron microprobe study of the U-Th-Pb systematics of metamorphosed monazite: the role of Pb diffusion versus overgrowth and recrystallisation. *Chemical Geology* 157, 285-302.
 21. Davis, G.A., C. Wang, Y. Zheng, J. Zhang, C. Zhang, G.E. Gehrels, 1998. The enigmatic Yinshan fold and thrust belt of northern China: new views on its intraplate contractional styles, *Geology*, 26, 43-46.
 22. Davis, G.A., Y.D. Zheng, C. Wang, B.J. Darby, C.H. Zhang, G.E. Gehrels, 2001. Mesozoic tectonic evolution of the Yanshan fold and thrust belt, with emphasis on Hebei and Liaoning Provinces, northern China, in: M.S. Hendrix, G.A. Davis (Eds.), *Paleozoic and Mesozoic Tectonic Evolution of Central Asia: Continental Assembly to Intracontinental Deformation*, *Geol. Soc. Am., Memoir*, vol.194, pp. 171-198.
 23. Deramond, J., Souquet, P., Fondécave-Wallez, M. J. and Specht, M., 1993, Relationships between thrust tectonics and sequence stratigraphy surfaces in foredeep: model and examples from the Pyrenees (Cretaceous-Eocene, France, Spain), in: Williams G. D. and Dobb, A., eds, *Tectonics and seismic sequence stratigraphy*, *Geological Society of London Special Publications*, v. 71: 193-219.
 24. Dewey, J. F. and Bird, J. M., 1970. Mountain belts and the new global tectonics. *Journal of*

- Geophysical Research, v. 75, 2625-2647.
25. Dickinson, W. R., and Snyder, W. S., 1978. Plate tectonics of the Laramide orogeny, in Matthews, V., ed., Laramide folding associated with Basement Block faulting in the Western United States: Geol. Soc. Am. Memoir, 151, 355–366.
 26. Ding, X., Chen, P. R., Chen, W. F., Huang, H. Y., and Zhou, X. M., 2005. LA-ICPMS zircon U-Pb age determination of the Weishan granite in Hunan: petrogenesis and significance: Sci. in China (D), v. 35, p. 606-616.
 27. Engebretson, D. C., Cox, A., and Gordon, R. G., 1985. Relative motion between oceanic and continental plates in the Pacific basin. Spec. Pap. Geol. Soc. Am., 206, 1 – 55.
 28. English, J. M., and Johnston, S. T., 2004. The Laramide orogeny: What were the driving forces?. Int. Geol. Rev., 46(9), 833-838.
 29. Enkelmann, E., Weislogel, A., Ratschbacher, L., Eide, E., Renno, A., Wooden, J., 2007. How was the Triassic Songpan-Ganzi basin filled? A provenance study. Tectonics 26, TC4007.
 30. Escher, A., and Beaumont, C., 1997. Formation, burial and exhumation of basement nappes at crustal scale: a geometric model based on the Western Swiss-Italian Alps. J. of Struct. Geol., 19, 955-974.
 31. Faure, M., and Charvet, J., 1987. Late Permian/early Triassic orogeny in Japan: piling up of nappes, transverse lineation and continental subduction of the Honshu block. Earth and Planetary Science Letters, 84(2-3), 295-308.
 32. Faure, M., Monié, P., and Fabbri, O., 1988. Microtectonics and ³⁹Ar-⁴⁰Ar dating of high pressure metamorphic rocks of the south Ryukyu Arc and their bearings on the pre-Eocene geodynamic evolution of Eastern Asia. Tectonophysics, 156(1-2), 133-143.
 33. Faure, M., Sun, Y., Shu, L., Monié, P., and Charvet, J., 1996. Extensional tectonics within a subduction-type orogen. The case study of the Wugongshan dome (Jiangxi Province, southeastern China). Tectonophysics, 263(1-4), 77-106.
 34. Faure, M., Lin, W., and Sun, Y., 1998. Doming in the southern foreland of the Dabieshan (Yangtse block, China). Terra Nova, 10(6), 307-311.
 35. Faure, M., Lin, W., Shu, L. S., Sun, Y., and Scharer, U., 1999. Tectonics of the Dabieshan (eastern China) and possible exhumation mechanism of ultra high-pressure rocks, Terra Nova, 11(6), 251-258.
 36. Faure, M., Lin, W., Scharer, U., Shu, L. S., Sun, Y., Arnaud, N., 2003. Continental subduction and exhumation of UHP rocks. Structural and geochronological insights from the Dabieshan (East China). Lithos 70, 213-241.
 37. Faure, M., Lin, W., Monié, P., and Meffre, S., 2008. Paleozoic collision between the North and South China blocks, Early Triassic tectonics and the problem of the ultrahigh-pressure metamorphism. CR Géosciences, special issue Triassic Tectonics in East Asia, 340(2-3), 139-150.

38. Faure, M., Shu, L., Wang, B., Charvet, J., Choulet, F., and Monié, P., 2009. Intracontinental subduction: a possible mechanism for the Early Palaeozoic Orogen of SE China. *Terra Nova*, 21(5), 360-368.
39. Gao, S., Ling, W.L., Qiu, Y.M., Lian, Z., Hartmann, G., Simon, K., 1999. Contrasting geochemical and Sm-Nd isotopic compositions of Archean metasediments from the Kongling high-grade terrain of the Yangtze craton: Evidence for cratonic evolution and redistribution of REE during crustal anatexis. *Geochim. Cosmochim. Acta* 63, 2071-2088.
40. Gao, S., Yang, J., Zhou, L., Li, M., Hu, Z., Guo, J., Yuan, H., Gong, H., Xiao, G., Wei, J., 2011. Age and growth of the Archean Kongling terrain, South China, with emphasis on 3.3 ga granitoid gneisses. *American Journal of Science* 311, 153-182.
41. Gilbert, C.K., 1890. Lake Bonneville. US Geological Survey Monographs, 1.
42. Gilder, S., Keller, G.R., Ming, L., and Goodell, P., 1991. Timing and spatial distribution of rifting in China. *Tectonophysics*, 197, 225-243.
43. Godin, L., Brown, R. L., Hanmer, S., and Parrish, R., 1999. Back folds in the core of the Himalayan orogen: An alternative interpretation. *Geology*, 27(2), 151-154.
44. Goleby, B. R., Shaw, R. D., Wright, C., Kennett, B. L. N., Lambeck, K., 1989. Geophysical evidence for thick-skinned crustal deformation in central Australia. *Nature*, 337, 325-330.
45. Greentree, M. R., Li, Z. X., Li, X. H. and Wu, H. C. 2006. Late Mesoproterozoic to earliest Neoproterozoic basin record of the Sibao orogenesis in western South China and relationship to the assembly of Rodinia. *Precambrian Research* 151(1-2), 79-100.
46. Gupta, S., 1989. Comments and Reply on "Mesozoic overthrust tectonics in south China". *Geology*, 17, 669 – 673.
47. Hacker, B. R., and Wang, Q. C., 1995. Ar/Ar Geochronology of Ultrahigh-Pressure Metamorphism in Central China. *Tectonics*, 14(4), 994-1006.
48. Hacker, B. R., Wallis, S. R., Ratschbacher, L., Grove, M., Gehrels, G., 2006. High-temperature geochronology constraints on the tectonic history and architecture of the ultrahigh-pressure Dabie-Sulu Orogen. *Tectonics* 25, 17.
49. Hand, M., and Sandiford, M., 1999. Intraplate deformation in central Australia, the link between subsidence and fault reactivation. *Tectonophysics*, 305(1-3), 121-140.
50. Harris, N., Massey, J., 1994. Decompression and anatexis of Himalayan metapelites. *Tectonics* 13, 1537-1546.
51. Harrowfield, M. J., and Wilson, C. J. L., 2005. Indosinian deformation of the Songpan Garze Fold Belt, northeast Tibetan Plateau. *J. Struc. Geol.*, 27(1), 101-117.
52. Hendrix, M. S., Graham, S. A., Carroll, A. R., Sobel, E. R., McKnight, C. L., Schulein, B. J., and Wang, Z., 1992. Sedimentary record and climatic implications of recurrent deformation in the Tian Shan: Evidence from Mesozoic strata of the north Tarim, south Junggar, and Turpan basins, northwest China. *Geol. Soc. Am. Bull.*, 104(1), 53-79.

53. Holdsworth, R. E., Hand, M., Miller, J. A., Buick, I. S. 2001. Continental reactivation and reworking: an introduction. In: *Continental Reactivation and Reworking* (edited by Miller, J., Holdsworth, R. E., Buick, I. S. & Hand, M.). Geological Society Special Publication 184. Geological Soc Publishing House, Bath, 1-12.
54. Hsu, K. J., Sun, S., Li, J., Chen, H., Pen, H., and Sengor, A. M. C., 1988. Mesozoic overthrust tectonics in South China. *Geology*, 16(5), 418-421.
55. Hsu, K. J., Li, J. L., Chen, H. H., Wang, Q. C., Sun, S., and Sengor, A. M. C., 1990. Tectonics of south China: Key to understanding West Pacific geology, *Tectonophysics*, 183, 9–39.
56. Huang, T.K., 1960. The main characteristics of the geologic structures of China: Preliminary conclusions. *Acta Geologica Sinica* 40, 1–37.
57. Huang, T. K., 1978. An outline of the tectonic characteristics of China. *Eclogae Geologicae Helveticae* 71, 611-635.
58. Jahn, B.M., Zhou, X.H., Li, J.L., 1990. Formation and tectonic evolution of southeastern China and Taiwan: isotopic and geochemical constraints. *Tectonophysics* 183, 145–160.
59. Lapierre, H., Jahn, B.M., Charvet, J., Yu, Y.W., 1997. Mesozoic felsic arc magmatism and continental olivine tholeiites in Zhejiang Province and their relationship with tectonic activity in SE China. *Tectonophysics* 274, 321–338.
60. Lepvrier, C., Maluski, H., Van Vuong, N., Roques, D., Axente, V., Rangin, C., 1997. Indosinian NW-trending shear zones within the Truong Son belt (Vietnam) 40Ar---39Ar Triassic ages and Cretaceous to Cenozoic overprints. *Tectonophysics* 283, 105-127.
61. Lepvrier, C., Maluski, H., Van Tich, V., Leyreloup, A., Truong Thi, P., and Van Vuong, N. 2004. The Early Triassic Indosinian orogeny in Vietnam (Truong Son Belt and Kontum Massif); implications for the geodynamic evolution of Indochina. *Tectonophysics*, 393(1-4), 87-118.
62. Lepvrier, C., Van Vuong, N., Maluski, H., Truong Thi, P., and Van Vu, T., 2008. Indosinian tectonics in Vietnam. *CR Géosciences*, special issue Triassic Tectonics in East Asia, 340(2-3).
63. Lepvrier, C., Faure, M., Van Vuong, N., Tich, Vu Van, Lin, W., Ta Trong Tang, 2011. North directed nappes in Northeastern Vietnam (East Bac Bo). *J. Asian Earth Sci.*, 41, 56-68.
64. Li, J. W., Zhou, M. F., Li, X. F., Fu, Z. R., Li, Z. J., 2001. The Hunan-Jiangxi strike-slip fault system in southern China: southern termination of the Tan-Lu fault. *Journal of Geodynamics* 32, 333-354.
65. Li, L. M., Sun, M., Wang, Y., Xing, G., Zhao, G., Lin, S., Xia, X., Chan, L., Zhang, F., Wong, J., 2011. U-Pb and Hf isotopic study of zircons from migmatized amphibolites in the Cathaysia Block: Implications for the early Paleozoic peak tectonothermal event in Southeastern China. *Gondwana Research* 19, 191-201.
66. Li, Q.L., Li, X. H., Liu, Y., Tang, G. Q., Yang, J. H., Zhu, W. G., 2010. Precise U-Pb and Pb-Pb dating of Phanerozoic baddeleyite by SIMS with oxygen flooding technique. *Journal*

- of Analytical Atomic Spectrometry 25, 1107-1113.
67. Li, S. Z., Zhao, G. C., Zhang, G. W., Liu, X. C., Dong, S. W., Wang, Y. J., Liu, X., Suo, Y. H., Dai, L. M., Jin, C., Liu, L. P., Hao, Y., Liu, E. S., Wang, J., and Wang, T., 2010. Not all folds and thrusts in the Yangtze foreland thrust belt are related to the Dabie Orogen. Insights from Mesozoic deformation south of the Yangtze River. *Geological Journal*, 45, 650-663.
 68. Li, S.Z., Kusky, T.M., Zhao, G.C., Liu, X.C., Kopp, H., Zhang, G.W., Wang, L., 2010. Two-Stage Triassic extrusion of the HP-UHP Terranes in the western Dabie-Sulu orogen of China: constraints from structural geology. *Tectonophysics*. 490, 267-293.
 69. Li, S.Z., Kusky, T.M., Zhao, G.C., Liu, X.C., Wang, L., Kopp, H., Hoernle, K., Zhang, G.W., Dong, S.W., 2011. Thermalchronological constrains to two-stage extrusion of the HP-UHP Terranes in the Dabie-Sulu Orogen, Central China. *Tectonophysics*. 504, 25-42.
 70. Li, X.H., 1991. Geochronology of the Wanyangshan-Zhuguangshan granitoid batholith: Implication for the crust development. *Science in China (B)* 34, 620-629.
 71. Li, X. H., 1994. A comprehensive U-Pb, Sm-Nd, Rb-Sr and ^{40}Ar - ^{39}Ar geochronological study on Guidong Granodiorite, southeast China: Records of multiple tectonothermal events in a single pluton. *Chemical Geology* 115, 283-295.
 72. Li, X. H., and McCulloch, M. T., 1996. Secular variation in the Nd isotopic composition of Neoproterozoic sediments from the southern margin of the Yangtze Block: evidence for a Proterozoic continental collision in southeast China. *Precambrian Research* 76(1-2), 67-76.
 73. Li, X. H., 1999. U-Pb zircon ages of granites from the southern margin of the Yangtze Block: timing of Neoproterozoic Jinning Orogeny in SE China and implications for Rodinia Assembly. *Precambrian Res.*, 97(1-2), 43-57.
 74. Li, X. H., 2000. Cretaceous magmatism and lithospheric extension in Southeast China. *Journal of Asian Earth Sciences* 18, 293-305.
 75. Li, X.-h., Li, Z.-X., Zhou, H., Liu, Y., Kinny, P. D., 2002. U-Pb zircon geochronology, geochemistry and Nd isotopic study of Neoproterozoic bimodal volcanic rocks in the Kangdian Rift of South China: implications for the initial rifting of Rodinia. *Precambrian Research* 113, 135-154.
 76. Li, X. H., Li, Z. X., Ge, W. C., Zhou, H. W., Li, W. X., Liu, Y., Wingate, M. T. D., 2003. Neoproterozoic granitoids in South China: crustal melting above a mantle plume at ca. 825 Ma? *Precambrian Research* 122, 45-83.
 77. Li, X. H., Li, Z. X., Li, W. X., and Wang, Y. J., 2006. Initiation of the Indosinian Orogeny in South China: Evidence for a Permian magmatic arc on Hainan Island. *J. Geol.*, 114(3), 341-353.
 78. Li, X. H., Li, W. X., Li, Z. X., Lo, C. H., Wang, J., Ye, M. F., Yang, Y. H., 2009a. Amalgamation between the Yangtze and Cathaysia Blocks in South China: Constraints from SHRIMP U-Pb zircon ages, geochemistry and Nd-Hf isotopes of the Shuangxiwu volcanic rocks. *Precambrian Research* 174, 117-128.

79. Li, X. H., Liu Y., Li Q. L., Guo C. H., Chamberlain K. R., 2009b. Precise determination of Phanerozoic zircon Pb/Pb age by multicollector SIMS without external standardization. *Geochemistry Geophysics Geosystems* 10, Q04010, doi:10.1029/2009GC002400.
80. Li, Z.X., 1998. Tectonic history of the major East Asian lithospheric blocks since the mid-Proterozoic—A synthesis, in Flower, M.J., Chung, S.-L., Lo, C.-H., and Lee, T.-Y., eds., *Mantle Dynamics and Plate Inter actions in East Asia*: Washington, D.C., American Geophysical Union, *Geodynamics Series* 27, 221–243.
81. Li, Z. X., Li, X. H., Kinny, P. D., Wang, J., 1999. The breakup of Rodinia: did it start with a mantle plume beneath South China? *Earth and Planetary Science Letters* 173, 171-181.
82. Li, Z. X., Li, X. H., Zhou, H. W., and Kinny, P. D., 2002. Grenvillian continental collision in south China: New SHRIMP U-Pb zircon results and implications for the configuration of Rodinia. *Geology* 30(2), 163-166.
83. Li, Z. X., and Li, X. H., 2007. Formation of the 1300-km-wide intracontinental orogen and postorogenic magmatic province in Mesozoic South China: A flat-slab subduction model. *Geology*, 35(2), 179-182.
84. Li, Z. X., Wartho, J. A., Occhipinti, S., Zhang, C. L., Li, X. H., Wang, J., Bao, C. M., 2007. Early history of the eastern Sibao Orogen (South China) during the assembly of Rodinia: New mica Ar-40/Ar-39 dating and SHRIMP U-Pb detrital zircon provenance constraints. *Precambrian Research* 159, 79-94.
85. Li, Z. X., Li, X. H., Wartho, J. A., Clark, C., Li, W. X., Zhang, C. L., and Bao. C., 2010. Magmatic and metamorphic events during the early Paleozoic Wuyi-Yunkai orogeny, southeastern South China: New age constraints and pressure-temperature conditions. *Geol. Soc. Am. Bull.*, 122(5-6), 772-793.
86. Lin, W., Faure, M., Monie, P., Scharer, U., Zhang, L. S., and Sun, Y., 2000. Tectonics of SE China: New insights from the Lushan massif (Jiangxi Province). *Tectonics*, 19(5), 852-871.
87. Lin, W., Wang, Q., and Chen, K., 2008. Phanerozoic tectonics of south China block: New insights from the polyphase deformation in the Yunkai massif. *Tectonics*, 27, TC6004, doi:10.1029/2007TC002207.
88. Lin, W., Shi, Y., Wang, Q., 2009a. Exhumation tectonics of the HP-UHP orogenic belt in Eastern China: New structural-petrological insights from the Tongcheng massif, Eastern Dabieshan. *Lithos* 109.
89. Lin, W., Faure, M., Shi, Y., Wang, Q., Li, Z., 2009b. Palaeozoic tectonics of the south-western Chinese Tianshan: new insights from a structural study of the high-pressure/low-temperature metamorphic belt. *International Journal of Earth Sciences*, doi: 10.1007/s00531-008-0371-7.
90. Liu, X., Hao, J., 1989. Structure and tectonic evolution of the Tongbai-Dabie Range in the east Qinling collisional belt, China. *Tectonics* 8, 637-645.
91. Ludwig, K.R., 2001. Users manual for Isoplot/Ex rev. 2.49. Berkeley Geochronology Centre

Special Publication. No. 1a, 56 pp.

92. Malavieille, J., 2010. Impact of erosion, sedimentation, and structural heritage on the structure and kinematics of orogenic wedges: Analog models and case studies, *GSA Today*, 20, 1, doi: 10.1130/GSATG48A.1.
93. Mattauer, M. 1980. Les déformation des matériaux de l'écorce terrestre. Ed. Herman. Paris.
94. Mattauer, M., Matte, P., Malavieille, J., Tapponnier, P., Maluski, H., Xu, Z., Lu, Y., Tang, Y., 1985. Tectonics of the Qinling belt: build-up and evolution of eastern Asia. *Nature* 317, 496–500.
95. McQuarrie, N., 2004. Crustal scale geometry of the Zagros fold-thrust belt, Iran. *J. Struct. Geol.*, 26(3), 519-535.
96. Morel, M. L. A., Nebel, O., Nebel-Jacobsen, Y. J., Miller, J. S., Vroon, P. Z., 2008. Hafnium isotope characterization of the GJ-1 zircon reference material by solution and laser-ablation MC-ICPMS. *Chemical Geology* 255, 231-235.
97. Montel, J. M., Marignac, C., Barbey, P., and Pichavant, M., 1992. Thermobarometry and granite genesis: the Hercynian low-P, high-T Velay anatectic dome (French Massif central). *Journal of Metamorphic Geology* 10, 1-15.
98. Molnar, P., and Tapponnier, P., 1975. Cenozoic Tectonics of Asia: Effects of a Continental Collision: Features of recent continental tectonics in Asia can be interpreted as results of the India-Eurasia collision. *Science* 189, 419-426.
99. Muñoz, J.A., 1992. Evolution of a continental collision belt: Ecore-Pyrenees crustal balanced cross-section, in: McClay, K.R., eds, *Thrust tectonics*, Chapman&Hall, London, 235-246.
100. Murphy, J.B., Nance, R.D., 1991. Supercontinent model for the contrasting character of Late Proterozoic orogenic belts. *Geology*, 19 (5), 469–472.
101. Nance, R.D., Murphy, J.B., 1994. Orogenic style and the configuration of supercontinents. In: Embry, A.F., Beauchamp, B., Glass, D.J. (Eds.), *Pangea: Global Environments and Resources. Memoir*, vol. 17. Canadian Society of Petroleum Geologists, Calgary, pp. 49–65.
102. Passchier, C. W., Trouw, R. A. J., 2005. *Microtectonics*. 2nd edition, Springer, Berlin, pp. 27–66.
103. Parrish, R., 1990. U-Pb dating of monazite and its application to geological problems. *Canadian Journal of Earth Sciences* 27, 1431-1450.
104. Pidgeon, R. T., 1992. Recrystallisation of oscillatory zoned zircon: Some geochronological and petrological implications. *Contrib Mineral Petrol*, 110: 463 - 472.
105. Pommier A., Cocherie, A., and Legendre, O., 2002. EPMA Dating User's manual: Age calculation from electron probe microanalyser measurements of U-Th-Pb. BRGM, 9 pp.
106. Qiu, Y. M., Gao, S., McNaughton, N. J., Groves, D. I., and Ling, W., 2000. First evidence of >3.2 Ga continental crust in the Yangtze craton of south China and its implications for Archean crustal evolution and Phanerozoic tectonics. *Geology* 28(1), 11-14.

107. Ren, J., 1991. On the geotectonics of southern China. *Acta Geologica Sinica* 44, 111-130.
108. Qiu, Y. X., Zhang Y. C., and Ma, W. P., 2000. The Tectonic Nature and Evolution of Xuefeng Mountains: One Model of Formation and Evolution of Intra-continental Orogenic Belt. Geological Publishing House, Beijing, 155pp.
109. Raimondo, T., Collins, A. S., Hand, M., Walker-Hallam, A., Smithies, R. H., Evins, P. M., and Howard, H. M., 2010. The anatomy of a deep intracontinental orogen. *Tectonics* 29, TC4024, 10.1029/2009tc002504.
110. Ramsay, J. G., and Huber, M.I., 1987. The techniques of Modern Structural geology Volume 2: Folds and Fractures, 700pp; Academic Press, London.
111. Ratschbacher, L., Hacker, B. R., Calvert, A., Webb, L. E., Grimmer, J. C., McWilliams, M. O., Ireland, T., Dong, S. W., Hu, J. M., 2003. Tectonics of the Qinling (Central China): tectonostratigraphy, geochronology, and deformation history. *Tectonophysics* 366, 1-53.
112. Rodgers, J., 1989. Comment on 'Mesozoic overthrust tectonics in south China'. *Geology*, 17, 671 – 672.
113. Roger, F., Leloup, P. H., Jolivet, M., Lacassin, R., Trinh, P. T., Brunel, M., Seward, D., 2000. Long and complex thermal history of the Song Chay metamorphic dome (Northern Vietnam) by multi-system geochronology. *Tectonophysics* 321, 449-466.
114. Roger, F., Jolivet, M., and Malavieille, J., 2008. Tectonic evolution of the Triassic fold belts of Tibet. *CR Géosciences*, special issue Triassic Tectonics in East Asia, 340(2-3), 180-189.
115. Roger, F., Jolivet, M., and Malavieille, J., 2010. The tectonic evolution of the Songpan-Garze(North Tibet) and adjacent areas from Proterozoic to Present: A synthesis. *J. Asian Earth Sci.*, 39(4), 254-269.
116. Roure, F., Choukroune, P., Berastegui, X., Munoz, J. A., Villien, A., Matheron, P. Bareyt, M., Seguret, M., Camara, P., and Deramond, J., 1989. ECORS Deep seismic data and balanced cross sections: geometric constraints on the evolution of the Pyrenees. *Tectonics*, 8, 41–50.
117. Rowley, D. B., Ziegler, A. M., and Nie, S., 1989. Comment on Mesozoic overthrust tectonics in south China. *Geology*, 17, 384 – 386.
118. Sandiford, M., Hand, M., and McLaren, S., 2001. Tectonic feedback, intraplate orogeny and the geochemical structure of the crust: a central Australian perspective. Geological Society, London, Special Publications, 184(1), 195-218.
119. Schmid, J. C., Ratschbacher, L., Hacker, B. R., Gaitzsch I., and Dong, S. W., 1999. How did the foreland react? Yangtze foreland fold-and-thrust belt deformation related to exhumation of the Dabie Shan ultrahigh pressure continental crust (eastern China). *Terra Nova*, 11, 266-272.
120. Schuchert, C., 1925. Significance of Taconic orogeny. *Geological Society of America Bulletin*, 36, 343-350.
121. Sengör, A. M. C., 1991. Plate tectonics and orogenic research after 25 years: Synopsis of a

- Tethyan perspective. *Tectonophysics*, 187, 315-344.
122. Sengör, A.M.C., Natal'in, B.A., Burtman, V.S., 1993. Evolution of the Alaid tectonic collage and Palaeozoic crustal growth in Eurasia. *Nature* 364, 299–307.
123. Sengör, A.M.C., Natal'in, B.A., 1996a. Paleotectonics of Asia: fragments of a synthesis. In: Yin, A., Harrison, T.M. (Eds.), *The Tectonic Evolution of Asia*. Cambridge University Press, pp. 486–640.
124. Sengör, A.M.C., Natal'in, B.A., 1996b. Turkic-type orogeny and its role in the making of the continental crust. *Annual Review of Earth and Planetary Sciences* 24, 263–337.
125. Shu, L. S., Zhou, G. Q., Shi, Y. S., and Yin, J., 1994. Study of the high-pressure metamorphic blueschist and its late Proterozoic age in the eastern Jiangnan belt. *Chin. Sci. Bull.*, 39(14), 1200-1204.
126. Shu, L. S. and Charvet, J. 1996. Kinematics and geochronology of the Proterozoic Dongxiang-Shexian ductile shear zone: with HP metamorphism and ophiolitic melange (Jiangnan region, South China). *Tectonophysics*, 267: 291-302.
127. Shu, L. S., Zhou, X. M., Deng, P., Wang, B., Jiang, S. Y., Yu, J. H., and Zhao, X. X., 2009. Mesozoic tectonic evolution of the Southeast China Block: New insights from basin analysis. *J. Asian Earth Sci.*, 34(3), 376-391.
128. Sibuet, J.-C., Srivastava, S. P., Spakman, W., 2004. Pyrenean orogeny and plate kinematics. *J. Geophys. Res.* 109, B08104.
129. Sláma, J., Košler, J., Condon, D. J., Crowley, J. L., Gerdes, A., Hanchar, J. M., Horstwood M. S.A., Morris G. A., Nasdala L., Norberg N., Schaltegger U., Schoene B., Tubrett M. N., and Whitehouse M. J., 2008. Plešovice zircon - A new natural reference material for U-Pb and Hf isotopic microanalysis. *Chemical Geology* 249, 1-35.
130. Stacey, J.S., Kramers, J.D., 1975. Approximation of terrestrial lead isotope evolution by a two-stage model. *Earth Planetary Science Letters* 26, 207-221.
131. Stipp, M., Stuitz, H., Heilbronner, R., Schmid, S. M., 2002. The eastern Tonale fault zone: a 'natural laboratory' for crystal plastic deformation of quartz over a temperature range from 250 to 700 °C. *Journal of Structural Geology* 24, 1861-1884.
132. Sun Y., Ma C. Q., Liu Y. Y., She Z. B. Geochronological and geochemical constraints on the petrogenesis of late Triassic aluminous A-type granites in southeast China. *Journal of Asian Earth Sciences*, in press.
133. Sutton, J. and Watson, J. V. 1986. Architecture of the continental lithosphere. *Philosophical Transactions of the Royal Society, London*, A317, 5-12.
134. Suzuki, K., Adachi, M., 1991. Precambrian provenance and Silurian metamorphism of the Tsubonosawa paragneiss in the south Kitakami terrane, northeast Japan, revealed by the chemical th-u-total pb isochron ages of monazite, zircon and xenotime. *Geochemical Journal* 25, 357-376.

135. Suzuki, K., Adachi, M., Kajizuka, I., 1994. Electron microprobe observations of Pb diffusion in metamorphosed detrital monazites. *Earth and Planetary Science Letters* 128, 391-405.
136. Suzuki, K., Kato, T., 2008. CHIME dating of monazite, xenotime, zircon and polycrase: protocol, pitfalls and chemical criterion of possibly discordant age data. *Gondwana Research* 14, 569–586.
137. Tapponnier, P., and Molnar, P., 1979. Active faulting and Cenozoic tectonics of the Tianshan, Mongolia, and Baykal regions. *J. Geophys. Res.*, 84(B7), 3425-3459.
138. Teixell, A., 1998. Crustal structure and orogenic material budget in the west central Pyrenees. *Tectonics*, 17, 395-406.
139. Teixell, A., Arboleya, M. L., Julivert, M., Charroud, M., 2003. Tectonic shortening and topography in the central High Atlas. *Tectonics*, 22, doi: 10.1029/2002TC00146.
140. Tullis, J. A. N., Christie, J. M., Griggs, D. T., 1973. Microstructures and Preferred Orientations of Experimentally Deformed Quartzites. *Geological Society of America Bulletin* 84, 297-314.
141. Vavra G, Gebauer, D., and Schmid, R., 1996. Multiple zircon growth and recrystallization during polyphase Late Carboniferous to Triassic metamorphism in granulites of the Ivrea Zone (Southern Alps) : An ion microprobe (SHRIMP) study. *Contrib Mineral Petrol*, 122: 337 - 358.
142. Wallis, S., Tsujimori, T., Aoya, M., Kawakami, T., Terada, K., Suzuki, K., and Hyodo, H., 2003. Cenozoic and Mesozoic metamorphism in the Longmenshan orogens: implications for geodynamic models of eastern Tibet. *Geology*, 31, 745-748.
143. Wan, Y.S., Liu, D.Y., Xu, M., Zhuang, J., Song, B. Shi, Y., Du, Y.L., 2007. SHRIMP U-Pb zircon geochronology and geochemistry of metavolcanic and metasedimentary rocks in Northwestern Fujian, Cathaysia block, China: Tectonic implications and the need to redefine lithostratigraphic units *Gondwana Research* 12(1-2), 166-183.
144. Wan, Y. S., Liu, D. Y., Wilde, S. A., Cao, J. J., Chen, B., Dong, C. Y., Song, B., and Du, L. L., 2010. Evolution of the Yunkai Terrane, south China: Evidence from SHRIMP zircon U-Pb dating, geochemistry and Nd isotope. *Journal of Asian Earth Sciences*, 37(2): 140-153.
145. Wang, D.Z., Chen, K.R., Zhou, J.C., 1990. Subvolcanic granitoids in southeastern China and their metallogenesis. *Sci. China (B)* 33 (4), 467–476.
146. Wang, J., and Li, Z. X., 2003. History of Neoproterozoic rift basins in South China: implications for Rodinia break-up. *Precambrian Res.*, 122(1-4), 141-158,.
147. Wang, X.F., Metcalfe, I., Jian, P., He, L.Q., Wang, C.S., 2000. The Jinshajiang–Ailaoshan Suture Zone, China: tectonostratigraphy, age and evolution. *Journal of Asian Earth Sciences* 18, 675–690.
148. Wang, X. L., Zhou, J. C., Qiu, J. S. and Gao, J. F., 2004. Geochemistry of the Meso- to Neoproterozoic basic-acid rocks from Hunan Province, South China: implications for the evolution of the western Jiangnan orogen. *Precambrian Research* 135(1-2), 79-103.

149. Wang, X. L., Zhou, J. C., Qiu, J. S., Zhang, W. L., Liu, X. M. and Zhang, G. L., 2006. LA-ICP-MS U-Pb zircon geochronology of the Neoproterozoic igneous rocks from Northern Guangxi, South China: Implications for tectonic evolution. *Precambrian Research* 145(1-2), 111-130.
150. Wang, X. L., Zhou, J. C., Griffin, W. L., Wang, R. C., Qiu, H. S., O'Reilly, S. Y., Xu, X. S., Liu, X. M. and Zhang, G. L., 2007. Detrital zircon geochronology of Precambrian basement sequences in the Jiangnan orogen: Dating the assembly of the Yangtze and Cathaysia Blocks. *Precambrian Research* 159(1-2), 117-131.
151. Wang, X. L., Zhao, G. C., Zhou, J. C., Liu, Y. S. and Hu, J., 2008. Geochronology and Hf isotopes of zircon from volcanic rocks of the Shuangqiaoshan Group, South China: Implications for the Neoproterozoic tectonic evolution of the eastern Jiangnan orogen. *Gondwana Research* 14(3), 355-367.
152. Wang, Y. J., Fan, W. M., Guo, F., Peng, T. P., Li, C. W., 2003. Geochemistry of Mesozoic mafic rocks adjacent to the Chenzhou-Linwu fault, South China: Implications for the lithospheric boundary between the Yangtze and Cathaysia blocks. *International Geology Review* 45, 263-286.
153. Wang, Y. J., Zhang, Y. H., Fan, W. M., and Peng, T. P., 2005. Structural signatures and Ar-40/Ar-39 geochronology of the Indosinian Xuefengshan tectonic belt, South China Block, *J. Struct. Geol.*, 27(6), 985-998.
154. Wang, Y. J., Fan, W. M., Sun, M., Liang, X. Q., Zhang, Y. H., and Peng, T. P., 2007a. Geochronological, geochemical and geothermal constraints on petrogenesis of the Indosinian peraluminous granites in the South China Block: A case study in the Hunan Province. *Lithos*, 96(3-4), 475-502.
155. Wang, Y. J., Fan, W. M., Zhao, G. C., Ji, S. C., and Peng, T. P., 2007b. Zircon U-Pb geochronology of gneissic rocks in the Yunkai massif and its implications on the Caledonian event in the South China Block. *Gondwana Res.*, 12(4), 404-416,.
156. Wang, Y. J., Fan, W. M., Cawood, P. A., Ji, S. C., Peng, T. P., and Chen, X. Y., 2007c. Indosinian high-strain deformation for the Yunkaidashan tectonic belt, south China: Kinematics and $^{40}\text{Ar}/^{39}\text{Ar}$ geochronological constraints. *Tectonics*, 26, TC6008, doi:10.1029/2007TC002099.
157. Wang, Y., Zhang, F., Fan, W., Zhang, G., Chen, S., Cawood, P. A., Zhang, A., 2010. Tectonic setting of the South China Block in the early Paleozoic: Resolving intracontinental and ocean closure models from detrital zircon U-Pb geochronology. *Tectonics* 29, TC6020.
158. Wang, Z. H., Lu, H. F., 2000. Ductile deformation and Ar-40/Ar-39 dating of the Changle-Nanao ductile shear zone, southeastern China. *Journal of Structural Geology* 22, 561-570.
159. Webb, L. E., Hacker, B. R., Ratschbacher, L., McWilliams, M. O., Dong, S., 1999. Thermochronologic constraints on deformation and cooling history of high- and ultrahigh-pressure rocks in the Qinling-Dabie orogen, eastern China. *Tectonics* 18.

160. Weislogel, A. L., Graham, S. A., Chang, E. Z., Wooden, J. L., Gehrels, G. E., Yang, H., 2006. Detrital zircon provenance of the Late Triassic Songpan-Ganzi complex: Sedimentary record of collision of the North and South China blocks. *Geology* 34, 97-100.
161. Weislogel, A. L., Graham, S. A., Chang, E. Z., Wooden, J. L., Gehrels, G. E., 2010. Detrital zircon provenance from three turbidite depocenters of the Middle-Upper Triassic Songpan-Ganzi complex, central China: Record of collisional tectonics, erosional exhumation, and sediment production. *Geological Society of America Bulletin* 122, 2041-2062.
162. Willett S.D., Beaumont, C., and Fullsack, P., 1993. Mechanical model for the tectonics of doubly vergent compressional orogens, *Geology*, 21, 371-374,.
163. Wilson, J.T., 1966. Did the Atlantic close and then re-open? *Nature* 211, 676–681.
164. Windley, B.F., 1992. Proterozoic collisional and accretionary orogens. In: Condie, K.C. (Ed.), *Proterozoic Crustal Evolution: Developments in Precambrian Geology*. Elsevier, Amsterdam, pp. 419–446.
165. Windley, B.F., 1993. Uniformitarianism today: plate tectonics is the key to the past. *Journal of the Geological Society (London)* 150, 7–19.
166. Woodhead, J. D., Hergt, J. M., 2005. A preliminary appraisal of seven natural zircon reference materials for in situ Hf isotope determination. *Geostandards and Geoanalytical Research* 29, 183-195.
167. Wu, F.Y., Yang, Y.H., Xie, L.W., Yang, J.H., Xu, P., 2006. Hf isotopic compositions of the standard zircons and baddeleyites used in U–Pb geochronology. *Chemical Geology* 234, 105–126.
168. Xiao, W. J., He, H. Q., 2005. Early Mesozoic thrust tectonics of the northwest Zhejiang region (Southeast China). *Geological Society of America Bulletin* 117, 945-961.
169. Xiao, W., Han, C., Yuan, C., Sun, M., Lin, S., Chen, H., Li, Z., Li, J., Sun, S., 2008. Middle Cambrian to Permian subduction-related accretionary orogenesis of Northern Xinjiang, NW China: Implications for the tectonic evolution of central Asia. *Journal of Asian Earth Sciences* 32, 102-117.
170. Xu, J. W., Zhu, G., Tong, W. X., Cui, K. R., and Liu, Q., 1987. Formation and evolution of the Tancheng-Lujiang wrench fault system: a major shear system to the northwest of the Pacific Ocean. *Tectonophysics*, 134(4), 273-310.
171. Xu, X. B., Zhang, Y. Q., Shu, L. S., Jia, D., 2011. La-ICP-MS U-Pb and $^{40}\text{Ar}/^{39}\text{Ar}$ geochronology of the sheared metamorphic rocks in the Wuyishan: Constraints on the timing of Early Paleozoic and Early Mesozoic tectono-thermal events in SE China. *Tectonophysics* 501, 71-86.
172. Xu, X. S., O'Reilly, S. Y., Griffin, W. L., Deng, P., Pearson, N. J., 2005. Relict proterozoic basement in the Nanling Mountains (SE China) and its tectonothermal overprinting. *Tectonics* 24, doi:10.1029/2004TC001652.

173. Yan, D. P., Zhou, M. F., Song, H. L., Wang, X. W., and Malpas, J., 2003. Origin and tectonic significance of a Mesozoic multi-layer over-thrust system within the Yangtze Block (South China). *Tectonophysics*, 361(3-4), 239-254.
174. Yan, D. P., Zhou, M. F., Wang, C. Y., Xia, B., 2006. Structural and geochronological constraints on the tectonic evolution of the Dulong-Song Chay tectonic dome in Yunnan Province, SW China. *Journal of Asian Earth Sciences* 28, 332-353.
175. Yan, D.-P., Zhang, B., Zhou, M.-F., Wei, G., Song, H.-L., Liu, S.-F., 2009. Constraints on the depth, geometry and kinematics of blind detachment faults provided by fault-propagation folds: An example from the Mesozoic fold belt of South China. *Journal of Structural Geology* 31, 150-162.
176. Yang, D. S., Li, X. H., Li, W. X., Liang, X. Q., Long, W. G., Xiong, X. L., 2010. U-Pb and ^{40}Ar - ^{39}Ar geochronology of the Baiyunshan gneiss (central Guangdong, south China): constraints on the timing of early Palaeozoic and Mesozoic tectonothermal events in the Wuyun (Wuyi-Yunkai) Orogen. *Geological Magazine* 147, 481-496.
177. Ye, K., Cong, B. L., and Ye, D. I., 2000a. The possible subduction of continental material to depths greater than 200 km. *Nature* 407(6805), 734-736.
178. Ye, K., Yao, Y. P., Katayama, I., Cong, B. L., Wang, Q. C., and Maruyama, S., 2000b. Large areal extent of ultrahigh-pressure metamorphism in the Sulu ultrahigh-pressure terrane of East China: new implications from coesite and omphacite inclusions in zircon of granitic gneiss. *Lithos* 52(1-4), 157-164.
179. Yin, A., Harrison, T. M., 2000. Geologic evolution of the Himalayan-Tibetan orogen. *Annual Review of Earth and Planetary Sciences* 28, 211-280.
180. Yin, A., Dubey, C. S., Kelty, T. K., Webb, A. A. G., Harrison, T. M., Chou, C. Y., Celerier, J., 2010. Geologic correlation of the Himalayan orogen and Indian craton: Part 2. Structural geology, geochronology, and tectonic evolution of the Eastern Himalaya. *Geological Society of America Bulletin* 122, 360-395.
181. Yu, J. H., O'Reilly, S. Y., Wang, L., Griffin, W. L., Zhang, M., Wang, R., Jiang, S., and Shu, L., 2008. Where was south China in the Rodinia supercontinent?: Evidence from U-Pb geochronology and Hf isotopes of detrital zircons. *Precambrian Research*, 164(1-2): 1-15.
182. Yu, J. H., O'Reilly, S. Y., Wang, L., Griffin, W. L., Zhou, M.-F., Zhang, M., Shu, L., 2010. Components and episodic growth of Precambrian crust in the Cathaysia Block, South China: Evidence from U-Pb ages and Hf isotopes of zircons in Neoproterozoic sediments. *Precambrian Research* 181, 97-114.
183. Zhang, F., Wang, Y., Chen, X., Fan, W., Zhang, Y., Zhang, G., Zhang, A., 2011. Triassic high-strain shear zones in Hainan Island (South China) and their implications on the amalgamation of the Indochina and South China Blocks: Kinematic and $^{40}\text{Ar}/^{39}\text{Ar}$ geochronological constraints. *Gondwana Research* 19, 910-925.
184. Zhang, S. B., Zheng, Y. F., Wu, Y. B., Zhao, Z. F., Gao, S., and Wu, F. Y., 2006a. Zircon U-Pb age and Hf isotope evidence for 3.8Ga crustal remnant and episodic reworking of Archean

- crust in South China. *Earth and Planetary Science Letters* 252(1-2), 56-71.
185. Zhang, S. B., Zheng, Y. F., Wu, Y. B., Zhao, Z. F., Gao, S., and Wu, F. Y., 2006b. Zircon isotope evidence for ≥ 3.5 Ga continental crust in the Yangtze craton of China. *Precambrian Research* 146(1-2), 16-34.
186. Zhao, G. C., Cawood, P. A., 1999. Tectonothermal evolution of the Mayuan assemblage in the Cathaysia Block: Implications for neoproterozoic collision-related assembly of the South China craton. *American Journal of Science* 299, 309-339.
187. Zheng, J. P., Griffin, W. L., Li, L. S., O'Reilly, S. Y., Pearson, N. J., Tang, H. Y., Liu, G. L., Zhao, J. H., Yu, C. M., Su, Y. P., 2010. Highly evolved Archean basement beneath the western Cathaysia Block, South China. *Geochimica et Cosmochimica Acta* 75, 242-255.
188. Zheng, Y.-F., Zhao, Z.-F., Wu, Y.-B., Zhang, S.-B., Liu, X., Wu, F.-Y., 2006. Zircon U-Pb age, Hf and O isotope constraints on protolith origin of ultrahigh-pressure eclogite and gneiss in the Dabie orogen. *Chemical Geology* 231, 135-158.
189. Zheng, Y. F., Zhang, S. B., Zhao, Z. F., Wu, Y. B., Li, X. H., Li, Z. X., Wu, F. Y., 2007. Contrasting zircon Hf and O isotopes in the two episodes of Neoproterozoic granitoids in South China: Implications for growth and reworking of continental crust. *Lithos* 96, 127-150.
190. Zhou, M. F., Yan, D. P., Kennedy, A. K., Li, Y. Q., and Ding, J., 2002. SHRIMP U-Pb zircon geochronological and geochemical evidence for Neoproterozoic arc-magmatism along the western margin of the Yangtze Block, South China. *Earth and Planetary Science Letters* 196(1-2), 51-67.
191. Zhou, M. F., Ma, Y. X., Yan, D. P., Xia, X. P., Zhao, J. H., and Sun, M., 2006. The Yanbian terrane (Southern Sichuan Province, SW China): A neoproterozoic arc assemblage in the western margin of the Yangtze block. *Precambrian Research* 144(1-2), 19-38.
192. Zhou, X. M., and Li, W. X., 2000. Origin of Late Mesozoic igneous rocks in Southeastern China: implications for lithosphere subduction and underplating of mafic magmas, *Tectonophysics*, 326(3-4), 269-287.
193. Zhou, X. M., Sun, T., Shen, W. Z., Shu, L. S., and Niu, Y. L., 2006. Petrogenesis of Mesozoic granitoids and volcanic rocks in South China: A response to tectonic evolution. *Episodes*, 29(1), 26-33.
194. Zhu, G., Wang, Y., Liu, G., Niu, M., Xie, C., Li, C., 2005. $^{40}\text{Ar}/^{39}\text{Ar}$ dating of strike-slip motion on the Tan-Lu fault zone, East China. *Journal of Structural Geology* 27, 1379-1398.
195. Zhu, G., Xie, C.-L., Chen, W., Xiang, B.-W., Hu, Z.-Q., 2010. Evolution of the Hongzhen metamorphic core complex: Evidence for Early Cretaceous extension in the eastern Yangtze craton, eastern China. *Geological Society of America Bulletin* 122, 506-516.
196. Zhu, X. K., O'Nions, R. K., Belshaw, N. S., Gibb, A. J., 1997. Significance of in situ SIMS chronometry of zoned monazite from the Lewisian granulites, northwest Scotland. *Chemical Geology* 135, 35-53.
197. Zhu, X. K., O'Nions, R. K., 1999. Zonation of monazite in metamorphic rocks and its

- implications for high temperature thermochronology: a case study from the Lewisian terrain. *Earth and Planetary Science Letters* 171, 209-220.
198. 福建省地质矿产局. 1985. 福建省区域地质志. 北京: 地质出版社. 1-671.
199. 广东省地质矿产局. 1988. 广东省区域地质志. 北京: 地质出版社. 1-941.
200. 广西壮族自治区地质矿产局. 1985. 广西壮族自治区区域地质志. 北京: 地质出版社, 1-853.
201. 湖南省地质矿产局. 1988. 湖南省区域地质志. 北京: 地质出版社. 1-507.
202. 江西省地质矿产局. 1984. 江西省区域地质志. 北京: 地质出版社. 1-921.
203. 柏道远, 周亮, 马铁球, 王先辉. 2007. 湘东南印支期花岗岩成因及构造背景. *岩石矿物学杂志*, 197-212.
204. 柏道远, 邹宾微, 赵龙辉, 李泽泓, 王先辉, 马铁球, 肖冬贵, 彭云益. 2009. 湘东太湖逆冲推覆构造基本特征研究. *中国地质*, 36(1): 54-64.
205. 陈海泓, 孙枢, 李继亮, 王清晨, 彭海波, 许靖华. 1992. 前陆盆地的构造制约——以湘西中生代沅麻盆地为例. 见: 李继亮主编: 中国东南海陆岩石圈结构与演化研究. 北京: 中国科学技术出版社. 17-31.
206. 陈海泓, 孙枢, 李继亮, 王清晨, 彭海波, 徐树桐, 许靖华. 1993. 雪峰山大地构造的基本特征初探. *地质科学*, 28(3): 201-210.
207. 陈科, 林伟, 王清晨. 2008. 扬子地块东南缘多期构造变形及其油气意义. *地质学报* 82, 308-316.
208. 陈卫锋, 陈培荣, 周新民, 黄宏业, 丁兴, 孙涛. 2006. 湖南阳明山岩体的 La-ICP-MS 锆石 U-Pb 定年及成因研究. *地质学报*, 80(7): 1065-1077.
209. 陈卫锋, 陈培荣, 黄宏业, 丁兴, 孙涛. 2007. 湖南白马山岩体花岗岩及其包体的年代学和地球化学研究. *中国科学(D 辑)*, 37(7): 873-893.
210. 褚杨, 陈科, 林伟, 严德天, 王清晨. 2009. 从多系统年代学透视云开地块古生代-中生代的构造演化. *地质科学* 44, 922-930.
211. 崔盛芹, 李锦蓉. 1983. 试论中国滨太平洋带的印支运动. *地质学报*, 57(1): 51-62.
212. 邓希光, 陈志刚, 李献华, 刘敦一. 2004. 桂东南地区大容山、十万大山花岗岩带 SHRIMP 锆石 U-Pb 定年. *地质论评* 50, 426-432.
213. 丁道桂, 郭彤楼, 胡明霞, 刘云黎. 2007. 论江南—雪峰基底拆离式构造. *石油实验地质*. 29(2): 120-128.
214. 丁兴, 陈培荣, 陈卫锋, 黄宏业, 周新民. 2005. 湖南沅山花岗岩中锆石 LA-ICPMS U-Pb 定年: 成岩启示和意义. *中国科学(D 辑)*, 35(7): 606-616.
215. 范小林, 陆国新, 蒋洪堪, 江兴歌. 1993. 雪峰北区深部地质构造及油气勘探远景. *江汉石油学院学报* 15, 9-15.
216. 范小林, 江兴歌, 蒋洪堪, 陆国新. 1994. 雪峰区(江口-洞口)深部地质构造初探. *石油*

- 实验地质 16, 128-135.
217. 高山, 张本仁. 1990. 扬子地台北部太古宙 TTG 片麻岩的发现及其意义. 地球科学: 中国地质大学学报 15, 675-679.
218. 郭令智, 施央申, 马瑞士. 1980. 华南大地构造格架和地壳演化. 国际交流地质学术论文集(1), 北京:地质出版社, 109-116.
219. 郭令智, 施央申, 马瑞士, 等. 1984. 中国东南部地体构造的研究. 南京大学学报(自然科学), 20 (4): 732-739.
220. 胡雄健等, 1991. 前寒武纪地质 (第 5 号): 浙西南前寒武纪地质. 北京: 地质出版社. 1-277.
221. 胡雄健. 1994. 浙西南下元古界八都群的地质年代学. 地球化学, 23(增刊): 18—24.
222. 胡召齐, 朱光, 张必龙, 张力. 2010. 雪峰隆起北部加里东事件的 K-Ar 年代学研究. 地质论评. 56(4): 490-500.
223. 侯光久, 索书田, 郑贵州, 魏启荣. 1998. 雪峰山加里东运动及其体制转换. 湖南地质. 17(3): 141-144.
224. 黄汲清. 1945. 中国主要地质构造单位. 中央地质调查所地质专报, 甲种第 20 号.
225. 李华芹, 王登红, 陈富文, 梅玉萍, 蔡红. 2008. 湖南雪峰山地区铲子坪和大坪金矿成矿作用年代学研究. 地质学报, 82(7): 900-905.
226. 李继亮, 郝杰, 柴育成, 杨美芳, 何海清. 1993. 赣南混杂带与增生弧联合体: 图尔基型碰撞造山带的缝合带. 见: 李继亮主编: 东南大陆岩石圈结构与地质演化. 北京: 冶金工业出版社. 2-11.
227. 李献华, 周国庆, 赵建新. 1994. 赣东北蛇绿岩的离子探针锆石 U-Pb 年龄及其构造意义. 地球化学, 23 (2): 125 131.
228. 刘宝珺主编. 1994. 华南岩相古地理图集. 北京: 科学出版社. 1-188.
229. 林伟, Faure M., Lepvrier C., 陈泽超, 褚杨, 王清晨, Van N., Vu T. 2011. 华南板块南缘早中生代的逆冲推覆构造及其相关的动力学背景. 地质科学, 46(01): 134-145.
230. 罗志高, 王岳军, 张菲菲, 张爱梅, 张玉芝. 2010. 金滩和白马山印支期花岗岩体 LA-ICP-MS 锆石 U-Pb 定年及其成岩启示. 大地构造与成矿学, 34(2): 282-290.
231. 马力, 陈焕疆, 甘克文. 2004. 中国南方大地构造和海相油气地质. 北京: 地质出版社.
232. 马文璞, 李学军, 刘和甫, 李永林. 1993. 雪峰隆起的构造性质及其对上扬子东南缘古生代盆地的改造. 见: 江南—雪峰地区的层滑作用及多期复合构造. 北京: 地质出版社. 120-147.
233. 梅廉夫, 刘昭茜, 汤济广, 沈传波, 凡元芳. 2010. 湘鄂西—川东中生代陆内递进扩展变形: 来自裂变径迹和平衡剖面的证据. 地球科学: 中国地质大学学报 35, 161-174.
234. 秦葆瑚. 1991. 台湾-四川黑水地学大断面所揭示的湖南深部构造. 湖南地质, 10(2): 89-96.

235. 丘元禧, 马文璞, 范小林, 张渝昌, 邓家瑞, 夏亮辉, 张旭亮. 1996. 雪峰古陆加里东起的构造性质和构造演化. 中国区域地质, 2: 150-160.
236. 丘元禧, 张渝昌, 马文璞. 1998. 雪峰山陆内造山带的构造特征与演化. 高校地质学报, 4(4): 432-443.
237. 丘元禧, 张渝昌, 马文璞. 1999. 雪峰山的构造性质与演化. 地质出版社. 1-155.
238. 舒良树, 施央申, 郭令智. 1995. 江南中段板块地体构造与碰撞造山运动学. 南京: 南京大学出版社, 1-174.
239. 舒良树, 卢华复, Charvet, J., Faure, M., 1997. 武夷山北缘断裂带运动学研究. 高校地质学报 3, 282-292.
240. 舒良树, 卢华复, 贾东, Charvet, J., Faure, M., 1999. 华南武夷山早古生代构造事件的 $40\text{Ar}/39\text{Ar}$ 同位素年龄研究. 南京大学学报(自然科学), 35(6): 668-674.
241. 舒良树, 周新民, 邓平, 余心起, 王彬, 祖辅平. 2004. 中国东南部中-新生代盆地特征与构造演化. 地质通报 23, 876-884.
242. 舒良树. 2006. 华南前泥盆纪构造演化: 从华夏地块到加里东造山带. 高校地质学报 12, 418-431.
243. 水涛. 1987. 中国东南大陆基底构造格局. 中国科学(B 辑), (4): 78-86.
244. 水涛等. 1988. 中国浙闽变质基底地质. 北京: 科学出版社. 1-88.
245. 孙涛, 王志成, 陈培荣, 周新民. 2007. 苗儿山—越城岭岩体. 见: 周新民. 南岭地区晚中生代花岗岩成因与岩石圈动力学演化. 北京: 科学出版社. 1-691.
246. 王清晨, 蔡立国. 2007. 中国南方显生宙大地构造演化简史. 地质学报 81, 1025-1040.
247. 王岳军, 范蔚茗, 梁新权, 彭头平, 石玉若. 2005. 湖南印支期花岗岩 SHRIMP 锆石 U-Pb 年龄及其成因启示. 科学通报, 1259-1266.
248. 吴福元, 李献华, 郑永飞, 高山. 2007. Lu-Hf 同位素体系及其岩石学应用. 岩石学报 23, 185-220.
249. 吴元保, 陈道公, 程昊, Etienne, D., 夏群科. 2001. 碧溪岭岩体中石榴橄榄岩的锆石显微结构及离子探针定年. 高校地质学报, 7 (3): 356 - 362.
250. 徐备, 乔广生. 1989. 赣东北晚元古代蛇绿岩的 Sm-Nd 同位素年龄及原始构造环境. 南京大学学报(地球科学), (3): 108 114.
251. 徐树桐, 刘贻灿, 江来利, 2002. 大别山造山带的构造几何学和运动学. 合肥, 中国科学技术大学出版社, 1—133.
252. 许志琴. 1984. 地壳变形与显微构造. 北京: 地质出版社. 1-133.
253. 杨奎峰, 杨坤光, 马昌前. 2004. 雪峰山安化—溆浦断裂带变形特征及 ESR 定年. 大地构造与成矿. 28(3): 263-269.
254. 于津海, 王丽娟, 周新民, 蒋少涌, 王汝成, 徐夕生, 邱检生;. 2006a. 粤东北基底变质岩的组成和形成时代. 地球科学-中国地质大学学报 31, 38-48.

255. 于津海, 魏震洋, 王丽娟, 舒良树, 孙涛. 2006b. 华夏地块: 一个由古老物质组成的年轻陆块. 高校地质学报 12, 440-447.
256. 于津海, 王丽娟, 魏震洋, 涛, 孙., 舒良树. 2007. 华夏地块显生宙的变质作用期次和特征. 高校地质学报 13, 474-483.
257. 于津海, Y.S.O'Reilly, 王丽娟, W.L.Griffin, 蒋少涌, 王汝成, 徐夕生. 2007. 华夏地块古老物质的发现和前寒武纪地壳的形成. 科学通报 52, 11-18.
258. 袁学诚主编. 1997. 阿尔泰-台湾地学断面论文集. 武汉: 中国地质大学出版社. 1-216.
259. 张爱梅, 王岳军, 范蔚茗, 张菲菲, 张玉芝. 2010. 闽西南清流地区加里东期花岗岩锆石 U-Pb 年代学及 Hf 同位素组成研究. 大地构造与成矿. 34(3): 408-418.
260. 张菲菲, 王岳军, 范蔚茗, 张爱梅, 张玉芝. 2010. 湘东-赣西地区早古生代晚期花岗岩体的 LA-ICPMS 锆石 U-Pb 定年研究. 地球化学. 39(5): 414-426.
261. 张国伟, 张本仁, 袁学诚, 肖庆辉. 2001. 秦岭造山带与大陆动力学. 北京: 科学出版社. 1-855.
262. 张进, 马宗晋, 杨健, 陈必河, 雷永亮, 王宗秀, 李涛. 2010. 雪峰山西麓中生代盆地属性及构造意义. 地质学报, 84(5): 631-650.
263. 张岳桥, 徐先兵, 贾东, 舒良树. 2009. 华南早中生代从印支期碰撞构造体系向燕山期俯冲构造体系转换的形变记录. 地学前缘, 16(1): 234-247.
264. 钟大赉等著. 1998. 滇川西部古特提斯造山带. 北京: 科学出版社. 1-231.
265. 周新民, 邹海波, 杨杰东. 1989. 安徽歙县伏川蛇绿岩套的 Sm-Nd 等时线年龄及其地质意义. 科学通报, 34(16): 1243-1245.
266. 周新民主编. 2007. 南岭地区晚中生代花岗岩成因与岩石圈动力学. 北京: 科学出版社. 1-691.
267. 朱宝贵等. 1988. 湘西北古丈背斜的地质构造特征及其区域构造意义. 中国区域地质.
268. 朱夏. 1980. 试论中国中生代油气盆地的地球动力学背景. 见: 朱夏, 论中国油气盆地构造. 北京: 石油工业出版社. 61-70.

发表文章目录

已发表或在审文章:

1. 褚杨, 林伟, Faure M., 王清晨. 2011. 雪峰山早中生代构造演化: 构造学和年代学分析. 地质科学, 46(01): 146-160.
2. 褚杨, 陈科, 林伟, 严德天, 王清晨. 2009. P 从多系统年代学透视云开地块古生代-中生代的构造演化. 地质科学, 44(3), 922-930.
3. 林伟, Faure M., Lepvrier C., 陈泽超, 褚杨, 王清晨, Van N., Vu T. 2011. 华南板块南缘早中生代的逆冲推覆构造及其相关的动力学背景. 地质科学, 46(01): 134-145.
4. 冀文斌, 林伟, 石永红, 王清晨, 褚杨. 2011. 大别山早白垩世变质核杂岩的结构与演化. 地质科学, 46(01): 161-180.
5. 王军, 褚杨, 林伟, 王清晨. 2010. 黄陵背斜的构造几何形态及其成因探讨. 地质科学, 45(03): 615-625.
6. Yan, D., Chen, D., Wang, Q., Wang, J. and **Chu, Y.** 2008. Environmental Redox Changes of the Ancient Sea in the Yangtze Area during the Ordo-Silurian Transition. *Acta Geologica Sinica – English Edition*, 82(3), 679-689.
7. **Chu Y.**, Faure M., Lin W. and Wang Q. Tectonic evolution of the Early Mesozoic (Indosinian) intracontinental Xuefengshan Belt, South China. Under review.
8. **Chu Y.**, Faure M., Lin W., Wang Q., Ji W. Structural analysis and chronological constraints on the decollement layer in an intracontinental orogen: Example of the Early Mesozoic Xuefengshan Belt, South China. Under review.
9. **Chu Y.**, Lin W., Faure M., Wang Q., Ji W. Phanerozoic tectonothermal events of the Xuefengshan Belt, central South China: implications from U-Pb age and Lu-Hf determinations of granites. Under review.

会议摘要

1. **Chu Y.**, Faure M., Lin W., Wang Q. 2010. Mesozoic Intracontinental Tectonic Evolution of the Xuefengshan Belt, South China. International Symposium on

- Gondwana to Asia, Qingdao, China. **Oral presentation.**
2. **Chu Y.**, Faure M., Lin W., Wang Q. 2011. Early Mesozoic intracontinental Xuefengshan Belt, South China: insights from structural analysis of polyphase deformation (Oral presentation). EGU meeting, Vienna, Austria. **Oral presentation.**
 3. Faure M., Lepvrier C., Lin W., Vuong N., Tich V., **Chu Y.** 2010. Triassic tectonics in the Southwestern margin of the South China Block and the welding of the South China-Indochina Blocks. International Symposium on Gondwana to Asia, Qingdao, China.
 4. Lin W., Faure M., Lepvrier C., Wang Q., Chen Z., **Chu Y.**, Van N., Vu V. 2010. The Early Mesozoic thrust and fold sheet structure along the southern margin of Yangtze block and its geodynamic significance. International Symposium on Gondwana to Asia, Qingdao, China.

致谢

时光荏苒，岁月如梭。5年的时光转瞬即逝，我的博士生生涯即将告一段落，而面对即将的工作生涯，这只不过是一个新的开始。

在导师钟大赉院士、林伟研究员和法国 Michel Faure 教授的悉心指导下，我的博士论文终于完成。这首先感谢林老师五年来对我的辛勤培养。导师严谨的治学风范，一丝不苟的工作态度、真诚热情的为人处事态度是我终生学习的榜样。五年来，林老师对我在学习上耐心的指导、学业上精心周密的安排，生活上无微不至的关怀与帮助，在野外工作中孜孜不倦的讲解，我都将铭记于心。而且没有林老师的支持，我就无法前去法国奥尔良大学，成为中法联合培养博士生，因此我在学业上的任何进步，无不倾注了林老师的心血和汗水！

感谢 Michel Faure 教授对我博士论文的指导，他渊博的知识、深厚的学术积淀、以及真诚的性格让我受益匪浅，在论文的写作上给了我耐心的指导，我所完成的论文，他都细心审阅并提出大量开拓性的建议，给了极大的帮助和提高。感谢钟大赉院士对我论文的指导，并对论文的选题方向和思路提出了建设性的意见。

五年的硕博连读，要感谢王清晨研究员，在野外，他对我细心讲解各种地质现象，在室内，又对我的论文提出各种想法和指导意见，良师般的教诲和长辈般的关怀让我获益匪浅。在法国联合培养的一年期间，陈岩教授在学习上给予了大量的启发，他一丝不苟的工作态度和专注用心的研究精神让我；生活上提供了许多帮助，并且让我在体育方面加强了锻炼，顺利的度过了法国的学习生活。通过这一段的学习和生活，让我对人生有了新的感悟。

感谢本所教育处苏宏老师和李铁胜老师在我五年的学习生活中提供的良好学习条件和环境，以及日常事务方面的热情帮助。同时还感谢课题组纪徐老师和合肥工大石永红老师在我学习期间的帮助。

感谢课题组司机李金雁师傅，带着我这五年来走南闯北经历了十多次野外，他的兢兢业业、不辞劳苦都让我深深感动，没有他的帮助我也无法如此顺利而有效率的完成我博士的全部野外工作。

攻读博士期间，严德天、韩登林、许承武、陈科、韩银学、刘嘉庆、邱振、王军、冀文斌、阳效法、陈泽超、姜琳、陶辉飞、卫巍等师兄弟的关心和帮助也

是我能够顺利完成论文的原因之一。感谢王伟同学和我在地球化学方面的讨论，虽然在不同的单位，但是我们学术交流仍然一如既往；感谢苏哲、冶小平、李陞以及无法在这里一一列出的同学，大家在学术上互相探讨、互相激励；在生活上互相关心、互相帮助，让我感到能在地质所学习和生活是一种莫大的幸运。也要感谢唐国强、刘宇、杨赛红在离子探针和锆石阴极发光实验中给予我的帮助。

在法国留学期间，感谢奥尔良大学 J. Charvet 教授、N. Lebreton、O. Rouer、I. Di Carlo、S. Janiec 老师们在专业和实验上对我的关心和帮助。N. Lebret、N. Charles、F. Choulet、M. Bellanger、P. Turrillot、J. Machault 在法国学习期间的帮助，也大大促进了我法语水平。感谢黎广荣、高强、梁鹏、谭忠明、张玉洁在法国生活和学习上给我的帮助。

最后，感谢为我默默奉献的父母和亲人，没有他们的支持和鼓励，我也无法一直坚持到现在，完成我所有的学业。感谢袁利娟对我学习上的激励和支持以及生活上无微不至的照顾，给予我一直向前的动力，不停地向前奋斗。

附表一 锆石 U-Pb 数据表

Sample spot	U (ppm)	Th (ppm)	Th/U	f_{206} (%)	$^{207}\text{Pb}/^{206}\text{Pb}$	$\pm\sigma$ (%)	$^{207}\text{Pb}/^{235}\text{U}$	$\pm\sigma$ (%)	$^{206}\text{Pb}/^{238}\text{U}$	$\pm\sigma$ (%)	$t_{207/206}$ (Ma)	$\pm\sigma$ (Ma)	$t_{207/235}$ (Ma)	$\pm\sigma$ (Ma)	$t_{206/238}$ (Ma)	$\pm\sigma$ (Ma)
XF17@01	666	442	0.664	0.39	0.05365	1.51	0.24175	2.39	0.0347	1.50	222.5	42.4	219.9	4.7	219.6	3.2
XF17@02	238	131	0.550	0.13	0.05104	2.51	0.24472	3.21	0.0355	1.72	196.7	61.8	222.3	6.4	224.7	3.8
XF17@03	683	294	0.430	0.03	0.05096	1.48	0.24833	2.15	0.0355	1.53	228.0	34.5	225.2	4.4	225.0	3.4
XF17@04	495	272	0.549	0.00	0.04990	1.35	0.23499	2.03	0.0342	1.52	190.5	31.2	214.3	3.9	216.5	3.2
XF17@05	265	165	0.624	0.06	0.04967	1.98	0.23242	2.49	0.0339	1.51	179.5	45.4	212.2	4.8	215.2	3.2
XF17@06	1098	465	0.423	0.00	0.05161	0.92	0.24650	1.77	0.0346	1.51	268.0	21.1	223.7	3.6	219.5	3.3
XF17@07	366	260	0.710	0.18	0.05215	2.70	0.24285	3.30	0.0347	1.50	230.8	66.5	220.7	6.6	219.8	3.2
XF17@08	516	265	0.512	0.03	0.05077	1.55	0.24284	2.16	0.0347	1.50	230.6	35.5	220.7	4.3	219.8	3.3
XF17@09	302	172	0.570	0.00	0.05098	1.74	0.24876	2.30	0.0354	1.51	239.7	39.6	225.6	4.7	224.2	3.3
XF17@11	1520	871	0.573	0.15	0.05210	0.78	0.24630	1.77	0.0351	1.51	237.5	21.0	223.6	3.6	222.2	3.3
XF17@12	993	348	0.350	0.14	0.05004	1.19	0.23386	2.01	0.0347	1.50	145.2	31.2	213.4	3.9	219.6	3.2
XF17@13	680	293	0.431	0.05	0.05074	1.27	0.24005	2.01	0.0346	1.50	211.6	30.6	218.5	4.0	219.1	3.2
XF17@14	1233	341	0.277	0.01	0.05076	1.07	0.23881	1.85	0.0341	1.51	229.9	24.5	217.4	3.6	216.3	3.2
XF73@01	863	449	0.520	0.06	0.05155	1.10	0.24034	1.92	0.0341	1.52	243.8	26.9	218.7	3.8	216.4	3.2
XF73@02	1211	268	0.221	0.09	0.05111	0.89	0.24968	1.79	0.0359	1.50	215.5	22.5	226.3	3.6	227.4	3.4
XF73@03	2200	493	0.224	0.03	0.05067	0.74	0.24355	1.68	0.0350	1.50	215.5	17.5	221.3	3.3	221.9	3.3
XF73@04	2486	1416	0.570	0.27	0.05341	0.66	0.24198	1.73	0.0342	1.50	252.7	19.5	220.0	3.4	217.0	3.2
XF73@05	297	336	1.132	0.71	0.05449	1.89	0.23049	3.60	0.0342	1.51	143.7	74.9	210.6	6.9	216.6	3.2
XF73@06	1298	532	0.410	0.21	0.05261	0.93	0.23321	1.91	0.0332	1.50	237.9	27.0	212.8	3.7	210.6	3.1
XF73@07	1302	415	0.319	0.12	0.05174	0.93	0.24549	1.83	0.0350	1.50	232.9	24.2	222.9	3.7	222.0	3.3
XF73@08	265	316	1.190	0.73	0.05454	2.22	0.23125	4.42	0.0344	1.53	139.0	94.7	211.2	8.5	217.8	3.3

附表一

(接附表一)

Sample spot	U (ppm)	Th (ppm)	Th/U	f_{206} (%)	$^{207}\text{Pb}/^{206}\text{Pb}$	$\pm\sigma$ (%)	$^{207}\text{Pb}/^{235}\text{U}$	$\pm\sigma$ (%)	$^{206}\text{Pb}/^{238}\text{U}$	$\pm\sigma$ (%)	$t_{207/206}$ (Ma)	$\pm\sigma$ (Ma)	$t_{207/235}$ (Ma)	$\pm\sigma$ (Ma)	$t_{206/238}$ (Ma)	$\pm\sigma$ (Ma)
XF73@09	724	597	0.825	0.18	0.05214	1.24	0.24007	2.11	0.0343	1.50	228.4	34.0	218.5	4.2	217.6	3.2
XF73@10	162	178	1.098	0.89	0.05378	2.60	0.24815	3.47	0.0351	1.57	250.6	69.7	225.1	7.0	222.6	3.4
XF73@11	2064	497	0.241	0.06	0.05013	1.22	0.24678	1.96	0.0360	1.50	179.5	29.2	224.0	4.0	228.2	3.4
XF73@12	167	259	1.553	0.87	0.05335	2.58	0.23755	3.82	0.0349	1.50	168.6	80.0	216.4	7.5	220.8	3.3
XF73@13	719	360	0.501	0.15	0.05127	1.38	0.23545	2.23	0.0341	1.53	198.7	37.1	214.7	4.3	216.2	3.3
XF73@14	164	154	0.936	0.65	0.05564	3.36	0.23879	5.64	0.0343	1.92	218.3	118.3	217.4	11.1	217.3	4.1
XF73@15	1452	544	0.375	0.18	0.05164	0.94	0.24301	1.89	0.0351	1.51	207.1	26.3	220.9	3.8	222.2	3.3
XF73@16	174	274	1.575	0.93	0.05275	2.94	0.23477	3.82	0.0342	1.52	187.0	79.7	214.1	7.4	216.6	3.2
XF213@01	1491	175	0.118	0.44	0.05047	0.68	0.24846	1.65	0.0357	1.50	216.8	15.7	225.3	3.3	226.1	3.3
XF213@02	622	62	0.100	0.02	0.06649	1.07	0.57108	1.86	0.0624	1.52	817.0	22.3	458.7	6.9	390.4	5.8
XF213@03	189	58	0.306	0.04	0.05304	1.90	0.28845	2.50	0.0397	1.60	315.6	43.2	257.3	5.7	251.0	3.9
XF213@04	190	115	0.604	0.19	0.11423	0.43	5.08504	1.60	0.3269	1.50	1845.5	10.0	1833.6	13.7	1823.1	23.9
XF213@05	878	29	0.033	0.04	0.10407	1.64	3.82769	2.59	0.2676	1.99	1692.1	30.1	1598.6	21.0	1528.6	27.2
XF213@06	124	103	0.834	0.02	0.09707	0.65	3.36541	1.64	0.2519	1.50	1565.0	12.2	1496.4	12.9	1448.4	19.5
XF213@07	284	65	0.230	0.03	0.07298	0.97	1.68660	1.80	0.1681	1.50	1008.0	19.9	1003.5	11.5	1001.4	13.9
XF213@08	207	23	0.111	0.03	0.06961	0.75	1.41308	2.51	0.1478	2.38	909.2	16.0	894.5	15.0	888.5	19.8
XF213@09	618	173	0.281	0.16	0.08845	0.47	2.03521	1.60	0.1692	1.52	1388.2	9.1	1127.4	11.0	1007.5	14.2
XF213@10	687	150	0.218	0.01	0.05853	0.72	0.66567	1.79	0.0826	1.64	545.8	15.8	518.1	7.3	511.8	8.1
XF213@11	547	373	0.681	0.05	0.05091	1.16	0.24029	1.94	0.0345	1.50	218.3	28.2	218.7	3.8	218.7	3.2
XF213@12	47	56	1.191	1.20	0.05196	4.71	0.24808	4.95	0.0346	1.54	283.6	104.3	225.0	10.0	219.4	3.3
XF213@13	977	80	0.082	0.03	0.05085	1.00	0.24459	1.82	0.0350	1.50	223.8	23.5	222.2	3.6	222.0	3.3
XF213@14	821	211	0.257	0.18	0.05299	1.34	0.25018	2.10	0.0352	1.51	265.4	33.2	226.7	4.3	223.0	3.3

(接附表一)

Sample spot	U (ppm)	Th (ppm)	Th/U	f_{206} (%)	$^{207}\text{Pb}/^{206}\text{Pb}$	$\pm\sigma$ (%)	$^{207}\text{Pb}/^{235}\text{U}$	$\pm\sigma$ (%)	$^{206}\text{Pb}/^{238}\text{U}$	$\pm\sigma$ (%)	$t_{207/206}$ (Ma)	$\pm\sigma$ (Ma)	$t_{207/235}$ (Ma)	$\pm\sigma$ (Ma)	$t_{206/238}$ (Ma)	$\pm\sigma$ (Ma)
XF213@15	649	45	0.070	0.03	0.05030	1.01	0.23875	1.84	0.0346	1.50	196.1	24.4	217.4	3.6	219.4	3.2
XF213@16	3047	54	0.018	0.04	0.05104	0.45	0.25360	1.57	0.0363	1.50	228.2	11.0	229.5	3.2	229.6	3.4
XF213@17	3964	37	0.009	0.18	0.05204	0.40	0.25627	1.63	0.0367	1.51	222.9	14.4	231.7	3.4	232.5	3.4
XF216@01	2258	1253	0.555	0.23	0.05153	2.07	0.25402	3.55	0.0358	2.89	264.6	46.7	229.8	7.3	226.4	6.4
XF216@02	898	706	0.786	0.07	0.05068	1.56	0.25801	2.20	0.0369	1.54	226.5	35.7	233.1	4.6	233.7	3.5
XF216@03	517	301	0.581	0.00	0.05109	1.85	0.25566	2.41	0.0363	1.55	245.0	42.0	231.2	5.0	229.8	3.5
XF216@04	1615	697	0.432	0.03	0.05045	0.98	0.25004	1.81	0.0359	1.52	215.6	22.5	226.6	3.7	227.7	3.4
XF216@05	924	385	0.417	0.04	0.04969	1.93	0.23980	2.66	0.0350	1.82	180.5	44.5	218.3	5.2	221.8	4.0
XF216@06	682	408	0.598	0.27	0.04992	2.02	0.24359	2.55	0.0354	1.55	191.1	46.3	221.4	5.1	224.2	3.4
XF216@07	582	520	0.894	0.59	0.05087	2.54	0.21617	2.98	0.0308	1.55	234.8	57.6	198.7	5.4	195.7	3.0
XF216@08	2218	1407	0.634	0.00	0.05001	0.93	0.25072	1.77	0.0364	1.50	195.4	21.5	227.2	3.6	230.2	3.4
XF216@12	839	567	0.676	0.07	0.05022	1.40	0.25519	2.10	0.0369	1.57	205.3	32.1	230.8	4.3	233.3	3.6
XF216@13	280	189	0.675	0.00	0.04945	2.24	0.24479	2.70	0.0359	1.50	169.4	51.6	222.3	5.4	227.4	3.4
XF216@16	1690	1299	0.769	0.10	0.05059	1.76	0.24048	2.31	0.0345	1.51	222.3	40.1	218.8	4.6	218.5	3.2
XF216@17	661	438	0.662	0.13	0.04918	1.62	0.24937	2.21	0.0368	1.51	156.5	37.6	226.1	4.5	232.8	3.4
XF216@18	1314	961	0.732	0.13	0.05167	1.23	0.25117	1.94	0.0353	1.50	270.7	27.9	227.5	4.0	223.4	3.3
XF216@19	879	654	0.744	0.00	0.04997	1.30	0.23967	1.99	0.0348	1.50	193.5	30.0	218.2	3.9	220.4	3.3
XF216@20	799	309	0.386	0.43	0.05048	2.08	0.24127	2.58	0.0347	1.52	217.0	47.6	219.5	5.1	219.7	3.3
XF216@21	4484	4577	1.021	0.04	0.05155	1.20	0.25104	1.92	0.0353	1.50	265.6	27.2	227.4	3.9	223.7	3.3
XF216@22	277	166	0.600	1.03	0.05396	4.02	0.25870	4.30	0.0348	1.53	369.4	88.1	233.6	9.0	220.3	3.3
XF221@01	964	254	0.263	0.19	0.05123	1.02	0.23895	1.85	0.0341	1.51	234.0	24.4	217.6	3.6	216.0	3.2

附表一

(接附表一)

Sample spot	U (ppm)	Th (ppm)	Th/U	f_{206} (%)	$^{207}\text{Pb}/^{206}\text{Pb}$	$\pm\sigma$ (%)	$^{207}\text{Pb}/^{235}\text{U}$	$\pm\sigma$ (%)	$^{206}\text{Pb}/^{238}\text{U}$	$\pm\sigma$ (%)	$t_{207/206}$ (Ma)	$\pm\sigma$ (Ma)	$t_{207/235}$ (Ma)	$\pm\sigma$ (Ma)	$t_{206/238}$ (Ma)	$\pm\sigma$ (Ma)
XF221@02	1090	303	0.278	0.14	0.05103	0.98	0.24704	1.83	0.0355	1.50	216.9	23.9	224.2	3.7	224.9	3.3
XF221@03	437	207	0.475	0.04	0.05269	1.30	0.22856	2.47	0.0338	1.51	148.9	45.3	209.0	4.7	214.4	3.2
XF221@04	515	384	0.746	0.18	0.05048	1.22	0.23679	1.95	0.0341	1.50	211.9	28.5	215.8	3.8	216.1	3.2
XF221@05	1559	713	0.457	0.16	0.05120	1.05	0.24029	2.01	0.0349	1.50	191.2	30.8	218.7	4.0	221.2	3.3
XF221@06	376	217	0.577	0.01	0.05197	1.60	0.23556	2.49	0.0338	1.51	221.6	45.2	214.8	4.8	214.2	3.2
XF221@07	1123	504	0.449	0.47	0.05052	0.86	0.24316	1.75	0.0351	1.50	204.4	20.6	221.0	3.5	222.6	3.3
XF221@08	377	152	0.402	0.07	0.05190	1.66	0.23591	2.39	0.0337	1.50	230.9	42.5	215.1	4.6	213.6	3.2
XF221@09	897	411	0.458	2.83	0.05180	0.98	0.23658	1.93	0.0341	1.50	207.8	27.7	215.6	3.8	216.3	3.2
XF221@10	1092	398	0.365	0.06	0.05088	1.41	0.24076	2.09	0.0346	1.50	213.7	33.3	219.0	4.1	219.5	3.2
XF221@11	530	187	0.354	0.52	0.05187	1.19	0.24238	1.99	0.0343	1.50	249.0	29.7	220.4	3.9	217.7	3.2
XF221@12	477	193	0.404	0.08	0.06869	1.09	0.22402	3.90	0.0335	1.51	125.0	82.6	205.3	7.3	212.3	3.2
XF221@13	700	201	0.287	2.56	0.05087	1.16	0.23652	1.98	0.0342	1.50	204.7	29.6	215.6	3.8	216.6	3.2
XF221@14	191	87	0.454	0.09	0.05089	1.99	0.24029	2.50	0.0342	1.51	235.8	45.2	218.7	4.9	217.1	3.2
XF221@15	796	328	0.412	0.06	0.05108	1.15	0.24161	1.96	0.0346	1.50	224.2	28.7	219.7	3.9	219.3	3.2
XF221@16	780	254	0.325	0.05	0.07408	2.35	0.24590	4.51	0.0344	1.51	280.9	94.5	223.2	9.1	217.8	3.2
XF76@01	490	207	0.421	0.04	0.05507	1.06	0.52654	1.87	0.0693	1.55	415.1	23.4	429.5	6.6	432.2	6.5
XF76@02	210	87	0.416	0.16	0.05546	1.85	0.52528	2.39	0.0687	1.50	430.9	40.8	428.7	8.4	428.3	6.2
XF76@03	396	97	0.245	0.00	0.07096	0.82	1.51573	1.71	0.1549	1.50	956.2	16.7	936.8	10.5	928.5	13.0
XF76@04	287	128	0.445	0.06	0.05589	1.36	0.54911	2.03	0.0713	1.51	447.8	29.9	444.4	7.3	443.8	6.5
XF76@05	384	251	0.652	0.07	0.05526	1.38	0.52878	2.09	0.0694	1.56	422.8	30.6	431.0	7.4	432.5	6.5
XF76@06	256	159	0.621	0.09	0.05654	1.49	0.52936	2.16	0.0679	1.57	473.5	32.6	431.4	7.6	423.6	6.4
XF76@07	281	77	0.275	0.00	0.05585	1.35	0.52495	2.02	0.0682	1.50	446.6	29.8	428.5	7.1	425.1	6.2

(接附表一)

Sample spot	U (ppm)	Th (ppm)	Th/U	f_{206} (%)	$^{207}\text{Pb}/^{206}\text{Pb}$	$\pm\sigma$ (%)	$^{207}\text{Pb}/^{235}\text{U}$	$\pm\sigma$ (%)	$^{206}\text{Pb}/^{238}\text{U}$	$\pm\sigma$ (%)	$t_{207/206}$ (Ma)	$\pm\sigma$ (Ma)	$t_{207/235}$ (Ma)	$\pm\sigma$ (Ma)	$t_{206/238}$ (Ma)	$\pm\sigma$ (Ma)
XF76@08	520	190	0.365	0.03	0.05571	1.00	0.53629	1.80	0.0698	1.50	441.0	22.0	436.0	6.4	435.0	6.3
XF76@09	333	162	0.485	0.00	0.05474	1.24	0.51230	1.96	0.0679	1.52	401.5	27.6	420.0	6.8	423.4	6.2
XF76@10	538	45	0.083	0.03	0.06652	0.81	1.26427	1.70	0.1379	1.50	822.6	16.8	829.8	9.7	832.5	11.7
XF76@11	515	66	0.128	0.03	0.06588	0.67	1.23547	1.64	0.1360	1.50	802.6	13.9	816.8	9.3	822.1	11.6
XF76@12	477	161	0.338	0.09	0.05416	1.32	0.51562	2.00	0.0690	1.50	377.7	29.5	422.2	6.9	430.4	6.3
XF76@13	436	171	0.392	0.00	0.05521	1.38	0.52085	2.04	0.0684	1.51	420.6	30.4	425.7	7.1	426.7	6.2
XF76@14	564	283	0.501	0.02	0.05572	0.93	0.52919	1.78	0.0689	1.51	441.3	20.6	431.3	6.3	429.4	6.3
XF76@15	257	79	0.308	0.00	0.05415	1.40	0.50685	2.06	0.0679	1.51	377.2	31.2	416.3	7.1	423.4	6.2
XF76@16	336	126	0.374	0.07	0.05633	1.29	0.53625	1.99	0.0690	1.51	465.4	28.4	436.0	7.1	430.4	6.3
XF93@01	413	141	0.342	0.03	0.05475	0.97	0.54711	1.78	0.0725	1.50	402.2	21.5	443.1	6.4	451.0	6.5
XF93@02	673	235	0.350	0.02	0.05623	0.83	0.54972	1.71	0.0709	1.50	461.4	18.2	444.8	6.2	441.6	6.4
XF93@03	473	160	0.337	2.66	0.05515	2.49	0.54734	2.93	0.0720	1.54	418.4	54.7	443.3	10.6	448.1	6.7
XF93@04	275	138	0.503	0.05	0.05601	1.10	0.53787	1.86	0.0696	1.50	452.8	24.2	437.0	6.6	434.0	6.3
XF93@05	327	104	0.318	0.08	0.05598	1.03	0.54216	1.82	0.0702	1.50	451.4	22.7	439.8	6.5	437.6	6.4
XF93@06	358	171	0.477	0.01	0.05594	1.38	0.55919	2.04	0.0725	1.50	449.8	30.3	451.0	7.4	451.2	6.5
XF93@07	272	98	0.359	0.06	0.05583	1.31	0.55021	2.00	0.0715	1.50	445.8	28.9	445.1	7.2	445.0	6.5
XF93@08	516	168	0.325	0.05	0.05589	1.01	0.54615	1.81	0.0709	1.50	448.1	22.4	442.5	6.5	441.4	6.4
XF93@09	378	147	0.388	0.03	0.05529	1.03	0.53315	1.82	0.0699	1.50	423.8	22.8	433.9	6.5	435.8	6.3
XF93@10	279	88	0.314	0.03	0.05690	1.15	0.54287	1.89	0.0692	1.50	487.8	25.1	440.3	6.8	431.3	6.3
XF93@11	381	163	0.429	0.02	0.05583	0.99	0.53741	1.80	0.0698	1.50	445.8	21.8	436.7	6.4	435.0	6.3
XF93@12	444	182	0.409	0.02	0.05498	0.98	0.52370	1.79	0.0691	1.50	411.6	21.7	427.6	6.3	430.6	6.3
XF93@12	444	182	0.409	0.02	0.05498	0.98	0.52370	1.79	0.0691	1.50	411.6	21.7	427.6	6.3	430.6	6.3

附表一

(接附表一)

Sample spot	U (ppm)	Th (ppm)	Th/U	f_{206} (%)	$^{207}\text{Pb}/^{206}\text{Pb}$	$\pm\sigma$ (%)	$^{207}\text{Pb}/^{235}\text{U}$	$\pm\sigma$ (%)	$^{206}\text{Pb}/^{238}\text{U}$	$\pm\sigma$ (%)	$t_{207/206}$ (Ma)	$\pm\sigma$ (Ma)	$t_{207/235}$ (Ma)	$\pm\sigma$ (Ma)	$t_{206/238}$ (Ma)	$\pm\sigma$ (Ma)
XF93@13	411	142	0.345	0.00	0.05612	1.17	0.53439	1.90	0.0691	1.50	457.1	25.6	434.7	6.7	430.5	6.3
XF93@14	334	141	0.421	0.04	0.05469	1.36	0.52883	2.04	0.0701	1.52	399.5	30.2	431.0	7.2	436.9	6.4
XF93@15	439	184	0.420	0.03	0.05563	1.37	0.52712	2.03	0.0687	1.50	437.4	30.2	429.9	7.1	428.5	6.2
XF93@16	347	99	0.286	0.03	0.05655	1.01	0.54457	1.83	0.0698	1.52	473.9	22.3	441.4	6.6	435.2	6.4
XF93@17	319	120	0.377	0.02	0.05592	1.06	0.54188	1.84	0.0703	1.50	449.0	23.4	439.7	6.6	437.9	6.4
XF93@18	452	142	0.313	0.04	0.05637	0.90	0.55279	1.75	0.0711	1.50	466.8	19.8	446.8	6.3	442.9	6.4
XF99@01	524	77	0.146	0.05	0.05540	1.04	0.53106	1.83	0.0695	1.50	428.4	23.1	432.5	6.5	433.3	6.3
XF99@02	778	164	0.210	0.03	0.05498	1.13	0.53757	1.88	0.0709	1.51	411.6	25.0	436.8	6.7	441.6	6.4
XF99@03	122	111	0.907	0.07	0.05555	2.58	0.52747	2.98	0.0689	1.50	434.6	56.5	430.1	10.5	429.3	6.2
XF99@05	174	56	0.321	0.00	0.05599	1.67	0.53522	2.24	0.0693	1.50	452.1	36.6	435.3	8.0	432.1	6.3
XF99@06	369	109	0.294	0.02	0.05542	1.50	0.52957	2.13	0.0693	1.50	429.4	33.2	431.5	7.5	431.9	6.3
XF99@07	642	175	0.273	0.00	0.05630	1.61	0.55317	2.20	0.0713	1.50	464.4	35.3	447.1	8.0	443.7	6.5
XF99@08	812	267	0.328	0.02	0.05502	0.84	0.54664	1.72	0.0721	1.50	412.9	18.6	442.8	6.2	448.6	6.5
XF99@09	484	134	0.278	0.04	0.05594	1.25	0.54669	1.95	0.0709	1.50	450.0	27.6	442.8	7.0	441.4	6.4
XF99@11	234	65	0.279	0.12	0.05398	1.64	0.51688	2.22	0.0694	1.50	370.4	36.4	423.1	7.7	432.8	6.3
XF99@12	148	49	0.328	0.12	0.05590	1.99	0.53937	2.50	0.0700	1.51	448.5	43.7	438.0	8.9	436.0	6.4
XF99@13	250	171	0.684	0.02	0.07037	0.84	1.52441	1.94	0.1571	1.74	939.0	17.2	940.3	11.9	940.8	15.3
XF99@14	280	130	0.465	0.06	0.05585	1.47	0.55208	2.10	0.0717	1.51	446.4	32.2	446.4	7.6	446.3	6.5
XF99@15	412	297	0.721	0.16	0.05488	1.27	0.53012	2.02	0.0701	1.57	407.4	28.2	431.9	7.1	436.5	6.6
XF219@01	1232	972	0.789	0.33	0.05754	0.52	0.50729	1.73	0.0669	1.50	411.3	19.2	416.6	5.9	417.6	6.1
XF219@02	318	289	0.910	0.17	0.05598	1.04	0.48974	1.93	0.0650	1.50	399.1	27.1	404.7	6.5	405.7	5.9

(接附表一)

Sample spot	U (ppm)	Th (ppm)	Th/U	f_{206} (%)	$^{207}\text{Pb}/^{206}\text{Pb}$	$\pm\sigma$ (%)	$^{207}\text{Pb}/^{235}\text{U}$	$\pm\sigma$ (%)	$^{206}\text{Pb}/^{238}\text{U}$	$\pm\sigma$ (%)	$t_{207/206}$ (Ma)	$\pm\sigma$ (Ma)	$t_{207/235}$ (Ma)	$\pm\sigma$ (Ma)	$t_{206/238}$ (Ma)	$\pm\sigma$ (Ma)
XF219@03	585	191	0.327	0.12	0.05571	0.78	0.49090	1.74	0.0650	1.50	403.6	19.5	405.5	5.8	405.9	5.9
XF219@04	769	683	0.888	0.35	0.05783	0.67	0.50189	1.77	0.0661	1.50	416.6	20.8	413.0	6.0	412.3	6.0
XF219@05	964	800	0.830	0.52	0.05907	0.60	0.49958	1.80	0.0659	1.50	411.3	22.0	411.4	6.1	411.4	6.0
XF219@07	1252	563	0.449	0.05	0.05512	0.54	0.50439	1.61	0.0669	1.50	400.5	13.0	414.7	5.5	417.2	6.1
XF219@08	932	661	0.709	0.14	0.05614	0.62	0.50914	1.66	0.0670	1.50	415.7	15.8	417.9	5.7	418.3	6.1
XF219@09	2086	1271	0.609	0.04	0.05478	0.41	0.51589	1.57	0.0687	1.50	389.6	10.0	422.4	5.4	428.4	6.2
XF219@10	1417	596	0.420	0.05	0.05506	0.71	0.50648	1.67	0.0672	1.50	397.6	16.4	416.1	5.7	419.4	6.1
XF219@11	489	217	0.444	0.73	0.06160	0.88	0.48225	2.09	0.0626	1.53	449.0	31.4	399.6	6.9	391.1	5.8
XF219@13	1133	549	0.484	0.14	0.05500	0.58	0.49072	1.64	0.0660	1.50	368.4	14.9	405.4	5.5	411.9	6.0
XF219@14	836	353	0.422	0.16	0.05608	1.28	0.49846	2.03	0.0659	1.50	406.1	30.2	410.7	6.9	411.5	6.0
XF219@15	888	299	0.336	0.05	0.05504	0.64	0.49775	1.66	0.0661	1.51	397.9	15.5	410.2	5.6	412.4	6.0
XF219@16	376	189	0.503	0.06	0.05566	1.12	0.50120	1.92	0.0658	1.50	421.3	26.6	412.5	6.5	411.0	6.0
XF270@01	1767	875	0.428	0.07	0.05554	0.51	0.51098	1.58	0.0667	1.50	433.9	11.3	419.1	5.5	416.4	6.1
XF270@02	1240	1032	0.509	0.52	0.05531	0.89	0.48803	1.75	0.0640	1.50	424.6	19.6	403.6	5.8	399.9	5.8
XF270@03	1134	504	0.383	0.89	0.05585	1.20	0.50038	1.92	0.0650	1.50	446.2	26.5	412.0	6.5	405.9	5.9
XF270@04	1827	1223	0.692	0.06	0.05465	0.50	0.51248	1.58	0.0680	1.50	397.7	11.1	420.1	5.5	424.2	6.2
XF270@05	1526	786	0.520	0.55	0.05404	0.77	0.50024	1.69	0.0671	1.50	372.9	17.4	411.9	5.7	418.9	6.1
XF270@06	793	329	0.409	0.18	0.05502	0.84	0.50177	1.72	0.0661	1.50	413.2	18.7	412.9	5.9	412.8	6.0
XF270@08	1293	722	0.484	0.16	0.05543	0.68	0.50875	1.65	0.0666	1.50	429.6	15.1	417.6	5.7	415.4	6.0
XF270@09	1335	586	0.422	0.04	0.05543	0.66	0.51779	1.64	0.0678	1.50	429.6	14.7	423.7	5.7	422.6	6.1
XF270@10	615	337	0.519	0.09	0.05498	1.25	0.50188	1.95	0.0662	1.50	411.6	27.7	413.0	6.7	413.2	6.0
XF270@11	1744	837	0.288	0.56	0.05446	0.88	0.47882	1.74	0.0638	1.50	390.1	19.7	397.3	5.7	398.5	5.8

(接附表一)

Sample spot	U (ppm)	Th (ppm)	Th/U	f_{206} (%)	$^{207}\text{Pb}/^{206}\text{Pb}$	$\pm\sigma$ (%)	$^{207}\text{Pb}/^{235}\text{U}$	$\pm\sigma$ (%)	$^{206}\text{Pb}/^{238}\text{U}$	$\pm\sigma$ (%)	$t_{207/206}$ (Ma)	$\pm\sigma$ (Ma)	$t_{207/235}$ (Ma)	$\pm\sigma$ (Ma)	$t_{206/238}$ (Ma)	$\pm\sigma$ (Ma)
XF270@13	1220	666	0.388	0.59	0.05470	0.90	0.49462	1.75	0.0656	1.50	399.9	20.1	408.1	5.9	409.5	6.0
XF270@15	802	385	0.486	0.08	0.05461	0.79	0.50522	1.71	0.0671	1.52	396.3	17.5	415.2	5.8	418.6	6.1
XF270@17	480	160	0.358	0.13	0.05388	1.07	0.49430	1.88	0.0665	1.54	366.1	24.0	407.8	6.3	415.3	6.2
XF270@18	1073	528	0.487	0.12	0.05432	0.86	0.49878	1.73	0.0666	1.50	384.2	19.1	410.9	5.9	415.6	6.0
XF274@02	281	249	0.875	0.05	0.05521	1.27	0.51176	1.98	0.0672	1.52	420.8	28.2	419.6	6.8	419.4	6.2
XF274@04	866	477	0.536	0.03	0.05547	1.01	0.52231	1.81	0.0683	1.51	431.2	22.4	426.7	6.3	425.9	6.2
XF274@05	1181	390	0.315	0.02	0.05541	0.60	0.52399	1.62	0.0686	1.50	428.8	13.3	427.8	5.7	427.6	6.2
XF274@06	1346	315	0.230	0.03	0.05464	0.57	0.52178	1.64	0.0693	1.54	397.5	12.8	426.3	5.7	431.7	6.4
XF274@07	1570	371	0.252	0.02	0.05478	0.52	0.53056	1.59	0.0702	1.50	403.4	11.7	432.2	5.6	437.6	6.3
XF274@08	560	164	0.322	0.08	0.05433	0.94	0.51716	1.78	0.0690	1.51	384.9	20.9	423.2	6.2	430.3	6.3
XF274@09	702	293	0.405	0.04	0.05506	1.04	0.51889	1.83	0.0683	1.50	414.7	23.1	424.4	6.4	426.2	6.2
XF274@10	813	360	0.417	0.05	0.05518	1.08	0.52424	1.85	0.0689	1.50	419.6	23.9	428.0	6.5	429.5	6.2
XF274@11	2453	951	0.380	0.01	0.05519	0.41	0.52662	1.56	0.0692	1.50	420.0	9.2	429.6	5.5	431.3	6.3
XF274@12	749	224	0.290	0.01	0.05543	0.74	0.52656	1.67	0.0689	1.50	429.7	16.4	429.5	5.9	429.5	6.2
XF274@14	268	223	0.756	0.13	0.05507	1.40	0.50843	2.05	0.0670	1.50	415.2	31.0	417.4	7.1	417.8	6.1
XF274@15	594	253	0.457	0.03	0.05441	1.09	0.49203	1.86	0.0656	1.50	387.9	24.3	406.3	6.2	409.5	6.0
XF274@16	551	320	0.579	0.02	0.05520	1.03	0.51334	1.83	0.0674	1.51	420.4	22.9	420.7	6.3	420.7	6.1
XF274@17	135	153	0.972	0.36	0.05620	2.72	0.52622	3.19	0.0679	1.68	460.4	59.1	429.3	11.2	423.5	6.9
XF274@18	300	260	0.663	0.13	0.05719	1.41	0.54791	2.06	0.0695	1.50	498.7	30.8	443.6	7.4	433.1	6.3
XF274@19	239	148	0.573	0.17	0.05586	1.77	0.53010	2.32	0.0688	1.50	446.7	38.9	431.9	8.2	429.1	6.2
XF274@20	342	418	1.082	0.17	0.05571	1.35	0.52734	2.02	0.0687	1.51	440.7	29.7	430.0	7.1	428.0	6.3
XF274@21	290	337	1.171	0.19	0.05448	1.69	0.51323	2.26	0.0683	1.50	391.0	37.5	420.6	7.8	426.1	6.2

(接附表一)

Sample spot	U (ppm)	Th (ppm)	Th/U	f_{206} (%)	$^{207}\text{Pb}/^{206}\text{Pb}$	$\pm\sigma$ (%)	$^{207}\text{Pb}/^{235}\text{U}$	$\pm\sigma$ (%)	$^{206}\text{Pb}/^{238}\text{U}$	$\pm\sigma$ (%)	$t_{207/206}$ (Ma)	$\pm\sigma$ (Ma)	$t_{207/235}$ (Ma)	$\pm\sigma$ (Ma)	$t_{206/238}$ (Ma)	$\pm\sigma$ (Ma)
XF274@22	266	139	0.485	0.19	0.05509	1.69	0.50955	2.27	0.0671	1.52	415.8	37.2	418.1	7.8	418.6	6.1
XF274@23	270	152	0.496	0.17	0.05509	1.56	0.50308	2.17	0.0662	1.50	416.0	34.6	413.8	7.4	413.4	6.0
XF274@24	317	230	0.669	0.12	0.05562	1.38	0.51418	2.04	0.0670	1.50	437.2	30.5	421.3	7.1	418.3	6.1
XF274@25	804	350	0.399	0.05	0.05562	0.89	0.52391	1.74	0.0683	1.50	437.2	19.6	427.8	6.1	426.0	6.2
XF274@26	116	144	1.263	0.58	0.05395	3.49	0.49311	3.80	0.0663	1.50	368.8	76.8	407.0	12.8	413.8	6.0
XF314@01	403	337	0.835	0.09	0.05554	1.13	0.51543	1.95	0.0681	1.52	406.4	27.1	422.1	6.8	425.0	6.2
XF314@02	182	195	1.069	0.19	0.05749	1.71	0.51900	2.58	0.0672	1.54	451.8	45.2	424.5	9.0	419.5	6.3
XF314@03	163	215	1.322	0.18	0.05506	1.90	0.48968	2.71	0.0662	1.52	357.6	49.9	404.7	9.1	413.0	6.1
XF314@04	352	335	0.951	0.10	0.05594	1.09	0.50961	1.94	0.0670	1.52	417.3	26.9	418.2	6.7	418.3	6.1
XF314@05	329	310	0.940	0.10	0.05476	1.14	0.49761	1.98	0.0668	1.52	370.7	28.3	410.1	6.7	417.1	6.1
XF314@06	575	374	0.650	0.05	0.05623	1.31	0.51524	2.03	0.0669	1.53	445.9	29.6	422.0	7.1	417.6	6.2
XF314@07	1497	500	0.334	0.03	0.05573	0.85	0.51957	1.74	0.0679	1.51	431.3	19.2	424.9	6.1	423.7	6.2
XF314@08	429	407	0.949	0.09	0.05533	1.32	0.50332	2.07	0.0668	1.51	397.7	31.2	413.9	7.0	416.9	6.1
XF314@09	489	316	0.647	0.18	0.05615	0.98	0.50054	1.91	0.0663	1.53	401.2	25.6	412.1	6.5	414.0	6.1
XF314@10	437	320	0.733	0.08	0.05603	1.52	0.51425	2.21	0.0674	1.51	427.4	35.5	421.3	7.6	420.2	6.2
XF314@11	451	262	0.581	0.10	0.05594	1.35	0.50216	2.11	0.0660	1.55	419.3	31.8	413.2	7.2	412.1	6.2
XF314@12	379	258	0.682	0.12	0.05595	1.06	0.50845	1.93	0.0670	1.51	412.9	26.4	417.4	6.6	418.2	6.1
XF314@13	491	304	0.619	0.04	0.05618	0.94	0.51119	1.81	0.0664	1.51	446.0	21.7	419.3	6.2	414.4	6.1
XF314@14	495	376	0.760	0.07	0.05577	0.92	0.51061	1.83	0.0671	1.52	420.0	22.4	418.9	6.3	418.7	6.2
XF314@15	1581	442	0.280	0.05	0.05507	0.57	0.51110	1.63	0.0678	1.51	398.7	13.6	419.2	5.6	422.9	6.2

 f_{206} (%) is the percentage of common ^{206}Pb in total ^{206}Pb

附表二 独居石数据表

REF	Age Ma	Error Age Ma	U ppm	Error U %	Error U ppm	Th ppm	Error Th %	Error Th ppm	Pb ppm	Error Pb %	Error Pb ppm	MPb	Th*(U) ppm	Error Th* %	Error Th* ppm	U*(Th) ppm	Error U* %	Error U* ppm	U/Pb	Error U/Pb %	Th/Pb	Error Th/Pb %	Corr
XF365g-4a	302	72	2890	5.19	150	42800	2.00	856	703	21.34	150	207.628	52183	2.57	1343	16072	2.57	414	4.111	21.96	60.887	21.43	0.967
XF365g-4a	262	74	2840	5.28	150	40940	2.00	819	585	25.65	150	207.621	50133	2.60	1304	15487	2.60	403	4.857	26.19	70.013	25.73	0.976
XF365g-4a	256	77	2700	5.56	150	38950	2.00	779	544	27.59	150	207.622	47686	2.65	1264	14738	2.65	391	4.966	28.14	71.633	27.66	0.978
XF365g-4a	291	65	2570	5.84	150	49660	2.00	993	752	19.96	150	207.698	57997	2.55	1480	17878	2.55	456	3.420	20.80	66.078	20.06	0.955
XF365g-4a	285	78	3020	4.97	150	37650	2.00	753	602	24.92	150	207.577	47443	2.61	1239	14631	2.61	382	5.018	25.41	62.559	25.00	0.978
XF365g-4a	321	71	3470	4.32	150	42050	2.00	841	764	19.62	150	207.567	53333	2.49	1329	16402	2.49	409	4.539	20.09	55.004	19.72	0.972
XF365g-4b	207	71	3300	4.55	150	40820	2.00	816	475	31.60	150	207.576	51459	2.53	1300	15962	2.53	403	6.952	31.92	85.988	31.66	0.988
XF365g-4b	247	57	3220	4.66	150	56010	2.00	1120	730	20.55	150	207.673	66421	2.42	1605	20542	2.42	496	4.411	21.07	76.726	20.65	0.971
XF365g-4b	230	43	3750	4.00	150	76890	2.00	1538	911	16.47	150	207.713	89000	2.27	2022	27560	2.27	626	4.116	16.94	84.401	16.59	0.965
XF365g-4b	198	67	3000	5.00	150	44520	2.00	890	477	31.45	150	207.631	54185	2.54	1374	16819	2.54	426	6.289	31.84	93.329	31.51	0.986
XF365g-4b	253	95	2680	5.60	150	29540	2.00	591	431	34.82	150	207.537	38210	2.82	1076	11812	2.82	333	6.222	35.27	68.576	34.88	0.986
XF365g-4b	283	74	2990	5.02	150	41020	2.00	820	639	23.46	150	207.606	50714	2.58	1307	15642	2.58	403	4.677	23.99	64.161	23.55	0.974
XF365g-4b	261	55	3140	4.78	150	59020	2.00	1180	804	18.65	150	207.692	69184	2.41	1666	21374	2.41	515	3.904	19.25	73.373	18.75	0.963
XF365g-4b	228	43	3820	3.93	150	75730	2.00	1515	893	16.79	150	207.705	88064	2.27	1999	27274	2.27	619	4.276	17.24	84.765	16.91	0.967
XF365g-4b	287	83	2800	5.36	150	35520	2.00	710	570	26.30	150	207.582	44601	2.68	1197	13752	2.68	369	4.910	26.84	62.287	26.38	0.977
XF365g-4b	259	94	2630	5.70	150	30490	2.00	610	449	33.38	150	207.554	39001	2.81	1095	12051	2.81	338	5.853	33.86	67.852	33.44	0.984
XF365g-4b	200	92	2630	5.70	150	30670	2.00	613	348	43.11	150	207.557	39144	2.80	1097	12149	2.80	340	7.558	43.48	88.144	43.16	0.990
XF365g-3a	257	74	2990	5.02	150	40360	2.00	807	572	26.22	150	207.602	50035	2.58	1293	15463	2.58	399	5.227	26.70	70.559	26.30	0.979
XF365g-3a	304	91	2530	5.93	150	32380	2.00	648	551	27.22	150	207.585	40596	2.80	1135	12501	2.80	349	4.591	27.85	58.752	27.29	0.974
XF365g-3a	313	84	2660	5.64	150	35990	2.00	720	622	24.10	150	207.602	44633	2.70	1207	13736	2.70	372	4.274	24.75	57.830	24.19	0.970
XF365g-3a	318	73	3280	4.57	150	40790	2.00	816	730	20.55	150	207.575	51453	2.53	1303	15828	2.53	401	4.493	21.05	55.877	20.65	0.972
XF365g-3b	206	60	3830	3.92	150	48540	2.00	971	559	26.82	150	207.583	60887	2.39	1454	18887	2.39	451	6.849	27.11	86.798	26.90	0.987
XF365g-3b	228	55	4080	3.68	150	55290	2.00	1106	696	21.55	150	207.604	68464	2.32	1590	21203	2.32	492	5.860	21.86	79.418	21.64	0.982

(接附表二)

REF	Age Ma	Error Age Ma	U ppm	Error U %	Error U ppm	Th ppm	Error Th %	Error Th ppm	Pb ppm	Error Pb %	Error Pb ppm	MPb	Th*(U) ppm	Error Th* %	Error Th* ppm	U*(Th) ppm	Error U* %	Error U* ppm	U/Pb	Error U/Pb %	Th/Pb	Error Th/Pb %	Corr
XF365g-3b	228	53	2690	5.58	150	61900	2.00	1238	716	20.96	150	207.738	70585	2.44	1722	21861	2.44	533	3.759	21.69	86.499	21.06	0.962
XF365g-3b	301	54	2740	5.47	150	63030	2.00	1261	966	15.53	150	207.737	71926	2.43	1748	22154	2.43	538	2.836	16.46	65.247	15.66	0.935
XF365g-3b	249	56	2770	5.42	150	58510	2.00	1170	748	20.06	150	207.719	67468	2.45	1655	20863	2.45	512	3.705	20.78	78.251	20.16	0.961
XF365g-3c	232	69	2910	5.15	150	44030	2.00	881	553	27.13	150	207.636	53429	2.55	1365	16542	2.55	423	5.263	27.61	79.633	27.20	0.980
XF365g-3c	230	40	2650	5.66	150	87310	2.00	1746	981	15.30	150	207.804	95868	2.33	2231	29687	2.33	691	2.702	16.31	89.034	15.43	0.930
XF365g-3c	236	45	2580	5.81	150	76140	2.00	1523	890	16.86	150	207.786	84476	2.38	2007	26146	2.38	621	2.900	17.83	85.583	16.98	0.939
XF365g-3c	292	79	2830	5.30	150	38220	2.00	764	618	24.28	150	207.601	47402	2.64	1251	14610	2.64	386	4.580	24.85	61.859	24.36	0.974
XF365g-3d	277	47	2530	5.93	150	75170	2.00	1503	1029	14.58	150	207.786	83369	2.39	1989	25726	2.39	614	2.459	15.74	73.047	14.71	0.918
XF365g-3d	196	54	2270	6.61	150	61150	2.00	1223	596	25.17	150	207.770	68462	2.49	1706	21254	2.49	530	3.810	26.03	102.627	25.25	0.964
XF365g-3d	261	73	3030	4.95	150	40960	2.00	819	590	25.41	150	207.602	50768	2.57	1305	15684	2.57	403	5.133	25.89	69.385	25.49	0.979
XF365g-2a	253	101	5860	2.56	150	16470	2.00	329	399	37.62	150	206.936	35427	2.30	815	10951	2.30	252	14.698	37.71	41.310	37.68	0.996
XF365g-1a	202	92	3230	4.64	150	28490	2.00	570	350	42.90	150	207.457	38899	2.71	1053	12070	2.71	327	9.238	43.15	81.479	42.95	0.993
XF365g-1a	321	129	3360	4.46	150	17230	2.00	345	402	37.28	150	207.224	28155	2.96	832	8659	2.96	256	8.351	37.55	42.825	37.34	0.991
XF365g-1a	260	132	3240	4.63	150	16710	2.00	334	315	47.61	150	207.228	27197	3.01	820	8403	3.01	253	10.284	47.84	53.040	47.65	0.994
XF365g-1a	220	132	3180	4.72	150	16720	2.00	334	264	56.85	150	207.238	26982	3.03	818	8361	3.03	254	12.053	57.05	63.371	56.89	0.996
XF365g-1a	222	71	4030	3.72	150	38690	2.00	774	511	29.38	150	207.489	51697	2.43	1258	16018	2.43	390	7.894	29.62	75.784	29.45	0.990
XF365g-1b	224	70	6380	2.35	150	31110	2.00	622	513	29.21	150	207.203	51703	2.14	1106	16018	2.14	343	12.426	29.31	60.590	29.28	0.994
XF365g-1b	268	86	3920	3.83	150	30040	2.00	601	511	29.37	150	207.401	42735	2.54	1087	13195	2.54	336	7.676	29.62	58.821	29.44	0.989
XF365g-1b	294	93	4930	3.04	150	23380	2.00	468	515	29.14	150	207.188	39377	2.42	954	12135	2.42	294	9.579	29.30	45.426	29.21	0.992
XF365g-1b	268	92	5060	2.96	150	23070	2.00	461	469	31.96	150	207.170	39456	2.40	947	12184	2.40	292	10.780	32.09	49.148	32.02	0.994
XF365c-3b	209	87	5170	2.90	150	24720	2.00	494	385	38.99	150	207.194	41390	2.36	978	12837	2.36	303	13.437	39.09	64.249	39.04	0.996
XF365c-3c	287	129	4140	3.62	150	14340	2.00	287	355	42.29	150	207.037	27767	2.78	773	8562	2.78	238	11.671	42.44	40.427	42.33	0.995
XF365c-3c	214	111	4690	3.20	150	16820	2.00	336	304	49.34	150	207.056	31948	2.57	820	9905	2.57	254	15.427	49.44	55.327	49.38	0.997
XF365c-3c	320	117	4060	3.69	150	17800	2.00	356	442	33.93	150	207.150	31000	2.72	844	9535	2.72	259	9.184	34.13	40.264	33.99	0.992

附表二

(接附表二)

REF	Age Ma	Error Age Ma	U ppm	Error U %	Error U ppm	Th ppm	Error Th %	Error Th ppm	Pb ppm	Error Pb %	Error Pb ppm	MPb	Th*(U) ppm	Error Th* %	Error Th* ppm	U*(Th) ppm	Error U* %	Error U* ppm	U/Pb	Error U/Pb %	Th/Pb	Error Th/Pb %	Corr
XF365c-3c	302	107	3990	3.76	150	21100	2.00	422	457	32.79	150	207.239	34055	2.67	909	10489	2.67	280	8.723	33.01	46.131	32.86	0.992
XF365c-3c	298	103	3950	3.80	150	22480	2.00	450	468	32.07	150	207.272	35301	2.65	936	10876	2.65	289	8.444	32.29	48.055	32.13	0.991
XF365c-2a	305	73	4500	3.33	150	36650	2.00	733	697	21.51	150	207.424	51264	2.38	1220	15785	2.38	376	6.454	21.77	52.568	21.61	0.984
XF365c-2a	178	65	5170	2.90	150	38840	2.00	777	438	34.24	150	207.395	55471	2.27	1259	17244	2.27	391	11.802	34.36	88.663	34.30	0.995
XF365c-2b	180	89	2720	5.51	150	31590	2.00	632	323	46.45	150	207.556	40341	2.76	1114	12538	2.76	346	8.423	46.77	97.820	46.49	0.992
XF365c-2b	210	86	2770	5.42	150	32910	2.00	658	390	38.45	150	207.563	41842	2.73	1142	12976	2.73	354	7.100	38.83	84.356	38.50	0.989
XF365c-2b	207	62	5970	2.51	150	39430	2.00	789	541	27.74	150	207.340	58677	2.17	1272	18200	2.17	395	11.040	27.85	72.914	27.81	0.993
XF365c-2b	239	62	5840	2.57	150	40590	2.00	812	633	23.69	150	207.361	59463	2.18	1297	18400	2.18	401	9.225	23.83	64.115	23.78	0.991
XF365c-2b	180	82	3350	4.48	150	33120	2.00	662	351	42.77	150	207.500	43898	2.61	1145	13644	2.61	356	9.551	43.00	94.431	42.81	0.993
XF365c-2b	318	76	2260	6.64	150	42590	2.00	852	709	21.15	150	207.692	49937	2.68	1339	15361	2.68	412	3.186	22.16	60.043	21.24	0.950
XF365c-2c	314	81	2450	6.12	150	38200	2.00	764	647	23.17	150	207.643	46162	2.71	1251	14204	2.71	385	3.785	23.97	59.012	23.26	0.963
XF365c-2c	272	50	3220	4.66	150	66350	2.00	1327	930	16.13	150	207.714	76781	2.36	1813	23702	2.36	560	3.463	16.79	71.352	16.25	0.953
XF365c-2c	210	40	3420	4.39	150	84930	2.00	1699	895	16.75	150	207.754	95958	2.27	2182	29759	2.27	677	3.820	17.32	94.860	16.87	0.961
XF365c-2c	226	65	2770	5.42	150	47960	2.00	959	573	26.19	150	207.672	56903	2.54	1443	17626	2.54	447	4.836	26.74	83.728	26.26	0.976
XF365d-3a	216	47	2110	7.11	150	73990	2.00	1480	778	19.27	150	207.813	80797	2.43	1964	25045	2.43	609	2.711	20.54	95.061	19.38	0.933
XF365d-3b	288	98	2750	5.45	150	28510	2.00	570	481	31.19	150	207.515	37430	2.82	1057	11540	2.82	326	5.718	31.66	59.277	31.25	0.983
XF365d-3b	182	101	2610	5.75	150	26830	2.00	537	286	52.53	150	207.514	35229	2.89	1019	10948	2.89	317	9.140	52.84	93.960	52.57	0.993
XF365d-3b	208	77	2570	5.84	150	38760	2.00	775	435	34.47	150	207.635	47046	2.68	1259	14592	2.68	390	5.906	34.96	89.074	34.53	0.984
XF365d-3c	244	63	2900	5.17	150	49810	2.00	996	643	23.32	150	207.670	59185	2.50	1481	18308	2.50	458	4.509	23.89	77.448	23.41	0.973
XF365d-3c	174	87	2870	5.23	150	31760	2.00	635	316	47.40	150	207.540	40990	2.73	1118	12746	2.73	348	9.069	47.69	100.363	47.44	0.993
XF365d-3c	238	105	2450	6.12	150	26320	2.00	526	363	41.34	150	207.528	34237	2.95	1011	10595	2.95	313	6.752	41.79	72.539	41.39	0.988
XF365d-3d	212	65	3020	4.97	150	47040	2.00	941	537	27.94	150	207.644	56780	2.51	1425	17605	2.51	442	5.625	28.38	87.622	28.01	0.982
XF365d-3d	221	60	2860	5.24	150	52240	2.00	1045	604	24.82	150	207.686	61470	2.49	1529	19048	2.49	474	4.732	25.36	86.427	24.90	0.975

(接附表二)

REF	Age Ma	Error Age Ma	U ppm	Error U %	Error U ppm	Th ppm	Error Th %	Error Th ppm	Pb ppm	Error Pb %	Error Pb ppm	MPb	Th*(U) ppm	Error Th* %	Error Th* ppm	U*(Th) ppm	Error U* %	Error U* ppm	U/Pb	Error U/Pb %	Th/Pb	Error Th/Pb %	Corr
XF376h-2c	165	93	2930	5.12	150	28730	2.00	575	280	53.53	150	207.498	38147	2.77	1057	11869	2.77	329	10.456	53.78	102.530	53.57	0.995
XF376h-2c	206	95	3480	4.31	150	26550	2.00	531	346	43.39	150	207.400	37768	2.69	1015	11716	2.69	315	10.067	43.61	76.803	43.44	0.994
XF376i-1d	240	94	3070	4.89	150	28470	2.00	569	411	36.53	150	207.475	38392	2.75	1054	11879	2.75	326	7.477	36.86	69.342	36.59	0.990
XF376i-2a	310	82	4040	3.71	150	31990	2.00	640	624	24.04	150	207.413	45115	2.50	1127	13886	2.50	347	6.474	24.32	51.261	24.12	0.985
XF376i-2b	178	90	3620	4.14	150	28040	2.00	561	314	47.84	150	207.407	39685	2.63	1043	12336	2.63	324	11.546	48.02	89.433	47.88	0.995
XF376j-1b	297	103	2830	5.30	150	26420	2.00	528	471	31.85	150	207.477	35605	2.85	1015	10970	2.85	313	6.010	32.29	56.104	31.92	0.984
XF376j-1b	185	91	3260	4.60	150	28730	2.00	575	322	46.54	150	207.458	39223	2.70	1057	12186	2.70	329	10.114	46.76	89.136	46.58	0.994
XF376j-1b	193	92	3420	4.39	150	27910	2.00	558	333	45.03	150	207.428	38924	2.68	1041	12087	2.68	323	10.267	45.24	83.783	45.07	0.994
XF376j-1b	232	101	3220	4.66	150	25170	2.00	503	368	40.80	150	207.409	35570	2.78	988	11013	2.78	306	8.759	41.07	68.465	40.85	0.992
XF376f-1a	185	92	4510	3.33	150	24340	2.00	487	320	46.93	150	207.251	38856	2.50	970	12072	2.50	301	14.109	47.04	76.146	46.97	0.997
XF376f-1a	232	95	4650	3.23	150	23010	2.00	460	393	38.19	150	207.210	38029	2.48	945	11774	2.48	292	11.838	38.32	58.581	38.24	0.995
XF376f-1a	242	97	3680	4.08	150	25230	2.00	505	399	37.61	150	207.355	37124	2.67	989	11486	2.67	306	9.226	37.83	63.252	37.66	0.993
XF376f-1b	242	95	3910	3.84	150	25390	2.00	508	409	36.69	150	207.332	38028	2.61	993	11765	2.61	307	9.563	36.89	62.097	36.74	0.993
XF376f-1b	190	94	4260	3.52	150	24080	2.00	482	319	46.96	150	207.272	37797	2.55	965	11739	2.55	300	13.337	47.09	75.389	47.00	0.996
XF376f-2a	252	85	3420	4.39	150	32110	2.00	642	485	30.93	150	207.480	43173	2.61	1127	13347	2.61	349	7.052	31.24	66.211	30.99	0.988
XF376e-1a	271	124	2470	6.07	150	21170	2.00	423	352	42.56	150	207.445	29171	3.12	909	9005	3.12	281	7.008	42.99	60.066	42.61	0.989
XF376e-1a	233	94	4120	3.64	150	24870	2.00	497	395	37.93	150	207.300	38178	2.57	982	11819	2.57	304	10.417	38.10	62.883	37.98	0.994
XF376e-1b	175	96	3770	3.98	150	24790	2.00	496	286	52.43	150	207.339	36915	2.65	978	11478	2.65	304	13.179	52.59	86.657	52.47	0.996
XF376e-1b	160	92	4190	3.58	150	25120	2.00	502	274	54.82	150	207.299	38581	2.55	984	12009	2.55	306	15.314	54.94	91.808	54.86	0.997
XF376b-1a	254	171	2440	6.15	150	12980	2.00	260	235	63.74	150	207.243	20873	3.57	745	6452	3.57	230	10.368	64.03	55.153	63.77	0.995
XF376b-1a	193	109	3040	4.93	150	22930	2.00	459	280	53.53	150	207.396	32720	2.88	942	10160	2.88	292	10.849	53.76	81.831	53.57	0.995
XF376b-1a	314	108	3200	4.69	150	23390	2.00	468	473	31.70	150	207.380	33789	2.83	955	10397	2.83	294	6.764	32.05	49.438	31.77	0.987
XF376b-1a	309	146	2650	5.66	150	16140	2.00	323	341	43.98	150	207.302	24749	3.27	810	7618	3.27	249	7.770	44.34	47.321	44.02	0.991
XF376b-1a	255	98	2970	5.05	150	27310	2.00	546	420	35.72	150	207.472	36919	2.79	1032	11411	2.79	319	7.073	36.08	65.042	35.78	0.989

附表二

(接附表二)

REF	Age Ma	Error Age Ma	U ppm	Error U %	Error U ppm	Th ppm	Error Th %	Error Th ppm	Pb ppm	Error Pb %	Error Pb ppm	MPb	Th*(U) ppm	Error Th* %	Error Th* ppm	U*(Th) ppm	Error U* %	Error U* ppm	U/Pb	Error U/Pb %	Th/Pb	Error Th/Pb %	Corr
XF376b-1b	252	135	2500	6.00	150	18410	2.00	368	297	50.57	150	207.385	26496	3.22	853	8192	3.22	264	8.429	50.93	62.072	50.61	0.992
XF376b-1b	149	102	2940	5.10	150	25000	2.00	500	228	65.82	150	207.445	34438	2.85	982	10728	2.85	306	12.900	66.01	109.695	65.85	0.997
XF376b-1b	223	107	3000	5.00	150	23750	2.00	475	332	45.18	150	207.415	33433	2.87	959	10358	2.87	297	9.036	45.46	71.539	45.23	0.993
XF376b-1b	301	105	2970	5.05	150	25280	2.00	506	469	31.99	150	207.441	34923	2.84	993	10756	2.84	306	6.334	32.39	53.916	32.05	0.986
xf205a1-t1	233	36	5840	2.57	150	88930	2.00	1779	1119	13.41	150	207.638	107794	2.10	2263	33372	2.10	701	5.219	13.65	79.479	13.55	0.971
xf205a1-t1	230	35	5520	2.72	150	92500	2.00	1850	1129	13.28	150	207.664	110326	2.12	2334	34164	2.12	723	4.887	13.56	81.901	13.43	0.969
xf205a1-t2	221	32	12990	2.00	260	81050	2.00	1621	1207	12.43	150	207.315	122971	2.00	2459	38105	2.00	762	10.763	12.59	67.153	12.59	0.975
xf205a1-t2	252	34	9430	2.00	189	84960	2.00	1699	1295	11.59	150	207.464	115463	2.00	2309	35696	2.00	714	7.283	11.76	65.619	11.76	0.971
xf205a1-t2	215	37	6390	2.35	150	82230	2.00	1645	984	15.25	150	207.588	102843	2.07	2128	31882	2.07	660	6.496	15.43	83.595	15.38	0.980
xf205a1-t2	223	49	1570	9.55	150	72550	2.00	1451	770	19.48	150	207.850	77617	2.49	1935	24048	2.49	600	2.039	21.70	94.235	19.59	0.893
xf205a1-t3	225	40	4160	3.61	150	82380	2.00	1648	960	15.63	150	207.705	95809	2.23	2132	29679	2.23	660	4.335	16.04	85.848	15.76	0.967
xf205a1-t3	242	46	1640	9.15	150	77750	2.00	1555	895	16.76	150	207.853	83051	2.46	2040	25695	2.46	631	1.833	19.10	86.885	16.88	0.872
xf205a1-t3	250	44	2040	7.35	150	81020	2.00	1620	977	15.35	150	207.831	87618	2.40	2106	27091	2.40	651	2.088	17.02	82.921	15.48	0.894
xf205a1-t3	231	43	1600	9.38	150	85760	2.00	1715	937	16.02	150	207.867	90927	2.42	2200	28154	2.42	681	1.708	18.56	91.572	16.14	0.856
xf205c1-t1	237	40	3360	4.46	150	86290	2.00	1726	1026	14.63	150	207.760	97146	2.28	2210	30067	2.28	684	3.276	15.29	84.135	14.76	0.948
xf205c1-t1	216	45	2040	7.35	150	78270	2.00	1565	817	18.37	150	207.826	84851	2.42	2049	26302	2.42	635	2.498	19.79	95.856	18.48	0.923
xf205c1-t1	227	57	1490	10.07	150	61310	2.00	1226	668	22.45	150	207.836	66121	2.59	1710	20480	2.59	530	2.230	24.61	91.767	22.54	0.909
xf205c1-t1	265	50	2150	6.98	150	69850	2.00	1397	908	16.52	150	207.801	76811	2.45	1883	23723	2.45	581	2.367	17.93	76.907	16.64	0.914
xf205c1-t1	205	50	1590	9.43	150	69580	2.00	1392	683	21.95	150	207.844	74705	2.51	1875	23175	2.51	582	2.326	23.89	101.801	22.04	0.915
xf205c1-t1	251	60	1970	7.61	150	55990	2.00	1120	697	21.52	150	207.779	62362	2.57	1605	19281	2.57	496	2.826	22.82	80.310	21.61	0.939
xf205c1-t1	243	45	2580	5.81	150	78080	2.00	1562	938	16.00	150	207.790	86420	2.37	2046	26734	2.37	633	2.752	17.02	83.284	16.12	0.933
xf205c1-t1	245	41	3480	4.31	150	84360	2.00	1687	1044	14.37	150	207.749	95611	2.27	2172	29574	2.27	672	3.333	15.00	80.801	14.51	0.949
xf205c1-t2	243	44	3010	4.98	150	77770	2.00	1555	949	15.81	150	207.761	87500	2.33	2040	27068	2.33	631	3.172	16.57	81.953	15.93	0.946

(接附表二)

REF	Age Ma	Error Age Ma	U ppm	Error U %	Error U ppm	Th ppm	Error Th %	Error Th ppm	Pb ppm	Error Pb %	Error Pb ppm	MPb	Th*(U) ppm	Error Th* %	Error Th* ppm	U*(Th) ppm	Error U* %	Error U* ppm	U/Pb	Error U/Pb %	Th/Pb	Error Th/Pb %	Corr
xf205c1-t2	217	44	3530	4.25	150	75230	2.00	1505	835	17.96	150	207.722	86618	2.30	1989	26849	2.30	616	4.226	18.46	90.071	18.07	0.967
xf205c1-t2	243	47	3390	4.42	150	71240	2.00	1425	889	16.86	150	207.718	82198	2.32	1910	25429	2.32	591	3.811	17.44	80.095	16.98	0.961
xf205c1-t2	244	41	4080	3.68	150	82160	2.00	1643	1035	14.50	150	207.709	95349	2.23	2128	29496	2.23	658	3.944	14.96	79.418	14.64	0.960
xf205c1-t3	246	41	4200	3.57	150	80390	2.00	1608	1032	14.54	150	207.697	93970	2.23	2093	29063	2.23	647	4.071	14.97	77.920	14.68	0.962
xf205c1-t3	226	43	4060	3.69	150	76320	2.00	1526	901	16.65	150	207.693	89428	2.25	2011	27700	2.25	623	4.505	17.05	84.691	16.77	0.969
xf205c1-t3	230	44	3860	3.89	150	75060	2.00	1501	898	16.71	150	207.701	87526	2.27	1986	27103	2.27	615	4.300	17.16	83.617	16.83	0.967
xf205c1-t3	246	45	3710	4.04	150	73700	2.00	1474	937	16.00	150	207.706	85695	2.29	1959	26506	2.29	606	3.957	16.50	78.616	16.13	0.962
xf205c1-t3	263	40	4260	3.52	150	84000	2.00	1680	1147	13.08	150	207.704	97791	2.21	2166	30207	2.21	669	3.714	13.54	73.239	13.23	0.955
xf205c1-t3	245	36	5220	2.87	150	93310	2.00	1866	1205	12.45	150	207.680	110187	2.13	2351	34081	2.13	727	4.333	12.78	77.462	12.61	0.962
xf205c1-t3	213	43	2570	5.84	150	80070	2.00	1601	838	17.91	150	207.795	88359	2.36	2085	27396	2.36	647	3.068	18.83	95.590	18.02	0.945
xf205c1-t4	204	32	6350	2.36	150	100620	2.00	2012	1098	13.66	150	207.649	121087	2.06	2496	37568	2.06	774	5.781	13.86	91.611	13.80	0.975
xf205c1-t4	215	31	7820	2.00	156	102560	2.00	2051	1220	12.30	150	207.594	127784	2.00	2556	39615	2.00	792	6.411	12.46	84.087	12.46	0.974
xf205c1-t4	268	41	3410	4.40	150	85480	2.00	1710	1152	13.02	150	207.755	96523	2.27	2195	29805	2.27	678	2.960	13.75	74.212	13.18	0.936
xf205c1-t4	223	40	3520	4.26	150	86170	2.00	1723	967	15.51	150	207.751	97531	2.26	2208	30218	2.26	684	3.639	16.08	89.081	15.64	0.956
xf205c1-t4	205	36	4390	3.42	150	93230	2.00	1865	981	15.29	150	207.721	107381	2.19	2348	33313	2.19	728	4.474	15.66	95.015	15.42	0.968
xf205c1-t4	224	35	5310	2.82	150	95900	2.00	1918	1126	13.32	150	207.683	113040	2.13	2402	35020	2.13	744	4.716	13.62	85.163	13.47	0.967
xf205c1-t4	242	35	5610	2.67	150	95140	2.00	1903	1221	12.28	150	207.666	113273	2.11	2388	35044	2.11	739	4.593	12.57	77.888	12.44	0.964
xf205e1-t1	215	35	2490	6.02	150	105470	2.00	2109	1087	13.80	150	207.840	113502	2.28	2593	35186	2.28	804	2.292	15.06	97.067	13.95	0.907
xf205e1-t1	245	40	4760	3.15	150	82780	2.00	1656	1071	14.00	150	207.673	98169	2.18	2141	30365	2.18	662	4.444	14.35	77.286	14.15	0.966
xf205e1-t1	247	32	13940	2.00	279	78700	2.00	1574	1358	11.04	150	207.270	123774	2.00	2475	38280	2.00	766	10.264	11.22	57.949	11.22	0.968
xf205e1-t1	229	35	8320	2.00	166	84320	2.00	1686	1131	13.26	150	207.508	111186	2.00	2224	34433	2.00	689	7.353	13.41	74.523	13.41	0.978
xf205e1-t1	259	45	2680	5.60	150	77440	2.00	1549	996	15.06	150	207.782	86114	2.36	2034	26607	2.36	629	2.690	16.06	77.728	15.19	0.929
xf205e1-t1	246	48	1900	7.89	150	74180	2.00	1484	880	17.04	150	207.829	80323	2.45	1969	24843	2.45	609	2.159	18.78	84.272	17.16	0.901
xf205e1-t1	240	49	1960	7.65	150	72560	2.00	1451	846	17.74	150	207.821	78894	2.45	1936	24411	2.45	599	2.318	19.32	85.816	17.85	0.912

附表二

(接附表二)

REF	Age Ma	Error Age Ma	U ppm	Error U %	Error U ppm	Th ppm	Error Th %	Error Th ppm	Pb ppm	Error Pb %	Error Pb ppm	MPb	Th*(U) ppm	Error Th* %	Error Th* ppm	U*(Th) ppm	Error U* %	Error U* ppm	U/Pb	Error U/Pb %	Th/Pb	Error Th/Pb %	Corr
xf205e1-t1	251	47	1930	7.77	150	76730	2.00	1535	927	16.18	150	207.831	82972	2.43	2020	25654	2.43	624	2.082	17.95	82.770	16.30	0.895
xf205e1-t2	238	37	3600	4.17	150	93200	2.00	1864	1111	13.50	150	207.762	104832	2.24	2349	32444	2.24	727	3.241	14.13	83.906	13.65	0.945
xf205e1-t2	195	43	2700	5.56	150	78460	2.00	1569	758	19.80	150	207.783	87157	2.35	2052	27059	2.35	637	3.563	20.56	103.548	19.90	0.958
xf205e1-t2	229	44	2360	6.36	150	80240	2.00	1605	896	16.73	150	207.809	87861	2.38	2089	27209	2.38	647	2.633	17.90	89.513	16.85	0.928
xf205e1-t2	227	29	15870	2.00	317	85980	2.00	1720	1387	10.82	150	207.252	137220	2.00	2744	42500	2.00	850	11.444	11.00	62.003	11.00	0.967
xf205e1-t2	204	39	5390	2.78	150	79010	2.00	1580	877	17.11	150	207.627	96383	2.14	2064	29903	2.14	640	6.149	17.34	90.133	17.23	0.980
xf205e1-t2	223	42	2840	5.28	150	81780	2.00	1636	903	16.61	150	207.781	90947	2.33	2120	28177	2.33	657	3.145	17.43	90.556	16.73	0.946
xf205e1-t2	218	44	2000	7.50	150	79440	2.00	1589	832	18.02	150	207.831	85893	2.41	2073	26622	2.41	642	2.403	19.52	95.433	18.13	0.918
xf205e1-t3	234	34	5210	2.88	150	97400	2.00	1948	1192	12.59	150	207.691	114230	2.13	2433	35361	2.13	753	4.371	12.91	81.721	12.74	0.963
xf205e1-t3	234	33	6160	2.44	150	97940	2.00	1959	1230	12.20	150	207.649	117839	2.07	2443	36478	2.07	756	5.009	12.44	79.640	12.36	0.968
xf205e1-t3	231	33	8780	2.00	176	90870	2.00	1817	1224	12.25	150	207.515	119225	2.00	2385	36917	2.00	738	7.172	12.41	74.226	12.41	0.974
xf205e1-t3	255	36	4690	3.20	150	95000	2.00	1900	1250	12.00	150	207.710	110173	2.17	2385	34054	2.17	737	3.753	12.42	76.022	12.17	0.953
xf205e1-t3	221	35	4830	3.11	150	96750	2.00	1935	1105	13.57	150	207.708	112337	2.15	2419	34810	2.15	750	4.371	13.93	87.554	13.72	0.964
xf205e1-t3	252	36	4500	3.33	150	95670	2.00	1913	1240	12.10	150	207.721	110226	2.18	2399	34076	2.18	742	3.629	12.55	77.163	12.26	0.951
xf205e1-t3	225	38	3800	3.95	150	89650	2.00	1793	1021	14.69	150	207.743	101917	2.23	2277	31571	2.23	705	3.721	15.21	87.791	14.82	0.957
xf205e1-t3	255	39	3690	4.07	150	87930	2.00	1759	1134	13.23	150	207.745	99868	2.25	2244	30868	2.25	694	3.254	13.84	77.532	13.38	0.945
xf205e1-t3	256	39	4040	3.71	150	88320	2.00	1766	1156	12.98	150	207.727	101392	2.22	2252	31337	2.22	696	3.496	13.50	76.429	13.13	0.950
xf205e1-t3	236	37	4390	3.42	150	91610	2.00	1832	1113	13.48	150	207.717	105793	2.19	2317	32745	2.19	717	3.946	13.91	82.342	13.63	0.959
xf205e1-t3	253	36	4760	3.15	150	93550	2.00	1871	1230	12.19	150	207.703	108949	2.16	2356	33678	2.16	728	3.870	12.60	76.054	12.36	0.955
xf205e1-t3	218	38	4300	3.49	150	88670	2.00	1773	994	15.09	150	207.714	102543	2.20	2257	31783	2.20	700	4.327	15.49	89.227	15.23	0.966
xf205e1-t3	248	37	4700	3.19	150	91290	2.00	1826	1176	12.75	150	207.700	106488	2.17	2311	32931	2.17	715	3.996	13.15	77.610	12.91	0.958
xf205e1-t3	205	35	4830	3.11	150	93710	2.00	1874	998	15.03	150	207.701	109279	2.16	2358	33902	2.16	731	4.840	15.35	93.907	15.16	0.971
xf205e1-t3	247	35	5360	2.80	150	97300	2.00	1946	1261	11.89	150	207.684	114631	2.12	2431	35452	2.12	752	4.250	12.22	77.158	12.06	0.960
xf205g1-t1	233	46	3510	4.27	150	71010	2.00	1420	855	17.55	150	207.710	82348	2.31	1905	25494	2.31	590	4.106	18.06	83.073	17.66	0.965

(接附表二)

REF	Age Ma	Error Age Ma	U ppm	Error U %	Error U ppm	Th ppm	Error Th %	Error Th ppm	Pb ppm	Error Pb %	Error Pb ppm	MPb	Th*(U) ppm	Error Th* %	Error Th* ppm	U*(Th) ppm	Error U* %	Error U* ppm	U/Pb	Error U/Pb %	Th/Pb	Error Th/Pb %	Corr
xf205g1-t1	238	67	2590	5.79	150	47140	2.00	943	587	25.54	150	207.685	55509	2.57	1427	17179	2.57	442	4.410	26.19	80.260	25.62	0.972
xf205g1-t1	252	49	3140	4.78	150	67700	2.00	1354	875	17.15	150	207.724	77857	2.36	1839	24069	2.36	569	3.590	17.80	77.403	17.27	0.957
xf205g1-t1	240	35	5440	2.76	150	95860	2.00	1917	1213	12.37	150	207.676	113441	2.12	2402	35102	2.12	743	4.484	12.67	79.021	12.53	0.964
xf205g1-t2	264	48	2600	5.77	150	73180	2.00	1464	962	15.60	150	207.777	81598	2.39	1949	25203	2.39	602	2.704	16.63	76.103	15.73	0.930
xf205g1-t2	252	52	2780	5.40	150	65020	2.00	1300	831	18.04	150	207.741	74012	2.41	1786	22881	2.41	552	3.344	18.83	78.218	18.16	0.952
xf205g1-t3	207	48	7080	2.12	150	53950	2.00	1079	707	21.22	150	207.400	76775	2.04	1563	23815	2.04	485	10.018	21.33	76.334	21.32	0.991
xf205g1-t3	193	47	5760	2.60	150	59250	2.00	1185	666	22.52	150	207.514	77800	2.14	1668	24158	2.14	518	8.647	22.67	88.944	22.61	0.989
xf205g1-t3	244	54	3290	4.56	150	59510	2.00	1190	763	19.65	150	207.683	70146	2.39	1675	21698	2.39	518	4.311	20.18	77.977	19.76	0.969
xf205g1-t3	262	48	2820	5.32	150	70830	2.00	1417	936	16.03	150	207.756	79959	2.38	1902	24700	2.38	588	3.014	16.89	75.691	16.15	0.942
xf205g1-t3	229	39	3500	4.29	150	89270	2.00	1785	1026	14.63	150	207.759	100572	2.26	2270	31146	2.26	703	3.413	15.24	87.049	14.76	0.951
xf205g1-t3	223	38	3980	3.77	150	90200	2.00	1804	1023	14.66	150	207.735	103046	2.22	2288	31926	2.22	709	3.890	15.14	88.163	14.80	0.960
xf205g1-t3	201	35	4600	3.26	150	94940	2.00	1899	980	15.31	150	207.715	109763	2.17	2382	34063	2.17	739	4.695	15.65	96.893	15.44	0.970
xf205g2-t1	212	32	6670	2.25	150	100090	2.00	2002	1148	13.07	150	207.634	121601	2.04	2486	37705	2.04	771	5.810	13.26	87.192	13.22	0.974
xf205g2-t1	221	31	7160	2.09	150	103910	2.00	2078	1251	11.99	150	207.624	127017	2.02	2562	39358	2.02	794	5.723	12.17	83.059	12.16	0.972
xf205g2-t1	208	34	4910	3.05	150	97030	2.00	1941	1047	14.32	150	207.705	112861	2.15	2424	35004	2.15	752	4.688	14.64	92.636	14.46	0.969
xf205g2-t1	257	42	3020	4.97	150	84570	2.00	1691	1082	13.86	150	207.776	94343	2.31	2177	29155	2.31	673	2.790	14.72	78.127	14.00	0.932
xf205g2-t2	217	29	16610	2.00	332	83360	2.00	1667	1319	11.38	150	207.217	136947	2.00	2739	42449	2.00	849	12.597	11.55	63.218	11.55	0.970
xf205g2-t2	230	31	15320	2.00	306	78890	2.00	1578	1312	11.43	150	207.228	128364	2.00	2567	39749	2.00	795	11.674	11.60	60.113	11.60	0.970
xf205g2-t2	224	32	11130	2.00	223	88270	2.00	1765	1237	12.12	150	207.415	124197	2.00	2484	38476	2.00	770	8.995	12.29	71.334	12.29	0.974
xf205g2-t2	244	31	12980	2.00	260	88170	2.00	1763	1412	10.63	150	207.351	130130	2.00	2603	40254	2.00	805	9.195	10.81	62.457	10.81	0.966
xf205g2-t3	233	27	22320	2.00	446	80710	2.00	1614	1580	9.49	150	207.060	152805	2.00	3056	47307	2.00	946	14.123	9.70	51.069	9.70	0.957
xf205g2-t3	230	31	17640	2.00	353	72600	2.00	1452	1324	11.33	150	207.123	129566	2.00	2591	40121	2.00	802	13.326	11.51	54.844	11.51	0.970
xf205g2-t3	255	30	18600	2.00	372	75710	2.00	1514	1538	9.75	150	207.117	135887	2.00	2718	42001	2.00	840	12.095	9.96	49.232	9.96	0.960
xf205g2-t3	221	29	20090	2.00	402	71430	2.00	1429	1340	11.20	150	207.052	136267	2.00	2725	42223	2.00	844	14.996	11.37	53.320	11.37	0.969

附表二

(接附表二)

REF	Age Ma	Error Age Ma	U ppm	Error U %	Error U ppm	Th ppm	Error Th %	Error Th ppm	Pb ppm	Error Pb %	Error Pb ppm	MPb	Th*(U) ppm	Error Th* %	Error Th* ppm	U*(Th) ppm	Error U* %	Error U* ppm	U/Pb	Error U/Pb %	Th/Pb	Error Th/Pb %	Corr
xf208c1-t1	247	35	2070	7.25	150	108260	2.00	2165	1266	11.84	150	207.864	114953	2.31	2650	35551	2.31	820	1.635	13.89	85.484	12.01	0.841
xf208c1-t1	230	40	1160	12.93	150	93040	2.00	1861	991	15.14	150	207.902	96786	2.42	2345	29972	2.42	726	1.171	19.91	93.912	15.27	0.754
xf208c1-t1	254	44	950	15.79	150	86790	2.00	1736	1020	14.71	150	207.910	89863	2.47	2221	27776	2.47	687	0.931	21.58	85.085	14.84	0.675
xf208c1-t1	218	47	890	16.85	150	77790	2.00	1556	782	19.17	150	207.908	80661	2.53	2040	25001	2.53	632	1.138	25.53	99.432	19.28	0.747
xf208c1-t1	248	40	1390	10.79	150	93550	2.00	1871	1084	13.83	150	207.888	98045	2.40	2356	30320	2.40	729	1.282	17.54	86.261	13.98	0.780
xf208c1-t1	190	44	1370	10.95	150	80820	2.00	1616	723	20.75	150	207.876	85231	2.46	2099	26470	2.46	652	1.895	23.46	111.801	20.85	0.880
xf208c1-t1	241	44	1360	11.03	150	84510	2.00	1690	955	15.70	150	207.881	88906	2.45	2175	27508	2.45	673	1.424	19.19	88.458	15.83	0.812
xf208c1-t1	214	44	1210	12.40	150	83760	2.00	1675	835	17.97	150	207.890	87663	2.46	2159	27179	2.46	669	1.450	21.83	100.364	18.08	0.818
xf208c1-t1	259	44	1620	9.26	150	83720	2.00	1674	1029	14.58	150	207.863	88963	2.43	2160	27488	2.43	667	1.574	17.27	81.357	14.71	0.836
xf208c1-t1	232	34	2730	5.49	150	108120	2.00	2162	1208	12.41	150	207.831	116937	2.26	2647	36206	2.26	820	2.259	13.58	89.484	12.57	0.903
xf208c1-t2	259	39	1460	10.27	150	98870	2.00	1977	1195	12.55	150	207.888	103595	2.38	2463	32011	2.38	761	1.222	16.22	82.739	12.71	0.764
xf208c1-t2	233	40	1260	11.90	150	94980	2.00	1900	1027	14.60	150	207.897	99050	2.41	2384	30666	2.41	738	1.227	18.84	92.458	14.74	0.768
xf208c1-t2	234	39	2090	7.18	150	92580	2.00	1852	1038	14.45	150	207.845	99332	2.35	2336	30749	2.35	723	2.014	16.14	89.214	14.59	0.887
xf208c1-t2	235	40	2310	6.49	150	91270	2.00	1825	1035	14.50	150	207.830	98733	2.34	2310	30562	2.34	715	2.233	15.89	88.222	14.64	0.904
xf208c1-t2	243	52	1100	13.64	150	70610	2.00	1412	803	18.68	150	207.884	74166	2.56	1897	22944	2.56	587	1.370	23.13	87.931	18.79	0.803
xf208c1-t2	243	47	740	20.27	150	79700	2.00	1594	890	16.86	150	207.920	82092	2.53	2079	25396	2.53	643	0.832	26.37	89.590	16.98	0.635
xf208c1-t2	206	43	1480	10.14	150	84610	2.00	1692	819	18.31	150	207.873	89381	2.43	2176	27728	2.43	675	1.807	20.93	103.283	18.42	0.870
xf208c1-t2	199	44	1290	11.63	150	81810	2.00	1636	763	19.65	150	207.883	85966	2.47	2120	26681	2.47	658	1.690	22.84	107.195	19.76	0.856
xf208c1-t2	215	43	1410	10.64	150	85740	2.00	1715	866	17.32	150	207.879	90288	2.44	2199	27989	2.44	682	1.628	20.33	99.011	17.44	0.846
xf208c1-t2	220	33	2340	6.41	150	110730	2.00	2215	1160	12.93	150	207.853	118281	2.28	2699	36654	2.28	836	2.017	14.43	95.453	13.08	0.885
xf208d2-t1	226	37	2450	6.12	150	96540	2.00	1931	1051	14.27	150	207.830	104449	2.31	2415	32354	2.31	748	2.331	15.53	91.859	14.41	0.910
xf208d2-t1	213	36	1950	7.69	150	102560	2.00	2051	1035	14.49	150	207.865	108850	2.33	2535	33748	2.33	786	1.884	16.40	99.069	14.63	0.875
xf208d2-t1	221	32	3550	4.23	150	113150	2.00	2263	1229	12.21	150	207.799	124607	2.20	2747	38610	2.20	851	2.889	12.92	92.080	12.37	0.933
xf208d2-t2	244	36	2640	5.68	150	102540	2.00	2051	1206	12.44	150	207.828	111074	2.28	2536	34360	2.28	784	2.189	13.68	85.032	12.60	0.898

(接附表二)

REF	Age Ma	Error Age Ma	U ppm	Error U %	Error U ppm	Th ppm	Error Th %	Error Th ppm	Pb ppm	Error Pb %	Error Pb ppm	MPb	Th*(U) ppm	Error Th* %	Error Th* ppm	U*(Th) ppm	Error U* %	Error U* ppm	U/Pb	Error U/Pb %	Th/Pb	Error Th/Pb %	Corr
xf208d2-t2	227	38	2450	6.12	150	95620	2.00	1912	1047	14.33	150	207.829	103530	2.31	2397	32067	2.31	742	2.341	15.59	91.371	14.47	0.911
xf208d2-t2	214	38	2620	5.73	150	92260	2.00	1845	958	15.65	150	207.814	100711	2.31	2329	31224	2.31	722	2.734	16.67	96.266	15.78	0.932
xf208e3-t1	195	39	1940	7.73	150	90300	2.00	1806	837	17.93	150	207.851	96549	2.37	2289	29976	2.37	711	2.319	19.53	107.932	18.04	0.913
xf208e3-t1	265	53	1500	10.00	150	67100	2.00	1342	851	17.63	150	207.846	71957	2.54	1828	22224	2.54	564	1.763	20.27	78.862	17.74	0.864
xf208e3-t1	250	46	1700	8.82	150	77760	2.00	1555	927	16.18	150	207.849	83258	2.45	2040	25744	2.45	631	1.834	18.43	83.886	16.30	0.871
xf208e3-t1	237	38	1870	8.02	150	97960	2.00	1959	1100	13.64	150	207.864	104002	2.35	2444	32188	2.35	756	1.701	15.83	89.094	13.79	0.853
xf208e3-t2	253	38	1520	9.87	150	100900	2.00	2018	1194	12.57	150	207.887	105817	2.37	2503	32711	2.37	774	1.274	15.98	84.539	12.73	0.777
xf208e3-t2	227	37	1820	8.24	150	100680	2.00	2014	1076	13.94	150	207.870	106556	2.34	2498	33004	2.34	774	1.691	16.19	93.565	14.08	0.852
xf208e3-t2	195	38	1520	9.87	150	96970	2.00	1939	886	16.93	150	207.884	101866	2.38	2423	31625	2.38	752	1.716	19.60	109.451	17.05	0.858
xf208e3-t2	240	39	1950	7.69	150	94770	2.00	1895	1082	13.86	150	207.856	101072	2.35	2380	31274	2.35	736	1.802	15.85	87.556	14.00	0.865
xf208e3-t2	244	39	1860	8.06	150	94060	2.00	1881	1090	13.76	150	207.860	100073	2.36	2366	30956	2.36	732	1.706	15.95	86.295	13.91	0.854
xf208e3-t2	249	43	1550	9.68	150	87030	2.00	1741	1024	14.65	150	207.871	92043	2.42	2226	28461	2.42	688	1.514	17.56	85.024	14.79	0.827
xf208e3-t2	255	48	1380	10.87	150	76480	2.00	1530	920	16.30	150	207.870	80945	2.49	2015	25019	2.49	623	1.500	19.59	83.127	16.43	0.826
xf208e3-t2	239	49	1360	11.03	150	73360	2.00	1467	828	18.11	150	207.867	77755	2.51	1952	24062	2.51	604	1.642	21.20	88.570	18.22	0.849
xf208e3-t3	205	41	1100	13.64	150	89230	2.00	1785	846	17.73	150	207.903	92776	2.44	2268	28783	2.44	704	1.300	22.37	105.473	17.84	0.788
xf208e3-t3	238	40	1680	8.93	150	92380	2.00	1848	1039	14.44	150	207.869	97809	2.38	2332	30269	2.38	722	1.617	16.98	88.943	14.58	0.843
xf208e3-t3	231	44	1730	8.67	150	82260	2.00	1645	903	16.61	150	207.853	87847	2.42	2130	27201	2.42	659	1.916	18.74	91.083	16.73	0.880
xf208e3-t3	250	45	1270	11.81	150	81960	2.00	1639	960	15.62	150	207.884	86067	2.47	2124	26612	2.47	657	1.323	19.58	85.356	15.75	0.791
xf208e3-t3	258	50	1450	10.34	150	72130	2.00	1443	885	16.94	150	207.858	76822	2.51	1928	23739	2.51	596	1.638	19.85	81.478	17.06	0.848
xf208e3-t3	191	42	1390	10.79	150	84570	2.00	1691	758	19.79	150	207.879	89046	2.44	2174	27653	2.44	675	1.833	22.54	111.549	19.89	0.873
xf208e3-t4	237	39	1440	10.42	150	95030	2.00	1901	1056	14.21	150	207.886	99683	2.39	2385	30850	2.39	738	1.364	17.62	90.027	14.35	0.799
xf208e3-t4	254	39	1480	10.14	150	95730	2.00	1915	1139	13.17	150	207.884	100518	2.39	2400	31071	2.39	742	1.300	16.62	84.079	13.33	0.784
xf208e3-t4	202	36	2640	5.68	150	99160	2.00	1983	967	15.52	150	207.824	107668	2.29	2467	33411	2.29	765	2.731	16.53	102.581	15.65	0.931
xf208e3-t4	226	37	2240	6.70	150	97330	2.00	1947	1051	14.28	150	207.843	104561	2.32	2431	32389	2.32	753	2.132	15.77	92.628	14.41	0.897

附表二

(接附表二)

REF	Age Ma	Error Age Ma	U ppm	Error U %	Error U ppm	Th ppm	Error Th %	Error Th ppm	Pb ppm	Error Pb %	Error Pb ppm	MPb	Th*(U) ppm	Error Th* %	Error Th* ppm	U*(Th) ppm	Error U* %	Error U* ppm	U/Pb	Error U/Pb %	Th/Pb	Error Th/Pb %	Corr
xf208e3-t5	211	43	1110	13.51	150	85370	2.00	1707	838	17.89	150	207.899	88950	2.46	2191	27582	2.46	679	1.324	22.42	101.840	18.01	0.793
xf208e3-t5	216	43	1060	14.15	150	86020	2.00	1720	861	17.41	150	207.903	89440	2.46	2204	27724	2.46	683	1.231	22.44	99.859	17.53	0.771
xf208e3-t5	240	40	1240	12.10	150	93100	2.00	1862	1037	14.46	150	207.897	97107	2.42	2347	30049	2.42	726	1.195	18.85	89.755	14.60	0.760
xf208f2-t1	242	48	1230	12.20	150	77060	2.00	1541	875	17.13	150	207.882	81036	2.50	2026	25071	2.50	627	1.405	21.03	88.026	17.25	0.809
xf208f2-t1	252	51	1240	12.10	150	71990	2.00	1440	853	17.59	150	207.874	76001	2.53	1925	23496	2.53	595	1.454	21.35	84.404	17.70	0.819
xf208f2-t1	244	40	1240	12.10	150	95520	2.00	1910	1084	13.83	150	207.899	99529	2.41	2395	30787	2.41	741	1.144	18.38	88.094	13.98	0.745
xf208f2-t1	220	38	1520	9.87	150	97630	2.00	1953	1005	14.93	150	207.884	102535	2.38	2437	31775	2.38	755	1.513	17.90	97.186	15.07	0.827
xf208f2-t2	220	44	1540	9.74	150	82640	2.00	1653	860	17.44	150	207.867	87610	2.44	2137	27149	2.44	662	1.790	19.97	96.069	17.55	0.867
xf208f2-t2	233	40	1140	13.16	150	92960	2.00	1859	1005	14.93	150	207.903	96642	2.43	2344	29919	2.43	726	1.135	19.90	92.514	15.06	0.744
xf208f2-t2	222	42	1530	9.80	150	86920	2.00	1738	907	16.53	150	207.873	91858	2.42	2223	28462	2.42	689	1.687	19.22	95.814	16.66	0.854
xf208f2-t2	251	51	1230	12.20	150	70920	2.00	1418	840	17.86	150	207.874	74898	2.54	1904	23156	2.54	589	1.464	21.63	84.438	17.97	0.821
xf208f2-t2	190	44	1090	13.76	150	82220	2.00	1644	724	20.71	150	207.897	85730	2.48	2127	26626	2.48	661	1.505	24.86	113.502	20.80	0.829
xf208f2-t2	248	39	1690	8.88	150	94970	2.00	1899	1110	13.51	150	207.871	100435	2.37	2384	31059	2.37	737	1.522	16.16	85.526	13.66	0.827
xf208f2-t2	214	40	1350	11.11	150	92810	2.00	1856	928	16.16	150	207.890	97165	2.41	2340	30123	2.41	725	1.455	19.61	100.003	16.29	0.818
xf208f2-t3	192	35	960	15.63	150	108820	2.00	2176	956	15.68	150	207.923	111911	2.38	2659	34753	2.38	826	1.004	22.14	113.769	15.81	0.703
xf208f2-t3	219	43	760	19.74	150	87560	2.00	1751	880	17.04	150	207.924	90012	2.48	2235	27895	2.48	693	0.864	26.08	99.495	17.16	0.649
xf208f2-t3	230	42	2200	6.82	150	86120	2.00	1722	956	15.69	150	207.829	93225	2.37	2207	28868	2.37	683	2.301	17.11	90.082	15.82	0.910
xf208f2-t3	210	40	1490	10.07	150	92710	2.00	1854	914	16.41	150	207.881	97515	2.40	2338	30240	2.40	725	1.630	19.25	101.404	16.53	0.846
xf208f2-t3	221	40	1450	10.34	150	93450	2.00	1869	966	15.52	150	207.884	98129	2.40	2353	30407	2.40	729	1.500	18.65	96.692	15.65	0.825
xf208g1-t1	232	36	3910	3.84	150	95720	2.00	1914	1121	13.38	150	207.751	108349	2.21	2399	33546	2.21	743	3.488	13.92	85.398	13.53	0.951
xf208g1-t1	239	40	2370	6.33	150	90290	2.00	1806	1043	14.38	150	207.825	97949	2.34	2291	30311	2.34	709	2.272	15.71	86.573	14.52	0.907
xf208g1-t1	264	42	1240	12.10	150	91640	2.00	1833	1125	13.33	150	207.895	95654	2.42	2318	29546	2.42	716	1.102	18.00	81.453	13.48	0.732
xf208g1-t1	226	35	2350	6.38	150	106720	2.00	2134	1152	13.02	150	207.848	114307	2.29	2619	35406	2.29	811	2.039	14.50	92.601	13.17	0.887
xf208g1-t1	204	35	1790	8.38	150	103760	2.00	2075	996	15.06	150	207.875	109529	2.34	2559	33982	2.34	794	1.797	17.23	104.173	15.19	0.866

(接附表二)

REF	Age Ma	Error Age Ma	U ppm	Error U %	Error U ppm	Th ppm	Error Th %	Error Th ppm	Pb ppm	Error Pb %	Error Pb ppm	MPb	Th*(U) ppm	Error Th* %	Error Th* ppm	U*(Th) ppm	Error U* %	Error U* ppm	U/Pb	Error U/Pb %	Th/Pb	Error Th/Pb %	Corr
xf208g1-t1	251	36	1720	8.72	150	105700	2.00	2114	1244	12.06	150	207.880	111263	2.34	2599	34400	2.34	804	1.382	14.88	84.959	12.22	0.799
xf208g1-t2	256	44	730	20.55	150	85990	2.00	1720	1008	14.88	150	207.925	88352	2.50	2205	27306	2.50	682	0.724	25.37	85.279	15.01	0.581
xf208g1-t2	249	39	3250	4.62	150	90910	2.00	1818	1127	13.31	150	207.776	101421	2.27	2303	31361	2.27	712	2.883	14.08	80.649	13.46	0.934
xf208g1-t3	249	41	1830	8.20	150	89000	2.00	1780	1052	14.26	150	207.856	94918	2.39	2265	29352	2.39	700	1.739	16.45	84.599	14.40	0.859
xf208g1-t3	232	38	1350	11.11	150	99520	2.00	1990	1076	13.94	150	207.895	103880	2.38	2475	32162	2.38	766	1.254	17.83	92.476	14.08	0.774
xf208f2-t2	264	42	1390	10.79	150	89450	2.00	1789	1108	13.54	150	207.884	93950	2.42	2275	29018	2.42	703	1.254	17.31	80.726	13.68	0.774
xf208g1-t2	263	40	1340	11.19	150	94570	2.00	1891	1159	12.95	150	207.892	98908	2.40	2377	30553	2.40	734	1.156	17.11	81.619	13.10	0.748
xf326-a1t1	203	31	7440	2.02	150	99670	2.00	1993	1115	13.45	150	207.601	123648	2.00	2477	38366	2.00	769	6.671	13.60	89.361	13.60	0.978
xf326-a1t1	203	31	7690	2.00	154	99610	2.00	1992	1126	13.32	150	207.590	124395	2.00	2488	38596	2.00	772	6.830	13.47	88.467	13.47	0.978
xf326-a1t1	207	29	7060	2.12	150	112450	2.00	2249	1247	12.03	150	207.650	135211	2.02	2733	41940	2.02	848	5.664	12.22	90.213	12.20	0.971
xf326-a1t1	229	30	6890	2.18	150	111730	2.00	2235	1368	10.97	150	207.655	133979	2.03	2719	41490	2.03	842	5.038	11.18	81.704	11.15	0.965
xf326-a1t1	210	30	6940	2.16	150	108890	2.00	2178	1227	12.22	150	207.646	131269	2.03	2661	40709	2.03	825	5.656	12.41	88.745	12.39	0.972
xf326-a1t1	238	31	6220	2.41	150	107030	2.00	2141	1347	11.13	150	207.670	127128	2.07	2625	39343	2.07	812	4.617	11.39	79.440	11.31	0.962
xf326-a1t1	234	32	6190	2.42	150	105870	2.00	2117	1310	11.45	150	207.669	125865	2.07	2602	38964	2.07	805	4.724	11.70	80.798	11.62	0.964
xf326-a1t1	243	32	6120	2.45	150	106730	2.00	2135	1371	10.94	150	207.674	126513	2.07	2619	39137	2.07	810	4.463	11.21	77.836	11.12	0.960
xf326-a1t1	234	32	6000	2.50	150	102670	2.00	2053	1271	11.80	150	207.669	122052	2.08	2538	37784	2.08	786	4.720	12.06	80.759	11.97	0.965
xf326-a1t1	221	35	4810	3.12	150	94870	2.00	1897	1085	13.83	150	207.704	110392	2.16	2381	34208	2.16	738	4.434	14.17	87.452	13.97	0.965
xf326-a1t2	238	33	7290	2.06	150	96200	2.00	1924	1268	11.83	150	207.595	119756	2.01	2409	37062	2.01	745	5.748	12.00	75.852	12.00	0.971
xf326-a1t2	223	32	7540	2.00	151	98560	2.00	1971	1222	12.27	150	207.593	122898	2.00	2458	38075	2.00	761	6.168	12.43	80.632	12.43	0.974
xf326-a1t2	201	31	7600	2.00	152	99860	2.00	1997	1114	13.46	150	207.595	124351	2.00	2487	38588	2.00	772	6.819	13.61	89.602	13.61	0.978
xf326-a1t2	223	31	6980	2.15	150	103890	2.00	2078	1256	11.95	150	207.631	126419	2.03	2562	39167	2.03	794	5.559	12.14	82.736	12.11	0.971
xf326-a1t2	224	30	6570	2.28	150	112500	2.00	2250	1333	11.26	150	207.669	133707	2.04	2734	41423	2.04	847	4.930	11.48	84.414	11.43	0.965
xf326-a1t2	237	31	6230	2.41	150	108010	2.00	2160	1353	11.08	150	207.672	128140	2.06	2645	39659	2.06	819	4.603	11.34	79.811	11.26	0.962

附表二

(接附表二)

REF	Age Ma	Error Age Ma	U ppm	Error U %	Error U ppm	Th ppm	Error Th %	Error Th ppm	Pb ppm	Error Pb %	Error Pb ppm	MPb	Th*(U) ppm	Error Th* %	Error Th* ppm	U*(Th) ppm	Error U* %	Error U* ppm	U/Pb	Error U/Pb %	Th/Pb	Error Th/Pb %	Corr
xf326-a1t2	212	31	6330	2.37	150	106700	2.00	2134	1200	12.51	150	207.665	127115	2.06	2618	39415	2.06	812	5.277	12.73	88.953	12.66	0.970
xf326-a1t2	217	31	5940	2.53	150	106430	2.00	2129	1211	12.39	150	207.681	125593	2.08	2613	38930	2.08	810	4.907	12.65	87.914	12.55	0.967
xf326-a1t2	219	32	5920	2.53	150	104340	2.00	2087	1201	12.49	150	207.677	123441	2.08	2571	38257	2.08	797	4.930	12.74	86.884	12.65	0.968
xf326-a1t2	195	32	5720	2.62	150	102070	2.00	2041	1045	14.35	150	207.680	120494	2.10	2525	37409	2.10	784	5.471	14.58	97.628	14.49	0.974
xf326-a1t2	212	33	5670	2.65	150	100390	2.00	2008	1120	13.40	150	207.678	118676	2.10	2492	36798	2.10	773	5.064	13.66	89.657	13.54	0.970
xf326-a1t3	237	31	7050	2.13	150	104420	2.00	2088	1345	11.15	150	207.630	127200	2.02	2573	39367	2.02	796	5.241	11.35	77.620	11.33	0.967
xf326-a1t3	236	31	6160	2.44	150	110610	2.00	2212	1373	10.92	150	207.681	130512	2.07	2697	40396	2.07	835	4.486	11.19	80.548	11.10	0.960
xf326-a1t3	230	31	5950	2.52	150	109310	2.00	2186	1316	11.40	150	207.687	128525	2.08	2671	39799	2.08	827	4.520	11.67	83.048	11.57	0.962
xf326-a1t3	234	31	6030	2.49	150	108110	2.00	2162	1327	11.30	150	207.681	127588	2.07	2647	39498	2.07	819	4.544	11.57	81.468	11.48	0.962
xf326-a1t3	219	32	5920	2.53	150	104860	2.00	2097	1208	12.42	150	207.678	123962	2.08	2581	38418	2.08	800	4.901	12.67	86.817	12.58	0.967
xf326-a1t3	195	31	6100	2.46	150	103600	2.00	2072	1067	14.06	150	207.668	123247	2.07	2555	38265	2.07	793	5.719	14.28	97.122	14.20	0.975
xf326-a3t1	255	45	1250	12.00	150	83160	2.00	1663	992	15.11	150	207.887	87204	2.46	2149	26953	2.46	664	1.260	19.30	83.793	15.25	0.776
xf326-b1t1	224	41	3400	4.41	150	82270	2.00	1645	929	16.14	150	207.749	93245	2.28	2130	28888	2.28	660	3.659	16.74	88.543	16.27	0.957
xf326-b1t1	246	40	3320	4.52	150	86580	2.00	1732	1068	14.05	150	207.763	97314	2.28	2217	30098	2.28	686	3.109	14.75	81.072	14.19	0.942
xf326-b1t1	239	40	3750	4.00	150	84180	2.00	1684	1026	14.62	150	207.733	96298	2.25	2168	29799	2.25	671	3.654	15.15	82.030	14.75	0.956
xf326-b1t1	228	42	6930	2.16	150	67470	2.00	1349	912	16.45	150	207.494	89846	2.04	1834	27826	2.04	568	7.600	16.59	73.993	16.57	0.984
xf326-b1t2	242	37	6140	2.44	150	85000	2.00	1700	1128	13.30	150	207.610	104845	2.08	2185	32438	2.08	676	5.443	13.52	75.352	13.45	0.973
xf326-b1t2	234	34	6260	2.40	150	94490	2.00	1890	1198	12.52	150	207.635	114713	2.07	2374	35510	2.07	735	5.227	12.75	78.891	12.68	0.970
xf326-b1t3	236	33	6530	2.30	150	98810	2.00	1976	1261	11.90	150	207.636	119907	2.05	2461	37113	2.05	762	5.179	12.12	78.369	12.06	0.968
xf326-b2t1	255	38	4360	3.44	150	88500	2.00	1770	1167	12.85	150	207.710	102607	2.20	2255	31713	2.20	697	3.736	13.30	75.826	13.01	0.954
xf326-b2t1	192	40	3220	4.66	150	84130	2.00	1683	808	18.57	150	207.764	94499	2.29	2166	29345	2.29	672	3.985	19.14	104.128	18.67	0.964
xf326-b2t1	201	43	4080	3.68	150	73810	2.00	1476	779	19.24	150	207.684	86958	2.25	1960	26984	2.25	608	5.234	19.59	94.695	19.35	0.977
xf326-b2t1	242	45	3110	4.82	150	75260	2.00	1505	918	16.33	150	207.748	85312	2.33	1990	26395	2.33	616	3.387	17.03	81.956	16.46	0.952
xf326-b2t2	269	41	3830	3.92	150	82910	2.00	1658	1145	13.10	150	207.725	95315	2.25	2144	29428	2.25	662	3.346	13.68	72.423	13.25	0.947

(接附表二)

REF	Age Ma	Error Age Ma	U ppm	Error U %	Error U ppm	Th ppm	Error Th %	Error Th ppm	Pb ppm	Error Pb %	Error Pb ppm	MPb	Th*(U) ppm	Error Th* %	Error Th* ppm	U*(Th) ppm	Error U* %	Error U* ppm	U/Pb	Error U/Pb %	Th/Pb	Error Th/Pb %	Corr
xf326-d111	259	59	4850	3.09	150	47470	2.00	949	728	20.61	150	207.495	63166	2.27	1435	19518	2.27	443	6.664	20.84	65.225	20.71	0.984
xf326-d111	256	59	5000	3.00	150	47630	2.00	953	728	20.60	150	207.485	63808	2.25	1438	19720	2.25	444	6.867	20.82	65.418	20.70	0.985
xf326-d112	277	60	4320	3.47	150	49190	2.00	984	780	19.23	150	207.547	63190	2.33	1470	19499	2.33	454	5.538	19.54	63.056	19.33	0.979
xf326-d112	270	61	4680	3.21	150	45810	2.00	916	732	20.49	150	207.495	60968	2.30	1402	18824	2.30	433	6.394	20.74	62.591	20.59	0.983
xf326-d112	236	59	6530	2.30	150	41070	2.00	821	651	23.04	150	207.318	62166	2.10	1306	19242	2.10	404	10.031	23.16	63.091	23.13	0.991
xf326-d3t1	219	52	2440	6.15	150	64000	2.00	1280	700	21.44	150	207.764	71873	2.45	1764	22275	2.45	547	3.487	22.30	91.474	21.53	0.957
xf326-d3t1	263	45	2060	7.28	150	79740	2.00	1595	1015	14.78	150	207.827	86409	2.41	2080	26691	2.41	643	2.029	16.47	78.545	14.91	0.889
xf326-e1t1	269	41	4970	3.02	150	80400	2.00	1608	1157	12.97	150	207.654	96497	2.17	2094	29794	2.17	646	4.296	13.31	69.502	13.12	0.963
xf326-e1t1	239	36	6780	2.21	150	87780	2.00	1756	1168	12.84	150	207.589	109690	2.04	2240	33943	2.04	693	5.802	13.03	75.124	12.99	0.974
xf326-e1t1	197	53	8520	2.00	170	41770	2.00	835	605	24.77	150	207.206	69217	2.00	1384	21486	2.00	430	14.071	24.85	68.986	24.85	0.994
xf326-e1t1	217	42	4930	3.04	150	74610	2.00	1492	876	17.13	150	207.636	90516	2.18	1976	28055	2.18	613	5.629	17.39	85.182	17.24	0.978
xf326-e1t1	228	44	3050	4.92	150	77880	2.00	1558	890	16.85	150	207.759	87728	2.33	2042	27170	2.33	632	3.425	17.55	87.461	16.96	0.953
xf326-e1t1	257	40	3890	3.86	150	85100	2.00	1702	1119	13.41	150	207.727	97687	2.24	2187	30189	2.24	676	3.478	13.95	76.080	13.56	0.951
xf326-e1t2	275	68	7460	2.01	150	29450	2.00	589	655	22.89	150	207.101	53622	2.00	1075	16549	2.00	332	11.382	22.97	44.933	22.97	0.992
xf326-e1t2	178	46	3380	4.44	150	69260	2.00	1385	635	23.62	150	207.714	80133	2.33	1868	24909	2.33	581	5.322	24.03	109.054	23.70	0.979
xf326-e1t2	206	44	3060	4.90	150	76770	2.00	1535	794	18.89	150	207.756	86634	2.33	2019	26875	2.33	626	3.854	19.52	96.686	19.00	0.963
xf326-e1t2	213	42	3320	4.52	150	79080	2.00	1582	852	17.60	150	207.746	89788	2.30	2065	27838	2.30	640	3.895	18.17	92.778	17.71	0.962
xf326-e1t4	182	76	6600	2.27	150	25580	2.00	512	379	39.58	150	207.095	46819	2.12	994	14549	2.12	309	17.416	39.65	67.501	39.63	0.997
xf326-e1t4	209	46	2380	6.30	150	75270	2.00	1505	772	19.42	150	207.797	82944	2.40	1989	25724	2.40	617	3.082	20.42	97.461	19.53	0.946
xf326-e1t4	244	40	3900	3.85	150	85160	2.00	1703	1064	14.10	150	207.727	97768	2.24	2188	30243	2.24	677	3.666	14.61	80.047	14.24	0.955
xf326-e2t3	190	38	7720	2.00	154	74770	2.00	1495	843	17.79	150	207.493	99627	2.00	1993	30941	2.00	619	9.157	17.90	88.690	17.90	0.988
xf326-e3t1	239	40	2120	7.08	150	89730	2.00	1795	1030	14.56	150	207.839	96581	2.36	2279	29886	2.36	705	2.057	16.19	87.083	14.69	0.891
xf326-e3t1	252	59	1540	9.74	150	58540	2.00	1171	714	21.00	150	207.825	63521	2.61	1656	19637	2.61	512	2.156	23.15	81.949	21.09	0.903
xf326-e3t1	273	70	2580	5.81	150	45180	2.00	904	651	23.03	150	207.674	53538	2.60	1390	16526	2.60	429	3.961	23.75	69.368	23.12	0.966

附表二

(接附表二)

REF	Age Ma	Error Age Ma	U ppm	Error U %	Error U ppm	Th ppm	Error Th %	Error Th ppm	Pb ppm	Error Pb %	Error Pb ppm	MPb	Th*(U) ppm	Error Th* %	Error Th* ppm	U*(Th) ppm	Error U* %	Error U* ppm	U/Pb	Error U/Pb %	Th/Pb	Error Th/Pb %	Corr
xf326-e3t1	240	71	2490	6.02	150	44310	2.00	886	559	26.85	150	207.679	52357	2.62	1371	16201	2.62	424	4.457	27.51	79.305	26.92	0.973
xf326-g1t2	230	38	5250	2.86	150	84540	2.00	1691	1040	14.43	150	207.653	101494	2.14	2175	31429	2.14	674	5.050	14.71	81.326	14.57	0.972
xf326-g1t3	188	50	4610	3.25	150	59070	2.00	1181	618	24.29	150	207.587	73911	2.25	1664	22959	2.25	517	7.464	24.50	95.642	24.37	0.988
xf326-g1t3	261	33	7290	2.06	150	96930	2.00	1939	1400	10.71	150	207.597	120526	2.01	2424	37236	2.01	749	5.206	10.91	69.225	10.90	0.965
XF366-t6	392	36	330	45.45	150	122140	2.00	2443	2162	6.94	150	207.960	123219	2.38	2933	37691	2.38	897	0.153	45.98	56.482	7.22	0.145
XF366-t2	369	58	320	46.88	150	68230	2.00	1365	1145	13.10	150	207.947	69274	2.68	1854	21227	2.68	568	0.280	48.67	59.595	13.25	0.266
XF366-t1	388	66	330	45.45	150	59830	2.00	1197	1058	14.18	150	207.942	60908	2.77	1687	18637	2.77	516	0.312	47.61	56.545	14.32	0.295
XF366-t2	407	61	440	34.09	150	65310	2.00	1306	1216	12.34	150	207.935	66750	2.69	1797	20395	2.69	549	0.362	36.25	53.718	12.50	0.336
XF366-t2	424	40	760	19.74	150	108890	2.00	2178	2117	7.08	150	207.933	111381	2.40	2669	33986	2.40	815	0.359	20.97	51.429	7.36	0.325
XF366-t2	370	53	550	27.27	150	75510	2.00	1510	1280	11.72	150	207.932	77305	2.59	2000	23686	2.59	613	0.430	29.68	58.982	11.89	0.389
XF366-t2	406	33	1020	14.71	150	135870	2.00	2717	2528	5.93	150	207.930	139208	2.30	3208	42538	2.30	980	0.403	15.86	53.740	6.26	0.355
XF366-t1	418	53	590	25.42	150	76580	2.00	1532	1469	10.21	150	207.929	78513	2.58	2023	23969	2.58	618	0.402	27.40	52.121	10.40	0.366
XF366-t4	441	81	390	38.46	150	47560	2.00	951	965	15.54	150	207.926	48840	2.96	1443	14883	2.96	440	0.404	41.48	49.271	15.67	0.372
XF366-t1	406	82	380	39.47	150	46300	2.00	926	865	17.35	150	207.926	47544	2.98	1417	14527	2.98	433	0.439	43.12	53.545	17.46	0.400
XF366-t2	350	61	550	27.27	150	63700	2.00	1274	1026	14.63	150	207.924	65492	2.69	1763	20098	2.69	541	0.536	30.95	62.110	14.76	0.468
XF366-t1	404	92	360	41.67	150	41140	2.00	823	766	19.59	150	207.923	42318	3.10	1314	12933	3.10	401	0.470	46.04	53.731	19.69	0.423
XF366-t6	374	55	630	23.81	150	71510	2.00	1430	1233	12.17	150	207.923	73567	2.61	1920	22534	2.61	588	0.511	26.74	58.010	12.33	0.449
XF366-t6	448	44	870	17.24	150	98640	2.00	1973	2039	7.36	150	207.922	101497	2.43	2465	30912	2.43	751	0.427	18.75	48.383	7.62	0.379
XF366-t1	353	100	330	45.45	150	36640	2.00	733	595	25.21	150	207.921	37716	3.24	1222	11572	3.24	375	0.555	51.98	61.591	25.29	0.484
XF366-t6	387	44	860	17.44	150	94320	2.00	1886	1682	8.92	150	207.921	97130	2.45	2377	29723	2.45	727	0.511	19.59	56.064	9.14	0.444
XF366-t6	433	46	840	17.86	150	92000	2.00	1840	1837	8.17	150	207.920	94755	2.46	2332	28894	2.46	711	0.457	19.64	50.088	8.41	0.404
XF366-t2	393	78	460	32.61	150	48740	2.00	975	884	16.97	150	207.919	50244	2.92	1465	15368	2.92	448	0.520	36.76	55.147	17.09	0.459
XF366-t6	406	48	810	18.52	150	85680	2.00	1714	1604	9.35	150	207.919	88331	2.50	2204	26991	2.50	674	0.505	20.74	53.404	9.56	0.441

(接附表二)

REF	Age Ma	Error Age Ma	U ppm	Error U %	Error U ppm	Th ppm	Error Th %	Error Th ppm	Pb ppm	Error Pb %	Error Pb ppm	MPb	Th*(U) ppm	Error Th* %	Error Th* ppm	U*(Th) ppm	Error U* %	Error U* ppm	U/Pb	Error U/Pb %	Th/Pb	Error Th/Pb %	Corr
XF366-t6	442	46	870	17.24	150	91390	2.00	1828	1866	8.04	150	207.918	94245	2.46	2320	28718	2.46	707	0.466	19.02	48.983	8.28	0.410
XF366-t6	452	50	800	18.75	150	83200	2.00	1664	1738	8.63	150	207.918	85827	2.51	2157	26133	2.51	657	0.460	20.64	47.883	8.86	0.407
XF366-t6	430	50	810	18.52	150	82170	2.00	1643	1636	9.17	150	207.916	84826	2.52	2135	25871	2.52	651	0.495	20.67	50.239	9.39	0.434
XF366-t2	387	78	480	31.25	150	48360	2.00	967	864	17.36	150	207.916	49929	2.92	1457	15279	2.92	446	0.556	35.75	55.984	17.48	0.483
XF366-t1	363	86	430	34.88	150	43050	2.00	861	721	20.81	150	207.916	44453	3.04	1350	13628	3.04	414	0.597	40.62	59.724	20.91	0.510
XF366-t6	453	46	930	16.13	150	91900	2.00	1838	1929	7.78	150	207.914	94955	2.45	2331	28909	2.45	710	0.482	17.91	47.647	8.03	0.421
XF366-t6	393	48	870	17.24	150	85120	2.00	1702	1547	9.70	150	207.914	87964	2.49	2193	26906	2.49	671	0.562	19.78	55.034	9.90	0.480
XF366-t6	414	52	840	17.86	150	77750	2.00	1555	1492	10.05	150	207.911	80501	2.54	2046	24583	2.54	625	0.563	20.49	52.117	10.25	0.481
XF366-t2	398	81	510	29.41	150	46330	2.00	927	856	17.53	150	207.909	47998	2.95	1417	14675	2.95	433	0.596	34.24	54.135	17.64	0.509
XF366-t6	440	64	700	21.43	150	61730	2.00	1235	1264	11.87	150	207.907	64027	2.70	1727	19512	2.70	526	0.554	24.50	48.844	12.04	0.478
XF366-t2	405	50	970	15.46	150	81270	2.00	1625	1533	9.78	150	207.904	84444	2.51	2116	25804	2.51	647	0.633	18.30	53.011	9.99	0.524
XF366-t6	447	62	760	19.74	150	63660	2.00	1273	1327	11.31	150	207.904	66155	2.67	1766	20150	2.67	538	0.573	22.75	47.982	11.48	0.489
XF366-t1	374	95	480	31.25	150	38850	2.00	777	675	22.21	150	207.902	40417	3.13	1267	12381	3.13	388	0.711	38.34	57.519	22.30	0.577
XF366-t1	385	91	540	27.78	150	40570	2.00	811	730	20.55	150	207.896	42334	3.07	1302	12956	3.07	398	0.740	34.55	55.575	20.65	0.592
XF366-t2	430	47	1170	12.82	150	86670	2.00	1733	1745	8.59	150	207.895	90506	2.46	2225	27603	2.46	679	0.670	15.43	49.653	8.82	0.542
XF366-t5	392	60	890	16.85	150	64180	2.00	1284	1176	12.75	150	207.893	67089	2.64	1774	20522	2.64	543	0.757	21.14	54.568	12.91	0.596
XF366-t2	411	45	1300	11.54	150	92270	2.00	1845	1779	8.43	150	207.891	96526	2.42	2337	29482	2.42	714	0.731	14.29	51.876	8.67	0.574
XF366-t2	467	59	970	15.46	150	68350	2.00	1367	1499	10.01	150	207.891	71540	2.60	1860	21756	2.60	566	0.647	18.42	45.607	10.21	0.533
XF366-t5	358	80	660	22.73	150	46300	2.00	926	776	19.33	150	207.891	48452	2.92	1415	14860	2.92	434	0.851	29.84	59.670	19.43	0.644
XF366-t6	384	60	910	16.48	150	63810	2.00	1276	1146	13.09	150	207.891	66783	2.64	1766	20442	2.64	541	0.794	21.05	55.674	13.24	0.615
XF366-t2	413	46	1260	11.90	150	87900	2.00	1758	1701	8.82	150	207.890	92026	2.44	2249	28105	2.44	687	0.741	14.81	51.665	9.04	0.580
XF366-t6	423	62	910	16.48	150	62400	2.00	1248	1238	12.11	150	207.889	65382	2.66	1740	19952	2.66	531	0.735	20.46	50.390	12.28	0.584
XF366-t5	432	53	1120	13.39	150	76290	2.00	1526	1547	9.70	150	207.888	79963	2.52	2018	24385	2.52	615	0.724	16.54	49.324	9.90	0.574
XF366-a2t2	429	83	670	22.39	150	45480	2.00	910	917	16.36	150	207.888	47677	2.94	1401	14542	2.94	427	0.731	27.73	49.616	16.49	0.586

附表二

(接附表二)

REF	Age Ma	Error Age Ma	U ppm	Error U %	Error U ppm	Th ppm	Error Th %	Error Th ppm	Pb ppm	Error Pb %	Error Pb ppm	MPb	Th*(U) ppm	Error Th* %	Error Th* ppm	U*(Th) ppm	Error U* %	Error U* ppm	U/Pb	Error U/Pb %	Th/Pb	Error Th/Pb %	Corr
XF366-t5	418	75	760	19.74	150	50070	2.00	1001	983	15.26	150	207.885	52559	2.84	1493	16046	2.84	456	0.773	24.95	50.929	15.39	0.606
XF366-t5	435	94	610	24.59	150	39420	2.00	788	808	18.57	150	207.883	41421	3.09	1280	12628	3.09	390	0.755	30.82	48.815	18.68	0.599
XF366-t5	372	74	790	18.99	150	50460	2.00	1009	882	17.02	150	207.883	53039	2.83	1499	16249	2.83	459	0.896	25.50	57.242	17.13	0.663
XF366-t5	416	76	800	18.75	150	49670	2.00	993	974	15.40	150	207.880	52290	2.84	1485	15965	2.84	453	0.821	24.26	50.984	15.53	0.629
XF366-t5	413	85	720	20.83	150	43370	2.00	867	846	17.74	150	207.877	45728	2.97	1359	13965	2.97	415	0.852	27.36	51.293	17.85	0.644
XF366-t5	420	75	830	18.07	150	49880	2.00	998	990	15.16	150	207.877	52599	2.83	1489	16055	2.83	454	0.839	23.59	50.402	15.29	0.637
XF366-t5	478	72	900	16.67	150	53660	2.00	1073	1213	12.37	150	207.876	56622	2.77	1567	17205	2.77	476	0.742	20.75	44.240	12.53	0.588
XF366-t5	443	68	970	15.46	150	56950	2.00	1139	1195	12.56	150	207.874	60134	2.71	1631	18321	2.71	497	0.812	19.92	47.667	12.71	0.622
XF366-t5	432	84	770	19.48	150	44100	2.00	882	903	16.61	150	207.872	46625	2.95	1374	14218	2.95	419	0.853	25.60	48.829	16.73	0.644
XF366-t6	428	55	1260	11.90	150	72080	2.00	1442	1461	10.27	150	207.872	76211	2.54	1933	23248	2.54	590	0.863	15.72	49.342	10.46	0.641
XF366-t5	389	73	900	16.67	150	50650	2.00	1013	933	16.07	150	207.871	53592	2.81	1503	16397	2.81	460	0.964	23.16	54.280	16.20	0.689
XF366-t5	459	76	890	16.85	150	49970	2.00	999	1088	13.79	150	207.870	52895	2.82	1492	16097	2.82	454	0.818	21.78	45.948	13.94	0.627
XF366-t5	412	55	1330	11.28	150	70840	2.00	1417	1386	10.82	150	207.865	75195	2.54	1908	22966	2.54	583	0.959	15.63	51.093	11.00	0.681
XF366-a2t1	399	82	840	17.86	150	44580	2.00	892	845	17.75	150	207.864	47328	2.92	1382	14469	2.92	423	0.994	25.18	52.764	17.87	0.701
XF366-a2t1	474	80	890	16.85	150	46990	2.00	940	1061	14.14	150	207.863	49918	2.87	1433	15173	2.87	436	0.839	22.00	44.299	14.28	0.636
XF366-t5	392	73	1000	15.00	150	50830	2.00	1017	948	15.82	150	207.860	54099	2.79	1507	16549	2.79	461	1.054	21.80	53.599	15.94	0.720
XF366-a2t1	452	79	940	15.96	150	47690	2.00	954	1029	14.58	150	207.859	50777	2.85	1446	15460	2.85	440	0.913	21.61	46.344	14.71	0.668
XF366-t5	407	62	1210	12.40	150	61120	2.00	1222	1187	12.64	150	207.859	65080	2.63	1713	19884	2.63	523	1.020	17.70	51.499	12.80	0.705
XF366-t5	442	77	970	15.46	150	48940	2.00	979	1033	14.51	150	207.859	52123	2.82	1471	15882	2.82	448	0.939	21.21	47.357	14.65	0.678
XF366-t5	425	57	1410	10.64	150	68070	2.00	1361	1384	10.84	150	207.854	72691	2.55	1853	22179	2.55	565	1.019	15.19	49.195	11.02	0.702
XF366-t5	455	84	920	16.30	150	44250	2.00	885	963	15.58	150	207.853	47272	2.91	1378	14390	2.91	419	0.955	22.55	45.949	15.70	0.685
XF366-t5	430	72	1110	13.51	150	52160	2.00	1043	1075	13.95	150	207.851	55799	2.75	1535	17018	2.75	468	1.033	19.42	48.519	14.10	0.711
XF366-a2t2	425	86	910	16.48	150	42460	2.00	849	864	17.36	150	207.850	45442	2.95	1341	13865	2.95	409	1.053	23.94	49.136	17.47	0.720
XF366-t6	393	98	830	18.07	150	36430	2.00	729	688	21.80	150	207.843	39144	3.11	1219	11973	3.11	373	1.206	28.32	52.939	21.89	0.767

(接附表二)

REF	Age Ma	Error Age Ma	U ppm	Error U %	Error U ppm	Th ppm	Error Th %	Error Th ppm	Pb ppm	Error Pb %	Error Pb ppm	MPb	Th*(U) ppm	Error Th* %	Error Th* ppm	U*(Th) ppm	Error U* %	Error U* ppm	U/Pb	Error U/Pb %	Th/Pb	Error Th/Pb %	Corr
XF366-t6	381	99	820	18.29	150	35820	2.00	716	656	22.88	150	207.842	38498	3.13	1206	11787	3.13	369	1.251	29.30	54.642	22.97	0.778
XF366-a2t2	496	93	920	16.30	150	39610	2.00	792	949	15.81	150	207.839	42642	3.02	1287	12939	3.02	390	0.970	22.71	41.745	15.93	0.691
XF366-t5	399	75	1150	13.04	150	48540	2.00	971	935	16.04	150	207.838	52302	2.79	1461	15989	2.79	447	1.230	20.68	51.918	16.17	0.770
XF366-t6	388	91	960	15.63	150	39290	2.00	786	736	20.38	150	207.834	42427	3.01	1276	12982	3.01	390	1.304	25.68	53.388	20.48	0.790
XF366-t6	422	104	860	17.44	150	33990	2.00	680	695	21.58	150	207.829	36808	3.18	1171	11233	3.18	357	1.237	27.75	48.904	21.67	0.774
XF366-t4	471	69	1410	10.64	150	54860	2.00	1097	1258	11.93	150	207.826	59498	2.67	1591	18088	2.67	484	1.121	15.98	43.622	12.09	0.736
XF366-t3	406	68	1410	10.64	150	54290	2.00	1086	1069	14.03	150	207.825	58904	2.68	1577	17999	2.68	482	1.319	17.61	50.780	14.17	0.789
XF366-t4	486	87	1110	13.51	150	42410	2.00	848	1004	14.95	150	207.823	46065	2.91	1342	13989	2.91	408	1.106	20.15	42.261	15.08	0.735
XF366-t3	466	71	1380	10.87	150	52570	2.00	1051	1193	12.57	150	207.823	57107	2.70	1545	17369	2.70	470	1.157	16.62	44.069	12.73	0.747
XF366-a2t2	431	90	1050	14.29	150	39640	2.00	793	831	18.05	150	207.822	43083	2.98	1285	13139	2.98	392	1.264	23.02	47.710	18.16	0.779
XF366-t3	460	115	820	18.29	150	30720	2.00	614	690	21.75	150	207.821	33415	3.31	1107	10167	3.31	337	1.189	28.42	44.551	21.85	0.762
XF366-t4	363	73	1330	11.28	150	49160	2.00	983	868	17.28	150	207.820	53498	2.75	1472	16401	2.75	451	1.532	20.63	56.620	17.39	0.832
XF366-t3	397	88	1110	13.51	150	40260	2.00	805	780	19.23	150	207.817	43890	2.95	1296	13420	2.95	396	1.423	23.50	51.614	19.33	0.814
XF366-t4	476	74	1390	10.79	150	50300	2.00	1006	1170	12.82	150	207.816	54874	2.73	1500	16677	2.73	456	1.188	16.76	42.983	12.97	0.756
XF366-t4	479	87	1150	13.04	150	41610	2.00	832	975	15.39	150	207.816	45395	2.92	1326	13793	2.92	403	1.180	20.18	42.697	15.52	0.757
XF366-t4	430	73	1380	10.87	150	49890	2.00	998	1047	14.33	150	207.816	54415	2.74	1490	16597	2.74	454	1.318	17.98	47.645	14.46	0.789
XF366-t4	416	92	1090	13.76	150	38590	2.00	772	786	19.09	150	207.813	42160	3.00	1263	12872	3.00	386	1.387	23.53	49.107	19.19	0.807
XF366-t4	442	91	1120	13.39	150	39460	2.00	789	854	17.57	150	207.812	43136	2.97	1281	13144	2.97	390	1.312	22.09	46.219	17.68	0.790
XF366-t3	332	109	890	16.85	150	31330	2.00	627	507	29.56	150	207.813	34226	3.26	1115	10518	3.26	343	1.754	34.03	61.737	29.63	0.867
XF366-a2t2	427	84	1220	12.30	150	42920	2.00	858	897	16.72	150	207.812	46919	2.88	1350	14313	2.88	412	1.360	20.75	47.830	16.84	0.800
XF366-t4	410	69	1530	9.80	150	52710	2.00	1054	1058	14.17	150	207.809	57719	2.68	1545	17632	2.68	472	1.446	17.23	49.810	14.32	0.814
XF366-a2t2	431	88	1190	12.61	150	40520	2.00	810	858	17.48	150	207.807	44422	2.93	1302	13547	2.93	397	1.387	21.55	47.213	17.59	0.806
XF366-a2t2	397	92	1140	13.16	150	38140	2.00	763	744	20.17	150	207.804	41868	2.99	1253	12802	2.99	383	1.533	24.08	51.282	20.27	0.833
XF366-t4	399	67	1630	9.20	150	53750	2.00	1075	1054	14.23	150	207.802	59081	2.65	1566	18063	2.65	479	1.547	16.95	51.001	14.37	0.832

附表二

(接附表二)

REF	Age Ma	Error Age Ma	U ppm	Error U %	Error U ppm	Th ppm	Error Th %	Error Th ppm	Pb ppm	Error Pb %	Error Pb ppm	MPb	Th*(U) ppm	Error Th* %	Error Th* ppm	U*(Th) ppm	Error U* %	Error U* ppm	U/Pb	Error U/Pb %	Th/Pb	Error Th/Pb %	Corr
XF366-t3	424	86	1260	11.90	150	41270	2.00	825	861	17.42	150	207.801	45399	2.90	1317	13853	2.90	402	1.463	21.10	47.915	17.53	0.820
XF366-a2t2	399	91	1180	12.71	150	38640	2.00	773	759	19.77	150	207.801	42500	2.97	1263	12993	2.97	386	1.555	23.50	50.919	19.87	0.837
XF366-t3	369	70	1570	9.55	150	50940	2.00	1019	925	16.21	150	207.800	56064	2.69	1508	17179	2.69	462	1.697	18.82	55.058	16.34	0.855
XF366-a2t2	415	80	1390	10.79	150	44120	2.00	882	905	16.58	150	207.796	48672	2.82	1374	14862	2.82	419	1.537	19.79	48.776	16.70	0.832
XF366-t3	394	87	1260	11.90	150	39990	2.00	800	777	19.30	150	207.796	44110	2.93	1290	13491	2.93	395	1.621	22.67	51.446	19.40	0.847
XF366-t3	472	112	1070	14.02	150	30940	2.00	619	729	20.56	150	207.779	34460	3.23	1112	10476	3.23	338	1.467	24.89	42.416	20.66	0.822
XF366-t3	405	97	1270	11.81	150	35560	2.00	711	719	20.86	150	207.774	39716	3.03	1202	12137	3.03	367	1.766	23.97	49.456	20.96	0.866
XF366-t3	433	103	1300	11.54	150	33160	2.00	663	726	20.67	150	207.756	37423	3.09	1155	11411	3.09	352	1.791	23.67	45.685	20.76	0.869
XF366-t1	438	98	1570	9.55	150	34340	2.00	687	774	19.38	150	207.725	39491	2.99	1179	12037	2.99	359	2.028	21.61	44.363	19.48	0.892

附表三 Hf 同位素数据表

Sample No.	Age (Ma)	$^{176}\text{Yb}/^{177}\text{Hf}$	2σ	$^{176}\text{Lu}/^{177}\text{Hf}$	2σ	$^{176}\text{Hf}/^{177}\text{Hf}$	2σ	$\epsilon_{\text{Hf}}(0)$	$\epsilon_{\text{Hf}}(t)$	$T_{\text{DM}}(\text{Ma})$	$T_{\text{DM}}^{\text{C}}(\text{Ma})$
XF17 01	220	0.027962	0.000212	0.000839	0.000003	0.282505	0.000024	-9.5	-4.8	1056	1561
XF17 02	220	0.037808	0.002016	0.001106	0.000060	0.282519	0.000021	-9.0	-4.4	1044	1532
XF17 03	220	0.027119	0.000689	0.000823	0.000021	0.282513	0.000019	-9.2	-4.5	1044	1543
XF17 04	220	0.022710	0.000316	0.000685	0.000008	0.282526	0.000020	-8.8	-4.0	1022	1513
XF17 05	220	0.028364	0.000162	0.000820	0.000006	0.282504	0.000021	-9.5	-4.8	1057	1563
XF17 06	220	0.029147	0.000949	0.000859	0.000027	0.282509	0.000018	-9.4	-4.7	1051	1552
XF17 07	220	0.028683	0.000208	0.000845	0.000003	0.282500	0.000020	-9.7	-5.0	1063	1572
XF17 08	220	0.037887	0.000265	0.001125	0.000008	0.282527	0.000018	-8.7	-4.1	1033	1514
XF17 09	220	0.022979	0.000244	0.000686	0.000007	0.282515	0.000018	-9.2	-4.4	1038	1537
XF17 10	220	0.027862	0.000177	0.000856	0.000003	0.282551	0.000019	-7.9	-3.2	992	1458
XF17 11	220	0.030732	0.001493	0.000901	0.000042	0.282529	0.000018	-8.7	-4.0	1024	1508
XF17 12	220	0.025457	0.000326	0.000764	0.000008	0.282524	0.000017	-8.8	-4.1	1027	1518
XF17 13	220	0.044609	0.000836	0.001289	0.000024	0.282561	0.000020	-7.5	-2.9	989	1440
XF17 14	220	0.036978	0.001113	0.001072	0.000030	0.282536	0.000018	-8.4	-3.7	1019	1494
XF17 17	220	0.029017	0.000701	0.000847	0.000018	0.282583	0.000017	-6.8	-2.1	947	1386
XF17 18	220	0.041880	0.001198	0.001184	0.000033	0.282552	0.000018	-7.9	-3.2	999	1459
XF17 19	220	0.037927	0.001703	0.001102	0.000047	0.282557	0.000020	-7.7	-3.0	990	1447
XF17 20	220	0.028717	0.000276	0.000849	0.000006	0.282531	0.000017	-8.6	-3.9	1020	1503
XF73 01	219	0.035201	0.000390	0.001023	0.000010	0.282444	0.000022	-11.7	-7.0	1147	1699
XF73 02	219	0.051097	0.000971	0.001359	0.000024	0.282438	0.000027	-11.9	-7.3	1166	1716
XF73 03	219	0.061500	0.000548	0.001615	0.000011	0.282490	0.000019	-10.0	-5.5	1099	1602

附表三

(接附表三)

Sample No.	Age (Ma)	$^{176}\text{Yb}/^{177}\text{Hf}$	2σ	$^{176}\text{Lu}/^{177}\text{Hf}$	2σ	$^{176}\text{Hf}/^{177}\text{Hf}$	2σ	$\epsilon_{\text{Hf}}(0)$	$\epsilon_{\text{Hf}}(t)$	$T_{\text{DM}}(\text{Ma})$	$T_{\text{DM}}^{\text{c}}(\text{Ma})$
XF73 04	219	0.083120	0.000320	0.002190	0.000005	0.282480	0.000020	-10.4	-5.9	1131	1630
XF73 05	219	0.052316	0.000853	0.001355	0.000020	0.282485	0.000021	-10.2	-5.6	1099	1611
XF73 06	219	0.043149	0.000545	0.001162	0.000012	0.282448	0.000018	-11.5	-6.9	1145	1692
XF73 07	219	0.039112	0.000185	0.001072	0.000002	0.282451	0.000017	-11.4	-6.8	1138	1684
XF73 08	219	0.040676	0.001472	0.001091	0.000037	0.282390	0.000020	-13.6	-8.9	1225	1820
XF73 09	219	0.034035	0.000721	0.000906	0.000017	0.282375	0.000018	-14.1	-9.4	1240	1852
XF73 10	219	0.037735	0.000253	0.001001	0.000006	0.282353	0.000017	-14.9	-10.2	1274	1901
XF73 11	219	0.070951	0.003445	0.001793	0.000072	0.282558	0.000023	-7.6	-3.1	1007	1452
XF73 12	219	0.068879	0.001518	0.001758	0.000042	0.282485	0.000021	-10.2	-5.7	1111	1614
XF73 13	219	0.031314	0.000695	0.000840	0.000015	0.282383	0.000018	-13.8	-9.1	1226	1833
XF73 14	219	0.038594	0.000186	0.001018	0.000003	0.282353	0.000019	-14.9	-10.2	1274	1902
XF73 15	219	0.064917	0.000591	0.001690	0.000015	0.282430	0.000019	-12.2	-7.6	1187	1736
XF73 16	219	0.034877	0.000909	0.000907	0.000021	0.282442	0.000019	-11.7	-7.1	1146	1703
XF73 17	219	0.034636	0.000399	0.000906	0.000008	0.282348	0.000016	-15.1	-10.4	1277	1912
XF73 18	219	0.073583	0.000892	0.001938	0.000027	0.282389	0.000015	-13.6	-9.1	1254	1830
XF73 19	219	0.060591	0.000119	0.001568	0.000005	0.282469	0.000017	-10.8	-6.2	1128	1648
XF205 01	222	0.059904	0.000762	0.001586	0.000017	0.282530	0.000025	-8.6	-4.0	1041	1511
XF205 02	222	0.060969	0.000693	0.001613	0.000014	0.282457	0.000020	-11.2	-6.6	1146	1674
XF205 03	222	0.045805	0.001676	0.001234	0.000042	0.282541	0.000021	-8.2	-3.6	1016	1483
XF205 04	222	0.078138	0.001215	0.002067	0.000027	0.282494	0.000020	-9.9	-5.3	1107	1596
XF205 05	222	0.051259	0.000827	0.001359	0.000019	0.282530	0.000019	-8.6	-4.0	1035	1509
XF205 06	222	0.071730	0.000700	0.001942	0.000014	0.282459	0.000015	-11.1	-6.6	1154	1673

(接附表三)

Sample No.	Age (Ma)	$^{176}\text{Yb}/^{177}\text{Hf}$	2σ	$^{176}\text{Lu}/^{177}\text{Hf}$	2σ	$^{176}\text{Hf}/^{177}\text{Hf}$	2σ	$\epsilon_{\text{Hf}}(0)$	$\epsilon_{\text{Hf}}(t)$	$T_{\text{DM}}(\text{Ma})$	$T_{\text{DM}}^{\text{c}}(\text{Ma})$
XF205 07	222	0.075955	0.002380	0.002011	0.000058	0.282542	0.000018	-8.2	-3.6	1036	1488
XF205 08	222	0.040104	0.000258	0.001084	0.000007	0.282513	0.000018	-9.2	-4.5	1051	1544
XF205 09	222	0.036404	0.000498	0.001021	0.000015	0.282508	0.000017	-9.4	-4.7	1057	1555
XF205 10	222	0.048117	0.000667	0.001302	0.000016	0.282461	0.000017	-11.1	-6.4	1131	1663
XF205 11	222	0.052667	0.001203	0.001506	0.000033	0.282556	0.000016	-7.7	-3.1	1002	1452
XF205 12	222	0.024948	0.000234	0.000694	0.000005	0.282469	0.000014	-10.8	-6.0	1102	1639
XF205 13	222	0.044796	0.000324	0.001190	0.000006	0.282534	0.000019	-8.5	-3.8	1025	1498
XF205 14	222	0.058166	0.002602	0.001555	0.000064	0.282529	0.000018	-8.7	-4.0	1042	1513
XF205 15	222	0.050914	0.001409	0.001363	0.000036	0.282494	0.000013	-9.9	-5.2	1086	1589
XF205 16	222	0.047596	0.000126	0.001259	0.000005	0.282532	0.000013	-8.6	-3.9	1029	1504
XF205 17	222	0.050343	0.001149	0.001325	0.000027	0.282466	0.000016	-10.9	-6.2	1125	1652
XF205 18	222	0.091342	0.003140	0.002448	0.000081	0.282489	0.000019	-10.1	-5.6	1126	1611
XF208 01	225	0.040510	0.000087	0.001106	0.000001	0.282508	0.000025	-9.4	-4.6	1059	1554
XF208 02	225	0.054163	0.000575	0.001445	0.000011	0.282558	0.000026	-7.6	-2.9	998	1445
XF208 03	225	0.055357	0.001207	0.001486	0.000029	0.282461	0.000022	-11.1	-6.3	1137	1662
XF208 04	225	0.033366	0.000038	0.000917	0.000002	0.282528	0.000024	-8.7	-3.9	1026	1507
XF208 05	225	0.045014	0.000471	0.001228	0.000016	0.282512	0.000028	-9.3	-4.5	1057	1546
XF208 06	225	0.054491	0.001092	0.001457	0.000026	0.282489	0.000023	-10.1	-5.4	1096	1599
XF208 07	225	0.027250	0.000311	0.000743	0.000008	0.282505	0.000019	-9.5	-4.7	1053	1557
XF208 08	225	0.045368	0.000255	0.001252	0.000005	0.282517	0.000020	-9.1	-4.3	1051	1535
XF208 09	225	0.043496	0.000396	0.001208	0.000010	0.282491	0.000018	-10.0	-5.2	1086	1593
XF208 10	225	0.032070	0.000627	0.000893	0.000014	0.282549	0.000017	-8.0	-3.1	996	1460

附表三

(接附表三)

Sample No.	Age (Ma)	$^{176}\text{Yb}/^{177}\text{Hf}$	2σ	$^{176}\text{Lu}/^{177}\text{Hf}$	2σ	$^{176}\text{Hf}/^{177}\text{Hf}$	2σ	$\epsilon_{\text{Hf}}(0)$	$\epsilon_{\text{Hf}}(t)$	$T_{\text{DM}}(\text{Ma})$	$T_{\text{DM}}^{\text{c}}(\text{Ma})$
XF208 11	225	0.050653	0.000770	0.001347	0.000019	0.282527	0.000019	-8.7	-4.0	1039	1513
XF208 12	225	0.051639	0.000266	0.001361	0.000005	0.282515	0.000020	-9.2	-4.4	1056	1540
XF208 13	225	0.040805	0.000879	0.001089	0.000020	0.282504	0.000020	-9.5	-4.8	1064	1562
XF208 14	225	0.037457	0.000194	0.001011	0.000006	0.282520	0.000018	-9.0	-4.2	1040	1526
XF208 15	225	0.045885	0.000309	0.001263	0.000005	0.282509	0.000020	-9.4	-4.6	1062	1553
XF208 16	225	0.093841	0.001761	0.002425	0.000041	0.282570	0.000020	-7.2	-2.6	1007	1427
XF208 17	225	0.042403	0.000320	0.001139	0.000007	0.282491	0.000016	-10.0	-5.2	1084	1592
XF213 01	224	0.042245	0.001059	0.001149	0.000026	0.282176	0.000028	-21.1	-16.4	1527	2292
XF213 03	257	0.026408	0.000836	0.000784	0.000025	0.282313	0.000019	-16.3	-10.8	1322	1967
XF213 04	1846	0.025845	0.000160	0.000655	0.000005	0.281425	0.000020	-47.7	-7.4	2535	2991
XF213 05	1692	0.042283	0.000482	0.001200	0.000011	0.281615	0.000018	-41.0	-4.7	2309	2701
XF213 07	1008	0.041506	0.001325	0.000970	0.000033	0.282101	0.000017	-23.8	-2.2	1624	2008
XF213 08	909	0.007521	0.000058	0.000236	0.000001	0.282365	0.000022	-14.5	5.5	1232	1444
XF213 09	1366	0.033931	0.000120	0.000987	0.000003	0.281708	0.000017	-37.7	-8.3	2168	2676
XF213 10	224	0.059296	0.001182	0.001519	0.000030	0.282535	0.000021	-8.5	-3.8	1032	1498
XF213 11	224	0.130216	0.001170	0.003325	0.000034	0.282630	0.000024	-5.1	-0.7	943	1302
XF213 12	224	0.003217	0.000039	0.000073	0.000001	0.282251	0.000018	-18.5	-13.6	1382	2117
XF213 13	224	0.040222	0.000324	0.001037	0.000009	0.282445	0.000019	-11.6	-6.9	1146	1695
XF213 15	224	0.004622	0.000043	0.000106	0.000001	0.282280	0.000017	-17.5	-12.6	1344	2053
XF213 16	224	0.094061	0.000867	0.002563	0.000027	0.282401	0.000019	-13.2	-8.7	1258	1807
XF213 17	224	0.127325	0.000933	0.003516	0.000024	0.282494	0.000016	-9.9	-5.5	1153	1608

(接附表三)

Sample No.	Age (Ma)	$^{176}\text{Yb}/^{177}\text{Hf}$	2σ	$^{176}\text{Lu}/^{177}\text{Hf}$	2σ	$^{176}\text{Hf}/^{177}\text{Hf}$	2σ	$\epsilon_{\text{Hf}}(0)$	$\epsilon_{\text{Hf}}(t)$	$T_{\text{DM}}(\text{Ma})$	$T_{\text{DM}}^{\text{c}}(\text{Ma})$
XF216 01	223	0.085280	0.003328	0.002138	0.000083	0.282476	0.000020	-10.5	-6.0	1135	1636
XF216 02	223	0.086322	0.007007	0.002210	0.000176	0.282584	0.000024	-6.7	-2.2	981	1395
XF216 03	223	0.052627	0.000792	0.001413	0.000021	0.282464	0.000020	-11.0	-6.3	1130	1656
XF216 04	223	0.051992	0.000312	0.001383	0.000007	0.282460	0.000020	-11.1	-6.4	1135	1665
XF216 05	223	0.070719	0.005650	0.001881	0.000146	0.282490	0.000021	-10.0	-5.4	1107	1603
XF216 06	223	0.048402	0.003869	0.001301	0.000102	0.282437	0.000022	-11.9	-7.2	1165	1715
XF216 07	223	0.051339	0.001849	0.001376	0.000049	0.282474	0.000018	-10.6	-5.9	1115	1634
XF216 08	223	0.032428	0.000856	0.000874	0.000022	0.282504	0.000016	-9.5	-4.8	1058	1562
XF216 09	223	0.045320	0.001111	0.001249	0.000028	0.282489	0.000017	-10.1	-5.4	1090	1599
XF216 10	223	0.060531	0.001804	0.001630	0.000044	0.282448	0.000019	-11.5	-6.9	1160	1694
XF216 11	223	0.064109	0.004038	0.001722	0.000103	0.282472	0.000019	-10.7	-6.0	1128	1641
XF216 12	223	0.048869	0.001758	0.001360	0.000047	0.282498	0.000014	-9.8	-5.1	1081	1580
XF216 13	223	0.039437	0.000847	0.001092	0.000022	0.282454	0.000019	-11.3	-6.6	1135	1676
XF216 14	223	0.066444	0.002093	0.001763	0.000054	0.282474	0.000019	-10.6	-6.0	1127	1637
XF216 15	223	0.035248	0.001262	0.000969	0.000034	0.282483	0.000018	-10.3	-5.5	1090	1610
XF216 16	223	0.054059	0.001329	0.001488	0.000034	0.282495	0.000019	-9.9	-5.2	1089	1588
XF216 17	223	0.049692	0.001360	0.001399	0.000035	0.282438	0.000020	-11.9	-7.2	1167	1714
XF216 18	223	0.056647	0.000494	0.001579	0.000015	0.282437	0.000022	-11.9	-7.3	1174	1718
XF216 19	223	0.035384	0.001125	0.001022	0.000031	0.282496	0.000021	-9.8	-5.1	1074	1581
XF216 20	223	0.029826	0.000338	0.000820	0.000008	0.282528	0.000018	-8.7	-3.9	1023	1508
XF216 21	223	0.105750	0.004794	0.002640	0.000133	0.282537	0.000024	-8.4	-3.9	1062	1505
XF216 22	223	0.070411	0.001550	0.001941	0.000037	0.282540	0.000027	-8.3	-3.7	1037	1491

附表三

(接附表三)

Sample No.	Age (Ma)	$^{176}\text{Yb}/^{177}\text{Hf}$	2σ	$^{176}\text{Lu}/^{177}\text{Hf}$	2σ	$^{176}\text{Hf}/^{177}\text{Hf}$	2σ	$\epsilon_{\text{Hf}}(0)$	$\epsilon_{\text{Hf}}(t)$	$T_{\text{DM}}(\text{Ma})$	$T_{\text{DM}}^{\text{c}}(\text{Ma})$
XF221 01	217	0.042916	0.000337	0.001163	0.000008	0.282481	0.000021	-10.4	-5.8	1099	1619
XF221 02	217	0.022280	0.000408	0.000611	0.000010	0.282447	0.000020	-11.6	-6.9	1130	1690
XF221 03	217	0.029083	0.000151	0.000814	0.000005	0.282470	0.000020	-10.8	-6.1	1104	1640
XF221 04	217	0.025506	0.000393	0.000710	0.000009	0.282415	0.000019	-12.7	-8.0	1178	1762
XF221 05	217	0.035025	0.000661	0.000945	0.000016	0.282463	0.000020	-11.0	-6.4	1118	1657
XF221 06	217	0.020038	0.000313	0.000548	0.000007	0.282496	0.000021	-9.8	-5.1	1060	1580
XF221 07	217	0.028398	0.000178	0.000775	0.000004	0.282448	0.000021	-11.5	-6.9	1134	1689
XF221 08	217	0.031445	0.000290	0.000887	0.000007	0.282398	0.000020	-13.3	-8.7	1207	1801
XF221 09	217	0.026121	0.000140	0.000708	0.000002	0.282487	0.000019	-10.1	-5.5	1077	1601
XF221 10	217	0.038774	0.001149	0.001040	0.000028	0.282460	0.000018	-11.1	-6.5	1125	1665
XF221 11	217	0.022962	0.000392	0.000635	0.000010	0.282473	0.000017	-10.6	-6.0	1095	1632
XF221 12	217	0.025225	0.000289	0.000708	0.000007	0.282458	0.000016	-11.2	-6.5	1118	1666
XF221 13	217	0.025542	0.000487	0.000717	0.000013	0.282457	0.000018	-11.2	-6.5	1119	1669
XF221 14	217	0.022719	0.000967	0.000629	0.000027	0.282525	0.000019	-8.8	-4.1	1022	1516
XF221 15	217	0.034215	0.000198	0.000932	0.000004	0.282497	0.000018	-9.8	-5.2	1070	1581
XF221 16	217	0.038497	0.000050	0.001066	0.000001	0.282480	0.000020	-10.4	-5.8	1097	1620
XF221 17	217	0.020871	0.000213	0.000581	0.000005	0.282480	0.000022	-10.4	-5.7	1084	1616
XF221 18	217	0.030208	0.000205	0.000816	0.000004	0.282461	0.000019	-11.1	-6.4	1117	1660
XF221 19	217	0.032007	0.000334	0.000859	0.000007	0.282498	0.000021	-9.8	-5.1	1066	1578
XF221 20	217	0.037898	0.000383	0.001018	0.000008	0.282517	0.000016	-9.1	-4.5	1044	1537
XF76 01	428	0.033163	0.000269	0.000913	0.000005	0.282342	0.000024	-15.3	-6.1	1286	1807
XF76 02	428	0.037185	0.000190	0.001018	0.000003	0.282292	0.000020	-17.0	-7.9	1360	1920

(接附表三)

Sample No.	Age (Ma)	$^{176}\text{Yb}/^{177}\text{Hf}$	2σ	$^{176}\text{Lu}/^{177}\text{Hf}$	2σ	$^{176}\text{Hf}/^{177}\text{Hf}$	2σ	$\epsilon_{\text{Hf}}(0)$	$\epsilon_{\text{Hf}}(t)$	$T_{\text{DM}}(\text{Ma})$	$T_{\text{DM}}^{\text{c}}(\text{Ma})$
XF76 03	956	0.027173	0.000060	0.000750	0.000000	0.282347	0.000022	-15.1	5.6	1274	1475
XF76 04	428	0.049128	0.000409	0.001342	0.000008	0.282279	0.000019	-17.5	-8.5	1390	1955
XF76 05	428	0.052682	0.000107	0.001411	0.000005	0.282314	0.000025	-16.3	-7.3	1343	1878
XF76 06	428	0.041456	0.000496	0.001115	0.000011	0.282354	0.000021	-14.9	-5.8	1276	1784
XF76 07	428	0.027948	0.000780	0.000748	0.000020	0.282273	0.000018	-17.7	-8.5	1376	1958
XF76 08	428	0.029003	0.000352	0.000808	0.000008	0.282309	0.000017	-16.4	-7.3	1328	1879
XF76 09	428	0.031073	0.000142	0.000838	0.000002	0.282313	0.000018	-16.3	-7.1	1324	1870
XF76 10	823	0.077052	0.000665	0.002070	0.000022	0.282209	0.000016	-20.0	-3.0	1518	1914
XF76 11	803	0.083997	0.001039	0.002259	0.000025	0.282156	0.000017	-21.9	-5.4	1602	2050
XF76 12	428	0.038481	0.001979	0.000987	0.000048	0.282274	0.000019	-17.7	-8.6	1384	1960
XF76 13	428	0.022638	0.000166	0.000621	0.000003	0.282272	0.000016	-17.8	-8.5	1373	1958
XF76 14	428	0.045302	0.000222	0.001184	0.000004	0.282323	0.000017	-15.9	-6.9	1322	1854
XF76 15	428	0.037387	0.000428	0.000999	0.000009	0.282269	0.000019	-17.9	-8.7	1391	1971
XF76 16	428	0.055192	0.000453	0.001454	0.000009	0.282269	0.000017	-17.9	-8.9	1408	1979
XF76 17	428	0.046632	0.000160	0.001250	0.000005	0.282286	0.000018	-17.3	-8.2	1376	1938
XF93 01	438	0.030938	0.000157	0.000861	0.000003	0.282397	0.000022	-13.3	-4.0	1208	1677
XF93 02	438	0.038221	0.000286	0.001059	0.000006	0.282400	0.000020	-13.2	-3.9	1210	1674
XF93 03	438	0.030586	0.000112	0.000838	0.000001	0.282376	0.000020	-14.1	-4.7	1236	1724
XF93 04	438	0.026446	0.000157	0.000720	0.000002	0.282378	0.000018	-14.0	-4.6	1230	1717
XF93 05	438	0.022098	0.000529	0.000611	0.000013	0.282346	0.000018	-15.1	-5.7	1270	1787
XF93 06	438	0.046132	0.000106	0.001247	0.000004	0.282366	0.000018	-14.4	-5.2	1264	1754
XF93 07	438	0.023307	0.000156	0.000633	0.000004	0.282294	0.000018	-17.0	-7.5	1343	1903

附表三

(接附表三)

Sample No.	Age (Ma)	$^{176}\text{Yb}/^{177}\text{Hf}$	2σ	$^{176}\text{Lu}/^{177}\text{Hf}$	2σ	$^{176}\text{Hf}/^{177}\text{Hf}$	2σ	$\epsilon_{\text{Hf}}(0)$	$\epsilon_{\text{Hf}}(t)$	$T_{\text{DM}}(\text{Ma})$	$T_{\text{DM}}^{\text{c}}(\text{Ma})$
XF93 08	438	0.051061	0.000310	0.001370	0.000005	0.282346	0.000018	-15.1	-5.9	1296	1800
XF93 09	438	0.036352	0.000146	0.000990	0.000002	0.282425	0.000016	-12.3	-3.0	1172	1617
XF93 10	438	0.039357	0.000181	0.001066	0.000005	0.282365	0.000017	-14.5	-5.1	1259	1752
XF93 11	438	0.030334	0.000148	0.000824	0.000002	0.282392	0.000018	-13.5	-4.1	1213	1688
XF93 12	438	0.031981	0.000140	0.000874	0.000002	0.282402	0.000018	-13.2	-3.8	1201	1666
XF93 13	438	0.035996	0.000261	0.000989	0.000005	0.282440	0.000017	-11.8	-2.5	1151	1583
XF93 14	438	0.023551	0.000575	0.000652	0.000013	0.282357	0.000018	-14.7	-5.3	1256	1763
XF93 15	438	0.035464	0.000124	0.000956	0.000002	0.282438	0.000016	-11.9	-2.5	1153	1587
XF93 16	438	0.041438	0.000593	0.001108	0.000017	0.282328	0.000019	-15.8	-6.5	1312	1836
XF93 17	438	0.032324	0.000128	0.000868	0.000004	0.282392	0.000018	-13.5	-4.1	1215	1688
XF93 18	438	0.035475	0.000310	0.000939	0.000007	0.282360	0.000017	-14.6	-5.3	1262	1761
XF93 19	438	0.037677	0.000642	0.001021	0.000018	0.282369	0.000018	-14.3	-5.0	1252	1743
XF93 20	438	0.037734	0.000100	0.001033	0.000005	0.282420	0.000017	-12.5	-3.2	1181	1629
XF93 21	438	0.032359	0.000084	0.000915	0.000001	0.282424	0.000018	-12.4	-3.0	1171	1618
XF93 22	438	0.033565	0.000115	0.000930	0.000002	0.282403	0.000019	-13.1	-3.8	1201	1665
XF99 01	437	0.062673	0.000682	0.001678	0.000015	0.282337	0.000016	-15.5	-6.3	1320	1827
XF99 02	437	0.058591	0.000664	0.001530	0.000019	0.282339	0.000018	-15.4	-6.2	1312	1820
XF99 03	437	0.078032	0.000936	0.001991	0.000027	0.282456	0.000023	-11.2	-2.2	1160	1566
XF99 04	437	0.032604	0.000442	0.000836	0.000010	0.282372	0.000018	-14.2	-4.9	1242	1733
XF99 05	437	0.056210	0.000293	0.001486	0.000007	0.282334	0.000019	-15.6	-6.4	1317	1830
XF99 06	437	0.057674	0.000720	0.001527	0.000017	0.282369	0.000017	-14.3	-5.2	1269	1753
XF99 07	437	0.051089	0.000476	0.001363	0.000010	0.282340	0.000018	-15.3	-6.1	1304	1814

(接附表三)

Sample No.	Age (Ma)	$^{176}\text{Yb}/^{177}\text{Hf}$	2σ	$^{176}\text{Lu}/^{177}\text{Hf}$	2σ	$^{176}\text{Hf}/^{177}\text{Hf}$	2σ	$\epsilon_{\text{Hf}}(0)$	$\epsilon_{\text{Hf}}(t)$	$T_{\text{DM}}(\text{Ma})$	$T_{\text{DM}}^{\text{c}}(\text{Ma})$
XF99 08	437	0.047418	0.001811	0.001262	0.000045	0.282275	0.000017	-17.6	-8.4	1392	1958
XF99 09	437	0.044427	0.001099	0.001199	0.000028	0.282322	0.000017	-16.0	-6.7	1324	1852
XF99 11	437	0.044545	0.001401	0.001166	0.000036	0.282307	0.000017	-16.5	-7.3	1344	1884
XF99 12	437	0.040732	0.001524	0.001094	0.000042	0.282358	0.000018	-14.7	-5.4	1270	1769
XF99 13	939	0.014695	0.000367	0.000342	0.000009	0.281946	0.000016	-29.3	-8.8	1809	2372
XF99 14	437	0.052697	0.000617	0.001404	0.000013	0.282371	0.000020	-14.3	-5.1	1262	1746
XF99 15	437	0.063033	0.001786	0.001693	0.000043	0.282385	0.000018	-13.8	-4.6	1252	1720
XF99 16	437	0.056484	0.000524	0.001530	0.000015	0.282380	0.000017	-13.9	-4.8	1253	1728
XF99 17	437	0.028200	0.000876	0.000775	0.000021	0.282199	0.000017	-20.3	-11.0	1480	2118
XF99 18	437	0.073541	0.000933	0.001986	0.000025	0.282375	0.000017	-14.1	-5.1	1276	1748
XF219 01	411	0.041321	0.000589	0.001145	0.000013	0.282399	0.000027	-13.3	-4.5	1214	1693
XF219 02	411	0.034234	0.001057	0.000924	0.000026	0.282329	0.000023	-15.7	-7.0	1305	1846
XF219 03	411	0.036932	0.000430	0.001080	0.000012	0.282374	0.000020	-14.1	-5.4	1247	1748
XF219 04	411	0.063325	0.000619	0.001766	0.000016	0.282372	0.000024	-14.2	-5.7	1273	1764
XF219 05	411	0.052810	0.000622	0.001509	0.000022	0.282409	0.000022	-12.9	-4.3	1211	1677
XF219 06	411	0.095006	0.000734	0.002435	0.000020	0.282421	0.000022	-12.5	-4.1	1225	1666
XF219 07	411	0.043054	0.000467	0.001206	0.000012	0.282378	0.000016	-14.0	-5.3	1245	1741
XF219 08	411	0.049518	0.000471	0.001387	0.000010	0.282427	0.000019	-12.3	-3.6	1182	1635
XF219 09	411	0.063633	0.000227	0.001781	0.000007	0.282450	0.000022	-11.5	-2.9	1162	1590
XF219 10	411	0.040820	0.000226	0.001152	0.000004	0.282395	0.000017	-13.4	-4.7	1220	1702
XF219 11	411	0.031305	0.000164	0.000902	0.000004	0.282403	0.000017	-13.1	-4.3	1200	1680
XF219 12	411	0.042146	0.000540	0.001202	0.000013	0.282405	0.000022	-13.0	-4.3	1207	1681

附表三

(接附表三)

Sample No.	Age (Ma)	$^{176}\text{Yb}/^{177}\text{Hf}$	2σ	$^{176}\text{Lu}/^{177}\text{Hf}$	2σ	$^{176}\text{Hf}/^{177}\text{Hf}$	2σ	$\epsilon_{\text{Hf}}(0)$	$\epsilon_{\text{Hf}}(t)$	$T_{\text{DM}}(\text{Ma})$	$T_{\text{DM}}^{\text{c}}(\text{Ma})$
XF219 14	411	0.037737	0.000153	0.001090	0.000004	0.282375	0.000013	-14.1	-5.4	1246	1746
XF219 15	411	0.033795	0.001364	0.000971	0.000037	0.282395	0.000017	-13.4	-4.6	1214	1699
XF219 16	411	0.052341	0.000681	0.001494	0.000021	0.282398	0.000023	-13.3	-4.7	1227	1702
XF219 17	411	0.053310	0.001381	0.001512	0.000039	0.282391	0.000020	-13.5	-4.9	1237	1718
XF219 18	411	0.053590	0.001827	0.001477	0.000050	0.282421	0.000023	-12.5	-3.9	1193	1650
XF219 19	411	0.031658	0.000088	0.000903	0.000002	0.282408	0.000017	-12.9	-4.2	1194	1669
XF270 01	412	0.044294	0.002187	0.001169	0.000056	0.282411	0.000018	-12.8	-4.1	1198	1666
XF270 02	412	0.042234	0.000443	0.001129	0.000009	0.282306	0.000020	-16.6	-7.8	1344	1900
XF270 03	412	0.036790	0.000840	0.001017	0.000021	0.282374	0.000017	-14.1	-5.4	1245	1746
XF270 04	412	0.049725	0.000652	0.001320	0.000016	0.282438	0.000019	-11.9	-3.2	1164	1608
XF270 05	412	0.037722	0.000796	0.001031	0.000021	0.282391	0.000018	-13.5	-4.8	1221	1708
XF270 06	412	0.026398	0.000797	0.000718	0.000019	0.282356	0.000018	-14.8	-5.9	1260	1781
XF270 07	412	0.032086	0.000453	0.000815	0.000008	0.282386	0.000019	-13.7	-4.9	1221	1716
XF270 08	412	0.041556	0.000324	0.001116	0.000007	0.282363	0.000017	-14.5	-5.8	1263	1772
XF270 09	412	0.033819	0.000093	0.000917	0.000001	0.282372	0.000017	-14.2	-5.4	1244	1749
XF270 10	412	0.030779	0.000072	0.000819	0.000003	0.282323	0.000018	-15.9	-7.1	1309	1857
XF270 11	412	0.050937	0.000730	0.001379	0.000017	0.282379	0.000016	-14.0	-5.3	1250	1741
XF270 12	412	0.039480	0.000732	0.001047	0.000023	0.282370	0.000018	-14.3	-5.5	1251	1756
XF270 13	412	0.039020	0.000904	0.001048	0.000023	0.282426	0.000019	-12.3	-3.5	1173	1630
XF270 14	412	0.035925	0.000121	0.000960	0.000002	0.282381	0.000018	-13.9	-5.1	1233	1730
XF270 15	412	0.053262	0.000484	0.001367	0.000014	0.282396	0.000020	-13.4	-4.7	1225	1703
XF270 16	412	0.068641	0.000515	0.001801	0.000014	0.282352	0.000018	-14.9	-6.4	1303	1809

(接附表三)

Sample No.	Age (Ma)	$^{176}\text{Yb}/^{177}\text{Hf}$	2σ	$^{176}\text{Lu}/^{177}\text{Hf}$	2σ	$^{176}\text{Hf}/^{177}\text{Hf}$	2σ	$\epsilon_{\text{Hf}}(0)$	$\epsilon_{\text{Hf}}(t)$	$T_{\text{DM}}(\text{Ma})$	$T_{\text{DM}}^{\text{c}}(\text{Ma})$
XF270 17	412	0.021747	0.000218	0.000602	0.000007	0.282404	0.000017	-13.1	-4.2	1190	1672
XF270 18	412	0.038918	0.000199	0.001003	0.000004	0.282388	0.000020	-13.7	-4.9	1225	1715
XF270 19	412	0.037950	0.000154	0.000958	0.000005	0.282463	0.000019	-11.0	-2.2	1118	1546
XF274 01	424	0.038692	0.001144	0.001054	0.000032	0.282343	0.000019	-15.2	-6.2	1289	1810
XF274 02	424	0.021986	0.000152	0.000593	0.000003	0.282364	0.000021	-14.5	-5.4	1245	1754
XF274 03	424	0.042386	0.001844	0.001254	0.000052	0.282469	0.000017	-10.8	-1.8	1118	1531
XF274 04	424	0.041166	0.000674	0.001073	0.000014	0.282366	0.000018	-14.4	-5.4	1258	1759
XF274 05	424	0.035442	0.000066	0.000941	0.000003	0.282362	0.000018	-14.6	-5.5	1259	1765
XF274 06	424	0.066411	0.000959	0.001753	0.000028	0.282414	0.000017	-12.7	-3.9	1212	1663
XF274 07	424	0.031318	0.000620	0.000850	0.000015	0.282421	0.000015	-12.5	-3.4	1174	1632
XF274 08	424	0.024335	0.000293	0.000655	0.000009	0.282368	0.000016	-14.4	-5.2	1241	1747
XF274 09	424	0.026226	0.000488	0.000697	0.000011	0.282370	0.000018	-14.3	-5.2	1240	1743
XF274 10	424	0.045042	0.001156	0.001187	0.000032	0.282382	0.000017	-13.9	-4.9	1239	1725
XF274 11	424	0.049589	0.000798	0.001278	0.000017	0.282361	0.000017	-14.6	-5.7	1272	1773
XF274 12	424	0.037093	0.000757	0.000973	0.000017	0.282337	0.000016	-15.5	-6.4	1295	1822
XF274 13	424	0.062836	0.000450	0.001618	0.000015	0.282376	0.000019	-14.1	-5.2	1262	1746
XF274 14	424	0.021006	0.000224	0.000563	0.000007	0.282371	0.000019	-14.3	-5.1	1234	1738
XF274 15	424	0.028553	0.000134	0.000760	0.000002	0.282522	0.000017	-8.9	0.2	1030	1403
XF274 16	424	0.021447	0.000153	0.000579	0.000003	0.282362	0.000019	-14.6	-5.4	1247	1759
XF274 17	424	0.026039	0.000085	0.000710	0.000004	0.282344	0.000020	-15.2	-6.1	1276	1801
XF274 20	424	0.032990	0.000263	0.000842	0.000005	0.282365	0.000018	-14.5	-5.4	1252	1757
XF274 22	424	0.017645	0.000606	0.000468	0.000016	0.282331	0.000016	-15.7	-6.5	1286	1826
XF274 23	424	0.025012	0.000107	0.000646	0.000001	0.282325	0.000018	-15.9	-6.7	1301	1843

$$\epsilon_{\text{Hf}}(0) = 10000 \left[\frac{{}^{176}\text{Hf}/{}^{177}\text{Hf}}{({}^{176}\text{Hf}/{}^{177}\text{Hf})_{\text{CHUR},0}} - 1 \right]$$

$$\epsilon_{\text{Hf}}(t) = 10000 \left\{ \left[\frac{{}^{176}\text{Hf}/{}^{177}\text{Hf}}{({}^{176}\text{Lu}/{}^{177}\text{Hf})_{\text{S}}} \times (e^{\lambda t} - 1) \right] / \left[\frac{{}^{176}\text{Hf}/{}^{177}\text{Hf}}{({}^{176}\text{Hf}/{}^{177}\text{Hf})_{\text{CHUR},0}} - \frac{{}^{176}\text{Lu}/{}^{177}\text{Hf}}{({}^{176}\text{Lu}/{}^{177}\text{Hf})_{\text{CHUR},0}} (e^{\lambda t} - 1) \right] - 1 \right\}$$

$$T_{\text{DM}} = 1/\lambda \times \ln \left\{ 1 + \left[\frac{{}^{176}\text{Hf}/{}^{177}\text{Hf}}{({}^{176}\text{Hf}/{}^{177}\text{Hf})_{\text{DM}}} - \frac{{}^{176}\text{Lu}/{}^{177}\text{Hf}}{({}^{176}\text{Lu}/{}^{177}\text{Hf})_{\text{S}}} - \frac{{}^{176}\text{Lu}/{}^{177}\text{Hf}}{({}^{176}\text{Lu}/{}^{177}\text{Hf})_{\text{DM}}} \right] \right\}$$

$$T_{\text{DM}}^{\text{C}} = 1/\lambda \times \ln \left\{ 1 + \left[\frac{{}^{176}\text{Hf}/{}^{177}\text{Hf}}{({}^{176}\text{Hf}/{}^{177}\text{Hf})_{\text{S},t}} - \frac{{}^{176}\text{Hf}/{}^{177}\text{Hf}}{({}^{176}\text{Hf}/{}^{177}\text{Hf})_{\text{DM},t}} \right] / \left[\frac{{}^{176}\text{Lu}/{}^{177}\text{Hf}}{({}^{176}\text{Lu}/{}^{177}\text{Hf})_{\text{C}}} - \frac{{}^{176}\text{Lu}/{}^{177}\text{Hf}}{({}^{176}\text{Lu}/{}^{177}\text{Hf})_{\text{DM}}} \right] \right\} + t$$

where, $({}^{176}\text{Lu}/{}^{177}\text{Hf})_{\text{S}}$ and $({}^{176}\text{Hf}/{}^{177}\text{Hf})_{\text{S}}$ are the measured values of the samples, $({}^{176}\text{Lu}/{}^{177}\text{Hf})_{\text{CHUR}} = 0.0332$ and $({}^{176}\text{Lu}/{}^{177}\text{Hf})_{\text{CHUR},0} = 0.282772$ (Bichert-Toft and Albarède, 1997); $({}^{176}\text{Lu}/{}^{177}\text{Hf})_{\text{DM}} = 0.0384$ and $({}^{176}\text{Hf}/{}^{177}\text{Hf})_{\text{DM}} = 0.28325$ (Griffin et al., 2000), $({}^{176}\text{Lu}/{}^{177}\text{Hf})_{\text{C}} = 0.015$, $t =$ crystallization age of zircon, ${}^{176}\text{Lu}$ decay constant $\lambda = 1.867 \times 10^{-5}$ m.y. (Soderlund et al., 2004).

附表四 图件目录

图 1-1 造山带分类示意图	2
图 1-2 比利牛斯山构造剖面图和 ECORS 剖面图	3
图 1-3 Alice Springs 造山带构造剖面图	4
图 2-1 华南构造简图	12
图 2-2 新元古代四堡（晋宁）造山带及扬子和华夏地块位置	14
图 2-3 雪峰山的综合地层柱状图	20
图 2-4 雪峰山中段的综合地质剖面	21
图 2-5 华盖山至雪峰山的综合地质剖面	22
图 2-6 雪峰山地质剖面图	23
图 2-7 华南板块构造演化模式	24
图 2-8 华南板块构造挤压模式	25
图 2-9 华南板块构造挤压模式	25
图 3-1 雪峰山构造地质图	27
图 3-2 雪峰山南部永州东北地质简图	28
图 3-3 主逆冲带南端区域地质图	32
图 3-4 主逆冲带南端构造剖面图	33
图 3-5 主逆冲带南端野外构造照片	34
图 3-6 西部区武陵山地质图	37
图 3-7 西部区（武陵山）野外构造照片	39
图 3-9 安化地区西北区构造典型照片	40
图 3-10 安化地区东南区构造典型照片	41
图 3-11 安化地区构造叠加示意图及野外照片	42
图 3-12 溆浦地区构造野外照片	44
图 3-13 洞口区域地质简图	46
图 3-14 洞口地区构造野外照片	47
图 3-15 涟源区域地质简图	49
图 3-14 东部区东缘涟源地区的典型构造的野外照片	50
图 4-1 雪峰山构造地质图及强应变带出露区域	53
图 4-2 城步地区构造地质图	55
图 4-3 城步地区典型构造的野外照片	56
图 4-4 云母片岩中石英脉的叠加褶皱	57
图 4-5 城步地区典型构造的显微照片	58
图 4-6 城步糜棱岩中两种石英组构的样式	59
图 4-7 城步糜棱岩石英 c 轴持平投影图	60
图 4-8 奉家-水车地区构造地质图	62

图 4-9 奉家-水车地区典型构造的野外照片	66
图 4-10 奉家-水车地区显微构造照片	67
图 4-11 沔山地区区域构造地质图	68
图 4-12 沔山地区显微构造照片	69
图 4-13 双峰地区区域构造地质图	71
图 4-14 双峰地区野外与显微构造照片	72
图 5-1 雪峰山花岗岩的显微照片	77
图 5-2 雪峰山变质岩的显微照片	78
图 5-3 研究区所采的花岗岩样品在区域上的分布	80
图 5-4 雪峰山早古生代和早中生代花岗岩中锆石阴极发光图像	81
图 5-5 研究区早古生代花岗岩锆石 U-Pb 谐和图	82
图 5-6 研究区早中生代花岗岩锆石 U-Pb 谐和图	84
图 5-7 研究区云母片岩和早中生代花岗岩中独居石照片。	87
图 5-8 研究区云母片岩和早中生代花岗岩的独居石年代学投图	89
图 5-9 研究区年代学数据总结	92
图 5-10 研究区花岗岩前人的年代学数据与本文对比	93
图 6-1 雪峰山早古生代花岗岩的 $\epsilon\text{Hf}(t)$ 的柱状分布图	96
图 6-2 雪峰山早古生代花岗岩样品的 T_{DM}° 的柱状分布图	97
图 6-3 雪峰山早中生代花岗岩的 $\epsilon\text{Hf}(t)$ 的柱状分布图	99
图 6-4 雪峰山早中生代花岗岩样品的 T_{DM}° 的柱状分布图	100
图 6-5 雪峰山早古生代和早中生代花岗岩的 $\epsilon\text{Hf}(t)$ 以及 T_{DM}° 的综合柱状分布图	103
图 6-6 雪峰山早古生代和早中生代花岗岩的年龄- $\epsilon\text{Hf}(t)$ 图解	104
图 7-1 雪峰山造山带早中生代多期构造变形图解	106
图 7-2 雪峰山造山带早中生代构造剖面图	112
图 7-3 华南板块早古生代至早中生代的构造演化模式图	116

**Tectonic evolution of the Early Mesozoic (Indosinian) intracontinental
Xuefengshan Belt, South China**

Yang Chu^{1,2}, Michel Faure^{1,2}, Wei Lin¹, Qingchen Wang¹

1. State Key Laboratory of Lithospheric Evolution, Institute of Geology and Geophysics, Chinese Academy of Sciences, Beijing 100029, China

2. Institut des Sciences de la Terre d'Orléans, Campus Géosciences, Université d'Orléans, 1A Rue de la Férollerie, 45071 Orléans Cedex 2, France

Abstract

Intracontinental orogens remain less understood than accretionary or collisional orogens that are related to plate margin interactions. In the center of the South China block, the Xuefengshan Belt provides a well-exposed example of such an intracontinental orogen of Early Mesozoic age. Detailed field tectonic observations indicate that the Xuefengshan Belt can be divided into a Western Outer Zone characterized by km-scale box-fold structures, and an Eastern Zone, separated from the Western Outer Zone by the SE-dipping Main Xuefengshan Thrust. In the Eastern Zone, NW verging folds coeval with a pervasive slaty cleavage and a NW-SE trending lineation are the dominant structures. From west to east, the dip of the cleavage surface exhibits a fan-like pattern. The bulk architecture of the Xuefengshan Belt results from polyphase deformation: D_1 is characterized by a top-to-the-NW ductile shearing; D_2 corresponds to SE-directed back thrusting and folding; D_3 consists of upright folds with vertical cleavage and lineation. At depth, a high strain zone characterized by greenschist facies metamorphic rocks and a top-to-the-NW ductile shearing corresponds to a ductile decollement layer that accommodated the deformation of the Neoproterozoic to Early Triassic sedimentary series. Kinematic compatibility suggests that the synmetamorphic ductile shearing was coeval with the D_1 event in the sedimentary cover. The Xuefengshan Belt is interpreted as an Early Mesozoic intracontinental orogen, which possibly originated from the SE-directed continental subduction of a piece of the South China block in response to northwestwards subduction of the Pacific plate.

Key words: Intracontinental orogen, Fold-and-Thrust belt, Xuefengshan Belt, South China block, Early Mesozoic orogeny

1. Introduction

The mechanisms of intracontinental orogeny have long been discussed, since intraplate mountain belts cannot be ascribed to the plate margin interaction paradigm that assumes that the interiors of a continent are rigid and hard to deform. However, it is now well accepted that the deformation of continental crust can be a far-field consequence of collision, as exemplified by the Miocene tectonics of Asia [e.g. *Tapponnier and Molnar, 1979; Avouac et al., 1993*]. Compared to collisional or accretionary orogens, evidence for oceanic subduction, ophiolites, accretionary complexes, mélangé, and arc-related magmatism are lacking. Conversely, fold-and-thrust belts, large-scale decollement, limited crustal melting, and even high temperature metamorphism are well developed tectonic elements in intracontinental orogens. These features are illustrated by the Cenozoic Tianshan Belt in Central Asia [*Tapponnier and Molnar, 1979; Hendrix et al., 1992; Avouac et al., 1993; Allen et al., 1999*], the Cenozoic Pyrenees in Europe [*Roure et al., 1989; Choukroune, 1992*], the Late Mesozoic to Cenozoic Laramide orogen in North America [*Dickinson and Snyder, 1978; English and Johnston, 2004*], the Paleozoic Alice Springs orogen in Central Australia [*Hand and Sandiford, 1999; Sandiford et al., 2001*], and the Early Paleozoic intracontinental belt of SE China [*Faure et al., 2009; Charvet et al., 2010*]. At the lithospheric plate scale, far-field consequence of continental collision or a flat-slab subduction are often the two main driving forces advocated to account for the origin of intracontinental orogens [*Dickinson and Snyder, 1978; Hendrix et al., 1992*].

The Xuefengshan Belt is an Early Mesozoic intracontinental orogen in the South China block (SCB) [e.g. *Qiu et al., 1998, 2000; Wang et al., 2005; Figure 1*]. Here, we present new detailed structural data from the Xuefengshan that aim to improve our understanding of the tectonic evolution of the central part of the SCB, and may provide general insights into the development of intracontinental belts.

2. Geological outline of the Xuefengshan belt in the South China block

2.1 The South China block

The South China block (SCB) formed in the Early Neoproterozoic (ca 900 Ma) by collision of the Yangtze block and the Cathaysia block to the northwest and southeast, respectively [Figure 1; *Shu et al., 1994; Charvet et al., 1996; Li, 1999; Li et al., 2009*, and enclosed references]. The Jiangshan-Shaoxing Fault represents the eastern part of the Neoproterozoic ophiolitic suture between these two blocks (Figure 1). Farther west, and southwest, this suture is hidden below the Paleozoic or Mesozoic sedimentary rocks. From the Late Neoproterozoic to the end of Early Paleozoic, the

SCB underwent continuous sedimentation, partly controlled in the Neoproterozoic by rifting [Wang and Li, 2003] until the Late Ordovician. An Early Paleozoic orogeny occurred around 450-420 Ma as indicated by a Middle Devonian regional unconformity and emplacement of post-orogenic plutons at ca. 410 Ma. The Early Paleozoic orogen of SE China is well developed to the south of the Jiangshan-Shaoxing Fault [Wang et al., 2007b; Faure et al., 2009; Li et al., 2010; Charvet et al., 2010]. In the Xuefengshan Belt, this event is weakly developed as argued below. The main orogenic episode of the SCB took place in the Early Mesozoic, as demonstrated by a Late Triassic unconformity widespread across the entire SCB. In terms of time, this Middle Triassic event is referred to as the “Indosinian Orogeny” [Chen, 1999; Wang et al., 2005, 2007c; Li and Li, 2007; Lin et al., 2008; Roger et al., 2008, 2010], but at the scale of the entire SCB, the “Indosinian Orogeny” cannot be seen as a single chain. The two main Triassic belts are exposed along the SCB margins. Namely, to the north, the S-Qinling-Dabie Belt is related to the northward subduction of the SCB below the North China block [Hacker and Wang, 1995; Faure et al., 1999, 2008]. To the southwest and south, the Jinshajiang and Song Ma sutures are associated with the collision of the SCB with the Indochina block [Lepvrier et al., 2004, 2008; Carter et al., 2001; Wallis et al., 2003; Harrowfield and Wilson, 2005; Carter and Clift, 2008; Roger et al., 2008, 2010].

When dealing with the Triassic tectonics of the SCB, the Xuefengshan Belt in Hunan Province presents a unique example of intracontinental orogens with folds and thrusts post-dated by Late Triassic undeformed post-orogenic plutons. However, the structural style, tectonic evolution, and geodynamic significance of the Xuefengshan Belt are still debated. The proposed tectonic interpretations are still at variance [Hsu et al., 1988, 1990; Gupta, 1989; Rodgers, 1989; Rowley, 1989]. For some authors, this belt was formed by a large-scale, multi-layer over-thrust system developed in the Late Mesozoic from the Xuefengshan Belt to the northeastern Sichuan Basin (Figure 1) [Yan et al., 2003]. Another interpretation emphasizes Triassic strike-slip faults leading to transpressional tectonics [Wang et al., 2005]. More recently, a NW-directed, flat slab subduction of the Pacific plate producing a propagating retroarc fold-and-thrust belt accompanied by NW-propagating magmatism during the 250-190 Ma interval has been suggested [Li and Li, 2007]. Although, as argued below, in section 4, this interpretation seems the most likely, structural analyses supporting this model are, up to now, not available.

During the Jurassic and Cretaceous, the tectonic activity in the SCB was characterized by NE-SW striking normal or strike-slip faults, synkinematic plutons, and syntectonic terrigenous sedimentation [Xu et al., 1987; Gilder et al., 1991; Faure

et al., 1996; Lin et al., 2000; Zhou et al., 2000, 2006; Shu et al., 2009]. In the Xuefengshan area, strike-slip faults parallel to the belt are rare. These brittle faults bound intramontane half-graben basins or offset the Triassic plutons.

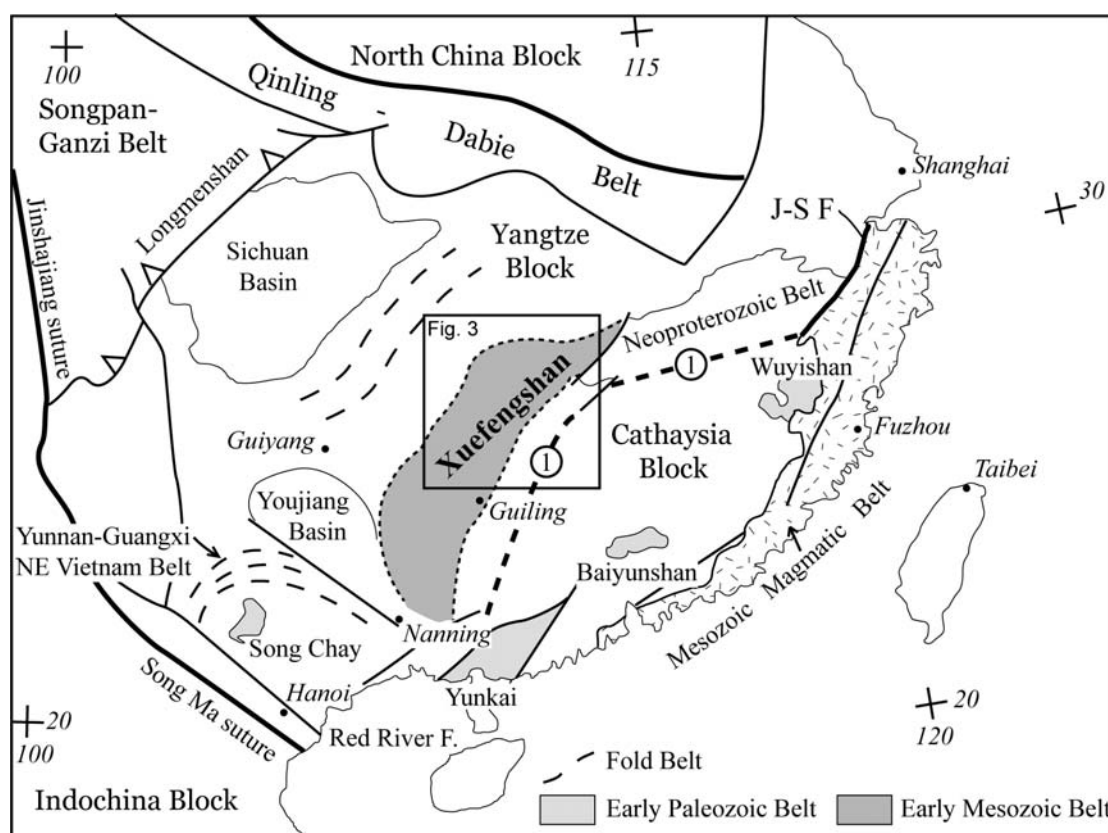


Figure 1. Tectonic map of the South China block with the location of the intracontinental Xuefengshan Belt (Modified after Faure et al., 2009). J-S F: Jiangshan-Shaoxing Fault. 1: Predicted boundary between the Yangtze Block and the Cathaysia Block.

2.2 Lithostratigraphy of the Xuefengshan Belt

The Xuefengshan Belt, located in the central area of the SCB, is a NNE-SSW trending range about 100 km wide and more than 300 km long (Figure 1). The Middle-Late Proterozoic Lengjiaxi group, formed by conglomerates, sandstones, siltstones, phyllites and slates, represents the oldest strata cropping out in the Xuefengshan Belt. The Lengjiaxi group is overlain by more than 3 km of turbidites and volcanic rocks assigned to the Neoproterozoic Banxi group [BGM_{MRHN}, 1988]. The Late Neoproterozoic (Sinian) strata include tillite, sandstone, chert and limestone. Until Early Silurian, and locally Middle Silurian, there is no obvious sedimentation gap in the stratigraphic sequence. However, the Cambrian and Ordovician lithology changes this uniform sedimentary pattern in the Xuefengshan Belt, with limestones and black shales to the north, and sandstones, silts, and slates to the south [BGM_{RGX}, 1985; BGM_{MRHN}, 1988]. In the study area, Silurian deposits are turbidites that can be

interpreted as the molasses derived from erosion of the Early Paleozoic orogen (Qiu et al., 1998, 2000; Faure et al., 2009).

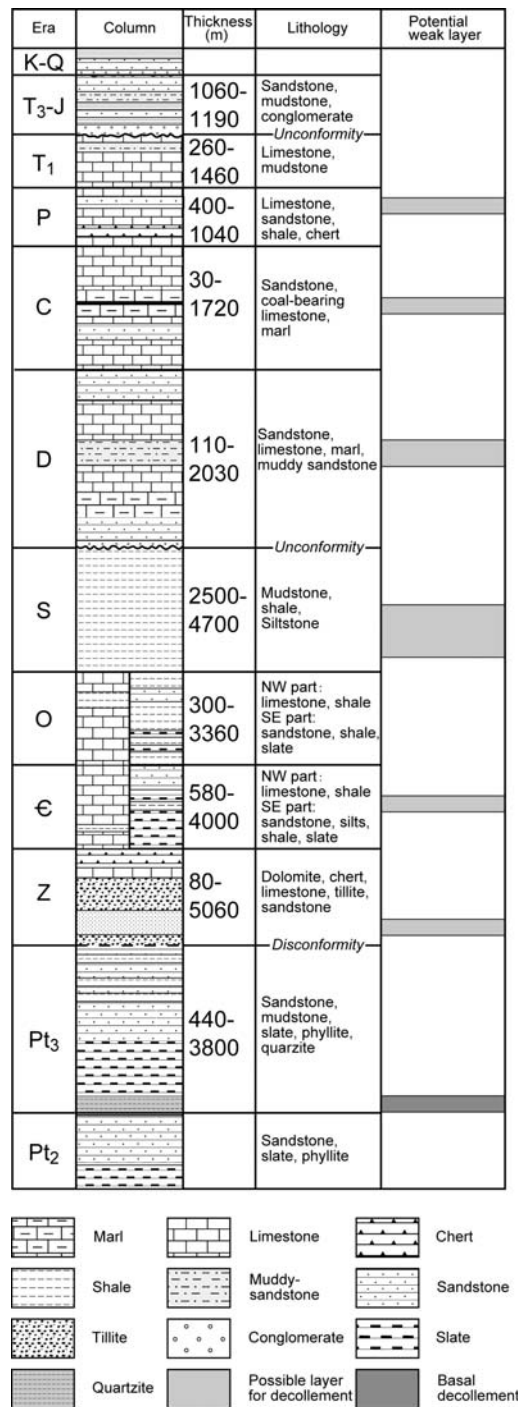


Figure 2. Stratigraphic column of the Xuefengshan Belt with location of potential decollement layers (BGMРН, 1988).

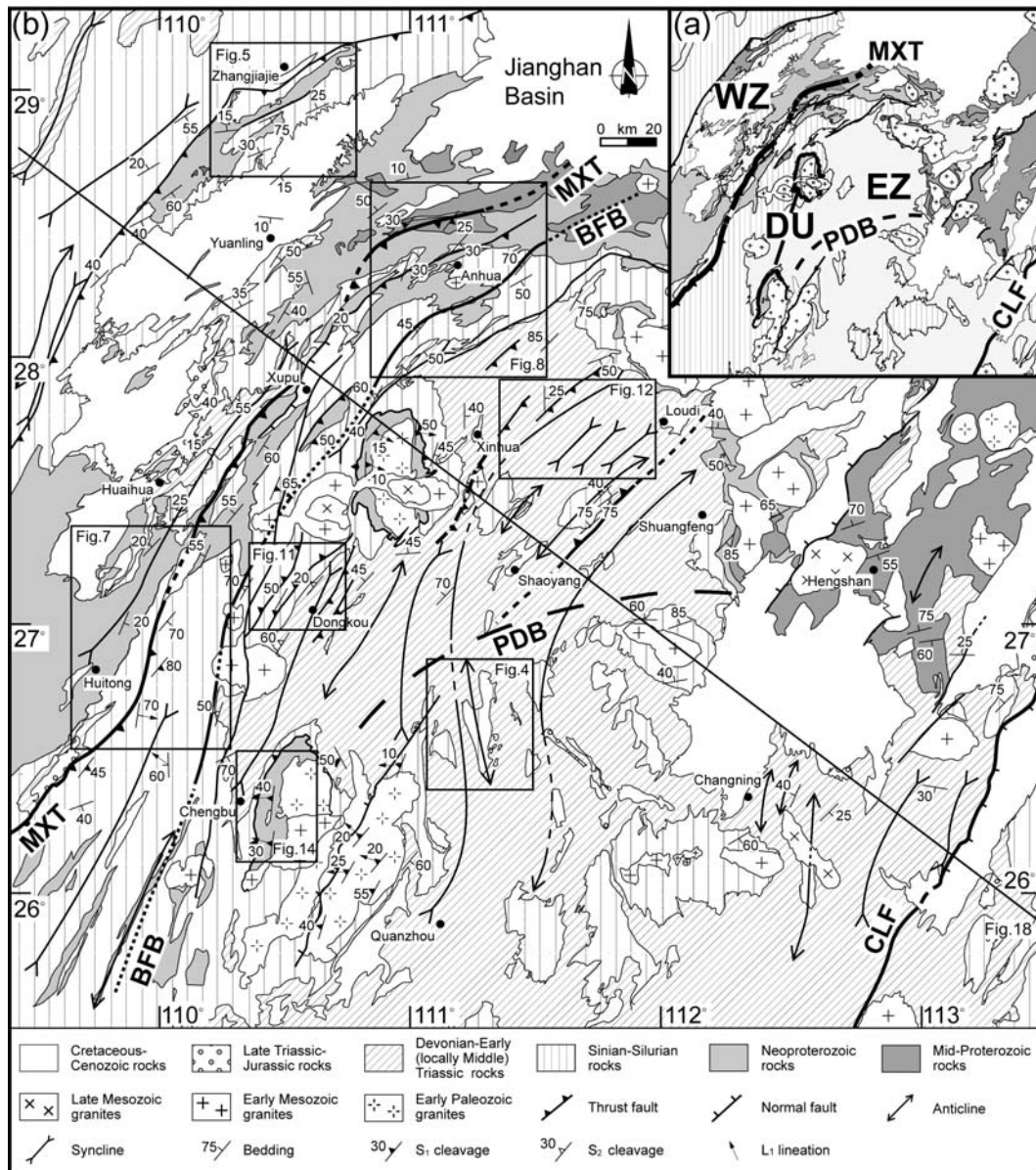


Figure 3. (a): Sketch map of the Xuefengshan Belt with tectonic division. (b): Structural map of the Xuefengshan Belt (Modified after 1:500 000 Geological map of Hunan, *BGMRHN*, 1988). WZ: Western Outer Zone. EZ: Eastern Zone. MXT: Main Xuefengshan Thrust. BFB: Back Folding Boundary. DU: Deep Metamorphic Unit. PDB: Pre-Devonian Boundary. North of this limit, pre-Devonian deformation is negligible. CLF: Chenzhou-Linwu Fault.

Upper Silurian to lower Devonian deposits are missing in the Xuefengshan area, and lower Paleozoic rocks are covered directly by Middle Devonian conglomerates. The late Devonian-Carboniferous-Permian and lower Triassic series consists of shallow-marine to littoral facies limestones, dolomites, and clastic rocks. All the rocks mentioned above are strongly deformed and unconformably overlain by Upper Triassic or Lower Jurassic sandstones and conglomerates that are distributed limitedly in intramontane basins. This unconformity is interpreted as a response to an Early

Mesozoic intracontinental orogeny [Chen, 1999; Wang *et al.*, 2005; Li and Li, 2007; Shu *et al.*, 2009]. From Middle Jurassic to Cretaceous, the sedimentary series consists of red terrestrial clastic rocks interbedded with volcanic rocks.

The pre-Late Triassic lithological succession contains several pelitic or shaly layers, some of them with coal measures, which could play a major role in shaping the tectonics of the Xuefengshan Belt. Due to their low yield stress, these soft layers act as decollement levels that accommodate the regional shortening. The Sinian pelite and graphitic layers, and the Cambrian black shales are the main decollement levels, but Devonian, Carboniferous, and Permian pelitic layers may also represent second order decollements (Figure 2) [Yan *et al.*, 2003].

Plutonic rocks are widespread in the Xuefengshan Belt (Figure 3). Undeformed Mesozoic peraluminous granites exposed in the Central and Eastern parts intrude the already deformed pre-Mesozoic series. These Mesozoic granites were generated between 245-210 Ma and postdate the Early Mesozoic orogeny [Chen *et al.*, 2006, 2007a, 2007b; Wang *et al.*, 2007a]. Furthermore, as described in section 3.4, Early Paleozoic plutons underwent a pervasive ductile deformation during the Early Mesozoic tectonics.

2.3. Pre-Devonian events in the Xuefengshan Belt

Due to the widespread occurrence of a Devonian unconformity, some geologists interpreted the Xuefengshan Belt as the product of an Early Paleozoic orogeny (e.g. Qiu *et al.*, 1998, 2000). However, according to our survey, the importance of the Early Paleozoic orogeny appears to be overestimated. In the southern part of the study area, Neoproterozoic, Cambrian, and Ordovician pelite-sandstone series are involved in E-W trending, south-verging folds (Figure 4). These early folds are unconformably covered by Devonian conglomerate and sandstone, followed by a continuous series of limestone and subordinate shale and mudstone. The entire sedimentary pile, from Neoproterozoic to Early Triassic, is deformed by N-S trending folds. This superimposed folding gives rise to a type 2 fold interference pattern [Ramsay and Huber, 1987].

In fact, in most parts of the study area, the angle of the Devonian unconformity is lower than 20°, and even in the northern and northwestern parts of the Xuefengshan Belt, only a parallel disconformity between Silurian and Devonian rocks is exposed. The Early Paleozoic folds are open, characterized by kilometer-scale gentle undulations without any axial planar cleavage. Furthermore, in the entire Xuefengshan area, when a slaty cleavage is observed in the Neoproterozoic to Silurian series, this cleavage is also developed in the unconformably overlying

Devonian rocks. Conversely, syn-schistose folds restricted to pre-Devonian series is hardly observed but in the southwestern area as described above (Figure 4). The northern boundary is outlined as the Pre-Devonian Boundary (PDB in Figure 3b). Additional microtectonic arguments for an Early Mesozoic deformation will be given in the following section. Therefore, the Early Paleozoic event is poorly developed in most parts of the Xuefengshan Belt, and thus we shall focus on the structural analysis of the Early Mesozoic orogeny, which is responsible for the bulk architecture of the belt.

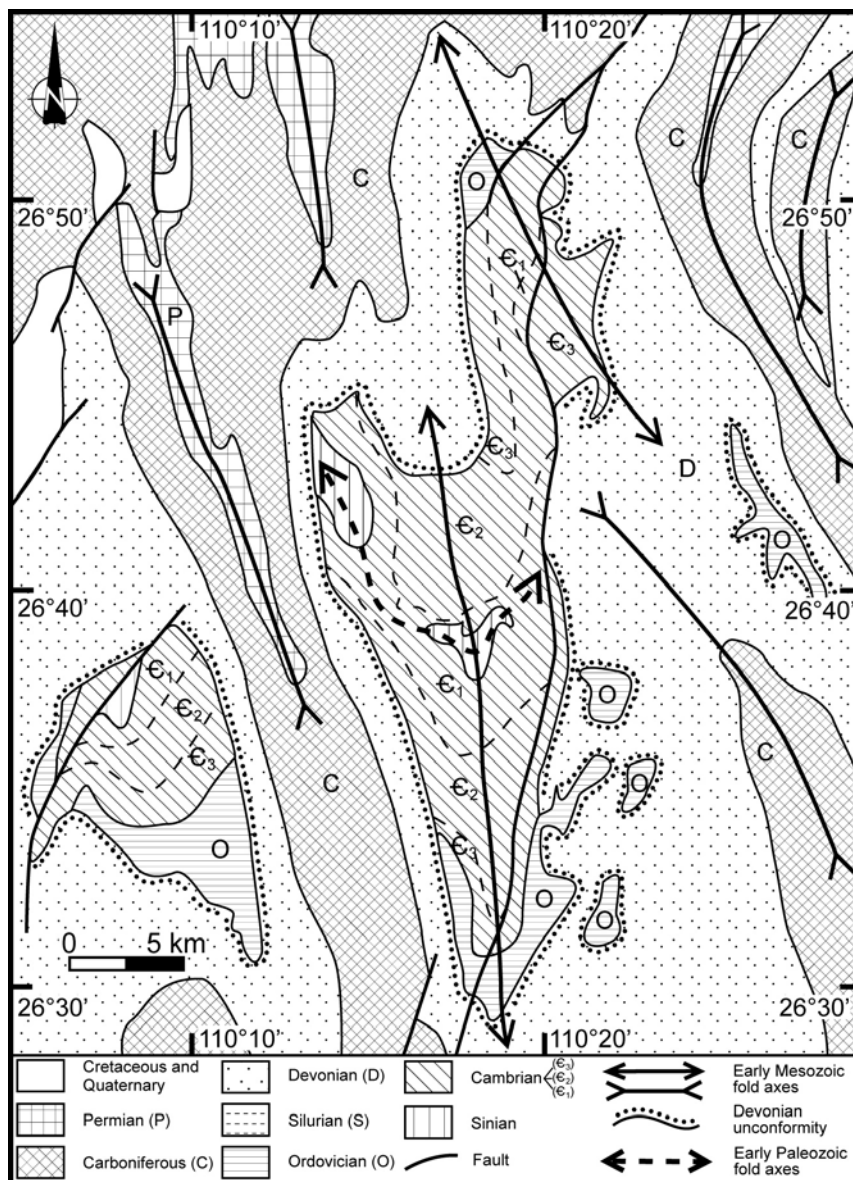


Figure 4. Geologic map of the southern part of the Xuefengshan Belt showing relics of pre-Triassic E-W trending fold axes, developed only in pre-Devonian rocks and refolded by Triassic N-S trending folds.

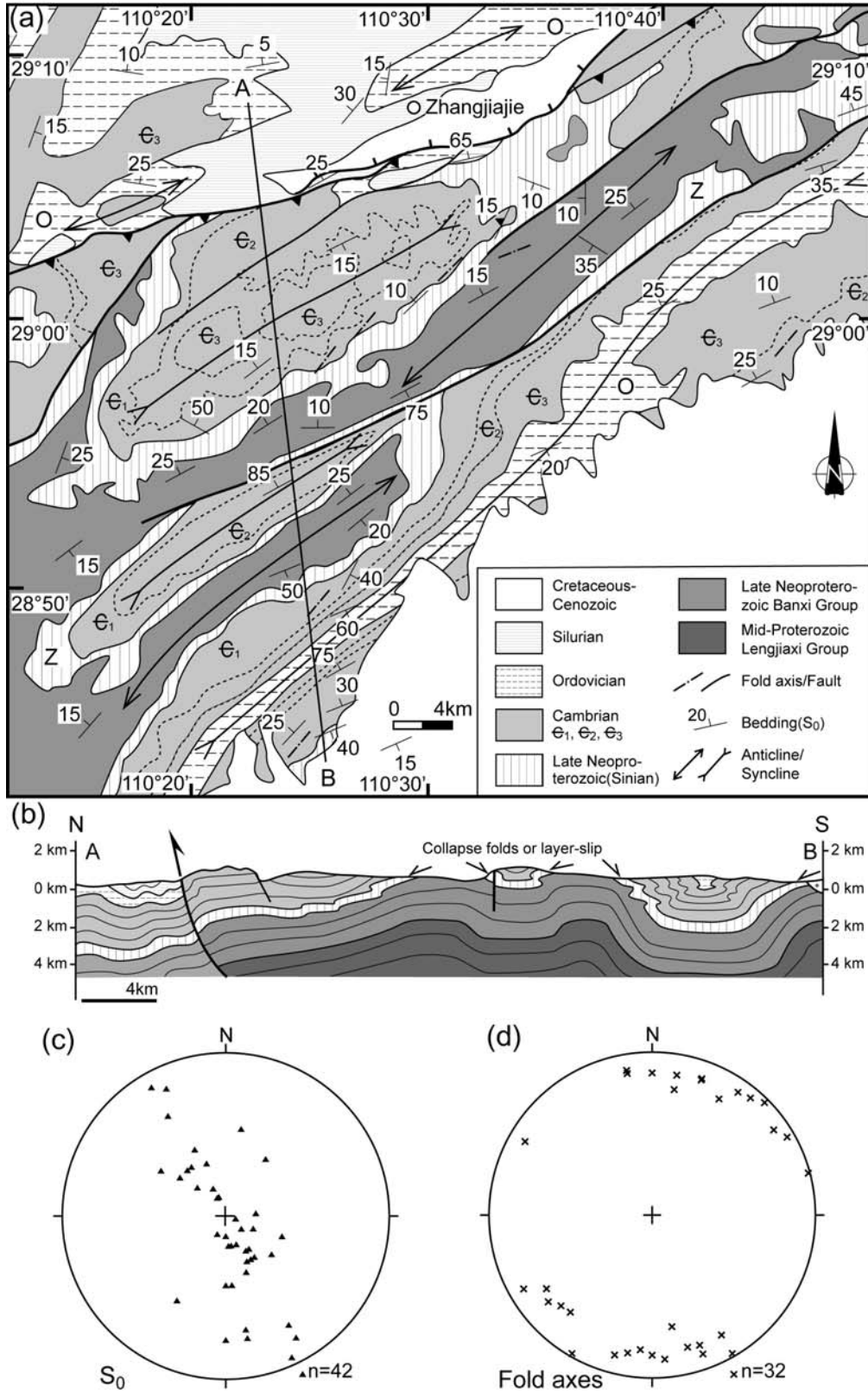


Figure 5. (a): Detailed geologic map of the Western Outer Zone in the Wuling Mountain (Modified after 1:500 000 Geological map of Hunan, BGMRHN, 1988). (b): Cross section showing the box-fold structure characteristic of this zone. Stereographic plots (Schmidt lower hemisphere projection) of the structural elements, (c): bedding, (d): fold axes.

3. Structural pattern of the Xuefengshan Belt

The Xuefengshan Belt can be subdivided into two tectonic zones (Figure 3a): the Western Outer Zone and the Eastern Zone. The Eastern Zone comprises the Xuefeng Mountain and a lowland area, to the west and to the east, respectively. The Xuefeng Mountain is an area with higher elevation, where the intensity of the deformation and metamorphism is the greatest. In the lowland area, Devonian to Early Triassic rocks are poorly exposed. The Western Outer Zone, exposed in the Wuling Mountain, is characterized by box-fold structures. The Main Xuefengshan Thrust (MXT, Figure 3) separates the Western Outer Zone and the Eastern Zone. It also corresponds to the cleavage front, as S_1 (described in section 3.2) is absent in the Western Outer Zone but is widely developed in the Eastern Zone. In this zone, NE-SW trending folds with an axial planar cleavage, NW or W-directed thrust faults, and E-W to WNW-ESE trending mineral and stretching lineation are the dominant structures.

Except in a few places around some plutons (e.g. near Chengbu, figure 3), highly metamorphosed rocks are not exposed in the study area. Another important structural boundary is the Back-Folding Boundary (BFB, Figure 3b), defined by the appearance of back-folds and back-thrusts (cf. section 3.3 for detailed descriptions). East of the BFB, east-verging folds, sometimes with inverted limbs are widespread in the Eastern Zone. Devonian to Triassic formations occupy a large area in the eastern part of the Eastern Zone, whereas pre-Devonian rocks are dominant in the west Eastern Zone. Nevertheless, except along the the decollement layers, there is not sharp discontinuity within the sedimentary series of the Eastern Zone. One of the main structural features is the progressive weakening, and even disappearance of the cleavage plane.

The whole belt experienced complex polyphase deformation. On the basis of cleavage plane geometry, fold-vergence, and overprinting relationship, in the Eastern Zone, we separate three deformation events. The first one, D_1 , is characterized by a top to the NW ductile shearing. The second one, D_2 , corresponds to a back-folding and back-thrusting stage with SE-verging folds. The last phase, D_3 , is represented by upright folds with vertical axial planar cleavage and vertical stretching lineation. For each zone, the typical deformation style relevant to the three events is described in selected areas (Figure 3b).

3.1 The Western Outer Zone

The Western Outer Zone, bounded to the east by the MXT, shows moderate deformation compared with that observed in the Eastern Zone. This zone has been investigated in the Wuling Mountain, South of Zhangjiajie (Figures 3, 5a, 5b, 5c and 5d). There, the Neoproterozoic to Silurian series is deformed by NE-SW trending,

kilometer-sized box-folds. In the core of anticlines and synclines, the bedding is flat without any macroscopically observable deformation, whereas highly dipping strata can be observed in the fold limbs (Figures 5b, 6a and 6b). Due to their weak rheology, the pelitic layers, namely Cambrian black shale, or Sinian pelite and coal measure are more intensely deformed than the limestone or sandstone beds. Where strata are tilted to dip angles of 70-90°, along these soft-layers, the deformation is accommodated by intense meter to centimeter-scale disharmonic folding and layer-parallel slip (Figure 5b). In the Western Outer Zone, the rocks do not record any metamorphism, even in the core of the anticlines where the deepest Middle-Late Proterozoic sandstone-pelite series crops out. In summary, the Western Outer Zone represents the structurally higher part of the Xuefengshan Belt which is deformed under brittle conditions accommodated by layer-parallel slip, box-folding, and brittle deformation concentrated in the fold hinges.

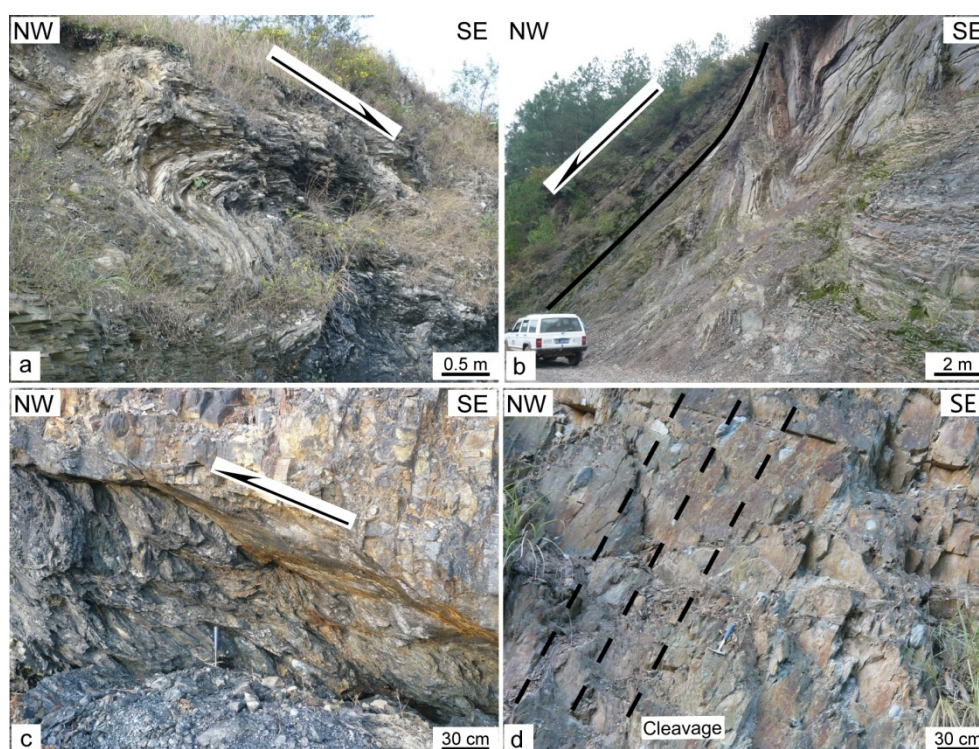


Figure 6. Photographs of representative structures observed in the Western Outer Zone and the Main Xuefengshan Thrust. (a): Gravitational collapse folds in Cambrian shale, south of Zhangjiajie (N29°00.406'/E110°28.804'). (b): Gravitational collapse structure in Neoproterozoic shale, northeast of Yuanling (N28°25.873'/E110°29.335'). (c): Shear zone in coal-bearing Cambrian black shale with sigmoidal shearing structure, east of Huitong (N26°56.422'/E109°56.097'). (d): Oriented pebbles in Sinian tillite with a NW-dipping cleavage, east of Huitong (N26°56.529'/E109°55.672').

3.2 The Main Xuefengshan Thrust (MXT)

The MXT is a northwest-directed reverse fault that corresponds also to the appearance of the main slaty cleavage (S_1 hereafter). This major structure is over 200 km long and extends farther south in the Youjiang Paleozoic-Early Mesozoic Basin (Figure 1). Locally, this thrust fault is reactivated as a normal fault that controls the opening of a Cretaceous half-graben. The northern part of the MXT, southwest to the Jiangnan Basin (Figure 3b), has not been directly observed in the field, due to outcrop conditions, but the sharp change between open folds devoid of axial planar cleavage to the NW, and well expressed overturned folds and slaty cleavage to the SE, argues for the existence of such a thrust. To the northeast, it is buried below the Cretaceous-Cenozoic Jiangnan Basin (Figure 3b).

In the southern part of the study area, east of Huitong (Figures 3b and 7a), a ca. 10m thick, moderately east dipping, high strain shear zone is developed in the Cambrian black shale, slate, and schist, separating weakly metamorphosed Sinian sandstone and tillite of the Eastern Zone in the hanging wall from undeformed and unmetamorphosed sub-horizontal Neoproterozoic-Cambrian rocks in the footwall (Figures 7a, 7b and 7c). In the vicinity of the shear zone, rocks are strongly deformed, whereas 2 km away from the contact, the thrusting-related tectonic fabrics disappear. Along the thrust plane, NW-SE trending striations, and kinematic indicators such as sigmoidal shaped lenses developed within Cambrian black shale show a top-to-the-W displacement (Figure 6c).

In the thrust hanging wall, the Sinian sandstone exhibits a high angle East-dipping or subvertical cleavage. In the footwall, ten-of-meters-wavelength folds, overturned to the west, are developed, and several meter-scale shear zones with layer-slip structures are conspicuous. In the Sinian tillite, 10 to 50 cm-sized pebbles are flattened, forming west-dipping cleavage planes (Figure 6d). This feature is related to a SE verging fold, analogous to those widely developed to the east (described in the section 3.3.2). However, this area is the only place where east-vergent structures have been observed in the Western Outer Zone. Thus, we tend to interpret it as a local reverse thrust, corresponding to a pop-up generated during D_1 rather than a true D_2 back-thrust.

At the regional scale, the deformation in the entire Proterozoic series that crops out to the west of the MXT is weak or almost absent. The bedding remains sub-horizontal over a large distance, and only joints, and kilometer-scale gentle upright folds represent the macroscopic deformation structures. Conversely, to the east of the MXT, folds coeval with a pervasive axial planar cleavage deform the sedimentary rocks (Figure 7b, 7c, 7d, 7e and 7f).

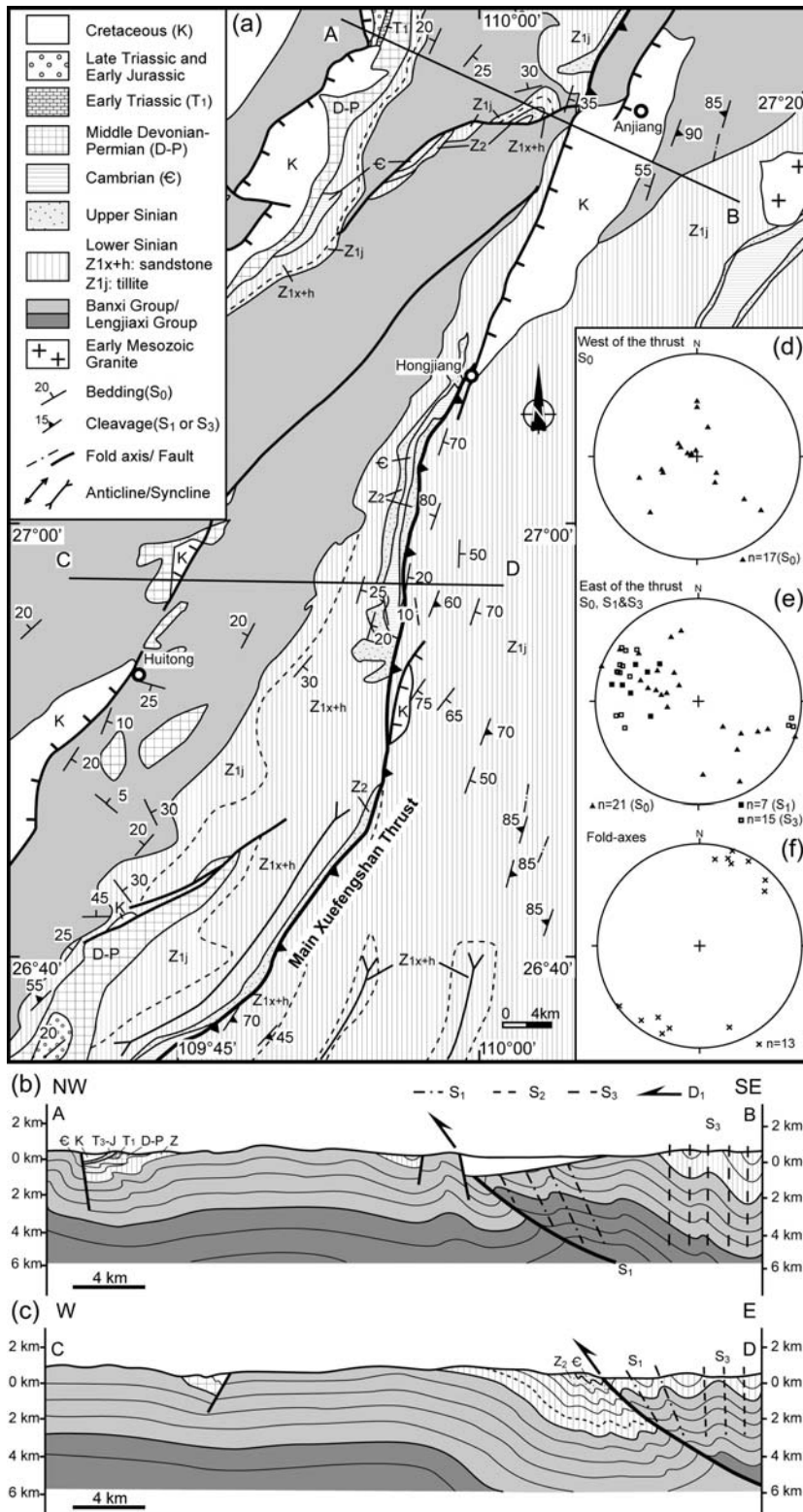


Figure 7. (a): Detailed geologic map of the Main Xuefengshan Thrust or Cleavage Front (Modified after 1:500 000 Geological map of Hunan, *BGMRHN*, 1988). (b) and (c): Cross sections showing the structure of the area close to the MXT. Stereographic plots (Schmidt lower hemisphere projection) of the structural elements, (d): bedding west of the thrust, (e): bedding (S₀, S₁ and S₃ cleavage, east of the thrust, (f): fold axes.

3.3 The Eastern Zone

Due to the high elevation and good exposure, the western part of the Eastern Zone provides important information to explore the geometry and kinematics of this zone. From west to east, different structural features are recognized. In the west, top-to-the-NW folding and shearing dominate, whereas in the east the opposite (i.e. eastward) vergence is predominant. These two contrasted vergences are not synchronous but successive, as demonstrated below (sections 3.3.1, 3.3.2 and 3.3.3), the eastward shearing overprints the westward one. These key areas are described as examples of the representative structure and of the superimposed deformation of the Eastern Zone. The timing question will be addressed in section 4.

3.3.1 Anhua section

In the northern part of the orogen, Middle to Late Proterozoic sandstone and argillite with a well-developed slaty cleavage occupy a large domain (Figure 8a and 8b). Northeast of Anhua, the N70-90E striking cleavage is steeply dipping to the SE, and from N to S, becomes more and more penetrative. S_1 gradually replaces the original S_0 bedding (Figure 9a), but the dip angle of S_1 changes slightly from place to place in different parts of the folds (Figure 8d). Nevertheless, the fold vergence determined by the S_0/S_1 relationships, is consistently to the NNW, even if cleavage refraction due to alternation of pelite and sandstone layers is locally well developed.

North of Anhua (Figure 8a), a several meters thick, highly deformed shear zone with top-to-the-north thrusting, separates the Neoproterozoic and Paleozoic rocks. In some places, the Neoproterozoic sandstone overthrusts onto the Devonian limestone. In the thrust footwall, the limestone is intensely folded and sheared whereas in the hanging wall, the sandstone is folded with a penetrative, SE-dipping, axial planar cleavage. Cataclasites are well developed along the fault zone. The foliated argillaceous matrix includes sigmoidal-shaped sandstone boudins with a top-to-the-NW sense of shear.

South of Anhua (Figure 8a), the cleavage surface gradually turns to vertical and then dips to the northwest. In the Sinian to Ordovician series, the verticalization of S_0 is coeval with the development of upright folds associated with an axial planar cleavage. Farther south, a NW-dipping slaty cleavage associated with SE verging folds is widely developed. As indicated by ripple marks, load casts and groove casts, the S_0 surface in the southeastern limb of anticlines is overturned in some places. Furthermore, the pelitic layers of the Silurian turbidite often exhibit a SE-dipping cleavage that cannot be related to these SE-verging folds (Figures 10a and 10b). We interpret this feature as a relic of the S_1 cleavage, coeval with the early NW-verging

folds, which is later involved in SE-verging folds. Thus, these overprinting relationships show that the SE-verging folds can be considered as back-folds formed during a second deformation stage (D_2) (Figures 8a, 8e and 8f).

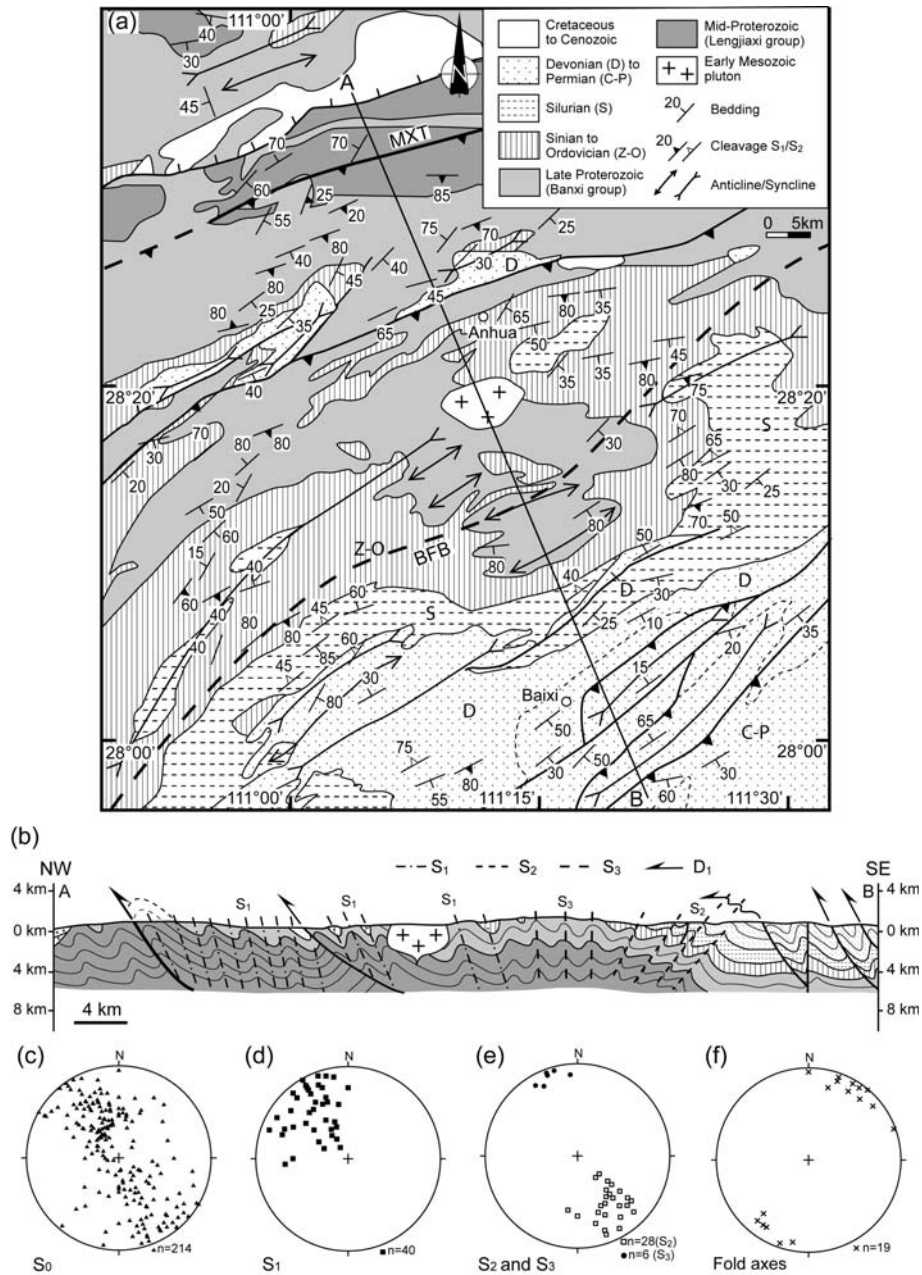


Figure 8. (a): Detailed geologic map of the Eastern Zone near Anhua (Modified after 1:500 000 Geological map of Hunan, *BGMRHN*, 1988). (b): Cross section showing the structure of the Anhua section. Stereographic plots (Schmidt lower hemisphere projection) of the structural elements, (c): bedding (S_0), (d): S_1 cleavage, (e): S_2 and S_3 cleavages, (f): fold axes.

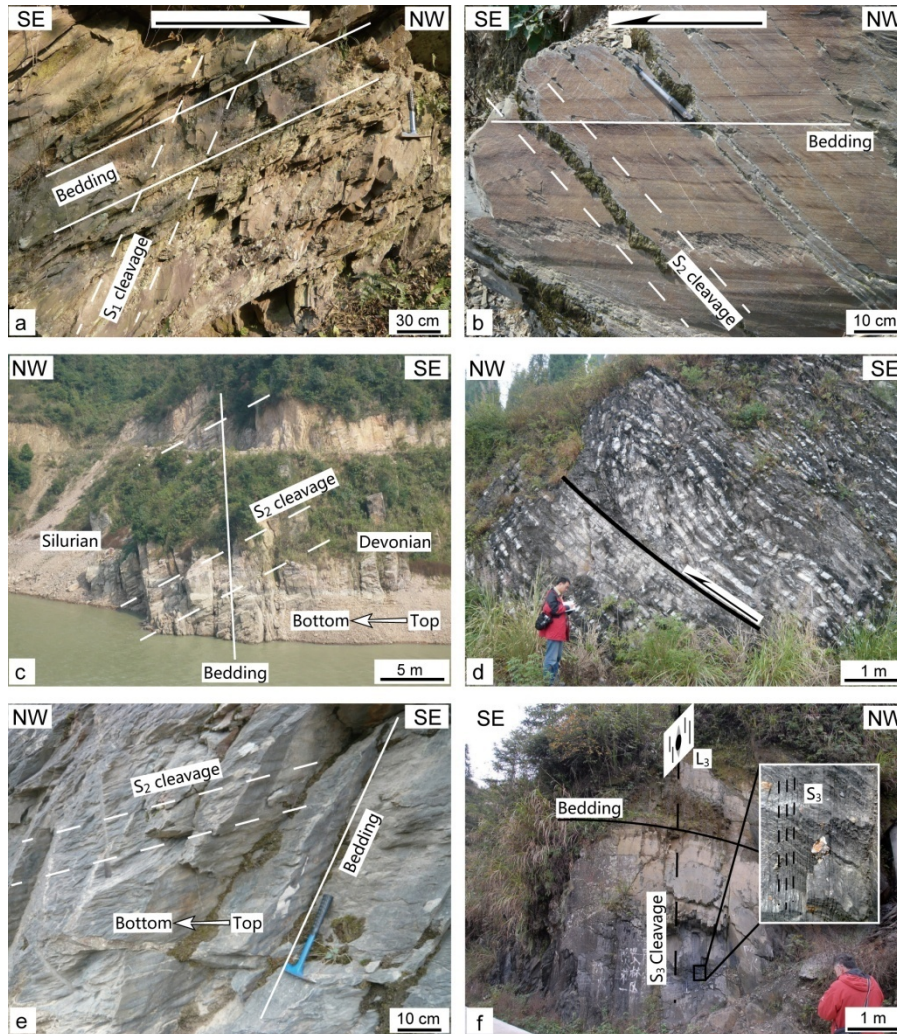


Figure 9. Photographs illustrating the deformation in Anhua and Dongkou sections. (a): SE dipping cleavage in Neoproterozoic sandstone, south of Anhua (N28°27.182'/E111°01.374'). (b): S₂ cleavage in Silurian mudstone in a normal limb of a SE-verging fold, south of Anhua (N28°02.531'/E111°02.792'). (c): S₂ cleavage in vertical layers of Devonian sandstone involved in a SE-vergent fold. The same cleavage affects the underlying Silurian strata, south of Anhua (N28°04.012'/E111°02.332'). (d): NW-directed reverse fault and associated fold in Carboniferous limestone, south of Anhua (N27°55.886'/E111°18.307'). (e): NW dipping S₂ cleavage in inverted Cambrian shale with ripple marks on the top surface (N27°04.762'/E110°31.480'). (f): Upright fold in Sinian shale with vertical pressure shadows, north of Dongkou (N27°27.604'/E110°24.581').

North of Baixi (Figure 8), the Silurian and Devonian bedding dips gently to the SE, striking N20-50E. SE-verging D₂ folds, associated with a northwest dipping cleavage, deform the entire series (Figures 9b and 9c). This structural consistency shows that the deformation occurred after the Devonian.

From Baixi to the south (Figure 8a), in the Carboniferous and Permian limestone and mudstone, thrust faults associated with NW-verging folds indicate again a

northwestward movement (Figure 9d). In this area, back folding is no longer observed. Nevertheless, the D_2 back-folding development is, to some extent, more intense in the Dongkou area, which will be discussed in the next section.

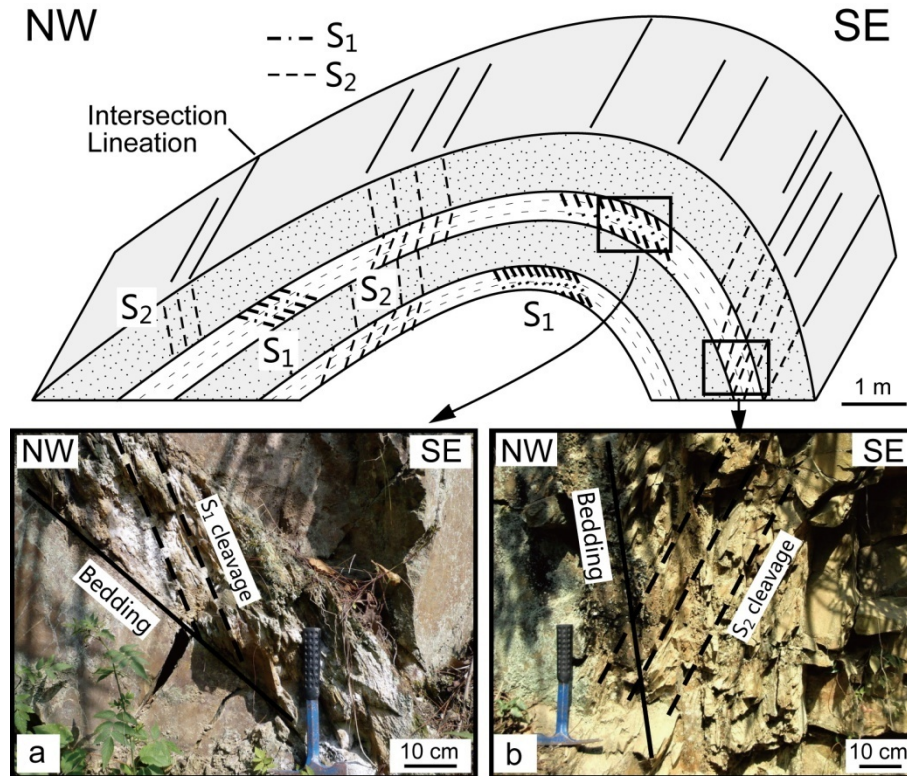


Figure 10. Field evidence of superimposed deformation. The S_1 cleavage is deformed by a SE-verging F_2 fold associated with a S_2 axial planar cleavage, northwest of Xinhua (N26°25.228'/E110°26.868'). (a): Relict S_1 cleavage in a mudstone layer. (b): Pervasive NW dipping S_2 cleavage.

3.3.2 The Dongkou section

The main structure of this area is represented by large scale overturned bedding involving Upper Neoproterozoic to Lower Devonian rocks (Figures 11a and 11b). Northwest of Dongkou, the slightly metamorphosed Cambrian to Silurian black shales and siltstones are deformed by NE-SW trending, SE-verging folds with axial-planar cleavage (Figures 9e and 11e). These structures are related to the D_2 back-folding event. Around Dongkou, the inverted limbs of the D_2 back-folds are less developed than to the west. The unconformable Devonian sandstone is generally rotated to vertical due to D_2 folding. A pervasive, NW-dipping S_2 cleavage is developed in the Devonian and Silurian strata (Figures 11b and 11d). However, evidence for an earlier, D_1 event, can be recognized too. The bedding (S_0) is generally parallel to S_1 cleavage, except in some rare hinges of isoclinal folds that are refolded by SE-verging F_2 folds.

East of Dongkou, top-to-the-NW thrusting dominates again with Devonian sandstone overthrusting onto the Carboniferous to Permian limestone. This structure is consistent with the one described in the Anhua section. Lastly, in this region, Cambrian and Ordovician black shales are deformed by up-right folds with vertical cleavage and vertical lineation. These folds are related to the D_3 event (Figure 9f).

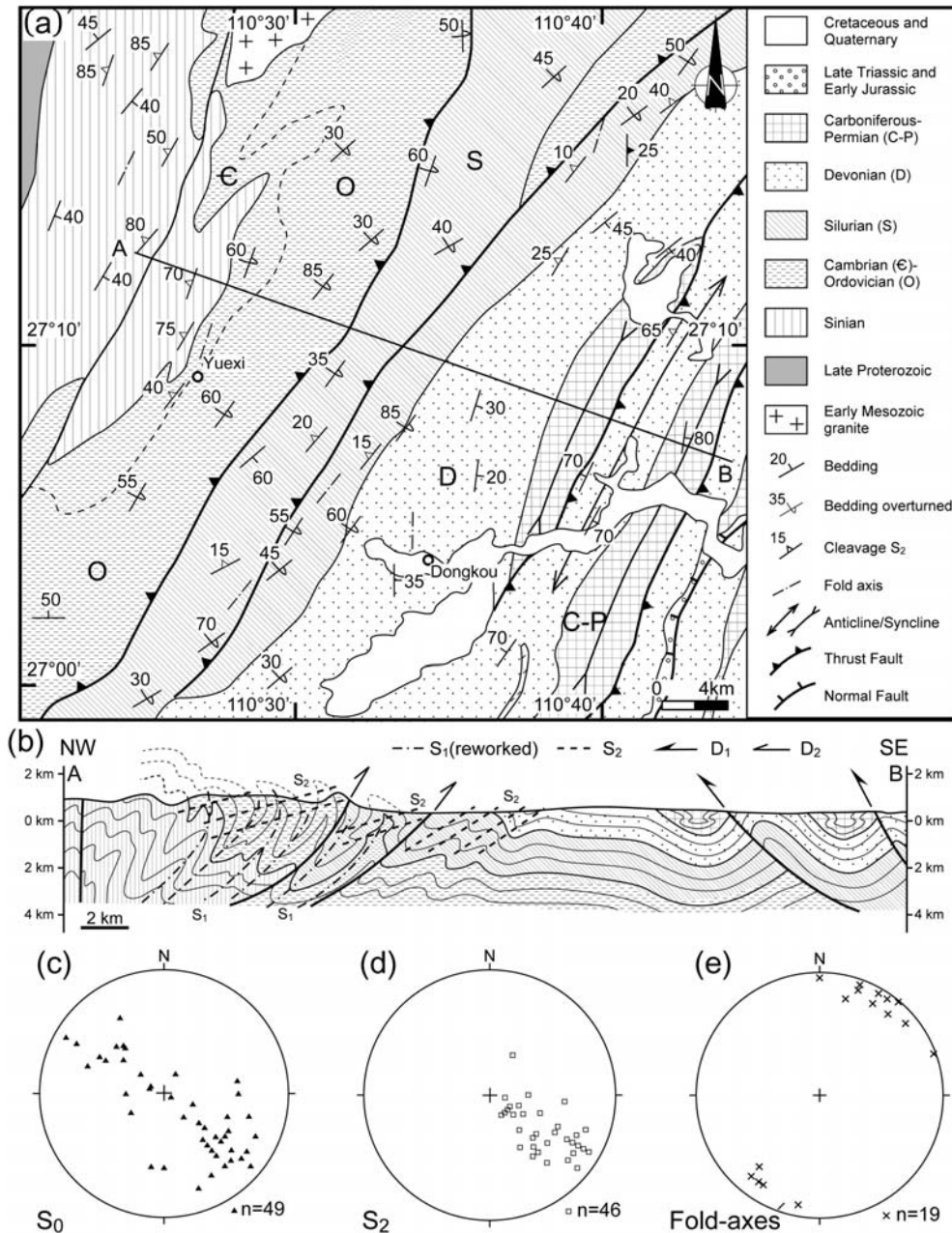


Figure 11. (a): Detailed geologic map of the Eastern Zone near Dongkou showing back-folding structure (Modified after 1:500 000 Geological map of Hunan, *BGMRHN*, 1988). (b): Cross section with F_1 folds refolded by F_2 folds. Stereographic plots (Schmidt lower hemisphere projection) of the structural elements, (c): bedding, (d): S_2 cleavage, (e): F_2 fold axes.

3.3.3 The Lianyuan section

To the east of the Anhua section, the Eastern Zone is mostly represented by Middle Devonian to Early Triassic sedimentary rocks (Figures 3 and 12). Upper Triassic clastic deposits unconformably overlie the older deformed series. This part of the Eastern Zone exhibits well-developed folds and thrusts but slaty cleavage is generally less penetrative than to the west (Figures 12a, 12b and 12e). This feature might be due to a higher structural level in this area. North of Lengshuijiang, Late Devonian sandstone overthrusts northwestwards onto Carboniferous limestone that in turn overthrusts onto Permian formations (Figures 12a and 12b). S_1 cleavage is well developed in mudstone layers interbedded by limestone (Figure 13a). In this thrust system, the coal-bearing argillite and shale layers in the Devonian, Carboniferous and Permian series acts as subordinate, locally developed decollement levels during the NW-directed thrusting. In the stronger limestone and sandstone layers, S_1 is generally absent. Hence, the deformation was largely accommodated in these soft layers. In the core of synclines, Early Triassic thin-bedded limestone is strongly folded (Figure 13b). In addition, SE-verging folds and thrust faults are also observed. For instance, northeast of Lengshuijiang, SE-vergent back-thrusting and back-folding of the D_2 event are well developed with relic of S_1 cleavage preserved in Carboniferous slaty layers (Figure 12c). Likewise, in Devonian mudstone interbedded with sandstone, the S_1 cleavage is refolded by an F_2 fold (Figure 13c). Moreover, north of Shaoyang (Figure 3b), a NW-dipping cleavage, associated with SE-verging folds, is also widely developed. These structures are interpreted here as the result of the D_2 back-folding, as described above in the other areas of the Eastern Zone.

Locally, several meters of inverted limbs can be observed (Figure 13d). Moreover, at the scale of a single 10-meter-wavelength fold, gravitational sliding along the anticline limbs is responsible for the development of collapse folds with contrasting kinematics. West- and east-verging folds formed on both sides of the anticline (Figure 13e). NE of Hengshan city, drilling reports describe a top-to-the-NW thrust of Neoproterozoic sandstone and slate onto Devonian limestone [Bai *et al.*, 2009].

Therefore, to summarize, the bulk geometry of the Eastern Zone is controlled by top-to-the-NW folding and thrusting (D_1 event) reworked by SE-verging back folding and back thrusting (D_2 event), but except in the westernmost part, both events developed without metamorphism. Structurally, the eastern part of the Eastern Zone can be considered as the eastern extension of the fold-and-thrust belt that is developed in the west Eastern Zone, but the difference lies in the thermobarometric conditions of

the polyphase deformation, which took place in the west under higher metamorphic conditions than in the east.

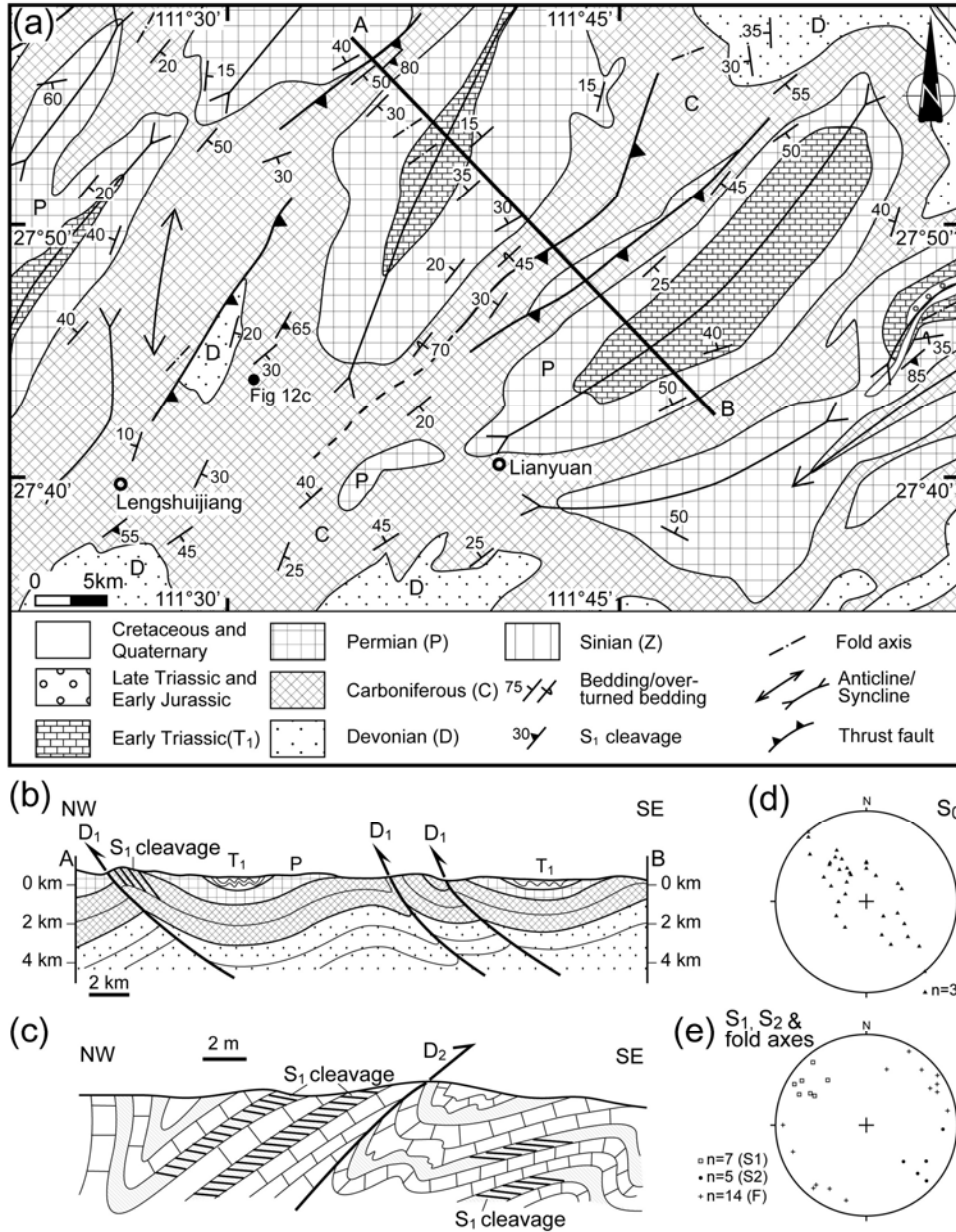


Figure 12. (a): Detailed geologic map of the Eastern Zone near Lianyuan (Modified after 1:500 000 Geological map of Hunan, *BGMRHN*, 1988). (b) and (c): Cross sections of the area. Stereographic plots (Schmidt lower hemisphere projection) of the structural elements, (d): bedding, (e): S₁, S₂ cleavage and fold axes.

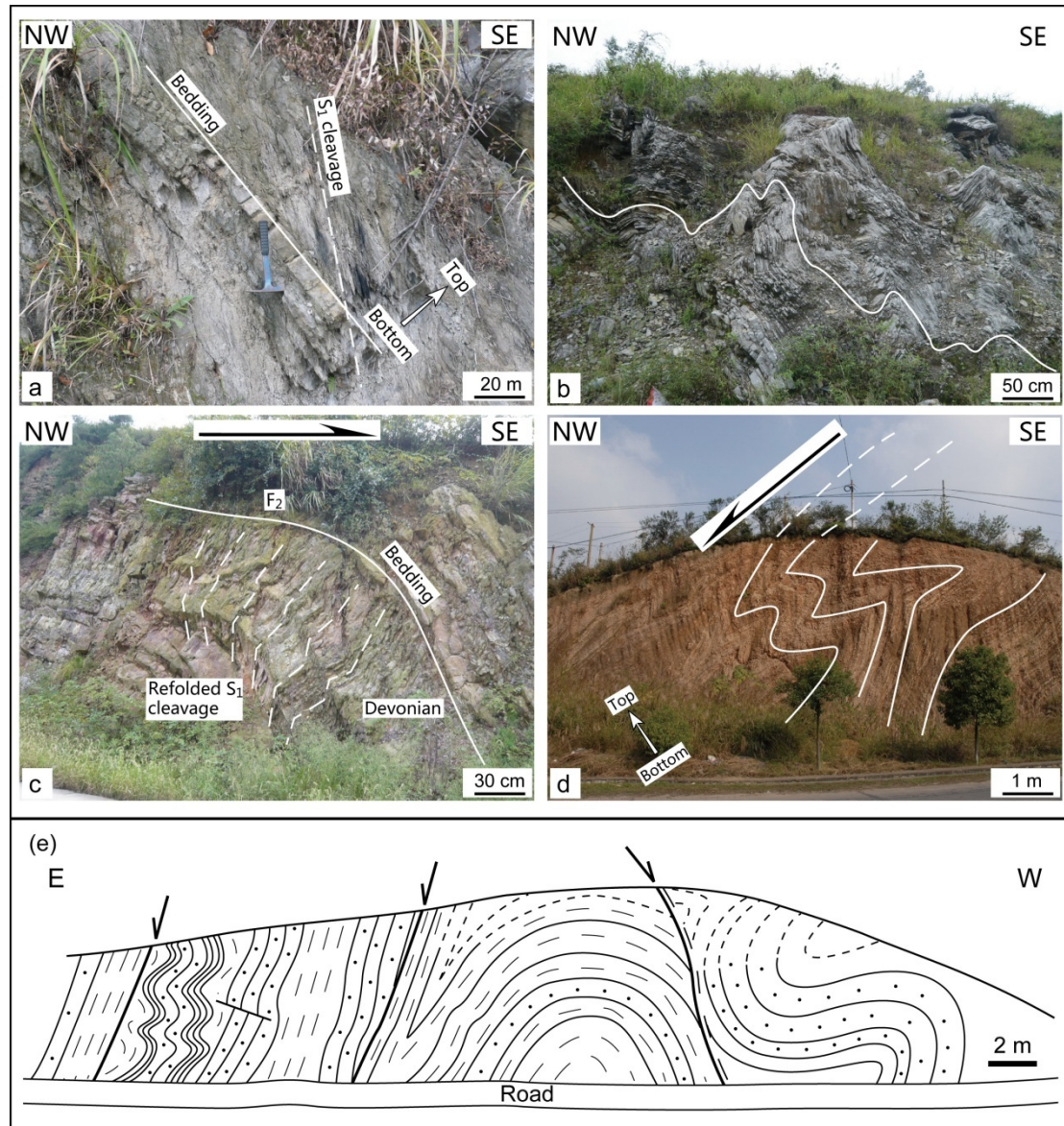


Figure 13. Examples of structures observed in the Eastern Zone. (a): S_0 bedding- S_1 cleavage relationships in Carboniferous limy-mudstone layers indicating a northwestward F_1 fold vergence, east of Anhua ($N27^{\circ}46.268'/E111^{\circ}31.012'$). (b): Strongly folded thin-layer Triassic limestone ($N27^{\circ}53.639'/E111^{\circ}37.699'$). (c) S_1 cleavage refolded in a SE-vergent fold in Late Devonian rocks, indicating that D_1 and D_2 both occurred in the Early Mesozoic ($N28^{\circ}09.767'/E112^{\circ}05.173'$). (d) Gravitational collapse folds in Triassic sandstone interlayered with mudstone, west of Changning ($N26^{\circ}23.541'/E112^{\circ}29.062'$). (e): Secondary collapse folds developed in both limbs of an upright fold in Permian sandstone and shale series, east of Changning ($N26^{\circ}23.434'/E112^{\circ}29.882'$).

3.4 The Deep Metamorphic Unit and the Decollement

Although most of rocks in the areas previously described in the Eastern Zone show only a low greenschist facies metamorphism coeval with the polyphase

deformation, metamorphic rocks are exposed in the deepest part of the Xuefengshan Belt, around some of the Mesozoic granitic plutons (Figures 3b, 14a and 14b).

East of Chengbu (Figure 3), and around Lanrong (Figure 14a), the Proterozoic rocks underlying the Late Neoproterozoic (Sinian) to Paleozoic series consists of slate, schistose sandstone, quartzite and garnet-bearing two-mica schist. These rocks show a pervasive foliation, and a mineral and stretching lineation. In some places, the well developed foliation, represented by a 1 to 5 mm compositional layering marked by alternation of quartz (light) and micaceous (dark) ribbons with a marked grain size reduction, corresponds to a mylonitic fabric (Figure 15a). In these metamorphic rocks, the sub-horizontal N-S trending foliation contains a WNW-ESE stretching lineation (Figures 14d and 14e). The top-to-the-NW shearing is documented by asymmetric pressure shadows surrounding garnet porphyroblasts, sigmoidal quartz clasts and quartz veins. Isoclinal folds with axes parallel to the lineation formed during the ductile shearing are also found (Figure 15b, 15c and 15d).

In the mica-schist, host rock of the Early Paleozoic Maoershan pluton, the mineral lineation is represented by andalusite grains that were formed by the contact metamorphism related to the granite emplacement, but reoriented during the ductile shearing (Figure 15e). The granitic intrusions, particularly the small monzogranitic Lanrong pluton east of the Maoershan pluton (Figure 14a), are also ductilely deformed. The granitic rocks are deformed and metamorphosed into orthogneiss, the foliation of which dips to the west or east in the western and eastern margins of the Lanrong body, respectively (Figure 15f). The mylonitic foliation formed by the alternation of quartz-feldspar layers and biotite-rich parts exhibits a stretching lineation oriented along the NW-SE trend, similar to that observed in the metamorphic aureole and the country rocks of the pluton. Around the orthogneiss massif, granitic dykes intruding into the micaschist and quartzite host rocks, are highly sheared, boudinaged, or folded. These asymmetric lenses show an unambiguous top-to-the-NW sense of shear. All the deformation features indicate that the ductile shearing occurred in a post-solidus stage after granite emplacement.

Upright folds and crenulations rework the synmetamorphic foliation and lineation. Sometimes a subvertical crenulation cleavage pervasively develops parallel to the upright fold axial plane (Figure 15e). The superimposition of the early fabric by a late one is also indicated by the refolding of isoclinally folded quartz veins in the micaschist (Figure 16).

In summary, ductile and synmetamorphic fabrics indicate that the deepest observed part of the Xuefengshan Belt was intensely deformed by a top-to-the-NW shearing, leading to the formation of mylonites. We interpret this high strain zone as a

ductile decollement along which the horizontal shortening, accommodated by folding and thrusting in the upper sedimentary units, is transferred. The decollement was folded in an antiformal pattern during the D₃ event. The tectonic significance of this decollement will be discussed in the forthcoming sections.

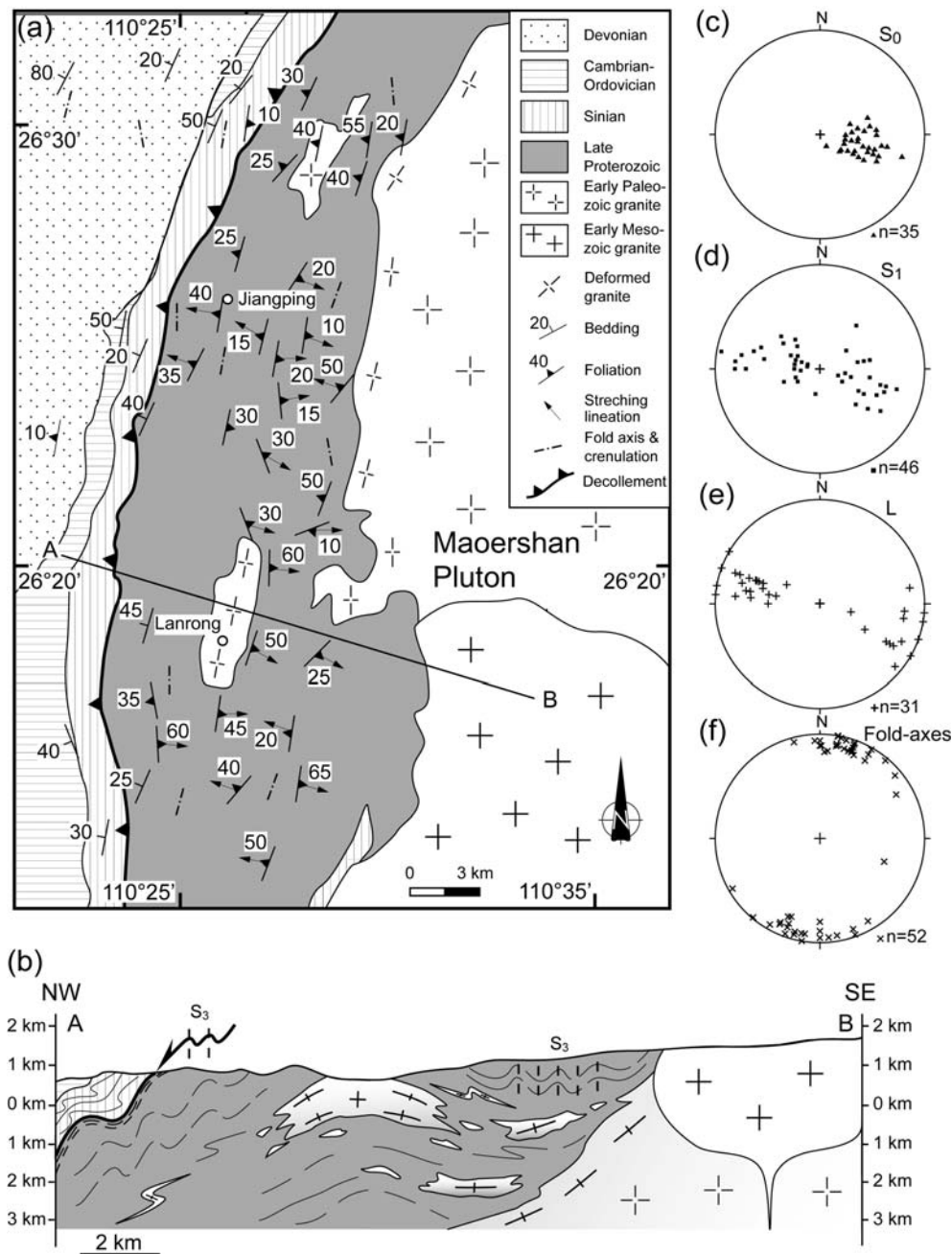


Figure 14. (a): Detailed geologic map of the decollement, east of Chengbu (Modified after 1:500 000 Geological map of Hunan, *BGMRHN*, 1988; Zhou, 2007). (b): General cross section of the area. Stereographic plots (Schmidt lower hemisphere projection) of the structural elements, (c): bedding, (d): S₁ foliation, (e): stretching lineation, (f): F₃ fold axes and crenulation lineation.

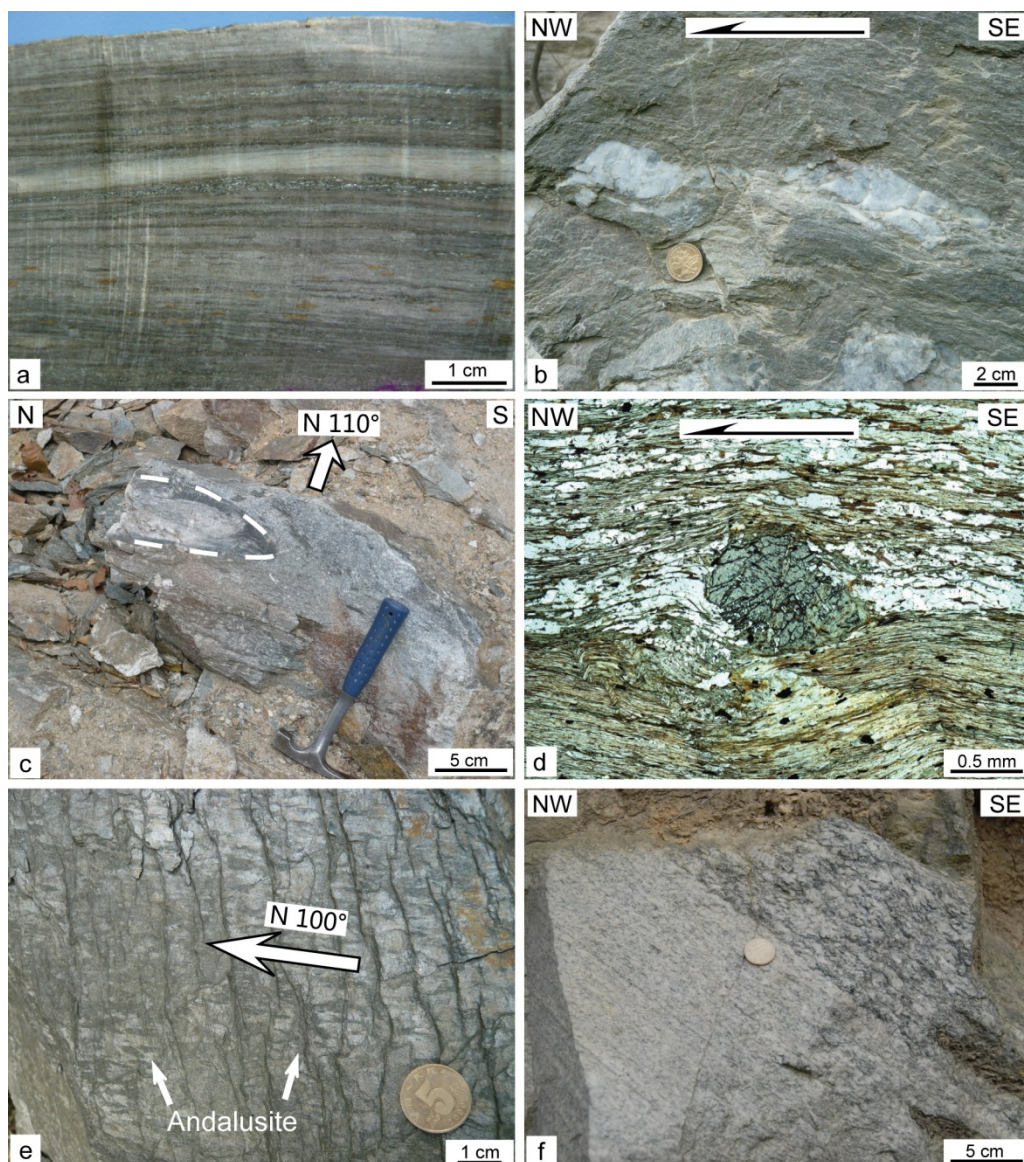


Figure 15. Deformation features along the decollement. (a): Mylonite showing a well developed banded foliation with alternations of quartz ribbons (light), and mica (dark), southeast of Jiangping ($N26^{\circ}25.228'/E110^{\circ}26.868'$). (b): Sigmoidal quartz veins in the mylonitic Neoproterozoic quartzite, east of Jiangping ($N26^{\circ}10.109'/E110^{\circ}43.674'$). (c): Isoclinal fold with fold axes parallel to the shearing direction, northeast of Lanrong ($N26^{\circ}17.885'/E110^{\circ}26.868'$). (d): Garnet porphyroclast with quartz pressure shadows showing the top-to-the NW sense of shear, southeast of Lanrong ($N26^{\circ}14.688'/E110^{\circ}25.811'$). (e): Crenulated micaschist foliation with folded mineral, and stretching lineation marked by reoriented andalusite grains crystallized during the emplacement of the Paleozoic granite, east of Lanrong ($N26^{\circ}21.002'/E110^{\circ}26.180'$). (f): Mylonitized Paleozoic granite with foliated porphyritic granite (top) and fine grained biotite granite (bottom), east of Lanrong ($N26^{\circ}19.743'/E110^{\circ}26.519'$).

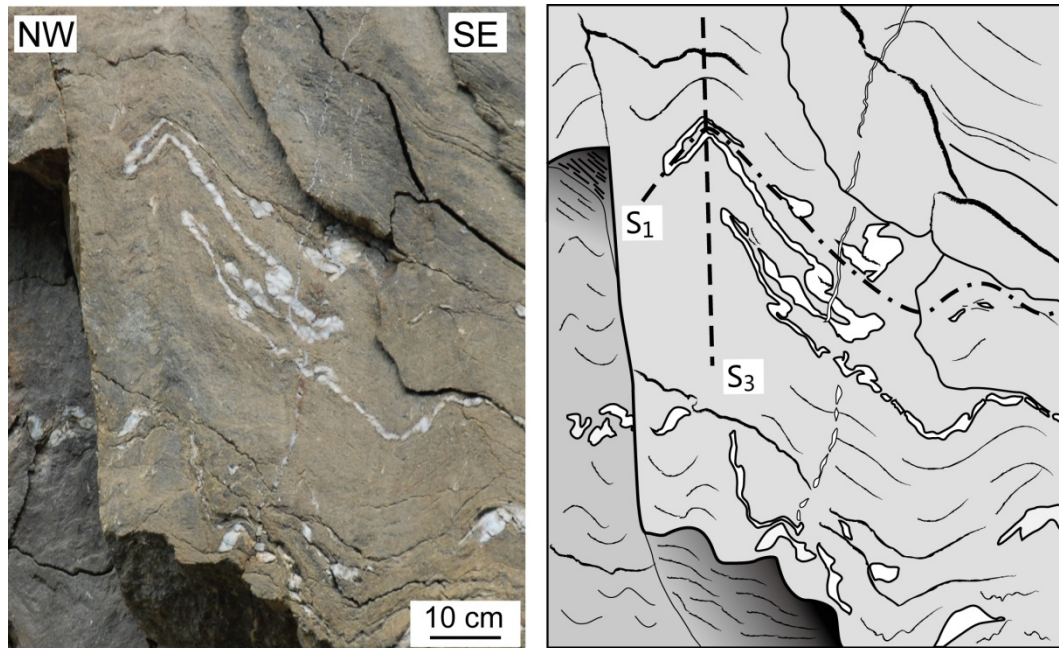


Figure 16. Field picture and interpretation of D_1 isoclinal folds reworked by D_3 NW-SE trending upright folds and crenulation in biotite-garnet micaschist of the decollement, southeast of Lanrong ($N26^{\circ}14.743'/E110^{\circ}25.979'$).

4. Polyphase deformation and timing

4.1 Polyphase deformation

As depicted in the previous section from several examples in the Xuefengshan Belt, the Neoproterozoic to Early Triassic rocks of the SCB experienced several deformation events. In this section the general features of each event are synthesized.

The D_1 event corresponds to the top-to-the-NW thrusting and folding developed in the entire Xuefengshan. Two different structural styles can be attributed to D_1 deformation (Figure 17). In the Western Outer Zone, box-fold structures with localized deformation in the fold hinges are the dominant structural element. Brittle to brittle-ductile structures such as layer-parallel slip, and disharmonic folding are the main features that accommodated shortening in the Western Outer Zone. In the Eastern Zone, the D_1 deformation is essentially ductile. The dominant S_1 slaty cleavage is axial planar to NW-vergent recumbent folds (F_1). S_1 contains a NW-SE striking mineral and stretching L_1 lineation. Shear criteria such as asymmetric quartz or calcite pressure shadows, sigmoidal veins and sheared pebbles in Sinian tillite consistently indicate a top-to-the-NW sense of shear, coeval with a greenschist facies metamorphism. Moving eastward, the D_1 event is also recognized in the eastern, and geometrically upper part of the Eastern Zone with similar structural features but without synkinematic metamorphism. The ductile deformation observed at depth in

the decollement which is developed along a NW-SE striking stretching lineation, and exhibits with the top-to-the-NW shearing sense. This deformation is also attributed to the D₁ event.

Wang et al. [2005] suggested that the top-to-the-WNW thrusting was accompanied by a significant sinistral N-S to NE-SW trending strike-slip component with subhorizontal lineation. However, based on our work, the D₁ deformation is characterized by NW-directed folds and thrusts only with a NW-SE lineation and top to the NW shear sense. Microstructural evidence for a strike-slip component, such as high-angle foliation and subhorizontal stretching lineation, has not been recognized in our study area.

The D₂ event is also widespread in the Eastern Zone. Several observations unambiguously demonstrate that SE verging F₂ folds associated with a S₂ cleavage overprint the D₁ structures. This event is not as intense as the first one since no metamorphism and high strain zones are observed. Due to the top-to-the-SE D₂ shearing, Sinian to Devonian strata, in the eastern part of the Eastern Zone, are largely overturned by SE directed folding. These D₂ structures are also recognized by *Wang et al.* [2005], but considered as coeval, not successive, with the NW-directed deformation. The overprint on D₁ by D₂, as shown above, is not in agreement with this interpretation.

Lastly, upright D₃ folds with a subvertical S₃ cleavage and down-dip L₃ stretching lineation are developed in the Eastern Zone. In the field, it is sometimes difficult to determine if this vertical cleavage represents S₁ turned to a steeper dip or a newly formed S₃ cleavage. However, since the surface folded by the tight upright folds sometimes exhibits a preferred orientation of platy phyllic minerals developed during D₁ metamorphism, the upright folds are attributed here to a D₃ event. In the same way, the upright folding of S₂ cleavage can be observed in a few places, for instance north of Chengbu.

Superimpositions of S₁-S₂, S₂-S₃, and S₁-S₃ cleavages recognized in several areas of the Eastern zone argue for a relative timing of the polyphase deformation. As a whole, the three deformation events correspond to the structural response of a bulk NW-SE shortening. The D₁ event characterized by top-to-the-NW asymmetric structures, and a deep-seated ductile decollement layer with similar kinematics suggests that the formation of the Xuefengshan Belt is related to northwest directed crustal scale shearing.


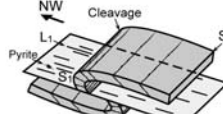
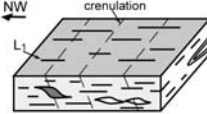
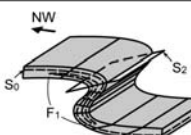
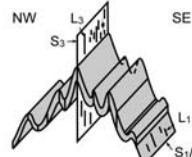
Deformation event	Western Outer Zone	Eastern Zone	Deep Metamorphic Unit
D ₁	 <p>Well developed box folds with gravity collapse folds in the vertical limbs. No cleavage.</p>	 <p>S₁, L₁ and F₁ with top-to-the-NW kinematics. Low greenschist facies metamorphism (sericite + chlorite).</p>	 <p>Mylonite with flat-lying S₁ foliation. NW-SE lineation with top-to-the-NW shearing. Greenschist facies metamorphism (biotite+garnet + muscovite).</p>
D ₂	Absent	 <p>S₁ and F₁ reworked by F₂ SE-directed folds with S₂ cleavage.</p>	Absent
D ₃	Absent	 <p>S₁, L₁, S₂ reworked by F₃ folds. Vertical S₃ with L₃ stretching lineation.</p>	

Figure 17. Summary of the main deformation structures. D₁, D₂ and D₃ events recognized in the Western Outer Zone, the Eastern Zone and the Deep Metamorphic Unit of the Xuefengshan Belt.

4.2 Timing of the D₁, D₂, and D₃ events

As mentioned in section 2.3, the Early Paleozoic event is restricted to the southeastern part of the Eastern Zone where the pre-Devonian structures are represented by south-verging folds (Figure 4). Furthermore, both Early Paleozoic synmetamorphic deformation and crustal partial melting are absent in the Xuefengshan. As already demonstrated to the east of the Xuefengshan (e.g. *Faure et al.*, 2009; *Charvet et al.*, 2010), the Late Silurian-Early Devonian plutons that intrude the Early Paleozoic folded series are undeformed. Middle Devonian or younger rocks directly overlie the granitoids. It is hereby concluded that, in the Xuefengshan Belt, the post-solidus ductile deformation of the granitoids took place after the Early Paleozoic orogeny. Thus, the Xuefengshan Belt shows hardly any evidence of the Early Paleozoic orogeny of SE China.

From Neoproterozoic to Early Triassic, the sedimentary rocks involved in the Xuefengshan Belt were deposited in a shallow sea environment except for during a short hiatus between Late Silurian and Early Devonian. But Middle Triassic strata are missing in the Xuefengshan Belt. The subsequent Late Triassic to Early Jurassic sedimentary series consists of clastic rocks conglomerate, sandstone and mudstone

derived from the erosion of the Xuefengshan Belt. These Mesozoic deposits are post-orogenic products accumulated in small intramontane basins. In contrast to the pre-Middle Triassic strata that are all involved in folding and thrusting, Late Triassic-Early Jurassic strata show only limited brittle deformation [BGMRHN, 1988; Shu *et al.*, 2009]. At depth, the ductile deformation related to the decollement described in section 3.4 involves mylonitized Early Paleozoic granitoids [BGMRHN, 1988; Zhou, 2007], and their Proterozoic country rocks. Thus, the ductile deformation along the D₁ decollement belongs to the Early Mesozoic event. Furthermore, the Triassic aluminous to peraluminous plutons, which intrude already deformed rocks are found widely distributed across the Xuefengshan Belt (Figure 3b). These magmatic rocks, devoid of any ductile deformation, are dated between in 225-200 Ma [Ding *et al.*, 2005; Chen *et al.*, 2006, 2007a, 2007b; Wang *et al.*, 2007a; Li and Li, 2007; Li *et al.*, 2008]. These lines of evidence indicate that the D₁ and D₂ events occurred between 240-220 Ma. The Late Triassic plutons crop out in the core of upright anticlines ascribed to the D₃ event. As observed in many belts, the granitic plutons are responsible for a regional deformation during their emplacement. Although radiometric dating of the D₃ folding is not available, it appears rather reasonable to consider that the D₃ event is coeval with granite emplacement, because the upright folding was formed due to locally compressional environment.

The three events can also be understood as three increments of the same deformation continuum. During the Early-Middle Triassic evolution of the Xuefengshan Belt, the regional NW-SE shortening was firstly accommodated by a NW-directed flat-lying ductile shearing. As in various orogenic belts for instance in the Alps, [e.g. Escher and Beaumont, 1997], Himalaya [Godin *et al.*, 1999] or Taiwan [Malavieille, 2010], a bi-vergent fold system develops in the Xuefengshan Belt. In agreement with analogue experiments and numerical modeling, [e.g. Willett *et al.*, 1993; Beaumont *et al.*, 1994; Malavieille, 2010], back-folding will form in the layers that cannot be underthrust below a frontal thrust, (i.e. the MXT in the case of the Xuefengshan Belt). The continuing convergence, responsible for overthickening in the western Eastern Zone of the Xuefengshan Belt, induces an instability that will be removed by back-folding and back-thrusting as illustrated in the Alps and Himalaya [Escher and Beaumont, 1997; Godin *et al.*, 1999]. Experiments also show that a conjugate deformation with NW- and SE-verging folds, may occur simultaneously. In the Xuefengshan Belt, the timing of box-folding in the Western Outer Zone is not well constrained. Thus, the eventuality that box-fold developed during the D₂ event cannot be excluded. Lastly, D₃ upright folding and vertical stretching accommodated the last stage of continuing shortening.

5. Discussion

5.1 Bulk architecture of the Xuefengshan Belt

The regional top to the NW ductile shearing with folding and thrusting in the Xuefengshan Belt has been recognized by other geologists in spite of differences, as stated in section 2, in the structural style, or the timing of the deformation [Qiu *et al.*, 1998, 2000; Yan *et al.*, 2003; Wang *et al.*, 2005]. Moreover, the general interpretations proposed in these models are not in agreement with the structural features described above. According to our survey, from west to east, we subdivide the Xuefengshan Belt into several zones, which correspond to different deformation types (Figures 3 and 17). Yan *et al.* [2003] considered that the Neoproterozoic rocks of the Wuling Mountain and Xuefeng Mountain form a klippe overthrust onto the in situ Paleozoic series. However, our field observations are not consistent with this interpretation. Indeed, superposition of older rocks above younger ones can be locally observed. This feature is the consequence of collapse folds formed by gravity sliding along highly dipping layers [Faure *et al.*, 1998]. Thus evidence for long-distance thrust is not confirmed by our survey.

In the western part of the Eastern Zone, east of the MXT, cleavage is widespread in Neoproterozoic and Paleozoic strata, and exhibits a fan-like pattern, with a dip to the SE associated with NW-verging folds, whereas in the east, the syn-schistose folds verge to the SE and the cleavage dips NW (Figures 8 and 11). Top-to-the-SE shearing indicated by folds and thrusts is interpreted as a back-folding or back-thrusting event. The large-scale inversion is well developed in Upper Sinian to Devonian sedimentary rocks where a back-folding boundary can be identified (BFB, Figure 3b). Superimposed folding shows that SE-vergent folding post-dates the NW-vergent folding.

East of the Chenzhou-Linwu fault (Figure 3), well preserved Early Paleozoic structures are weakly reworked by the Triassic deformation. The Late Neoproterozoic to Ordovician, sedimentary series is deformed by E-W to NW-SE trending folds, with SW-vergence and a NE-dipping slaty cleavage. A ductile decollement that separates the folded sedimentary series from underlying metamorphic rocks is described in Jiangxi Province, east of the study area [Faure *et al.*, 2009]. A similar structure is also inferred east of the Chenzhou-Linwu fault. Thus, this fault represents the eastern limit of the Early Mesozoic Xuefengshan Belt.

In the outer zones of collision belts (e.g. Alpine Jura or Zagros Fold-and-Thrust Belt), decollement layers develop in low strength rocks such as evaporites or black shales to accommodate the bulk regional shortening [e.g. Escher and Beaumont, 1997; McQuarrie, 2004]. Below the decollement layer, basement rocks lack strong and

pervasive deformation. In the Xuefengshan Belt, a major crustal decollement must be formed at the base of the Proterozoic to Early Triassic sedimentary series in order to accommodate the NW-SE shortening recorded by the D_1 event. The Early Neoproterozoic mudstone and siltstone series corresponds to this decollement layer (Figure 2). Due to the D_3 upright folding, a portion of this high strain discontinuity is exposed in the Chengbu area in the core of a D_3 antiform (Figures 14 and 18), but the underlying basement is not observed in the Xuefengshan Belt. In the study area, available crustal scale seismic data that may constrain the deep geometry of the decollement are rare, and inaccurate [Qin, 1991]. A SE dipping reflector that might correspond to a decollement is imaged in Central Hunan, below the Eastern Zone. Thus, we argue that the MXT and other thrusts are rooted in this decollement layer. We interpret the upper crustal deformation responsible for thrusts, folds, and slaty cleavage as thin-skin tectonics underlain by a major decollement, rather than a thick skinned thrusting [Yan *et al.*, 2003]. However, a thick skin tectonic style involving the basement of the Eastern Zone cannot be ruled out since seismic data are not available.

A question arises about the eastern extension of the decollement. Two possibilities can be put forward. The simplest one is to assume a single decollement layer that deepens eastward up to the Chengzhou -Linwu fault. Such a structure will develop southeastward for more than 300km that might be considered as unrealistic. Furthermore, in this case, the origin of the D_2 back folding in the Eastern Zone can be the result of SE-directed thrusting through the decollement (Figure 18a). Another possibility would be to consider that the decollement deepens eastward below the Eastern Zone (Figure 18b). In this interpretation, the east of the Eastern Zone would be underlain by a second decollement. Such a geometric pattern may account for the development of the D_2 back folding and back-thrusting that would be rooted within the decollement. Whatever the right interpretation, the intracontinental Xuefengshan Belt is clearly underlain by a high strain layer that separates the upper crustal rocks that deformed by thrusting and folding and the middle to lower crustal rocks that are not exposed. This hidden basement corresponds to a piece of the SCB. In order to accommodate the shortening experienced by the Late Neoproterozoic (Sinian) to Early Triassic sedimentary series, the underlying basement must have experienced intracontinental underthrusting during the Triassic. Since East of the Chenzhou-Linwu fault the Triassic deformation is weak, and the Early Paleozoic tectonics is the main feature, this fault that represents the eastern tectonic boundary of the Xuefengshan Belt can be interpreted as a back-stop.

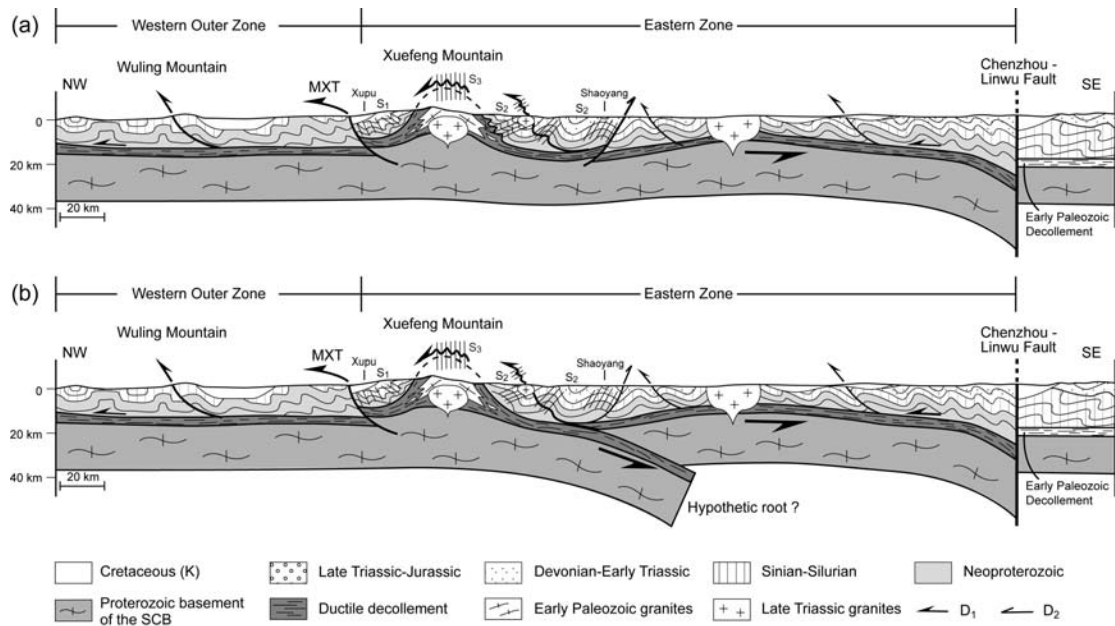


Figure 18. Two possible interpretative bulk cross-sections of the Xuefengshan Belt: (a) and (b), located in Figure 3b. The Triassic decollement, observed in the core of the D_3 anticlines, separates the upper crust deformed by NW-directed folding and thrusting, and the middle-lower crust deepening to the SE. The Xuefengshan Belt is intruded by late Triassic peraluminous granitic plutons. SE of Shaoyang, the pre-Devonian series are folded by S-verging folds, but these folds parallel to the line of section are not represented. East of the Chenzhou-Linwu fault, the Triassic deformation is weak. The main structure developed during the Early Paleozoic orogeny corresponds to S or SE-verging folds underlain by a decollement (cf. Faure et al., 2009). The crustal structure of the Xuefengshan Belt can be explained in two cases. For hypothesis (a), one decollement is depicted rooted in the Chenzhou-Linwu fault. SE of Shaoyang, due to the second phase of top-to-the SE shearing, the decollement is cut by a D_2 SE-directed thrust coeval with S_2 cleavage. In hypothesis (b), two layers of decollement are inferred. The western one is rooted below the Eastern Zone, whereas the eastern one deepens eastward, and is rooted in the Chenzhou-Linwu fault. The D_2 event, top-to-the-SE, reworks the Neoproterozoic to Early Triassic sedimentary series, but the D_2 thrust is rooted in the decollement.

5.2 Tectonic implications for the SCB

During the Early Triassic, the SCB underwent several orogenic events along its boundaries. To the north, the SCB subducted beneath the North China Craton [Hacker and Wang, 1995; Faure et al., 1999; 2008]; to the west, the Songpan-Ganzi and Longmenshan Belts record evidence for Triassic deformation [Wallis et al., 2003; Harrowfield and Wilson, 2005; Roger et al., 2008, 2010], and to the southwest, the Yunnan-Guangxi-NE Vietnam Belt separates the SCB from Indochina [Lepvrier et al., 2008, 2011; Carter et al., 2001; Carter and Clift, 2008]. While the tectonic evolution models of the SCB must obviously also consider these three orogenic events, an extensive discussion of the tectonics of the SCB is beyond the scope of this paper.

The Xuefengshan Belt has been interpreted as the result of the westward progressive collision of the Yangtze Block with the North China Block during the Late Jurassic to Cretaceous [Yan *et al.*, 2003], but the Middle Triassic event, which is clearly postdated by the Late Triassic plutons and the regional Late Triassic unconformity, is not distinguished from the Cretaceous one. Other authors proposed that this belt is the western part of an Early Mesozoic oblique convergent zone, with another structural belt in western Fujian Province as its eastern part, formed due to the relatively weak mechanical behavior of the SCB that was surrounded by the more rigid North China and Indochina blocks. The entire SCB was deformed in a diffuse manner with a bi-vergent structure, that is, top to the NW thrusting in the Xuefengshan Belt and top to the SE thrusting in western Fujian Province, east of the Chenzhou-Linwu Fault [Chen, 1999; Wang *et al.*, 2005, 2007c]. However, the top-to-the-SE structures in the southeastern part of the SCB are assigned to a Late Jurassic event [Chen, 1999], while the Xuefengshan Belt is formed in Early Mesozoic. Thus, the two parts of the flower structure across the entire SCB did not form in the same time.

Recently, the South China fold belt was interpreted as a 1300-km wide intracontinental orogen [Li and Li, 2007]. The temporally and geographically restricted Late Triassic shallow terrestrial or lacustrine basins represent post-orogenic deposits, and the Early Triassic marine limestone strata of Hunan and Jiangxi provinces both indicate similar platform depositional environment [BGMRJX, 1984; BGMРН, 1988]. According to this model, folding and thrusting, syn-orogenic magmatism, and foreland basin deposition migrated toward the SCB continental interior in response to the flat-slab subduction of the Pacific plate. However, the timing of the onset of the Pacific plate subduction is still under debate. Some authors suggest that west-directed subduction did not start until ~125 Ma [Engebretson *et al.*, 1985], but others argue that subduction already started in the Early Mesozoic, even in Late Permian [Li *et al.*, 2006]. Moreover, at the scale of the SCB, the radiometric ages of the Triassic plutons, ranging from 220 Ma to 208 Ma, are randomly distributed [Ding *et al.*, 2005; Chen *et al.*, 2006, 2007a, 2007b; Wang *et al.*, 2007a; Li and Li, 2007; Li *et al.*, 2008]. These granitic plutons do not show a magmatic trend younging from SE to NW that might be related to the progressive flat-slab subduction of the Pacific plate as proposed by Li and Li [2007]. However, Triassic NW-directed subduction is preferable, as suggested not only by Permian arc magmatism in Hainan Island to the south, but also by Late Permian to Early-Middle Triassic high pressure metamorphism in the Japanese islands [Faure and Charvet, 1987; Faure *et al.*, 1988; Li *et al.*, 2006]. Although still speculative, in the present state of knowledge of the SCB geology, the far-field effect of the Paleo-Pacific subduction model accounts well

for the structural features described in this paper, and the overall tectonic evolution of the Xuefengshan Belt.

5.3 Insights for intracontinental orogenic belts

In the past 20 years, numerous intracontinental orogens have been studied by multidisciplinary approaches [*Hendrix et al., 1992; Avouac et al., 1993; Choukroune, 1992; Hand and Sandiford, 1999; Sandiford et al., 2001; English and Johnston, 2004; Faure et al., 2009; Charvet et al., 2010* and enclosed references]. In the Alice Springs and the Pyrenees belts, for example, deep crustal or lithospheric structures are revealed by seismic profiles. It is noteworthy that most of intracontinental belts are characterized by thick-skinned tectonics, induced by remarkable crustal displacement or continental subduction [*Goleby et al., 1989; Choukroune, 1992*]. However, the Xuefengshan Belt is a particular chain with a regional high-strain decollement layer but no exposure of high-grade metamorphic rocks. Thus a thin-skinned tectonic evolution is preferred here. Among the intracontinental belts worldwide, the Jura belt is also a well established thin-skinned orogens with a basal decollement represented by Triassic salt formations. On the contrary, without detailed seismic data, the deep structure of the Xuefengshan cannot be well constrained. Therefore, a thick-skinned model cannot be completely ruled out.

As a regional back-stop boundary for the Xuefengshan Belt, the Chenzhou-Linwu fault played an important role in the Early Mesozoic tectonics. This fault is also considered to be the potential suture zone between the Yangtze block and the Cathaysia block during the Neoproterozoic collision [*Wang et al., 2007c*].

Furthermore, in intracontinental tectonics, an internal weak zone is the place to localize the deformation induced by the compressional stress developed in response to subduction or collision at plate margins, and thereby triggers an intracontinental deformation. In the Pyrenees orogen, the most intense Cenozoic deformation was accommodated within the pre-orogenic continental rifts basins opened during the Cretaceous [*Choukroune, 1992*]. The Alice Springs orogen is a reactivated Paleozoic belt superimposed upon the Neoproterozoic-Early Paleozoic Petermann orogen [*Hand and Sandiford, 1999; Sandiford et al., 2001*]. The Late Paleozoic Tianshan orogen was compressed and uplifted again during the Cenozoic, due to the Indo-Asia collision [*Hendrix et al., 1992; Avouac et al., 1993*]. Therefore, the weak zone along which an intracontinental belt will develop is a pre-existing crustal weak zone such as a rift, or a regional fault zone formed during an older orogeny, along which the continental crust has been rheologically softened. In our case, we infer that the Early

Mesozoic Xuefengshan Belt was an intracontinental belt developed as a result of the reactivation of the Neoproterozoic Chenzhou-Linwu fault.

The geodynamic cause of intracontinental orogens is still a matter of debate. Far-field effects of either remote flat-slab subduction or continental collision are the favored interpretations [e.g. *Dickinson and Snyder, 1978; Avouac et al., 1993; English and Johnston, 2004*]. Nevertheless, a peripheral compressional stress perpendicular to the orogenic belt is a prerequisite to the formation of an intracontinental orogen, no matter this push is originated from subduction, collision, or ocean ridge extension.

6. Conclusion

Our new structural data, combined with previous works, allow us to establish the following statements.

1. The Xuefengshan Belt can be divided into two tectonic zones. (1) The Western Outer Zone is characterized by box-fold structures with gravity collapse folds and layer slip in the fold hinges; (2) The Eastern Zone represents the most complex domain in which ductile deformation is coeval with weak greenschist facies metamorphism. NW-directed thrust and folds associated with a pervasive axial planar slaty cleavage are reworked by two superimposed deformation events. The folded Neoproterozoic to Early Triassic sedimentary series is never overthrust by old basement rocks.

2. The bulk architecture of the whole belt results from polyphase deformation. The D_1 event, characterized by a top-to-the-NW ductile shearing, is responsible for the main structure of the Xuefengshan Belt. The D_2 event, observed in the Eastern Zone, corresponds to a back-folding and back-thrusting stage with NW-dipping cleavage. The D_2 folds superimpose upon the D_1 ones. D_3 is responsible for upright folds with vertical axial planar cleavage, and vertical stretching lineation. The deformed rocks belong to the upper continental crust, which is underlain by a ductile decollement layer that can be observed in a few places due to the D_3 upright folding. Since this decollement layer is characterized by a NW-SE striking lineation, and a synmetamorphic top-to-the-NW ductile shearing that complies well with the northward vergence of the entire belt, the ductile deformation along the decollement likely developed during D_1 . As a whole, the Xuefengshan Belt is the result of a NW-SE shortening that involved the entire Early Triassic to Late Neoproterozoic sedimentary upper crust of the SCB. The Proterozoic basement of the SCB is not involved in the bulk structure of the Xuefengshan Belt.

3. The main deformation of the Xuefengshan Belt began after the Early Triassic and was completed before the deposition of the Late Triassic continental to lacustrine

terrigenous deposits, and also before the emplacement of the Late Triassic peraluminous granitic plutons. The deformation lasted around 20 Ma, from 240 Ma to 220 Ma.

4. The Xuefengshan Belt formed contemporaneously to the South Qinling-Dabie, and Longmenshan-Jinshajiang–SW China-NE Vietnam belts that developed along the northern and southwestern margins of the SCB, respectively. Although the two belts can be related to interactions between the margins of the SCB and, the North China Block and Indochina Block respectively, the geodynamic setting of the Xuefengshan Belt remains speculative. In spite of lack of reliable geophysical data on its deep crustal structure, the Xuefengshan Belt is interpreted as an Early Mesozoic intracontinental orogen, in which southeastward underthrusting of the SCB accommodated the folding and thrusting of the upper crustal sedimentary rocks. This early Triassic orogen possibly originated as a far-field effect of the northwestward Pacific subduction below the SCB.

Acknowledgements Fieldwork has been funded by the Innovative Project of the Chinese Academy of Sciences (Grant No. KZCX1-YW-15-1) and Major State Basic Research Development Program of China (2005CB422101, 2009CB825008). NSFC grants n° 90714007 and 40730315 are also acknowledged. Constructive reviews by the associate editor and three anonymous reviewers helped us to improve this manuscript.

Reference

- Allen, M. B., S. J. Vincent, and P. J. Wheeler (1999), Late Cenozoic tectonics of the Kepingtage thrust zone: Interactions of the Tien Shan and Tarim Basin, northwest China, *Tectonics*, 18(4), 639-654, doi:10.1029/1999TC900019.
- Avouac, J. P., P. Tapponnier, M. Bai, H. You, and G. Wang (1993), Active Thrusting and Folding Along the Northern Tien Shan and Late Cenozoic Rotation of the Tarim Relative to Dzungaria and Kazakhstan, *J. Geophys. Res.*, 98(B4), 6755-6804, doi:10.1029/92JB01963.
- Bai D. Y., B. W. Zou, L. H. Zhao, Z. H. Li, X. H. Wang, T. Q. Ma, D. G. Xiao and Y. Y. Peng (2009), Basic characteristics of Taihu Thrust System in Eastern Hunan (in Chinese with English abstract), *Geology in China*, 36(1), 54-65.
- Beaumont C., P. Fullsack and J. Hamilton (1994), Styles of crustal deformation in compressional orogens caused by subduction of the underlying lithosphere, *Tectonophysics*, 232, 119-132, doi:10.1016/0040-1951(94)90079-5.

- Bureau of Geology and Mineral Resources of Guangxi province (BGMRGX) (1985), *Regional Geology of the Guangxi Zhuang Autonomous Region*, 853 pp., Geol. Publishing House, Beijing.
- Bureau of Geology and Mineral Resources of Hunan province(BGMRHN) (1988), *Regional Geology of the Hunan Province*, 507 pp., Geol. Publishing House, Beijing.
- Bureau of Geology and Mineral Resources of Jiangxi Province (BGMRJX) (1984), *Regional Geology of the Jiangxi Province*, 921 pp., Geol. Publishing House, Beijing.
- Carter, A., and P. D. Clift (2008), Was the Indosinian orogeny a Triassic mountain building or a thermotectonic reactivation event?, *CR Géosci.*, 340(2-3), 83-93, doi:10.1016/j.crte.2007.08.011.
- Carter, A., D. Roques, C. Bristow, and P. Kinny (2001), Understanding Mesozoic accretion in Southeast Asia: Significance of Triassic thermotectonism (Indosinian orogeny) in Vietnam, *Geology*, 29(3), 211-214, doi:10.1130/0091-7613(2001)029<0211:UMAIISA>2.0.CO;2.
- Charvet, J., L. S. Shu, Y. S. Shi, L. Z. Guo, and M. Faure (1996), The building of south China: Collision of Yangzi and Cathaysia blocks, problems and tentative answers, *J. Southeast Asian Earth Sci.*, 13(3-5), 223-235, doi:10.1016/0743-9547(96)00029-3.
- Charvet, J., L. Shu, M. Faure, F. Choulet, B. Wang, H. Lu, and N. Le Breton (2010), Structural development of the Lower Paleozoic belt of South China: Genesis of an intracontinental orogen, *J. Asian Earth Sci.*, 39(4), 309-330, doi:10.1016/j.jseaes.2010.03.006.
- Chen, A. (1999), Mirror-image thrusting in the South China Orogenic Belt: tectonic evidence from western Fujian, southeastern China, *Tectonophysics*, 305(4), 497-519, doi:10.1016/S0040-1951(99)00036-0.
- Chen, W. F., P. R. Chen, X. M. Zhou, H. Y. Huang, X. Ding, and T. Sun (2006), Single-zircon La-ICP-MS U-Pb Dating of the Yangmingshan Granitic Pluton in Hunan, South China and its Petrogenetic Study (in Chinese with English abstract), *Acta Geol. Sin.*, 80(7), 1065-1077.
- Chen, W. F., P. R. Chen, H. Y. Huang, X. Ding, and T. Sun (2007a), Chronological and geochemical studies of granite and enclave in Baimashan pluton, Hunan, South China, *Sci. in China (D)*, 50(11), 1606-1627, doi:10.1007/s11430-007-0073-1.
- Chen, W. F., P. R. Chen, X. M. Zhou, H. Y. Huang, X. Ding, and T. Sun (2007b), Single Zircon LA-ICP-MS U-Pb Dating of the Guandimiao and Wawutang

- Granitic Plutons in Hunan, South China and its Petrogenetic Significance, *Acta Geol. Sin.*, 81, 81-89.
- Choukroune, P. (1992), Tectonic evolution of the Pyrenees, *Annu. Rev. Earth Planet. Sci.*, 20, 143-158, doi:10.1146/annurev.ea.20.050192.001043.
- Dickinson, W. R., and W. S. Snyder (1978), Plate tectonics of the Laramide orogeny, in Matthews Ili, V., ed., Laramide folding associated with Basement Block faulting in the Western United States: *Geol. Soc. Am. Memoir*, 151, 355–366.
- Ding, X., P. R. Chen, W. F. Chen, H. Y. Huang, and X. M. Zhou (2005), LA-ICPMS zircon U-Pb age determination of the Weishan granite in Hunan: petrogenesis and significance: *Sci. in China (D)*, v. 35, p. 606-616, doi:10.1007/s11430-006-0816-4.
- Engebretson, D. C., A. Cox, and R. G. Gordon (1985), Relative motion between oceanic and continental plates in the Pacific basin, *Spec. Pap. Geol. Soc. Am.*, 206, 1 – 55.
- English, J. M., and S. T. Johnston (2004), The Laramide orogeny: What were the driving forces?, *Int. Geol. Rev.*, 46(9), 833-838, doi:10.2747/0020-6814.46.9.833.
- Escher, A., and C. Beaumont (1997), Formation, burial and exhumation of basement nappes at crustal scale: a geometric model based on the Western Swiss-Italian Alps, *J. of Struc. Geol.*, 19, 955-974, doi:10.1016/S0191-8141(97)00022-9.
- Faure, M., and J. Charvet (1987), Late Permian/early Triassic orogeny in Japan: piling up of nappes, transverse lineation and continental subduction of the Honshu block, *Earth and Planetary Science Letters*, 84(2-3), 295-308, doi:10.1016/0012-821X(87)90094-X.
- Faure, M., P. Monié, and O. Fabbri (1988), Microtectonics and ^{39}Ar - ^{40}Ar dating of high pressure metamorphic rocks of the south Ryukyu Arc and their bearings on the pre-Eocene geodynamic evolution of Eastern Asia, *Tectonophysics*, 156(1-2), 133-143, doi:10.1016/0040-1951(88)90287-9.
- Faure, M., Y. Sun, L. Shu, P. Monié, and J. Charvet (1996), Extensional tectonics within a subduction-type orogen. The case study of the Wugongshan dome (Jiangxi Province, southeastern China), *Tectonophysics*, 263(1-4), 77-106, doi:10.1016/S0040-1951(97)81487-4.
- Faure, M., W. Lin, and Y. Sun (1998), Doming in the southern foreland of the Dabieshan (Yangtse block, China), *Terra Nova*, 10(6), 307-311.

- Faure, M., W. Lin, L. S. Shu, Y. Sun, and U. Scharer (1999), Tectonics of the Dabieshan (eastern China) and possible exhumation mechanism of ultra high-pressure rocks, *Terra Nova*, 11(6), 251-258, doi:10.1046/j.1365-3121.1999.00257.x.
- Faure, M. W. Lin, P. Monié, S. Meffre (2008), Paleozoic collision between the North and South China blocks, Early Triassic tectonics and the problem of the ultrahigh-pressure metamorphism. *CR Géosciences, special issue Triassic Tectonics in East Asia*, 340(2-3), 139-150, doi:10.1016/j.crte.2007.10.007.
- Faure, M., L. Shu, B. Wang, J. Charvet, F. Choulet, and P. Monié (2009), Intracontinental subduction: a possible mechanism for the Early Palaeozoic Orogen of SE China, *Terra Nova*, 21(5), 360-368, doi:10.1111/j.1365-3121.2009.00888.x.
- Gilder, S., G.R. Keller, L. Ming, and P. Goodell (1991), Timing and spatial distribution of rifting in China, *Tectonophysics*, 197, 225-243, doi:10.1016/0040-1951(91)90043-R.
- Godin, L., R. L. Brown, S. Hanmer, and R. Parrish (1999), Back folds in the core of the Himalayan orogen: An alternative interpretation, *Geology*, 27(2), 151-154, doi:10.1130/0091-7613(1999)027<0151:BFITCO>2.3.CO;2.
- Goleby, B. R., Shaw, R. D., Wright, C., Kennett, B. L. N., Lambeck, K., 1989. Geophysical evidence for thick-skinned crustal deformation in central Australia, *Nature*, 337, 325-330.
- Gupta, S. (1989), Comments and Reply on "Mesozoic overthrust tectonics in south China", *Geology*, 17, 669 – 673, doi:10.1130/0091-7613(1989)017<0669:CAROMO>2.3.CO;2.
- Hacker, B. R., and Q. C. Wang (1995), Ar/Ar Geochronology of Ultrahigh-Pressure Metamorphism in Central China, *Tectonics*, 14(4), 994-1006, doi:10.1029/95TC00932.
- Hand, M., and M. Sandiford (1999), Intraplate deformation in central Australia, the link between subsidence and fault reactivation, *Tectonophysics*, 305(1-3), 121-140, doi:10.1016/S0040-1951(99)00009-8.
- Harrowfield, M. J., and C. J. L. Wilson (2005), Indosinian deformation of the Songpan Garze Fold Belt, northeast Tibetan Plateau, *J. Struc. Geol.*, 27(1), 101-117, doi:10.1016/j.jsg.2004.06.010.
- Hendrix, M. S., S. A. Graham, A. R. Carroll, E. R. Sobel, C. L. McKnight, B. J. Schulein, and Z. Wang (1992), Sedimentary record and climatic implications of recurrent deformation in the Tian Shan: Evidence from Mesozoic strata of the north Tarim, south Junggar, and Turpan basins, northwest China, *Geol.*

- Soc. Am. Bull.*, 104(1), 53-79,
doi:10.1130/0016-7606(1992)104<0053:SRACIO>2.3.CO;2.
- Hsu, K. J., S. Sun, J. Li, H. Chen, H. Pen, and A. M. C. Sengor (1988), Mesozoic overthrust tectonics in South China, *Geology*, 16(5), 418-421,
doi:10.1130/0091-7613(1988)016<0418:MOTISC>2.3.CO;2.
- Hsu, K. J., J. L. Li, H. H. Chen, Q. C. Wang, S. Sun, and A. M. C. Sengor (1990), Tectonics of south China: Key to understanding West Pacific geology, *Tectonophysics*, 183, 9 – 39, doi:10.1016/0040-1951(90)90186-C.
- Lepvrier, C., H. Maluski, V. Van Tich, A. Leyreloup, P. Truong Thi, and N. Van Vuong (2004), The Early Triassic Indosinian orogeny in Vietnam (Truong Son Belt and Kontum Massif); implications for the geodynamic evolution of Indochina, *Tectonophysics*, 393(1-4), 87-118,
doi:10.1016/j.tecto.2004.07.030.
- Lepvrier, C., N. Van Vuong, H. Maluski, P. Truong Thi, and T. Van Vu (2008), Indosinian tectonics in Vietnam, *CR Géosciences, special issue Triassic Tectonics in East Asia*, 340(2-3), 94-111, doi:10.1016/j.crte.2007.10.005.
- Lepvrier, C., M. Faure, Van Vuong, N'guyen, Tich, Vu Van W. Lin, Ta Trong Tang (2011), North directed nappes in Northeastern Vietnam (East Bac Bo). *J. Asian Earth Sci.*, 41, 56-68, doi:10.1016/j.jseaes.2011.01.002
- Li, H. Q., D. H. Wang, F. W. Chen, Y.P. Mei and H. Cai (2008), Study on Chronology of the Chanziping and Daping gold deposit in Xuefeng Mountains, Hunan Province (in Chinese with English abstract), *Acta Geologica Sinica*, 82(7), 900-905.
- Li, X. H. (1999), U-Pb zircon ages of granites from the southern margin of the Yangtze Block: timing of Neoproterozoic Jinning: Orogeny in SE China and implications for Rodinia Assembly, *Precambrian Res.*, 97(1-2), 43-57,
doi:10.1016/S0301-9268(99)00020-0.
- Li, X. H., Z. X. Li, W. X. Li, and Y. J. Wang (2006), Initiation of the Indosinian Orogeny in South China: Evidence for a Permian magmatic arc on Hainan Island, *J. Geol.*, 114(3), 341-353, doi:10.1086/501222.
- Li, X. H., W. X. Li, Z.X. Li, C. H. Lo, J. Wang, M.-F. Ye, and Y.-H. Yang (2009), Amalgamation between the Yangtze and Cathaysia Blocks in South China: Constraints from SHRIMP U-Pb zircon ages, geochemistry and Nd-Hf isotopes of the Shuangxiwu volcanic rocks, *Precambrian Res.*, 174(1-2), 117-128, doi:10.1016/j.precamres.2009.07.004.
- Li, Z. X., and X. H. Li (2007), Formation of the 1300-km-wide intracontinental orogen and postorogenic magmatic province in Mesozoic South China: A

- flat-slab subduction model, *Geology*, 35(2), 179-182,
doi:10.1130/G23193A.1.
- Li, Z. X., X. H. Li, J. A. Wartho, C. Clark, W. X. Li, C. L. Zhang, and C. Bao (2010), Magmatic and metamorphic events during the early Paleozoic Wuyi-Yunkai orogeny, southeastern South China: New age constraints and pressure-temperature conditions, *Geol. Soc. Am. Bull.*, 122(5-6), 772-793, doi:10.1130/B30021.1.
- Lin, W., M. Faure, P. Monie, U. Scharer, L. S. Zhang, and Y. Sun (2000), Tectonics of SE China: New insights from the Lushan massif (Jiangxi Province), *Tectonics*, 19(5), 852-871, doi:10.1029/2000TC900009.
- Lin, W., Q. Wang, and K. Chen (2008), Phanerozoic tectonics of south China block: New insights from the polyphase deformation in the Yunkai massif, *Tectonics*, 27, TC6004, doi:10.1029/2007TC002207.
- Malavieille, J. (2010), Impact of erosion, sedimentation, and structural heritage on the structure and kinematics of orogenic wedges: Analog models and case studies, *GSA Today*, 20, 1, doi: 10.1130/GSATG48A.1.
- McQuarrie, N. (2004), Crustal scale geometry of the Zagros fold-thrust belt, Iran, *J. Struc. Geol.*, 26(3), 519-535, doi:10.1016/j.jsg.2003.08.009.
- Qin, B.H. (1991), Deep seated structure beneath Hunan Province revealed by Taiwan-Heshui geotraverse, *Hunan Geology*, 15, 89-96.
- Qiu, Y. X., Y. C. Zhang, and W. P. Ma (1998), Tectonics and Geological Evolution of Xuefeng Intra-continental Orogen, South China (in Chinese with English abstract), *Geol. J. China Universities*, 4(4), 432-443.
- Qiu, Y. X., Y. C. Zhang, and W. P. Ma (2000), *The Tectonic Nature and Evolution of Xuefeng Mountains: One Model of Formation and Evolution of Intra-continental Orogenic Belt*, 155pp, Geol. Publishing House, Beijing.
- Ramsay, J. G, and M.I. Huber (1987), *The techniques of Modern Structural geology Volume 2: Folds and Fractures*, 700pp ; Academic Press, London.
- Rodgers, J. (1989), Comment on 'Mesozoic overthrust tectonics in south China', *Geology*, 17, 671 – 672.
- Roger, F., M. Jolivet, and J. Malavieille (2008), Tectonic evolution of the Triassic fold belts of Tibet, *CR Géosciences, special issue Triassic Tectonics in East Asia*, 340(2-3), 180-189, doi:10.1016/j.crte.2007.10.014.
- Roger, F., M. Jolivet, and J. Malavieille (2010), The tectonic evolution of the Songpan-Garze(North Tibet) and adjacent areas from Proterozoic to Present: A synthesis, *J. Asian Earth Sci.*, 39(4), 254-269, doi:10.1016/j.jseas.2010.03.008.

- Roure, F., P. Choukroune, X. Berastegui, J. A. Munoz, A. Villien, P. Matheron, M. Bareyt, M. Seguret, P. Camara, and J. Deramond (1989), ECORS Deep seismic data and balanced cross sections: geometric constraints on the evolution of the Pyrenees, *Tectonics*, 8, 41–50, doi:10.1029/TC008i001p00041.
- Rowley, D. B., A. M. Ziegler, and S. Nie (1989), Comment on Mesozoic overthrust tectonics in south China, *Geology*, 17, 384 – 386, doi:10.1130/0091-7613(1989)017<0384:CAROMO>2.3.CO;2.
- Sandiford, M., M. Hand, and S. McLaren (2001), Tectonic feedback, intraplate orogeny and the geochemical structure of the crust: a central Australian perspective, *Geological Society, London, Special Publications*, 184(1), 195-218, doi:10.1144/GSL.SP.2001.184.01.10.
- Shu, L. S., G. Q. Zhou, Y. S. Shi, and J. Yin (1994), Study of the high-pressure metamorphic blueschist and its late Proterozoic age in the eastern Jiangnan belt, *Chin. Sci. Bull.*, 39(14), 1200-1204.
- Shu, L. S., X. M. Zhou, P. Deng, B. Wang, S. Y. Jiang, J. H. Yu, and X. X. Zhao (2009), Mesozoic tectonic evolution of the Southeast China Block: New insights from basin analysis, *J. Asian Earth Sci.*, 34(3), 376-391, doi:10.1016/j.jseaes.2008.06.004.
- Tapponnier, P., and P. Molnar (1979), Active faulting and Cenozoic tectonics of the Tianshan, Mongolia, and Baykal regions, *J. Geophys. Res.*, 84(B7), 3425-3459, doi:10.1029/JB084iB07p03425.
- Wallis, S., T. Tsujimori, M. Aoya, T. Kawakami, K. Terada, K. Suzuki, and H. Hyodo (2003), Cenozoic and Mesozoic metamorphism in the Longmenshan orogens: implications for geodynamic models of eastern Tibet, *Geology*, 31, 745-748, doi:10.1130/G19562.1.
- Wang, J., and Z-X. Li (2003), History of Neoproterozoic rift basins in South China: implications for Rodinia break-up, *Precambrian Res.*, 122(1-4), 141-158, doi:10.1016/S0301-9268(02)00209-7.
- Wang, Y. J., Y. H. Zhang, W. M. Fan, and T. P. Peng (2005), Structural signatures and Ar-40/Ar-39 geochronology of the Indosinian Xuefengshan tectonic belt, South China Block, *J. Struct. Geol.*, 27(6), 985-998, doi:10.1016/j.jsg.2005.04.004.
- Wang, Y. J., W. M. Fan, M. Sun, X. Q. Liang, Y. H. Zhang, and T. P. Peng (2007a), Geochronological, geochemical and geothermal constraints on petrogenesis of the Indosinian peraluminous granites in the South China Block: A case

- study in the Hunan Province, *Lithos*, 96(3-4), 475-502,
doi:10.1016/j.lithos.2006.11.010.
- Wang, Y. J., W. M. Fan, G. C. Zhao, S. C. Ji, and T. P. Peng (2007b), Zircon U-Pb geochronology of gneissic rocks in the Yunkai massif and its implications on the Caledonian event in the South China Block, *Gondwana Res.*, 12(4), 404-416, doi:10.1016/j.gr.2006.10.003.
- Wang, Y. J., W. M. Fan, P. A. Cawood, S. C. Ji, T. P. Peng, and X. Y. Chen (2007c), Indosinian high-strain deformation for the Yunkaidashan tectonic belt, south China: Kinematics and $^{40}\text{Ar}/^{39}\text{Ar}$ geochronological constraints, *Tectonics*, 26, TC6008, doi:10.1029/2007TC002099.
- Willett S.D., C. Beaumont, and P. Fullsack (1993), Mechanical model for the tectonics of doubly vergent compressional orogens, *Geology*, 21, 371-374, doi:10.1130/0091-7613(1993)021<0371:MMFTTO>2.3.CO;2.
- Xu, J. W., G. Zhu, W. X. Tong, K. R. Cui, and Q. Liu (1987), Formation and evolution of the Tancheng-Lujiang wrench fault system: a major shear system to the northwest of the Pacific Ocean, *Tectonophysics*, 134(4), 273-310, doi:10.1016/0040-1951(87)90342-8.
- Yan, D. P., M. F. Zhou, H. L. Song, X. W. Wang, and J. Malpas (2003), Origin and tectonic significance of a Mesozoic multi-layer over-thrust system within the Yangtze Block (South China), *Tectonophysics*, 361(3-4), 239-254, doi:10.1016/S0040-1951(02)00646-7.
- Zhou, X. M., and W. X. Li (2000), Origin of Late Mesozoic igneous rocks in Southeastern China: implications for lithosphere subduction and underplating of mafic magmas, *Tectonophysics*, 326(3-4), 269-287, doi:10.1016/S0040-1951(00)00120-7.
- Zhou, X. M., T. Sun, W. Z. Shen, L. S. Shu, and Y. L. Niu (2006), Petrogenesis of Mesozoic granitoids and volcanic rocks in South China: A response to tectonic evolution, *Episodes*, 29(1), 26-33.
- Zhou, X. M., ed. (2007), *Genesis of Late Mesozoic Granites in Nanling Region and Geodynamic Evolution of Lithosphere*. Beijing: Science Press, 691pp.

Structural analysis and chronological constraints on the basal decollement layer in an intracontinental orogen: Example of the Early Mesozoic Xuefengshan Belt, South China

Yang Chu^{1,2,3}, Michel Faure^{1,2}, Wei Lin^{1,*}, Qingchen Wang¹, Wenbin Ji^{1,3}

1. State Key Laboratory of Lithospheric Evolution, Institute of Geology and Geophysics, Chinese Academy of Sciences, Beijing 100029, China
2. Institut des Sciences de la Terre d'Orléans, Campus Géosciences, Université d'Orléans, 1A, Rue de la Férollerie, 45071 Orléans Cedex 2, France
3. Graduate University of Chinese Academy of Sciences, Beijing 100049, China

Abstract: In intracontinental belts, a basal decollement layer often develops to accommodate the shortening at depth due to folding and thrusting of the sedimentary cover. In the Early Mesozoic intracontinental Xuefengshan Belt of South China, such a decollement layer is exposed in the core of anticlines formed by the emplacement of the late orogenic granitic plutons. The detailed, multi-scale structural analysis of the basal decollement layer documents the synmetamorphic ductile deformation. In the basal decollement, the Neoproterozoic pelite and sandstone and the intruding Early Paleozoic granites are changed into mylonites and orthogneiss, respectively. The metamorphic foliation contains a NW-SE striking stretching lineation associated with top-to-the-NW kinematic indicators. These high-strain rocks can be correlated with the NW-verging folds and thrusts recognized in the Neoproterozoic to Early Triassic sedimentary cover. Monazite U-Th-Pb chemical dating, and zircon SIMS U-Pb dating provide age constraints of the ductile shearing between 242 and 226 Ma, and late orogenic granite emplacement around 235-215 Ma. In agreement with recent geochronological data, these new results show that the Xuefengshan Belt is an Early Mesozoic intracontinental orogen, dominated by the NW-directed shearing and thrusting, and not a Precambrian or Early Paleozoic one. At the scale of the South China block, to the SE of the Xuefengshan Belt, the Chenzhou-Linwu fault separates the Early Mesozoic and the Early Paleozoic domains, to the NW and the SE, respectively. This fault acted as a major boundary in the orogenic evolution of the intracontinental Xuefengshan Belt. The architecture of this belt was possibly originated from the continental underthrusting to the SE of the South China block in response to the northwest directed subduction of the Paleo-Pacific plate.

Key words: Intracontinental Belt, Basal decollement layer, Xuefengshan, South China block, Triassic tectonics

1. Introduction

Because of their considerable distance, 1000 km or more, from active plate boundaries, the intracontinental orogens remain an enigmatic tectonic feature for geologists. Compared to collisional or accretionary orogens, evidence for oceanic subduction such as ophiolites, accretionary complex, serpentinite, mélangé, and arc-related magmatism are lacking in intracontinental belts. Examples of intracontinental belts are provided by the Miocene Tianshan orogen of Central Asia (e.g. Molnar and Tapponnier, 1975; Tapponnier and Molnar, 1979; Hendrix et al., 1992; Avouac et al., 1993), the Cenozoic Laramide orogens in Western USA (e.g. Dickinson and Snyder, 1978; English and Johnston, 2004), the Cenozoic Pyrenees in Europe (Roure et al., 1989; Choukroune, 1992), the Neoproterozoic Petermann and Paleozoic Alice Springs orogens in Central Australia (Hand and Sandiford, 1999; Sandiford et al., 2001; Raimondo et al., 2010), and the Early Paleozoic intracontinental belt of SE China (Faure et al., 2009; Charvet et al., 2010). These intracontinental orogens are characterized by fold-and-thrust belts, large-scale decollement layers, and limited or even absent crustal melting and metamorphism. Consequently, a far-field effect of continental collision or a flat-slab subduction are now well accepted as possible mechanisms to account for the formation of intracontinental orogens.

In the South China block (SCB), the Early Mesozoic Xuefengshan Belt preserves well exposed structures ascribed to a typical intracontinental belt (Qiu et al., 1998, 2000; Yan et al., 2003; Wang et al., 2005; Chu et al., submitted). Despite of significant compressional deformation in the subsurface sedimentary strata, no highly metamorphosed basement rocks are exposed, indicating the existence of large, in-between decollement layer, which accommodates the discrepancy of deformation. Although decollement layers present in many collisional orogens, such as the Alps (Escher and Beaumont, 1997), and the Zagros (McQuarrie, 2004), little less attention has been paid to basal decollement layers in intracontinental belts. The decollement layer exposed in the Xuefengshan Belt makes this intracontinental orogen a typical example to analyse this major structure. In order to better document the structural features of an intracontinental orogen, this paper presents detailed field and microscope-scale structural analyses of the ductile decollement layer that accommodates most of the crustal deformation in the Xuefengshan Belt. In order to

better constrain the timing of the deformation, new monazite U-Th-Pb and zircon U-Pb geochronological data of the syn-kinematic metamorphism coeval with the activity of the ductile decollement layer and the late-orogenic granites that post-date the deformation are presented.

2. Geological setting

2.1. The South China block (SCB)

The SCB formed and experienced contractional tectonics in the Early Neoproterozoic, around ca 900 Ma, due to the collision of the Yangtze and Cathaysia blocks during the Jiangnan orogeny. In the eastern part of this belt, the Jiangshan-Shaoxing Fault represents the ophiolitic suture (Fig. 1a; Shu et al., 1994; Charvet et al., 1996; Li, 1999; Li et al., 2009b and references therein), but its southwestern extension is not well established due to poor exposure and subsequent tectonic modification. From Late Neoproterozoic to Middle Silurian, a ca.10 km-thick, a continuous terrigenous sedimentation took place in the southern part of the SCB, whereas in the northern part of the SCB, the Cambrian-Ordovician sedimentation is characterized by black shale and limestone, and followed by a thick Silurian turbidite formation (Wang and Li, 2003; BGMRJX, 1984; BGMRHN, 1988). From Late Ordovician, (around 450 Ma) to Silurian, an intracontinental orogeny that partly reworked the Jiangshan-Shaoxing suture occurred as indicated by intermediate pressure-intermediate temperature metamorphism, crustal melting at ca 440-430 Ma, emplacement of post-orogenic plutons at ca. 410 Ma-400 Ma, and Middle Devonian regional unconformity (Wang et al., 2007b; Faure et al., 2009; Li et al., 2010a; Charvet et al., 2010).

The Early Mesozoic is the most important period for the tectonics of the SCB. To the north, the SCB subducted beneath the North China block, forming the southern part of the Qinling-Dabie Belt, which is also an intracontinental belt developed after the Ordovician collision between the North China and the South China blocks (e. g. Mattauer et al, 1985; Hacker and Wang, 1995; Faure et al., 1999, 2008). To the southwest, the over 1000-km-long Jinshajiang-Song Ma suture extends from western Yunnan to north Vietnam and the South China sea to the south. Although incompletely described, this major belt is likely related to the collision of the SCB with the Indochina block (Lepvrier et al., 1997, 2004, 2008, 2011; Wang et al., 2000; Carter et al., 2001; Wallis et al., 2003; Harrowfield and Wilson, 2005; Carter and Clift, 2008; Roger et al., 2008; Chen et al., 2011). Triassic deformation also exists by places in Jiangxi, Zhejiang, and Fujian Provinces, as documented by a Late Triassic unconformity, and locally by a ca. 235-225 Ma magmatism(BGMRJX, 1984;

BGMRFJ, 1985; BGMRZJ, 1989; Faure et al., 1996; Chen, 1999; Xiao et He, 2005). Furthermore, in the central part of the SCB, mostly in Hunan Province, but also in the northern part of Guangxi Province and the northwestern part of Jiangxi Province, the deformation pattern is characterized by NE-SW to NNE-SSW striking folds and faults with an overall northwest vergence. The age and the structures of the Xuefengshan Belt (XFSB) are still controversial. Some authors argue for an Early Paleozoic age (Qiu et al., 1998, 2000), others propose a Cretaceous age (Yan et al., 2003). However, recent studies suggest that the XFSB developed in Middle Triassic since Early Triassic rocks are folded, but Jurassic terrigenous rocks unconformably overly the deformed series (BGMRHN, 1988; Wang et al., 2005; Chu et al., 2011).

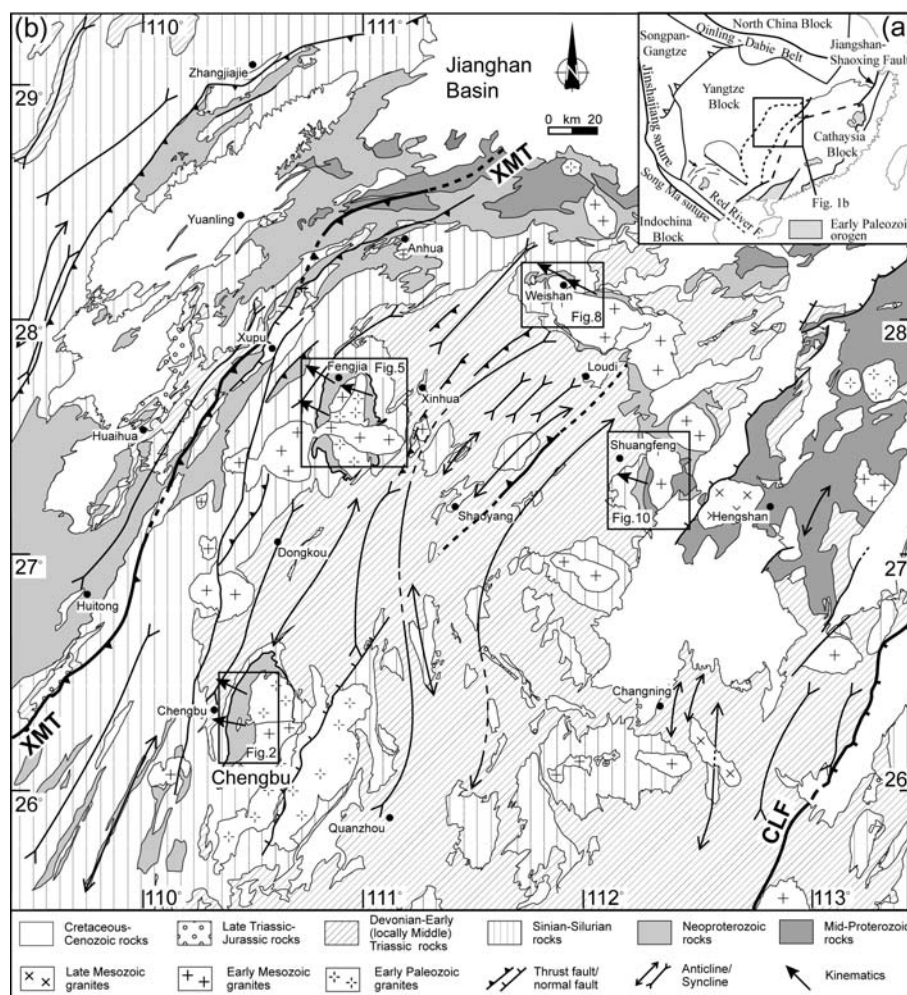


Fig. 1. (a): Tectonic map of the South China block with the location of the study area (Modified after Faure et al., 2009; Chu et al., submitted). ① Southwestern extension of the Jiangshan-Shaoxing Fault. (b): Structural map of the Xuefengshan Belt (Modified after 1:500 000 Geological map of Hunan, BGMRHN, 1988; Chu et al., submitted). MXT: The Main Xuefengshan Thrust.

2.2. The Xuefengshan Belt (XFSB)

Located in the center of the SCB, the XFSB is generally considered as a Triassic intracontinental belt (Wang et al., 2005; Chu et al., submitted). As for most parts of the SCB, the sedimentary cover includes thick layers of sandstone, siltstone, shale and limestone from Late Proterozoic to Silurian, then followed, with a low angle unconformity by dominantly carbonate series ranging from Middle Devonian to early Triassic with a sedimentary hiatus between Late Silurian and Early Devonian (BGMRHN, 1988). The Late Triassic rocks are absent, and the folded marine series is unconformably covered by Early Jurassic-Cretaceous terrigenous rocks, represented by red sandstone, conglomerate, and mudstone.

Unlike the southerly areas of the SCB, the XFSB exposes a weak Early Paleozoic deformation, as indicated by a low angle (not higher than $\sim 20^\circ$) unconformity between Devonian and pre-Devonian rocks. In the XFSB, kilometer-scale gentle open folds devoid of any cleavage characterize this Early Paleozoic event. Moreover, when present, the slaty cleavage is observed on both sides of the unconformity, i.e., if a slaty cleavage is observed in the Neoproterozoic to Silurian series, this cleavage is also developed in the unconformably overlying Devonian rocks. Thus, in the XFSB, the main tectonic event appears to develop during Early Mesozoic.

The XFSB is divided into two zones: the Western Outer Zone and the Eastern Inner Zone, separated by the Main Xuefengshan Thrust (Fig. 1b). Three main stages of deformation, namely D_1 , D_2 , D_3 have been recognized (Chu et al., submitted). The D_1 structures are characterized by NW-verging folds and thrusts often associated with a SE dipping, axial planar, slaty cleavage (S_1), and locally, a NW-SE mineral and stretching lineation (L_1), represented by elongated clasts in terrigenous rocks, quartz pressure shadows around pyrite in slates, and sericite or chlorite fibers. Kinematic indicators such as asymmetric pressure shadows or shear bands show a top-to-the-NW shearing that complies with fold vergence. The D_1 structures are subsequently reworked by SE-directed folds and thrusts attributed to a D_2 event. A NW-dipping fracture or slaty cleavage (S_2) in the axial planes of D_2 folds, but the (L_2) stretching lineation is rare. Lastly, upright folds associated with a vertical cleavage (S_3) and a vertical stretching lineation (L_3) formed during the D_3 phase. The whole belt experienced a low greenschist facies metamorphism developed during D_1 . Thermobarometric estimates indicate 300-400 °C and 4-6 Kbar, respectively (BGMRHN, 1988).

Plutonic rocks are widespread in the XFSB (Figure 1b). On the basis on their ages, lithology, and deformation, these granitic rocks can be divided into an Early

Paleozoic group and a Triassic group. The Early Paleozoic plutons (ca 430-410 Ma) underwent a ductile deformation during the Middle Triassic tectonics whereas the undeformed Triassic granites intrude the deformed pre-Mesozoic series. The Triassic granitic plutons that occupy an area of more than 5600 km² (BGM RHN, 1988) consist of two-mica granite, biotite monzonite, two-mica monzonite, and biotite-hornblende granite, with less distributed granodiorite and tourmaline granite (BGM RHN, 1988, Wang et al., 2007a). Previous geochemical studies show that these peraluminous granitic magmas formed by crustal melting after the Early Triassic compression (Chen et al., 2006, 2007a, 2007b; Wang et al., 2007a, and references therein).

In the litho-stratigraphic series of the XFSB, the Late Neoproterozoic (Sinian) pelite and graphitic layers, Early Triassic pelite, Cambrian black shale, as well as Devonian, Carboniferous, and Permian pelitic layers, some of them including coal measures, played an important role in the structural evolution of the XFSB (Yan et al., 2003; Chu et al., submitted). These soft layers with a low yield stress acted as decollement levels that accommodated the regional shortening during the Triassic folding and thrusting. The deepest layer of the Xuefengshan series is represented by micaschist and schistosed siltstones of Neoproterozoic (pre-Sinian) age. This 2 to 5 km thick ductile shear zone crops out due to the structural high formed during the emplacement of the Late Triassic granites, and was exposed to the surface by subsequent erosion. This litho-tectonic unit is interpreted as a basal decollement layer that separates the sedimentary cover and the basement rocks. This decollement layer appears as the main structural discontinuity of the XFSB, whereas the Sinian and Paleozoic pelitic layers are secondary decollement levels. In the following section, the structural features of the main decollement layer are presented.

3. Structural analysis of the basal decollement layer

During its polyphase deformation, the sedimentary cover of the XFSB experienced a shortening, accommodated by box-folding, estimated to ca 20% in the Western Outer Zone (Yan et al., 2003). However, the total amount of shortening is probably larger, since the ductile shortening due to pressure solution, the slip on the layers, and the total displacement on brittle thrust faults is not taken into account. Conversely to the Neoproterozoic to Early Triassic series that does not present any significant metamorphism, the basal decollement layer exhibits a synmetamorphic ductile deformation. Detailed structural investigations were carried out in four representative areas where metamorphic rocks are well cropping out (Fig. 1b). In the next sections, we shall describe the mesoscale features, such as the planar and linear

fabrics, folds observed in the decollement layer, and the microstructures, including quartz texture, and *c*-axis fabrics.

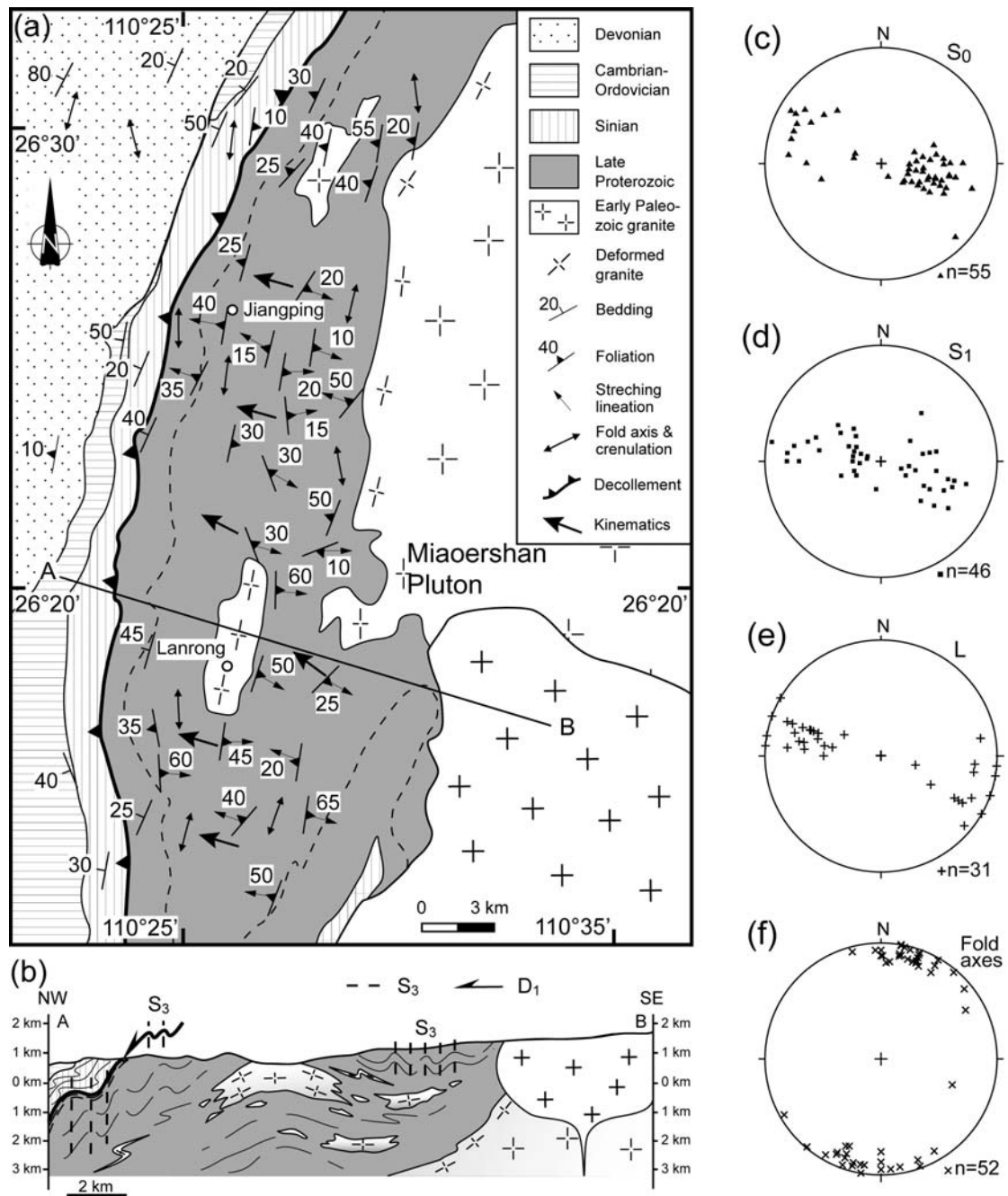


Fig. 2. (a): Detailed geologic map of the basal decollement layer, east of Chengbu (Modified after 1:500 000 Geological map of Hunan, BGMRHN, 1988; Chu et al., submitted). (b): General cross section of the area. Stereographic plots (Schmidt lower hemisphere projection) of the structural elements, (c): bedding, (d): S_1 foliation, (e): stretching lineation, (f): F_3 fold axes and crenulation lineation.

3.1. Chengbu area

East of Chengbu, the Miaoershan granitic massif consists of Early Paleozoic and Early Mesozoic plutons (BMGRHN, 1984; Zhou, 2007). Mid-Late Proterozoic rocks that experienced a greenschist facies metamorphism, are exposed in the vicinity of the Miaoershan pluton (Figs. 2a-b). These metamorphic rocks consist of slate, schistose sandstone, quartzite and garnet-bearing two-mica schist; they show a penetrative foliation gently dipping to the NW or SE, a NW-SE striking mineral and stretching lineation, and a NE-SW striking crenulation (Figs. 2c-f). Mylonites and ultramylonites are observed near Lanrong and east of Jiangping. Thus, this zone that represents the deepest unit of the XFSB is interpreted as a high-strain basal decollement layer. The dominant event is characterized by NW-directed structures, which are reworked by upright folds and crenulations similar to the D₃ event described in the sedimentary series (Chu et al., submitted).

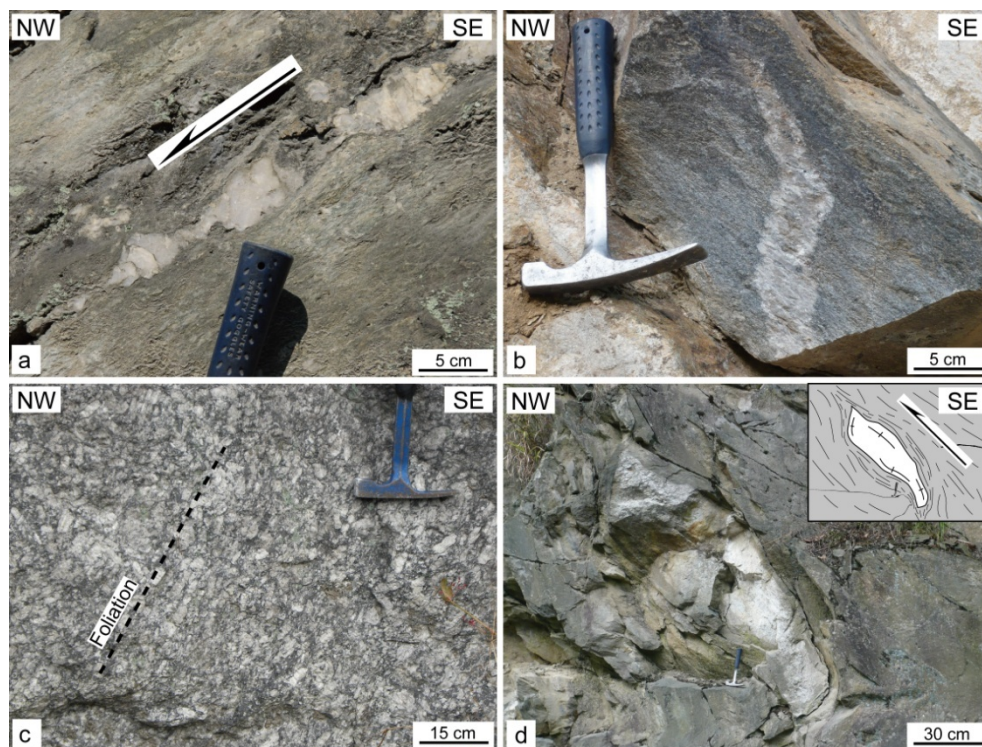


Fig. 3. Examples of structures observed in the basal decollement layer in Chengbu area. (a): Sigmoidal quartz veins in the mylonitic Neoproterozoic quartzite, east of Jiangping. (b): Deformed granitic lense within a micaschist matrix, east of Lanrong. (c): Foliated Paleozoic granite, Lanrong. (d): Sheared granitic dyke in micaschist, northeast of Lanrong.

3.1.1. Mesoscopic deformation

As already depicted by Chu et al. (2011), here we emphasize some macroscopic structures in order to better understand the mechanism of deformation which is our main objective in this section (3.1). Above the decollement layer, the Late Neoproterozoic (Sinian) to Paleozoic series is weakly metamorphosed and deformed by NW verging folds related to the D₁ event. The underlying mylonitic sandstone and mudstone show a pervasive foliation. Numerous quartz lenses distributed in the micaschists argue for important fluid circulations. In outcrop-scale sections perpendicular to the foliation and parallel to the lineation, quartz lenses asymmetry indicates a top-to-the-NW sense of shear (Fig. 3a-b). Moreover, The Paleozoic granite is intensely mylonitized with gneissic structure, and some sheared granitic dykes, intruding into the micaschists, yield an asymmetric sigmoidal shape with a top-to-the-NW sense of shear (Fig. 3f). All the above mentioned structures indicate a post-solidus shearing developed after granite emplacement, and thus the deformation occurred after the Early Paleozoic, and probably in Early Mesozoic.

3.1.2 Microfabrics

At the microscopic scale, shear sense is clearly shown by numerous kinematic indicators such as sigma-type porphyroclast systems, micafish, and shear bands. In meta-sandstone, quartz clasts are surrounded by chlorite or mica pressure shadows, and the matrix is deformed by shear bands. The concentration of phyllosilicates in the foliation planes, pressure shadows around clasts, and dissolution features indicate that the main deformation mechanism in these rocks is pressure solution (Fig. 4a-b). This mechanism plays an important role at grain boundaries under high differential stress in low to intermediate temperature such as that of greenschist facies. Pressure solution develops at quartz grain contacts where the solubility is higher in an aqueous fluid and stress is likewise relatively high, because the grain lattice near contact points is strongly compressed, and thus material is dissolved there and then redeposited in the low strain areas, such as pressure shadows along the stretching direction (Passchier and Trouw, 2005). In quartzite, the metamorphic crystallization of white mica and the recrystallization of quartz are pervasively developed. East of Jiangping (Fig. 2a), quartzite is deformed into mylonite with sigmoidal mica fish arranged along shear bands, indicating a top-to-the-NW shear sense (Fig. 4c). In mica-schist, in spite of the subsequent alteration that changed the garnet porphyroblast into a chlorite-quartz assemblage, the asymmetric quartz pressure shadows indicate also a top-to-the-NW sense of shear (Fig. 4d).

In order to decipher the deformation pattern of the high-strain decollement layer, we investigated the quartz *c*-axis preferred orientation with respect to the texture of the quartz aggregates observed in some mylonitic samples.

In the analyzed mylonite, two types of quartz microstructures can be recognized. The first type occurs generally in micaschist. It consists of anhedral or subhedral quartz grains with straight boundaries and platen shape (Fig. 5a). In some cases, the grain boundaries tend to arrange in triple junctions with interfacial angles close to 120°. No obvious dynamic recrystallization is observed. The second one is developed in quartzite or micaceous quartzite. In these rocks, two groups of quartz grains, namely ~1 mm sized clasts, and ~70 μm grains in matrix, are identified (Fig. 5b). Quartz clasts are generally elongated parallel to the foliation and subdivided into several subgrains with oblique subgrain boundaries. These grains exhibit undulose extinction, along the clast boundaries, newly formed, anhedral fine grains are isolated from the host grain by subgrain rotation recrystallization.

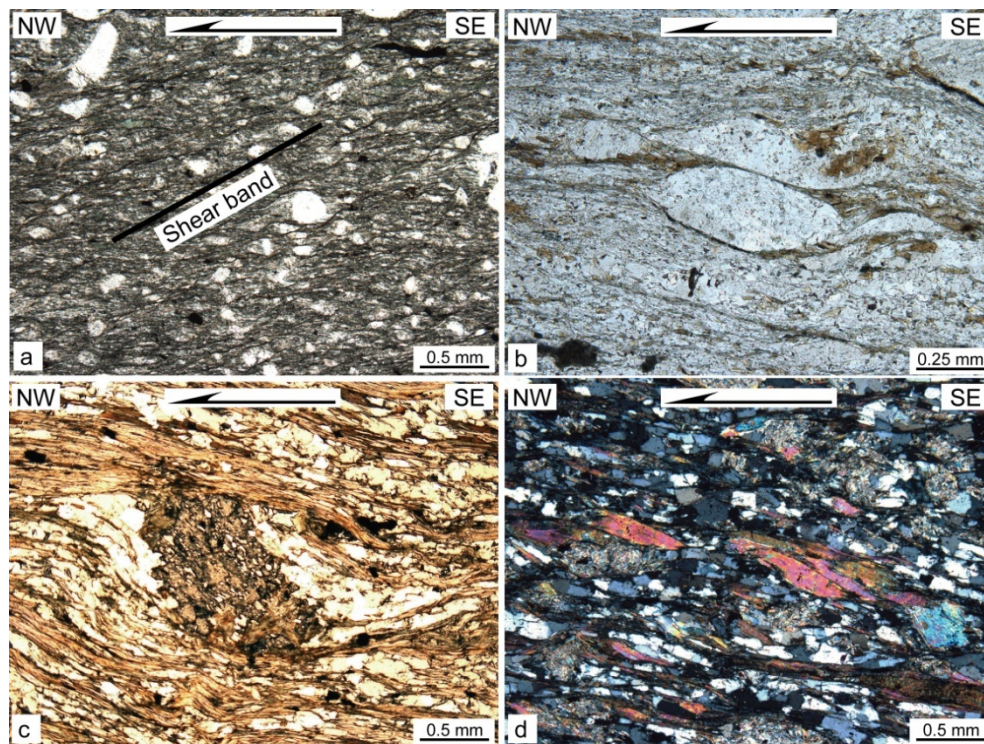


Fig. 4. Microscopic deformational features of the basal decollement layer of Chengbu area. (a): Sheared Neoproterozoic conglomerate with shear bands structure and quartz clasts with asymmetric pressure shadows showing a top-to-the-NW sense of shear, west of Lanrong. (b): Sigmoidal feldspar porphyroblast in sandstone with a top-to-the-NW shear sense, east of Jiangping. (c): Garnet porphyroblast with quartz pressure shadows showing the top-to-the NW sense of shear. (d): Mica fish structures in micaschist with a top-to-the-NW shear sense, southeast of Jiangping.

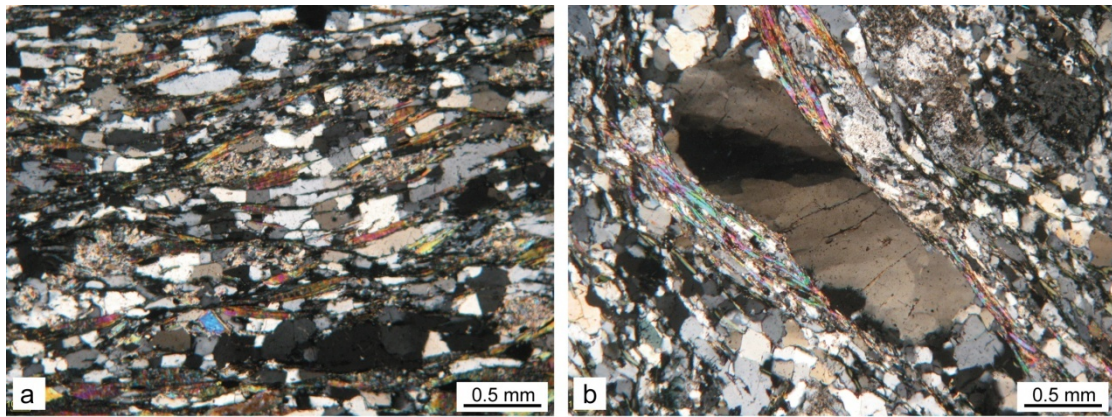


Fig. 5. Microscopic photos showing deformation pattern of quartz grains in the basal decollement in Chengbu area. (a): Anhedral or subhedral quartz grains with straight boundaries and platen shape. (b): Quartz clasts elongated parallel to the foliation and subdivided into several subgrains with oblique subgrain boundaries, and undulose extinction.

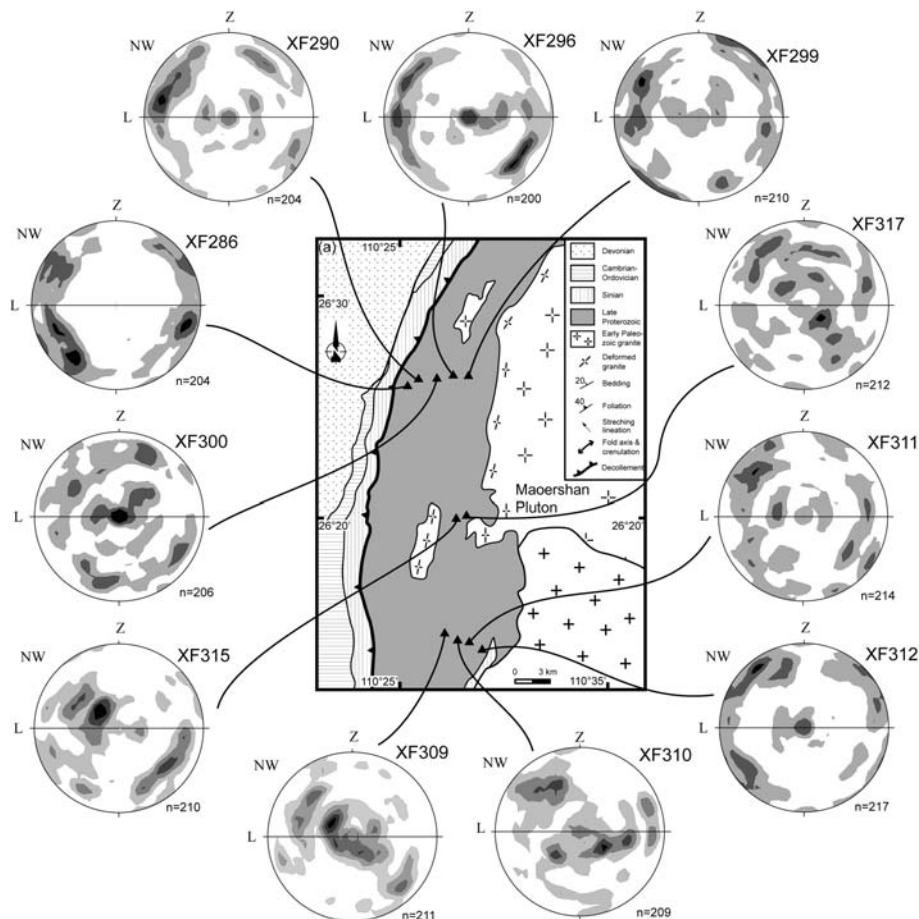


Fig. 6. Quartz *c*-axis orientation projections (Schmid diagram, lower hemisphere, equal area) for the mylonitic rocks in the basal decollement layer of Chengbu area. Contour intervals are 1%.

Quartz *c*-axis measurements were performed from thin sections cut in the XZ plane with in a universal stage (i.e. perpendicular to the foliation and parallel to the lineation) from 11 samples in which quartz aggregates belong to one of the two types described above. The *c*-axis patterns can be grouped in two types. One type consists of crossed girdles with an opening angle of $\sim 75^\circ$, and a point maximum close to the Y axis. Along the girdles, point maxima in the XZ plane, and inclined at low angles (less than 45°) to Z, are consistent with the dominance of basal $\langle a \rangle$ slip mechanism. *C*-axis concentration around Y indicate prism $\langle a \rangle$ slip. This type is observed in samples XF286, XF290, XF296, XF299, XF311, XF312 (Fig. 6). Another pattern of quartz *c*-axis fabric exhibits maxima close to the Y axis, and a single oblique girdle, pointing to basal, rhomb and prism slip systems active at the same time. Such a pattern corresponds to samples XF300, XF309, XF310, XF315, XF317 (Fig. 6). Both types of quartz *c*-axis patterns indicate that the preferred orientation in the mylonite was developed under low-temperature metamorphic conditions, and probably in presence of hydrous material (Passchier and Trouw, 2005).

3.2. Fengjia-Shuiche area

Low greenschist facies metamorphic rocks, including meta-sandstone, quartzite and micaschist, crop out around the Baimashan granite. This massif is composed of Paleozoic and Early Mesozoic plutons, the mapping of which is not clearly settled (Figs. 1 and 7a). The metamorphic rocks are exposed in a ca. 20 km large anticline, with a core of Early Paleozoic and Late Triassic plutons. These rocks are pervasively ductilely deformed, and overlain by unmetamorphosed Late Neoproterozoic (Sinian) to Paleozoic sedimentary rocks. The deformed metamorphic rocks are interpreted as the basal decollement layer (Fig. 7a-b), in which the intensity of ductile deformation increases downward.

3.2.1. Mesoscopic deformation

The penetrative S_1 foliation is well developed in the decollement layer around the Baimashan pluton. At the regional scale, the S_1 foliation dips to the NW and the SE to the west and the east of the pluton, respectively, indicating an anticlinal structure (Fig. 7b-d). At the outcrop scale, the metamorphic and deformation style shows some difference between the western and eastern sides of the anticline.

To the west of Fengjia, close to the sedimentary Neoproterozoic-Paleozoic series, in spite of the ductile deformation, the sedimentary structures are still preserved. When moving eastwards, the intensity of deformation and metamorphism increases, and the sedimentary bedding is transposed by the S_1 foliation. Around Fengjia, the S_1

foliation exhibits a flat-lying attitude, but small changes in dip indicate that S_1 is involved in a late upright folding. The NNE-SSW crenulation, centimeter to meter-scale folds and a vertical cleavage are in agreement with this late upright folding event (Fig. 8a). Close to the pluton, S_1 is tilted to subvertical, and deformed by centimeter- to meter-scale NE-SW striking fold axes with subhorizontal axial planes, locally associated with a foliation represented by the preferred orientation of mica flakes. These flat-lying structures argue for vertical shortening that might be due to the intrusion of the Early Mesozoic granite (Figs. 7b and 8b). Syn- S_1 intrafolial folds are also refolded during this event. Our field observations show that the most pervasively deformed rocks crop out in the lowermost part of the series where biotite appears.

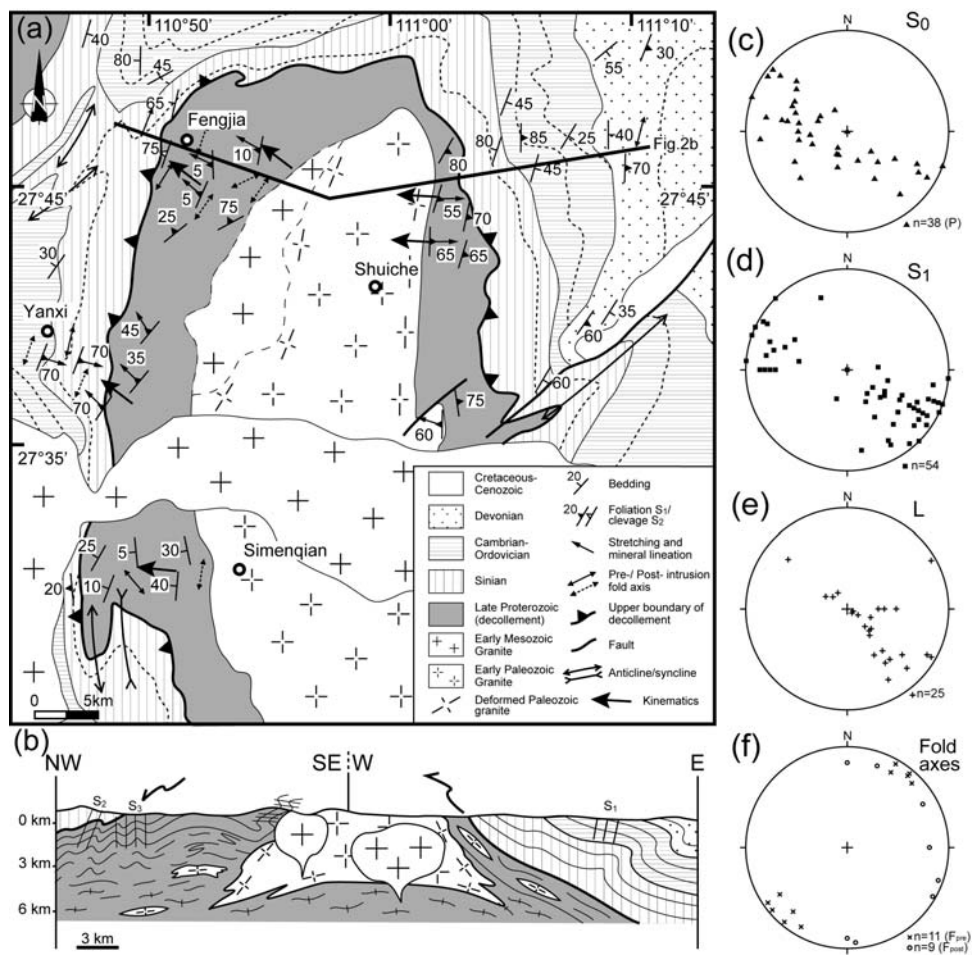


Fig. 7. (a): Detailed geologic map of Fengjia-Shuiche area (Modified after 1:500 000 Geological map of Hunan, BGMRHN, 1988). (b): Cross sections of the area. Stereographic plots (Schmidt lower hemisphere projection) of the structural elements, (c): bedding, (d): S_1 foliation, (e): stretching lineation, (f): fold axes and crenulation lineation. F_{pre} and F_{post} : fold axes before and after the intrusion of the pluton.



Fig. 8. Photographs illustrating the deformation of Fengjia-Shuiche area. (a): Upright folds in the high-strain zone, southeast of Fengjia. (b): Vertical foliation with a horizontal crenulation, southeast of Fengjia. (c): Stretched pebbles trending NW-SE in meta-conglomerate, east of Yanxi. (d): Boudinaged quartz vein in quartzite, west of Simenqian. (e): Meter-scale recumbent fold in quartzite, west of Simenqian. (f): Fractured feldspar clast in Neoproterozoic (Sinian) conglomerate, indicating a top-to-the-NW shear sense, northeast of Shuiche. (g): Mineral lineation due to the reorientation of andalusite crystallized during the contact metamorphism of the Early Paleozoic Baimashan pluton, northeast of Shuiche. (h): Foliated Early Paleozoic granite with mylonitic compositional layering, southeast of Shuiche.

South of Fengjia, near Yanxi, a well-pronounced foliation develops in the Neoproterozoic conglomerate in which the pebbles exhibit a N120° striking preferred orientation consistent with the regional lineation observed in the micaschists and metasandstones (Figs. 7e and 8c). In the sedimentary cover, the rocks are deformed in accordance with the structure observed in the decollement layer. For instance, a closely spaced cleavage and a NW-SE mineral and stretching lineation marked by elongated mineral aggregates is conspicuous.

More southerly, west of Simenqian, the decollement is represented by a near-horizontal foliation in meta-sandstone and conglomerate. In some places, quartz veins are boudinaged and sheared (Fig. 8d). Moreover, intra-folial recumbent folds are also observed in weakly metamorphosed sandstone indicating that the original bedding is totally transposed by the S_1 foliation (Fig. 8e).

To the east of the pluton and northeast of Shuiche, likewise in the western part, meta-conglomerate, meta-pelite, and micaschist that crop out in the decollement are more metamorphic than to the west. In the Neoproterozoic meta-conglomerate, the cleavage is represented by a penetrative slaty cleavage, along which variably sized pebbles are oriented and sheared. Some of them exhibit a sigmoidal shape. The cleavage intensity decreases in Sinian and lower Paleozoic rocks which contain generally a spaced cleavage or fold-related axial planar cleavage. Shear sense is indicated by asymmetric pressure shadow around centimeter-scale gravels and fracturing in feldspathic pebble (Fig. 8f). As described in the Chengbu area, in the vicinity of the Early Paleozoic pluton, andalusite formed by contact metamorphism during the granite intrusion is deformed along the direction of the regional lineation (Fig. 8g). The granitic pluton, especially south of Shuiche, is ductilely deformed and metamorphosed into orthogneiss. The mylonitic foliation is characterized by the alternation of light and dark layers corresponding to quartz-feldspar and biotite-rich parts, respectively (Fig. 8h). In some places, mafic enclaves are also elongated in the NW-SE direction. All the kinematic indicators are consistent with a top-to-the NW ductile shearing.

3.2.2 Microfabrics

In thin sections cut in the XZ plane of the strain ellipsoid, deformation features are well developed. In the metapelite, quartz pressure shadows around pyrites, with fibers length ranging from ~0.1 mm to more than 0.5 mm long, develop with a consistent top-to-the-NW sense of shear (Fig. 9a). Top-to-the NW kinematics is also shown by sigma-type feldspar porphyroclasts (Fig. 9b).

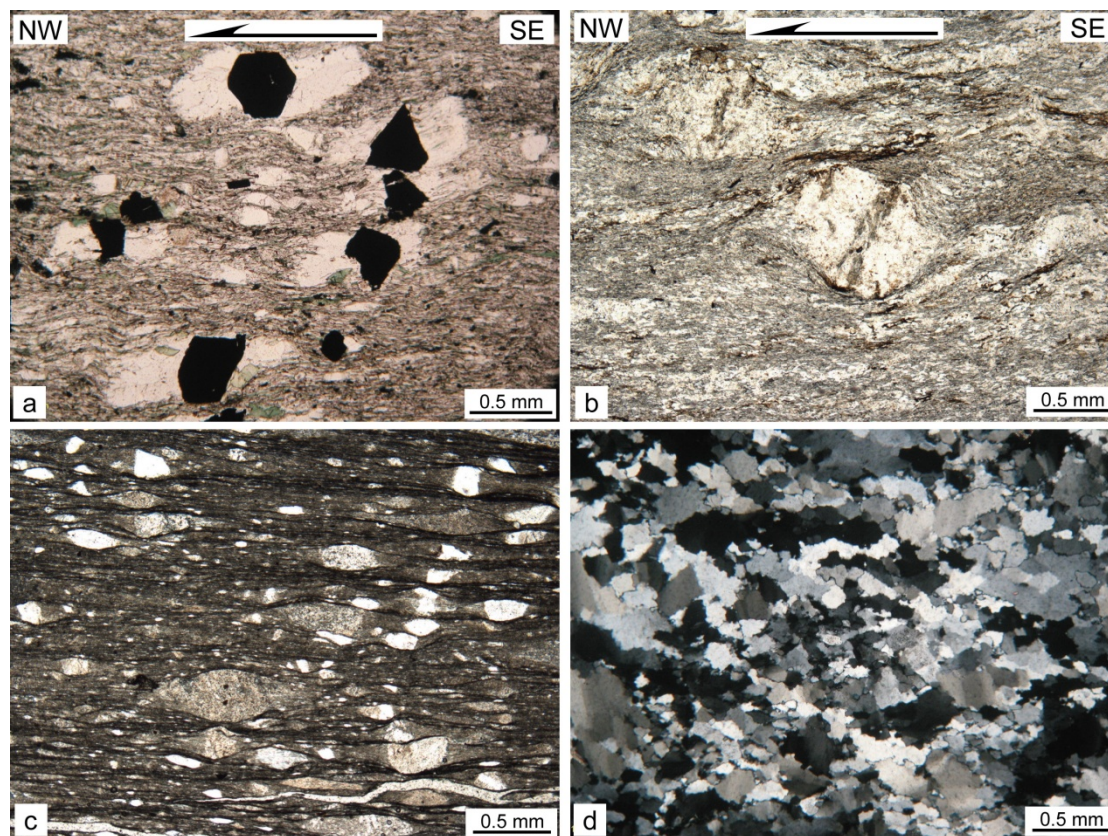


Fig. 9. Microscopic photographs showing the deformation of Fengjia-Shuiche area. (a): Pressure shadows around pyrites in meta-sandstone showing the top-to-the NW sense of shear, west of Simenqian. (b): Strongly deformed meta-sandstone with oriented quartz grains showing dissolution along the grain long boundaries (perpendicular to the maximum shortening Z direction), and pressure shadows in the X direction, west of Fengjia. (c): Sigmoidal feldspar porphyroclasts in sandstone with a top-to-the-NW shear sense, east of Fengjia. (d): Dynamically recrystallized quartz grains with serrated boundaries and oblique shape preferred orientation, east of Yanxi.

From outer to inner areas, the deformation mechanism is also changing from top to bottom of the decollement layer as mentioned above in the section 3.1.2. In meta-sandstone or meta-conglomerate, quartz clasts are sheared and oriented parallel to the foliation. The participation of fluid, as shown by the development of foliation-parallel phyllosilicates, and pressure shadows along elongated clasts (Fig. 9b-c), indicates that the dominant deformation mechanism is pressure solution. This pattern complies with low temperature metamorphic conditions, and fluid circulation hampered intragranular deformation (Passchier and Trouw, 2005). In the lower part of the decollement layer, polycrystalline aggregates, with grain size varying from $\sim 50 \mu\text{m}$ to $\sim 400 \mu\text{m}$, exhibit a typical “core and mantle” texture formed by dynamic recrystallization (Fig. 9d). Old, large clastic grains are replaced by elongated

aggregates with numerous small neograins probably developed by subgrain rotation recrystallization. Locally old grains are entirely replaced by a new grain network.

Thus, due to the increase in differential stress and temperature, intracrystalline slip turns to be the predominant deformation mechanism. In summary, alike for the Chengbu area, the deepest observed part of the XFSB is exposed in the Fengjia-Shuiche area due to the uplifting of the Triassic pluton, and this litho-tectonic unit composed of lower greenschist facies metapelites and metasandstones is interpreted as the basal decollement layer that separates the ductilely deformed upper sedimentary cover series and the unexposed Proterozoic basement. Within this high-strain zone, the Neoproterozoic sedimentary rocks, and the intruding early Paleozoic granites are changed into low temperature mylonites and orthogneiss, respectively. Along the NW-SE striking lineation, various and abundant kinematic indicators argue for a top-to-the-NW shearing. At the mineral size, fluid-assisted deformation (i.e. pressure solution) appears as the main deformation mechanism, although in the deepest part of the decollement layer, dynamically recrystallized quartz aggregates suggest that plasticity might become an important deformation mechanism.

3.3. Weishan area

The Weishan pluton is the largest Early Mesozoic granitic body cropped out in the XFSB, however, in this area well exposed the high-strain decollement layer is restricted to the northwestern margin of the pluton (Figs. 1b and 10a). Above the decollement layer, Sinian to Devonian sedimentary rocks are deformed both by the NW-verging D_1 folds and the D_2 SE-verging backfolds. To the west of the Weishan pluton, the regionally NE-SW striking D_1 fold axes turn to the NNE or N in the vicinity of the pluton. The Neoproterozoic meta-sandstone and micaschist are observed west and south of Huangcai (Fig. 10a). Due to the emplacement of the Weishan pluton, the original attitude of the foliation is modified to become parallel with the pluton boundaries, that is, the foliation dips to the NE and W in the northeastern and western borders, respectively (Fig. 10a). Moreover, a contact metamorphism aureole indicated by large, and randomly oriented biotite and muscovite grains develops around the entire granitic body. In order to avoid the influence of the contact metamorphism overprint, the macroscopic and microscopic observations have been done outside of the thermal aureole.

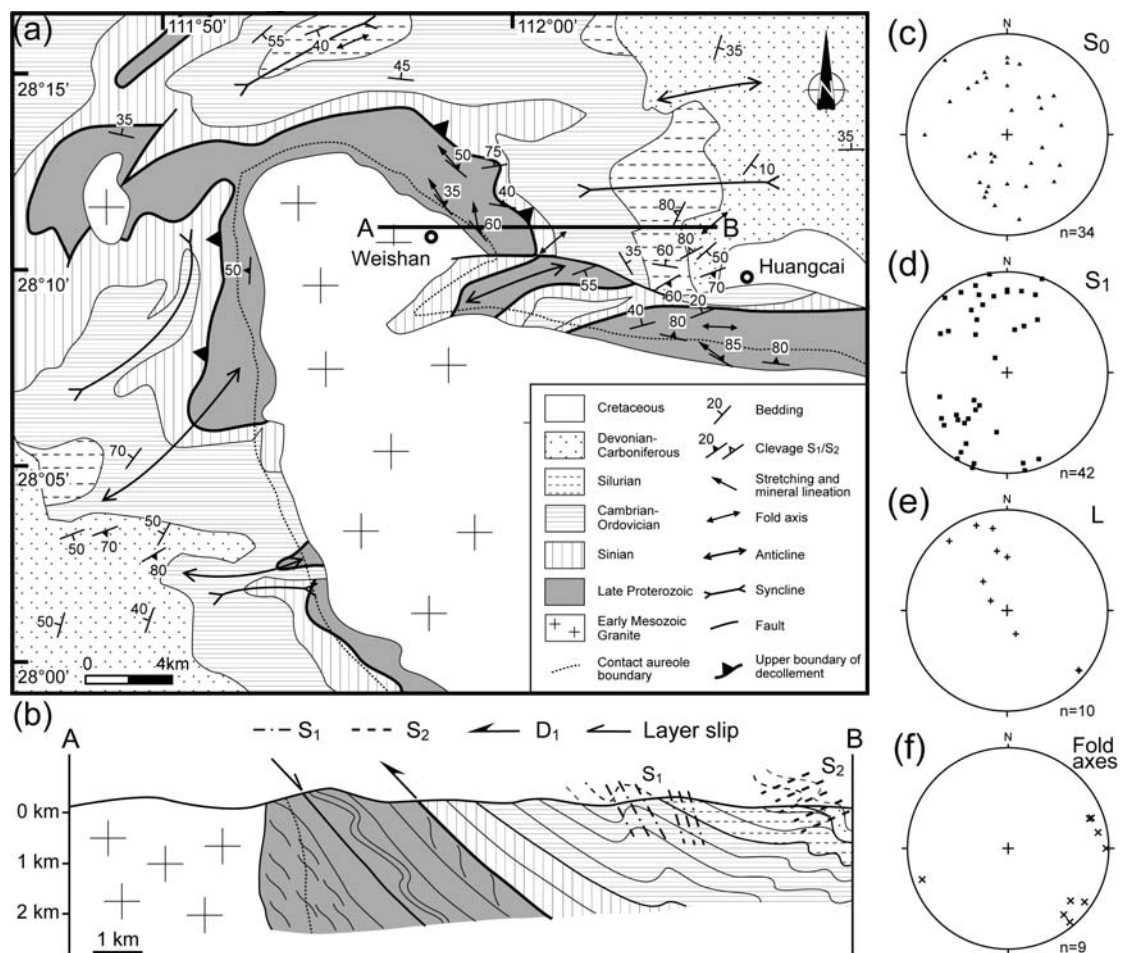


Fig. 10. (a): Detailed geologic map of Weishan area (Modified after 1:500 000 Geological map of Hunan, BGMRHN, 1988). (b): Cross sections of the area. Stereographic plots (Schmidt lower hemisphere projection) of the structural elements, (c): bedding, (d): S₁ foliation, (e): stretching lineation, (f): fold axes.

East of Weishan, in quartzite and micaschist, the foliation characterized by the preferred orientation of muscovite, biotite, and quartz grains, dips to the NE (Fig. 10d). A NNW-SSE trending mineral and stretching lineation, expressed by oriented biotite and quartz aggregates, is consistent with the regional L₁ lineation direction observed in the deformed sedimentary series of the XFSB. At the microscope scale, in metasandstone, clastic quartz grains with undulose extinction are elongated, and locally present a sigmoidal shape indicating a top-to-the-NW shearing. In quartzite, shear bands show a top-to-the-NW shear sense (Fig. 11a). Quartz aggregates consist of recrystallized grains with sutured or straight boundaries, locally an oblique shape fabric of the new grains, consistent with the top-to-the-NW sense of shear can be observed (Fig. 11b). Locally, quartz grains exhibit a euhedral shape, plane grain boundaries, and triple junctions. These features suggest that the quartz aggregates

experienced a thermal annealing, likely during the development of the thermal aureole coeval with the Weishan pluton emplacement. Nevertheless, our field and laboratory observations argue for a development of a synmetamorphic, top-to-the NW, ductile shearing before the Weishan pluton intrusion. Moreover, in the metapelite, a fibrous sillimanite-muscovite assemblage argue for a high temperature metamorphism predating the thermal aureole (Fig. 11c).

3.4. Shuangfeng area

Neighboring to the Ziyunshan pluton, ductilely deformed metamorphic rocks are well exposed in the pluton western margin, SE of Shuanfeng (Fig. 12a). In the study area, all the planar fabric elements, such as bedding, slaty cleavage, and metamorphic foliation, strike NE-SW (Fig.12c-d). Away from the Ziyunshan pluton, the Neoproterozoic to Devonian rocks are deformed by SE-verging folds related to the D₂ event. The sandstone and tillite formations are tilted, and become nearly vertical close to the pluton, and hereby post-intrusion collapse folds and layer slip faults develop in agreement with a vertical shortening possibly related to granite emplacement (Fig. 11e-f). Micaschist and quartzite are less metamorphosed than in the previous three areas, but vertical planar cleavage can be identified particularly along a few folded quartz veins (Fig. 11d). Under the microscope, the bedding surface S₀ is superimposed by the S₁ cleavage (Fig. 11g). Although only weakly metamorphosed rocks are exposed in this area, a contact metamorphic aureole marked by andalusite and biotite develops around the pluton. Conversely to the previous areas, the stretching lineation is weakly developed, and kinematic indicators are rare. This feature can be understood by considering that the exposed metapelites correspond to the upper part of the decollement layer, or alternatively that the linear structure and related kinematic indicators have been erased by recrystallisation.

In conclusion, the ductilely sheared metamorphic rocks exposed in the deepest part of the XFSB exhibit the same kinematic features as the D₁ structures developed in the Neoproterozoic to Early Triassic rocks . Thus we interpret these sheared rocks as the basal ductile decollement layer that accommodated the the NW verging folds shortening in the upper part of the orogen.

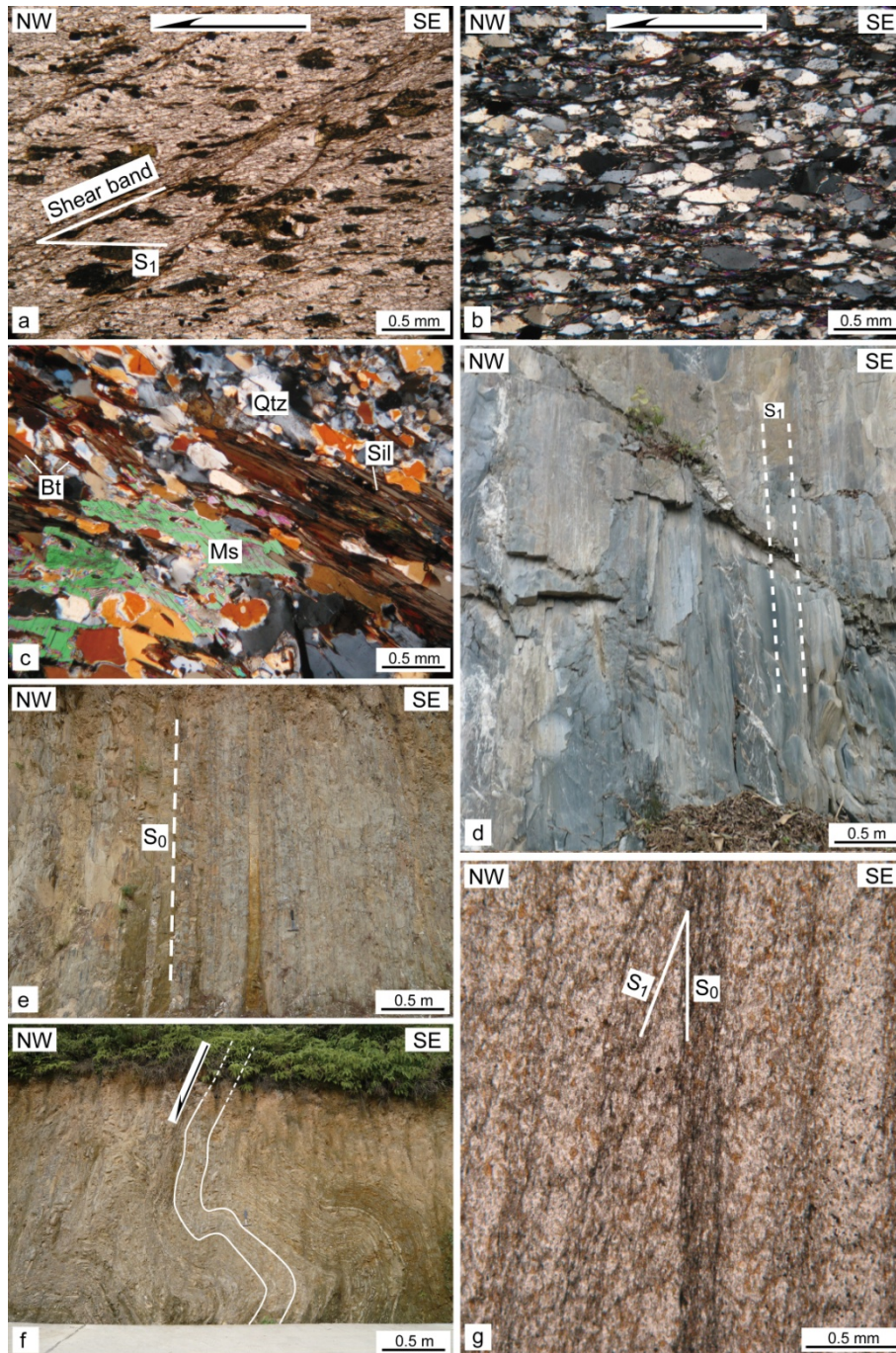


Fig. 11. Photographs illustrating the deformation of Weishan and Shuangfeng areas. (a): Shear band structure with horizontal foliation and oblique shear plane, west of Huangcai. (b): Equigranular recrystallized quartz with a few sigmoidal grains indicating a top-to-the-NW shearing, west of Huangcai. (c): Biotite (Bt)-sillimanite (Sil)-bearing micaschist with muscovite (Ms), and quartz (Qtz). (d): Vertical S_1 foliation in quartzite, east of Shuangfeng. (e): Vertical original bedding in pelite-sandstone alternation, southeast of Shuangfeng. (f): Gravitational collapse folds in Neoproterozoic sandstone, southeast of Shuangfeng. (g): Microscopic photo of original bedding (S_0) superimposed by cleavage (S_1), east of Shuangfeng.

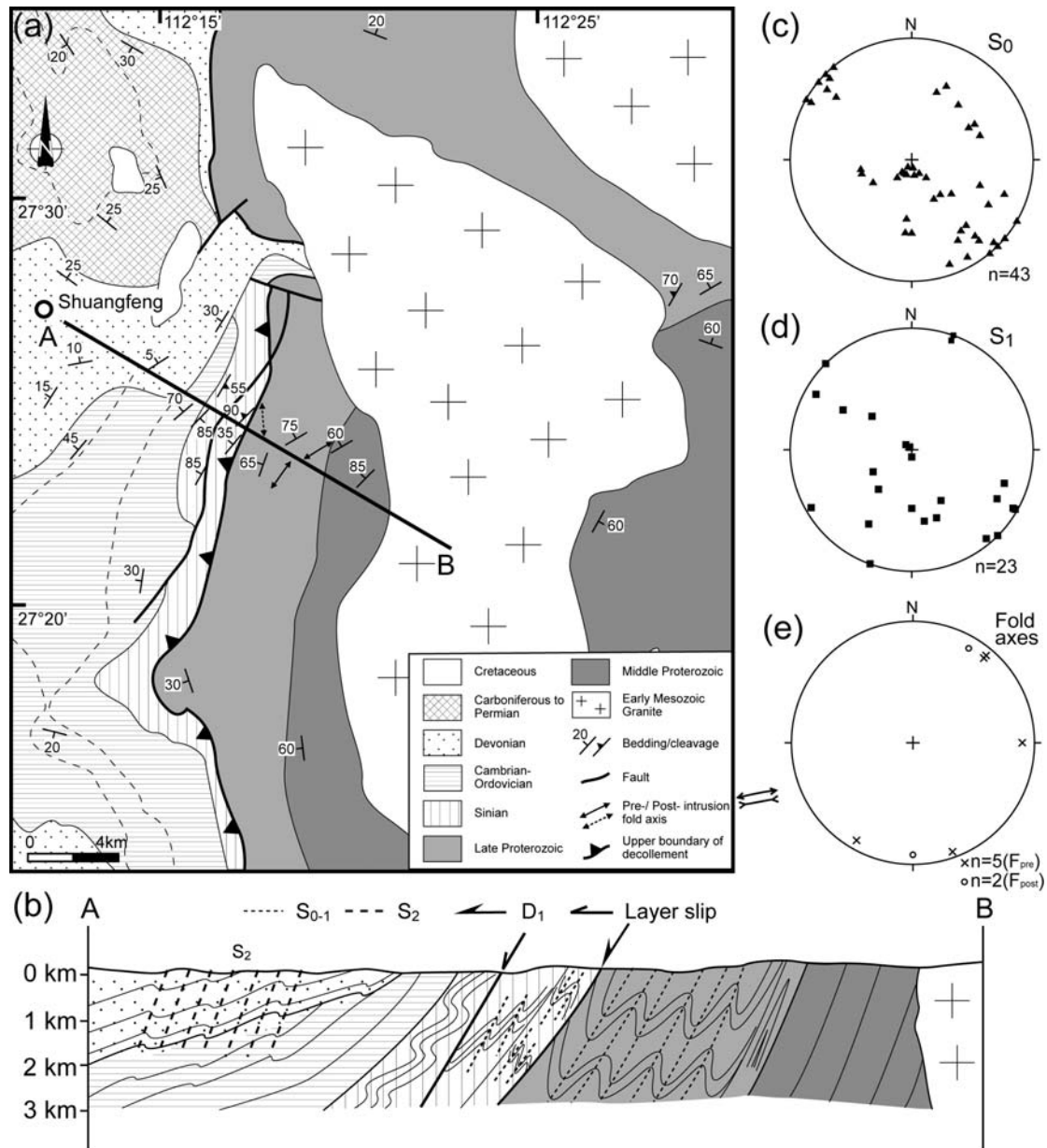


Fig. 12. (a): Detailed geologic map of Shuangfeng area (Modified after 1:500 000 Geological map of Hunan, BGMRHN, 1988). (b): Cross sections of the area. Stereographic plots (Schmidt lower hemisphere projection) of the structural elements, (c): bedding, (d): S_1 foliation, (e): fold axes and crenulation lineation. F_{pre} and F_{post} : fold axes before and after the intrusion of the pluton.

4. Geochronological constraints

In order to place time constraints on the ductile and synmetamorphic deformation described above in the decollement layer, monazite U-Th-Pb dating of metamorphic rocks has been carried out. In addition, SIMS zircon U-Pb and monazite U-Th-Pb dating have been performed on the granitoids that intrude into the basal decollement layer.

4.1. Analytical methods

4.1.1 Monazite U-Th-Pb chemical dating

Over the past 15 years, chemical geochronology on monazite has become possible (e.g. Suzuki and Adachi, 1991; Montel et al., 1996; Cocherie et al., 1998, 2005). Three starting assumptions are required to determine U–Th–Pb_{tot} age by using EPMA: 1) common Pb is negligible as compared to the amount of thorogenic and uraniumogenic lead (Parrish, 1990); 2) no radiogenic Pb loss has occurred since system closure, Pb content is not significantly affected by diffusion (e. g. Cocherie et al., 1998; Crowley and Ghent, 1999; Zhu and O'Nions, 1999); 3) a single age is involved at the size level of each individual spot analysis.

Monazite grains were analyzed with a Cameca SX 50 microprobe co-operated by ISTO (Institut des Sciences de la Terre d'Orléans, Campus Géosciences, Université d'Orléans) and BRGM (Bureau de recherches géologiques et minières) following the detailed analytical procedure provided by Cocherie et al. (1998), with 20 kV for acceleration voltage, 100 nA for beam current and 150 ppm for U, Th and Pb absolute errors. Individual and isochron age calculations and data sorting were realized by using EPMA/ex program written by Pommier et al. (2002). Following Cocherie and Albarède's isochron method (2001), data were plotted in U/Pb vs. Th/Pb diagram by using Isoplot (Ludwig, 2001). Results validity is given by several parameters such as comparison of best fit line with theoretical isochron or comparison of theoretical and calculated Mean Square Weight Deviation (MSWD). When the U/Pb and Th/Pb ratios are too close, their plots on the Th/Pb vs U/Pb diagram does not allow the definition of a regression line, and a reliable age cannot be derived by this method. Thus, the age is calculated by the average method.

4.1.2. SIMS U-Pb dating

Samples for U-Pb analysis were processed by conventional magnetic and density techniques to concentrate the non-magnetic, heavy fractions. Zircon grains, together with zircon standard Plešovice were mounted in epoxy mounts which were then polished to section the crystals in half for analysis. All zircons were documented with transmitted and reflected light micrographs as well as cathodoluminescence (CL) images in order to reveal their internal structures, and the mount was vacuum-coated with high-purity gold prior to secondary ion mass spectrometry (SIMS) analysis.

Measurements of U, Th and Pb were conducted *in situ* using the Cameca IMS-1280 SIMS at the Institute of Geology and Geophysics, Chinese Academy of Sciences in Beijing. U-Th-Pb ratios and absolute abundances were determined relative to the standard zircon Plešovice (Sláma et al., 2008), analyses of which were

interspersed with those of unknown grains, using operating and data processing procedures similar to those described by Li et al. (2009b). A long-term uncertainty of 1.5% (1 RSD) for $^{206}\text{Pb}/^{238}\text{U}$ measurements of the standard zircons was propagated to the unknowns (Li et al., 2010b), despite that the measured $^{206}\text{Pb}/^{238}\text{U}$ error in a specific session is generally around 1% (1 RSD) or less. Measured compositions were corrected for common Pb using non-radiogenic ^{204}Pb . Corrections are sufficiently small to be insensitive to the choice of common Pb composition, and an average of present-day crustal composition (Stacey and Kramers, 1975) is used for the common Pb assuming that the common Pb is largely surface contamination introduced during sample preparation. Uncertainties on individual analyses in data tables are reported at a 1σ level; mean ages for pooled U/Pb (and Pb/Pb) analyses are quoted with 95% confidence interval. Data reduction was carried out using the Isoplot program (Ludwig, 2001).

4.2. Geochronological results of the metamorphic rocks in the basal decollement layer

4.2.1. Sample XF365

Sample XF 365 (N26°16.467', E110°24.269'), is a garnet-muscovite-biotite-quartz-chlorite micaschist collected from the decollement layer in the Chengbu area. In thin section, the main fabric is the S_1 foliation with a top-to-the-NW shear sense shown by asymmetric pressure shadows around garnet porphyroblasts. Monazite grains are located in matrix with chloritized biotite and range in size from 10 to 80 μm without zonation (Fig.13a). The grains are mostly prismatic with long axes parallel to the S_1 foliation, thus, we interpret them as syn-metamorphic minerals crystallized during the D_1 ductile deformation. U-Th-Pb electron probe analyses were performed *in situ*. This approach allowed us to select the largest and unzoned grains in contact with biotite that formed during the D_1 event. With MSWD of 1.2 that makes the 74 data points in agreement with a reliable single age, a weighted average age of 243 ± 9 is calculated here, interpreted as the time of the ductile deformation (Fig. 14a).

4.2.2. Sample XF376

Sample XF376 (N28°11.317', E111°58.108') is a sillimanite-muscovite-quartz-biotite micaschist from the northeast of the Weishan pluton. Back-scattered electron images reveal that monazite grains are prismatic and range from 20 to 50 μm (Fig. 13b). Due to the low composition of radiogenic Pb, the calculated ages for single spot give a large error. Nevertheless, twenty-eight analyses in 13 grains yields a reliable weighted average age of 226 ± 18 Ma, with an

acceptable MSWD of 0.95 (Fig. 14b). It is interpreted as the time of the tectonic-metamorphism coeval with the crystallization of sillimanite.

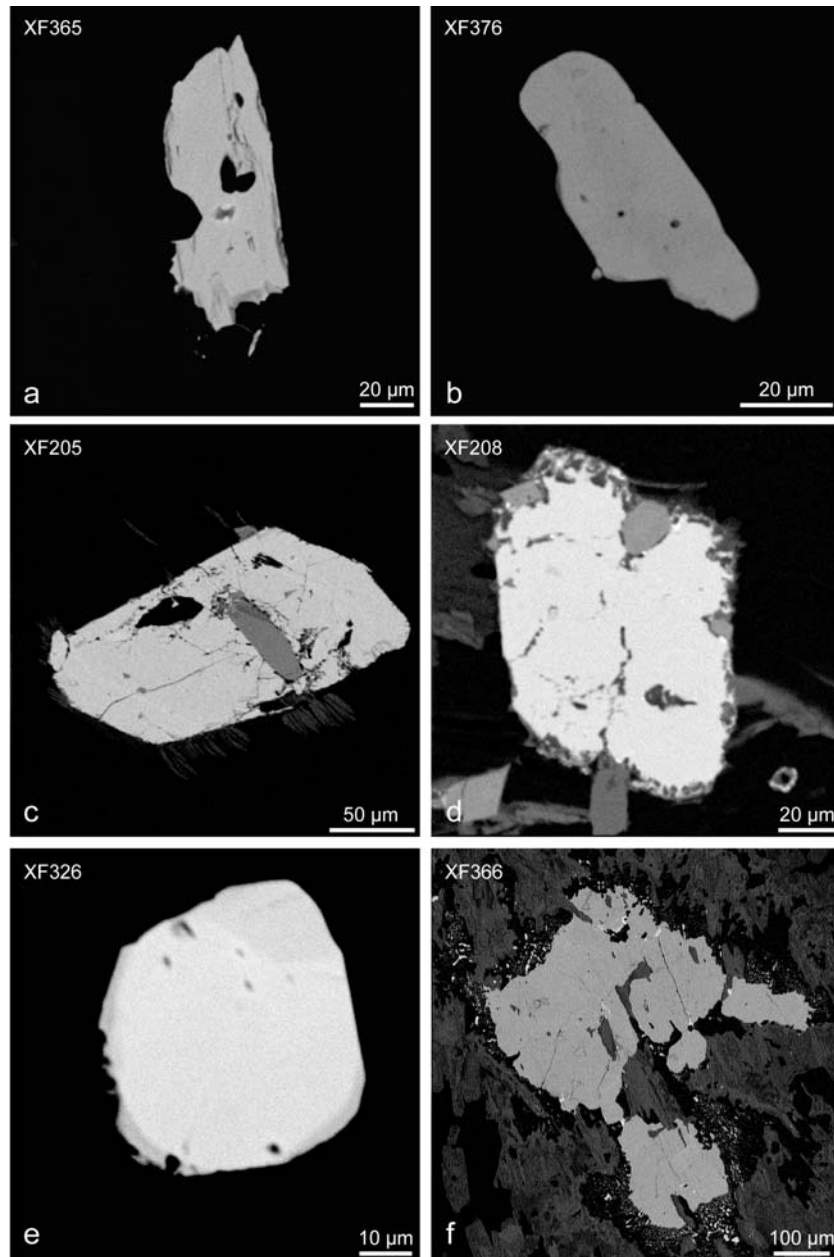


Fig. 13. BSE images of the dated monazite grains without chemical zonation. (a): Garnet-bearing micaschist from the Chengbu area. (b): Biotite-sillimanite-bearing micaschist from the Weishan area. (c): Weishan granite. (d): Ziyunshan granite. (e): Wawutang granite. (f): Lanrong deformed granite.

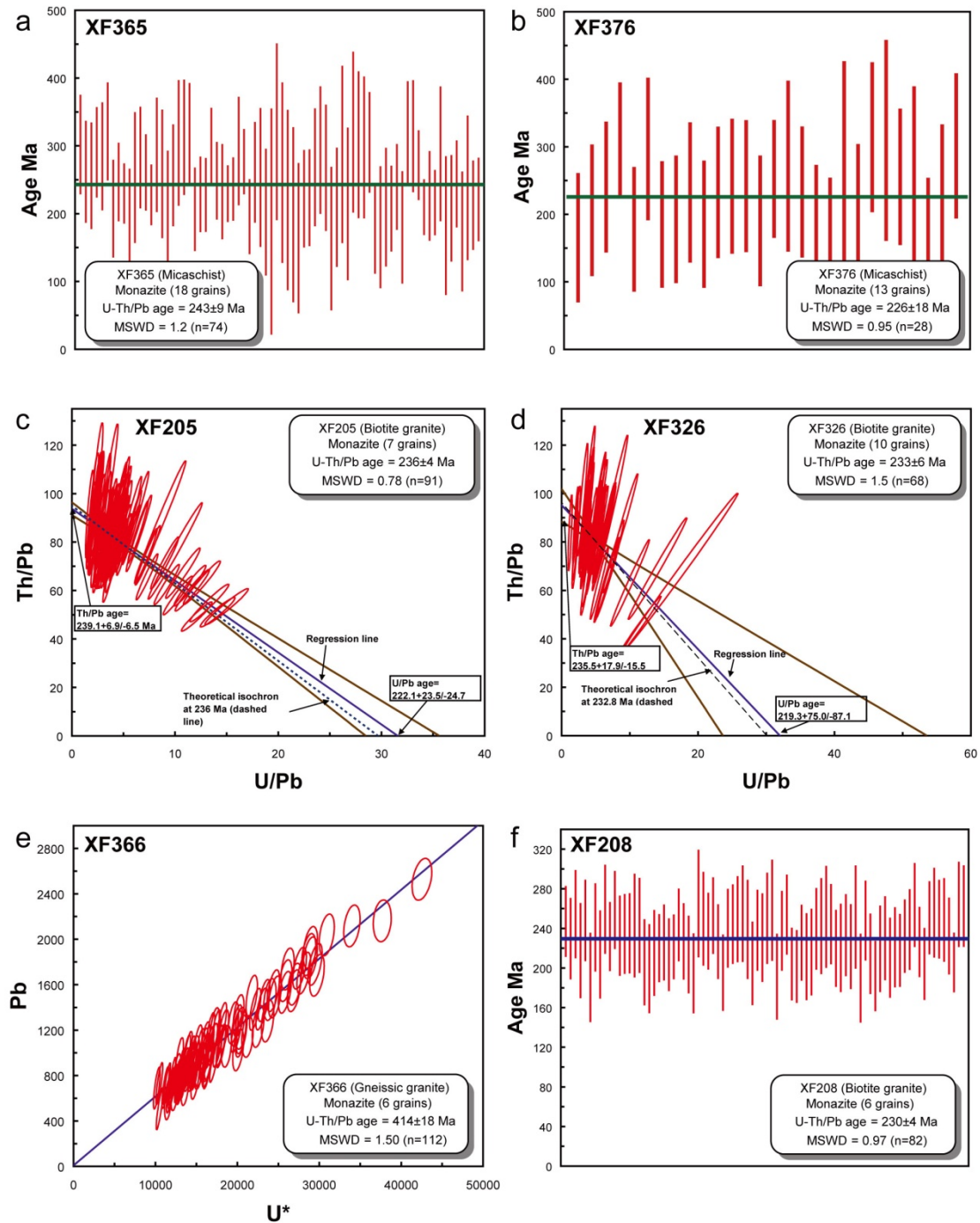


Fig. 14. Diagrams of monazite U-Th-Pb dating. (a): Garnet-bearing micaschist from Chengbu area. (b): Biotite-sillimanite-bearing micaschist from weishan area. (c): Weishan granite. (d): Ziyunshan granite. (e): Wawutang granite. (f): Lanrong granite.

4.3. Geochronological results on the plutonic rocks

4.3.1. U-Th-Pb_{tot} monazite dating

Four granitic samples, XF205, XF208, XF326, and XF366, are selected for monazite dating. The monazite grains occur as inclusions in biotite and range in size

from 50 to 500 μm (Fig. 13c-f). These monazite grains were analyzed directly from petrographic thin sections.

In sample XF205 (N28°00.255', E112°00.455'), large ranges in Th/U indicates that the chemical composition is favorable for using the Th/Pb vs. U/Pb diagram (Cocherie and Albarede, 2001). Ninety-one analyses of 7 grains yield well defined intercept ages (U/Pb age: $222 + 24/ - 25$ Ma and Th/Pb age: 239 ± 7 Ma). An isochron age of 236 ± 4 Ma is calculated at the centroid of the population (Fig.14c).

Sample XF326 is a monzonitic granite collected from the Wawutang pluton (N26°46.013', E110°20.266'). Sixty-eight spot analyses were performed on ten grains by using EPMA technique. Due to rather constant Th/U ratio, the spot analyses are clustered in the Th/Pb vs. U/Pb diagram (Fig. 14d), leading to large errors on the intercept ages (U/Pb age: $219 + 75/ - 87$ Ma and Th/Pb age: $236 + 18/ - 16$ Ma). Nevertheless, it is noteworthy that the slope of the regression line is very close to the theoretical isochron. A mean age of 233 ± 6 Ma was calculated at the centroid of the population.

Sample XF366 (N26°19.743', E110°26.519') is a gneissic granite collected from deformed Lanrong pluton. The constant Th/U ratio is not suitable for using the Th/Pb vs. U/Pb diagram to calculate a mean age. In such case, as the $U+Th_{\text{tot}}$ concentration is very high and changes significantly, the most suitable diagram is that of Suzuki and Adachi (1991). All the analyses, with an intercept very close to the origin, yield a precise age at 414 ± 18 Ma (Fig. 14e), which is similar within errors to the result of zircon U-Pb dating method (XF314).

For sample XF208 (N27°27.802', E112°22.327'), eighty-two analyses of six grains were performed. However, due to more concentrated Th/U ratios, neither the Th/Pb vs. U/Pb diagram nor Pb-Th* diagram of Suzuki and Adachi is appropriate to calculate the mean age, a weighted average age of 230 ± 4 is preferred here to represent the timing of the emplacement (Fig. 14f).

4.3.2. U-Pb zircon dating

Sample XF205 is a biotite monzonitic granite collected from Weishan pluton. Concentric zoning is distinctly demonstrated in euhedral zircon, which is 100 to 250 μm in length with length-width ratios of 2:1 to 3:1 (Fig. 15a). Fourteen analyses on 14 zircons have 1202-7648 ppm of U, 192-2176 ppm of Th, with 0.067-0.347 of Th/U ratios (Table 1). Five spots with U contents over 4000 ppm are discarded because of their abnormal old age related to high U. Similar phenomenon has also been reported during SIMS zircon U-Pb analyses (e.g., Li et al., 2010a). Hence, excluding these 5

spots, the other 9 analyses yield a concordia $^{206}\text{Pb}/^{238}\text{U}$ age of 222 ± 3 Ma (Fig. 16a), which likely represents the emplacement age.

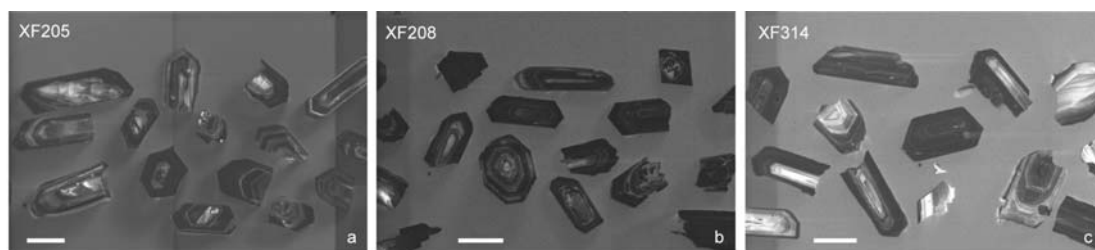


Fig. 15. Examples of cathodoluminescence images of the dated zircons from samples XF205, XF208 and XF314.

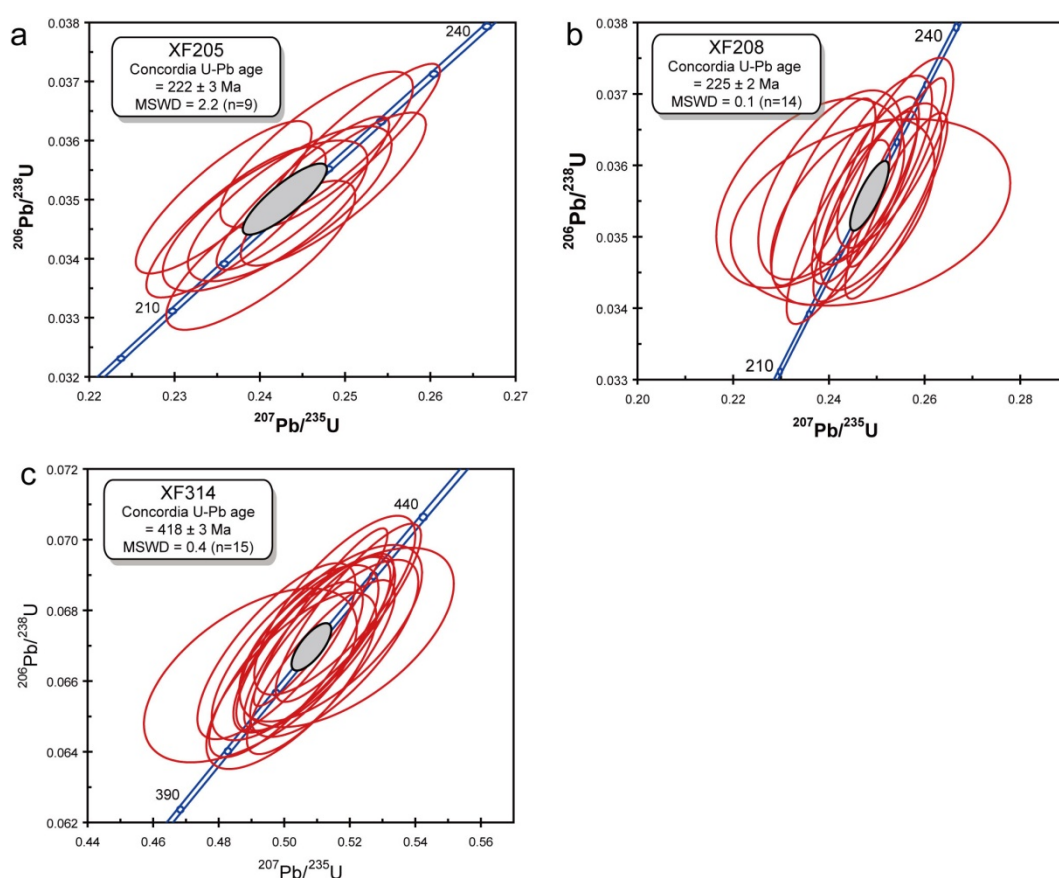


Fig. 16. Concordia diagrams of SIMS zircon U-Pb data. (a): Weishan granite. (b): Ziyunshan granite. (c): Lanrong granite.

Table 1. SIMS U-Pb zircon analyses from samples XF205, XF208 and XF314(See Appendix table 1).

Sample XF208 is a two mica granite collected from Ziyunshan pluton. Relatively transparent and colorless, euhedral or subhedral zircons with concentric zoning are commonly observed in this sample (Fig. 15b). Zircons are 50 to 150 μm

long with length-width ratios of 1:1 to 2:1. Fourteen analyses on 14 fourteen zircons, with 851-1603 ppm of U, 172-817 ppm of Th and 0.203-0.538 of Th/U ratios (Table 1), gives indistinguishable U-Pb isotopic compositions within errors, which correspond to a single age population with a concordia $^{206}\text{Pb}/^{238}\text{U}$ of 226 ± 2 Ma (Fig. 16b), indicating the intrusion of Ziyunshan pluton.

Sample XF314 is a gneissic granite collected from Lanrong pluton beside the location of sample XF366. Zircons from this sample are mostly subhedral to anhedral, and 50-200 μm long with mostly 2:1 to 3:1 of length-width ratios (Fig. 15c). Fifteen analyses of fifteen zircons were performed, with 163-1581 ppm of U, 195-500 ppm of Th, 0.280-1.322 of Th/U ratios, and a concordia age of 418 ± 3 Ma (Table 1, Fig. 16c). This Paleozoic age represents the crystallization age of this pluton.

5. Discussion

5.1. Summary of the deformational characteristics in the basal decollement layer

The Xuefengshan intracontinental belt experienced a polyphase deformation with a dominant D_1 phase of top-to-the-NW compression and shearing, followed by a SE-verging back-folding and back thrusting D_2 phase, and lastly a D_3 phase of upright folding (Wang et al., 2005; Chu et al., submitted). Neoproterozoic to Early Triassic sedimentary rocks, with rarely developed low greenschist facies metamorphism, were intensely deformed. However, unlike many orogenic belts, high-grade metamorphic rocks, like amphibolite or migmatite, are absent in this chain (BGMРН, 1988). In order to accommodate the important shortening observed in shallow crustal rocks, a basal decollement layer must develop at depth within ductilely deformed metamorphic rocks. Such a decollement layer crops out in the core of anticlines formed during the emplacement of post-tectonic Late Triassic plutons, like the Miaoershan and the Baimashan. As shown above, the ductile deformation is characterized by a flat-lying foliation, a NW-SE stretching lineation, and a top-to-the-NW shearing. Thus the ductile deformation recorded in the basal decollement layer can be attributed to the D_1 event recognized in the sedimentary cover.

By comparison with the Alpine Jura or Zagros Fold-and-Thrust Belt, high strain decollement layers are well developed in the outer zone of collisional belts, commonly in low strength rocks such as evaporites or black shales (Escher and Beaumont, 1997; McQuarrie, 2004). Below the basal decollement layer, basement rocks lack strong and pervasive deformation. In the XFSB, the main crustal decollement located at the base of the Proterozoic to Early Triassic sedimentary series allows the NW-SE shortening recorded by the D_1 event to be accommodated at depth.

Furthermore, although not clearly mentioned, the existence of a ductile decollement layer is consistent with previous studies of the architecture of the XFSB (Wang et al., 2005 and references therein).

In the decollement layer, the flat lying foliation, NW-SE striking stretching lineation, and intrafolial folds developed during a top-to-the-NW shearing, as documented by numerous kinematic indicators such as sigmoidal quartz veins, garnet porphyroblast with pressure shadows, sigma-type porphyroclasts, shear bands, etc... Paleozoic granites were also involved in this shearing, producing orthogneiss and mylonites in the pluton margins. Paleozoic granitic dykes intruding the country rocks were boudinaged giving rise to sigmoidal lenses that comply with the regional sense of shear. The top-to-the-NW kinematics observed in the basal decollement layer is in agreement with the NW vergence of D_1 synschistose folds coeval with slaty cleavage, and the NW-SE lineation observed in the sedimentary cover rocks.

At the microscope scale, pressure solution appears as the main deformation mechanism responsible for the development of the ductile fabrics under low-grade metamorphic conditions. However, in the deepest parts of the decollement, the ductile deformation increases as indicated by quartz microstructures and quartz *c*-axis fabrics. The diagrams indicate that quartzite and micaschist mylonites developed at low temperature (ca 300-400 °C) where pressure solution is the dominant mechanism, and dislocation glide and dynamic recrystallization become effective when temperature increases (Tullis et al., 1973; Stipp et al., 2002; Passchier and Trouw, 2005).

5.2. Time constraints

5.2.1. Ductile deformation and crustal melting in the Xuefengshan Belt

The monazite U-Th-Pb, and the zircon U/Pb ages presented above provide new time constraints on the evolution of the XFSB. In spite of a large uncertainty, monazites from micaschist of the basal decollement layer yield chemical age constraints about 243-226 Ma, indicating that the top-to-the-NW shearing occurred during Middle Triassic.

The Triassic aluminous to peraluminous plutons, which intrude already deformed rocks are widely distributed across the Xuefengshan Belt (Fig. 1b). Although these granites are dated with different isotopic methods, the ages still remain in debate (Ding et al., 2005; Chen et al., 2006, 2007a, 2007b; Wang et al., 2007a; Li and Li, 2007; Li et al., 2008, and references therein). The synthesis of the available age data is shown in Fig. 17. Our zircon U-Pb, and monazite U-Th-Pb geochronological data allow us to narrow the time interval of the magmatic activity in

the XFSB. These new time constraints show that pluton emplacement occurred between 235 and 215 Ma, at the end of the entire orogenic process.

It is worth to note that the monazite U-Th-Pb age, at ca 226 Ma, of the biotite-sillimanite micaschist (sample XF 376) picked around the Weishan pluton is similar, within the errors, with the monazite and zircon ages of the undeformed granites that post-date the activity of the basal decollement layer. This biotite-sillimanite rock argue for a high temperature metamorphism that might be interpreted as a consequence of the thermal event responsible for crustal melting and the emplacement of the Triassic granites at the end of the Xuefengshan orogeny.

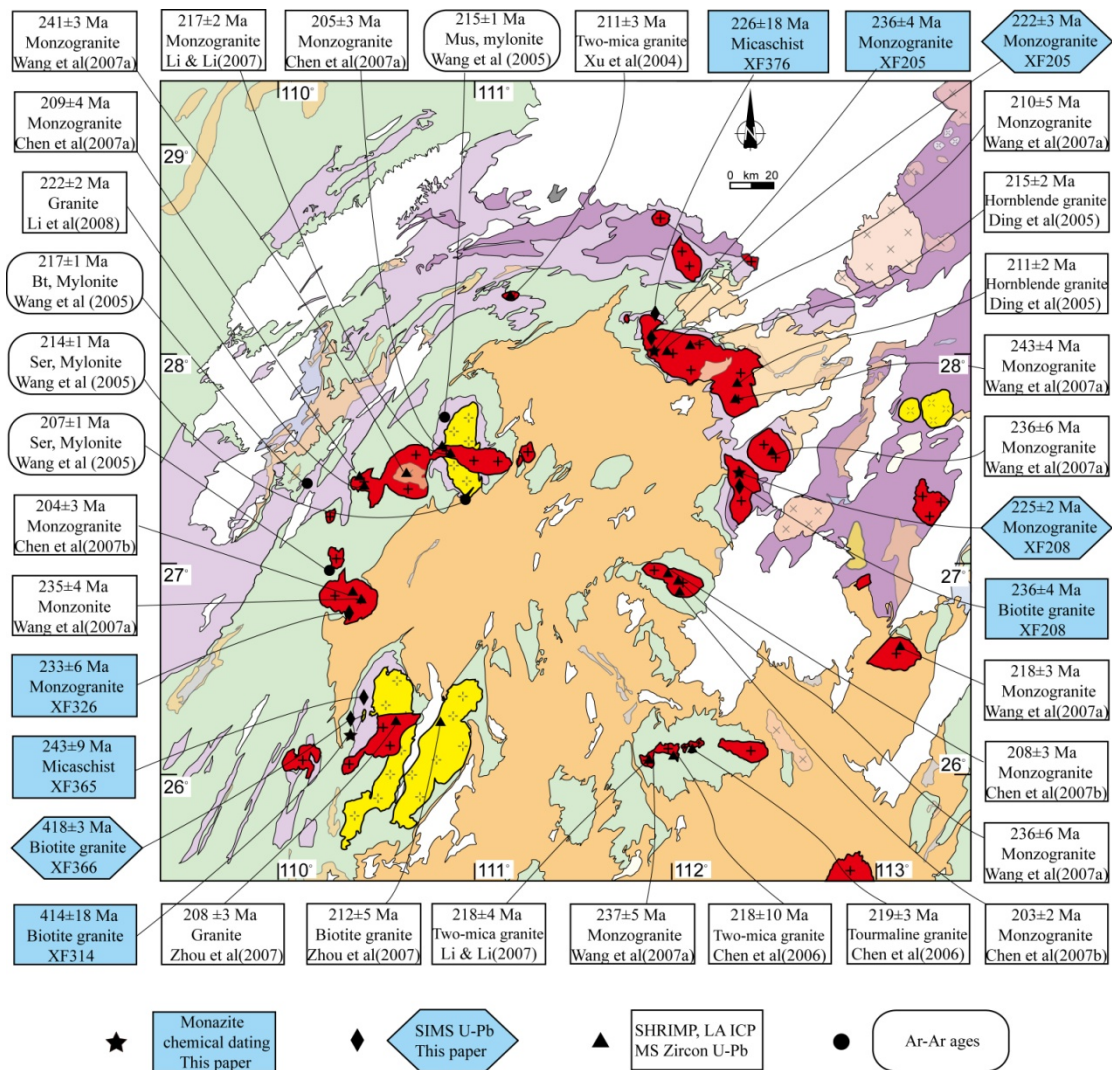


Fig. 17. Synthetic map of the Xuefengshan Belt showing the available radiometric data.

5.2.2. Tectonic evolution of the XFSB

As already described, the SCB experienced a ductile deformation, middle-high grade metamorphism, and widespread crustal partial melting during the Early Paleozoic orogeny in Late Ordovician to early Silurian (Faure et al., 2009; Li et al., 2010a; Charvet et al., 2010). However, the XFSB was almost not influenced by this event, except in the southeastern part of the belt (see Chu et al. submitted for details). Most of the regional faults, cleavage or foliation direction, fold axial planes are trending NE-SW, and the deformation pattern of the XFSB is similar in both pre- and post-Devonian rocks, including the entire Paleozoic series, and the Early and Middle Triassic one. The late Triassic, Jurassic and Cretaceous rocks that unconformably overly the deformed series place the time constraint on the deformation. The geometric and kinematic consistency between the Paleozoic and Early Triassic rocks strongly suggests that the structure of the Xuefengshan Belt is the product of the same deformation event, i.e., the Early Mesozoic Orogeny. Furthermore, a very significant criteria to distinguish the Early Mesozoic structures from the Early Paleozoic ones is that the Early Paleozoic granites that represent the post-orogenic plutons of the Early Paleozoic orogen, are ductilely deformed into orthogneiss when involved into the Early Mesozoic Orogeny. Moreover, the Early Mesozoic granites are not deformed. In the country rocks around the Paleozoic plutons, contact metamorphism andalusite was reoriented during the Early Mesozoic D₁ event. These lines of evidence are in agreement with previous sericite and biotite ⁴⁰Ar-³⁹Ar data (Wang et al. 2005).

5.3. Geodynamic significance of the XFSB in the SCB framework

Our detailed, multi-scale structural analysis and geochronological study on monazite and zircon, allow us to clarify the deformational pattern in the decollement layer and the timing of the orogen. The regional top-to-the-NW ductile shearing with folding and thrusting sculpted the outlines of the XFSB.

Nevertheless, the general tectonic interpretation of the belt is still controversial. An Early Paleozoic orogeny (Qiu et al., 1998, 2000) has been proposed, but the available stratigraphic and radiometric constraints do not support this view. Wang et al. (2005) proposed an asymmetric positive flower-shaped, transpressional model to explain the ductile shearing with a sinistral strike-slip component. Based on stratigraphic and geochronological data, the main deformation occurred between the middle Triassic and early Jurassic, but our structural studies do not support the sinistral flower-shaped transpressional model. Indeed, in the XFSB, strike-slip faults are brittle structures cutting through the undeformed granitic plutons. Yan et al. (2003) interpreted the XFSB as the result of the westward progressive collision of the

Yangtze Block with the North China Block during the Late Jurassic to Cretaceous, but in this model, the Triassic event, which is clearly postdated by the Late Triassic plutons and the regional Late Triassic unconformity, is not distinguished from the Cretaceous one. The structural analysis of the decollement presented above, argue for a large scale thin-skinned tectonic model with a high strain basal decollement layer, rooted in the Chenzhou-Linwu Fault, between the sedimentary cover and basement rocks (Fig. 18). West of the Chenzhou-Linwu Fault, the XFSB is characterized by NE-SW trending structures. In order to accommodate the shortening experienced by the Late Neoproterozoic (Sinian) to Early Triassic sedimentary series, the underlying basement must have experienced an intracontinental underthrusting to the SE during the Triassic.

To the east of the Chenzhou-Linwu Fault, in Jiangxi province, well preserved Early Paleozoic structures, interpreted as an intracontinental orogen (Faure et al., 2009), are weakly reworked by the Triassic deformation. Consequently, the Chenzhou-Linwu Fault appears as an important regional boundary, which separates the Early Mesozoic deformation dominated to the west, and Early Paleozoic deformation dominated domains to the east. The Chenzhou-Linwu fault and also a significant boundary in the entire SCB (Wang et al., 2007b).

During the Early Triassic, the SCB underwent several orogenic events along its boundaries. To the north, the SCB subducted beneath the North China Craton (Hacker and Wang, 1995; Faure et al., 1999; 2008); to the northwest, the Songpan-Ganzi and Longmenshan Belts record evidence for a Triassic deformation (Wallis et al., 2003; Harrowfield and Wilson, 2005; Roger et al., 2008, 2010); to the west, the Jinshajiang suture zone is characterized by east-directed deformation (Wang et al., 2000) and to the southwest, the Yunnan-Guangxi-NE Vietnam Belt separates the SCB from Indochina (Lepvrier et al., 2011; Carter et al., 2001; Carter and Clift, 2008). Nevertheless, none of these orogens is directly related to the intracontinental XFSB.

During the Mesozoic, Early Mesozoic (Indosinian) granitic rocks are widespread not only in the XFSB, but also entire SCB (Faure et al., 1996; Xu et al., 2003; Deng et al., 2004; Li and Li, 2007; Wang et al., 2007b; Zhou, 2007; Lin et al., 2008; Kusky et al., 2010). A flat slab subduction model has been brought forward to account for the inland-directed propagation of Triassic plutonism (Li and Li, 2007). This model may generate a volume of magma scattered in a wide area in the upper plate of the subduction system. Such a mechanism is often invoked to account for the Laramide orogen in the Western North American Cordillera, and the Andes in South America (Haschke et al., 2002; English and Johnston, 2004). However, this model is still in testing, as the onset of the Pacific plate subduction remains in debate, and the spatial

and temporal distribution of the Triassic magmatism does not show a clear regional trend (Engebretson et al., 1985; Li et al., 2006; Ding et al., 2005; Chen et al., 2006, 2007a, 2007b; Wang et al., 2007a; Li and Li, 2007; Li et al., 2008).

As well exemplified by the Petermann and Alice Springs orogens of Australia, a weak crustal zone, such as a fault, an old suture, or a rift, might be easily reactivated in continental orogens (Hand and Sandiford, 1999; Holdsworth et al., 2001; Sandiford et al., 2001). The reactivation of a fault zone in the SCB is a likely interpretation for the localization of the XFSB. After the completion of the Early Neoproterozoic Jiangnan orogeny that produced the welding of the Yangtze and Cathaysia blocks, the development of rifts within the newly formed South China Block was a suitable setting to accumulate more than 10 km thick Neoproterozoic terrigenous sediments followed by black shales and limestones until Ordovician, and covered by Silurian turbidite series that corresponds to the erosion of the early Paleozoic orogen (BGMJRJX, 1984; BGMRGX, 1985; BGMRHN, 1988; Faure et al., 2009; Charvet et al., 2010).

The Chenzhou-Linwu Fault absorbed the deformation transferred from the subduction of the Pacific plate below the active margin of the South China Block. As a consequence, the intracontinental deformation generated the ductile decollement layer, and the top-to-the-NW thrusting and folding of the sedimentary cover in the XFSB.

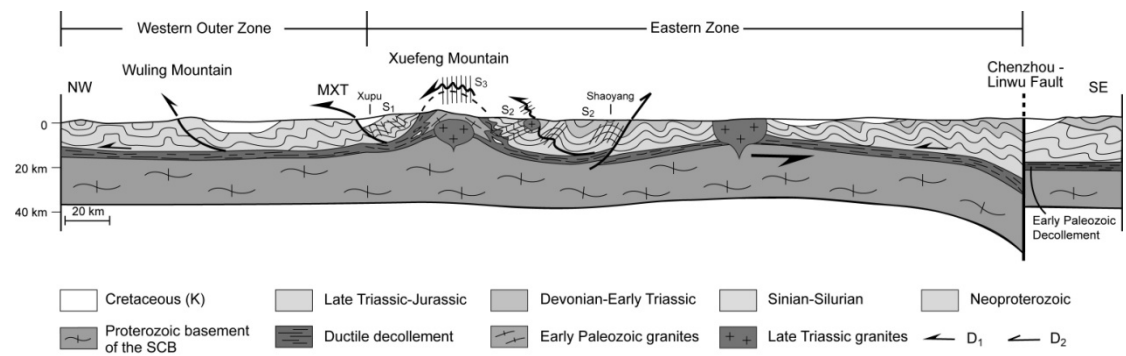


Fig. 18. Interpretative bulk cross-sections of the Xuefengshan Belt: The Triassic basal decollement, observed in the core of the D₃ anticlines, separates the upper crust deformed by NW-directed folding and thrusting, and the middle-lower crust deepening to the SE. The Xuefengshan Belt is intruded by late Triassic peraluminous granitic plutons. SE of Shaoyang, the pre-Devonian series are folded by S-verging folds, but these folds parallel to the line of section are not represented. East of the Chenzhou-Linwu fault, the Triassic deformation is weak. The main structure developed during the Early Paleozoic orogeny corresponds to South or SE-verging folds underlain by a decollement (cf. Faure et al., 2009). One decollement is depicted

rooted in the Chenzhou-Linwu fault. SE of Shaoyang, due to the second phase of top-to-the SE shearing, the decollement is cut by a D₂ SE-directed thrust coeval with S₂ cleavage.

6. Conclusion

The XFSB represents another example of an intracontinental orogen in which the shortening represented by NW-verging folding and thrusting is well developed in the Neoproterozoic-Early Triassic sedimentary series. At depth, this deformation is accommodated by a basal ductile decollement with a pervasively developed, synmetamorphic top-to-the-NW ductile shearing. The monazite U-Th-Pb chemical dating is in agreement with a Triassic age for the synmetamorphic ductile deformation. Widespread granites, which cut the Early Mesozoic structures, are dated by the zircon U-Pb method. Based on these results, the XFSB occurred between 245 and 215 Ma, with the NW-directed folding, thrusting and shearing around 245-226 Ma, and late orogenic granites of 235-215 Ma.

Acknowledgements. Field works have been funded by the Innovative Project of the Chinese Academy of Sciences (Grant No. KZCX1-YW-15-1) and Major State Basic Research Development Program of China (2009CB825008). NSFC grants n° 90714007 and 40730315 are also acknowledged.

Reference

- Avouac, J. P., Tapponnier, P., Bai, M., You, H., Wang, G., 1993. Active Thrusting and Folding Along the Northern Tien Shan and Late Cenozoic Rotation of the Tarim Relative to Dzungaria and Kazakhstan. *Journal of Geophysical Research* 98, 6755-6804.
- Bureau of Geology and Mineral Resources of Fujian Province (BGMRFJ), 1985. *Regional Geology of the Jiangxi Province*. Geological Publishing House, 675 pp.
- Bureau of Geology and Mineral Resources of Guangxi province (BGMRGX), 1985. *Regional Geology of the Guangxi Zhuang Autonomous Region*. Geological Publishing House, 853 pp.
- Bureau of Geology and Mineral Resources of Hunan province (BGMRHN), 1988. *Regional Geology of the Hunan Province*. Geological Publishing House, Beijing, 507 pp.

- Bureau of Geology and Mineral Resources of Jiangxi Province (BGMJRJX), 1984. Regional Geology of the Jiangxi Province. Geological Publishing House, 921 pp.
- Bureau of Geology and Mineral Resources of Zhejiang Province (BGMJRZJ), 1989. Regional Geology of the Jiangxi Province. Geological Publishing House, 617 pp.
- Carter, A., Clift, P. D., 2008. Was the Indosinian orogeny a Triassic mountain building or a thermotectonic reactivation event? *Comptes Rendus Geosciences* 340, 83-93.
- Carter, A., Roques, D., Bristow, C., Kinny, P., 2001. Understanding Mesozoic accretion in Southeast Asia: Significance of Triassic thermotectonism (Indosinian orogeny) in Vietnam. *Geology* 29, 211-214.
- Charvet, J., Shu, L. S., Shi, Y. S., Guo, L. Z., Faure, M., 1996. The building of south China: Collision of Yangzi and Cathaysia blocks, problems and tentative answers. *Journal of Southeast Asian Earth Science* 13, 223-235.
- Charvet, J., Shu, L. S., Faure, M., Choulet, F., Wang, B., Lu, H. F., Le Breton, N., 2010. Structural development of the Lower Paleozoic belt of South China: Genesis of an intracontinental orogen. *Journal of Asian Earth Science* 39, 309-330.
- Chen, A., 1999. Mirror-image thrusting in the South China Orogenic Belt: tectonic evidence from western Fujian, southeastern China. *Tectonophysics* 305, 497-519.
- Chen, C. H., Hsieh, P. S., Lee, C. Y., Zhou, H. W., 2011. Two episodes of the Indosinian thermal event on the South China Block: Constraints from LA-ICPMS U-Pb zircon and electron microprobe monazite ages of the Darongshan S-type granitic suite. *Gondwana Research* 19, 1008-1023.
- Chen, W. F., Chen, P. R., Zhou, X. M., Huang, H. Y., Ding, X., Sun, T., 2006. Single-zircon La-ICP-MS U-Pb Dating of the Yangmingshan Granitic Pluton in Hunan, South China and its Petrogenetic Study (in Chinese with English abstract). *Acta Geologica Sinica* 80, 1065-1077.
- Chen, W. F., Chen, P. R., Huang, H. Y., Ding, X., Sun, T., 2007a. Chronological and geochemical studies of granite and enclave in Baimashan pluton, Hunan, South China. *Science in China (D)* 50, 1606-1627.
- Chen, W. F., Chen, P. R., Zhou, X. M., Huang, H. Y., Ding, X., Sun, T., 2007b. Single Zircon LA-ICP-MS U-Pb Dating of the Guandimiao and Wawutang Granitic Plutons in Hunan, South China and its Petrogenetic Significance. *Acta Geologica Sinica* 81, 81-89.

- Choukroune, P., 1992. Tectonic evolution of the Pyrenees. *Annual Review of Earth Planetary Sciences* 20, 143-158.
- Chu Y., Faure M., Lin W., Wang Q. 2011. Early Mesozoic intracontinental Xuefengshan Belt, South China: insights from structural analysis of polyphase deformation; EGU meeting, Vienna, Austria.
- Chu Y., Faure, M., Lin, W., Wang, Q. C. Tectonic evolution of the Early Mesozoic (Indosinian) intracontinental Xuefengshan Belt, South China. Submitted.
- Cocherie, A., Legendre, O., Peucat, J. J., Kouamelan, A. N., 1998. Geochronology of polygenetic monazites constrained by in situ electron microprobe Th-U-total lead determination: implications for lead behaviour in monazite. *Geochimica et Cosmochimica Acta* 62, 2475-2497.
- Cocherie, A., Albarede, F., 2001. An improved U-Th-Pb age calculation for electron microprobe dating of monazite. *Geochimica et Cosmochimica Acta* 65, 4509-4522.
- Cocherie, A., Mezeme, E. B., Legendre, O., Fanning, C. M., Faure, M., Rossi, P., 2005. Electron-microprobe dating as a tool for determining the closure of Th-U-Pb systems in migmatitic monazites. *American Mineralogist* 90, 607-618.
- Crowley, J.L., Ghent, E.D., 1999. An electron microprobe study of the U-Th-Pb systematics of metamorphosed monazite: the role of Pb diffusion versus overgrowth and recrystallisation. *Chemical Geology* 157, 285-302.
- Deng, X.G., Chen, Z.G, Li, X.H., 2004. SHRIMP U-Pb zircon dating of the Darongshan-Shiwandashan. *Geological Review* 50, 426-432.
- Dickinson, W. R., Snyder, W. S., 1978. Plate tectonics of the Laramide orogeny. In: Matthews Ili, V. (ed), *Laramide folding associated with Basement Block faulting in the Western United States*. Geological Society of America Memoir 151, 355-366.
- Ding, X., Chen, P. R., Chen, W. F., Huang, H. Y., Zhou, X. M., 2005. LA-ICPMS zircon U-Pb age determination of the Weishan granite in Hunan: petrogenesis and significance. *Science in China (D)* 35, 606-616.
- Engebretson, D. C., Cox, A., Gordon, R. G., 1985. Relative motion between oceanic and continental plates in the Pacific basin, Geological Society of America, Special Paper 206, 1 – 55.
- English, J. M., Johnston, S. T., 2004. The Laramide orogeny: What were the driving forces? *International Geology Review* 46, 833-838.
- Escher, A., Beaumont, C., 1997. Formation, burial and exhumation of basement nappes at crustal scale: a geometric model based on the Western Swiss-Italian Alps. *Journal of Structural Geology* 19, 955-974.

- Faure, M., Sun, Y., Shu, L., Moni, P., Charvet, J., 1996. Extensional tectonics within a subduction-type orogen. The case study of the Wugongshan dome (Jiangxi Province, southeastern China). *Tectonophysics* 263, 77-106.
- Faure, M., Lin W., Shu L. S., Sun Y., Scharer U., 1999. Tectonics of the Dabieshan (eastern China) and possible exhumation mechanism of ultra high-pressure rocks. *Terra Nova* 11, 251-258.
- Faure, M. Lin, W., Monié, P., Meffre, S., 2008. Paleozoic collision between the North and South China blocks, Early Triassic tectonics and the problem of the ultrahigh-pressure metamorphism. *Comptes Rendus Geosciences* 340, 139-150.
- Faure, M., Shu, L.S., Wang, B., Charvet, J., Choulet, F., Monie, P., 2009. Intracontinental subduction: a possible mechanism for the Early Palaeozoic Orogen of SE China. *Terra Nova* 21, 360-368.
- Hacker, B. R., Wang, Q. C., 1995. Ar/Ar Geochronology of Ultrahigh-Pressure Metamorphism in Central China. *Tectonics* 14, 994-1006.
- Hand, M., Sandiford, M., 1999. Intraplate deformation in central Australia, the link between subsidence and fault reactivation. *Tectonophysics* 305, 121-140.
- Harrowfield, M. J., Wilson, C. J. L., 2005. Indosinian deformation of the Songpan Garze Fold Belt, northeast Tibetan Plateau. *Journal of Structural Geology* 27(1), 101-117.
- Hendrix, M. S., Graham, S. A., Carroll, A. R., Sobel, E. R., McKnight, C. L., Schulein, B. J., Wang, Z., 1992. Sedimentary record and climatic implications of recurrent deformation in the Tian Shan: Evidence from Mesozoic strata of the north Tarim, south Junggar, and Turpan basins, northwest China. *Geological Society of America Bulletin* 104, 53-79.
- Kusky, T.M., Ye, M., Wang, J.P., and Wang, L., 2010. Geological evolution of Longhushan World Geopark in relation to global tectonics, *Journal of Earth Science* 21, 1-18.
- Lepvrier, C., Maluski, H., Van Vuong, N., Roques, D., Axente, V., Rangin, C., 1997. Indosinian NW-trending shear zones within the Truong Son belt (Vietnam) ^{40}Ar - ^{39}Ar Triassic ages and Cretaceous to Cenozoic overprints. *Tectonophysics* 283, 105-127.
- Lepvrier, C., Maluski, H., Van Tich, V., Leyreloup, A., Truong Thi, P., Van Vuong, N., 2004. The Early Triassic Indosinian orogeny in Vietnam (Truong Son Belt and Kontum Massif); implications for the geodynamic evolution of Indochina. *Tectonophysics* 393, 87-118.
- Lepvrier, C., Van Vuong, N., Maluski, H., Truong Thi, P., Van Vu, T., 2008. Indosinian tectonics in Vietnam. *Comptes Rendus Geosciences* 340, 94-111.

- Li, H. Q., Wang D. H., Chen F. W., Mei Y.P., Cai H., 2008. Study on Chronology of the Chanziping and Daping gold deposit in Xuefeng Mountains, Hunan Province. *Acta Geologica Sinica* 82, 900-905 (in Chinese with English abstract).
- Li, Q.L., Li, X.H., Liu, Y., Tang, G.Q., Yang, J.H., Zhu, W.G., 2010. Precise U-Pb and Pb-Pb dating of Phanerozoic baddeleyite by SIMS with oxygen flooding technique. *Journal of Analytical Atomic Spectrometry* 25, 1107-1113.
- Li, X. H., 1999. U-Pb zircon ages of granites from the southern margin of the Yangtze Block: timing of Neoproterozoic Jinning Orogeny in SE China and implications for Rodinia Assembly. *Precambrian Research* 97, 43-57.
- Li, X. H., Li, Z. X., Li, W. X., Wang, Y. J., 2006. Initiation of the Indosinian Orogeny in South China: Evidence for a Permian magmatic arc on Hainan Island. *The Journal of Geology* 114, 341-353.
- Li, X. H., Liu Y., Li Q. L., Guo C. H., Chamberlain K. R., 2009a. Precise determination of Phanerozoic zircon Pb/Pb age by multicollector SIMS without external standardization. *Geochemistry Geophysics Geosystems* 10, Q04010, doi:10.1029/2009GC002400.
- Li, X. H., Li, W. X., Li, Z. X., Lo, C. H., Wang, J., Ye, M. F., Yang, Y. H., 2009b. Amalgamation between the Yangtze and Cathaysia Blocks in South China: Constraints from SHRIMP U-Pb zircon ages, geochemistry and Nd-Hf isotopes of the Shuangxiwu volcanic rocks. *Precambrian Research* 174, 117-128.
- Li, Z. X., Li, X. H., 2007. Formation of the 1300-km-wide intracontinental orogen and postorogenic magmatic province in Mesozoic South China: A flat-slab subduction model. *Geology* 35, 179-182.
- Li, Z. X., Li, X. H., Wartho, J. A., Clark, C., Li, W.-X., Zhang, C. L., Bao, C., 2010. Magmatic and metamorphic events during the early Paleozoic Wuyi-Yunkai orogeny, southeastern South China: New age constraints and pressure-temperature conditions. *Geological Society of America Bulletin* 122, 772-793.
- Lin, W., Wang, Q. C., Chen, K., 2008. Phanerozoic tectonics of south China block: New insights from the polyphase deformation in the Yunkai massif, *Tectonics* 27, TC6004, doi:10.1029/2007TC002207.
- Ludwig, K.R., 2001. Users manual for Isoplot/Ex rev. 2.49. Berkeley Geochronology Centre Special Publication. No. 1a, 56 pp.
- McQuarrie, N., 2004. Crustal scale geometry of the Zagros fold-thrust belt, Iran. *Journal of Structural Geology* 26, 519-535.

- Montel, J. M., Marignac, C., Barbey, P., Pichavant, M., 1992. Thermobarometry and granite genesis: the Hercynian low-P, high-T Velay anatectic dome (French Massif central). *Journal of Metamorphic Geology* 10, 1-15.
- Molnar, P., Tapponnier, P., 1975. Cenozoic Tectonics of Asia: Effects of a Continental Collision: Features of recent continental tectonics in Asia can be interpreted as results of the India-Eurasia collision. *Science* 189, 419-426.
- Passchier, C.W., Trouw, R.A.J., 2005. *Microtectonics*. 2nd edition. Springer, Berlin, pp. 27–66.
- Parrish, R., 1990. U-Pb dating of monazite and its application to geological problems. *Canadian Journal of Earth Sciences* 27, 1431-1450.
- Peng, P., Zhai, M.-G., Li, Q., Wu, F., Hou, Q., Li, Z., Li, T., Zhang, Y., 2011. Neoproterozoic (~900 Ma) Sariwon sills in North Korea: Geochronology, geochemistry and implications for the evolution of the south-eastern margin of the North China Craton. *Gondwana Research*, 20(1): 243-254.
- Pommier A., Cocherie, A., Legendre, O., 2002. EPMA Dating User's manual: Age calculation from electron probe microanalyser measurements of U-Th-Pb. BRGM, 9 pp.
- Qiu, Y. X., Zhang Y. C., Ma W. P., 1998. Tectonics and Geological Evolution of Xuefeng Intra-continental Orogen, South China. *Geological Journal of China Universities* 4, 432-443 (in Chinese with English abstract).
- Qiu, Y. X., Zhang Y. C., Ma W. P., 2000. *The Tectonic Nature and Evolution of Xuefeng Mountains: One Model of Formation and Evolution of Intra-continental Orogenic Belt*, Geological Publishing House, Beijing, 155pp,
- Raimondo, T., Collins, A. S., Hand, M., Walker-Hallam, A., Smithies, R. H., Evins, P. M., Howard, H. M. 2010. The anatomy of a deep intracontinental orogen. *Tectonics* 29, TC4024, 10.1029/2009tc002504.
- Roger, F., Jolivet, M., Malavieille, J., 2008. Tectonic evolution of the Triassic fold belts of Tibet. *Comptes Rendus Geosciences* 340, 180-189.
- Roger, F., Jolivet, M., Malavieille, J., 2010. The tectonic evolution of the Songpan-Garze (North Tibet) and adjacent areas from Proterozoic to Present: A synthesis. *Journal of Asian Earth Sciences* 39, 254-269.
- Roure, F., Choukroune, P., Berastegui, X., Munoz, J. A., Villien, A., Matheron, P., Bareyt, M., Seguret, M., Camara, P., Deramond, J., 1989. ECORS Deep seismic data and balanced cross sections: geometric constraints on the evolution of the Pyrenees. *Tectonics*, 8, 41–50.

- Sandiford, M., Hand, M., McLaren, S., 2001. Tectonic feedback, intraplate orogeny and the geochemical structure of the crust: a central Australian perspective. Geological Society, London, Special Publications 184, 195-218.
- Shu, L. S., Zhou, G. Q., Shi, Y. S., Yin, J., 1994. Study of the high-pressure metamorphic blueschist and its Late Proterozoic age in the Eastern Jiangnan Belt. Chinese Science Bulletin 39, 1200-1204.
- Sláma, J., Košler, J., Condon, D. J., Crowley, J. L., Gerdes, A., Hanchar, J. M., Horstwood M. S.A., Morris G. A., Nasdala L., Norberg N., Schaltegger U., Schoene B., Tubrett M. N., Whitehouse M. J., 2008. Plešovice zircon - A new natural reference material for U-Pb and Hf isotopic microanalysis. Chemical Geology 249, 1-35.
- Stacey, J.S., Kramers, J.D., 1975. Approximation of terrestrial lead isotope evolution by a two-stage model. Earth Planetary Science Letters 26, 207-221.
- Stipp, M., Stuitz, H., Heilbronner, R., Schmid, S. M., 2002. The eastern Tonale fault zone: a 'natural laboratory' for crystal plastic deformation of quartz over a temperature range from 250 to 700 °C. Journal of Structural Geology 24, 1861-1884.
- Suzuki, K., Adachi, M., 1991. Precambrian provenance and Silurian metamorphism of the Tsubonosawa paragneiss in the south Kitakami terrane, northeast Japan, revealed by the chemical th-u-total pb isochron ages of monazite, zircon and xenotime. Geochemical Journal 25, 357-376.
- Tapponnier, P., Molnar P., 1979. Active faulting and Cenozoic tectonics of the Tianshan, Mongolia, and Baykal regions. Journal of Geophysical Research 84, 3425-3459.
- Wallis, S., Tsujimori, T., Aoya, M., Kawakami, T., Terada, K., Suzuki, K., Hyodo, H., 2003. Cenozoic and Mesozoic metamorphism in the Longmenshan orogens: implications for geodynamic models of eastern Tibet. Geology 31, 745-748
- Wang, X.F., Metcalfe, I., Jian, P., He, L.Q., Wang, C.S., 2000. The Jinshajiang - Ailaoshan Suture Zone, China: tectonostratigraphy, age and evolution. Journal of Asian Earth Sciences 18, 675 - 690.
- Wang, J., Li, Z. X., 2003. History of Neoproterozoic rift basins in South China: implications for Rodinia break-up. Precambrian Research 122, 141-158.
- Wang, Y. J., Zhang, Y. H., Fan, W. M., Peng, T. P., 2005. Structural signatures and Ar-40/Ar-39 geochronology of the Indosinian Xuefengshan tectonic belt, South China Block. Journal of Structural Geology 27, 985-998.
- Wang, Y. J., Fan, W. M., Sun, M., Liang, X. Q., Zhang, Y. H., Peng, T. P., 2007a. Geochronological, geochemical and geothermal constraints on petrogenesis of

- the Indosinian peraluminous granites in the South China Block: A case study in the Hunan Province. *Lithos* 96, 475-502.
- Wang, Y. J., Fan, W. M., Zhao, G. C., Ji, S. C., Peng, T. P., 2007b. Zircon U-Pb geochronology of gneissic rocks in the Yunkai massif and its implications on the Caledonian event in the South China Block. *Gondwana Research* 12, 404-416.
- Xiao, W. J., He, H. Q., 2005. Early Mesozoic thrust tectonics of the northwest Zhejiang region (Southeast China). *Geological Society of America Bulletin* 117, 945-961.
- Xu, H. J., Ma, C. Q., Zhong, Y. F., She, Z. B., 2004. Zircon SHRIMP dating of Taojiang and Dashenshan granite: Lower limit on the timing of the amalgamation between Yangtze and Cathaysia blocks. Annual meeting of Petrology and Geodynamics, China.
- Yan, D. P., Zhou, M. F., Song, H. L., Wang, X. W., Malpas, J., 2003. Origin and tectonic significance of a Mesozoic multi-layer over-thrust system within the Yangtze Block (South China). *Tectonophysics* 361, 239-254.
- Zhou, X. M. (Eds), 2007. *Genesis of Late Mesozoic Granites in Nanling Region and Geodynamic Evolution of Lithosphere*. Science Press, Beijing, 691pp.
- Zhu, X.K., O'Nions, R.K., 1999. Zonation of monazite in metamorphic rocks and its implications for high temperature thermochronology: a case study from the Lewisian terrain. *Earth and Planetary Science Letters* 171, 209-220.

Phanerozoic tectonothermal events of the Xuefengshan Belt, central South China: implications from U-Pb age and Lu-Hf determinations of granites

Yang Chu^{1,2,3}, Wei Lin^{1,*}, Michel Faure^{1,2}, Qingchen Wang¹, Wenbin Ji^{1,3}

1. State Key Laboratory of Lithospheric Evolution, Institute of Geology and Geophysics, Chinese Academy of Sciences, Beijing 100029, China
2. Institut des Sciences de la Terre d'Orléans, Campus Géosciences, Université d'Orléans, 1A, Rue de la Férellerie, 45071 Orléans Cedex 2, France
3. Graduate University of Chinese Academy of Sciences, Beijing 100049, China

*Corresponding author. Email address: linwei@mail.iggcas.ac.cn (Wei Lin).

Institute of Geology and Geophysics, Chinese Academy of Sciences

19 Beitucheng western Road, Chaoyang District

100029 Beijing, China P. R.

Tel: +861082998546 Fax: +861062010846

Abstract:

The Xuefengshan Belt, characterized by large-scale fold and thrust structures and widespread granites, is a key area to decipher the tectonic evolution of the South China block. Two episodes of magmatism are recorded by Early Paleozoic and Early Mesozoic granites of this belt. In this paper, we carried out precise SIMS zircon U-Pb dating and *in situ* Lu-Hf isotopes measurements on these granitic plutons. Our study indicates that the Early Paleozoic and the Early Mesozoic granites are late-orogenic products of the Early Paleozoic orogen and the Middle Triassic Xuefengshan orogen, respectively. In the Xuefengshan Belt, the Early Paleozoic event is poorly registered except Silurian-Early Devonian granites, implying a compressional regime localized in the Wuyi-Baiyun-Yunkai belt but a widespread, subsequent extensional event in central and eastern South China. On the other hand, Triassic granites are formed in an intracontinental environment with weakly to strongly peraluminous signatures. U-Pb ages on zircons of granites presented here, associated with a summary of newly acquired data in the same region, suggest that the emplacement of anatectic granites occurred around 225-215 Ma, not in a rather wide range of ca. 245-200 Ma. *In situ* zircon $\varepsilon_{\text{Hf}}(t)$ values, from -0.7 to -16.4 with a peak at ca. -5.5, indicate an unlikely

existence of a subducted slab. Combining our data with recent studies, we infer that these Early Mesozoic granites can be the late-orogenic products of the intracontinental Xuefengshan orogen, most likely manifesting the far field effect by the subduction of the Paleo-Pacific ocean plate at the southeastern margin of the South China block.

Key words: Phanerozoic tectonothermal events, the Xuefengshan Belt, U-Pb zircon age, Lu-Hf isotopes, South China

1. Introduction

Similar to remarkable shortening and thickening of continental crust, crustal melting is a widespread and concomitant phenomenon in many orogenic belts, such as Himalaya, Qinling-Dabie, and Variscan belts (Harris and Massey, 1994; Faure et al., 2003; Brown, 2005; Chung et al., 2005; Faure et al., 2008). This feature represents the thermal relaxation during late-, or post-collisional removal or unthickening process of the uplifted mountain belts.

In South China, granites provide a window to investigate the tectonic evolution. It has been well accepted that polyphase tectonothermal events occurred in the Phanerozoic, namely in Early Paleozoic, Early Mesozoic and Late Mesozoic, respectively (Chen, 1999; Zhou and Li, 2000; Yan et al., 2003; Wang et al., 2005; Zhou et al., 2006; Li and Li, 2007; Faure et al., 2009; Li et al., 2010b). Contemporaneous with considerable granitic intrusions, coeval volcanism and syn-tectonic terrigenous sedimentary basins, the Yanshannian event is systematically studied in multidisciplinary approaches, and interpreted as an extensional tectonics in response to the SE-directed subduction of the Pacific Plate (Faure et al., 1996; Lin et al., 2000; Shu et al., 2009; Zhou et al., 2006). However, the Early Paleozoic and the Early Mesozoic events remain poorly understood in spite of their recognition several decades ago (Huang, 1960, 1978). Recent studies suggest that these two orogens are both intracontinental (Wang et al., 2005; Faure et al., 2009; Charvet et al., 2010; Li et al., 2010b; Chu et al., 2011a, 2011b). The Early Paleozoic orogenic belt in South China (Fig. 1), demonstrated by a regional Devonian unconformity, Silurian- Early Devonian magmatism and high-grade metamorphism, is located in the southeastern part of the South China block from the Wuyi in the northeast, the Baiyun in the middle, to the Yunkai in the southwest (Wang et al., 2007b; Wan et al., 2010; Yang et al., 2010; Li et al., 2010b; Li et al., 2011). Now it is accepted that the Early Paleozoic belt was an intracontinental orogen in response to the closure of the Nanhua rift (Faure et al., 2009; Charvet et al., 2010; Li et al., 2010b).

Except the Sichuan Basin, the entire South China block was involved the Early Mesozoic event (Fig. 1), where Early Paleozoic structures underwent intensive overprinting. In the central part, another intracontinental orogen, that is, the Xuefengshan Belt, was identified to be of Triassic age by detailed structural analysis (Chu et al., 2011a, 2011b). Previous studies suggest that Early Mesozoic igneous rocks are widespread in the South China block, especially in Hunan province, as syn- or late-orogenic products (BGMHRN, 1988; Xu et al., 2004; Ding et al., 2005; Xu et al., 2005; Chen et al., 2006, 2007a, 2007b; Li and Li, 2007; Wang et al., 2007a; Li et al., 2008 and reference therein). However, the timing of the magmatism, lasting from 245 Ma to 200 Ma, is still in variance, and their petrogenesis and geodynamic background are also in debate.

In this work, we report SIMS U-Pb zircon ages and *in situ* Lu-Hf isotopic data of the Early Paleozoic and Early Mesozoic granites from the Xuefengshan Belt, Hunan Province, in order to precisely constrain the timing of magmatic activities. We demonstrate that these granites represent orogenic products related to the Xuefengshan Belt. A possible interpretation of their potential source, and tectonic implications of the two tectonothermal events with respect to the South China block are also discussed.

2. Geological setting

From Neoproterozoic to Cenozoic, over 10-km-thick sedimentation covers mostly the South China block. Nevertheless, unexposed Archean to Paleoproterozoic crustal information is added by locally distributed basement rocks and chronological data of detrital zircons in the Yangtze block and the Cathaysia block (Qiu et al., 2000; Zhang et al., 2006; Yu et al., 2010).

During Neoproterozoic, the South China Block was finally amalgamated by the Yangtze Block and the Cathaysia Block, separated by the Jinning or Sibao orogen (Fig. 1, cf. Li et al., 2009a), which has been proved by abundant structural, geochemical and geochronological data (Shu et al., 1994; Charvet et al., 1996; Li, 1999; Li et al., 2009 and references therein). Since then, the South China Block experienced a relatively peaceful period of ~400 Ma until the Early Paleozoic intracontinental tectonics, or named as Wuyi-Yunkai orogen, occurred with ductile shearing, regional unconformity and high-grade metamorphism (Huang et al., 1980; BGMHRN, 1984; Ren, 1991; Wan et al., 2007; Faure et al., 2009; Charvet et al., 2010; Li et al., 2010). At the end of this orogeny, widespread Silurian-Devonian plutons intruded in pre-Devonian syntectonic metamorphic rocks. In the Xuefengshan area (Fig. 2), in spite of several granites, the Early Paleozoic event is not as pervasive as in

the Wuyi-Baiyun-Yunkai area, as its distance from the Wuyi-Yunkai orogen is over 500 km. Conversely, the NE-SW trending structures are dominated by the Early Mesozoic event, which is called the Xuefengshan orogeny. This Middle Triassic orogeny is revealed by a regional unconformity between the Late Triassic-Early Jurassic terrigenous rocks and pre-Middle Triassic deformed rocks (BGMRGX, 1985; BGMRHN, 1988).

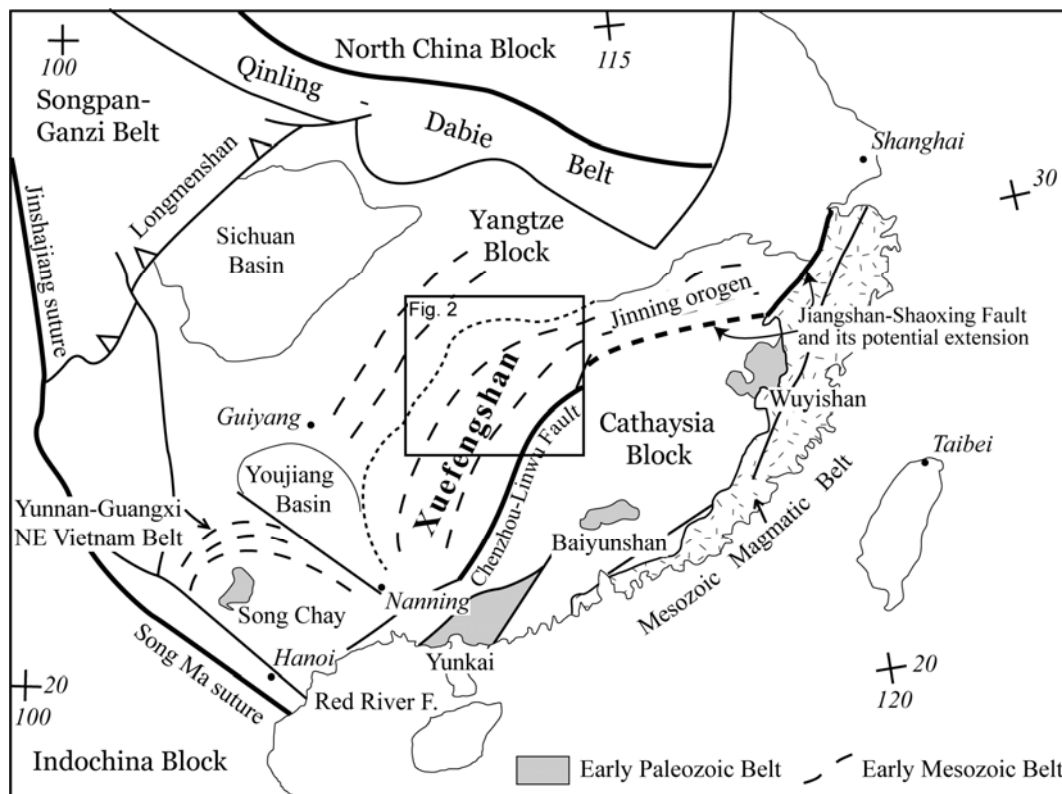


Fig. 1 Tectonic framework of the South China block (Modified after Faure et al., 2009).

The Early Mesozoic event in South China is previously called the Indosinian Orogeny, but in fact this name is originally recorded by unconformities between pre-Norian and pre-Rhaetian during Triassic in Vietnam (Deprat, 1914; Fromagat, 1932). Therefore, it is better to separate this one from the simultaneous orogeny in South China with different names to avoid confusion. In central South China, the Middle Triassic intracontinental Xuefengshan Belt is characterized by well developed folds, thrust faults and pervasive cleavages in the sedimentary cover, and ductile deformation with a NE-SW striking foliation and a NW-SE trending lineation in the decollement layer and basement rocks. Late Triassic granites intruded into the folded strata as late-orogenic products (Qiu et al., 2000; Wang et al., 2007; Chu et al., 2011a, 2011b). To the east of the Chenzhou-Linwu fault (Fig. 2), this region is dominated by

WNW-ESE trending structures of Early Paleozoic, whereas to the west, Early Mesozoic structures in the NE-SW direction is the most notable phenomenon. Hence, this fault acts as an important boundary fault in central South China, and is also postulated to be the southwest extension of the Neoproterozoic suture zone (Wang et al., 2003, 2007b).

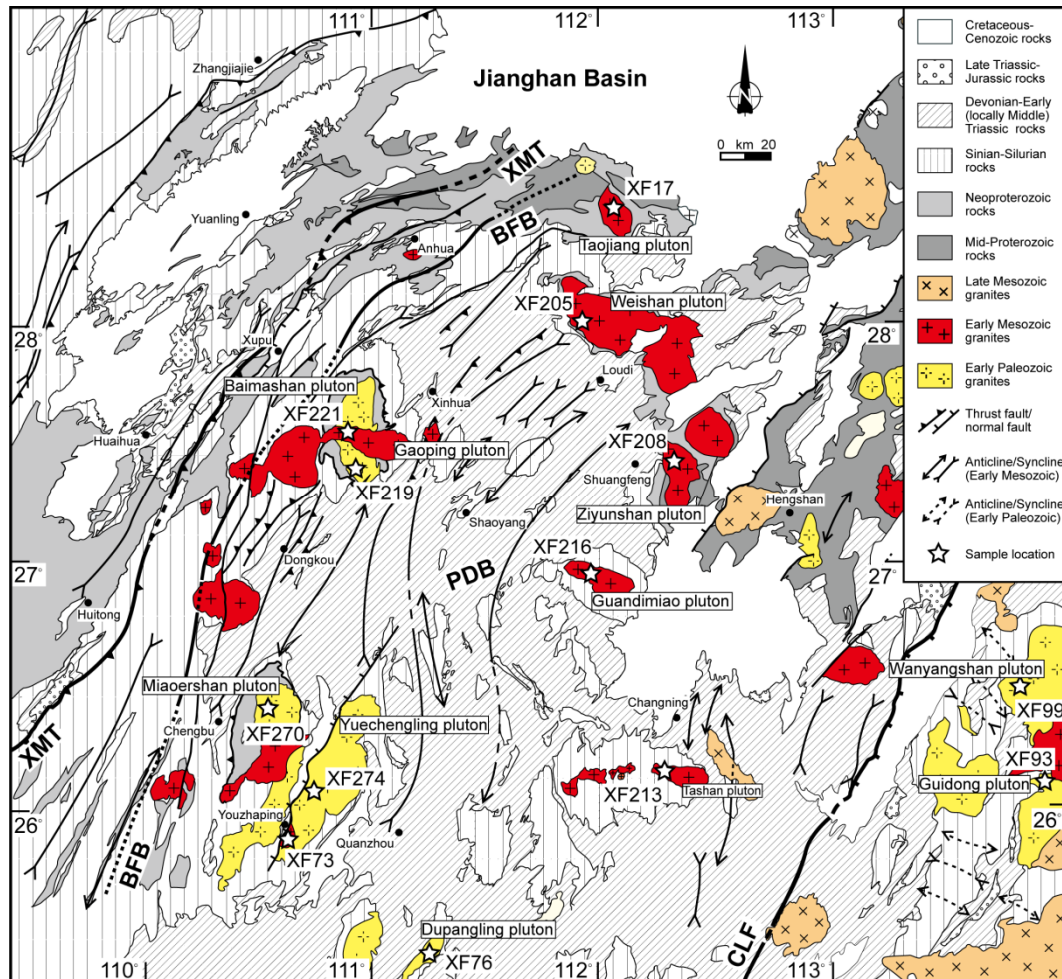


Fig. 2 Geologic map of the Xuefengshan Belt with sample locations of granites (Modified after BGRMGX, 1985; BGRMHN, 1988).

3. Petrography

The Early Paleozoic granites are mostly distributed in the southern and eastern parts of the Xuefengshan Belt with a total area over 3000 km². The selected samples (XF76, XF93, XF99, XF219, XF270, and XF274) are dominantly biotite monzogranite, biotite granite and hornblende-bearing granite with intermediate to coarse-grained texture. They commonly consist of biotite (~10%), K-feldspar (~25%), plagioclase (~35%) and quartz (~30%), with a minor amount of hornblende or muscovite and other accessory minerals.

Early Mesozoic granites make up the largest portion, over 5000 km² in area (BGMРН, 1988). Similar to Early Paleozoic granites, these Triassic granites (XF17, XF73, XF205, XF208, XF213, XF216 and XF221) are comprised of biotite monzogranite and biotite granite, whereas two types are divided by the presence of hornblende or muscovite (Fig. 3a-b). The mineral assemblage is biotite (~8%), plagioclase (~40%), K-feldspar (~20%), and quartz (30%), with minor hornblende (~2%) or muscovite (~2%). A good consistence is shown by that the A/CNK index of the hornblende bearing granites (XF17, XF216 and XF221) are 1.0 to 1.1 as a aluminous type, whereas the index of the muscovite-bearing granites (XF73, XF205, XF208 and XF213) are > 1.1, indicating peraluminous magmatic type (Wang et al., 2007a).

Additionally, the dominant structures are different. At the boundary of Early Paleozoic granites (e.g. Baimashan pluton), due to the Early Mesozoic event, rocks are sheared with a deformed zone of several hundred meters wide. In this zone, quartz are strongly sheared into recrystallized grains around plagioclases, which also show undulose or flame-shape extinction (Fig. 3c). In contrast, a magmatic structure, such as mymekite, is dominant in Early Mesozoic granites, where the deformation structure is rare or absent (Fig. 3d).

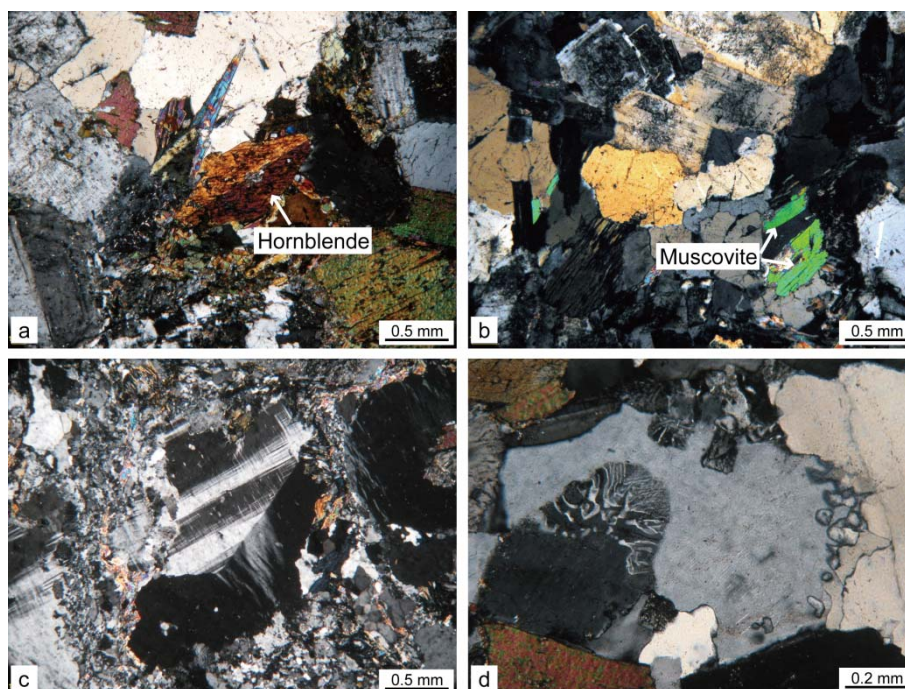


Fig. 3 Microscopic photos of granites. Two types of Triassic granites: (a): Hornblende-bearing granite. (b): Muscovite-bearing granite. Different deformation patterns in (c) the Paleozoic granite with quartz dynamic recrystallization and twins in plagioclases, and (d) the Mesozoic granite with no obvious ductile deformation but mymekites as an indicator of pre-solidus deformation.

Table 1 Summary of sample localities of Early Paleozoic and Early Mesozoic granites in the Xuefengshan Belt.

Pluton	No.	Lithology	GPS	Age	Reference
Early Mesozoic plutons					
Taojiang	XF17	Hornblende biotite granite	N28°28.624', E112°04.268'	220±2	This study
Yuechengling-Youzhaping	XF73	Biotite granite	N25°56.121', E110°38.082'	219±2	This study
Tashan	XF213	Biotite granite	N26°11.709', E112°16.528'	224±2	This study
Guandimiao	XF216	Hornblend monzogranite	N26°57.392', E112°08.094'	225±2	This study
Baimashan (Gaoping)	XF221	Hornblend granite	N27°35.756', E110°58.355'	217±2	This study
Weishan	XF205	Biotite monzogranite	N28°00.255', E112°00.455'	222±3	Chu et al., 2011b
Ziyunshan	XF208	Biotite monzogranite	N27°27.802', E112°22.327'	225±2	Chu et al., 2011b
Early Paleozoic plutons					
Dupangling	XF76	Biotite monzogranite	N25°20.102', E111°05.427'	428±4	This study
Guidong	XF93	Hornblend granite	N26°05.496', E113°58.364'	438±3	This study
Wanyangshan	XF99	Two-mica granite	N26°27.393', E113°49.097'	437±4	This study
Baimashan (Main)	XF219	Hornblend granite	N27°27.948', E110°57.279'	411±4	This study
Miaoershan	XF270	Biotite granite	N26°27.690', E110°30.608'	412±4	This study
Yuechengling (Main)	XF274	Biotite granite	N26°10.109', E110°43.674'	424±3	This study

4. Analytical procedures

4.1. Zircon U-Pb dating

Zircons were separated from samples using standard density and magnetic separation techniques. Zircon grains, together with standard Plešovice zircon and Qinghu were mounted in epoxy mounts which were then polished to section the crystals in half for analysis. All zircons were photographed in transmitted and reflected light, and the cathodoluminescence (CL) image to reveal their internal structures, and the mount was vacuum-coated with high-purity gold for SIMS analyses.

The U-Pb determination was conducted using a Cameca IMS 1280 large-radius SIMS at the Institute of Geology and Geophysics, Chinese Academy of Sciences (CAS) in Beijing. U-Th-Pb ratios and absolute abundances were determined relative to the standard zircon Plešovice (Sláma et al., 2008). Analytical procedures are the same as those described by Li et al. (2009b). The ellipsoidal spot is about 20×30 μm in size. Positive secondary ions were extracted with a 10 kV potential. A long-term uncertainty of 1.5% (1 RSD) for $^{206}\text{Pb}/^{238}\text{U}$ measurements of the standard zircons was propagated to the unknowns (Li et al., 2010a), despite that the measured $^{206}\text{Pb}/^{238}\text{U}$

error in a specific session is generally around 1% (1 RSD) or less. Correction of common lead was made by measuring ^{204}Pb . An average Pb of present-day crustal composition (Stacey and Kramers, 1975) is used for the common Pb assuming that it is largely due to surface contamination introduced during sample preparation. Uncertainties on individual analyses in data tables are reported at a 1σ level; mean ages for pooled U/Pb (and Pb/Pb) analyses are quoted with 95% confidence interval. Data reduction was carried out using the Isoplot program (Ludwig, 2001).

4.2. Zircon Lu-Hf isotopes

Zircon Lu-Hf isotopic analysis was carried out *in situ* on a Neptune multi-collector ICP-MS equipped with a Geolas-193 laser ablation system at the Institute of Geology and Geophysics, Chinese Academy of Sciences. Detailed analytical procedures are given in Wu et al. (2006). Previously analyzed zircon grains for U-Pb isotopes were chosen for Lu-Hf isotopic analyses. The beam diameter is either 44 or 60 μm , with a laser repetition rate of 10 Hz at 100 mJ. During the analytical period, the weighted mean $^{176}\text{Hf}/^{177}\text{Hf}$ ratios of the zircon standards GJ-1 (0.281999 ± 6 , 2σ , $n=34$) and MUD (0.282503 ± 7 , 2σ , $n=34$) are in good agreement with reported values (Woodhead and Hergt, 2005; Morel et al., 2008).

5. Results

Sample locations are shown in the Fig.1. The analytical data of U-Pb data are listed in table 2, and concordia ages are presented in Fig. 5-6. Lu-Hf isotopic results are listed in table 3, and diagrams of $\epsilon_{\text{Hf}}(t)$ and Hf crustal model ages are shown in Fig. 7.

5.1. SIMS zircon U-Pb age

5.1.1 Samples of Early Paleozoic granites

Six sample were collected from Early Paleozoic granites of the Xuefengshan Belt with detailed GPS location in table 1. Zircons separated from these samples are mostly euhedral to subhedral, transparent and colorless, ranging from 50 μm to 250 μm in length, and have length to width ratio between 1:1 to 4:1. Concentric zoning is common in most crystals in cathodoluminescence (CL) image (Fig. 4). The Th/U ratios of all samples are between 0.1 and 1.6, indicating a magmatic origin, except a few older zircons with low Th/U ratios.

5.1.1.1. XF76

Sample XF76 is a monzonite from the Dupangling pluton, south of the study area. Sixteen spots on these zircons have relatively low U (210-564 ppm) and Th (45-283 ppm) contents, with Th/U ratios from 0.128 to 0.652, except one zircon of 832.5 Ma age. A concordia age at 428 ± 4 is calculated as the emplacement time without 3 inherited zircons of 926 Ma, 833 Ma and 822 Ma (Fig. 5a).

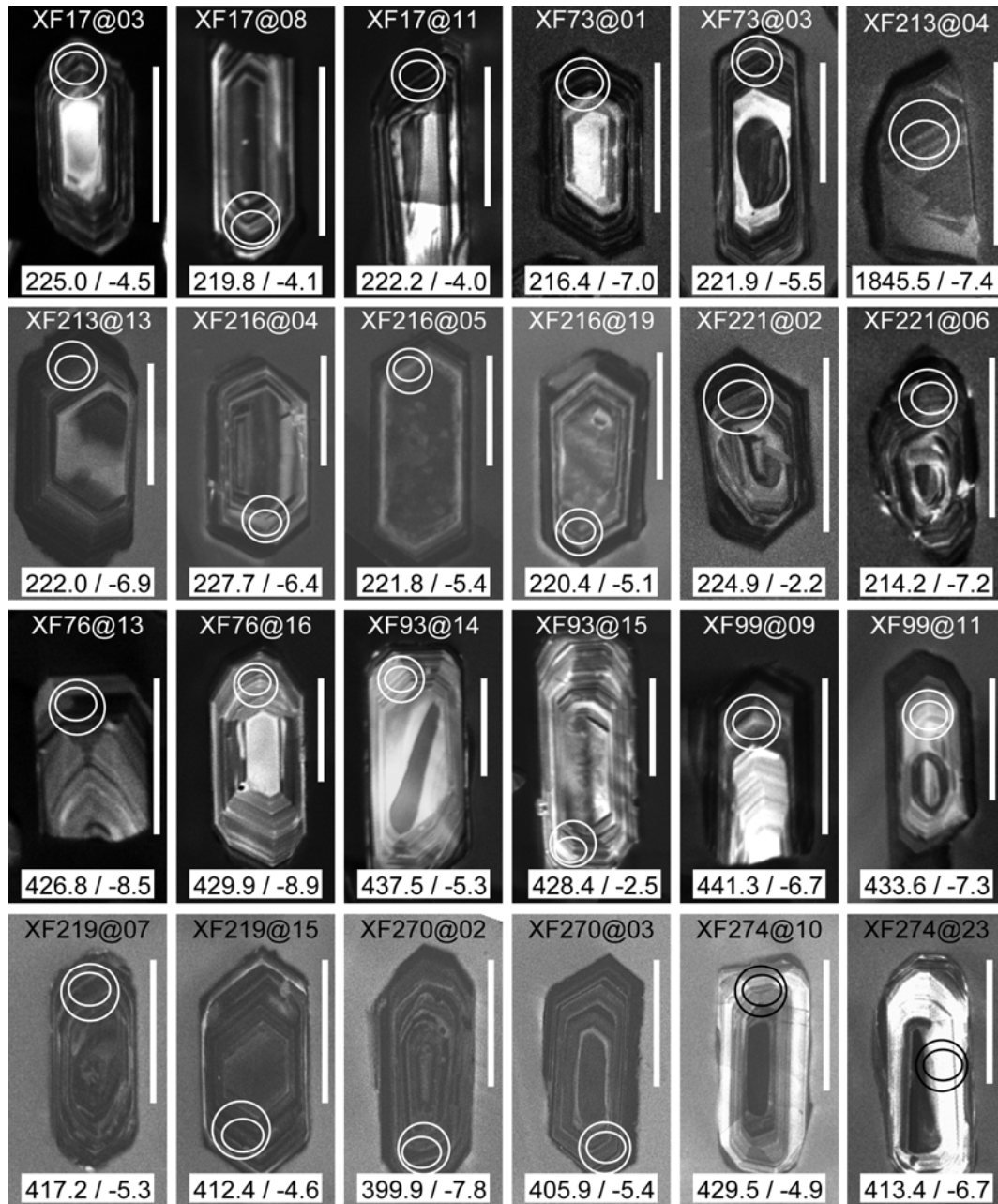


Fig. 4 Cathodoluminescence (CL) images of representative zircons from collected granite samples. Small ellipses are locations of SIMS U-Pb analysis spots and circles indicate the locations of LA-MC-ICPMS Hf analyses. Age and $\epsilon_{\text{Hf}}(t)$ data are listed under individual zircons with ages ahead. The scale bar is 50 μm .

5.1.1.2. XF93

Sample XF93 is collected from the Guidong pluton. Eighteen analyses were performed on magmatic rims. The U concentrations ranges from 272 to 673 ppm, Th from 88 to 235 ppm, and Th/U ratios from 0.286 to 0.503. A concordia age of 438 ± 3 Ma is given (Fig. 5b), representing the crystallization time of the pluton. This age is a little older than the zircon age (426 ± 2 Ma and 427 ± 2 Ma) obtained by Li (1991) and Li (1994).

5.1.1.3. XF99

Thirteen analyses on 13 zircons were carried on sample XF99 from the Wanyangshan pluton, with 122 to 812 ppm of U, 49 to 297 ppm of Th, and 0.146 to 0.907 of Th/U ratios. These zircons yield a concordia age of 437 ± 4 Ma as the crystallization age of the pluton (Fig. 5c). This age is consistent in error with the previous age of 434 ± 1 Ma (Li, 1991).

5.1.1.4. XF219

Zircons from sample XF219 of the Baimashan pluton give the U concentrations from 318 to 2086 ppm, Th from 191 to 1271 ppm, and Th/U ratios from 0.327 to 0.910. Fourteen analyses yield a concordia age of 411 ± 4 Ma as the crystallization age (Fig. 5d).

5.1.1.5. XF270

Sample XF270 is collected from the Miaoershan pluton. Fourteen analyses of 14 zircons were obtained, with moderate U (480-1827 ppm) and Th (160-1223 ppm) concentrations. The Th/U ratios vary from 0.288 to 0.692. All analyses yield a concordia age of 412 ± 4 Ma (Fig. 5e), which is interpreted as the crystallization age.

5.1.1.6. XF274

Sample XF274 is collected from the Yuechengling pluton. Twenty-three analyses of 23 zircons were obtained. The U, Th, and Th/U ratios vary from 116 to 2453, 139 to 951 and 0.230 to 1.263, respectively. A concordia age of 424 ± 3 Ma is calculated and interpreted as the crystallization age of the pluton (Fig. 5f).

5.1.2 Samples of Early Mesozoic granites

Five samples were collected from Early Mesozoic plutons and dated by SIMS U-Pb methods. Most zircons are euhedral to subhedral, transparent and colorless with prismatic shapes and concentric zoning indicating a magmatic origin. Sample XF213

of the Tashan pluton is an exception with a large portion of inherited zircons, similar to the results of the Yangmingshan pluton to the east of this pluton (Wang et al., 2007b).

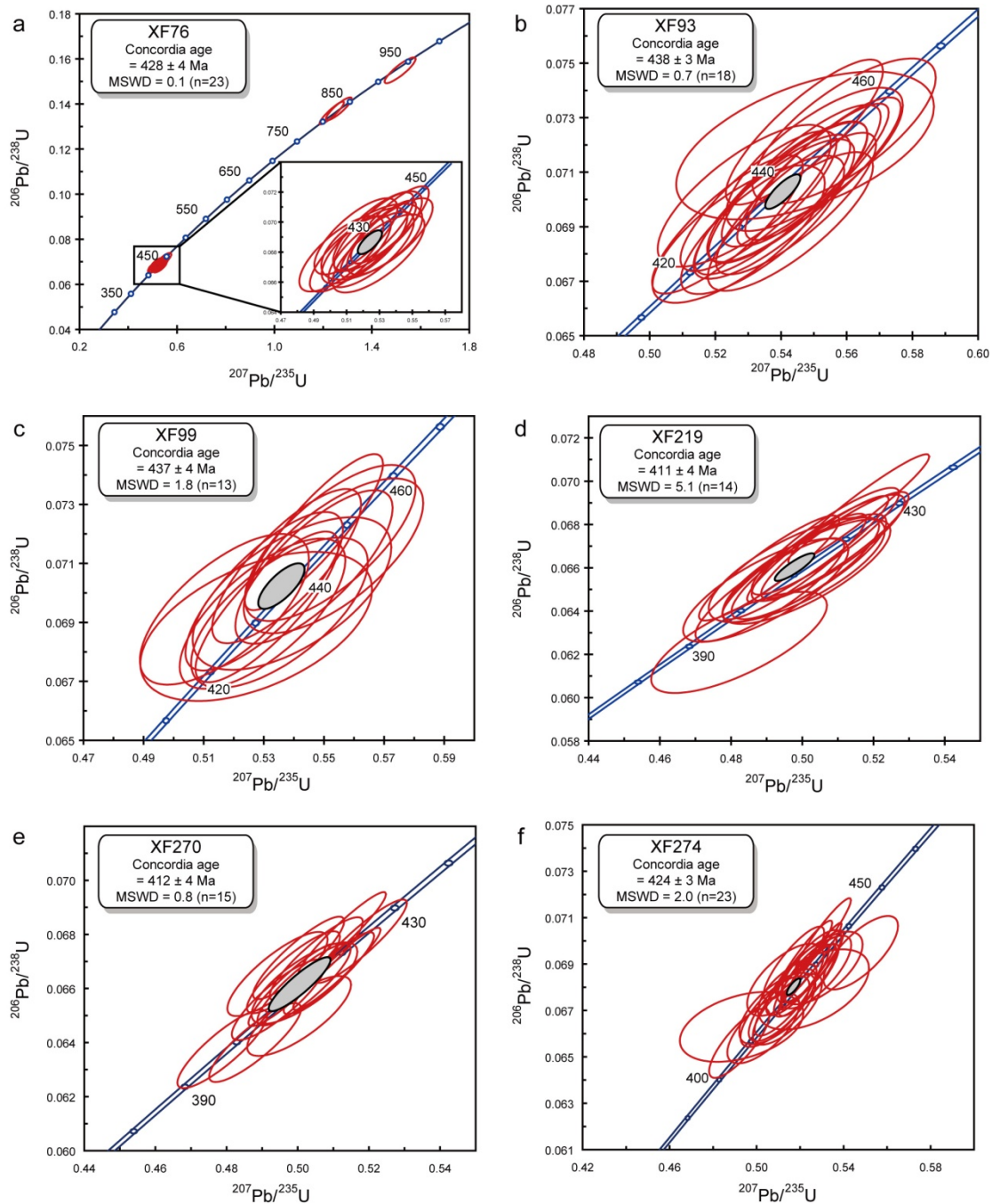


Fig. 5 SIMS U-Pb concordia diagrams of Early Paleozoic granite samples.

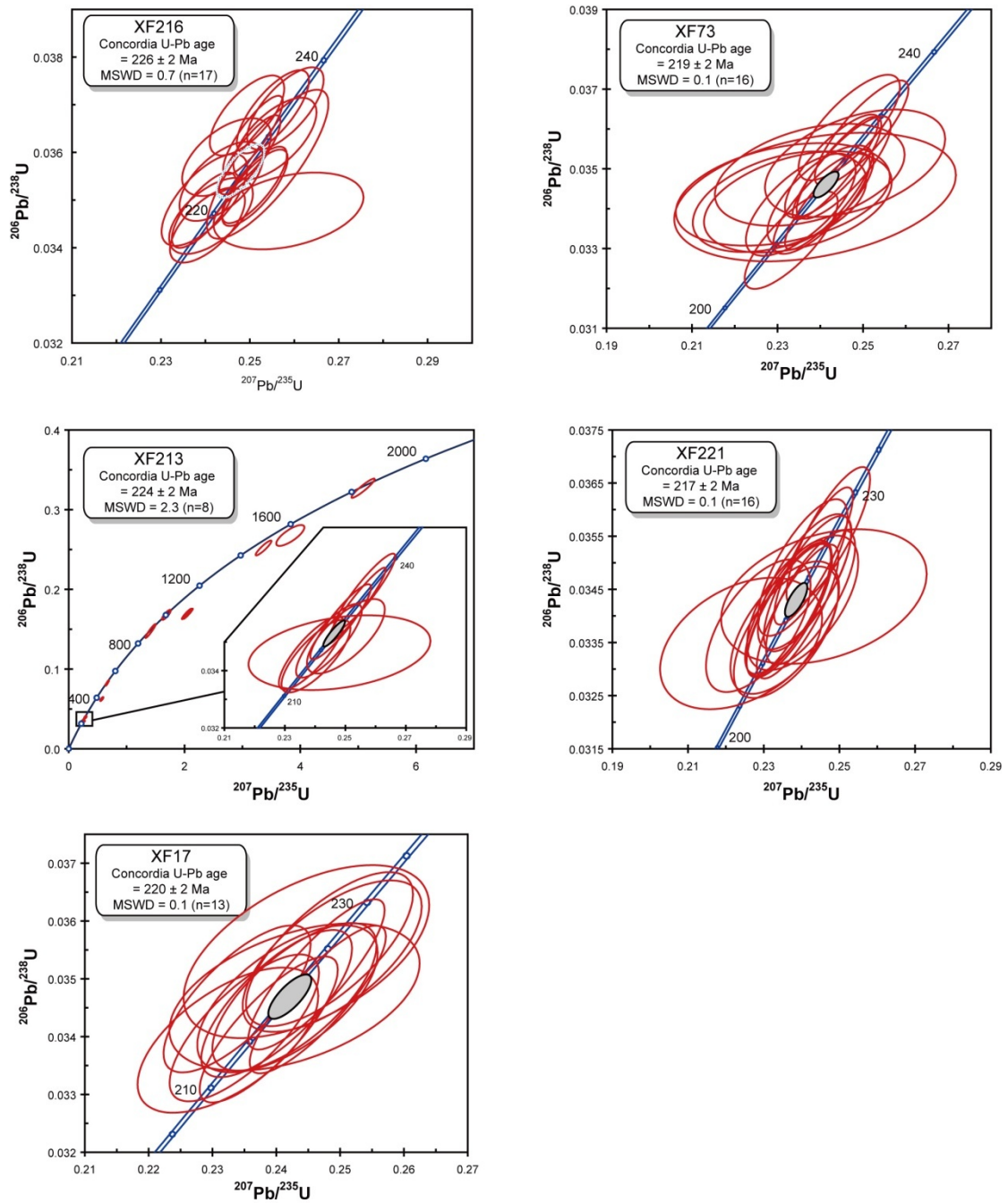


Fig. 6 SIMS U-Pb concordia diagrams of Early Mesozoic granite samples.

5.1.2.1 XF17

Sample XF17 is a biotite granite collected from Taojiang pluton. Thirteen analyses of thirteen zircons were obtained. The U concentrations ranges from 238 to 1520 ppm, Th from 131 to 871 ppm, and Th/U ratios from 0.277 to 0.710. All analyses have a concordia age of 220 ± 2 Ma (Fig. 6a), which is interpreted as the emplacement age of the granitic pluton.

5.1.2.2. XF73

Sample XF73 is a monzonitic granite collected from Yuechengling complex pluton. Sixteen analyses of sixteen zircons were obtained. These zircons have intermediate U (162-2486 ppm) and Th (154-1416 ppm) contents, with Th/U ratios from 0.221 to 1.575. A concordia age of 219 ± 2 Ma is given (Fig. 6b), representing the crystallization time of the pluton.

5.1.2.3. XF213

Sample XF213 is a biotite granite collected from Tashan pluton. Some of them shows inherited core and variable-sized concentric zoning, whereas others are magmatic without cores. Seventeen analyses of 17 zircons have variable U contents of 47 to 3964 ppm, low Th of 23 to 373 ppm; Th/U ratios ranges from 0.009 to 1.191. Eight out of 17 analyses yield a coherent age cluster with a concordia age of 224 ± 4 Ma, which is taken as the crystallization age of the granite (Fig. 6c). The remaining 9 analyses are plotted along the concordia curve and give variable apparent ages between 251 and 1823 Ma, including some less concordant ages like 1002, 1448 and 1528 Ma. These zircons are interpreted as inherited ones from the magma source.

5.1.2.4. XF216

Sample XF216 is collected from a amphibole-bearing granite in the Guandimiao pluton. Nineteen analyses of 19 zircons, with 280 to 4484 ppm of U, 189 to 4577 ppm of Th, and 0.386 to 1.021 of Th/U ratios, yield a concordia age of 225 ± 2 Ma, except XF216@9 with an abnormal young age (Fig. 6d), representing the crystallization age for this sample.

5.1.2.5. XF221

Sample XF221 is a monzonitic granite collected from the Baimashan (Gaoping) complex pluton. Sixteen analyses of sixteen zircons were obtained with 191 to 1559 ppm of U, 87 to 713 ppm of Th, and 0.263 to 0.746 of Th/U ratios, yielding a concordia age of 217 ± 2 Ma (Fig. 6e). This age is consistent with abovementioned ages and is treated as the emplacement age similar to the age of Li and Li (2007).

5.2. Zircon Lu-Hf isotopes

Most of the Lu-Hf isotope analyses were performed on spot within the same internal structure domains that were analyzed for U/Pb isotopic compositions. Except abovementioned samples, XF205 of the Weishan pluton and XF208 of the Ziyunshan pluton (Table 1) were analyzed for the Lu-Hf composition. The concordia ages of the plutons obtained from zircons of the same sample were used for calculating their

initial Hf isotopic ratios and the crustal model ages. 113 analyses were performed on 7 samples from Early Mesozoic granites, and 148 analyses were performed on 7 samples from Early Mesozoic granites, including XF205 and XF208, which were dated by Chu et al. (2011b). These results are presented in the Table 3. Diagram of $\epsilon_{\text{Hf}}(t)$ values is shown in Fig. 7.

5.2.1. Samples from Early Paleozoic granites

5.2.1.1. XF76

Seventeen zircons were chosen to perform Hf analyses. In the zircons of Early Paleozoic ages, the calculated $\epsilon_{\text{Hf}}(t)$ values range from -8.9 to -6.1, and their T_{DM}^{C} ages vary from 1807 to 1979 Ma. Additionally, in three inherited zircons, a positive $\epsilon_{\text{Hf}}(t)$ value (+5.6) is obtained with a T_{DM}^{C} age at 1475 Ma. The other two zircons give $\epsilon_{\text{Hf}}(t)$ values of -3.0 and -5.4, and T_{DM}^{C} ages of 1914 and 2050 Ma, respectively.

5.2.1.2. XF93

Twenty-two analyses of 22 zircons show that the calculated $\epsilon_{\text{Hf}}(t)$ values range from -7.5 to -2.5, and their T_{DM}^{C} ages are between 1583 to 1903 Ma.

5.2.1.3. XF99

Seventeen zircons were chosen to perform Hf analyses. The calculated $\epsilon_{\text{Hf}}(t)$ values range from -11.0 to -2.2, and their T_{DM}^{C} ages vary from 1720 to 2118 Ma. One inherited zircon of 939 Ma has a $\epsilon_{\text{Hf}}(t)$ value of -8.8 and a T_{DM}^{C} age of 2372 Ma.

5.2.1.4. XF219

Eighteen zircons were chosen to perform Hf analyses, with calculated $\epsilon_{\text{Hf}}(t)$ values from -7.0 to -2.9, and their T_{DM}^{C} ages from 1590 to 1846 Ma.

5.2.1.5. XF270

Nineteen analyses of 19 zircons were obtained. The calculated $\epsilon_{\text{Hf}}(t)$ values range from -7.8 to -2.2, and their T_{DM}^{C} ages vary from 1546 to 1900 Ma.

5.2.1.6. XF274

A total of twenty zircons were chosen to perform Hf analyses. The calculated $\epsilon_{\text{Hf}}(t)$ values vary from -6.7 to -1.8, with their T_{DM}^{C} ages from 1531 to 1843 Ma. Only one slightly positive $\epsilon_{\text{Hf}}(t)$ value of +0.2 is obtained, with a T_{DM}^{C} age at 1407 Ma.

5.2.2. Samples from Early Mesozoic granites

5.2.2.1. XF17

For the XF17 of the Taojiang pluton, cores of zircons were not selected. Eighteen zircons were analyzed for the Hf isotopes, yielding relatively narrow $\varepsilon_{\text{Hf}}(t)$ value from -5.0 to -2.1. Their T_{DM}^{C} ages range from 1386 to 1572 Ma.

5.2.2.2. XF73

Nineteen zircons were chosen from the Yuchengling (Youzhaping) pluton to perform Hf analyses. The calculated $\varepsilon_{\text{Hf}}(t)$ values range from -10.4 to -3.1, and their T_{DM}^{C} ages vary from 1451 to 1912 Ma.

5.2.2.3. XF205

Eighteen zircons were analyzed for the quartz diorite sample XF205. Their $\varepsilon_{\text{Hf}}(t)$ values are mainly negative from -6.6 to -3.1. These zircons show T_{DM}^{C} ages from 1452 to 1674 Ma.

5.2.2.4. XF208

A total of 17 analyses on seventeen zircons from sample XF208 give a $\varepsilon_{\text{Hf}}(t)$ range between -6.3 to -2.6. The T_{DM}^{C} ages of these zircons are from 1427 to 1662 Ma.

5.2.2.5. XF213

The sample XF213 from the Tashan pluton has a large portion of inherited zircons. In these analytical spots of inherited zircons, the $\varepsilon_{\text{Hf}}(t)$ value ranges from -10.8 to -2.2, with one positive value of +5.5. The analyses of Triassic magmatic zircons show a wide range of $\varepsilon_{\text{Hf}}(t)$ value from -16.4 to -0.7. Both types of zircons yield T_{DM}^{C} ages from 1444 to 2991 Ma.

5.2.2.6. XF216

Twenty-two zircon grains from the sample XF216 of the Guandimiao pluton were analyzed and give $\varepsilon_{\text{Hf}}(t)$ values from -7.3 to -2.2. These zircons show a relatively narrow range of T_{DM}^{C} age between 1395 to 1718 Ma.

5.2.2.7. XF221

Twenty analyses on zircons from the Baimashan pluton were analyzed with $\varepsilon_{\text{Hf}}(t)$ values from -8.7 to -4.1. The T_{DM}^{C} ages of these zircons vary from 1516 to 1801 Ma.

Table 2 SIMS zircon U-Pb data of the collected granites. (See Appendix Table 1)

Table 3 LA-ICP-MS zircon Lu-Hf isotopic data. (See Appendix Table 3)

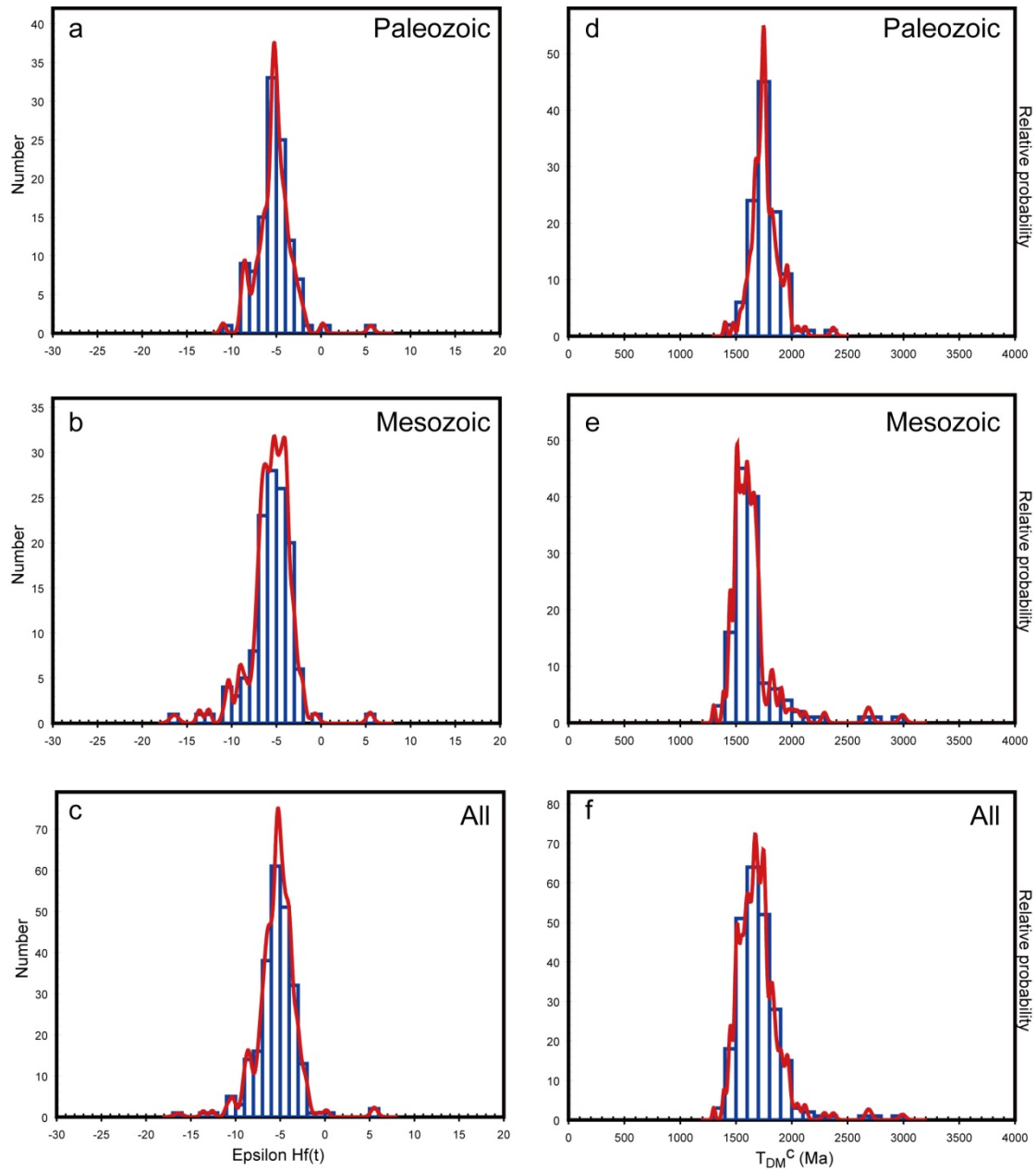


Fig. 7 Diagrams of $\epsilon_{\text{Hf}}(t)$ and T_{DM}^{C} values from Early Paleozoic granites (a-b), Early Mesozoic granites (c-d) and all samples (e-f) in the Xuefengshan Belt.

6. Discussion

6.1. Potential source of the granites

According to the geochemical characteristics, the Early Paleozoic and Early Mesozoic granites in the Xuefengshan Belt are aluminous or peraluminous late-orogenic products (Li, 1991, 1994; Zhou and Li, 2000; Chen et al., 2007a, 2007b; Wang et al., 2007a; Zhou et al., 2006; Zhang et al., 2011). Moreover, several inherited

zircons also provide useful information that the potential source may be the lower-middle crustal rocks of sedimentary origins.

The zircon $\epsilon_{\text{Hf}}(t)$ values of the Early Paleozoic granite samples show a relatively concentrated distribution from -10 to -1, with a peak at -5 (Fig. 7a). Hf crustal model ages (T_{DM}^{C}) of all the zircons give a range from 2.4 to 1.5 Ga, with a peak at ~ 1.75 Ga (Fig. 7b), implying a uniform parental magma source. In combination with the $\epsilon_{\text{Hf}}(t)$ values and the Hf model ages, a homogenous lower crust with Early Mesoproterozoic and Paleoproterozoic materials is preferred as the source area for Early Paleozoic granites. This result is also consistent with whole rock Nd model age of the Guidong pluton (Li, 1994).

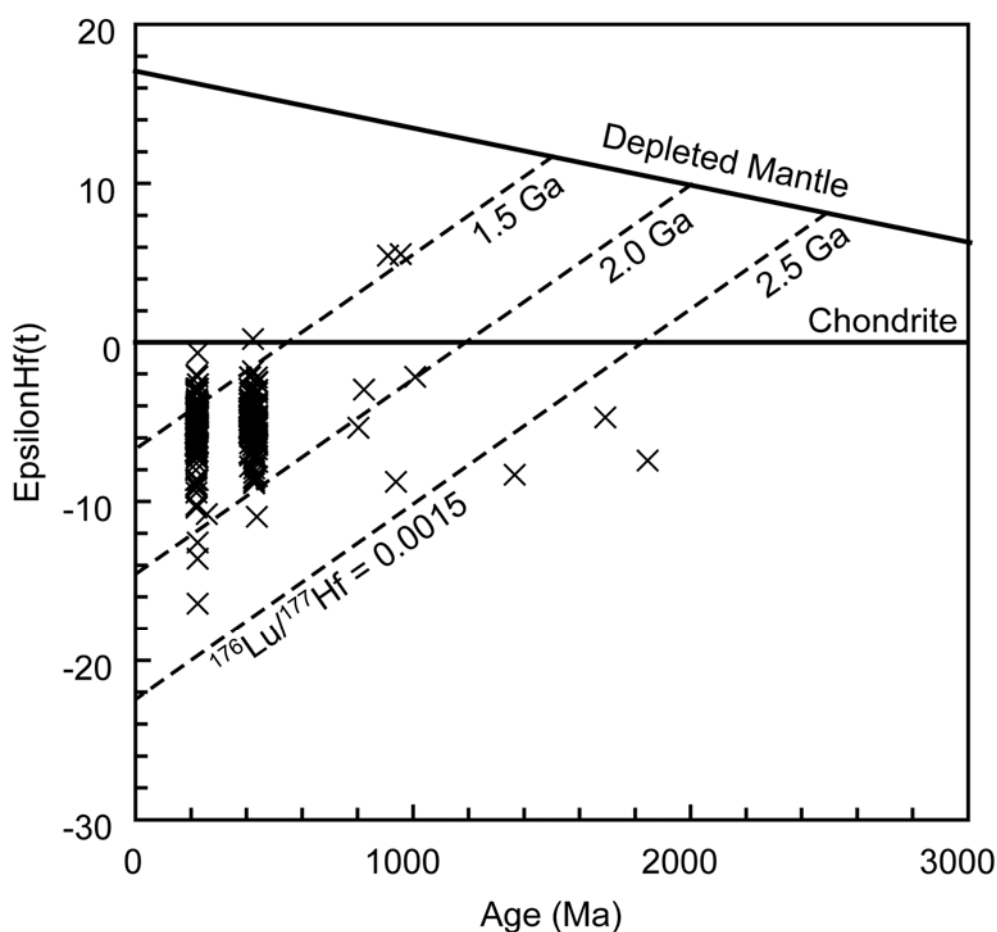


Fig. 8 Diagram of $\epsilon_{\text{Hf}}(t)$ vs. U-Pb ages of all of zircons from Early Paleozoic and Early Mesozoic granite samples.

The Early Mesozoic granite samples have a similar pattern of zircon $\epsilon_{\text{Hf}}(t)$ values as the Early Paleozoic granites (from -10 to -1), with a peak at around -5 (Fig. 7c). However, the Hf crustal model ages of the Early Mesozoic granites vary from 2.3 Ga to 1.4 Ga, and the peak age (~ 1.55 Ga) is younger than that of the Early Paleozoic

granites (Fig. 7d). Hence, we interpret that the Early Mesozoic granites are produced by the partial melting of Late Paleoproterozoic and Early Mesoproterozoic crustal materials. Previously reported whole rock Sm-Nd isotopic data of Early Mesozoic granites in the Xuefengshan Belt also exhibit a narrow $\varepsilon_{\text{Nd}}(t)$ range from -11 to -6, and likewise Nd crustal model ages around 1.5 Ga (Wang et al., 2007a). In addition, inherited zircons of ~1.8 Ga, ~1.6 Ga and 1.0 to 0.9 Ga are found in some samples, probably indicating a Proterozoic crust survived from the partial melting. It is noteworthy that two zircons with positive $\varepsilon_{\text{Hf}}(t)$ values are found in the samples XF213 and XF76, dated at 909 Ma and 956 Ma, respectively, an indicative of crustal extraction from the depleted mantle during Neoproterozoic (Fig. 8). Because zircons with positive $\varepsilon_{\text{Hf}}(t)$ values are absent in this group of Triassic age, we interpret that the Early Mesozoic magmatism is not effected by mantle-derived addition, but only with lower crustal materials.

In summary, two generations of Phanerozoic granitoids in the Xuefengshan Belt, Early Paleozoic and Early Mesozoic, show similar features of zircon Lu-Hf isotopes. Both generations have close $\varepsilon_{\text{Hf}}(t)$ values ranging from -10 to -1, with a peak at -5 (Fig. 7e). In spite of the little timing difference between the two groups of T_{DM}^{C} ages (Fig. 7f), Late Paleoproterozoic to Early Mesoproterozoic materials appear to be the dominant source of the two generations of granites. Thus, it is well established that these granites were mainly derived from the lower crust without addition of depleted mantle source related to the subduction.

6.2. The Early Paleozoic magmatism and its tectonic significance

An Early Paleozoic orogen extended over 2000 km in length and 600 km in width in the southeastern region of South China. Amphibolite-facies and even granulite-facies metamorphism are documented in Wuyi and Yunkai, during an interval of ca. 460-440 Ma (Wang et al., 2007b; Wan et al., 2010; Li et al., 2010b). In contrast, late-orogenic granitoids are widespread in this orogen. Previous U-Pb results show that this magmatism probably started at ~450 Ma and ended at ~410 Ma. Our data provide a further constraint on granitoids in the western extension of this orogen. In the Xuefengshan Belt, compared with the Wuyi-Yunkai area, the influence of the Early Paleozoic orogeny is limited. The ductile deformation of Early Paleozoic age has not been reported in this region. Another important clue is revealed by that the angle of the unconformity between Middle to Late Devonian conglomerate or sandstone and pre-Devonian rocks is decreased, and disconformity appeared to the northwest (BGRMHN, 1988; Chu et al., 2011a).

Moreover, in the central part of the Early Paleozoic orogen, the climax of syn-orogenic or late-orogenic granitoids ranges from 450 Ma to 420 Ma (Wang et al., 2007b; Wan et al., 2010; Yang et al., 2010; Li et al., 2010b; Xu et al., 2011 and reference therein), however, in the Xuefengshan Belt, to the west of the Chenzhou-Linwu fault, the granites were emplaced ranging from 430 Ma to 410 Ma, exhibiting a time interval of ~20 Ma. This difference could be interpreted that the Xuefengshan Belt is partly involved in the Early Paleozoic orogen as indicated by E-W or WNW-ESE trending fold axes in pre-Devonian rocks, whereas the major portion of the belt is dominated by the Early Mesozoic event. During the Early Paleozoic orogeny, the Wuyi-Baiyun-Yunkai region experienced crustal thickening during 460-440 Ma, characterized by high-grade metamorphism and ductile deformation, but the Xuefengshan Belt is weakly affected at the same time (BMGRFJ, 1985; BMGRGD, 1988, Li et al., 2010; Chu et al., 2011a). After the main contractional phase, widespread magmatism occurred in an extensional regime in the central and eastern regions with late-orogenic peraluminous granitoids, indicating an orogenic collapse or delamination event (Lin et al., 2008; Li et al., 2010b).

Although more and more geochronological data have been published, the geodynamics of this Early Paleozoic orogen is still debated. It is well acknowledged that a subsequent rifting, called the Nanhua rift, was developed after the Neoproterozoic collision of the Yangtze and Cathaysia blocks along the Jinning or Sibao orogen (Charvet et al., 1996; Li, 1998; Wang and Li, 2003; Li et al., 2009a). However, this rift remained in a failed or immature state without breaking the South China block but a potential weak zone. Based on this failed rift, several models have been proposed to explain the inland tectonics of the South China block. According to studies on metamorphic event in the Yunkai region, Wang et al. (2007b) proposed an Early Paleozoic intracontinental orogen in response to the subduction of the Paleo-Qinling ocean the beneath the Yangtze block. However, Yan et al. (2006) interpreted the igneous activity in the Dulong-Song Chay massif as a result of the collision between the Yangtze block and the Cathaysia block by the closure of Paleo-Tethys ocean. Recently, comprehensive studies on structural geology, petrology and geochronology point to an intracontinental orogeny reactivated at a failed rift or Paleo-suture zone, however, the kinematics of this orogeny is still controversial between a SE or S-directed or a NW-directed shearing (Faure et al., 2009; Charvet et al., 2010; Li et al., 2010b). Nevertheless, it is preferred that an intracontinental belt occurred during Early Paleozoic, accompanied with late-orogenic magmatism of 450-410 Ma rose by collapse of the orogen or delamination.

6.3. The Early Mesozoic magmatism and its tectonic significance

In the Xuefengshan Belt, central South China, previous studies give a relatively large range of crystallization ages of granites, resulting in various interpretations (Xu et al., 2004; Ding et al., 2005; Chen et al., 2006, 2007a, 2007b; Zhou et al., 2006; Li and Li, 2007; Wang et al., 2007a; Zhou, 2007; Li et al., 2008). Wang et al. (2005, 2007a) suggest that two-stage evolution of the Early Mesozoic granites according to two age-groups. The first episode of magmatism is between ~245 Ma and 228 Ma, which was generated by readjusting of the over-thickened crust after the peak metamorphism; while the second episode (220-206 Ma), is a likely result of the magma underplating event. However, our precise SIMS U-Pb dating demonstrates that the Early Mesozoic magmatism of central South China occurred between 225 to 215 Ma, rather than from 245 to 200 Ma. The previous ages at ~240 Ma are questionable. Hence, we argue that these granites represent a single magmatic event (Fig. 9). Some authors infer that these plutons were derived from crustal materials by decompressional melting in a Late Triassic post-collisional tectonic setting during spontaneous thinning of the overthickened crust (Ding et al., 2005; Chen et al., 2006, 2007a, 2007b). However, this long-distance effect that they suggested is ca. 500 km away from the Indosinian suture zone in north Vietnam. On the contrary, Triassic granites were lacking in in-between regions from the Vietnamese Indosinian belt to the Xuefengshan Belt, and the trend of dominant structures of the Xuefengshan Belt is perpendicular to that of the Indosinian belt. It is thereby impossible to connect the two events. Li and Li (2007) synthesize available chronological data and propose a flat-slab subduction model to interpret the intraplate magmatism in the South China block. Nonetheless, our Hf isotopic results imply that a single source of the granites with any input of mantle-derived materials. Thus, it is reasonable to conclude that the flat-slab subduction did not reach the asthenosphere beneath the Xuefengshan Belt.

On the basis of structural analysis, the Xuefengshan Belt is well acknowledged as an intracontinental orogen, which was possibly triggered by the Paleo-Pacific subduction. In addition, the orogenic stages is well constrained our precise SIMS zircon U-Pb ages and previously obtained EMPA monazite U-Th-Pb dating, that is, the ductile deformation occurred in an interval of 243-226 Ma, while the subsequent late-orogenic magmatism was developed between 225 Ma and 215 Ma (Chu et al., 2011a, 2011b).

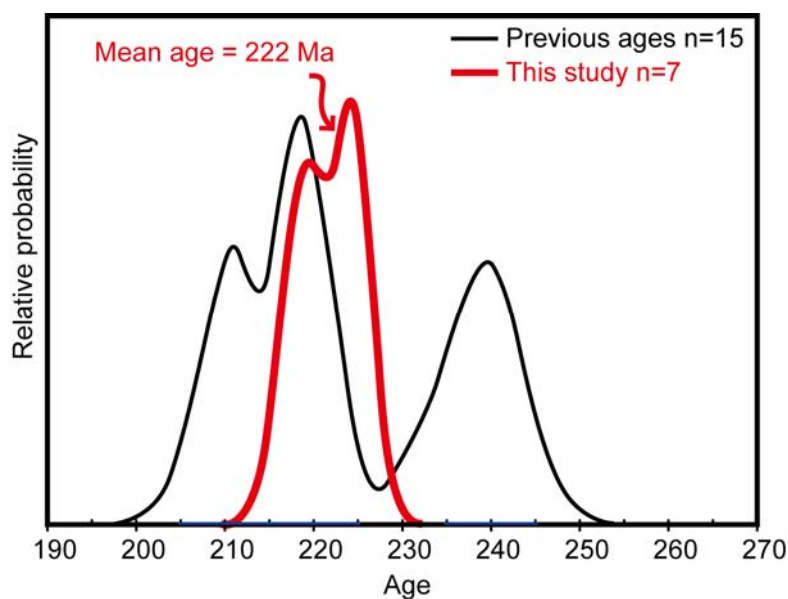


Fig. 9 Relative probability plots of isotopic ages of Triassic granites. Previous age data are from the following references (Xu et al., 2004; Ding et al., 2005; Chen et al., 2006, 2007a, 2007b; Li and Li, 2007; Wang et al., 2007a; Li et al., 2008).

During Early Mesozoic, the South China block and its adjacent regions, including the western Yunnan-Indochina block, the Songpan-Gantze flysch belt, and the Qinling-Dabie-Sulu belt, experienced considerable Early Mesozoic tectonics (BGMJRJX, 1984; BGMRGX, 1985; Hacker and Wang, 1995; Lepvrier et al., 1997, 2011; Carter et al., 2001; Harrowfield and Wilson, 2005; Li et al., 2006; Carter and Clift, 2008; Roger et al., 2010), but the internal part of the block has merely raised abroad attention since recent years (Wang et al., 2005; Chu et al., 2011a, 2011b). Because of contradicting structural vergences, none of abovementioned events can be attributed to the geodynamic origin of the Xuefengshan Belt, which was simultaneously triggered during Early Mesozoic in the center of the South China block. Thus, the introduction of a Paleo-Pacific subduction is in good coincidence with the occurrence of this intracontinental belt (Li et al., 2006; Li and Li, 2007). Furthermore, the Late Permian to Early Triassic subduction is also well evidenced by contemporary deformation on the Japanese islands (Faure and Charvet, 1987; Faure et al., 1988). Accordingly, after a continuous deposition of ca. 400-260 Ma, the South China block stepped out the stable period firstly evidenced by the onset of the Paleo-Pacific subduction around 260-250 Ma. As the push force propagated to the inland weak zone, the Chenzhou-Linwu fault, the Xuefengshan Belt commenced its activity with folds and thrusts.

Analogous to other orogenic belts, such as the Alice springs orogen, the Laramide orogen and the Pyrenees orogen (Choukroune, 1992; Hand and Sandiford,

1999; Sandiford et al., 2001; English and Johnston, 2004), a preexisting weak zone plays an important role in triggering the orogeny. The Early Mesozoic Xuefengshan Belt is thereby a typical intracontinental orogen reactivated at a weak zone in response to the far-field effect of the subduction at the continental margin. Late-orogenic magmatism was generated in the last stage of the orogeny as indicative of cessation of the contraction.

7. Conclusions

Phanerozoic aluminous to prealuminous granitoids are widespread in the Xuefengshan Belt. Combined with a synthesis of previous researches, geochronological and Lu-Hf isotopic data of representative plutons allow us to establish that:

(1) The Early Paleozoic granites in the Xuefengshan Belt were emplaced during 430-410 Ma, with a time interval of ~20 Ma later than the central part of the Wuyi-Baiyun-Yunkai orogen. Together with structural observations, it is implied that the Xuefengshan Belt is partly involved in the Early Paleozoic deformation, but affected by the extension-induced magmatism.

(2) The Xuefengshan Belt is dominated by the Early Mesozoic contractional deformation and a subsequent magmatism intruding the folded strata.

(3) Early Mesozoic magmatism is well constrained during 225-215 Ma, indicating a transition from contraction to extension in the Xuefengshan Belt.

(4) The flat-slab subduction did not reach to the Xuefengshan Belt as there is no input of mantle-derived materials in the Late Triassic granites.

Acknowledgements. Field works have been funded by the Innovative Project of the Chinese Academy of Sciences (Grant No. KZCX1-YW-15-1) and Major State Basic Research Development Program of China (2009CB825008). We thank Xin Yan and Saihong Yang for help with zircon CL imaging, Qiuli Li, Guoqiang Tang and Yu Liu for help with zircon U–Pb analysis, and Zhichao Liu and Yue-Heng Yang for help with zircon Hf analysis.

Reference

Brown, M., 2005. Synergistic effects of melting and deformation: an example from the Variscan belt, western France. In: Gapais, D., Brun, J.P., Cobbold, P. (Eds.), *Deformation mechanisms, rheology and tectonics: from minerals to the*

- lithosphere: Geological Society, London, Special Publication, 243, pp. 205-226.
- Bureau of Geology and Mineral Resources of Guangxi province (BGMRGX), 1985. Regional Geology of the Guangxi Zhuang Autonomous Region. Geological Publishing House, 853 p.
- Bureau of Geology and Mineral Resources of Hunan province (BGMRHN), 1988. Regional Geology of the Hunan Province. Geological Publishing House, Beijing, 507 p.
- Bureau of Geology and Mineral Resources of Jiangxi Province (BGMRJX), 1984. Regional Geology of the Jiangxi Province. Geological Publishing House, 921 p.
- Carter, A., Clift, P. D., 2008. Was the Indosinian orogeny a Triassic mountain building or a thermotectonic reactivation event? *Comptes Rendus Geosciences* 340, 83-93.
- Carter, A., Roques, D., Bristow, C., Kinny, P., 2001. Understanding Mesozoic accretion in Southeast Asia: Significance of Triassic thermotectonism (Indosinian orogeny) in Vietnam. *Geology* 29, 211-214.
- Charvet, J., Shu, L. S., Shi, Y. S., Guo, L. Z., Faure, M., 1996. The building of south China: Collision of Yangzi and Cathaysia blocks, problems and tentative answers. *Journal of Southeast Asian Earth Science* 13, 223-235.
- Charvet, J., Shu, L. S., Faure, M., Choulet, F., Wang, B., Lu, H. F., Le Breton, N., 2010. Structural development of the Lower Paleozoic belt of South China: Genesis of an intracontinental orogen. *Journal of Asian Earth Science* 39, 309-330.
- Chen, A., 1999. Mirror-image thrusting in the South China Orogenic Belt: tectonic evidence from western Fujian, southeastern China. *Tectonophysics* 305, 497-519.
- Chen, W. F., Chen, P. R., Zhou, X. M., Huang, H. Y., Ding, X., Sun, T., 2006. Single-zircon La-ICP-MS U-Pb Dating of the Yangmingshan Granitic Pluton in Hunan, South China and its Petrogenetic Study (in Chinese with English abstract). *Acta Geologica Sinica* 80, 1065-1077.
- Chen, W. F., Chen, P. R., Huang, H. Y., Ding, X., Sun, T., 2007a. Chronological and geochemical studies of granite and enclave in Baimashan pluton, Hunan, South China. *Science in China (D)* 50, 1606-1627.
- Chen, W. F., Chen, P. R., Zhou, X. M., Huang, H. Y., Ding, X., Sun, T., 2007b. Single Zircon LA-ICP-MS U-Pb Dating of the Guandimiao and Wawutang Granitic Plutons in Hunan, South China and its Petrogenetic Significance. *Acta Geologica Sinica* 81, 81-89.

- Choukroune, P., 1992. Tectonic evolution of the Pyrenees. *Annual Review of Earth Planetary Sciences* 20, 143-158.
- Chu Y., Faure M., Lin W., Wang Q., 2011a. Early Mesozoic intracontinental Xuefengshan Belt, South China: insights from structural analysis of polyphase deformation, EGU meeting, Vienna, Austria.
- Chu Y., Faure, M., Lin, W., Wang, Q. C., Ji W. B., 2011b. Tectonics of the Middle Triassic intracontinental Xuefengshan Belt, South China: new insights from structural and chronological constraints on the basal decollement layer. Submitted.
- Chung, S. L., Chu, M. F., Zhang, Y., Xie, Y., Lo, C. H., Lee, T.-Y., Lan, C. Y., Li, X., Zhang, Q., Wang, Y., 2005. Tibetan tectonic evolution inferred from spatial and temporal variations in post-collisional magmatism. *Earth-Science Reviews* 68, 173-196.
- Ding, X., Chen, P. R., Chen, W. F., Huang, H. Y., Zhou, X. M., 2005. LA-ICPMS zircon U-Pb age determination of the Weishan granite in Hunan: petrogenesis and significance. *Science in China (D)* 35, 606-616.
- English, J. M., Johnston, S. T., 2004. The Laramide orogeny: What were the driving forces? *International Geology Review* 46, 833-838.
- Faure, M., Charvet J., 1987. Late Permian/early Triassic orogeny in Japan: piling up of nappes, transverse lineation and continental subduction of the Honshu block, *Earth and Planetary Science Letters* 84, 295-308.
- Faure, M., Monié P., Fabbri O., 1988. Microtectonics and ^{39}Ar - ^{40}Ar dating of high pressure metamorphic rocks of the south Ryukyu Arc and their bearings on the pre-Eocene geodynamic evolution of Eastern Asia, *Tectonophysics* 156, 133-143.
- Faure, M., Sun, Y., Shu, L., Monié, P., Charvet, J., 1996. Extensional tectonics within a subduction-type orogen. The case study of the Wugongshan dome (Jiangxi Province, southeastern China). *Tectonophysics* 263, 77-106.
- Faure, M., Lin W., Shu L. S., Sun Y., Scharer U., 1999. Tectonics of the Dabieshan (eastern China) and possible exhumation mechanism of ultra high-pressure rocks. *Terra Nova* 11, 251-258.
- Faure, M., Lin, W., Scharer, U., Shu, L. S., Sun, Y., Arnaud, N., 2003. Continental subduction and exhumation of UHP rocks. Structural and geochronological insights from the Dabieshan (East China). *Lithos* 70, 213-241.
- Faure, M. Lin, W., Monié, P., Meffre, S., 2008. Paleozoic collision between the North and South China blocks, Early Triassic tectonics and the problem of the ultrahigh-pressure metamorphism. *Comptes Rendus Geosciences* 340, 139-150.

- Faure, M., Shu, L.S., Wang, B., Charvet, J., Choulet, F., Monie, P., 2009. Intracontinental subduction: a possible mechanism for the Early Palaeozoic Orogen of SE China. *Terra Nova* 21, 360-368.
- Hacker, B. R., Wang, Q. C., 1995. Ar/Ar Geochronology of Ultrahigh-Pressure Metamorphism in Central China. *Tectonics* 14, 994-1006.
- Hand, M., Sandiford, M., 1999. Intraplate deformation in central Australia, the link between subsidence and fault reactivation. *Tectonophysics* 305, 121-140.
- Harris, N., Massey, J., 1994. Decompression and anatexis of Himalayan metapelites. *Tectonics* 13, 1537 - 1546.
- Harrowfield, M. J., Wilson, C. J. L., 2005. Indosinian deformation of the Songpan Garze Fold Belt, northeast Tibetan Plateau. *Journal of Structural Geology* 27(1), 101-117.
- Huang, T.K., 1960. The main characteristics of the geologic structures of China: Preliminary conclusions. *Acta Geologica Sinica* 40, 1-37.
- Huang, T. K., 1978. An outline of the tectonic characteristics of China. *Eclogae Geologicae Helveticae* 71, 611-635.
- Lepvrier, C., Maluski, H., Van Vuong, N., Roques, D., Axente, V., Rangin, C., 1997. Indosinian NW-trending shear zones within the Truong Son belt (Vietnam) ^{40}Ar - ^{39}Ar Triassic ages and Cretaceous to Cenozoic overprints. *Tectonophysics* 283, 105-127.
- Lepvrier, C., Faure, M., Van, V. N., Vu, T. V., Lin, W., Trong, T. T., Hoa, P. T., 2011. North-directed Triassic nappes in Northeastern Vietnam (East Bac Bo). *Journal of Asian Earth Sciences* 41, 56-68.
- Li, H. Q., Wang D. H., Chen F. W., Mei Y.P., Cai H., 2008. Study on Chronology of the Chanziping and Daping gold deposit in Xuefeng Mountains, Hunan Province. *Acta Geologica Sinica* 82, 900-905 (in Chinese with English abstract).
- Li, L. M., Sun, M., Wang, Y., Xing, G., Zhao, G., Lin, S., Xia, X., Chan, L., Zhang, F., Wong, J., 2011. U-Pb and Hf isotopic study of zircons from migmatized amphibolites in the Cathaysia Block: Implications for the early Paleozoic peak tectonothermal event in Southeastern China. *Gondwana Research* 19, 191-201.
- Li, Q.L., Li, X.H., Liu, Y., Tang, G.Q., Yang, J.H., Zhu, W.G., 2010a. Precise U-Pb and Pb-Pb dating of Phanerozoic baddeleyite by SIMS with oxygen flooding technique. *Journal of Analytical Atomic Spectrometry* 25, 1107-1113.
- Li, X.H., 1991. Geochronology of the Wanyangshan-Zhuguangshan granitoid batholith: Implication for the crust development. *Science in China (B)* 34, 620-629.

- Li, X. H., 1994. A comprehensive U-Pb, Sm-Nd, Rb-Sr and ^{40}Ar - ^{39}Ar geochronological study on Guidong Granodiorite, southeast China: Records of multiple tectonothermal events in a single pluton. *Chemical Geology* 115, 283-295.
- Li, X. H., 1999. U-Pb zircon ages of granites from the southern margin of the Yangtze Block: timing of Neoproterozoic Jinning Orogeny in SE China and implications for Rodinia Assembly. *Precambrian Research* 97, 43-57.
- Li, X. H., Li, Z. X., Li, W. X., Wang, Y. J., 2006. Initiation of the Indosinian Orogeny in South China: Evidence for a Permian magmatic arc on Hainan Island. *The Journal of Geology* 114, 341-353.
- Li, X. H., Li, W. X., Li, Z. X., Lo, C. H., Wang, J., Ye, M. F., Yang, Y. H., 2009a. Amalgamation between the Yangtze and Cathaysia Blocks in South China: Constraints from SHRIMP U-Pb zircon ages, geochemistry and Nd-Hf isotopes of the Shuangxiwu volcanic rocks. *Precambrian Research* 174, 117-128.
- Li, X. H., Liu Y., Li Q. L., Guo C. H., Chamberlain K. R., 2009b. Precise determination of Phanerozoic zircon Pb/Pb age by multicollector SIMS without external standardization. *Geochemistry Geophysics Geosystems* 10, Q04010, doi:10.1029/2009GC002400.
- Li, Z.X., 1998. Tectonic history of the major East Asian lithospheric blocks since the mid-Proterozoic—A synthesis, in Flower, M.J., Chung, S.-L., Lo, C.-H., and Lee, T.-Y., eds., *Mantle Dynamics and Plate Interactions in East Asia*: Washington, D.C., American Geophysical Union, *Geodynamics Series* 27, 221–243.
- Li, Z. X., Li, X. H., 2007. Formation of the 1300-km-wide intracontinental orogen and postorogenic magmatic province in Mesozoic South China: A flat-slab subduction model. *Geology* 35, 179-182.
- Li, Z. X., Li, X. H., Wartho, J. A., Clark, C., Li, W.-X., Zhang, C. L., Bao, C., 2010. Magmatic and metamorphic events during the early Paleozoic Wuyi-Yunkai orogeny, southeastern South China: New age constraints and pressure-temperature conditions. *Geological Society of America Bulletin* 122, 772-793.
- Lin, W., Faure, M., Monie, P., Scharer, U., Zhang, L. S., Sun, Y., 2000. Tectonics of SE China: New insights from the Lushan massif (Jiangxi Province). *Tectonics* 19, 852-871.
- Lin, W., Wang, Q. C., Chen, K., 2008. Phanerozoic tectonics of south China block: New insights from the polyphase deformation in the Yunkai massif, *Tectonics* 27, TC6004, doi:10.1029/2007TC002207.

- Ludwig, K.R., 2001. Users manual for Isoplot/Ex rev. 2.49. Berkeley Geochronology Centre Special Publication. No. 1a, 56 pp.
- Morel, M. L. A., Nebel, O., Nebel-Jacobsen, Y. J., Miller, J. S., Vroon, P. Z., 2008. Hafnium isotope characterization of the GJ-1 zircon reference material by solution and laser-ablation MC-ICPMS. *Chemical Geology* 255, 231-235.
- Qiu, Y. M., Gao, S., McNaughton, N. J., Groves, D. I., Ling, W., 2000. First evidence of > 3.2 Ga continental crust in the Yangtze craton of south China and its implications for Archean crustal evolution and Phanerozoic tectonics. *Geology* 28, 11-14.
- Qiu, Y. X., Zhang Y. C., Ma W. P., 2000. The Tectonic Nature and Evolution of Xuefeng Mountains: One Model of Formation and Evolution of Intra-continental Orogenic Belt, Geological Publishing House, Beijing, 155pp.
- Ren, J., 1991. On the geotectonics of southern China. *Acta Geologica Sinica* 44, 111-130.
- Roger, F., Jolivet, M., Malavieille, J., 2010. The tectonic evolution of the Songpan-Garze(North Tibet) and adjacent areas from Proterozoic to Present: A synthesis. *Journal of Asian Earth Sciences* 39, 254-269.
- Sandiford, M., Hand, M., McLaren, S., 2001. Tectonic feedback, intraplate orogeny and the geochemical structure of the crust: a central Australian perspective. Geological Society, London, Special Publications 184, 195-218.
- Shu, L. S., Zhou, G. Q., Shi, Y. S., Yin, J., 1994. Study of the high-pressure metamorphic blueschist and its Late Proterozoic age in the Eastern Jiangnan Belt. *Chinese Science Bulletin* 39, 1200-1204.
- Shu, L. S., Zhou, X. M., Deng, P., Wang, B., Jiang, S. Y., Yu, J. H., Zhao, X. X., 2009. Mesozoic tectonic evolution of the Southeast China Block: New insights from basin analysis. *Journal of Asian Earth Sciences* 34, 376-391.
- Sláma, J., Košler, J., Condon, D. J., Crowley, J. L., Gerdes, A., Hanchar, J. M., Horstwood M. S.A., Morris G. A., Nasdala L., Norberg N., Schaltegger U., Schoene B., Tubrett M. N., Whitehouse M. J., 2008. Plešovice zircon - A new natural reference material for U-Pb and Hf isotopic microanalysis. *Chemical Geology* 249, 1-35.
- Stacey, J.S., Kramers, J.D., 1975. Approximation of terrestrial lead isotope evolution by a two-stage model. *Earth Planetary Science Letters* 26, 207-221.
- Wan, Y., Liu, D., Wilde, S. A., Cao, J., Chen, B., Dong, C., Song, B., Du, L., 2009. Evolution of the Yunkai Terrane, South China: Evidence from SHRIMP zircon U-Pb dating, geochemistry and Nd isotope. *Journal of Asian Earth Sciences* 37, 140-153.

- Wang, J., Li, Z. X., 2003. History of Neoproterozoic rift basins in South China: implications for Rodinia break-up. *Precambrian Research* 122, 141-158.
- Wang, Y. J., Fan, W. M., Guo, F., Peng, T. P., Li, C. W., 2003. Geochemistry of Mesozoic mafic rocks adjacent to the Chenzhou-Linwu fault, South China: Implications for the lithospheric boundary between the Yangtze and Cathaysia blocks. *International Geology Review* 45, 263-286.
- Wang, Y. J., Zhang, Y. H., Fan, W. M., Peng, T. P., 2005. Structural signatures and Ar-40/Ar-39 geochronology of the Indosinian Xuefengshan tectonic belt, South China Block. *Journal of Structural Geology* 27, 985-998.
- Wang, Y. J., Fan, W. M., Sun, M., Liang, X. Q., Zhang, Y. H., Peng, T. P., 2007a. Geochronological, geochemical and geothermal constraints on petrogenesis of the Indosinian peraluminous granites in the South China Block: A case study in the Hunan Province. *Lithos* 96, 475-502.
- Wang, Y. J., Fan, W. M., Zhao, G. C., Ji, S. C., Peng, T. P., 2007b. Zircon U-Pb geochronology of gneissic rocks in the Yunkai massif and its implications on the Caledonian event in the South China Block. *Gondwana Research* 12, 404-416.
- Woodhead, J. D., Hergt, J. M., 2005. A preliminary appraisal of seven natural zircon reference materials for in situ Hf isotope determination. *Geostandards and Geoanalytical Research* 29, 183-195.
- Wu, F. Y., Yang, Y. H., Xie, L. W., Yang, J. H., Xu, P., 2006. Hf isotopic compositions of the standard zircons and baddeleyites used in U-Pb geochronology. *Chemical Geology* 234, 105-126.
- Xu, H. J., Ma, C. Q., Zhong, Y. F., She, Z. B., 2004. Zircon SHRIMP dating of Taojiang and Dashenshan granite: Lower limit on the timing of the amalgamation between Yangtze and Cathaysia blocks. Annual meeting of Petrology and Geodynamics, China.
- Xu, X. B., Zhang, Y. Q., Shu, L. S., Jia, D., 2011. La-ICP-MS U-Pb and $^{40}\text{Ar}/^{39}\text{Ar}$ geochronology of the sheared metamorphic rocks in the Wuyishan: Constraints on the timing of Early Paleozoic and Early Mesozoic tectono-thermal events in SE China. *Tectonophysics* 501, 71-86.
- Xu, X. S., O'Reilly, S. Y., Griffin, W. L., Deng, P., Pearson, N. J., 2005. Relict proterozoic basement in the Nanling Mountains (SE China) and its tectonothermal overprinting. *Tectonics* 24, doi:10.1029/2004TC001652.
- Yan, D. P., Zhou, M. F., Song, H. L., Wang, X. W., Malpas, J., 2003. Origin and tectonic significance of a Mesozoic multi-layer over-thrust system within the Yangtze Block (South China). *Tectonophysics* 361, 239-254.

- Yan, D. P., Zhou, M. F., Wang, C. Y., Xia, B., 2006. Structural and geochronological constraints on the tectonic evolution of the Dulong-Song Chay tectonic dome in Yunnan Province, SW China. *Journal of Asian Earth Sciences* 28, 332-353.
- Yang, D. S., Li, X. H., Li, W. X., Liang, X. Q., Long, W. G., Xiong, X. L., 2010. U-Pb and ^{40}Ar - ^{39}Ar geochronology of the Baiyunshan gneiss (central Guangdong, south China): constraints on the timing of early Palaeozoic and Mesozoic tectonothermal events in the Wuyun (Wuyi-Yunkai) Orogen. *Geological Magazine* 147, 481-496.
- Yu, J. H., O'Reilly, S. Y., Wang, L., Griffin, W. L., Zhou, M.-F., Zhang, M., Shu, L., 2010. Components and episodic growth of Precambrian crust in the Cathaysia Block, South China: Evidence from U-Pb ages and Hf isotopes of zircons in Neoproterozoic sediments. *Precambrian Research* 181, 97-114.
- Zhang, F., Wang, Y., Chen, X., Fan, W., Zhang, Y., Zhang, G., Zhang, A., 2011. Triassic high-strain shear zones in Hainan Island (South China) and their implications on the amalgamation of the Indochina and South China Blocks: Kinematic and $^{40}\text{Ar}/^{39}\text{Ar}$ geochronological constraints. *Gondwana Research* 19, 910-925.
- Zhang, S. B., Zheng, Y.-F., Wu, Y.-B., Zhao, Z.-F., Gao, S., Wu, F.-Y., 2006a. Zircon U-Pb age and Hf isotope evidence for 3.8Ga crustal remnant and episodic reworking of Archean crust in South China. *Earth and Planetary Science Letters* 252, 56-71.
- Zhou, X. M., Li, W. X., 2000. Origin of Late Mesozoic igneous rocks in Southeastern China: implications for lithosphere subduction and underplating of mafic magmas. *Tectonophysics* 326, 269-287.
- Zhou, X. M., Sun, T., Shen, W. Z., Shu, L. S., Niu, Y. L., 2006. Petrogenesis of Mesozoic granitoids and volcanic rocks in South China: A response to tectonic evolution. *Episodes* 29, 26-33.
- Zhou, X. M. (Eds), 2007. *Genesis of Late Mesozoic Granites in Nanling Region and Geodynamic Evolution of Lithosphere*. Science Press, Beijing, 691pp.

Discussion

1. Polyphase deformation

The Xuefengshan is located in the center of the South China block and a key to understanding the intraplate deformation. In the Xuefengshan belt, a regional fault, named as the Main Xuefengshan Thrust, has been recognized with top-to-the-NW kinematics. This fault separates the Western (Outer) Zone and Eastern (Inner) Zone, and also represents the cleavage front. In the study area, Neoproterozoic to Early Triassic rocks experienced 3 events of deformation. D1 corresponds to the top-to-the-NW thrusting and folding across the whole Xuefengshan belt, interpreted as the dominant phase during the Early Mesozoic orogeny (Fig. 7-1). In the Western Zone, kilometer-scale box folds are principal structures with subvertical hinges and broad and flat cores of anticlines and synclines. In addition to the large scale shortening, the deformational features are located in the hinges, such as layer parallel slip and gravitational collapse folds. The Eastern Zone is characterized by ductile deformation in a lower structural level. NW vergent isoclinal folds are widespread with closely spaced axial planar cleavages. On the cleavage plane, NW-SE trending mineral and stretching lineation is well developed by elongated minerals, pebbles, and mineral fibers in the pressure shadow. In the XZ plane, which is perpendicular to the foliation or cleavage and parallel to the lineation, kinematic criteria, such as asymmetrical pressure shadow of quartz or calcite, sigmoidal quartz vein and strongly sheared pebbles in Sinian (late Neoproterozoic) tillites, is clearly expressed with a top-to-the-NW shear sense. The rocks of the Eastern Zone experienced syn-tectonic greenschist facies metamorphism contemporaneous with the ductile shearing.

In contrast, across the eastern part of the Eastern Zone, Devonian to Early Triassic rocks are intensely deformed in a brittle to ductile structural level. Dissimilar to the western part, top-to-the-NW structures are widespread without any metamorphism in the eastern part. The deformation is featured by asymmetrical

folding and NW-directed thrusting. For example, in the Lianyuan area, the Carboniferous to Triassic interbedded limestone and mudstone are involved in multiple thrusts and fault-related folds, indicating a top-to-the-NW shear sense.

Compared with the D1 structures, the D2 deformation is localized in the Eastern Zone. According to our investigation, the D1 structures are superposed by SE vergent folds with NW-dipping cleavages. Absent syn-tectonic metamorphism and high-strain decollement, this event is less penetrative and intense than the D1 event. Along the linear zone of Anhua-Xinhua-Dongkou-Chengbu, a regional overturned structure is developed in Sinian to Devonian strata, resulted from SE vergent folding.

The last phase, D3, is characterized by upright fold with vertical S3 cleavages and L3 lineation, localized in the Eastern Zone. This phase is interpreted as the product of uplift-induced local compression during the emplacement of granites. In outcrop scale, it is difficult to distinguish the vertical S3 cleavage and the subvertical S1 cleavage in some places. However, in D3 domains, the folded planes are S1 foliation with likewise folded lineation on the surface, whereas the plane folded by D1 with cleavages is original bedding. Similarly, to the west of Chengbu, the NW-dipping S2 cleavages are superposed by upright S3 cleavages.

Wang et al. (2005) suggest that the WNW-directed fold and thrust structures are accompanied with sinistral strike-slip movement with a N-S or NNE-SSW trending lineation. Simultaneously, top-to-the-SE shearing is considered to be the result of back-thrusting. However, based on our field observation, the top-to-the-NW D1 structures are demonstrated by fold and thrust with a NW-SE trending lineation, and there is no strike-slip component during Triassic, and if any, it should belong to a late event as the late-orogenic granites were cut and displaced by their regional faults. Qiu et al. (1998, 1999) consider that the Xuefengshan belt is due to an autochthonous NW vergent thrusting during Early Paleozoic, while the top-to-the-SE shearing is a later gravitational slide-induced thrusting. Both folds and cleavages only involved the pre-Devonian rocks with a superposition of Early Mesozoic (Indosinian) event with the same kinematics. Nevertheless, this interpretation is strongly challenged by the fact that the D1 thrust and the D2 back-thrust occurred in both Early Paleozoic and

Late Paleozoic rocks.

To summarize, the D1, D2 and D3 events are recorded in the Eastern Zone, suggesting that the Xuefengshan belt experienced a polyphase deformation during the Early Mesozoic orogeny. The superposition of S1-S2, S1-S3 and S2-S3 indicates a continuous deformation from D1 to D3 in a single geodynamic setting of NW-SE compression.

2. Time constraints of the polyphase deformation

In the Xuefengshan belt, the Early Paleozoic event is dominated by E-W trending folds and Silurian-Early Devonian granites. However, there are no ductile deformation and metamorphism in the study area. To the east of the Xuefengshan belt, ca. 440-400 Ma granitic plutons are emplaced into the folded strata which were deformed during 460-440 Ma (Faure et al., 2009; Charvet et al., 2010), and then were covered by middle to late Devonian conglomerate and sandstone. According to the presence of mylonitized Early Paleozoic granites, we thus infer that these structures are formed under the solidus facies as a result of post-Devonian deformation. This phenomenon is analogous to that of the Wuyishan and Yunkaidashan area, where the Early Paleozoic granites were strongly sheared into orthogneiss with 240-210 Ma of Ar-Ar and zircon ages (Wang et al., 2007b, 2007c; Yang et al., 2010; Xu et al., 2011). Nevertheless, compared to the eastern South China block, the Xuefengshan belt is weakly affected by the Early Paleozoic orogeny.

The sedimentary rocks involved in the Early Mesozoic orogeny are mostly deposited in a shallow sea environment, except the hiatus from Late Silurian to Early Devonian due to the uniform uplift of the South China block and the successive Middle Devonian terrestrial sedimentation (BRMGJX, 1984; BRGMFJ, 1985, BRGMHN, 1988; BRGMZJ, 1989; Shu et al., 2009). From Middle Triassic, the environment changed abruptly from marine to terrestrial facies in the Xuefengshan belt. Meanwhile, the South China block was uplifted to land of approximate present elevation. Late Triassic to Early Jurassic sequence is composed of clastic rocks such

as conglomerate, gritstone and mudstone, which are deposited in small intermontane basins from the erosion of the Xuefengshan belt (Zhang et al., 2010). Conversely, the pre-Middle Triassic strata are involved folds and thrusts.

According to the regional unconformity, Jia (1994) and Qiu et al. (1999) suggest that the main event of the Xuefengshan belt is in Early Paleozoic. Furthermore, they find that the cleavage in the Silurian strata does not penetrate the unconformity. However, on the basis of our observation, the Early Paleozoic post-orogenic granites were deformed. The slaty cleavage are well developed on the both sides of the unconformity, that is, the Silurian and Devonian rocks are of similar deformational character. Hence, the deformation occurred after the unconformity. Yan et al. (2003, 2009) propose that the Xuefengshan belt is a Late Mesozoic klippe with Neoproterozoic rocks thrust onto the Early Paleozoic rocks. Approaching westerly to the eastern Sichuan, the thick skinned tectonics is changed to thin skinned tectonics. In fact, the principal structures of the Xuefengshan belt are formed during Triassic, and the contact between the Neoproterozoic and Early Paleozoic rocks is sedimentary. Therefore, the Xuefengshan belt and the Sichuan fold belt are products of different tectonic events.

Beneath the sedimentary cover of the Xuefengshan belt, a basal decollement generated high strain mylonitic rocks, including Early Paleozoic granites and their host rocks. During the mylonitization, the granite is transformed into orthogneiss and the host rock is changed to quartz mylonite. The basal decollement is characterized by top-to-the-NW shearing, indicative of products by the D1 event in Early Mesozoic. We dated two strongly sheared micaschist collected from the basal decollement, yielding ages of 243 Ma and 226 Ma by the Electron Microprobe monazite U-Th-Pb dating method. It can be inferred that the ductile deformation and syn-tectonic metamorphism occurred between 242 and 226 Ma. Moreover, the folded strata were cut by late Triassic aluminous-peraluminous plutons widely outcropped in the Xuefengshan belt. As these granites are undeformed late- or post-orogenic products, the timing of emplacement can be interpreted as the upper limit of the orogeny. Combined with previous studies, the granites are mostly emplaced during 225-215 Ma

(Ding et al., 2005; Chen et al., 2006, 2007a, 2007b; Wang et al., 2007a; Li and Li, 2007; Li et al., 2008), implying that the crustal shortening probably ceased after 225 Ma and was replaced by a regional extensional regime. These granites are located in the cores of anticlines, and generated localized weak compression. Although it is difficult to get the any chronological age of the D3 folding, we think that it is contemporaneous with the granite intrusion.

Wang et al. (2005) have dated 5 mylonitic samples of major faults in the Xuefengshan belt, giving a range from 217 to 195 Ma. However, these ages imply late Triassic to Early Jurassic tectonics, but even younger than the late-orogenic granites. In addition, the major faults, to which they have paid a lot attention, displace the granite by sinistral strike-slip movement, indicating a post-orogenic faulting. Accordingly, the Ar-Ar ages of 217-195 Ma represent the cooling age after the emplacement of Triassic plutons, rather than the age of ductile deformation.

In a word, the three phases of deformation in the Xuefengshan belt can be considered as a continuum of NW-SE shortening. The D1 and D2 events occurred between 243 and 226 Ma, and the D3 event is coeval with the magmatism at 225-215 Ma. The age range of 217-195 Ma suggests the cooling stage after the orogen.

3. Tectonic evolution of the Xuefengshan belt

Previous studies on the top-to-the-NW ductile deformation reveal several tectonic models of the Xuefengshan belt, but they are not in accord with our investigation. Qiu et al. (1999) suggest that the Xuefengshan belt is shaped during Early Paleozoic with weak Early Mesozoic superposition. Its central area in southeastern Guizhou and northern Guangxi is dominant by autochthonous thrusting and subsequent slide-induced back-thrusting; Yan et al. (2003) consider that the Xuefengshan and Wulingshan are both klippe in a multi-layer thrust system, consistent with the viewpoint of Hsu et al. (1988, 1990) who proposed a large scale, long-distance thrust. However, the so-called thrust between the Neoproterozoic and Early Paleozoic rocks is, in fact, a sedimentary contact or gravitational collapse when the dip angle is high

(Faure et al., 1998).

Across the Xuefengshan belt, the Western Zone is characterized by box folds. To the north of the Wulingshan, Cambrian to Ordovician limestone were thrust onto Silurian mudstone by the SE-dipping Dayong fault, which also uplifted the Neoproterozoic rocks. In the Xuefengshan, cleavage is widespread in Neoproterozoic to Devonian strata with a fan-like pattern (Fig. 7-2), that is, the cleavage dips to the SE in the west and to the NW in the east. The NW-dipping cleavages are products of back-folding event. In most classical orogens, back folding are very common under compressional stress field, such as the Taiwan belt, Himalaya orogenic belt and the Alps (Godin et al., 1999; Willett et al., 1993; Malavieille, 2010).

In the eastern part of the Eastern Zone, NW-directed folds and thrusts are dominant structures. The Chenzhou-Linwu fault is an important boundary in the Xuefengshan belt. To the east, the Early Paleozoic structures are well preserved with limited Triassic effect. Across the eastern South China block, the Early Paleozoic orogeny generated regional Devonian unconformity, widespread post-orogenic magmatism and migmatization (BRMGFJ, 1985; BRMGGD, 1988; BRMGGX, 1985; BRMGJX, 1984; Shu et al., 1997, 1999; Wang et al., 2007a; Wan et al., 2007, 2010; Chen et al., 2008; Faure et al., 2009; Charvet et al., 2010; Li ZX et al., 2010; Zhang et al., 2010; Zhang et al., 2010; Yang et al., 2010; Chen et al., 2011; Xu et al., 2011). In Jiangxi province, Neoproterozoic to Ordovician strata were deformed by E-W or NW-SE trending folds with SW vergent asymmetrical folds and NE dipping cleavages. The sedimentary cover and the metamorphic basement are separated by a basal decollement. Post-orogenic extension and granite intrusion resulted in the uplift of the basement, including migmatite, amphibolite and granulite in some places (BRMGJX, 1985; Faure et al., 2009; Yu et al., 2009). On the contrary, to the west of the Chenzhou-Linwu fault, in spite of Silurian granites and Devonian unconformity, the Xuefengshan belt is dominated by Early Mesozoic deformation. In fact, in most parts of the study area, the angle of the Devonian unconformity is lower than 20°, and even in the northern and northwestern parts of the Xuefengshan Belt, only a parallel disconformity between Silurian and Devonian rocks is exposed. The Early Paleozoic

folds are open, characterized by kilometer-scale gentle undulations without any axial planar cleavage. Thus, we infer that the Chenzhou-Linwu fault represent the eastern boundary of the Xuefengshan belt (Fig. 7-2).

In the outer zones of collision belts (e.g. Alpine Jura or Zagros Fold-and-Thrust Belt), decollement layers develop in low strength rocks such as evaporites or black shales to accommodate the bulk regional shortening [e.g. Escher and Beaumont, 1997; McQuarrie, 2004]. Below the decollement layer, basement rocks lack strong and pervasive deformation. In the Xuefengshan Belt, a major crustal decollement must be formed at the base of the Proterozoic to Early Triassic sedimentary series in order to accommodate the NW-SE shortening recorded by the D1 event. The Early Neoproterozoic mudstone and siltstone series corresponds to this decollement layer. Due to the D3 upright folding, a portion of this high strain discontinuity is exposed in the Chengbu area in the core of a D3 antiform (Fig. 7-2), but the underlying basement is not observed in the Xuefengshan Belt.

In the study area, available crustal scale seismic data that may constrain the deep geometry of the decollement are rare, and inaccurate [Qin, 1991]. A SE dipping reflector that might correspond to a decollement is imaged in Central Hunan, below the Eastern Zone. Furthermore, according to the reinterpretation of seismic data, Ding et al. (2007) suggest that a shallowly dipping low velocity layer is likely to be a basal decollement beneath the Eastern Zone. Thus, we argue that the MXT and other thrusts are rooted in this decollement layer. We interpret the upper crustal deformation responsible for thrusts, folds, and slaty cleavage as thin-skin tectonics underlain by a major decollement, rather than a thick skinned thrusting [Yan et al., 2003]. However, a thick skin tectonic style involving the basement of the Eastern Zone cannot be ruled out since seismic data are not available.

A question arises about the eastern extension of the decollement. Two possibilities can be put forward. The simplest one is to assume a single decollement layer that deepens eastward up to the Chengzhou -Linwu fault. Such a structure will develop southeastward for more than 300km that might be considered as unrealistic. Furthermore, in this case, the origin of the D2 back folding in the Eastern Zone can be

the result of SE-directed thrusting through the decollement (Figure 7-2a). Another possibility would be to consider that the decollement deepens eastward below the Eastern Zone (Figure 7-2b). In this interpretation, the east of the Eastern Zone would be underlain by a second decollement. Such a geometric pattern may account for the development of the D2 back folding and back-thrusting that would be rooted within the decollement. Whatever the right interpretation, the intracontinental Xuefengshan Belt is clearly underlain by a high strain layer that separates the upper crustal rocks that deformed by thrusting and folding and the middle to lower crustal rocks that are not exposed. This hidden basement corresponds to a piece of the SCB. In order to accommodate the shortening experienced by the Late Neoproterozoic (Sinian) to Early Triassic sedimentary series, the underlying basement must have experienced intracontinental underthrusting during the Triassic. Since East of the Chenzhou-Linwu fault the Triassic deformation is weak, and the Early Paleozoic tectonics is the main feature, this fault that represents the eastern tectonic boundary of the Xuefengshan Belt can be interpreted as a back-stop.

4. Early Mesozoic tectonic evolution of the South China block: Insights from the Xuefengshan belt

Across the whole South China block, several orogenic belts occurred along its boundary during Early Mesozoic. To the north, the SCB subducted beneath the North China Craton [Hacker and Wang, 1995; Faure et al., 1999; 2008]; to the west, the Songpan-Ganzi and Longmenshan Belts record evidence for Triassic deformation [Wallis et al., 2003; Harrowfield and Wilson, 2005; Roger et al., 2008, 2010], and to the southwest, the Yunnan-Guangxi-NE Vietnam Belt separates the SCB from Indochina [Lepvrier et al., 1997, 2004, 2008, 2011; Carter et al., 2001; Carter and Clift, 2008, Zhang et al., 2011].

When the Jiangnan old land was firstly proposed by Huang (1945), the interior of the South China block has raised wide attention of geologists. In the 1980s and 1990s, the deformation, magmatism, metamorphism and architecture were largely and

thoroughly investigated, but are still controversial. Firstly, the timing of the dominant deformation is in debate. Huang (1945) suggest the inland is controlled by Early Paleozoic tectonics, and this viewpoint is supported by Ren (1991), Li et al. (1993), Jia (1994), and Qiu et al. (1998, 1999). The other viewpoint is that the Early Mesozoic event dominates the internal structures by collisional orogeny (Hsu et al., 1988, 1990). Chen et al. (1993) and Ma et al. (1993) share the same idea of the timing constraint. The second controversy is related to the orogenic type. The collisional orogeny is supported by Guo (1980), Hsu et al. (1988), Li et al. (1993) and Chen et al. (1993), while intracontinental orogenic model is also proposed (Ma et al., 1993; Qiu et al., 1998, 1999) and accepted by more and more geologists.

From 2000s, as research funds and analytical techniques have been largely increased, the study of the internal South China block, such as the Xuefengshan belt, is greatly advanced. Based on seismic data and structural analysis, the Xuefengshan Belt has been interpreted as the result of the westward progressive collision of the Yangtze Block with the North China Block during the Late Jurassic to Cretaceous [Yan et al., 2003], but the Middle Triassic event, which is clearly postdated by the Late Triassic plutons and the regional Late Triassic unconformity, is not distinguished from the Cretaceous one. Wang et al. (2005, 2007c) proposed that this belt is the western part of an Early Mesozoic oblique convergent zone, with another structural belt in western Fujian Province as its eastern part, formed due to the relatively weak mechanical behavior of the SCB that was surrounded by the more rigid North China and Indochina blocks. The entire SCB was deformed in a diffuse manner with a bi-vergent structure, that is, top to the NW thrusting in the Xuefengshan Belt and top to the SE thrusting in western Fujian Province, east of the Chenzhou-Linwu Fault. However, the top-to-the-SE structures in the southeastern part of the SCB are assigned to a Late Jurassic event [Chen, 1999], while the Xuefengshan Belt is formed in Early Mesozoic. Thus, the two parts of the flower structure across the entire SCB did not form in the same time.

Recently, the South China fold belt was interpreted as a 1300-km wide intracontinental orogen [Li and Li, 2007]. The temporally and geographically

restricted Late Triassic shallow terrestrial or lacustrine basins represent post-orogenic deposits, and the Early Triassic marine limestone strata of Hunan and Jiangxi provinces both indicate similar platform depositional environment [BGMJRJX, 1984; BGMRHN, 1988]. According to this model, folding and thrusting, syn-orogenic magmatism, and foreland basin deposition migrated toward the SCB continental interior in response to the flat-slab subduction of the Pacific plate. However, the timing of the onset of the Pacific plate subduction is still under debate. Some authors suggest that west-directed subduction did not start until ~125 Ma [Engebretson et al., 1985], but others argue that subduction already started in the Early Mesozoic, even in Late Permian [Li et al., 2006]. Moreover, at the scale of the SCB, the radiometric ages of the Triassic plutons, ranging from 220 Ma to 208 Ma, are randomly distributed [Ding et al., 2005; Chen et al., 2006, 2007a, 2007b; Wang et al., 2007a; Li and Li, 2007; Li et al., 2008]. These granitic plutons do not show a magmatic trend younging from SE to NW that might be related to the progressive flat-slab subduction of the Pacific plate as proposed by Li and Li [2007]. However, Triassic NW-directed subduction is preferable, as suggested not only by Permian arc magmatism in Hainan Island to the south, but also by Early-Middle Triassic high pressure blueschist facies metamorphism of an Ar-Ar age at ~245 Ma in the Japanese islands [Faure and Charvet, 1987; Faure et al., 1988; Li et al., 2006]. Therefore, it is likely that the Paleo-Pacific subduction was ongoing during Early Mesozoic, and probably started in Late Permian. According to our study, the Xuefengshan Belt was not generated until Early Mesozoic along the potential weak zone, the Chenzhou-Linwu fault. Moreover, in the southeastern margin of the South China block, compressional deformation is recorded since Middle Triassic, with a delay of ca. 20 My to the arc-related magmatism (Chen, 1999), and Late Permian to Early Triassic plutons are interpreted as A-type granites emplaced in a transtensional setting (Wang et al., 2005a). Thus it is inferred that a transition from extension to compression occurred in Early Triassic, probably on account of the shallowing of the subducted plate angle. Consequently, in the centre of the South China block, the Xuefengshan orogeny took place during Middle to Late Triassic. Although still speculative, in the present state of knowledge

of the SCB geology, the far-field effect of the Paleo-Pacific subduction model accounts well for the structural features described in this paper, and the overall tectonic evolution of the Xuefengshan Belt. Based on our structural, petrological and chronological evidence, we propose a new model to discuss the tectonic evolution of the South China block from Early Paleozoic to Early Mesozoic. Since the Yangtze and Cathaysia blocks were amalgamated in Neoproterozoic, the suture zone is located in the South China block as a weak zone. Furthermore, other weak zones can be originated from the subsequent Nanhua rifting. During late Paleozoic, the South China block experienced intense deformation with S- or SE-directed shearing in a compressional setting. In spite that the geodynamic source is still unclear, the orogeny is well preserved by ductile deformation and syn-tectonic metamorphism between 460 and 440 Ma (Fig. 7-3a). After 440 Ma, according to the gravitational readjustment of thickened crust, crustal extension and collapse of the orogen are characterized by regional strike-slip faults and voluminous granites (Fig. 7-3b). The whole South China block was uplifted to land from Late Silurian to Middle Devonian by this orogeny, and the sedimentary record is almost missing with Middle Devonian post-orogenic molasse deposited on the pre-Devonian strata. The intensity of this event decreased as approaching to the western part, indicated by the transition from unconformity to disconformity. In the eras of Late Devonian to Permian, the South China block entered a peaceful stage without large-scale tectonic event (Fig. 7-3c). In Late Permian, at the southeastern margin, the Paleo-pacific plate started to subduct beneath the South China block with ductile shearing in the peripheral regions (Fig. 7-3d). Until Triassic, around 250 Ma, the compressional stress was transported to the interior of the block. In this situation, the weak zone, such as the Chenzhou-Linwu fault, was reactivated and generated top-to-the-NW deformation with folds, thrusts, cleavages and etc. The Xuefengshan Belt was formed during the Early to Late Triassic accordingly.

To summarize, the deformation of the internal part of the South China block is expressed by intracontinental orogeny, which is caused by the far-field effect from the subduction at plate margins. During Early Mesozoic, over 500 km long

intracontinental fold-and-thrust belt was developed from Guangxi, Hunan to Jiangxi, and finally established the architecture of the South China block.

5. Insights for intracontinental orogenic belts

In the past 20 years, numerous intracontinental orogens have been studied by multidisciplinary approaches [Hendrix et al., 1992; Avouac et al., 1993; Choukroune, 1992; Hand and Sandiford, 1999; Sandiford et al., 2001; English and Johnston, 2004; Faure et al., 2009; Charvet et al., 2010 and enclosed references]. In East Asia, several intracontinental belts have been reported, such as the Cenozoic Chinese Tianshan (Tapponnier and Molnar, 1979; Avouac et al., 1993), the Yanshan-Yinshan belt (Davies et al., 1998; Darby et al., 2001), and the Early Paleozoic South China belt (Faure et al., 2009; Charvet et al., 2010; Li et al., 2010). Comparable to the Xuefengshan Belt, high-grade metamorphic rocks of a Cenozoic age are poorly outcropped or even absent in the Cenozoic Tianshan Belt, while the exposed basement rocks are Paleozoic orogenic products overprinted by Cenozoic brittle deformation (Avouac et al., 1993 and reference therein). The Yanshan-Yinshan intracontinental belt, however, demonstrates an Archean unit-involved thin-skinned fold-and-thrust system above a low angle main thrust fault (Davies et al., 1998, 2001; Darby et al., 2001, 2007). In this belt, the Precambrian rocks are often overlaid directly by Jurassic to Cretaceous sedimentation, lacking the entire Paleozoic sequence. The Early Paleozoic South China belt is analogous to the Xuefengshan Belt with a basal decollement, except the exhumation of high-grade metamorphic rocks by extension.

On the contrary, in the Alice Springs and the Pyrenees belts, for example, deep crustal or lithospheric structures are revealed by seismic profiles. They are typical intracontinental belts characterized by thick-skinned tectonics, induced by remarkable crustal displacement or continental subduction [Goleby et al., 1989; Choukroune, 1992]. However, the Xuefengshan Belt is a particular chain with an over 10-km-thick sedimentary cover and a regional high-strain decollement layer but no exposure of high-grade metamorphic rocks. Thus a thin-skinned tectonic evolution is preferred here. Among the intracontinental belts, the Early Paleozoic South China belt and the

Yanshan-Yinshan belt both suggest a thin-skinned structure by basal thrust faulting. In addition, the Jura belt, resulted from the collision between Europe and the Apulian promontory, is also a well established thin-skinned thrust belt with a basal decollement represented by Triassic salt formations. Nevertheless, without detailed seismic data, the deep structure of the Xuefengshan cannot be well constrained, and thereby a thick-skinned model cannot be completely ruled out.

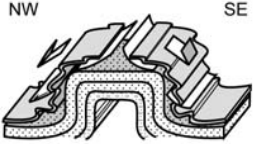
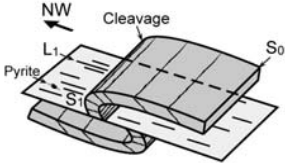
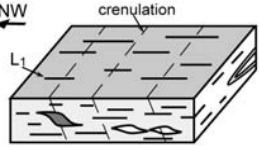
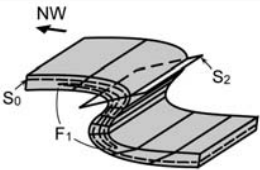
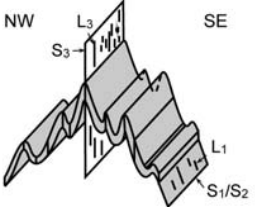
As a regional back-stop boundary for the Xuefengshan Belt, the Chenzhou-Linwu fault played an important role in the Early Mesozoic tectonics. This fault is also considered to be the potential suture zone between the Yangtze block and the Cathaysia block during the Neoproterozoic collision [Wang et al., 2007c].

Furthermore, in intracontinental tectonics, an internal weak zone is the place to localize the deformation induced by the compressional stress developed in response to subduction or collision at plate margins, and thereby triggers an intracontinental deformation. In the Pyrenees orogen, the most intense Cenozoic deformation was accommodated within the pre-orogenic continental rifts basins opened during the Cretaceous [Choukroune, 1992]. The Alice Springs orogen is a reactivated Paleozoic belt superimposed upon the Neoproterozoic-Early Paleozoic Petermann orogen [Hand and Sandiford, 1999; Sandiford et al., 2001]. The Late Paleozoic Tianshan orogen was compressed and uplifted again during the Cenozoic, due to the Indo-Asia collision [Hendrix et al., 1992; Avouac et al., 1993]. Therefore, the weak zone along which an intracontinental belt will develop is a pre-existing crustal weak zone such as a rift, or a regional fault zone formed during an older orogeny, along which the continental crust has been rheologically softened. In our case, we infer that the Early Mesozoic Xuefengshan Belt was an intracontinental belt developed as a result of the reactivation of the Neoproterozoic Chenzhou-Linwu fault.

The geodynamic cause of intracontinental orogens is still a matter of debate. Far-field effects of either remote flat-slab subduction or continental collision are the favored interpretations [e.g. Dickinson and Snyder, 1978; Avouac et al., 1993; English and Johnston, 2004]. Nevertheless, a peripheral compressional stress perpendicular to the orogenic belt is a prerequisite to the formation of an intracontinental orogen, no

matter this push is originated from subduction, collision, or ocean ridge extension.

The Xuefengshan belt was formed in this mechanism, however, without available geophysical data, we cannot integrate the surface architecture with the deep structure, neither can we estimate the amount of the shortening. Nevertheless, we believe that the deep structure will be reveal soon and this intracontinental belt will be, at that time, more understood by the geologists.

Deformation event	Western Outer Zone	Eastern Zone	Deep Metamorphic Unit
D ₁	 <p>Well developed box folds with gravity collapse folds in the vertical limbs. No cleavage.</p>	 <p>S₁, L₁ and F₁ with top-to-the-NW kinematics. Low greenschist facies metamorphism (sericite + chlorite).</p>	 <p>Mylonite with flat-lying S₁ foliation. NW-SE lineation with top-to-the-NW shearing. Greenschist facies metamorphism (biotite+garnet +muscovite).</p>
D ₂	Absent	 <p>S₁ and F₁ reworked by F₂ SE-directed folds with S₂ cleavage.</p>	Absent
D ₃	Absent	 <p>S₁, L₁, S₂ reworked by F₃ folds. Vertical S₃ with L₃ stretching lineation.</p>	

Main Xuefengshan Thrust

Decollement

Fig. 7-1. Polyphase deformation in the Xuefengshan belt.

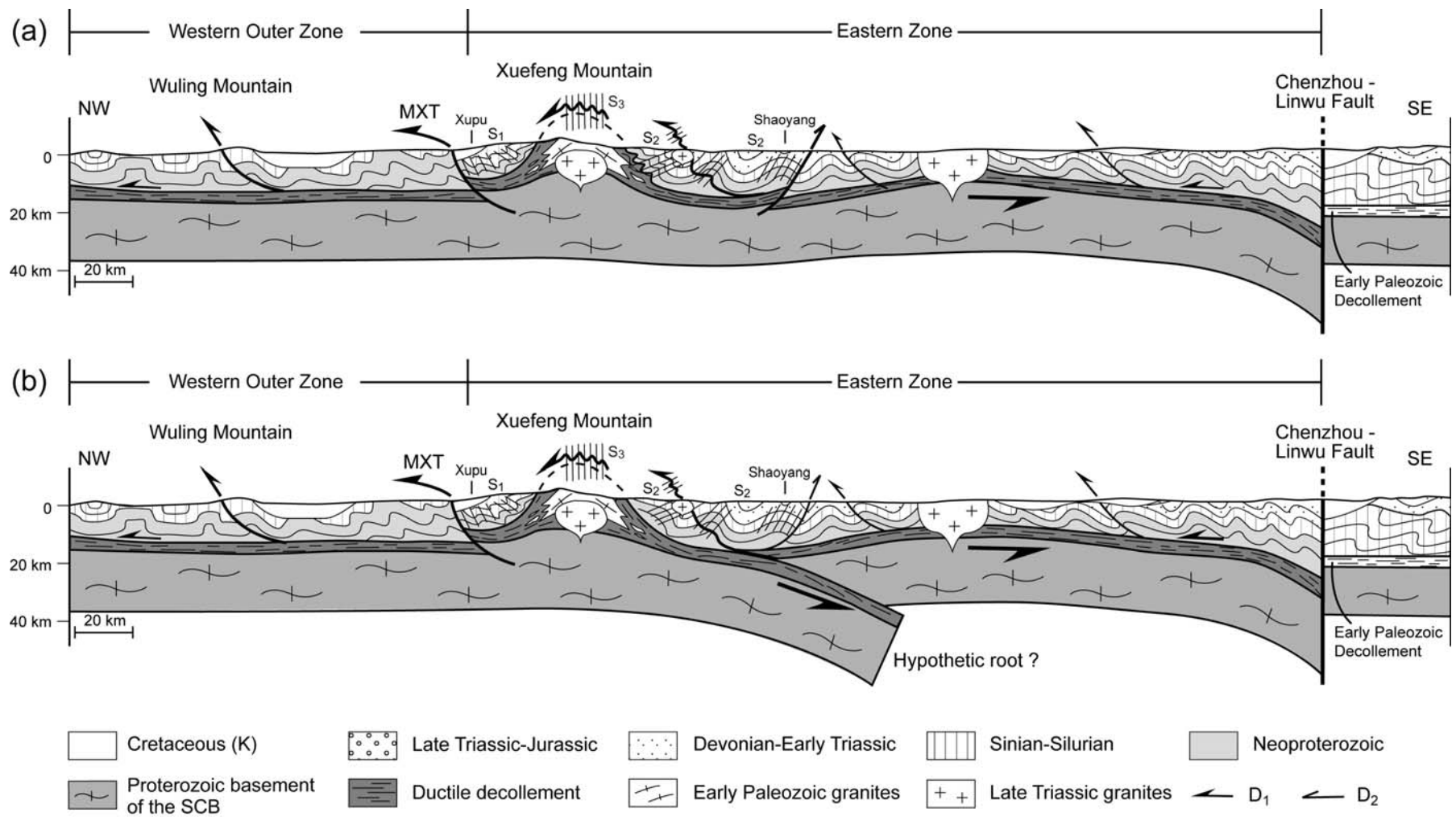


Fig. 7-2. Two possible interpretative bulk cross-sections of the Xuefengshan Belt

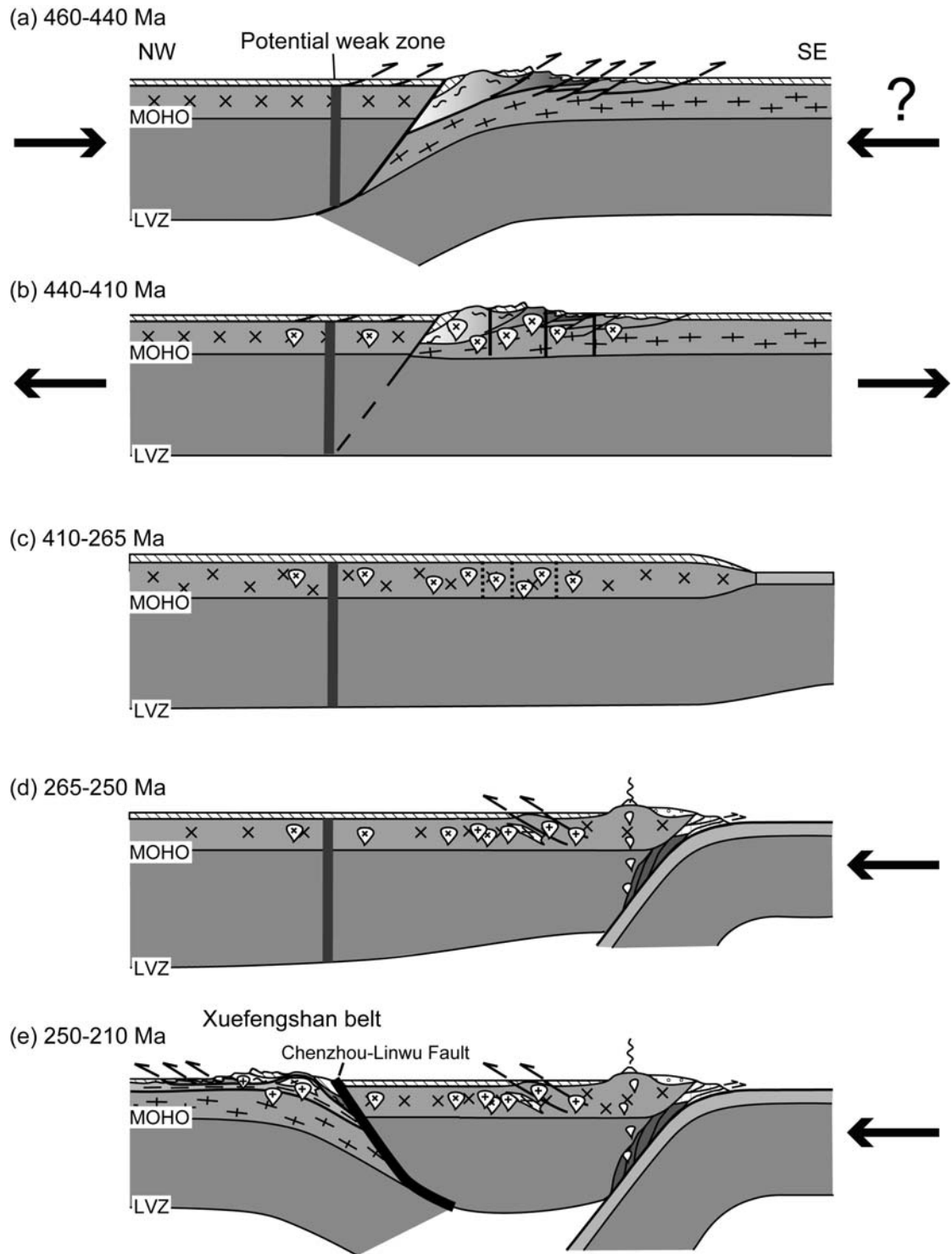


Fig. 7-3. Tectonic evolution of the eastern South China block from Late Early Paleozoic to Early Mesozoic.

Conclusion

In this thesis, the Xuefengshan intracontinental belt is investigated in detail by multidisciplinary methods, and the architecture and tectonic evolution are discussed. The thesis can be divided into two parts. Firstly, on the basis of structural analysis from macro- to micro-scope scale, we establish the geometrical model of the belt. The second part are integrated with zircon SIMS U-Pb dating results, monazite Electron Microprobe U-Th-Pb chronological data, and zircon Hf isotopic data to discuss the timing of the deformation, magmatism and crustal information. Some results are listed below:

1. The strata from the Neoproterozoic to Early Triassic are intensely deformed during the Early Mesozoic Xuefengshan orogeny. Despite the crustal shortening, amphibolite facies metamorphism and large scale magmatism to the east, the Xuefengshan belt is weakly influenced with sparsely distributed granitic intrusions and pre-Devonian E-W trending folds in the south.
2. The Xuefengshan belt can be divided into the Western (Outer) Zone and the Eastern (Inner) Zone, which are separated by the Main Xuefengshan Thrust. The Western Zone is characterized by kilometer-scale box fold with layer-slip and collapse folds in hinges. No penetrative cleavage and metamorphism are developed. In the Eastern Zone, closely spaced cleavages are demonstrated in a fan-like pattern, indicative of a lower part of the orogen. Approaching the east, the intensity of deformation is decreased with the promotion of the structural level. A basal decollement and greenschist facies metamorphic rocks, such as garnet-bearing micaschist, are outcropped in the Eastern Zone. These rocks are interpreted as the upper part of the basement. High grade metamorphic rocks, for instance amphibolite and granulite, are absent in the exposed part of the orogen.
3. The Xuefengshan belt experienced a polyphase deformation during Early Mesozoic. D1 is characterized by a top-to-the-NW ductile shearing and widely spread in the whole belt. NW-SE trending stretching and mineral lineation are developed on the NE-SW striking cleavage planes. D2 corresponds to SE-directed back thrusting and folding, D1 cleavages and folds were refolded by the D2 fold. D3 consists of upright folds with vertical cleavage and lineation, indicating a NW-SE horizontal shortening.
4. Two tectonothermal events are recorded in the Xuefengshan belt, one in Early Paleozoic and the other in Early Mesozoic. Although the Early Paleozoic shortening is weakly developed, the extensional event may cause the 440-410 Ma magmatism in Xuefengshan. Triassic granites, dated between 225 and 215 Ma, were emplaced in the cores of anticlines, leading to the uplift of the basal decollement.

5. According to our Hf isotopic data, both generations of granites have a similar range of $\epsilon_{\text{Hf}}(t)$ between -10 and -1, and 2.4-1.3 Ga Hf model age, representing that the middle-lower crustal material are the source of the granites without any input of mantle derived source.
6. The youngest strata involved in the orogeny is Early Triassic thin-layered limestone, which was deposited from 251 to 245 Ma, and the late-orogenic magmatism ceased at 215 Ma. The timing of the orogeny is thereby inferred to be between 245 and 215 Ma.
7. The Chenzhou-Linwu fault is regarded as the suture zone of the Neoproterozoic orogen which amalgamated the Yangtze block and the Cathaysia block. As the eastern boundary of the Xuefengshan belt, it separates the Xuefengshan Early Mesozoic tectonic domain and the eastern Early Paleozoic domain.
8. As a typical intracontinental orogen, the Xuefengshan belt resulted from the far-field effect of the Triassic NW-directed subduction of the Paleo-Pacific plate beneath the South China block. Compared with the Cenozoic Tianshan, the widespread fold-and-thrust belt of the Xuefengshan belt is attributed to the reactivation of the Chenzhou-Linwu fault.

Yang CHU

Tectonique intracontinentale dans le bloc de Chine du sud. Exemple de la chaîne du Xuefengshan

Les observations détaillées indiquent que la chaîne de Xuefengshan peut être divisée en deux parties, la zone Ouest, caractérisée par des plis-coffrés, et la zone Est à déformation ductile polyphasée. Elles sont séparées par le chevauchement principal vers l'Ouest. Dans la zone Est, les structures dominantes sont des plis à vergence NW associés à des schistosités pénétratives de plan axial et des linéations NW-SE. De l'ouest vers l'est, la schistosité montre un style en éventail. Les roches du socle affleurent seulement autour des plutons triasiques. Les roches de la chaîne de Xuefengshan sont généralement déformées ductilement mais faiblement métamorphosées, toutefois, sous la croûte supérieure, on met en évidence un décollement ductile et synmétamorphe qui accommode les différences de déformation entre les roches sédimentaires et le socle. L'architecture de la chaîne de Xuefengshan résulte de la déformation polyphasée: la première phase (D_1) est caractérisée par un cisaillement vers le nord-ouest. La deuxième phase (D_2) correspond au rétro-plissement vers le SE. La dernière phase (D_3) est un événement de raccourcissement NW-SE avec des plis droits et schistosités verticales. En combinant ces nouveaux résultats structuraux avec les données géochronologiques, la chaîne de Xuefengshan est interprétée comme un orogène intracontinental formé au Trias moyen. Cette chaîne résulte du sous-charriage continental d'une partie du bloc de Chine du Sud, en réponse à l'effet lointain de la subduction de la plaque de Paleo-Pacifique vers le nord-ouest.

Mots clés: Xuefengshan, chaîne intracontinentale, déformation polyphasée, décollement basal, Chine

Intracontinental tectonics in the South China block. Example of the Xuefengshan Belt

Detail field observations indicate that the Xuefengshan Belt can be divided into a Western Outer Zone, characterized by km-scale box-fold structures, and an Eastern Zone, separated from the Western Outer Zone by the Main Xuefengshan Thrust. In the Eastern Zone, NW verging folds coeval with a pervasive slaty cleavage and a NW-SE trending lineation are the dominant structure. From west to east, the dip of the cleavage surface exhibits a fan-like pattern. Basement rocks are sparsely located around some Triassic plutons. The rocks of the Xuefengshan Belt are generally ductilely deformed but weakly metamorphosed, however, below this upper crustal level, a high strain decollement accommodates the difference of deformation between the sedimentary and the basement rocks. The architecture of the Xuefengshan Belt results from polyphase deformation: the first one (D_1) is characterized by a top-to-the-NW shearing. The second one (D_2) corresponds to a back-folding and back-thrusting stage. The last phase (D_3) is a NW-SE shortening event associated with upright folds with vertical axial plane cleavages. Combined with geochronological data, the Xuefengshan Belt is interpreted as an Early Mesozoic intracontinental orogen, which possibly originated from the continental underthrusting to the SE of a piece of the South China block in response to the far-field effect of the northwest directed subduction of the Paleo-Pacific plate.

Key words: Xuefengshan, intracontinental belt, polyphase deformation, basal decollement, far-field effect



Institut des Sciences de la Terre d'Orléans
1A, rue de Férollerie, 45071 ORLÉANS, France
Institut de Géologie et Géophysique, CAS
19, rue Beituchengxi, Chaoyang, 100029 Pékin, Chine

